# Transactions of the ASME


Symposium on Design for and Operating Experience With Outdoor Power Plants . . . . . 671

Flow in Corners of Passages With Noncircular Cross Sections . . . . . *E. R. G. Eckert and T. F. Irvine, Jr.* 709

Laminar Pipe Flow With Injection and Suction Through a Porous Wall . . . . . *S. W. Yuan and A. B. Finkelstein* 719

Radiation Analysis by the Network Method . . . . . *A. K. Oppenheim* 725

Self-Excited Vibrations of Systems With Two Degrees of Freedom . . . . . *Ernst Saljé* 737

A New Method of Evaluating Dynamic Response of Counterflow and Parallel-Flow Heat Exchangers . . . . . *H. M. Paynter and Yasundo Takahashi* 749

The Dynamic Response of Industrial Thermometers in Wells . . . . . *T. C. Linahan* 759

Flow of a Compressible Fluid in a Thin Passage . . . . . *S. K. Grimsell* 765

The Effect of Oil-Column Acoustic Resonance on Hydraulic Valve "Squeal" . . *F. W. Ainsworth* 773

On the Maximum and Minimum Velocities and the Accelerations in Four-Link Mechanisms. . . . . *Ferdinand Freudenstein* 779

Long-Shoe Block Brake With Floating Anchor. . . . . *M. F. Spotts* 789

Determination of Radius of Curvature for Radial and Swinging-Follower Cam Systems . . . . . *Martin Kloomok and R. V. Muffley* 795

Determination of Pressure Angles for Swinging-Follower Cam Systems . . . . . *Martin Kloomok and R. V. Muffley* 803

The Relation Between Grinding Conditions and Thermal Damage in the Workpiece. *R. S. Hahn* 807

Measuring the Thermal Diffusivity of Metals at Elevated Temperatures . . . . . *M. A. El-Hifnî and B. T. Chao* 813

On the Relations Between Various Laboratory Fracture Tests . . . *E. M. Lape and J. D. Lubahn* 823

The Effects of High-Frequency Vibrations in Grinding . . . . . *L. V. Colwell* 837

The Role of Chip Thickness in Grinding . . . . . *G. S. Reichenbach, J. E. Mayer, S. Kalpakcioglu, and M. C. Shaw* 847

Inorganic Grinding Fluids for Titanium Alloys . . . . . *M. C. Shaw and C. T. Yang* 861

Selective Silica Carry-Over in Steam . . . . . *E. E. Coulter, E. A. Pirsh, and E. J. Wagner, Jr.* 869

Demineralized Make-Up for 1250-Psi Installation at East Millinocket Mill of Great Northern Paper Company . . . . . *E. F. Davidson* 875

Power Removal From Boiling Nuclear Reactors . . . . . *P. C. Zmola and R. V. Bailey* 881



TRANSACTIONS OF THE AMERICAN SOCIETY OF MECHANICAL ENGINEERS

VOLUME 78 MAY 1956 NUMBER 4

# Transactions

## of The American Society of Mechanical Engineers

Published on the tenth of every month, except March, June, September, and December

OFFICERS OF THE SOCIETY:

J. W. Barker, *President*

Joseph L. Koss, *Treasurer* — C. E. Davies, *Secretary*

Edgar J. Kates, *Asst. Treasurer*

COMMITTEE ON PUBLICATIONS:

Otto de Lorenzi, *Chairman*

W. E. Reaser — John de S. Coutinho

Kerr Atkinson — B. G. A. Skrotzki

R. A. Cederberg, H. N. Wentzel } *Junior Advisory Members*

George A. Stetson, *Editor* — K. W. Clendinning, *Managing Editor*; J. A. North, *Asst. Managing Editor*

REGIONAL ADVISORY BOARD OF THE PUBLICATIONS COMMITTEE:

Roy L. Parsell—I
A. D. Blake—II
C. C. France—III
Francis C. Smith—IV
H. M. Cather—V
C. R. Earle—VI
M. B. Hogan—VII
Linn Helander—VIII

Published monthly by The American Society of Mechanical Engineers. Publication office at 20th and Northampton Streets, Easton, Pa. The editorial department is located at the headquarters of the Society, 29 West Thirty-Ninth Street, New York 18, N. Y. Cable address, "Dynamic," New York. Price $1.50 a copy, $12.00 annually for Transactions and the *Journal of Applied Mechanics;* to members, $1.00 a copy, $6.00 annually. Add $1.50 for postage to all countries outside the United States, Canada, and Pan American Union. Changes of address must be received at Society headquarters seven weeks before they are to be effective on the mailing list. Please send old as well as new address.... By-Law: The Society shall not be responsible for statements or opinions advanced in papers or... printed in its publications (B13, Par. 4).... Entered as second-class matter March 2, 1928, at the Post Office at Easton, Pa., under the Act of August 24, 1912.... Copyrighted, 1956, by The American Society of Mechanical Engineers. Reprints from this publication may be made on condition that full credit be given the Transactions of the ASME and the author, and that date of publication be stated.

# Symposium on Design for and Operating Experience With Outdoor Power Plants

By J. N. LANDIS,[1] SAN FRANCISCO, CALIF.

## Introduction

ALTHOUGH outdoor power plants have been built for a number of years and technical literature contains many articles on them, it was felt that a carefully prepared group of papers dealing with the design for and operation of outdoor plants would bring out a useful body of information based on the very considerable volume of experience with such plants. A work group consisting of Messrs. Argue, Duffy, Friend, Estcourt, and Landis undertook to organize a symposium. At the outset a review was made of the outstanding articles in the technical literature to single out the more important issues involved, with the thought that papers dealing with these particular issues would be invited. However, as the work group dealt with the problem this approach was abandoned, because it was concluded that asking specific authors to contribute papers on definite subjects would be less likely to bring out a cross-section background of experience. Consequently a number of qualified individuals were invited to present discussions, the only limitation being that the material should fall under the symposium title "Design for and Operating Experience with Outdoor Power Plants." It was hoped that this procedure would bring out the issues as they had developed in the individual experience of the participant or his company.

Participants fell into one group giving longer, somewhat analytical, papers, and another group giving shorter experience papers. Since all papers were prepared ahead of the meeting, even the shorter papers cannot be regarded as being normal "discussion" papers. It was very unfortunate that time did not permit discussion from the floor.

The organizing group weighed the question of whether discussion should be secured from proponents of indoor construction. In order to obviate the charge that the presentation was completely biased and did not permit any discussion by indoor station proponents, it was decided to request two such papers, one from M. K. Drewry, the other from E. C. Gaston.

It was decided to invite a general historical paper, preferably from someone who by having lived through the developmental era of outdoor power plants could give a distilled history of the trend. Mr. Louis Elliott stood out pre-eminently among those considered for this part. Unfortunately, for the symposium, Mr. Elliott was currently in Switzerland and his paper had to be read by Mr. Estcourt, thus depriving Mr. Elliott's very many friends in the audience of the pleasure of hearing him personally review the opening era of outdoor plants which he so strongly championed over a period of many years.

Directly in line with the recognition that the symposium should do something to give the reader some statistical basis for weighing the relative importance of outdoor and indoor construction, Mr. B. G. A. Skrotzki was requested to canvass the utility industry to ascertain the extent of use of indoor and outdoor construction as related to specific major important items of equipment in modern plants. Limitation of time necessitated Mr. Skrotzki's presentation at the meeting being in abbreviated form.

Subsequent to the presentations in the symposium, a systematic analysis of all the papers has been made to draw out a composite of all the views expressed. Credit goes to Messrs. V. F. Estcourt and B. V. Marcellus for exhaustive study of the papers to single out and collate the material from which the digest of papers constituting the "Summary" was made.

# Outdoor-Type Steam-Electric Stations Early Types and Development

By LOUIS ELLIOTT,[2] NEW YORK, N. Y.

IT is pleasant to have this opportunity of sending a greeting from Switzerland to my friends and fellow members of THE AMERICAN SOCIETY OF MECHANICAL ENGINEERS.

Switzerland began its co-operative existence in 1296 by a pact of mutual loyalty and aid entered into by the rugged mountaineers of three little cantons. Since that medieval time, the sturdy Swiss have built a firm and fine democracy, tiny though it be in comparison with our United States.

Like the Swiss federation, our electric-power industry in America has grown by boldness and hard work. The industry has benefited by ingenuity, by keen analysis, and by the co-operation of engineers, power companies, and manufacturers. No new development has sprung from one man alone or one company alone. The magnitude, the efficiency, and the excellent performance of our power system are the result of accretion from many sources.

The engineering company by which I have been employed for 40 years, early in electric-utility history became prominent in

[1] Vice-President, Bechtel Corporation. Mem. ASME.

[2] Consulting Power Engineer, Ebasco Services Incorporated. Fellow ASME.

Contributed by the Power Division and presented at a joint session of the Power, Hydraulic, and Fuels Divisions, at the Annual Meeting, New York, N. Y., November 29–December 4, 1953, of THE AMERICAN SOCIETY OF MECHANICAL ENGINEERS.

NOTE: Statements and opinions advanced in papers are to be understood as individual expressions of their authors and not those of the Society. Manuscript received at ASME Headquarters December 2, 1953.

promoting the development of so-called "outdoor" designs for substations, switchyards, and power plants. Outdoor is a convenient and nowadays a conventional term for denoting plants in which one or more important equipment units are installed without protection from the weather. My remarks apply primarily to thermal stations, but hydroelectric plants also have their history of outdoor installation.

### First Outdoor Installation

In 1910 my company designed and built the first 110-kv substation in which the transformers and high-voltage switches were not completely enclosed within a building. In 1912 it engineered the first outdoor hydroelectric plant, preceding the first such steam plant by 17 years. The company has now designed and built 25 outdoor hydroelectric plants for nine of its clients—six of those utility companies have authorized a second outdoor plant. One company is now operating nine of them and is planning to build four additional. There are more than 600 plant-years of successful operation of outdoor hydroelectric plants on the record.

The reduction and resulting modification of structures serving a steam-power station had its beginning years ago. The movement was encouraged by the study of industrial installations, including oil refineries. Boiler shelters in the tropics have for many years consisted of a simple roof, frequently of corrugated steel.

### Outdoor Turbines and Boilers

About 1932 utility companies in New York City worked on the design of a large steam installation, placing the turbines on an open deck with gantry crane. The design was apparently considered too radical for adoption. A little later, General Electric Company installed a 6000-kw outdoor-type steam turbine at Schenectady, as an element of a steam-mercury plant. During the 1930's, at Glendale and Burbank—two of the smaller cities in southern California—steam stations were constructed with the turbines on an open deck, provided with partial housing, but with the boilers quite well protected.

In 1930 the power company at Phoenix, Arizona, built a station with boiler-room walls somewhat skeletonized. The Utah company, in 1937, constructed an 18,750-kw stoker-fired plant near Provo, with important outdoor features. About the same time, a number of utility boilers were installed outdoors, among them one in Arizona and one in Ohio. This partial list of early installations in America is intended merely to sketch the development up to about 1940.

From that year there has been a rapid increase in number and size of outdoor installations of various types. The outdoor plants designed and built by my company, and now in course of design and construction, through the years 1936 to 1953, include 164 steam generators and 155 turbine-generators, in 70 stations; the aggregate capability is approximately 10,100,000 kw. The largest boiler produces over 1,000,000 lb of steam per hour, and the largest turbine unit is rated at something over 150,000 kw. As to location, the range has been from the Gulf of Mexico on the south to Montana and New York on the north, with additional installations in other countries. If I may be permitted to single out one engineer, I wish to say that Paul Gourdon has been foremost in developing the designs, in general and in detail, for the installations mentioned.

### Developing Outdoor Designs

At the beginning of the outdoor development, the only available designs for good-sized turbines, boilers, and most of the other major equipment, were primarily for installation and operation within a building. The introduction of outdoor plants called for corresponding modifications by makers of equipment, and plant designing engineers have worked continuously with the manufacturers' engineers in developing the elements of outdoor design and installation. The manufacturers have been most co-operative.

I recall an incident, humorous in retrospect, relating to the introduction of high-voltage equipment suitable for service outdoors; it may illustrate the problems of manufacturers in modifying, for new conditions, the designs of successful equipment. In 1913 several members of our company, myself included, made a visit to Schenectady, hoping to persuade the manufacturer to supply 110-kv outdoor-type transformers and breakers, for service on a new system in Utah. We consulted C. P. Steinmetz, and he expressed the opinion that the materials and construction entering into high-voltage transformers and breakers were unsuitable for exposure to temperatures from minus 40 to plus 110 F and to dust, rain, and snow. However, certain others of the maker's engineers gave encouragement, and the Utah step-up and step-down stations then adopted outdoor construction. Steinmetz was a grand man—pioneer, scientist, mathematician, and engineer, but no one can be infallible. As the saying goes, even Jove nods occasionally.

Similarly, the installation outdoors of large boilers and turbines has run the gauntlet of ridicule, doubt, criticism, and gradual acceptance, until the volume of such installations, the successful performance, and the substantial economy in investment have commanded approval. I remember that, in years past, in the meetings of utility-industry committees, radical new ideas have more than once encountered a tolerant pity from the conservatives.

No engineer advocates universal utilization of the outdoor principle, or of any one particular plan or design. However, outdoor transformers and high-voltage switching equipment have become almost universal. That ultimate state is not here predicted for steam plants, but as planning for new plants is initiated nowadays, outdoor features are becoming more frequent.

### Reasons for Outdoor Design

There are two main reasons for adopting outdoor designs, the saving accomplished in the first cost and, in most cases, the reduction in the time required for construction. In an outdoor design, with foundation slab at, or near, ground level, the slab can often be poured shortly after the construction force is organized, permitting the erection of boiler steel to start soon thereafter and the turbine-pedestal construction to follow shortly. In operation, there are certain advantages inherent in the outdoor principle, especially when air temperatures are high. The heat from boiler and turbine is not "boxed in." It has been my experience that many southern operators strongly prefer the unhoused type.

There are of course certain disadvantages accruing to the outdoor type, especially under conditions of extreme low temperatures and during storms. Maintenance of equipment may cost somewhat more and take a little longer than with a fully housed plant. Maintenance cost of buildings is of course reduced in the outdoor installation. The disadvantages of the outdoor design, which are indeed much less important than anticipated, are for most situations much overweighed by the saving in investment.

I do not wish to magnify the importance of the reduction and simplification in structures, which indeed constitute a devolution rather than an evolution. The design represents one of the many advances in the art that have made the power industry what it is. Each engineer will of course study his individual conditions, make comparison of investment and of operating and maintenance costs, for various designs involving "outdoorness" as well as other features, and reach his decision as to the form of plant best suiting his situation. He will take into account the economic and all other elements.

### Philosophy of the Outdoor Plant

The low over-all plant-investment costs prevailing in the "good old days," when the outdoor economies were first realized, may never be seen again. Recalling them serves only to emphasize the difficult problems now confronting executives and engineers, who must contend with the radically higher present-day cost levels. Today we should exercise close economy in structures and equipment—still obtaining reasonable reliability and good economy; we should select as large units as the estimated loads over a future period make permissible; we should adopt steam conditions and cycle at least as good as the economics justify, over the foreseeable future; we should supply a minimum of spare equipment—"working our investment hard," as an old operating executive expressed it; we should sacrifice unwarranted refinements.

Outdoor plants possess dignity; they look what they are—the modern term is "functional"; they satisfy, in so far as is practicable, the commercial and engineering requirements by their moderate cost and their reliability and economy in operation; and they contribute to the success of the utility industry and its companies. Finally, these well-planned and well-wrought creations will give to ourselves, the engineers, the personal satisfaction of work well done.

# Economic Factors in Design of Power-Station Enclosures

By F. W. ARGUE,[1] BOSTON, MASS.

POWER plants are enclosed for three major purposes: (1) As protection or comfort for operating and maintenance personnel; (2) as protection for equipment; (3) to preserve the good will of neighbors. This third reason is obviously not influenced directly by economic considerations and thus will not be discussed further. Decision regarding the first two reasons, however, may well be affected by their economic justification, and it is the purpose of this paper to stimulate interest in developing useful data for evaluating the many pertinent factors.

### Acceptance of Outdoor Design

Outdoor construction, while employed by industrial plants for many years, did not receive widespread acceptance by power-station operators until instrumentation and automatic control had reached the stage where routine operations could be performed from a remote point. By grouping controls in a relatively small room which could be conditioned for operator comfort at moderate expense, the necessity for enclosing the balance of the plant for weather protection of the operators was minimized. There remained the requirement that equipment must be protected while in service and, more particularly, during maintenance periods. It was recognized, also, that maintenance personnel required protection from the elements if the work was to be performed expeditiously. Various methods have been employed to meet these requirements, most of which have been adequately publicized.

It is unfortunate that controversy has developed regarding the feasibility of outdoor construction and opinions have been formed without adequate factual basis. At one extreme, there is doubt that outdoor stations are practical for other than the most favorable climate; at the other, there is the feeling that the maximum reliability, efficiency, and operating convenience can be combined with minimum first cost simply by omitting enclosures. What is needed, of course, is an engineering approach to the problem with the substitution of facts or reasonable probabilities for opinions.

### The Engineering Approach

In developing an engineering approach, the problem confronting the designer in evaluating types and extent of enclosures is similar to that of other station components: "What does it cost and what do you get for your money?"

Before attempting to estimate installation cost, it is necessary to set forth the design criterion and, as a basis for illustration, three criteria have been assumed:

*Outdoor Construction.* There should be no enclosures except for the space where the operators spend the major part of their time.

*Minimum Enclosed Construction.* The major components must be enclosed for equipment protection and facility of maintenance. Provision for operator comfort should only be extended to the space where the operators spend the major part of their time. The purpose of establishing this criterion was to determine what the cost of enclosure would be if no more provision for operator comfort were made than in outdoor plants.

*Conventional Enclosure.* The major components must be enclosed and all enclosed space should be treated as working space, suitably heated and ventilated for operator comfort.

A further subdivision of the third criterion has been made to take into account complete housing for a mild climate where uninsulated walls would be satisfactory and for a more severe climate requiring insulated wall construction.

### Basic Plants for Comparison

With these criteria, estimates of construction cost have been made for two designs of stations, one an arrangement made specifically for an enclosed station and the other, for an outdoor station. It is believed that use of the two designs provides a more equitable basis of comparison because the equipment arrangement is not necessarily the same in both. It also provides a source of unit cost data for the various additions and deductions which are less subject to controversy than estimates, no matter how carefully the latter may be prepared. For example, if the completed costs of an enclosed station show $2 per square ft for wall construction, the fairness of using this figure as the estimate for adding walls to an outdoor design can scarcely be questioned.

*Indoor Plant Designs.* Station 1 was designed and built as a totally enclosed plant with the exception of fans, dust collectors, and chimneys, which are external. It is located in an area of mild climate and thus has uninsulated walls. Its capacity is nominally rated at 200,000 kw and it is coal-fired. Features of lighting, ventilation, and other building services are more or less conventional for completely enclosed stations. It does not have completely centralized control, and control centers are not separated from other working areas by partitions.

[1] Assistant Chief Power Engineer, Stone & Webster Engineering Corporation. Mem. ASME.

The estimated costs for outdoor construction of Station 1 were based upon the same equipment arrangement, but with housing omitted. Weather protection for mechanical and electrical equipment was added, where necessary, and a gantry-type crane substituted for the indoor bridge crane which, in the original design, was supported on conventional dual-purpose steel. An allowance was made for a control house similar to that provided in a contemporary design of outdoor station. No allowance was made, however, for mechanical and electrical costs required for centralized controls.

For so-called minimum enclosure, as the concept was not to provide for operator comfort, lighting and other building services were limited to those required for equipment protection and operator safety. A control room, partitioned off and air conditioned, was considered necessary but the size was only sufficient for the most essential and frequently used controls. It also was believed that omission of weather protection on equipment required an insulated roof in order to provide equivalent protection.

For mild-climate conventional enclosure, the actual station design was used.

For severe-climate conventional enclosure, the actual station design was used except that an allowance was included for insulated panel wall construction.

*Outdoor Design.* Station 2 was designed and built as a completely outdoor plant in a mild climate, of 250,000-kw nominal capacity, oil and gas-fired. Estimates for the three types of enclosure were treated similarly to Station 1, except that, as Station 2 employs centralized control, the control room was included in each case.

As the detailed estimates are too voluminous to be intelligible in this brief presentation, bar graphs have been prepared of the incremental differences. In each case, the outdoor construction cost is represented by the zero line.

## Comparative Costs

Fig. 1 is a comparison for Station 1 of the cost differences broken down into structural, building services, electrical equipment, and mechanical equipment. As would be expected, the additional costs of structural and building-service features are compensated for, to some extent, by decreased electrical and mechanical costs. The significant differences between the various types is in the building-service account, where heating, ventilating, and similar requirements increase the costs of conventionally enclosed station designs by a substantial amount.

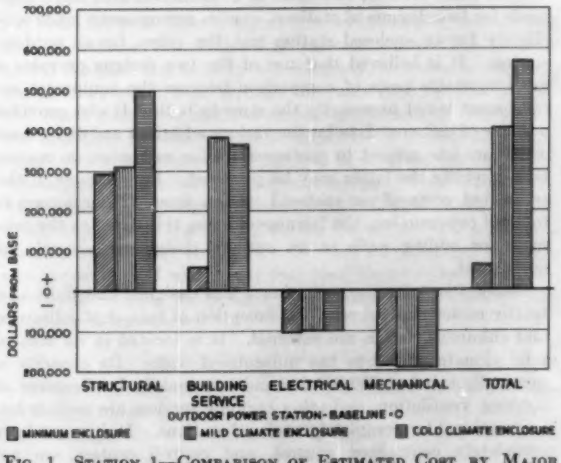


Fig. 1 Station 1—Comparison of Estimated Cost by Major Accounts for Outdoor and Enclosed Power Stations

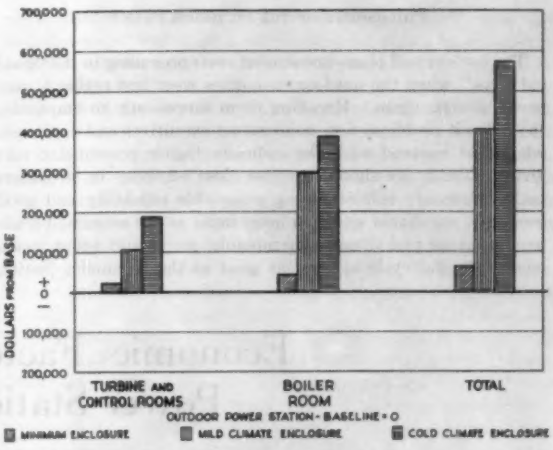


Fig. 2 Station 1—Comparison of Estimated Cost by Sections of Plant—Outdoor and Enclosed Power Stations

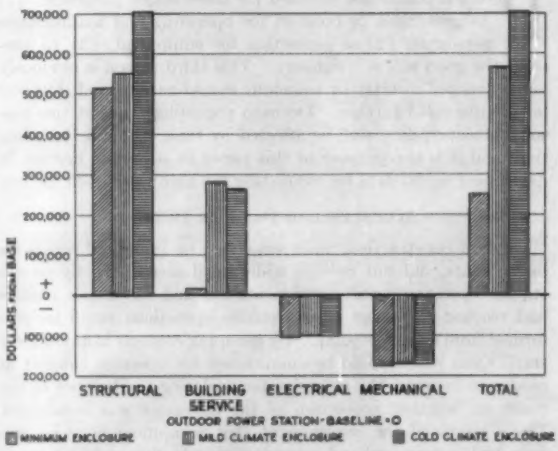


Fig. 3 Station 2—Comparison of Estimated Cost by Major Accounts for Outdoor and Enclosed Power Stations

Fig. 2 is a comparison for Station 1 separated into turbine room (including auxiliary and control sections) and boiler room. It is evident that, in this example at least, the major cost differences between open and enclosed types lie in the boiler room, although it must be recognized that, with the usual disposition of auxiliary equipment, the division between departments has to be somewhat arbitrary.

Fig. 3 is a comparison for Station 2, broken down into the same accounts as in Fig. 1. Because this basic design was for outdoor construction where it is usually economically feasible to provide more "elbow room," the change in structural costs is higher than for Station 1.

Fig. 4 is a breakdown of estimates for Station 2 by sections of the plant. This differs from Station 1 to the extent that an auxiliary bay and control house are separately identifiable. Here again, the major difference is in the boiler room.

Cost differences are frequently expressed as a percentage of the total. Fig. 5 is prepared on this basis, using 100 per cent cost of outdoor plant as the base line. It is the author's opinion that percentages, while not actually misleading, fail to express the full significance of cost differences, especially in the case of high-ca-

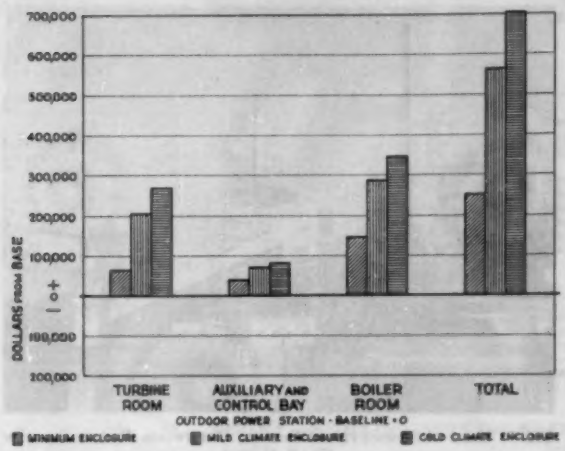


FIG. 4 STATION 2—COMPARISON OF ESTIMATED COST BY SECTIONS OF PLANT FOR OUTDOOR AND ENCLOSED POWER STATIONS

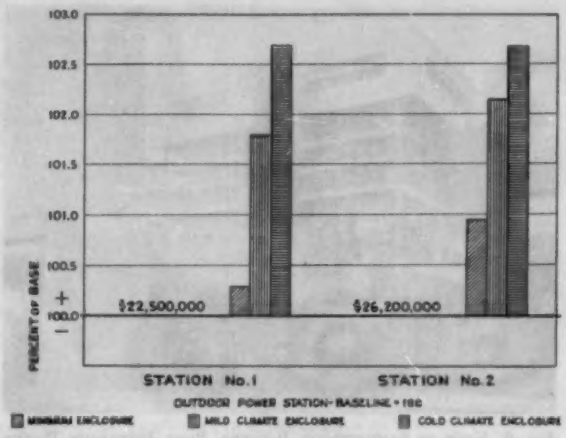


FIG. 5 STATIONS 1 AND 2—PERCENTAGE COMPARISON OF ESTIMATED COST FOR OUTDOOR AND ENCLOSED POWER STATIONS

pacity plants. The total estimated costs shown are for the portion of plant and equipment affected by building considerations. Thus switchyard, external fuel handling, and similar components are not included.

It should be pointed out also that, in each case, enclosures were strictly functional, and relied for pleasing appearance on well-arranged masses and outlines. No special features which might affect costs were provided for architecturally esthetic effects. Obviously, masonry walls, tiled interiors, and similar treatment would add greatly to the cost of enclosures and thus increase the first-cost advantage of outdoor construction.

Exception may be taken to the validity of the comparison on the grounds that the alternative plans may not represent the most desirable designs for the stated conditions. The estimates were prepared, however, by as nearly a factual method as could be devised starting from completed designs for which revised estimates based on expenditures and commitments were available.

### RESULTS OF STUDY

It is believed that, by presenting two cases, one of which tends to favor enclosed construction and the other outdoor, the cost differences, while not defined with absolute accuracy, are sufficiently bracketed for evaluation purposes.

It is apparent from the comparisons that the degree of operator comfort provided in the infrequently used portions of the station has a significant effect on the cost of enclosures. There is, in fact, a remarkably small difference between the so-called minimum enclosure design and the outdoor station. The practicability of the minimum enclosure design would depend on climatic conditions. For areas of limited precipitation and high average temperatures, the outdoor plant would have definite advantages from a personnel-comfort standpoint. With greater precipitation and lower temperatures, this advantage conceivably could be reversed.

It also appears that greater savings in initial cost can be made by having the boilers out of doors than other plant components.

No attempt is made to draw conclusions from these comparisons. Obviously, they only illustrate one phase of the problem, and for an answer to the question, "What do you get for your money?" we must utilize the data accumulated by actual operating experience with various types of plants. From these data, the effect of enclosure on reliability, availability, and maintenance expense can be determined. It is hoped that operators of outdoor and semioutdoor stations will continue to report their experiences so that eventually we can get a more accurate measure of the importance of many of the factors which are now regarded as intangible.

# Cost Data, Design Progress, and Experience Through Six Major Installations

BY E. C. DUFFY,[4] MINEOLA, N. Y.

SINCE the inception of the Long Island Lighting Company's first semioutdoor steam-generating unit at Port Jefferson in 1946, the trend of design of its power stations has been increasing toward more outdoor construction. This type of construction was initiated with full consideration given to prevailing climatic conditions, the problems of operation and maintenance that would be posed, effect on performance of personnel, and savings that would be realized. The trend has been continued and expanded only after carefully reviewing experience gained at each step and studying the merits of furthering outdoor designs. The early experiences not only demonstrated that a saving of approximately $4 per kw would be realized, but that greater personnel comfort would be gained 8 to 10 months per year through elimination of costly enclosures and at no sacrifice in the costs and reliability of operation.

### SEMIOUTDOOR BOILERS

The earlier power stations in the system had employed the

[4] Vice-President, Long Island Lighting Company. Mem. ASME.

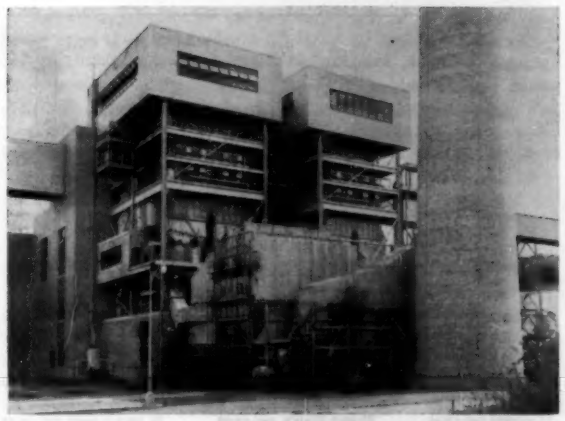

FIG. 6 VIEW OF SEMIOUTDOOR BOILERS, PORT JEFFERSON POWER STATION, UNITS 1 AND 2

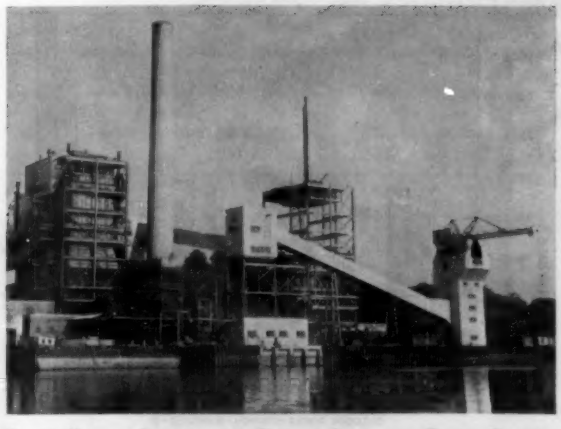

FIG. 7 VIEW OF SEMIOUTDOOR BOILER, GLENWOOD POWER STATION NO. 3, UNIT 4

conventional boiler and turbine-room housings of brick construction. Two 40/44-mw units at Port Jefferson Power Station, which were placed in operation in 1948 and 1950, were the first units to depart radically from this type of construction.

The boilers of these units are of the semioutdoor design, which set the pattern of boiler enclosure for subsequent units. Fig. 6 illustrates the extent of enclosures at Port Jefferson. Corrugated transite siding and its supporting steel girt framing attached to the boiler columns are provided around the boiler at the drum elevation and around the rear and sides of the furnace at the burner level. Brick walls at ground elevation enclose the bottom furnace area and the forced-draft fans. The front of the boiler faces the brick wall-enclosed coal bunkers and coal-tripper room. Air preheaters, gas breeching, mechanical and electrical dust collectors, and induced-draft fans are outdoors. Portions of the hot-air duct work and soot-blower piping are outdoors. Outdoor duct work and equipment in the duct system are weatherproofed. In addition, all outdoor instrument and control air lines are grouped and wrapped with electric-resistance heating wire and insulated and weatherproofed. All outdoor water lines are similarly grouped with a steam tracer line. Outdoor air-operated equipment such as soot-blower heads and fan damper and control drives are enclosed in flat transite housings and provided with strip heaters.

Three similar 90/99-mw units at Glenwood and Far Rockaway Power Stations also employ semioutdoor boiler design. The first of these, Glenwood Power Station No. 3, Unit 4, was placed in operation in November, 1952, a second, Unit 4 at Far Rockaway Power Station No. 2, placed in operation in November, 1953, and the third, Unit 5 at Glenwood, is scheduled for late 1954 operation.

Fig. 7 illustrates the typical boiler enclosure of the semioutdoor boilers at the three 90/99-mw installations. Although the scope of boiler enclosure is the same as at Port Jefferson, the actual boiler area enclosed is somewhat greater owing to the larger boiler size, and to the difference in design of unit. Whereas the boiler drums at Port Jefferson are located near the rear of the boiler, and therefore necessitate a complete enclosure around the boiler-drum elevation, the drum of the 90/99-mw units is located at the front of the boiler and thus reduces the extent of enclosure at the drum level. On the other hand, the amount of siding around the burner elevations of the 90/99-mw units is considerably greater than that at Port Jefferson, because two

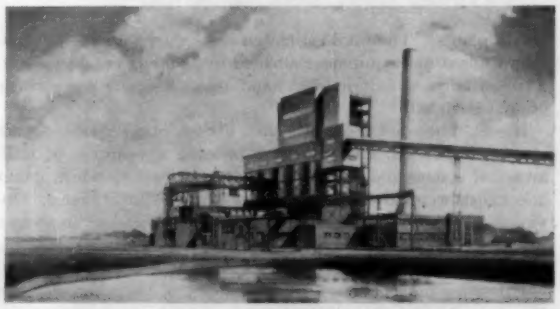

FIG. 8 SKETCH OF EDWARD F. BARRETT POWER STATION, UNIT 1

levels of burners are required for the larger steam-generating units, as opposed to one level at Port Jefferson.

Outdoor breeching, air ducts, mechanical and electrical dust collectors, induced-draft fans, and piping are weatherproofed similarly to those at Port Jefferson. In order to conserve valuable enclosed power-plant space, the main steam, reheat, crossover, and boiler feed lines are run partially outdoors and are insulated with an additional $^1/_2$ in. of insulation and weatherproofed with asphalt-saturated asbestos felt and plastic asphaltic coating.

Experiences at Port Jefferson indicated that the costly electric heating of outdoor instrument and control air lines could be eliminated by running these lines close to the boiler casing where possible and heavily insulating the lines where it is necessary that they be located away from the boiler. This decision was augmented by the installation of an air drier in the instrument air lines at all units subsequent to initial operation at Port Jefferson. Electric operated and controlled soot blowers to be installed at Glenwood Station, Unit 5, will obviate the necessity for soot-blower covers and electric heaters.

The Edward F. Barrett Power Station, Unit 1, a 156-mw unit which is scheduled for initial operation in 1956, will employ a further reduced scope of boiler enclosure. This unit is illustrated by the sketch shown in Fig. 8. Experience at both Port Jefferson and at Glenwood indicates that a burner-belt enclosure is not necessary and that elimination of the enclosure around the forced-draft fans will reduce noise within the power-station building. Furthermore, grouping of the main steam and reheater outlet headers at the front of the boiler has reduced the extent of

TABLE 1 ESTIMATED REDUCTION IN CAPITAL COSTS WITH SEMIOUTDOOR BOILER DESIGN

| Power station | Port Jefferson, Units 1 and 2 | | Glenwood No. 3, Unit 4 Far Rockaway No. 2, Unit 4 | | Glenwood No. 3, Unit 5 | | Edward F. Barrett, Unit 1 | |
|---|---|---|---|---|---|---|---|---|
| Unit rating | 40 mw | | 90 mw | | 90 mw | | 156 mw | |
| Initial operation | 1948 and 1950 | | 1952 and 1953 | | 1954 | | 1956 | |
| | Semioutdoor | Indoor | Semioutdoor | Indoor | Semioutdoor | Indoor | Semioutdoor | Indoor |
| Substructure | $ 68,000 | $ 88,000 | $150,000 | $175,000 | $150,000 | $175,000 | $237,000 | $ 207,000 |
| Structural and miscellaneous steel | 70,000 | 141,000 | 161,000 | 242,000 | 161,000 | 242,000 | 255,000 | 355,000 |
| Corrugated siding and girts | 15,000 | ... | 40,000 | ... | 40,000 | ... | 88,000 | ... |
| Brick walls | 13,000 | 72,000 | 14,000 | 106,000 | 14,000 | 106,000 | 6,000 | 187,000 |
| Floors (differential) | ... | 3,000 | ... | 4,500 | ... | 4,500 | ... | ... |
| Doors and windows | 10,000 | 28,000 | 12,000 | 30,000 | 12,000 | 30,000 | 8,000 | 34,000 |
| Roof | 5,000 | 9,000 | 8,000 | 12,000 | 11,000 | 12,000 | 8,000 | 16,000 |
| Painting and finishing | 14,000 | 19,000 | 18,000 | 23,000 | 18,000 | 23,000 | 21,000 | 27,000 |
| Heating and ventilating | 4,000 | 8,000 | 5,500 | 8,500 | 5,500 | 8,500 | 2,000 | 10,000 |
| Weatherproofing piping and duct work | 3,000 | ... | 5,000 | ... | 5,000 | ... | 5,000 | ... |
| Flashing between boiler and concrete floors | 2,000 | ... | 5,000 | ... | 5,000 | ... | 2,000 | ... |
| Soot-blower covers and antifreeze protection | 21,000 | ... | 10,000 | ... | ... | ... | ... | ... |
| Weatherproofing FD fans and motors | ... | ... | ... | ... | ... | ... | 20,000 | ... |
| | $225,000 | $368,000 | $428,500 | $601,000 | $421,500 | $601,000 | $652,000 | $ 896,500 |
| Omissions, contingencies, and overheads—25% | $ 56,200 | $ 92,000 | $107,100 | $150,200 | $105,400 | $150,200 | $163,000 | $ 224,100 |
| Total costs | $281,200 | $460,000 | $535,600 | $751,200 | $526,900 | $751,200 | $815,000 | $1,120,600 |
| Net savings per unit | $178,800 | ... | $215,600 | ... | $224,300 | ... | $305,600 | ... |

TABLE 2 ESTIMATED COSTS FOR WEATHERPROOFING SEMIOUTDOOR BOILERS

| Power station | Port Jefferson Units 1 and 2 | Glenwood No. 3, Unit 4 Far Rockaway No. 2, Unit 4 | Glenwood No. 3, Unit 5 | Edward F. Barrett, Unit 1 |
|---|---|---|---|---|
| Unit rating, mw | 40 | 90 | 90 | 156 |
| Year of initial operation | 1948 and 1950 | 1952 and 1953 | 1954 | 1956 |
| Corrugated asbestos siding and girt steel | $15,000 | $ 40,000 | $ 40,000 | $ 88,000 |
| Brick walls | 13,000 | 14,000 | 14,000 | 6,000 |
| Concrete floors required for partial enclosures | (−) 3,000 | (−) 4,500 | (−) 4,500 | ... |
| Roof | 5,000 | 8,000 | 11,000 | 8,000 |
| Doors and windows | 10,000 | 12,000 | 12,000 | 8,000 |
| Flashing between boiler and concrete floors | 2,000 | 5,000 | 5,000 | 2,000 |
| Weatherproofing ducts and piping | 3,000 | 5,000 | 5,000 | 5,000 |
| Soot-blower covers and antifreeze heating | 21,000 | 10,000 | ... | ... |
| Weatherproofing FD fan motors and FD fan inlet boxes | ... | ... | ... | 20,000 |
| | $66,000 | $ 89,500 | $ 82,500 | $137,000 |
| Omissions, contingencies, and overheads—25% | 16,500 | 22,400 | 20,600 | 34,200 |
| Total cost per unit | $82,500 | $111,900 | $103,100 | $171,200 |

the boiler drum-level enclosure. This arrangement has also made it possible to run main steam, crossover, and reheat piping in an indoor pipe chase between the front boiler platforms and the coal silos. Weatherproofing and antifreeze protection of duct work and equipment will be similar to that employed for Unit 5 at Glenwood.

A detailed comparison of the capital savings effected through adoption of progressive stages of semioutdoor boiler design is shown in Table 1. This comparison is based on the assumption that an indoor boiler enclosure would be comprised of a brick housing having a separate steel structure outside of the boiler columns, completely enclosing the sides and rear of the boiler, soot blowers, forced-draft fans, air preheaters, and hot-air duct work. The breeching and associated equipment, however, are assumed to remain outdoors, as enclosing this equipment either would involve a large superfluous structure or would involve a complete redesign of the power station, both of which would cloud the issue at hand. It is felt that the indoor arrangement selected most closely approaches the conventional indoor boiler room at a single-boiler single-turbine power plant.

It is to be noted that future labor and material-cost increases have not been shown for Glenwood Power Station No. 3, Unit 5 or Edward F. Barrett Power Station as these are not known accurately at this time. Furthermore, it is felt that the increased savings gained through larger-sized units and progressive changes in outdoor design could be magnified if predicted-cost increases were applied.

Costs for weatherproofing of outdoor equipment, shown in Table 2, are largely differential costs over those that would apply if the boiler had been indoors. Therefore total costs for weatherproofing of gas breeching, dust collectors, and so on, which would be outdoors in either case, were not included.

### Outdoor Turbine-Generators

Turbine-generator Unit 4 at Glenwood Station, Fig. 9, was the first outdoor unit to be placed in operation in the northeastern area of the United States. All subsequent units embody outdoor turbine-generators having essentially the same general weatherproofing provisions as those used for this unit.

Walk-in lighted and ventilated enclosures, furnished by the turbine-generator manufacturer, comprise the weatherproofing over the governor end of the turbine and the exciter. In addition, a weatherproof housing is provided over the turning gear. A turbine start-up panel board and valves for gland sealing and leak-off control are located in the governor-end enclosure and are included in the costs shown in Tables 3 and 4.

The turbine deck is pitched to afford complete drainage in all areas. In addition, a special gutter is provided beneath the joint between the turbine-generator pedestal and the turbine deck. Turbine-deck snow-melting systems were provided for Glenwood Unit 4 and Far Rockaway Unit 4 but have been eliminated at the later installations, operating experience having proved their usefulness to be very limited.

Capital savings gained through adoption of the outdoor turbine-generator design are shown in Table 3. This comparison is based on the assumption that an indoor turbine room would be constructed similar to that at Port Jefferson Power Station which was comprised of a high turbine room of outside brick-wall construction with inside walls of glazed tile, Fig. 10. While the outdoor gantry crane is more costly than the indoor bridge crane the additional structural steel required to support the bridge crane reduces the differential.

### Other Outdoor Construction

In addition to the outdoor boiler and turbine-generator design

TABLE 3 ESTIMATED REDUCTION IN CAPITAL COSTS WITH OUTDOOR TURBINE-GENERATOR DESIGN

| Power station | Glenwood No. 3, Unit 4 and Far Rockaway No. 2, Unit 4 | | Glenwood No. 3, Unit 5 | | Edward F. Barrett, Unit 1 | |
|---|---|---|---|---|---|---|
| Unit rating | 90 mw | | 90 mw | | 156 mw | |
| Initial operation | 1952–1953 | | 1954 | | 1956 | |
| | Outdoor | Indoor | Outdoor | Indoor | Outdoor | Indoor |
| Structural and miscellaneous steel | ... | $ 40,000 | ... | $ 40,000 | ... | $ 70,000 |
| Roof, drains, flashing | $ 1,000 | 30,000 | $ 1,000 | 30,000 | $ 2,000 | 47,000 |
| Brick, glazed tile walls, including windows | ... | 80,000 | ... | 80,000 | ... | 144,000 |
| Heating and ventilating | ... | 15,000 | ... | 15,000 | ... | 25,000 |
| Lighting | 3,000 | 5,000 | 3,000 | 5,000 | 4,000 | 6,500 |
| Painting | 8,000 | 13,000 | 8,000 | 13,000 | 10,000 | 16,000 |
| Walk-in enclosures over turbine head end and exciter | 18,500 | ... | 18,500 | ... | 58,500 | ... |
| Steel canopy for erection and maintenance | 6,500 | ... | 6,500 | ... | 7,500 | ... |
| Turbine-room crane | 77,000 | 60,000 | 77,000 | 60,000 | 142,000 | 117,000 |
| Snow-melting system in turbine deck | 3,000 | ... | ... | ... | ... | ... |
| Additions erection costs for outdoor turbine | 7,500 | ... | 7,500 | ... | 10,000 | ... |
| | $124,500 | $243,000 | $121,500 | $243,000 | $224,000 | $425,500 |
| Omissions, contingencies, and overheads—25% | 31,100 | 60,800 | 30,400 | 60,800 | 56,000 | 106,400 |
| Totals | $155,600 | $303,800 | $151,900 | $303,800 | $280,000 | $531,900 |
| Net savings per unit | $148,200 | ... | $151,900 | ... | $251,900 | ... |

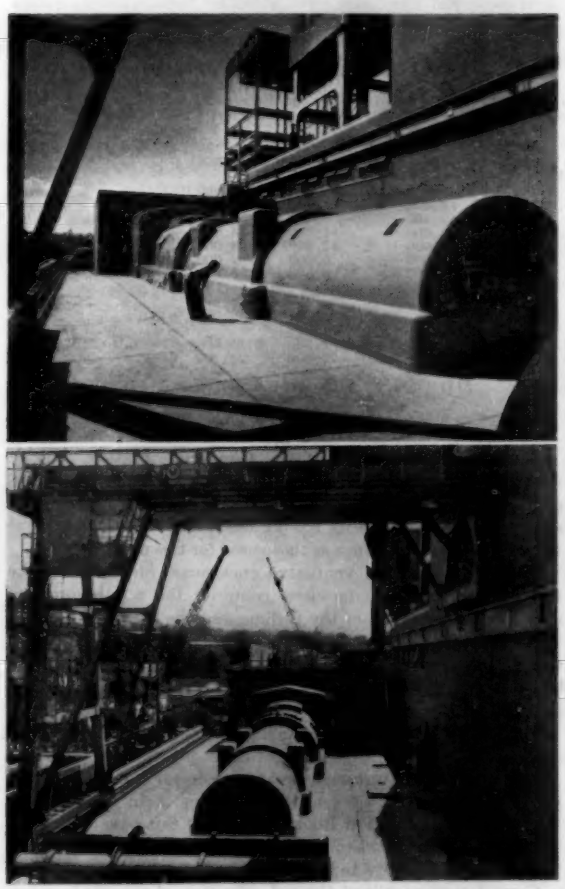

Fig. 9 View of Outdoor Turbine-Generator, Glenwood Power Station No. 3, Unit 4

TABLE 4 ESTIMATED COST OF WEATHERPROOFING OUTDOOR TURBINE-GENERATOR UNITS

| Power station | Glenwood No. 3, Unit 4 and Far Rockaway No. 2, Unit 4 | Glenwood No. 3, Unit 5 | Edward F. Barrett, Unit 1 |
|---|---|---|---|
| Unit rating, mw | 90 | 90 | 156 |
| Initial operation | 1952–1953 | 1954 | 1956 |
| Walk-in enclosures | $18,500 | $18,500 | $58,500 |
| Steel canopy for erection and maintenance | 6,500 | 6,500 | 7,500 |
| Snow-melting system in turbine deck | 3,000 | ... | ... |
| Totals | $28,000 | $25,000 | $66,000 |
| Omissions, contingencies, and overheads—25% | 7,000 | 6,300 | 16,500 |
| Total cost per unit | $35,000 | $31,300 | $82,500 |

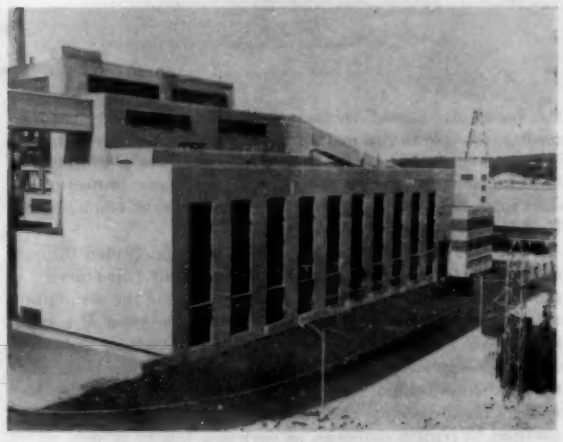

Fig. 10 View of Turbine-Generator Room, Port Jefferson Power Station, Units 1 and 2

at the Edward F. Barrett Station, capital expenditures have been reduced by deleting enclosures around other equipment in the station. Greater reduced costs for the Barrett unit are shown in Table 1. Elimination of the enclosure around the forced-draft fans and the burners has been mentioned. It was decided to gain a further saving by sealing the space between the coal silos and eliminating the brick-wall siding covering the front and sides of this coal-storage space as had been provided on earlier units. Similarly, as has been done in many plants, but for the first time on Long Island Lighting installations, the corrugated transite siding and roof of the coal-conveyer galleries were replaced with an aluminum-alloy hood over the conveyer belt only, and an open grating walkway alongside the belt. The circulating-water intake structure which had been enclosed at all previous units, was eliminated at the Barrett Station since the intake is located on a channel which is in a relatively sheltered area and because frequent access to the circulating-water intake equipment is not necessary. Furthermore, it had previously been decided that only local controls of the motors would be provided and that all starters and other motor auxiliary electrical equipment would be centrally located within the plant.

Through operating experiences at all our power stations, as well as those of other companies, it was decided that the scope of

TABLE 5 PROGRESSIVE CHANGES IN OUTDOOR DESIGN AND THE SAVINGS EFFECTED THEREBY

| | Savings | |
|---|---|---|
| *Glenwood Power Station No. 3, Unit 4 and Far Rockaway Power Station No. 2, Unit 4* | | |
| Outdoor turbine-generator | $148,200 | |
| Simplified soot-blower covers and elimination of resistance wiring on air tubing 11,000 + 25% | 13,800 | |
| Additional savings over previous design | $162,000 | $162,000 |
| *Glenwood Power Station No. 3, Unit 5* | | |
| Elimination of soot-blower covers and heaters | $ 10,000 | |
| Elimination of turbine deck snow-melting system | 3,000 | |
| Addition of roof over back end of boiler for additional protection during construction | (−)3,000 | |
| | $ 10,000 | |
| 25% for overhead, etc. | 2,500 | |
| Additional savings over previous design | $ 12,500 | $ 12,500 |
| *Edward F. Barrett Power Station, Unit 1* | | |
| Elimination of front and side walls around coal silos | $ 22,000 | |
| Elimination of side walls on coal-conveyer galleries | 45,000 | |
| Elimination of enclosure over circulating-water intake less cost of weatherproofing of equipment | 18,400 | |
| Reduction in main power-plant heating and ventilating equipment | 25,000 | |
| Elimination of boiler enclosure around burner elevations | 46,800 | |
| Elimination of enclosure around FD fans less cost of weatherproofing equipment | .... | |
| | $157,200 | |
| 25% for overheads, etc. | 39,300 | |
| Savings over previous design | $196,500 | $196,500 |

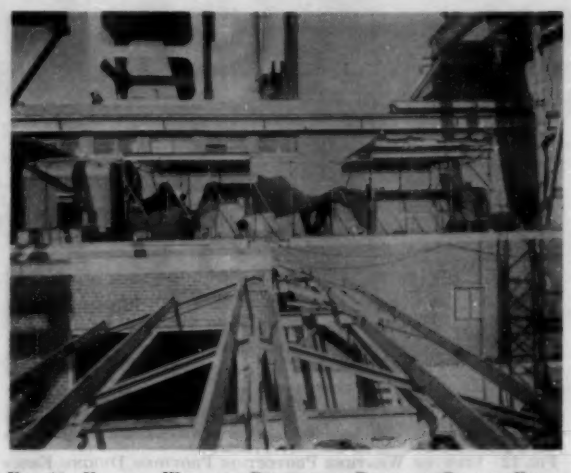

FIG. 11 VIEW OF WEATHER PROTECTION PROVIDED DURING ERECTION OF TURBINE-GENERATOR, FAR ROCKAWAY POWER STATION NO. 2, UNIT 4

TABLE 6 SUMMARY OF OVER-ALL SAVINGS BY INCREASING SCOPE OF OUTDOOR DESIGN

| Power station | Port Jefferson, Units 1 and 2 | Glenwood No. 3, Unit 4 Far Rockaway No. 2, Unit 4 | Glenwood No. 3, Unit 5 | Edward F. Barrett, Unit 1 |
|---|---|---|---|---|
| Unit rating, mw | 40 | 90 | 90 | 156 |
| Initial operation | 1948–1950 | 1952–1953 | 1954 | 1956 |
| Semioutdoor boiler | $178,800 | $215,600 | $224,300 | $305,600 |
| Outdoor turbine-generator | ... | 148,200 | 151,900 | 251,900 |
| Semioutdoor coal silo | .... | .... | .... | 27,500 |
| Outdoor coal-conveyer galleries | ... | ... | ... | 56,200 |
| Outdoor circulating-water intake | ... | ... | ... | 23,000 |
| Reduction in main power-plant heating and ventilating | ... | .... | .... | 31,200 |
| Total savings—outdoor design—per unit | $178,800 | $363,800 | $376,200 | $695,400 |
| Savings per kw rating | $4.47 | $4.04 | $4.18 | $4.45 |

heating and ventilating equipment could be reduced markedly. At the Barrett Station there are no elevations below grade. Ventilation during the summer months for the area below the turbine will be achieved by opening hatches in the turbine deck. Removal of wall panels will permit circulation in the lower boiler region and pulverizer area.

A tabulation of the savings represented by each item of outdoor construction made possible by progressive outdoor design changes is shown in Table 5.

Over-all savings obtained through the progressive increases in the extent of outdoor design are shown in Table 6. The tabulation indicates that increased savings for the latter units is due primarily to the increase in the extent of outdoor construction. Furthermore, if the scope of outdoor design had not been progressively increased, the savings per kilowatt would have reduced as the sizes of the units increased.

## CONSTRUCTION

It has been found that there has been very little additional cost for erection of outdoor turbine-generator units due to weather conditions. This partially results from the fact that the major construction of both the boilers and turbines has been scheduled during the warmer months, and is also due in part to the mild winters that have been experienced in this area in the past few years. Moreover, partial weather protection has been provided for both boiler and turbine erectors.

Concrete roofs over the boilers at Port Jefferson, Glenwood Station No. 3, Unit 4, and Far Rockaway Station No. 2, Unit 4, cover the enclosed drum-level area only. Inasmuch as the entire drum elevation is enclosed at Port Jefferson a full boiler roof is provided and therefore a maximum of rain and snow protection during erection was afforded. However, since the drum-level enclosures at Glenwood and at Far Rockway include only the front portion of the boiler, only a partial boiler roof was provided. It was found during erection at Glenwood that the additional roof was necessary in order to reduce lost time during inclement weather. Accordingly, a complete boiler roof will be provided for Unit 5 at Glenwood and Unit 1 at the Edward F. Barrett Station.

A portable canopy with canvas sides is provided the turbine erector, Fig. 11, for partially enclosing the turbine-generator unit during erection. This canopy is designed so that it can be used at any of the three 90/99-mw units for both erection and maintenance purposes. This removable structure consists of diagonally braced conventional-type pipe scaffolding set in fittings inserted in the turbine deck. The roof is supported on light aluminum trusses and is made in three large panel sections. The total cost of this canopy was $6500.

In addition to the partial weather protection provided, it has been found necessary to supplement this protection with local protection of areas where work is in progress during rainy weather or high winds. Canvas tarpaulins have been erected when necessary around local areas when welding tubes and when heat-treating alloy welds, Fig. 12. In some cases plywood wind shields have been erected around heating-treating equipment. Generally, there is sufficient work on the steam-generating unit to permit the boiler erector to shift the erection crews to work in more protected areas during short periods of inclement weather.

Owing to the corrosive salt atmosphere in this area, the turbine erector has found it necessary to grease and wrap all open ma-

FIG. 12 VIEW OF WEATHER PROTECTION PROVIDED DURING ERECTION OF BOILER NO. 2, PORT JEFFERSON POWER STATION

chinery when erection work is not actually in progress. Furthermore, during rainy or foggy weather, it is not possible for millwrights to work on the turbine deck because of the possible corrosive effect on the unit.

It has been estimated that total construction lost time due to inclement weather has not exceeded 5 per cent in the case of the boiler and 10 to 15 per cent in the case of the turbine-generator. Turbine-erection costs have been estimated to be between $5000 and $10,000 higher because of the outdoor design.

### OPERATION AND MAINTENANCE

Operation and maintenance experiences at the outdoor stations indicate not only that ventilation of the station is far superior, but that maintenance time in previous high-temperature areas has been reduced and outweighs lost time due to low temperatures during the short period of two to four months during the winter season. Moreover, during five years of operation at Port Jefferson, it has only been necessary to erect a temporary heated enclosure on two occasions of emergency maintenance. A survey of the operating personnel also indicates that they definitely prefer the outdoor station to the indoor.

Fear that noise would emanate from the outdoor plants was a matter of concern until operation of the outdoor boilers and turbines had proved that the noise level at various distances from the plant created no noise problem. Previous operating experience with brick enclosures indicated that their effect was similar to a piano sounding board, resulting in amplification of the power-plant noise, not only inside the plant but to surrounding areas. Furthermore, sound emanating from a single piece of equipment at an outdoor installation is permitted to attenuate rapidly as opposed to the noise inside an indoor installation where the noise from all equipment is confined to a single enclosed space resulting in a cumulative loud rumbling noise. Although originally under consideration, soundproofing of equipment has not been found necessary, nor is it expected to be necessary.

Other than the design changes previously mentioned in the development of the newer power stations, no alterations or additions have been made at the present stations occasioned by the outdoor design.

### CONCLUSION

In conclusion it should be mentioned that adoption of a program of outdoor construction is not only in large measure a reflection of company policy, but requires for its successful prosecution full collaborative effort on the part of all personnel comprising the engineering and operating organizations. The savings gained through reduction of power-plant building walls and enclosures are of real significance. The improvement in employee comfort and contentment, while intangible, is equally significant. It is our opinion after five years of experience that semioutdoor boilers are practical and are here to stay. We are confident that an outdoor turbine will be similarly regarded. It is also felt that as operating experience is gained the scope of outdoor construction will be increased to an even greater extent than that presently contemplated.

# Adapting Outdoor Plants to Their Environment

BY W. F. FRIEND,[1] NEW YORK, N. Y.

IN the historical sketch by Louis Elliott, sent from Switzerland, the evolution of steam power plants is traced—as to type and extent of structure and enclosure. In a biological sense, "evolution" is a term denoting physical and functional adaptation to the environment, through a series of steps or changes. For power plants, the economic element in environment has been a strong influence, but it is by no means the sole factor identified in progressively reducing the extent of housing provided for equipment and personnel.

Concurrent developments toward simplified plant designs during the past two decades, which facilitated the outdoor trend, have included among others:

(*a*) Unit boiler-and-turbine arrangement.
(*b*) Reduction of cross connections and spare equipment.
(*c*) Low-headroom designs for condensers.
(*d*) Centralized controls, combined for boiler and turbine.
(*e*) Plant foundation using a simple concrete slab at grade level.
(*f*) Wall construction of lightweight panel types, without masonry.

This evolution has paralleled the practices in industrial plant design, notably for petroleum refineries and in chemical manufacture.

Today, the kind and extent of housing for a power plant are generally decided after consideration has been given to such factors as:

1 Topography of site, whether:
(*a*) Exposed to or sheltered from storms.
(*b*) Subjected to mist or to ocean spray.

[1] Mechanical Engineer, Ebasco Services Incorporated. Mem. ASME.

(*c*) Situated in desert or dust-bowl country.
(*d*) Exposed to rockfall from cliffs.

2 Climatic extremes, such as:
(*a*) Low temperature in winter.
(*b*) Winds of gale or hurricane force.
(*c*) Rainfall, especially sustained rains or tropical downpours.
(*d*) Sleet storms.
(*e*) Heavy snowfall.

3 Other local conditions, including:
(*a*) Character of community.
(*b*) Preference expressed by executives and operators.
(*c*) Economic factors.

All of these must receive individual consideration and compromise, attaching due weight not only to physical and economic factors, but also to the less tangible psychological and public-relations elements, when deciding the degree of outdoorness for any specific situation.

### Community Acceptance

With generating stations as with step-down substations placed in populated areas, appearance acceptable within the community is recognized today as a public-relations opportunity and obligation. Rational methods for securing good appearance embrace:

(*a*) Functional design, with attention wherever feasible to symmetry and proportion.
(*b*) Selection of construction materials.
(*c*) Choice of color treatment.
(*d*) Landscaping and "buffer-zone" provisions.
(*e*) Night-lighting effect, including reduction of sky glow.

In addition, the control of noise may be a "good-neighbor" requisite. The considerable knowledge acquired through experience in the control of noise from outdoor-type plants has been assembled and analyzed in a paper given by the author at the 1952 American Power Conference paper under the title, "Noise Problems and Prevention of Noise on Public-Utility Properties."

Construction economies and penalties are covered in today's symposium by other speakers and discussers, from several viewpoints. In the earlier years, the talk was commonly about savings to be realized by curtailing structures. Nowadays, the "yardstick" basis used for analysis by the author's organization is more often the full outdoor design, with differentials estimated for providing anything beyond the practicable minimum of housing.

### Conclusion

Modern outdoor designs have demonstrated their adaptability for fitting successfully into any environment. Greater foresight and imagination are needed than with fully housed installations, but the ingenuity of engineers can provide adequate solutions and good compromises to meet all the local requirements.

# Survey of Equipment Placement in New Steam Central Stations—1953–1956

By B. G. A. SKROTZKI,[8] NEW YORK, N. Y.

DURING the fall of 1953, questionnaires were sent to all central-station utilities in the United States to determine which units of equipment were placed outdoors, semi-outdoors, or indoors. The survey was limited to new units, those starting operation in 1953 and scheduled for initial operation up to and including 1956.

Data received on 267 units represent almost 70 per cent of the number of new units, and about 80 per cent of the total mw capacity. These units were distributed among 40 states in all sorts of climates and precipitation conditions.

Bar charts in Fig. 13 show the disposition of 58 items of plant equipment in the 267 units. Each bar represents 100 per cent of the total capacity reported. Open sections on the bars represent per cent of equipment placed outdoors. Horizontally hatched sections represent percentage of equipment placed semi-outdoors. Solid sections are the percentages of equipment placed indoors. Gray sections show the percentage of capacity not using or reporting that type of equipment.

Outdoor and semioutdoor percentages for each item were added together and plotted to the left of the zero-centered ordinate. Sum of the indoor and nonreported percentages are plotted to the right of the zero ordinate. The items were arranged in descending order of outdoorness.

When plotting results in percentage of total number of units, some of the figures differ from the percentages shown in Fig. 13. These differences, however (less than 3 per cent on the average) do not change significantly the order of the items in Fig. 13. For this reason we have not reported the analysis on a number-of-units basis.

### Results

Only 11 items of equipment were indicated for outdoor installation by more than 50 per cent of the capacity. The next 11 were outdoors in 25 to 50 per cent of the capacity. The remaining 36 items were outdoors in less than 25 per cent of the capacity.

High-tension switchgear, transformers, and house transformers are almost always outdoors. After these, acceptance of outdoor placement decreases rapidly. Of the main equipment, the steam generator is outdoors, or partly so, in 38 per cent of the capacity, the turbine-generator in 21 per cent, the condenser in 12 per cent, the boiler feed pumps in only 7.7 per cent.

Forced-draft fans are outdoors in 33.8 per cent and semi-indoors in 1.6 per cent of the total capacity. Induced-draft fans stand outdoors in 65.0 per cent and semi-indoors in 1.0 per cent of the capacity, but they are not used at all in 7.5 per cent of the capacity.

Meaning of semi-indoor or semioutdoor varies. Often an item has an overhead shelter without sides, or it is partly outdoors, or of similar items in one plant, some are indoors, others outdoors.

Outdoor installations stand in all parts of the country, regardless of climate or precipitation, Fig. 14. The only exception appears to be the northwest which is predominantly hydro. Outdoor plants seem to concentrate largely in the south and southwest. A notable exception is the Southern System in the states of Alabama, Georgia, Mississippi, and Florida. They do not use outdoor plants, as such, but they do place some of the

[8] Engineering and Management Editor, *Power*, McGraw-Hill Publishing Company, Inc. Mem. ASME.

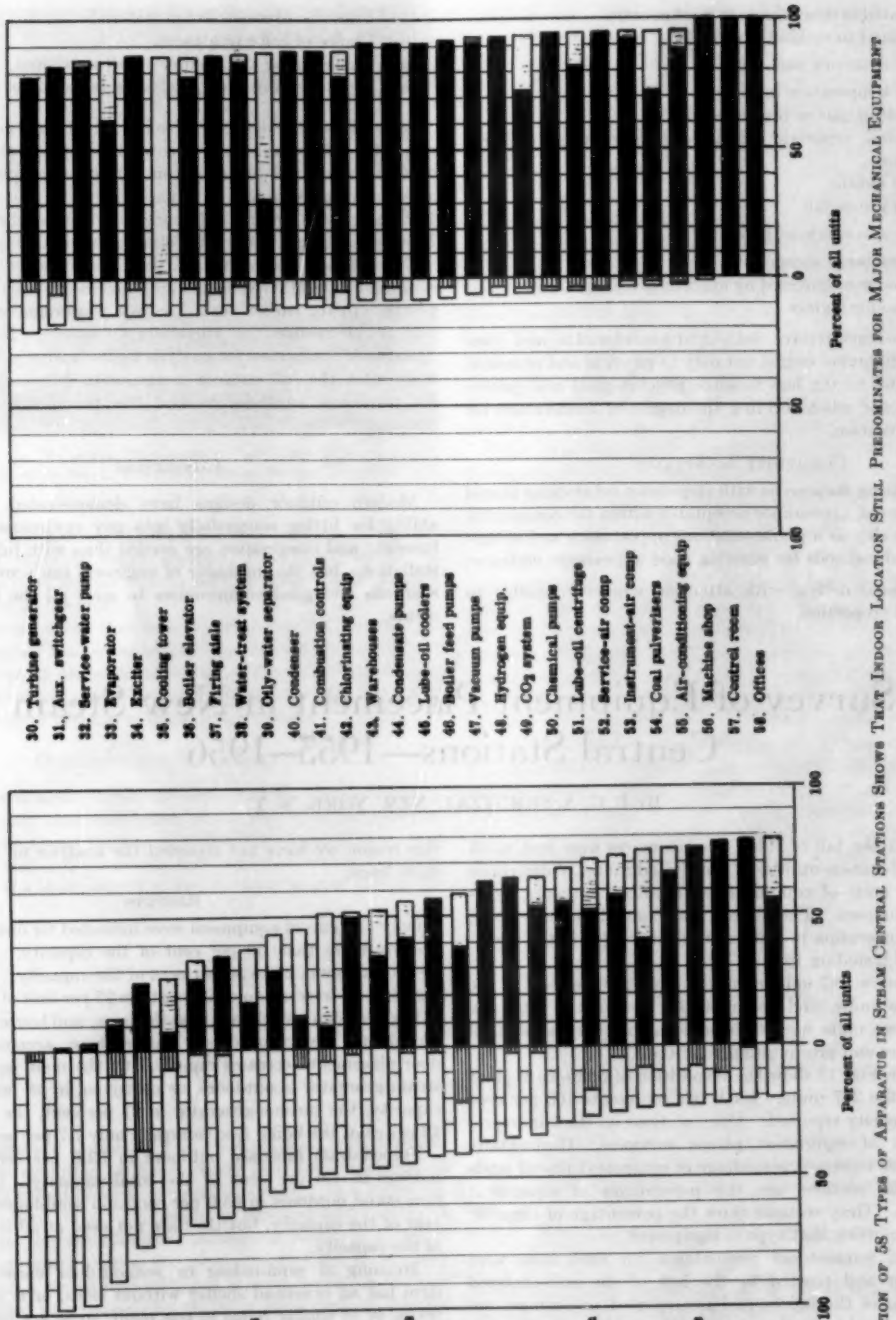


FIG. 13 DISPOSITION OF 58 TYPES OF APPARATUS IN STEAM CENTRAL STATIONS SHOWS THAT INDOOR LOCATION STILL PREDOMINATES FOR MAJOR MECHANICAL EQUIPMENT

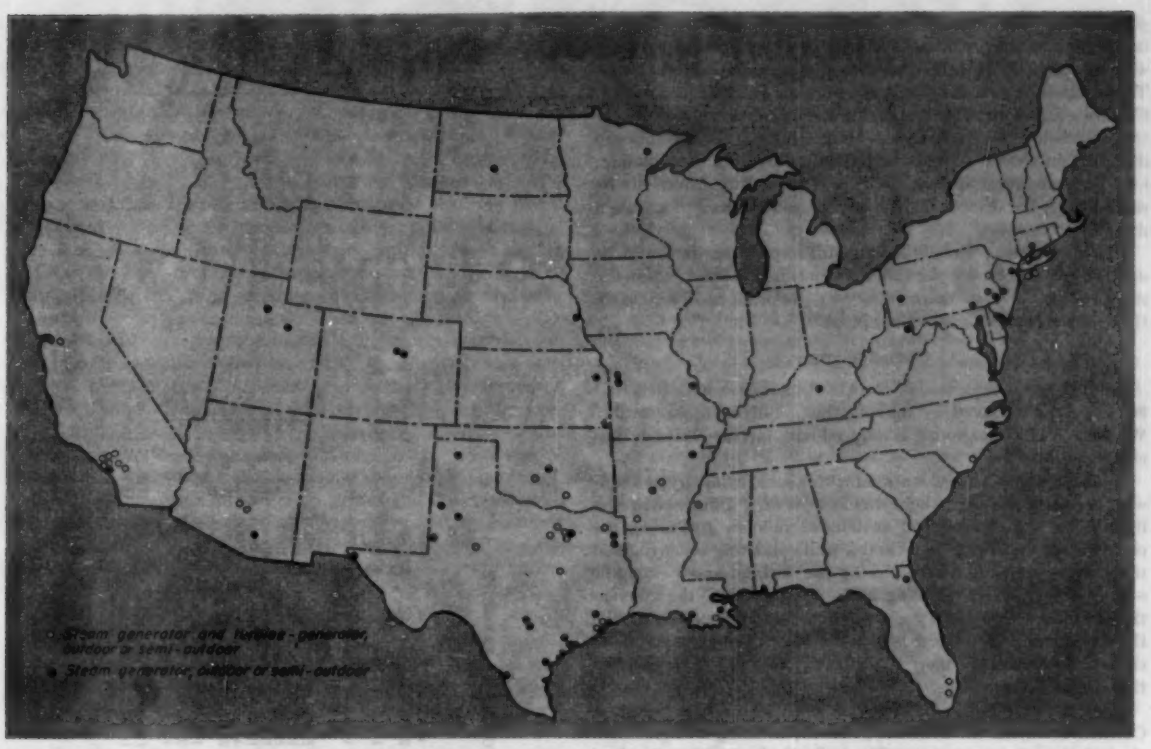


FIG. 14 NEW STEAM CENTRAL STATIONS WITH OUTDOOR AND SEMIOUTDOOR BOILERS AND TURBINES APPEAR IN ALL PARTS OF U. S. A. WITH EXCEPTION OF NORTHWEST

plant auxiliaries outdoors at ground level. This system does its major overhauling during a heavy rainy season, which reduces attractiveness of an outdoor plant.

The survey, Fig. 13, also shows the degree to which certain items of equipment are not used by the reported capacity. Items that stand out include cooling towers, coal towers, fuel-oil heaters, deaerators, oily-water separators, $CO_2$ systems, and coal pulverizers.

Oddities in the survey are one outdoor machine shop and outdoor firing aisles in 8.9 per cent of the capacity and semioutdoor aisles in 5.1 per cent.

The reports received from 174 steam central stations have been summarized elsewhere.[7]

### CONCLUSIONS

Some electrical equipment is always placed outdoors. For major station equipment, such as boilers, turbines, condensers, and feed pumps, indoor locations still predominate. Induced-draft fans are major boiler auxiliaries placed outdoors, others are more often placed under shelter.

[7] Listed in the March, 1954, issue of *Power*, pp. 81–85.

# Design and Experience With Outdoor Power Plants

BY G. A. GAFFERT,[8] CHICAGO, ILL.

IN 1931 Sargent & Lundy designed a steam-electric plant with one novel feature—the outer walls of the building were in the same plane as the outer walls of the steam-generating units. The boiler design was arranged with natural-gas firing, using an air-cooled furnace setting. Two boilers were installed with one 5000-kw turbine-generator. A recent inspection and discussion with the operators indicated no unusual difficulties over a period of years.

[8] Chief Mechanical Engineer, Sargent & Lundy. Fellow ASME (since deceased).

Many years later, in 1945, the Central Louisiana Electric Company planned to build a new steam-electric station in central Louisiana, and wished to consider as many outdoor features as practicable to hold down initial investment. An arrangement of steam-generating units, wherein the boiler was located outdoors and the firing aisle indoors, was adopted.

Further, the turbines were to be located on an outdoor deck with condensing equipment mounted below. Turbines were to be served with a gantry crane. Switchgear also was to be located outdoors on the turbine-room deck and weatherproofed. This plant has now grown to a four-unit station following the same

pattern, the only deviation being the installation of a pressurized boiler for the fourth unit. Experience over a period of years with this plant has indicated no outstanding operating difficulties. The weather bureau is consulted before an overhaul is planned. Control equipment is located on an operating control-board central area below the main deck. In this station the turbines are mounted on a deck poured integral with the rest of the building, i.e., no foundation isolation. This feature has proved to be satisfactory, the deck being sloped for drainage away from each machine.

The only unusual item is the amount of painting that must be applied yearly, because the rain and sunshine at this location are rather severe. Also, there is more deterioration of insulation than for the conventional indoor plant.

## Cost Aspects

A study and comparison of costs for this station indicated that $6 per kw were saved by making this a fully outdoor station. We believe that this saving is reduced with increased size of generating unit.

A later design of a new station for this same company at Baldwin, La., indicated that there was little, if any, difference in cost by placing the turbine and switchgear indoors and using the conventional overhead crane and a wall consisting of corrugated transite, as compared with placing the turbine and switchgear out of doors, weatherproofing both, and replacing the conventional crane with a gantry crane. The cost of weatherproofing the turbine and switchgear is considerable. The gantry type of crane is considerably more expensive than the indoor conventional type of crane.

The Interstate Power Company, in 1947, built a new station at Clinton, Iowa, on the Mississippi River, utilizing a single-boiler single-turbine arrangement. The boiler is fired with pulverized fuel, and that portion of the boiler above the main operating floor is out of doors, the front firing aisle being indoors. This unit is of the water-cooled integral-furnace type of construction. The induced-draft fan is located on the deck behind the boiler. This fan gave trouble initially, because the oil congealed in the bearings during cold weather. Also, the hydraulic-coupling oil cooler was subject to freezing. By relocating this cooler below deck, the difficulty was overcome. This boiler has gone through several winters with only minor annoyances to the operators, due to exposure to weather of the soot-blower elements.

Two steam power stations were built simultaneously of outdoor design (both boiler and turbine); one for the Oklahoma Gas & Electric Company, at Sulphur, Okla., and a second plant for the Public Service Company of Oklahoma, at Washita, Okla. One boiler per turbine was used in the first case and two boilers per turbine in the second case, all of the pressurized type. The main turbines and switchgear were located on outdoor decks. Walk-in type of housings protected the operators at the steam and exciter ends. In both cases, a central control room for the boilers, turbines, and switchgear was utilized, this room being located on an upper deck and completely housed. During erection of the main turbine, a quonset house was built around the turbine for weather protection, in one case these machines being erected during winter time.

## Two General Types of Plant

Since that time, Sargent & Lundy have designed a number of outdoor steam-electric stations following two general patterns. In the first pattern, the boilers alone are out of doors, with the front face inside, facing the firing aisle. In the second pattern, the turbine-generators are also out of doors on an outdoor deck and weatherproofed by using walk-in type of housings on both the turbine and exciter ends. Also, the switchgear is weather-

TABLE 7 OUTDOOR PLANTS DESIGNED BY SARGENT & LUNDY

| Station | Owner | State | Year first unit oper. | Press. and temp. | Fuel | Boiler make outdoor | Type casing | Turbine size | Turbine make | Turbine location | Turbine and exciter protection | Switchgear location | Condensing water |
|---|---|---|---|---|---|---|---|---|---|---|---|---|---|
| Coughlin | Central Louisiana Elec. Co. | Louisiana | 1946 | 600/825 | Nat. gas | 2/B&W | Steel | 2/7500 | G-E | Outdoor deck | Weather-proofed | Outdoor | River |
| Coughlin | Central Louisiana Elec. Co. | Louisiana | 1948 | 600/825 | Nat. gas | 1 CE | Steel | 1/10000 | G-E | Outdoor deck | Weather-proofed | Outdoor | River |
| Coughlin | Central Louisiana Elec. Co. | Louisiana | 1949 | 850/900 | Nat. gas | 1 B&W | Steel press. | 1/20000 | G-E | Outdoor deck | Weather-proofed walk-in encl. | Outdoor | River |
| Beaver Channel | Interstate Power Co. | Iowa | 1950 | 600/825 | Pulv. fuel | B&W | Steel | 1/15000 | WEM | Indoor[a] | — | Indoor | River |
| Lieberman | Southwestern Gas & Elec. Co. | Shreveport, La. | 1950 | 850/900 | Nat. gas | B&W | Steel | 2/30000 | G-E | Indoor[a] | — | Indoor | Lake |
| Laredo | Central Power & Light Co. | Texas | 1951 | 800/900 | Nat. gas | B&W | Steel press. | 2/30000 | G-E | Indoor[a] | — | Indoor | Cool. tower |
| South | Oklahoma Gas & Elec. Co. | Oklahoma | 1951 | 850/900 | Nat. gas | B&W | Steel press. | 1/60000 | G-E | Outdoor | Walk-in encl. | Outdoor | Cool. tower |
| Southwestern | Public Service Co. of Oklahoma | Washita, Okla. | 1951 | 850/900 | Nat. gas | B&W | Steel press. | 2/60000 | WEM | Outdoor | Walk-in encl. | Outdoor deck | Cool. tower |
| Knox Lee | Southwestern Gas & Elec. Co. | Longview, Texas | 1951 | 850/900 | Nat. gas | 3/B&W | Steel | 3/30000 | G-E | Indoor[a] | — | Indoor | Lake |
| Victoria | Central Power & Light Co. | Victoria, Texas | 1952 | 850/900 | Nat. gas | 2/B&W | Steel press. | 1/30000 | West. | Indoor[a] | — | Indoor | River |
| | | | | | | | | 1/60000 | West. | | | | |
| Teche | Central Louisiana Elec. Co. | Baldwin, La. | 1953 | 850/900 | Nat. gas | 1/B&W | Steel press. | 1/20000 | G-E | Indoor[b] | — | Indoor | River |
| Paint Creek | West Texas Utilities Co. | Texas | 1953 | 850/900 | Nat. gas | 2/B&W | Steel press. | 2/30000 | G-E | Indoor[b] | — | Indoor | Lake |
| Mullergren | Western Light & Telephone Co. | Great Bend, Kan. | 1953 | 850/900 | Nat. gas, oil | 1 CE | Steel | 1/15000 | G-E | Indoor[b] | — | Indoor | Cool. tower |
| Lon C. Hill | Central Power & Light Co. | Texas | 1954 | 850/900 | Nat. gas | 1/B&W | Steel press. | 1/60000 | G-E | Indoor[a] | — | Indoor | Cool. tower |
| Lone Star | Southwestern Gas & Elec. Co. | Daingerfield, Texas | 1954 | 850/900 | Nat. gas | 1/B&W | Steel press. | 1/40000 | G-E | Indoor[a] | — | Indoor | Lake |

[a] Brick turbine wall.
[b] Transite turbine wall.

proofed and located out of doors. In addition, the generating heater, evaporator, and miscellaneous tanks are mounted out of doors. The steam-generating units in late designs have been of the pressurized type in the South, using only pressure blowers to supply combustion air and remove the furnace gases.

Table 7 indicates the details in connection with each of these stations. We believe that the outdoor boiler is firmly established. We do believe, however, that there is an open question as to whether the outdoor type of turbine saves any appreciable investment. We also feel that for the outdoor boiler and turbine plants, an enclosed central control room with adequate glazing will give the operators needed weather protection, will improve their vision of operating conditions, and will reduce operating manpower.

It is also necessary with outdoor design to weatherproof certain pipe lines, which cannot be drained or wherein water may freeze. We have applied antifreeze protection to our more recent outdoor plants. This has been done with electric strip heaters, either with or without monitoring indicators. Protection also can be done by steam tracing various pipe lines. Costs can be reduced by grouping various lines around a central source of heat.

In all, our firm has under design, or has completed, some 25 station units for outdoor service. We believe that the outdoor plant has its place particularly in the type of climate where the plant is not subject to extremes of weather.

## General Discussion

W. L. Chadwick.[9] The advantages of outdoor stations and the opportunities for economies in construction and operation which they present have long been recognized in Southern California. The feasibility of operating outdoor stations in this area has been demonstrated by the petroleum industry with many years of successful operation of outdoor refineries including complex high-temperature and high-pressure equipment.

In 1947 the design features of the semienclosed Redondo No. 1 Plant of the Southern California Edison Company were reported. At the 1952 Spring Meeting of the Society a report[10] was presented on the design features of Etiwanda Steam Station, the first all-outdoor plant of the Southern California Edison Company, which was then under construction. The decision to use an outdoor design here was based on numerous reports from and observations of outdoor plants which had given satisfactory service elsewhere, on the favorable experiences with outdoor oil refineries, and on the reliable operation of many outdoor synchronous condensers on the Edison system going back to 1930.

In that report several advantages of outdoor design were mentioned.

1 The elimination of the usual boiler and turbine buildings with an attendant saving of between $5 and $8 per kilowatt in first cost.

2 Simplifications of design and construction with further savings in first cost and improvement in reliability.

3 Elimination of most of the ventilation problems, thereby saving not less than $75,000 in the first cost of fans as well as saving the continued cost of power and maintenance for such equipment.

4 Increased ease of cleaning and the attendant saving by permitting the washing down of open areas rather than sweeping or vacuum cleaning.

5 Finally, the outdoor station is safer in case of fire. The exposures to heat, smoke, and water are less and the accessibility for fire suppression is much improved. This is an advantage which is often overlooked. Several central-station fires have been reported recently in which the heat and smoke from a relatively small fire, concentrated in an enclosed area, made it impossible for the operating force to get close enough either to fight the fire properly or to shut down equipment. Major damage resulted.

To date our experience has been that we have not only realized all of the advantages, but have obtained other incidental benefits. The improved accessibility of the outdoor station has been an important aid during construction. It has been possible to use motorized moving and lifting equipment to better advantage. The elimination of walls extended the reach range of derricks. Construction supervision has been noticeably more effective in the open station, and there has been less interference between structural workers and equipment erectors.

There has been distinctly better operator morale at the outdoor station. Operators prefer the outside duties, often resisting transfers to assignment on which they will be required to work in enclosed areas.

One objection frequently raised to outdoor stations is the exposure during overhaul and repair. Our experience has been that some form of temporary portable housing is essential but quite satisfactory. During initial alignment of the units such housing is necessary to prevent uneven expansion from uneven solar heating. After erection, the shelter can be set aside, but yet used to enable any necessary maintenance work to be continued during unfavorable weather. We do not believe that any walk-in enclosure is desirable because it would provide no protection which cannot be obtained in a weatherproofed unit, yet it presents the same problems in ventilation and much the same exposure to hazard from fire and accidents as in fully enclosed stations.

We believe that the outdoor station design is a natural step in the development of the central station. The first electrical apparatus was all housed, but as designers and manufacturers improved equipment, advantage has been taken of the economy, reliability, and safety which may be gained by moving the generating, transforming, and distributing stations outdoors.

We concede that at some station sites, the problems of noise control may be serious enough to practically eliminate the possibility of outdoor stations. In other areas where low temperatures are encountered the outdoor station may seem unsuitable, but it is often possible to use outdoor boilers and turbine-generators and yet enclose the area beneath the turbine deck at comparatively small cost, thereby providing a protective enclosure for most of the auxiliary equipment.

Our experience with the outdoor station has been so successful that we are incorporating it to the limits of feasibility in two new stations now under construction.

C. C. Whelchel.[11] The Pittsburgh Steam Plant, consisting initially of four units, is scheduled to go into operation during the spring and summer of 1954. It will be a so-called full-outdoor plant. The estimated gross normal operating station capability will be 600,000 kw, making Pittsburgh the largest steam-electric generating station in the west. The estimated cost of the plant, excluding the high-voltage switchyard, is about $120 per kw of plant.

The weather at this site is mild, with dry summers, and a rainy season averaging about 20 in. per year extending from about November through April. The major problem is expected to come from wind and dust, but the dust will be minimized by planting and yard paving.

---

[9] Vice-President, Southern California Edison Company, Los Angeles, Calif. Mem. ASME.

[10] *Mechanical Engineering*, vol. 74, 1952, pp. 543–550.

[11] Chief, Steam Engineering Division, Pacific Gas & Electric Company, San Francisco, Calif. Mem. ASME.

This very brief discussion will be limited to the general arrangement and the outdoor features.

The turbine-generators, except for the head end, are out in the open. The boilers are protected only by an umbrella-type roof extending some 9 ft below drum center line. The principal enclosure contains the control room and firing aisle. The protected areas under the boilers and the turbine pedestals also provide economical space for enclosed location of some equipment.

The four turbine-generators are set in parallel with axes normal to the boiler drums, resulting in a minimum piping distance from boiler to turbine. The turbines project from a combination auxiliary equipment bay and firing aisle, with the governor ends of the turbines thus being located inside the auxiliary bay-firing aisle area and accessible to the operators. This feature eliminates the need for the typical walk-in weatherproof enclosure on the governor end of the turbine but a walk-in enclosure is installed over each exciter.

The central control room for the four units is located between units Nos. 2 and 3 in the enclosed combination firing aisle and turbine operating area just discussed.

The turbine-generators are serviced by a 60-ton semigantry crane, having access also to the high-pressure feedwater heaters, to the spur track, and to an open lay-down area at grade adjacent to the machine shop. During construction and when required for maintenance on a turbine-generator, a mobile canvas shelter on an aluminum tubular frame is provided.

Fans are located outdoors on the ground behind the boilers, with two forced and two induced-draft units per boiler.

While the Pittsburgh Steam Plant would be designated as a full-outdoor plant, the over-all design has attained a considerable degree of enclosure for operators and certain equipment by taking full advantage of numerous structural situations where low-cost enclosure could be made at desirable points.

The arrangement of the Pittsburgh plant is the end result of a continuous effort by PG&E to build stations that are economical from the standpoint of investment, and operating and maintenance costs. At this plant the largest item of saving came from the decision to make this a completely outdoor plant—the first such plant on our system—although we have a number of other outdoor boilers. Along with this the decision to rearrange our turbine-generator layout from the in-line or common-axis arrangement greatly reduced piping and electrical costs. The total savings for the outdoor over a masonry-enclosed arrangement plus the improved turbine-generator arrangement was estimated at between $1,000,000 and $1,500,000.

We cannot as yet fully evaluate the effect of the outdoor turbine arrangement on possible operating and maintenance problems and costs, but we anticipate that the plant will be a practical and simple one to operate and maintain, and that over-all operating costs will not be increased by the outdoor features.

J. W. Keck.[12] We have eight major plants with a total of 21 units installed. Of these units, ten are conventional indoor plants, three semioutdoor plants, i.e., outdoor boiler, two are something between semi and full-outdoor, having a low steel enclosure over the entire turbogenerator, and five are full-outdoor plants. With one exception, the indoor plants were built prior to 1940, the semioutdoor plants were built in the period 1942-1946, and since 1948 eight units have been built in progressive degrees of full-outdoor construction. (One indoor plant was built in 1948 in an existing building.)

Over the years we have averaged about one hurricane per year on our system and, depending on the path of the storm, one or more plants might be affected. The older indoor plants have, of course, weathered more storms than the newer plants and two of our newer outdoor plants have not yet been exposed to storms of hurricane force.

With the exception of several auxiliary motor failures in two of the early semioutdoor plants, we have had no plant shutdown during hurricanes as a result of design features of either indoor, semioutdoor, or full-outdoor construction, and our operating experience indicates that the three types properly designed are equally reliable under hurricane conditions.

The last hurricane affecting our system occured in October, 1950, when three plants in the Miami area were exposed to winds approaching 125 mph. Four outdoor units, one semioutdoor unit, and five indoor units were involved. All three plants are on, or near, the ocean and there was considerable wind-driven rain and salt spray. One plant was shut down by salt spray on the outdoor switchyard which, though protected by a nearby building, is less than 100 yd from salt water. The other two plants continued to operate, though at reduced load occasioned by loss of transmission and distribution lines.

In the earlier versions of the outdoor plant, it was necessary to adapt much equipment for outdoor use, such as turbines, exciters, motors, instrument panels, etc. Co-operation between the designer and manufacturers has eliminated the need for adaptation and, in general, equipment for outdoor use is readily available today.

We have several types of enclosure for the turbine and generator, but as a result of our experiences have now standardized on small walk-in enclosures for the governor end of the turbine and the exciter end.

C. W. Geue.[13] The request for information on operating difficulties with outdoor plants in dust storms posed a problem, since we found it difficult to discover any serious cases of trouble that could be traced to dust storms. From three to five years of experience with outdoor steam-electric generating stations in West Texas, during one of the worst droughts in history, has definitely shown that no serious operating or maintenance problems are caused by dust or sand storms. It is very likely that had these stations been completely enclosed, the dust and sand nuisance would have been worse, since dust and sand would have accumulated in the enclosed areas.

Aside from the nuisance of these dust or sand storms we have not found any distinction between operating an indoor or outdoor plant under these conditions. The key operators are in an air-conditioned control room and others are in sheltered areas. Clear glass goggles are available to assist operators in seeing properly while inspecting equipment during a severe sand storm.

Good housekeeping is necessary in any plant whether indoors or outdoors. The following minor problems have come up in outdoor stations which would also occur in an indoor type of plant located in areas where dust storms are prevalent:

1 Leaky oil seals on motor bearings will result in an accumulation of oily dirt on the motor windings. Pressurising these seals eliminated the problem.

2 Grease and oil on valve stems, regulator-valve stems, and reciprocating pump shafts, etc., will catch sand or grit and result in more rapid wear and leaky packing.

3 Some sparking and more rapid wear of brushes on commutators and collector rings have been noted during severe sand storms, especially so in one case where a high wind blew dust into the exhaust-air duct from the exciter hood. This was corrected by modifying the exhaust outlet. Protection of exciters is such that they are as well enclosed as in indoor plants and the dust

[12] Superintendent of Generating Stations, Florida Power & Light Company, Miami, Fla. Mem. ASME.

[13] Superintendent of Power, Texas Electric Service Company, Fort Worth, Texas.

nuisance has not had any more effect on this equipment than if the machine had been indoors.

4 During maintenance, severe dust storms may stop work on exposed machinery, which must be covered to protect bearings, journals, and open oil lines from sand. Careful cleaning of such parts afterwards is very important.

5 Auxiliary power-switch cubicles should be made dust-tight.

Summarizing our experiences, we have not had any operating problems that could not have been prevented by good housekeeping.

H. G. Hiebeler.[14] The Houston Lighting and Power Company is now operating at two plants six completely outdoor unit installations totaling over half a million kilowatts in capability, ranging in size from the two 60/66 mw preferred standard machines which went into service at Greens Bayou in 1949, to the two 80/100 mw units completed there this year. In addition, there are on the system four outdoor steam-generator installations of 135-mw total rating serving two indoor and two semioutdoor (covered) turbine-generators. The first of these, a 25,000-kw unit at the Gable Street Station, has been in service almost 15 years and one at another plant for over 10 years.

Under construction or in design are four major capacity additions, two 80/100 mw units for the new Webster Station scheduled for initial operation in 1954 and 1955 and two 125/156 mw Joppa-type reheat machines, one for completion in 1955 as an addition to the Deepwater Station, and the other for 1956 for the new Sam R. Bertron Plant. All, with the exception of the Deepwater extension, will be of completely outdoor design. The Deepwater machine will be installed in an extension of the present turbine room in order to utilize existing crane, circulating-water tunnels, and other facilities, and to simplify operation of the combined plant. The steam generator and its auxiliaries will be outdoors.

When this expansion program is completed in 1956 total outdoor plant capability will approximate 900 mw and the outdoor boiler plant 1200 mw. All of the newer and about 85 per cent of total system boiler capacity will be outdoors as well as almost 60 per cent of the total installed turbine-generator capacity of one and a half million kilowatts. The reliability of the outdoor plant has necessarily been carefully considered by our engineers and operators.

While the mild climate of South Texas may be thought more favorable to outdoor operations than that of other sections of the country, changes of weather there are often sudden and accompanied by squalls with high winds and driving rain. The warm southerly winds from the Gulf contribute high humidity and, at certain seasons, fog. Heavy tropical deluges are not infrequent and annual rainfall is in excess of 40 in. Hurricanes occasionally whip through the area.

The operating experience with the outdoor equipment has not been substantially different than that at the indoor stations. A few failures of splashproof motors in outdoor service have been experienced due to moisture; but on all installations prior to 1950 the only motors available were inadequate adaptions of indoor designs. Details of the difficulties in this regard have been previously reported.[15] Manufacturers have developed and now offer greatly improved weatherproof designs for outdoor application with well-protected ventilation openings, air filters, and adequate heaters.

To combat dampness and prevent condensation on sudden atmospheric temperature changes, all outdoor motors are provided with heaters to be turned on when a motor is not in service. Some of our motor troubles are believed due to the operator's failure to observe this precaution where this operation is a manual one. However, similar protection is also required or desirable in our climate for motors and electrical equipment in all but a few locations even in the indoor plants.

Since the heaviest loads and highest outputs of the system come in summer due to air conditioning, irrigation pumping, and other seasonal loads, the maintenance falls into an October 15 through mid-May period. This usually involves some cold and rainy weather which may slow the work slightly but has never stopped it. The majority of these days are actually the most favorable of the year for outdoor activities.

An unscheduled test of the ability to do maintenance under extreme weather conditions developed when on January 29, 1951, a generator-coil insulation failure occurred on one of the 60/66 mw units at Greens Bayou. This was not due to outdoor operation. The wet freezing sleeting "Norther" on at that time continued over 120 hr to establish the longest continuous period of subfreezing temperatures ever reported by the Houston Weather Bureau. During that time, under protection of a temporary tarpaulin-covered canopy, the exciter and generator-end bells were removed and the field was pulled to allow examination of the windings. Sleet, coating the trolley wires of the gantry crane, delayed work several hours. The generator was down about four weeks for replacement of 18 coils. The work proceeded day and night under tarpaulin covers with space heaters being used to prevent sweating. As this difficult job was accomplished under the most adverse conditions the operators are now confident of their ability to handle any foreseeable future maintenance problem.

The completely outdoor plants here have been tested by only one hurricane of comparatively short duration, although the older outdoor boiler units have experienced major storms. Heavy driving rains give frequent fairly complete short-time tests. No difficulties have been experienced. Of course, the indoor stations during a tropical storm are not exactly as snug and tight as those who have not enjoyed such experience might imagine. Large ventilator windows necessary for summer cooling are almost impossible to make tight against rain and 100-mile winds, and in consequence water may be showered down on equipment not designed for such contingency.

Some extra and more frequent painting is required by the outdoor plant if protection and appearance are to be maintained. Valve stems and similar parts present corrosion problems. The extra costs here are offset by building and roof-maintenance savings.

The individual operators and maintenance workers generally prefer assignments at the outdoor stations. The supervisors also favor these plants. When comparing semioutdoor, completely outdoor, and the outdoor units with walk-in turbine-end enclosures, all of which we are operating, there is practically 100 per cent preference in all ranks for the totally outdoor arrangement. It was, however, found desirable to add walk-in enclosures over the standard roll-away exciter housings of the original Greens Bayou units although no trouble actually developed from lack of them in three years of operation; and this will be standard practice hereafter.

Our organization has been well satisfied with the reliability of results from, and experience with, the outdoor plants to date. As stated, plans for the future include a 125/156 mw outdoor installation for the new Sam R. Bertron Station. As the first unit there, it defines, in general, the character of future design for this site which our engineers estimate has an ultimate possible capacity of over a million kilowatts. It is believed that above anything else this confirms the satisfaction of our engineers, operators, and the company management with the outdoor plant.

[14] Superintendent of Power, Houston Lighting and Power Company, Houston, Texas. Mem. ASME.

[15] "The Outdoor Power Station in South Texas," by H. G. Hiebeler, presented at ASME Fall Meeting, Chicago, Ill., Sept. 8–11, 1952.

PAUL BLANCHARD.[16] Utah Power & Light has 425,000 kw installed capacity of which 245,000 kw is in steam. It has under construction two steam plants to add 166,000 kw within the next 18 months.

Temperatures in the area average a little over 50 F with a minimum of minus 35 F. The average annual precipitation is 16 in. including an average of 54 in. of snow. Wind averages 8 mph with maximums of over 50 miles per hour. Under such weather conditions,, the first outdoor boiler has operated since 1936. Three more outdoor boilers have been completed and two additional ones are under construction.

An outdoor boiler installation materially reduces the first cost of a plant by eliminating a large section of building, together with accessories such as heating, ventilating, and cleaning equipment. Operating costs are reduced by eliminating building maintenance and power for heating and ventilating equipment. Savings exceed the additional cost of an outdoor boiler with the necessary weather protection, such as steam or electric tracing and waterproofing. The convenience and accessibility of an outdoor boiler outweigh any disadvantages due to inclement weather. Personnel have been well pleased with operating conditions.

With all the advantages just mentioned, there are still some difficulties that must be solved before satisfactory operation can be maintained.

Freezing weather is the principal problem encountered. In subzero weather safety valves, blowdown valves, water columns, air lines, control lines, and many drain lines, have frozen at one time or another, even though every effort had been made to have these items insulated and traced.

The results of a good stiff breeze in subzero weather are unpredictable. Water columns have been frozen within 2 ft of a steam drum even when heavily insulated. Any openings in the protective covering may result in frozen lines even when tracing is in service. Steam escaping from a safety valve or vent line can be condensed and frozen so fast that the vent can actually be sealed closed.

Steam or electric tracing is used on all accessory equipment. Steam tracing is usually turned on and off seasonally. Some tracing lines vented to atmosphere are controlled by throttling to keep a small plume of steam at the end of the line at all times. This system is generally used with small $^3/_{16}$ or $^1/_4$-in. copper tubing on short runs where the operator can see the end of the tracing line from the control point.

Other tracing lines are drained by means of a steam trap. Such systems are generally used with $^3/_8$ to $^1/_2$-in. copper tubing and impulse traps. An impulse trap has a safety feature in that it usually fails in an open position. Care must be taken to avoid pockets where condensate might collect and freeze.

Electric tracing cannot be used on drain lines from superheaters when high temperatures are encountered during part of the time. Electric tracing is generally easier to maintain than steam tracing and has the added advantage that at very little cost a contact-making thermometer can be used to cut it on or off automatically at any desired temperature.

Large lines, 6 in. and over, are usually protected by spiraling copper tubing or heating cable around the pipe inside the pipe covering. Smaller lines can be protected by paralleling the pipe with the heating element. Lines, 1 in. and under, can often be grouped and wrapped with a spiral heating element and then the whole group enclosed in a pipe covering of an appropriate size. Care must be taken to see that control lines requiring constant head, such as water-level controls, are not in contact with some hot drain line that would affect the water density. Variations in boiler-water level due to this phenomenon have occurred.

[16] Manager of Steam Plants, Utah Power & Light Company, Salt Lake City, Utah.

Control air is carefully dried so that freezing due to condensation is reduced to a minimum.

Electric space heaters are used to protect a full boiler when it is down for maintenance during freezing weather and it is necessary to work in the gas passes. Electric strip heaters are used in totally enclosed motors and in pneumatic controllers to avoid condensation and freezing.

We are thoroughly satisfied with outdoor boilers and have had no insurmountable problems due to the outdoor installations.

R. A. REID.[17] The F. W. Bird Plant of The Montana Power Company at Billings, Montana, is the farthest north of any outdoor plant built to date. The plant went into operation on December 1, 1951. An outdoor plant embodying the design features of this plant is satisfactory for the severe climatic condition of the Montana area.

There have been very few instances where working conditions would have been improved by having the boiler and turbine enclosed, and after two years of operation we feel additional expenditure for enclosure would not be warranted. From an operating standpoint, the personnel prefers the outdoor boiler because of reduced heat, less noise, and fewer cleaning problems encountered. The fact of the installation being outdoor type has not affected the operator pay scale or required additional operators under any conditions experienced—in fact it is believed that with the outdoor design fewer personnel are required. Normal maintenance has not had to be deferred because of weather conditions so far. Major outages are scheduled during mild weather. Although during overhaul of the turbine there could be times when certain phases of the work might have to be postponed for a short time due to inclement weather, there usually is enough other work going on so that the outage schedule would not have to be prolonged by having to wait for the weather to improve.

On the point of the relative cost of maintenance in comparison with an indoor plant, we doubt if cold weather, while admittedly disagreeable, is much of a handicap or that it increases the maintenance cost. Men are more productive in cold weather than under hot conditions. The cost of rigging canvas enclosures is not excessive, due to sufficient structural steel members around the boiler from which temporary enclosures can be hung, such as for soot-blower maintenance, and the like. As for maintenance inside of the boiler proper, the stored heat is sufficient for two or three days' work even in the coldest weather. Outdoor painting costs may be increased somewhat but probably will be offset by the fact of not having extensive turbine and boiler enclosing structures to paint.

Inasmuch as this plant was the first one designed for the Montana weather conditions, which have the most extreme temperature conditions of any outdoor job to date, initial troubles were experienced at a number of points, which have been corrected. The principal items of this kind were:

Trouble was experienced with retractable soot blowers due to inadequate piping drainage coupled with insufficient heating cable and pipe insulation. The piping drainage was modified and additional electrical heating added.

Trouble was encountered during winter months with traps freezing up. The fuel oil lines to the day and oil storage tank are steam traced. The line also furnishes steam for the suction heaters and floor heating coils in the main storage tank. The traps and return lines were exposed with the condensate going to waste. Frozen traps had to be thawed with blow torches.

The drains from the boiler safety valves were originally piped several feet. In mid-winter these drains froze and ice formed on the discharge side of the safety valves, making them inoperative.

[17] Superintendent of Generation, The Montana Power Company, Butte, Mont.

The drains were shortened so they now contain no more than one short nipple and an elbow, which solves the problem. This difficulty could occur on an indoor design.

The forced-draft fans are installed in a plenum chamber with Aerofin sectional coil-type heating coils in the walls. During the first winter season about 150 leaks occurred as a result of frozen tubes occasioned by improper condensate-return piping. The condensate returns from all heating coils, unit heaters, and auxiliary headers terminate in a common condensate tank. Leaky traps caused pressure to build up in this tank which, in turn, retarded the free flow of condensate from the heating coils. This piping has been changed to eliminate the back pressure.

For prolonged shutdowns in cold weather, the boiler is completely drainable, but when it is desired to leave the water in the boiler, salamanders are used to maintain temperatures above freezing. Stand-by electric power is necessary to supply electric tracing and to operate the gas-fired house boiler used for building heat, tracing on the condenser hot well, and instrument piping tracing. Because of limited capacity of the house boiler, equipment taking load from it must be operated at reduced ratings.

Flue gas-sampling lines to the orsat froze on occasions when temperature dropped to the dew point. Considerable trouble was experienced with this until an electric air heater was installed which blows heated station air through the orsat lines back into the boiler when they are not in use sampling gas.

The control valve which admits steam to a heater jacket to control the fuel-gas temperature to the gas-metering house became inoperative during cold weather because it used steam as a valve-operating medium. It has been replaced. The new type uses gas as an operating medium.

The outdoor Foster-Wheeler steam generator has heated walk-in enclosures at each end of the single boiler drum. Instrument piping from the drum to the firing level is enclosed in insulated ducts containing the water column and gage-glass drains, drum-level indicator, recorder and controller lines, drum-pressure gage line, continuous blowdown and water-sampling lines, steam-sampling lines, and chemical feed line. The ducts are heated by radiation from the steam supply and condensate return lines of the unit heaters in the walk-in drum enclosures. A freeze-up occurred when the unit-heater blowers were inadvertently left off. This damaged a bourdon tube of the drum-pressure gage. The feedwater control was put on hand until the ducts could be heated and the lever controller was again made to function.

Cold air pulled through a building vent in the cable vault under the control room froze some instrument lines. This has been remedied by closing off the outside vent.

The soot-blower steam pressure-reducing station is located in the forced-draft-fan room and has a Fisher valve for pressure reducing. This regulator froze during an outage in mid-winter causing the bourdon tube in the controller to rupture. In case of future subzero outages, the normal air inlets through the heating coils will have to be covered with tarpaulins, and this area heated either from the main building with salamanders or with unit heaters.

The induced-draft-fan inlet and outlet damper-control drives and fuel-gas control valve are located outside. The control air lines to this equipment are unheated and depend upon the silica-gel to maintain the dew point below ambient. One case of icing in the induced-draft-fan inlet damper-control-drive pilot valve caused faulty operation. This will be overcome by additional heating of the silica-gel in the air driers. The composite drain header from superheater, economizer, and extended surface-boiler headers froze because it was unprotected. It had to be thawed with blow torches. Damage to the superheater tubes could result from this type of freezing in case of loss of load.

Considerable difficulty was experienced with the induced-draft-fan inlet and outlet dampers due to sticking. The original design and the cold temperatures encountered were contributing factors which caused corrosive flue-gas deposits to build up between the damper shaft and bearing spacer causing the vanes to bind. The damper shaft became immobile to such an extent that drive arms were bent on a load rejection and the connecting shaft between dampers sheared all universal bolts. The trouble was remedied by removing the pipe-bearing spacer and substituting a stuffing box with two rings of packing.

Expansion joints in the exit-gas ducts show signs of considerable corrosion. These are uninsulated and consequently in cold weather severe condensation is experienced. It is planned to insulate or heat these joints in question.

The first winter's operation of this first steam plant on a previously all hydro system presented some difficulties for operating and maintenance personnel with no previous steam experience. However, an outdoor plant in this climate is practical. The problems encountered were mainly due to lack of previous design experience for Montana weather conditions and operating inexperience. It is believed that our difficulties have been overcome.

T. M. Morong,[18] C. T. Eyring,[19] and J. O. Rich, Jr.[20] The Southwestern location of our system, in a region having around 300 days per year of sunshine, led to the early consideration of an outdoor design. After a year and a half of operation, the decision to construct Kyrene as an outdoor plant has been well justified from all major aspects of design and performance (Fig. 15).

The basic thought underlying the design was to erect a plant for the optimum ultimate economy. Consideration was also given to the extremes of temperature in this locality, the range at times being from 20 to 120 F. Direct radiation during the summer increases the upper limit of this range to 140 F. Periodic rains of torrential intensity and heavy dust storms also shaped our thinking.

All the recognized advantages of outdoor construction were realized at Kyrene. A savings of $6 to $7/kw resulted from the outdoor construction. A 50 per cent decrease in operating personnel was realized over an older installation of slightly smaller capacity. This latter fact is attributed to the two main features of the plant: (*a*) Compact arrangement, yet with ease of accessibility to all of the equipment; and (*b*) the use of completely centralized instruments and controls.

*Plant-Design Features.*[21] The main plant design departed slightly from a completely outdoor design, the first of these departures being a curtain wall enclosing all of the major auxiliaries below the turbine deck. This curtain wall is of lightweight concrete block, reinforced for earthquake resistance. Such an arrangement provides adequate climatic protection, both from rain and dust. It also assured a minimum building volume for the plant. Several other advantages resulted from this design. We were able to use standard indoor equipment, both for auxiliaries and auxiliary drives. It was also possible to eliminate the necessity for exterior administration and service buildings on the site. The superintendent's office and control room are located on the turbine deck. Mechanical, electrical, and instrument repair rooms and laboratory are all included in the enclosed structure under the deck. Air washers are used to provide cool dust-free air to the interior of the enclosure, resulting in an extremely clean and dust-free plant, since there are no below-deck

---

[18] Chief Engineer, Salt River Power District, Phoenix, Ariz.

[19] Assistant Chief Engineer, Salt River Power District, Phoenix, Ariz. Mem. ASME.

[20] Superintendent of Steam Plants, Salt River Power District, Phoenix, Ariz. Mem. ASME.

[21] Plant descriptions in *Combustion*, October, 1952, and in *Electrical West*, August, 1952.

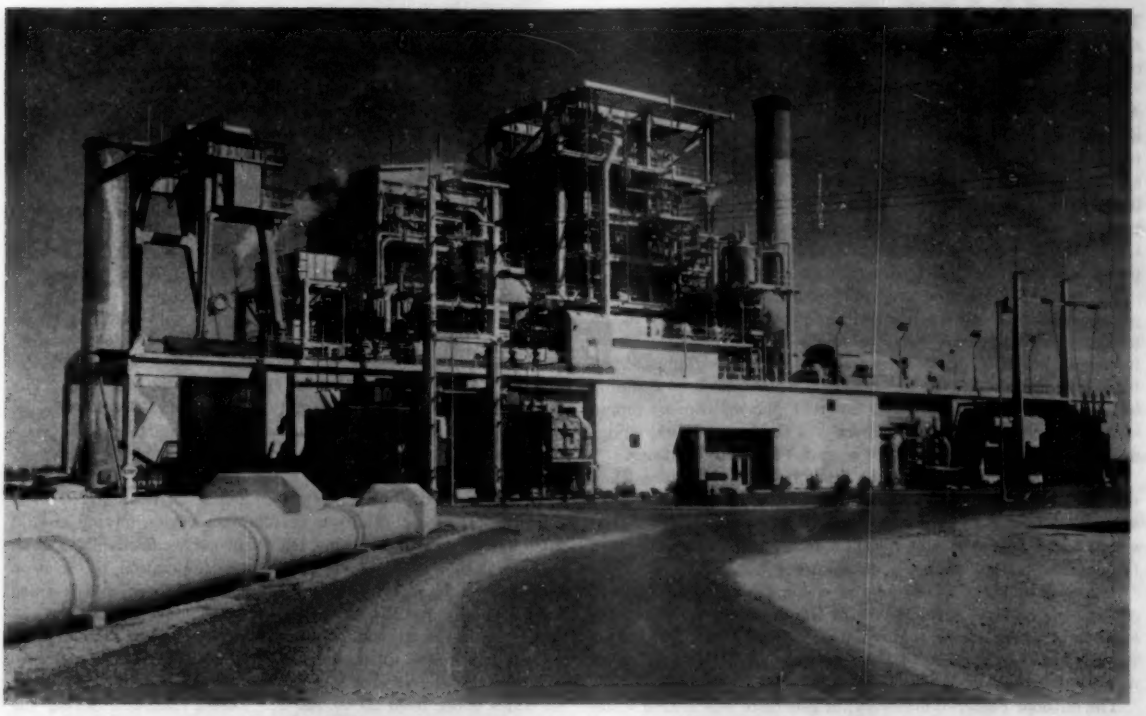

FIG. 15 KYRENE—OUTDOOR STEAM PLANT OF SALT RIVER POWER DISTRICT

windows. This enclosure also gave us the advantage of better maintenance conditions for the day-to-day work on station auxiliaries.

The boiler firing aisle is at the deck level adjacent to the control room. It is completely enclosed for climatic protection.

The 30,000-kw turbine-generator located on the deck or roof of the enclosure has the control end of the turbine in a steel house. The balance of the turbine and the generator are the manufacturer's standard outdoor design. This particular arrangement was the intermediate design of the manufacturer prior to the completely outdoor turbine. Delivery problems prevented our use of a completely outdoor design. A second unit, rated at 60,000 kw, is now under construction at this location. Its turbine-generator is a complete outdoor design.

*Operating Experience.*

*Below Deck Enclosure.*

The small below-deck enclosure has shown itself to need considerably more ventilation than would normally be required in a volume of this size. The incoming heat load per unit volume is high with much radiant pickup from windows and building walls, as well as from the boiler and other thermal vessels. The ventilating-equipment duty is therefore higher than would be needed in a conventional power building. High ambient temperatures were experienced in the switchgear room and resulted in some relay trouble. Additional ventilation of the switchgear was required to correct this. The operators experienced some discomfort in going from a completely air-conditioned control room at 70 F into a station ambient of 100 F. The station hot spot proved to be a stair well with several windows at the top.

These problems were solved by the installation of additional ventilating equipment and by the removal of some windows to decrease the radiant-heat load. This latter move is, of course, effective only in the summertime. But this is, of course, the period of the highest solar-heat load.

*Turbine Enclosure.* The present housing has proved inconvenient during repairs. It is difficult to dismantle and re erect at time of turbine outages. Valuable lay-down space is required to store it at such times. The enclosure requires considerable forced ventilation and adequate air filters to maintain any degree of cleanliness. As previously mentioned, the second unit now being installed at this station has no such enclosure.

*Enclosed Firing Aisle.* The aisle is small in volume with a high ambient temperature. There is a great deal of radiation from the burner fronts. It was found necessary to increase the ventilating equipment and the rate of air change in the area. A more adequate form of boiler-front insulation is required. We feel the advantages of the enclosed firing aisle outweigh any of the disadvantages mentioned here.

*General Operating Experience.* Anyone designing and building an outdoor plant should give considerable attention to the sealing of combination slabs used both as a floor and a roof. If insulation is used under a wearing deck on a roof slab, such insulation should be rigid, such as perlite concrete, foam glass, or a silicate-type insulation. All construction and expansion joints should be sealed with a cast-in-place rubber water stop. These joints should be checked periodically for deterioration and kept well calked.

The outdoor installation of our chlorinator presented some problems because it was basically an indoor type. Extreme climatic temperature changes resulted in some reliquefaction and damage to the expansion-valve seat. Additional insulation of exposed lines corrected this problem.

Painting this type of plant in our Arizona climate also has its problems. Thermal vessels subjected to internal heating have a short paint life when exposed to direct sunlight. We are still

experimenting with a number of paints as a means of solving this problem.

Weatherproof pipe insulation was used on all exposed piping. Repairs to the weatherproofing must be made as soon as the trouble is noted. The deterioration of the inner insulation is rapid once the weatherproofing is broken.

It was found necessary to acoustically insulate the main gas line where it passes adjacent to the chemical laboratory. The small building volume also resulted in some uncomfortable temperatures in an office adjacent to a pipe chase. Increased ventilation of the chase corrected this.

During major turbine outages, it is necessary to secure and protect all dismantled parts to a greater degree than would be required in a conventional station.

We have found that the extreme-temperature variations have resulted in more colds and an increase in time off for operating personnel, over an older conventional installation.

The operators' satisfaction, however, is very high at this plant. Operators have turned down chances for advancement when such advancement required their returning to an older conventional installation. Supervision at the plant also feels very satisfied with the design and operating experience to date. We have also had a good reaction from our maintenance personnel, working both indoors and outdoors at this location.

Management is well pleased with the operating experience and costs at this plant. It is convinced that the curtain-wall protection of auxiliaries is paramount for successful operation of outdoor plants, rather than the somewhat stylized refinery-type outdoor plants in other locations. Satisfactory operation also requires adequate supervisory instrumentation for remote checking. It is also felt by management that the cost of adequate centralized controls has been well worth the investment in reduced personnel requirements. The fact that we are building a second unit of this type is good evidence of our over-all satisfaction with outdoor plants.

J. A. Inwright.[21] Four units are in service at Sewaren; two went in service in 1948 (one in November and one in December), one in October, 1949, and one in July, 1951. The units are as follows:

No. 1—110,000 kw
No. 2—110,000 kw
No. 3—110,000 kw
No. 4—125,000 kw (reheat)

Each is served by its own boiler with no cross connection between units.

The boilers are of semioutdoor construction. The furnaces are all indoors. Part of the superheaters and the remainder of the gas passages are outside. Certain mechanical equipment is outdoors, such as air preheaters, forced and induced-draft fans, and precipitators. The combustion control is pneumatic. The soot blowers are air-operated, air-controlled. Some of these are out of doors.

With this amount of outdoor equipment, certain conditions must be watched. The air for combustion control and for control of the soot blowers must be dry. Driers remove moisture in the air to insure that there will be no freezing down to —40 F. The air is periodically checked for dew point to make sure of this.

The bearings of the forced and induced-draft fans are air-cooled by drawing outside air through cored spaces around the bearings to the suction side of the induced-draft fans. This has been found to be sufficient.

[21] Superintendent, Sewaren Generating Station, Public Service Electric and Gas Company, Sewaren, N. J.

Since the superheaters are of the pendant type and cannot be drained, the temperature within the superheater bank is watched closely during overhaul periods in extreme cold weather. Sometimes warm air is blown into the furnace by erecting a steam coil and blower at the furnace access door.

Oil for use in the outdoor equipment is specified to have the proper viscosity at low temperature. The same oil is used summer and winter and has been found satisfactory for ring-oiled bearings and in the hydraulic couplings.

Most of the time, the outdoor equipment can be easily maintained. At times wind breaks made of tarpaulins have been required to protect the men. It has been found that in extremely cold weather it takes two to three times as long to do close tolerance work such as lining up rotary equipment.

There is a considerable amount of exposed steel which must be painted both for protection as well as looks. Experience with this has been limited because of the short period of service.

In the five years the plant has been running, there has been only one time when the temperature was below freezing for a long period of time. This was in February, 1950, when the average temperature was about 24 F for 12 days. The minimum temperature during this period was 8 or 10 F. An extended outage of No. 1 unit included this period. It was possible to schedule the work so that the effect of the low temperature on the over-all maintenance work was negligible.

Because the forced-draft fans are outdoors the air-heater inlet temperatures are controlled to reduce fouling. This is done by recirculation in three of the boilers and by heating the inlet air with steam in the fourth boiler. When burning oil even with these precautions, the air heaters have to be washed several times a year.

The operators who handle the equipment are stationed inside, but make periodic inspection trips outside and visit each piece of apparatus. The temperatures of the bearings and motors are remotely indicated in the control room.

All in all, for this area and its weather conditions, operation with semioutdoor construction is satisfactory.

J. B. Saxe.[22] This subject is extremely pertinent as it constitutes the most important means of combating the inflationary rise in the cost of power-plant construction. While little can be done to reduce costs in many components of the power plant, engineers have been able to assume control of the situation to a limited degree by minimizing the structure and placing some of the equipment outdoors.

There is no question but that a substantial saving in first cost can be achieved by so doing. The savings will vary widely depending on the basis of the comparison, that is, whether the enclosure to be eliminated is corrugated asbestos or brick exterior and tile interior, but appear to revolve around a figure of $5 to $7 per kilowatt of capability.

Even with some increased maintenance and inconvenience, a saving on this order is most attractive. It would therefore be of greater interest, instead of discussion whether equipment should be placed outdoors, to discuss the extent to which it should be placed outdoors.

Examination of the source of the savings reveals that most of the gain comes from placing the boilers and heaters outdoors. In its essence, the saving consists in elimination of the siding and its supporting girts, of the roof, and of the ventilation, less provisions for outdoor operation. The boilers and heaters are the major dissipators of heat and in southern climates it is practically impossible to provide satisfactory ventilation if they are enclosed. The only fully satisfactory means of providing comfort is to elim-

[22] Chief Engineer, Gibbs and Hill, Inc., New York, N. Y. Mem. ASME.

inate the enclosure. In locations of considerable precipitation, it is necessary to build and take down a temporary roof over the boilers during construction. Since the cost of this operation very nearly approaches that of a permanent roof, the construction of the latter is more logical. In northern climates, enclosure of the steam drum still appears desirable. The oil industry has employed plastic casings outdoors with results that would not be considered acceptable by the utility industry. If a plastic casing is acceptable when enclosed and steel-cased setting necessary outdoors, a substantial portion of the saving disappears. However, there are now some plastic settings on outdoor installations which show promise of considerable permanency and it is questionable whether such a difference is proper in the comparison. Even in the severest climates, there appears to be little justification for enclosing dust collectors, induced-draft fans, and tanks. In cold climates, facing a hot casing with winter on the back while handlancing a furnace is not conducive to good health of the operator. In such locations, particularly liberal furnaces and ample means for cleaning the furnace from a more comfortable spot are important. With the introduction of furnace television, a great many operations formerly conducted manually at the burners can now be conducted safely, remotely from the control room, and enclosure of the burners if located at the rear of the boiler no longer appears necessary. Electrically driven and controlled soot blowers appear to be superior for outdoor installations. The problem of cold air on the cold end of the air heater appears to have been satisfactorily and economically solved by introduction of the steam air preheater. While some of the outdoor boilers in northern climates have not yet experienced a really severe winter, many of the problems have been solved and such an installation appears feasible and economically attractive.

While considerable structure is eliminated in placing the turbine outdoors, the saving is relatively small due to the high cost of the gantry crane and walk-in housings. So far, attempts to lower the cost of these two elements have not been very successful. Also only a relatively small amount of heat is dissipated in the turbine room and the ventilation necessary is not very costly. In warm and arid areas, the taking of this relatively small saving appears to be amply warranted, particularly if the climate is being promoted and the utility is part of the act. However, in the colder and higher-precipitation climates, the operators are inconvenienced, and to some extent maintenance costs are increased and outages prolonged so that the question as to whether the saving should be taken is much more debatable.

The problems involved in protecting instrument and control lines against freezing appear to have been solved satisfactorily. Some outdoor installations have experienced excessive repainting costs. More attention should be given to this subject and to the use of materials which do not require painting.

M. D. Engle.[24] Present economic conditions require that we find ways to continuously reduce the unit cost of the facilities required to supply electrical service to our customers. This, of course, applies to all facilities, generating stations, transmission, distribution, and service facilities.

While it is true that over the past years we have done a good job in increasing the thermal efficiency and reliability and in reducing the number of men required to operate and maintain our generating stations, this is not enough. Even though our present-day stations, with all these improvements, cost less per kilowatt of capacity than the stations of years ago, when we correct the present costs for the lower value of our dollars, it is still not good enough in view of the fact that our income is in present-day dollars which are not corrected for inflation. We must retain and improve upon these achievements of the past and at the same time find ways to reduce the unit cost of construction.

As our interconnections are increased in capacity we should take full advantage of the possibilities and economics of larger and larger units. Staggered construction between interconnected systems and proper short-term firm power contracts should permit economical financing of the larger-size units.

The adoption of the outdoor or semioutdoor design of generating station also should help materially in finding a way to construct the generating stations at a lower cost per kilowatt of capacity and many companies are proceeding along this line.

In these semioutdoor stations, by proper design, all of the equipment which needs "walk-in" enclosures can be enclosed in low unit-cost enclosures, and most of the operating personnel also will be located inside.

Feedwater regulators, hp heater drainage controls, evaporator drainage controls, and other similar equipment, sometimes installed out of doors in such stations, can just as well be located inside.

However, there are many other features of design which should be considered seriously and should further reduce the unit cost of construction. Some of these are as follows:

1 The turbine-room basement should only be as far below grade as necessary to obtain an economical foundation below the turbine-room mat. Many studies have shown that it is not economical to lower the condenser just to reduce the head that must be developed by the circulating-water pumps. Neither is it economical to raise the condenser basement to the operating grade just in order to have it at that level.

2 If the level of the condenser above the water level in the river is such that a siphon cannot recover all of this difference in level, then the head which must be lost can be utilized to force the water back to the river at a higher velocity through a smaller than normal discharge conduit and a worth-while saving in the cost of construction can be obtained.

3 When the condenser is located closer to the operating grade, the intake and discharge tunnels do not need to be as far below grade and consequently cost less to install.

4 Reinforced-concrete pipe in place of "formed-in place" concrete tunnels are usually less expensive.

5 Most of the industrial buildings constructed today are of concrete block. Good-quality concrete blocks have demonstrated that they have a long life and are a satisfactory and economical material of construction. It would appear logical therefore that concrete blocks should be considered seriously for the principal buildings and enclosing walls at a generating station.

6 Reinforced concrete silos with offset conical bottoms have been used as coal bunkers for many years and have been found very satisfactory. They are more self-clearing than rectangular bunkers, they are cheaper per ton of coal stored, and they also can support the coal conveyers and housing above them. It would appear that the reinforced-concrete silo is the logical type coal bunker for coal-fired steam-electric stations.

7 While tile floors for turbine rooms and boiler rooms are much better looking, concrete floors are less costly.

8 A porous crushed-gravel surface for the station yard is low in cost, areas that settle can be filled to grade cheaply, and rain water can usually be allowed to seep into the ground below without requiring an expensive pipe drainage system. It would appear that the same type of gravel surface should be suitable below the outdoor boiler instead of the concrete pavement frequently provided.

9 A large-capacity caterpillar crane can be used at outdoor stations for many purposes in place of permanent steel structures and hoists. Some of these are as follows:

(*a*) Lifting intake bar racks and screens.

[24] Mechanical Engineer, Pennsylvania Power & Light Company, Allentown, Pa. Fellow ASME.

(*b*) Installing and removing stop logs at intake and discharge structures.

(*c*) Lifting rotors and motors of ID and FD fans.

(*d*) Overhaul of outdoor pumps and motors.

(*e*) Repair of bulldozers and carryalls and locomotives.

(*f*) Repair of car dumpers and coal grids.

(*g*) Maintenance of transformer and OCB bushings.

10 The outdoor steel standpipe, supported at grade, has been found to be an economical means of water storage by most all municipal water supply systems. It would appear to be the most economical means of storing service water and condensate at steam-electric stations. A fire pump can be installed for any higher pressures required.

11 A single-track hopper for unloading railroad cars and reclaiming coal from storage can usually be used instead of separate pits for the two purposes.

12 A recent survey has indicated that the capacity to unload railroad cars by means of a "car shakeout" is usually limited by the capacity of the hopper provided. By installing a track hopper of adequate capacity, the large investment for a car dumper might be delayed a number of years or omitted at a new station.

13 Where the ash-disposal line is not too long, the jet pump is lower in first cost than motor-driven ash-pump installations.

14 A single three-phase step-up transformer for the main generator is considerably less expensive than three single-phase transformers and operating experience indicates that the additional cost of the single-phase transformers and a spare cannot be justified.

15 Service at 4000 volts to the larger auxiliary motors results in lower cost than 2300 volts.

16 A single 4000-volt bus for each unit seems to be in keeping with the unit construction used elsewhere in station design. The economics of a second or third auxiliary bus bears careful scrutiny.

17 Some studies have shown an engine-driven fire pump less expensive than a separate source of electrical service.

These few examples are presented only as an indication that even after we adopt the outdoor or semioutdoor design of station, there are still many features of design that may be changed to reduce further the unit cost of construction. It can and must be done.

M. K. Drewry.[35] Cost reduction appears the single impelling urge of omitting enclosures. Evaluation of cost reduction is therefore vital.

The investment savings in omitting a typical brick wall costing $3.50 per sq ft contrast importantly with the investment savings when omitting asbestos-cement siding costing 70 cents per sq ft, only $^1/_5$ as much. That outdoor design should be compared with minimum-cost practical enclosures seems obvious.

Asbestos-cement siding ("corrugated transite" is one name for it) has been found to be a practical and desirable boiler-room enclosure. For turbine-room enclosure, 1 in. of insulation can be justified, causing doubling of the 70-cent cost to $1.40 per sq ft, erected. These costs obviously do not include supporting steel, to be treated later.

Twenty-five years' experience in an unfavorable environment has proved this material of practically zero maintenance and of continued good appearance. The asbestos fibers and the particular siding design result in a concrete that is more nearly permanent than even typical concrete.

With a maintenance-free weatherproof enclosure protecting the great area of all boiler-room and turbine-room surfaces, some of which are of high maintenance when exposed to the elements, long-time structural maintenance costs reach a minimum.

Boiler casings, containing flue gas of 100 F moisture dew point and with corrosive sulphur compounds that condense at higher temperatures, though protected to a degree by brickwork and insulation, seem vulnerable to the low metal temperatures of the outdoors. Walkways and platforms of open grating to avoid snow shoveling and cleaning need to be galvanized or equally corrosionproofed to qualify for reasonable maintenance. Painting of all surfaces needs to be more frequent than for indoor equipment. Thus there seems a good probability that asbestos-cement enclosed plants will prove of considerably lower structural maintenance than will outdoor ones.

Construction time and temporary construction sheltering during winter weather are importantly related to outdoor construction, at least in the northern states. Experience proves the need of sheltering workmen and equipment during construction if erection is not to be delayed substantially. The added time of erection can vary markedly, which precludes stating any estimates, but possibly some readers are acquainted with 50 per cent erection labor efficiency resulting from half the time being spent in men warming themselves during coldest weather conditions. In a recent 120,000-kw installation, $100,000 direct saving in using asbestos-cement siding instead of brickwork was augmented by very approximately an equal indirect saving because of greatly more rapid siding erection permitting enclosure before coldest weather. Delays in starting new apparatus are usually very costly.

Heat saving resulting from boiler-room enclosure pays investment charges of a substantial share of low-cost shelter. The boiler-unit heat-loss difference of indoor and outdoor construction of the foregoing case is estimated at $^3/_4$ per cent of the boiler thermal output. The resulting net coal-cost difference is estimated at $^1/_4$ per cent assuming that this $^3/_4$ per cent greater heat loss of the outdoor boiler plant would be replaced by steam extracted from the turbine after doing $^2/_3$ of the work it would do otherwise. In the case mentioned the capitalized value of $^1/_4$ per cent is $75,000, or 94 per cent of the cost of the boiler-room siding, its supporting steel, windows, and roof, as follows:

Boiler-Room Enclosure Costs

| | | |
|---|---|---|
| Corrugated asbestos siding | $27,000 | |
| Structural steel (roof purlins, horizontal girts, and vertical girt posts) | 30,000 | |
| Aluminum-frame windows | 6,300 | |
| Aluminum coping | 2,200 | |
| Monolithic concrete roof and parapet walls | 8,000 | |
| Roofing | 6,600 | |
| Total net cost of enclosure | $80,100 | |
| Heat saving value of enclosure | $75,000 | (94% of $80,100) |

Wall and roof supporting steel is usually integrated with boiler unit, access, and other steelwork, minimizing its incremental cost. In the case cited practically no columns or beams could be omitted upon omission of siding and roof, whereas outdoor construction necessitates many compensatory extra costs.

Simply the boiler-room comparison is cited because there seems no adequate inducement to take the long chance of needed turbine maintenance in mid-winter in this climate without complete turbine-room shelter.

That outdoor construction is a necessary defense against destructive turbine-oil fires may be stated in favor of omitting shelter. However, in the foregoing case, shelter costs include favorable isolation of the oil system of each unit, effectively permitting other units to continue in service and helpfully providing adjacent walls through which to fight the fire. That this isola-

[35] Chief Engineer of Power Plants, Wisconsin Electric Power Company, Milwaukee, Wis. Life Member ASME.

tion system solves the problem better than does outdoor construction seems a fact.

Outage time is usually impressibly expensive. An extra day per year of the unit mentioned is as costly as $60,000 added investment. Thus, if unfavorable weather prolongs outages a total of 1 1/3 days per year, the $80,100 incremental cost for roof and walls can be paid, with the heat saving as computed left as a net gain.

That the question of indoor-versus-outdoor power plants is one of geography and circumstance probably will never have a simple answer is suggested. For northern states our company's experience suggests that inexpensive shelters are well warranted. Heat savings paid 94 per cent of their cost in a recent case. The substantial gains of importantly facilitating construction and maintenance that enhance the availability of the expensive apparatus are net savings of no little magnitude.

E. C. GASTON.[3] The Southern Company system embracing Alabama Power Company, Georgia Power Company, Mississippi Power Company, and Gulf Power Company will by the latter part of 1955 and since 1949 have completed 37 new steam-generating units with a total capacity of 2,234,000 kw.

Although this system is located in an area where it might be generally expected that outdoor or semioutdoor designs would be employed, this has not been the case. At only one location has this type of construction been employed, namely, at Albany, Georgia, which is in the south-central part of that state. At this location two 22,500-kw units are installed in one plant, utilizing a semioutdoor type of construction where the boilers only are located outdoors. This plant was constructed in the 1947–1949 period.

A number of considerations may explain why the outdoor or semioutdoor type of plant has not been employed more frequently in the plant designs on this system. In the first place, it is a combination hydro and steam system, the ratio of capacity being approximately 25 per cent hydro and 75 per cent steam. The annual wet season generally occurs in the early part of each year. Likewise, seasonal load variations are such that the system load is lowest in this same period. Because of this particular combination of factors, the plant outages for maintenance must generally be scheduled during the first five months in each year.

Owing to the large number of units now installed and because of an established practice of removing turbines for inspection every two years, there is a large number of units which must be inspected each year and this fact makes it necessary to plan and schedule these outages with accuracy and with requirement for minimum amounts of time for each unit. Since the outages must be scheduled during the rainy and colder season of the year, maintenance work can be more efficiently accomplished and more quickly completed where it can be performed inside the protection of a building.

Because the system covers a tremendous territorial area (approximately 113,000 sq miles) with plants scattered throughout the area, there are wide variations in fuel and operating costs between the individual plants. Fuel costs may vary from a low of less than 15 cents per million Btu to a high of more than 30 cents per million Btu. When a low-cost unit is down for inspection, the energy which it would have produced must be supplied from other and higher-cost sources. It is therefore most important that outage time be limited to only that time which is absolutely essential for maintenance, since an increase in outage time could involve costs of $1000 to $3000, or more, per day for displacement energy depending on size of the unit and the source and location of the substitute unit.

[3] Vice-President and Chief Engineer, Southern Services, Inc., Birmingham, Ala. Mem. ASME.

The greatest savings from the construction of an outdoor or semioutdoor type of plant are effected when a "ranch-style" layout can be employed. This type of layout spreads the plant over a wider area and all major equipment, foundations, etc., are located at ground level. A majority of our plants are located on rivers which fluctuate 30 to 40 ft between extreme low flow and maximum flood-water elevations. In such locations, the condenser and other major equipment cannot be elevated sufficiently to be protected against flood damage without incurring prohibitive cooling-water pumping costs under low water and even under normal water-flow conditions. In a plant design of this type it will be generally found that approximately 1/3 of the powerhouse building will be below ground level and 2/3 above ground level. Since building volume below ground level costs approximately twice as much per cubic foot as it does above grade, it develops that the superstructure represents only 50 per cent of the total building cost. The potential savings resulting from the use of outdoor construction is therefore proportionately reduced.

In any plant, whether it be an indoor or outdoor type of design, consideration must be given not only to the initial cost of the plant but also to the maintenance and operating costs which will be incurred after it has been placed in operation. Because of the heavy rainfall (approximately 60 in. average per year) and also because of extreme and frequent changes in atmospheric conditions, including temperature, a judgment factor must be applied to cover the extra maintenance which undoubtedly will be incurred in adopting outdoor or semioutdoor designs. The cost of this added maintenance, after being capitalized, must be charged against the outdoor design and the amount of this penalty will vary according to judgment after making an unbiased evaluation of all of the factors which contribute to maintenance.

Despite the fact that there is only one plant constructed on this system which utilizes semioutdoor construction, the outdoor idea has not been completely overlooked. On the plant designs, which are currently being used, the induced-draft fans, dust collectors, stacks, recirculating fan, oil pumps, oil heaters, storage tanks, etc., are located outdoors. All of this equipment is located at ground level, and most of it had previously consumed building space. By locating these and other smaller items of equipment outdoors, it has been possible to effect a substantial reduction in building volume, structural steel, and other major components of building cost.

Since the basic problem is to reduce the cost of building structures, there can be only two avenues of approach, namely, either to reduce the cost to an acceptable minimum, or to disregard the value of a protective housing and completely eliminate the enclosure. Our studies have dictated that we should follow the first approach. Recent experience has demonstrated that building costs can be substantially reduced through the utilization of less expensive materials and the elimination of nonessential ornamental features. As an example, corrugated-asbestos siding has been found by experience to be an adequate substitute for brick walls. Its use effects a saving of approximately $3 per sq ft and the resulting architectural appearance of the building is not at all displeasing.

Numerous studies have been made and many figures have been quoted covering the estimated amount of saving in construction costs which can be affected by utilizing outdoor or semioutdoor designs. There is a wide variation in the cost reductions which have been predicted and which have been reported. Perhaps the primary reason for the wide variation in the figures is that the actual saving which can be effected is a function of the base cost of the plant on which the savings are measured. Employing principles and methods of reasoning as generally outlined in the foregoing and without the use of outdoor or semioutdoor designs, the costs of new steam-generating units added to The Southern

Company system have been most encouraging and compare favorably with the very lowest costs reported by other companies without regard to the type of construction used.

E. J. GARBARINI.[27] An inherent advantage for the constructor in an outdoor power plant is the accessibility afforded for placing equipment and erecting component parts of the structure and apparatus. With the improved accessibility and with proper scheduling to have foundations and supports ready to receive apparatus upon its arrival at the job site, very often equipment and material can be unloaded from a railroad car by a truck crane and hauled directly to its permanent position, thus reducing cost by eliminating rehandling and also minimizing storage space requirements.

Better accessibility permits increased and more efficient use of mobile-power equipment to erect plant equipment and piping. Trucks and truck cranes can be utilized fully to place many items of apparatus in final position.

Scaffolding costs are reduced as a result of the omission of lighting and painting work in high places over operating levels.

Natural daylight affords better visibility than artificial lighting, and unless night shifts are used the cost of maintaining lights during construction is reduced.

Eliminating the building structure removes the need for some relatively high unit-cost operations, such as placing reinforced-concrete floors and roof decking at considerable heights above ground level.

Where the main crane does not have the capacity to lift the heaviest piece of the generator to be set during erection, the rigging and handling operations which are required are simplified by outdoor over indoor construction, especially as compared with indoor construction involving temporary omission of masonry building walls until getting heavy pieces moved inside.

The over-all field construction cost of an outdoor plant is normally less than for an enclosed plant of comparable design because of omitting certain elements of construction and thus reducing the number of units of work to be accomplished.

As the total number of work units is reduced, the total labor force can be smaller. This is of special importance in an area where manpower is in short supply.

However, the advantage of easy access is somewhat counterbalanced by the lack of protection for performing certain operations. As the severity of climatic conditions increases, this lack of protection can more than completely offset the gain from accessibility.

It is generally necessary to provide temporary shelters for a number of reasons, such as the following:

(*a*) Protection of workmen from sun, wind, rain, and cold.

(*b*) Protection of equipment from wind-borne dirt and rain.

(*c*) Protection of equipment from temperature changes during alignment or setting to close tolerances. The main turbine-generator is the most critical piece of apparatus in this connection.

(*d*) Protection of insulation from rain during application.

Some items of work are more expensive for outdoor construction, as for example, exposed conduit must be weatherproof, some slabs must have weatherproof membranes to act as roofs, and so on.

Inclement weather can be a problem if the schedule is tight, particularly if critical operations like turbine erection must be done in bad weather.

Although specific conditions will determine individual situations, in general, the over-all field construction costs are lower for outdoor plants than for indoor plants.

[27] Area Manager, Power Division, Bechtel Corporation, Los Angeles, Calif.

M. W. BURLESON[28] AND V. L. WHITACRE.[29] Since we are interested in this development only to the extent that it affects the life and performance of the thermal insulation, we are in no position to comment on the relative advantages and disadvantages except from the insulator's viewpoint. While we believe many people think of the insulation as a minor item in this era of high temperatures, it actually is no longer so minor, constituting about 5 per cent of the total cost of the plant. It, therefore, does deserve some close attention.

There is no question but that the insulation problem is vastly complicated when the protection of the building is removed. Unfortunately, insulation is not elastic and will not stretch. The inevitable result is that when equipment and piping expands the insulation must move and open up in places.

Where the plant is protected by a building, the problem is relatively simple. A poor job makes its own expansion joints in the insulation when the equipment expands and while the appearance may leave much to be desired the insulation will perform after a fashion. With a high-grade job, expansion joints are normally provided in the insulation so that the finish is not cracked by movement, the appearance is good and the insulation performs as it should. But even on a high-grade job there are, owing to interference and congestion, many places where the insulation cannot really be applied properly.

When the protection of the building is removed, all of this insulation must be weatherproofed. This is accomplished with asphalt-saturated felts, asphalts, sheet metal, asbestos-cement sheets, and other materials. It is relatively easy to apply many of the sheet or felt materials to straight piping effectively, but becomes extremely complicated over irregular surfaces, fittings, and similar equipment. The only practical means at present is to protect these areas with asphalt mastics.

The contact of mastics with hot-metal parts, the improper application of mastics, disregard of movement due to expansion (refer to Figs. 16, 17, 18), and other factors result in protection of the insulation which cannot be entirely weatherproofed.

[28] Johns-Manville Company, New York, N. Y.

[29] Insulation Manager, New York Power Products Department, Johns-Manville Sales Corporation, New York, N. Y. Mem. ASME.

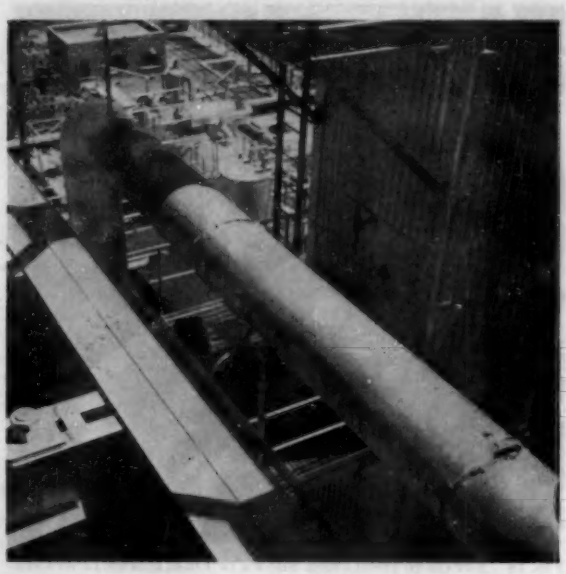

FIG. 16 VIEW SHOWING EFFECT OF EXPANSION AND SINGLE-LAYER CONSTRUCTION ON PIPE INSULATION WEATHERPROOFING

When the unit is in operation, the majority of the piping is sufficiently hot so that water which enters the insulation is quickly evaporated. In such cases, little harm apparently is done other than to increase the heat loss from the equipment. On the other hand, where the unit is shut down, water remains in the insulation and may result in serious corrosion of piping and equipment and increased insulation maintenance costs.

All of these factors add up the following:

1 Equipment and piping must be designed to be insulated (Figs. 19 and 20).

2 The specifications covering the application and weatherproofing of insulation must be far more complete than previously. In present practice, the weatherproofing details are largely designed by the insulator who applies it.

3 The reliability of the insulation contractor becomes of greatest importance.

4 Some areas are so complicated that they should be housed anyway. Examples are feedwater heaters and the piping that surrounds them.

5 Frequent close inspection and maintenance of insulation.

There is another problem. Where outdoor power plants are built in climates that produce below-freezing temperatures at

FIG. 17 CLOSE-UP OF INSULATION SHOWN IN FIG. 16

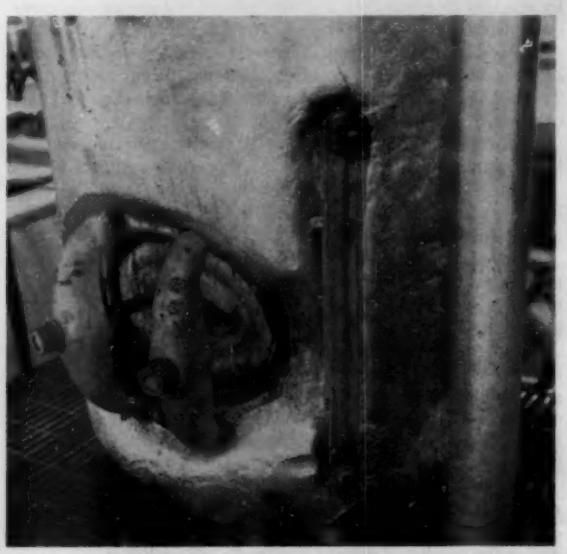

FIG. 19 INSULATION DESIGN INADEQUATE
(Glass should have been far enough from deaerating heater to permit proper insulation.)

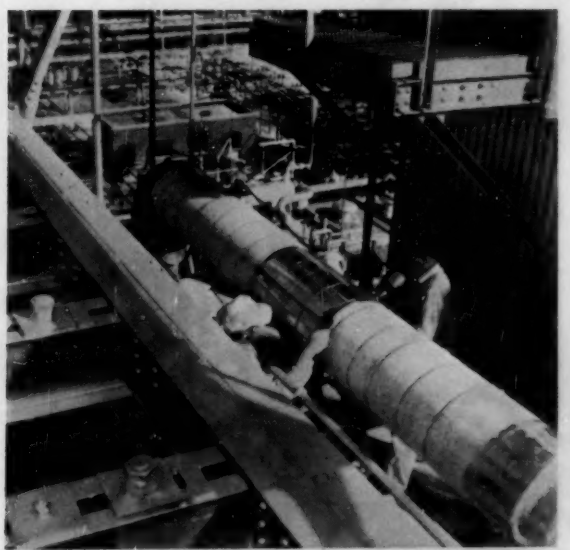

FIG. 18 REPAIR TO INSULATION SHOWN IN FIGS. 16 AND 17 BY CONSTRUCTION OF EXPANSION JOINTS AND APPLICATION OF NEW WEATHERPROOFING

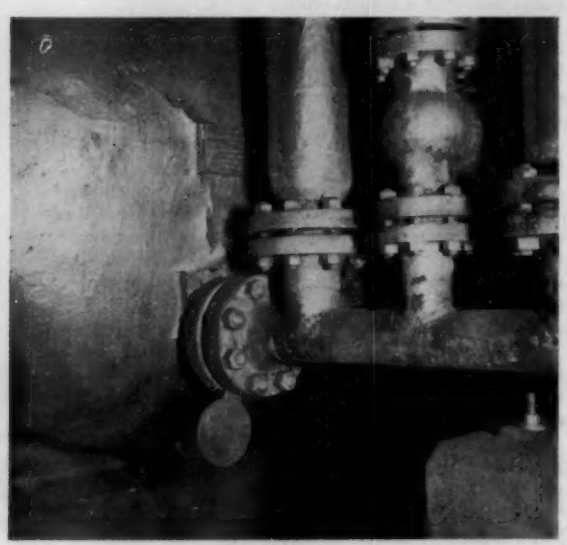

FIG. 20 BLOWDOWN TANK PIPING CONNECTION
(Original insulation failed and was not replaced. Congestion is too great to permit proper weatherproofing. This type equipment would be better under cover.)

times, all control lines and intermittent lines must be protected. This requires heaters of some sort on the piping and insulation to enable the heaters to be effective. Since these are not operating a large part of the time, there is no heat in the piping to dry out water that may leak into the insulation. Unless carefully weatherproofed, this condition can be a problem. Since the major problem is produced by shutdown periods on all heated piping and equipment, we have here a class of piping which is a major problem all of the time.

In conclusion, provisions for metal expansion and insulation protection for indoor installations cannot be translated directly into outdoor installations. Because of climatic conditions an outdoor insulation-protection specification acceptable in the southern climates would not be suitable for the northern climates.

The art of insulation protection has not progressed to the point where it is entirely acceptable to the exacting requirements of utilities, and it is only by close co-operation between the user and the manufacturer of insulation and insulation protections that a suitable specification can be developed.

H. C. Drake[30] and W. E. Moore.[31] In selecting insulation for outdoor service, it is well to keep in mind three major points: (1) Will it stand up well under the more rigorous conditions of outdoor service? (2) Will its efficiency remain fairly constant during exposure over long periods—5 years, 10 years, or more? (3) What additional allowance should be made for labor costs and erection time, as compared with an indoor job?

A standard method of assuring durability and sustained efficiency is the application of a 22-gage metal jacket over conventional insulating material. Higher labor costs for this additional weather protection are to be anticipated as a result. Hunter aluminum insulation simplifies the problem of choosing outdoor protective insulating materials by meeting the heavier demands of outdoor service with one prefabricated covering, thereby reducing erection time and costs. This material is equally effective for indoor application, but for the purposes of this discussion its outdoor features will be stressed.

*Product Description.* (*a*) *Physical.* Unlike most conventional materials, this product is designed in individual units, completely shop-fabricated and easily handled. Each unit is composed of a series of aluminum-alloy sheets, separated by $\frac{1}{2}$-in. dead air spaces, and held in place and supported by material of low heat conductivity.

The Hunter Aluminum Insulated Expansion Joint and/or Hanger Cover is engineered and fabricated to fit over existing hangers. The cutouts for the hanger support are incorporated in the insulation to receive the hanger support proper. The general design arrangement is similar to Hunter Aluminum Pipe Covering with the exception that it nests over adjoining pipe insulation.

One end of the expansion joint is mechanically secured to the adjoining pipe covering and is packed and sealed with calking compound. The opposite end of the expansion joint incorporates a self-sealing device that nests around the outer periphery of the adjoining pipe covering which extends partially into the expansion joint body. This arrangement permits expansion and contraction within the expansion joint itself, eliminating cracks and fractures as experienced in conventional block-type insulating material.

(*b*) *Technical.* An understanding of the heat-transfer principles used in the design of Hunter aluminum insulation is helpful, we think, in appreciating its value as an outdoor insulation. Fig. 26 illustrates the three principles used, namely, radiant, convection, and conduction heat transfer.

Heat emitted from the pipe heats up the adjacent confined air

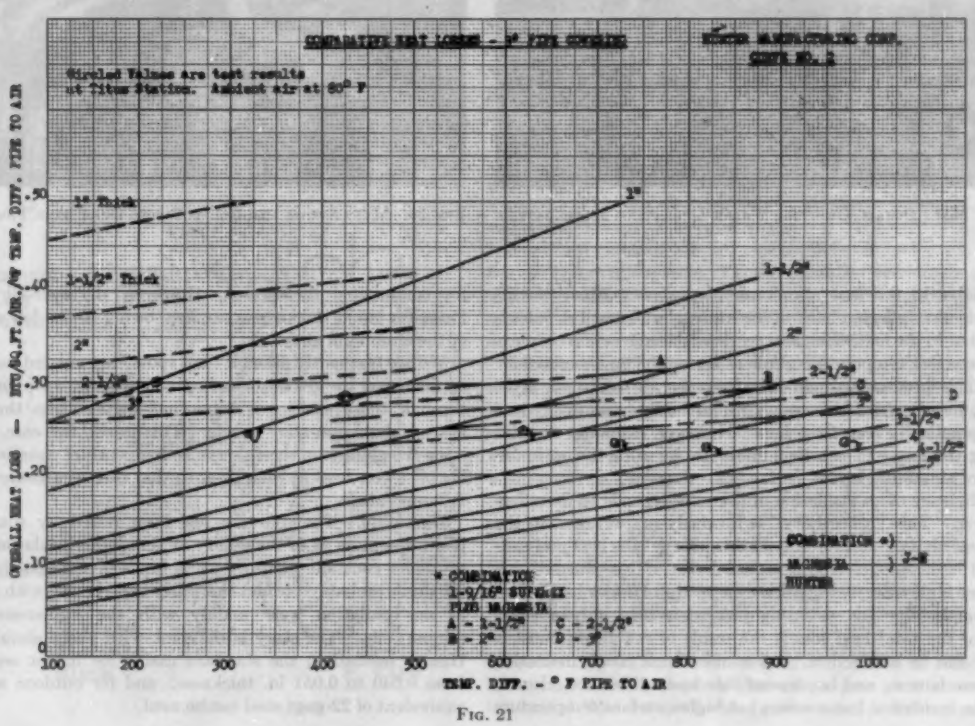


Fig. 21

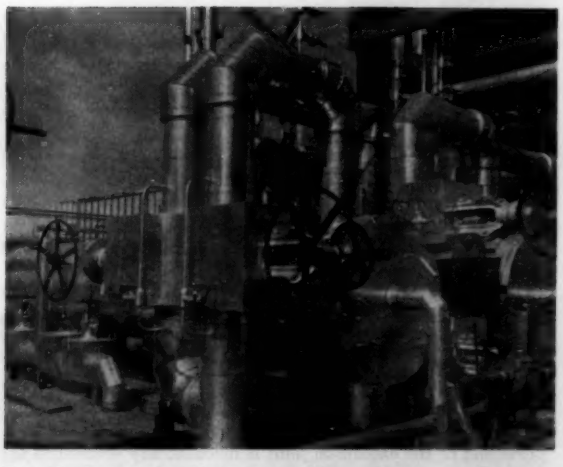

FIG. 22 FEEDWATER HEATERS AND PIPING OPERATING TEMPERATURE 800 F

FIG. 24 INDUCED-DRAFT FAN OPERATING TEMPERATURE 360 F

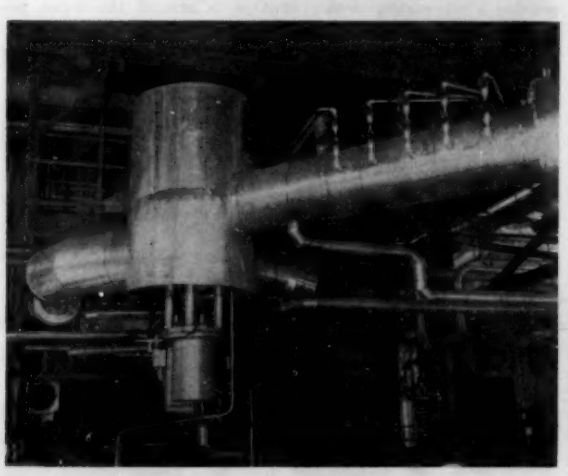

FIG. 23 MAIN STEAM THROTTLE VALVE OPERATING TEMPERATURE 1000 F

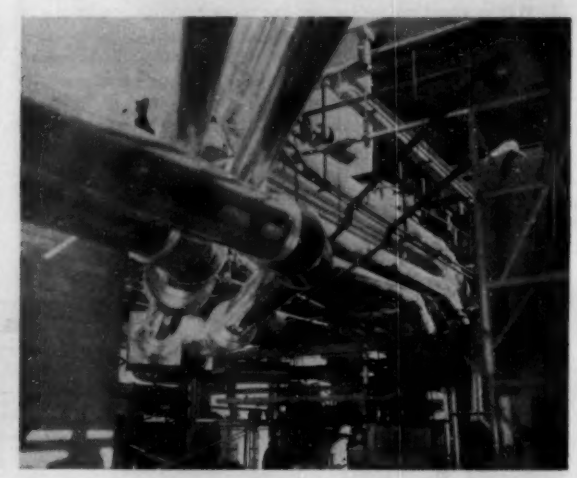

FIG. 25 MAIN STEAM AND BLEED PIPING OPERATING TEMPERATURE 1000 F

and radiates to the first aluminum-alloy sheet. Most of this radiated heat is reflected back to the source, but a small portion is transmitted to the first sheet, as a result of the convection currents set up through a temperature gradient across the first confined air space. This progressive heat-transfer process is repeated, layer by layer, and if carried far enough, would finally result in a reduction to practically zero heat loss. However, economy dictates confining the loss to a practical minimum by using the optimum number of aluminum layers.

The efficiency of an insulation of this sort depends on its reflective power. This "reflectivity" is inversely proportional to the metal's emissivity—or radiating power. To get the best performance and highest efficiency, a material of very low emissivity—hence very high reflective qualities—is used in Hunter insulation.

Since emissivity—or radiating power—is low, only a small portion of the total heat loss is the result of radiation; most is actually due to convection. On conventional block insulation the reverse is true, and because of this basic difference, Hunter aluminum insulation has a somewhat higher surface temperature for comparable thicknesses. However, the over-all Btu heat losses for equal thicknesses are less, owing to the low emissivity of the aluminum alloy.

We are frequently asked if "hot spots" are created on the outer surfaces over the low heat conductivity spacers, since conductivity through these spacers is somewhat higher than through the spaced aluminum-alloy sheets. This is not the case, however, since the aluminum sheets serve as temperature equalizers, drawing off excess heat at each layer so that surface areas are uniform in temperature.

*Durability.* The question has been raised by some power-plant operators as to the ability of aluminum insulation to stand up under constant exposure to all kinds of weather. The basis for this is probably the fact that early experiments with aluminum as an insulation were mainly with the lighter-weight aluminum foils. The story is different with sheet aluminum. In Hunter insulation, the standard casing for indoor service runs from 0.040 to 0.051 in. thickness; and for outdoor service the equivalent of 22-gage steel can be used.

Because Hunter aluminum insulation is composed of a metal, primarily, it has certain features of durability not present in conventional insulating materials, which are of particular value in outdoor use:

1 It is resistant to thermal shock (or the sudden application of high-temperature gradients), either wet or dry. Damage in the form of stress-relieving cracks or disintegration, which sometimes occurs with bulk materials, is completely eliminated.

2 It will withstand physical vibration to a greater degree than other materials. There have been instances where conventional insulation has been fractured by vibration of ducts, from burner pulsation, by unbalanced fans or pulverizers, or by water hammer. With an aluminum alloy, this cannot happen.

3 It is dimensionally stable—wet or dry. Each individual insulating unit is designed to allow for expansion and contraction within the unit, with no stress or strain. Units are joined together so that expansion and contraction occur at predetermined locations, with expansion joints provided in the insulation at these points.

4 Because this material is a corrosion-resistant metal, it is naturally weatherproof and needs no additional protective paint or casing. Insulating units are fitted together to form mechanical seals which act as a protection from water penetration.

The retaining material of low conductivity is practically nonabsorbent. (On prolonged immersion, there is no more than 2 per cent surface wetting.) In addition, it is protected by the overlapped aluminum-alloy casings.

If an internal steam or water leak occurs—say, at a hanger, a joint, or at instrument connections—water from the inside should weep out without seriously affecting the insulating material. Location of the leak may be simplified, as well, since moisture from one leak should not travel beyond the section in which it occurs, causing further damage and lowering efficiency.

To prevent moisture penetration at joints, calking at cutouts for hanger supports and instrument connections, and special seals at expansion joints are provided, as required.

This greater weather resistance of Hunter aluminum insulation reduces the danger of corrosion of piping and equipment caused by retained moisture. With conventional bulk insulation—particularly on piping and equipment which is cold part, or all, of the time—corrosion may occur without a direct break in the basic insulation. When lines are cold, the empty air spaces in bulk material will absorb whatever moisture exists in the ambient air through any joints that are not completely vapor sealed. These air cells are under a partial vacuum, developed when the moisture is initially driven out of the air cells on heating. With the lines cold, moisture is driven back into the air cells. In time, repetition of this process can cause loss of efficiency and progressive deterioration of the insulation, owing to the force of expanding steam in the cellular air spaces. In Hunter insulation, this phenomenon is negligible, since block-form insulation occupies only a small fraction of the total volume.

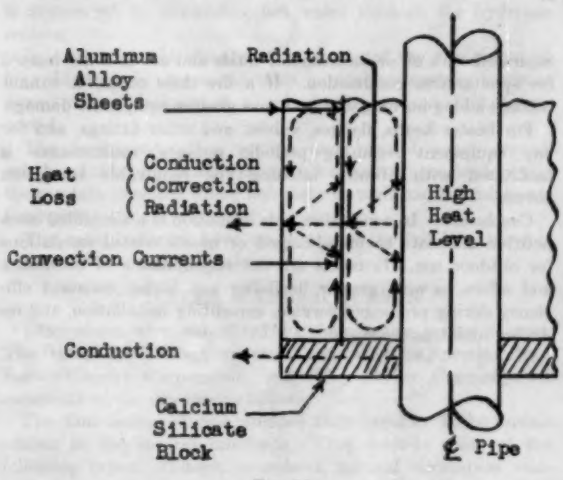


FIG. 26

*Efficiency.* Fig. 21 compares heat losses from Hunter aluminum insulation with several standard materials. In all cases the Hunter product is more efficient for equivalent thicknesses, with efficiency increasing at higher temperatures. Actual operating results at the Titus Station of Metropolitan Edison Company, an indoor station where Hunter insulation is being used on all three units, have borne this out. After two years of operation, insulation efficiency was 98 to 100 per cent of the predicted and published values. (Actual heat losses on 3-in. pipe at this station are indicated by the circled values in Fig. 21.)

The ability of an insulating material to retain efficiency during prolonged operation without additional protective covering is of especial importance in outdoor service.

Bulk insulations, when used outdoors, are seldom 100 per cent dry, and the actual heat loss of such material in practice may be somewhat greater than the theoretical value. This is due to capillarity, which causes the retention of moisture in the material, even on hot surfaces. In contrast, Hunter insulation exhibits little or no dropoff in efficiency over long periods because of moisture or water accumulation.

Sustained higher insulation efficiency would reflect attractive savings in fuel costs over the life of the insulation that, though probably difficult to evaluate, have a tangible economic advantage.

*Application.* The third point to be considered in choosing an outdoor insulation is the comparative application time and total installed cost. Such a comparison should include not only initial cost but the expense of removing and replacing insulation during equipment maintenance. In this respect Hunter aluminum insulation offers several advantages readily reflected in dollar savings.

The need for protective painting or covering is entirely eliminated, since insulation surfaces are naturally durable and attractive. This is a direct saving in application time and material cost and in future maintenance costs.

Since this material will not absorb moisture and needs no drying out before application, it can be installed even under extreme weather conditions. One continuous erection period can be scheduled in advance, and no additional clean-up time is required, since there is no accumulation of dust or debris.

Labor and application costs are further reduced because only a single application is involved. Installation is also facilitated by the lighter weight of this insulation (about $1/_2$ the weight of standard materials) and by the ease with which insulating units can be snapped into place. This advantage is repeated each time equipment or piping is dismantled for maintenance; outage time is reduced, and replacement of insulation destroyed through removal is eliminated.

On projects that are a considerable distance from the Hunter Plant in Bristol, Pa., the manufacturer can arrange for job-site fabrication of all straight pipe covering and flat surface insulation. Special pieces—valve and fitting covers, etc.—are produced at the home plant.

*Special Applications.* The reflective qualities of Hunter aluminum insulation serve an additional purpose on steam and electric-traced lines for antifreeze protection. A resistance-heating

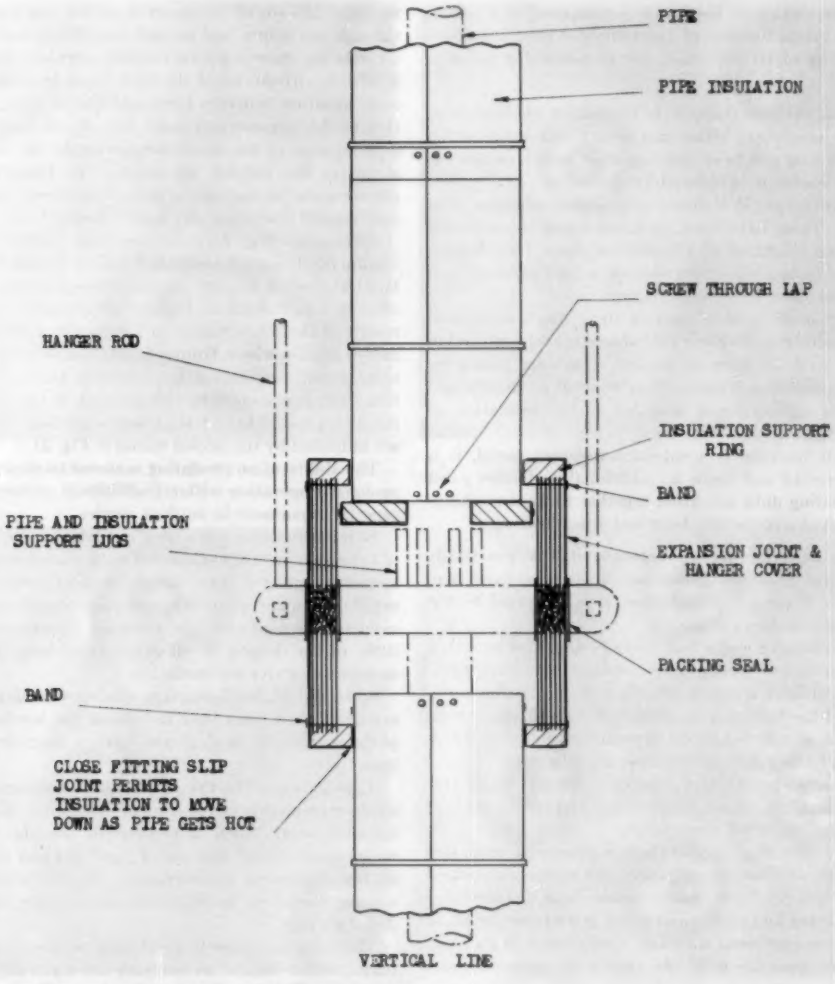


FIG. 27

cable may be run adjacent to the pipe or, if it is desired, to limit the maximum contact temperature of the tracer, in the $^1/_2$-in. space between insulating layers. In either case, the heat from the tracer is well distributed around the pipe because of the reflectivity of the aluminum-alloy sheets, obviating the need for conventional contact heating. Notches are made during fabrication in the low conductivity material supporting spacers at the parting line to allow for passage of the heating cable and yet retain the removable features of the insulation.

On throttle valves, main steam leads, and bleed lines under turbines, that are situated close to lubricating-oil lines, this material is of considerable protective value. Being for all practical purposes nonabsorbent, the insulation cannot become saturated with oil or inflammable fluids and act as a fire hazard for spontaneous combustion. If a fire does occur, it cannot become a long-burning wick to cause greater equipment damage.

For heater heads, flanges, valves, and other fittings, and for any equipment requiring periodic outages, maintenance is facilitated with Hunter latching-type removable insulation covers.

*Conclusion.* In conclusion, this insulation is a simplified competitive alternate to metal-lagged or mastic-coated insulations for outdoor use. It meets all the requirements of durability and offers, as well, greater flexibility and higher constant efficiency during prolonged service, expediting installation, and reducing maintenance costs.

# Digests of Manufacturer Discussions

## TURBINE MANUFACTURERS

The following constitutes a composite digest of written discussions submitted by the General Electric Company and Westinghouse Electric Corporation, in response to invitation:

Over the past 15 years approximately 50 turbine-generators have been put in operation with some degree of outdoor construction. Installations have been made in Florida on the sea coast where they are subject to ocean spray and hurricanes, in Texas where the climate is hot and dry with sandstorms, and in Montana where they have encountered winter snow and ice and temperatures as low as —40 F. These units are reliable and generally satisfactory with no significant difficulties.

Because of the lack of a building over the unit, both the initial installations and maintenance work have sometimes been delayed to some extent, but this has been accepted and generally the operators have liked the outdoor units.

The manufacturers believe that either of two arrangements will be most generally acceptable. The first is an arrangement with the turbine completely outdoors, the front standard weatherproofed with all control devices coming through packings so they are completely accessible. The space between the turbine and generator is covered with metal lagging, with the turning gear inside. The turbine metal lagging itself is made in as large pieces as can be handled with only a few bolts to be removed or clamping devices to be operated, so that access for maintenance is quick and easy. Weathertight doors with internal stairs and platforms are provided for access to the control valves and the turning gear. The generator itself is completely weatherproofed. The exciter has a walk-in-type housing so that brush inspection and minor maintenance work can be done regardless of the weather. While a few exciters have been furnished with weatherproofed enclosure and no walk-in housing, this has not generally been satisfactory and a walk-in-type housing is strongly recommended.

In regions where temperatures of zero or lower may be encountered for extended periods of time, it is considered necessary to provide heat insulation around the generator stator casing to be able to maintain a minimum temperature of 15 C inside. Heat is introduced by circulating hot water through the hydrogen coolers.

In extremely cold climates, the heating of the lubricating oil for cold starts is necessary. Also, provisions must be made to insure proper drainage if a unit has an extended shutdown period.

The hydrogen-treating system and control panel are all weatherproofed for outdoor installations with space heaters and thermostats provided where necessary to maintain the minimum temperatures.

The manufacturers have no hesitation in building turbine-generators for outdoor service.

## BOILER MANUFACTURERS

Discussions were submitted by four boiler manufacturers: The Babcock & Wilcox Company, Combustion Engineering, Inc., Foster-Wheeler Corporation, and Riley Stoker Company. A composite of the discussions follows:

The four manufacturers number their outdoor boiler installations in the several hundreds. They include units of the following types: Reheat, nonreheat, natural circulation, controlled circulation, suction-fired, and pressure-fired, up to 2350 psi pressure and to 1,450,000 lb/hr. Practically every type of fuel firing is represented in the group. Neither the geographical location nor the elevation of plants now prohibits the use of entirely outdoor steam-generating equipment. Individual boiler units vary greatly as to the portions of the total equipment exposed to the weather, starting with units just having the air heaters, dust collectors, and fans outdoors, and extending through the complete range to those which have no part of the unit indoors or even supplementarily housed.

Weather protection for the operating and maintenance personnel varies from complete enclosures at the firing and drum levels to no special provision. The enclosures are usually constructed of transite and have provisions for both natural and artificial light, heat, and ventilation. The floors of these enclosures are concrete, arranged with proper pitch for drainage and to permit hosing down for good housekeeping. The roofs are either of transite construction, the extension of the boiler steel casing, or in the case of lower-most enclosures, concrete.

The development of automatic and remote manually operated controls for combustion, lighting off, soot blowers, and valves, together with television observation of furnace conditions and water level, is rapidly reducing the necessity for a large part of these enclosures as far as operating personnel is concerned.

Particular attention should be paid to the design of the weather-exposed structure so that all portions are self-draining and free from pockets in which water can accumulate.

Exposed horizontal steel preferably should be provided with sloping covers. Platforms and floors other than the main concrete floors are of the open galvanized grating type requiring little cleaning and no painting.

Experience has indicated that tarpaulins suspended from hooks connected to the supporting structure can provide satisfactory protection for maintenance crews if repairs must be made during inclement weather.

It is essential that all of the outside piping be completely drainable. As far as possible, it should be brought down at the side of the boiler to benefit from the radiated heat from the setting and be grouped so it can be easily and conveniently insulated and steel lagged. These enclosures are usually supplied with cord-type electric heaters or with steam tracing for use when the unit is out of service.

Except on outdoor boilers in mild-weather climates free from freezing, the recommendation is to house safety valves, water columns, and water-gage glasses.

Duct-work systems are arranged with their tops pitched for drainage and insulation may be applied either on the inside or the outside. If outside, the insulation is metal-sheathed or plastic-covered.

The forced-draft fans should be so located that the inlets will not pick up moisture and sand.

All bearings of all rotating equipment exposed to cold weather should be air-cooled if possible. In some cases where air cooling cannot be applied and subfreezing temperatures may be encountered, small thermostatically controlled electrical heaters are installed in the water-cooling system.

It is felt that the subject of boiler casings requires specific discussion, as sometimes the opinion is held that an indoor boiler can be insulated, then covered with a sealing coat of waterproof compound, but that an outdoor boiler requires a steel casing. The ready adaptation of boilers from indoor to outdoor use was possible from the very first because initially indoor boilers and their associated accessories were basically steel-encased equipment, which was reasonably pressure and watertight. Even up to very recently some manufacturers have been continuous exponents of a steel-cased design, first with bolted construction, then progressing to all-welded construction. How-

ever, steel shortages during the war years made it necessary to devise alternate weatherproofing material as a substitute for the steel casings which were being used. This led first to the use of transite casings, and then with the advancement of boiler and furnace design came walls which were insulated and covered with a coat of waterproof compound.

When properly designed the latter is economical and satisfactory for both indoor and outdoor types of installations. It inherently does not have the ruggedness of an outer steel casing, and as both designs are now available, decision as to the one to be used depends on the evaluation made by the client.

All the major builders have dropped exclusive advocacy of outside steel casings. Some manufacturers are currently marketing a design in which there is a pressure-type steel skin mounted directly on the boiler tubes, which is then backed with adequate insulating material, and then, in turn, covered with a waterproofing compound which is reinforced with glass-fiber material. Such a casing can be made positively tight, entirely weatherproof, and can be painted to be as attractive as a completely outside steel casing.

In summary, all builders take the stand that boiler units can be designed readily for complete or partial outdoor service at small additional cost over indoor installation. They report also that it is their opinion from discussions with operators who have outdoor boiler units properly designed for their specific climatic conditions that there are no serious operating or maintenance problems.

## Centralized Control Manufacturers

Discussions were submitted by four manufacturers of control equipment: Bailey Meter Company, Hagan Corporation, Leeds & Northrup, and Republic. A composite of the discussions follows:

The control room is usually air conditioned just as with an indoor plant, with the result that instruments and control apparatus located therein operate under conditions which favor excellent performance and reduced maintenance. However, sensing and signaling devices for the various measurements of flow, level, pressure, and temperature are quite frequently located out of doors where they must combat a much wider temperature range, increased exposure to water and ice, sand and dirt, with strong winds increasing the adverse effects of these factors. In addition there may be the problem of increased distances between the central control room and the outlying controlled elements.

Manufacturers are paying more design attention to secure weathertight enclosure.

Exposed equipment will in general be less convenient for maintenance since the men involved will also be subjected to the prevailing weather conditions, and maintenance is made more difficult due to the necessity of opening weathertight enclosures not ordinarily required for indoor installations. There will naturally be a search for designs requiring even less maintenance than in the past, and increased use of corrosion-resistant materials to reduce maintenance on components located outdoors. One manufacturer states that because measuring and controlling units are generally small and can be taken to an indoor shop for repair or overhaul the maintenance cost on these devices located outdoors is not likely to be appreciably higher than on similar units located indoors.

Hydraulic transmission of signals is giving way to pneumatic or electric transmission because long small high-pressure lines of hydraulic systems are difficult to protect against physical damage, freezing, and overheating when protected by heating.

Pneumatic systems in cold climates require driers to reduce the dew point of the compressed air below the minimum ambient temperature encountered. No special precaution is needed for the lines connecting to outdoor apparatus. With a suitable drier and a storage tank providing at least 15-min reserve, reliable power for signaling and control is assured for the outdoor plant.

Manufacturers with electrical transmission systems advocate their use. The requirement of weatherproof protection for conduits and connections to the outdoor apparatus to guard against insulation breakdown is pointed out. Outdoor motor operators require special attention to lubrication to insure reliable performance. Suitable outdoor electrical apparatus is available, although the cost of such equipment is somewhat higher than for indoor equipment.

Ice may form on forced-draft-fan vanes or dampers and on the connecting linkage between operators and dampers located out of doors. Power units for such devices should be made somewhat oversize to allow for ice-forming tendencies, and during icing conditions the power units should be operated periodically to break up any ice. Damper linkage should be protected against direct moisture impingement in icing areas.

It is always desirable where it can be done to install all measuring and control devices and panels within the building structure in enclosures provided for other operating reasons.

In many plants the outdoor mounted control equipment is limited to the forced and induced-draft fans, with a relatively trivial cost increase. If, however, the design is carried to the extent that measurement and control of water level, fuel, air flow, and furnace draft are all located outdoors, the installed cost will increase rather rapidly and maintenance cost also will be affected adversely.

The additional control cost for outdoor installations usually is not excessive, maintenance poses no severe problems, and the performance of a well-engineered outdoor job will equal the indoor plant installation.

## Piping Fabricators

The M. W. Kellogg Company comments that the only difference found on outdoor jobs as compared to indoor jobs is in the insulation requirements and the need for special housing of complicated hangers exposed to icing conditions. Midwest Piping Company notes the necessity of metal sheathing or bituminous coating on the insulation of outdoor piping to withstand the elements, coupled with provision of steam or electric tracers to prevent freezing; points out that on outdoor construction the absence of building steel may complicate the job of designing adequate hangers and supports, and states that erection experience to date has been fortunate, without sufficient bad weather to impede erection of the outdoor piping handled.

# Summarization of Symposium Papers

By V. F. ESTCOURT[32] and B. V. MARCELLUS,[33] SAN FRANCISCO, CALIF.

THE papers composing the symposium have been reviewed to collate the views of the several authors on points of similar nature.

### Investment Costs Chargeable to Design

The two main reasons cited for adopting outdoor design are savings in first cost and reduction in construction time (Louis Elliott). In this section we will attempt to analyze the former. In the several papers there exists a wide variation in cost reductions reported for outdoor plants. E. C. Gaston rightly states that the actual saving is a function of the base cost on which the savings are measured. Two other yardstick bases for analysis have been suggested: Ebasco Services Incorporated use the full outdoor design, with penalties estimated for providing anything beyond the practical minimum of housing (W. F. Friend), while M. K. Drewry believes that outdoor design should be compared with minimum-cost practical enclosures.

F. W. Argue presents still another approach. In his paper, one comparison of savings is made by adjusting the costs of an existing conventional plant to that of the same plant in an outdoor arrangement and another, by adjusting the differences of cost in an existing outdoor plant versus the same plant in conventional design.

The different bases which the several authors have used in their cost analyses have resulted in a variety of predicted capital savings. It was noted that climatic conditions and the degree of outdoorness had a great bearing on the possible initial savings. The following is an attempt to correlate these data and explain the apparent discrepancies.

*Over-All Cost Savings on Total Plant.* The greatest savings of from $6 to $7 per kw of installed capacity can be made by adopting a fully outdoor design over a conventionally designed plant having brick or heavy masonry enclosures (T. M. Morong, G. A. Gaffert). A lesser saving of $4 per kw is gained by installing only outdoor boilers and units with the remaining enclosure of brick or heavy masonry walls (E. C. Duffy) serving as protection for indoor-type auxiliary equipment.

A saving of $1.66 to $2.50 per kw was obtained in P.G.&E's Pittsburgh plant by adopting outdoor boilers and units with the remaining enclosure of heavy masonry as compared to a similar size plant with outdoor boilers and a heavy masonry enclosure for the turbine-generators. These savings include the gain reflected by optimum placement of the units (C. C. Whelchel). The governor ends of the turbines project into the enclosed area thus eliminating walk-in enclosures and long runs of steam piping.

However, savings of only $0.66 to $2.85 per kw will be realized in adopting outdoor design if the enclosures to be eliminated are strictly functional, of inexpensive contruction, and relying upon well-arranged masses for pleasing appearance (F. W. Argue). This variation in saving can be attributed to climatic conditions determining the type of enclosure being eliminated. In colder climates cost of enclosures will be increased by the required insulation.

*Savings From Outdoor Boiler Installation.* The outdoor boiler is firmly established (G. A. Gaffert) and materially reduces the first cost of a plant by eliminating a large section of building, together with accessories such as heating, ventilating, and cleaning equipment. Savings will exceed the additional cost for an outdoor boiler with the necessary weather protection, waterproofing, and steam tracing of lines (Paul Blanchard). Most of the over-all gain in savings comes from placing the boilers and heaters outdoors (John B. Saxe).

As noted before, the savings in placing any equipment outdoors is affected by the type of enclosure eliminated. If this is a functional enclosure, the savings with outdoor boilers will approximate only $0.40 to $2 per kw of installed capacity, depending upon whether the enclosure was designed for mild or cold-weather conditions (F. W. Argue). The size or capacity of the boiler also affects the savings. The savings decrease in inverse proportion to the size of the boiler. For example, E. C. Duffy's paper indicates the reduction in first cost by adopting semi-outdoor boiler design for single-boiler single-unit installations by the Long Island Lighting Company were $4.47 for a 40,000-kw job, $2.44 for a 90,000-kw unit, and $1.96 for a 156,000-kw installation. In all cases the enclosures eliminated were of brick.

M. K. Drewry believes the saving in first cost by entirely omitting the boiler enclosure is not exactly justified for a steam plant located in a northern climate. The cost of an enclosure built from inexpensive materials such as corrugated transite will be recovered by reducing heat losses from the boiler. He estimates the cost of such an enclosure to be $80,000 for a 120,000-kw installation ($0.76 per kw) and the reduction in heat losses per year from such an enclosure to be $75,000. Also, he estimates that a totally enclosed plant using transite-type walls and indoor equipment would approximate the cost of a fully outdoor plant of the same capacity.

*Savings From Outdoor Turbine Installation.* Placing the turbine-generator outdoors results in relatively small savings owing to the high cost of the gantry crane and walk-in housings (John B. Saxe). Also, there is very little difference between the cost of placing the turbine and switchgear indoors using conventional overhead crane and walls of corrugated transite and by adopting an outdoor unit and switchgear and using the more expensive gantry crane (G. A. Gaffert).

E. C. Duffy estimates the reduction of cost in an outdoor turbine installation including gantry crane, but exclusive of cost of unit, to be from $1.64 to $1.53 per kw of installed capacity for unit sizes from 90 mw to 156 mw, inclusive. In these cases, the eliminated enclosures were of brick construction.

W. D. Marsh and A. G. Mellor of the General Electric Company report that the additional cost of weatherproofing turbine-generators is between 2 and 4 per cent of the cost of the machine or $0.50 to $1.25 per kw.

F. W. Argue in his paper implies that the over-all saving in placing turbine-generator and related control room in an outdoor setting will vary between $0.53 and $0.72 per installed kw. These costs are based on the eliminated enclosure being of strictly functional design.

*Savings Realized by Minimizing Enclosures.* The elimination of usual boiler and turbine buildings will result in savings of from $5 to $8 per kw of capability depending upon whether the enclosure to be eliminated is of brick or of less expensive construction (John B. Saxe, W. L. Chadwick). Corrugated-asbestos siding is approximately $3 per sq ft less than brick walls (E. C. Gaston).

Where the eliminated enclosure is of functional design, utilizing inexpensive materials, the initial savings will only be from

[32] General Superintendent of Steam Generation, Pacific Gas & Electric Company. Fellow ASME.

[33] Technical Engineer, Pacific Gas & Electric Company. Mem. ASME.

$1.85 to $2.35 per installed kw in an outdoor plant (F. W. Argue).

*Miscellaneous Savings in Outdoor Design.* The decrease in building services such as lighting, heating, and ventilation will amount to $0.76 to $1.35 per installed kw in an outdoor plant (F. W. Argue). The decrease will depend upon climatic conditions. At the Etiwanda Steam Station in Los Angeles, Calif., the reduction in the amount of necessary ventilating fans resulted in a savings of $0.55 per installed kw (W. L. Chadwick). Mr. E. C. Duffy states that net savings for ventilation equipment in plants on Long Island, N. Y., were found to be approximately $0.06 per kw of installed capacity.

*Increased Cost of Mechanical and Electrical Equipment.* Weatherproofing equipment for outdoor service increases its cost. F. W. Argue estimates the increase for electrical equipment to be from $0.40 to $0.50 per installed kw. W. D. Marsh and A. G. Mellor of the General Electric Company are in agreement with this as they say the total increase in cost of an outdoor turbine unit plus switchgear, exciters, motors, etc., will amount to $1.65 per kw for a 100-mw installation while the increased cost of weatherproofing the unit alone is $0.50 to $1.25 per kw, depending upon the capacity. Thus $1.65 minus $1.25 would give $0.40 per kw as the additional cost for electrical equipment for the larger unit.

The cost of mechanical equipment for outdoor service will average $0.68 to $1 per installed kw over that for indoor equipment (F. W. Argue).

*Conclusion.* The authors vary in the summation of all costs for conventional versus outdoor design plants. They show a variation of savings for outdoor designs amounting to anywhere from approximately zero (M. K. Drewry) to $8 (W. L. Chadwick) per kw of installed capacity. This amount is dependent upon climatic conditions, installed capacity, and type of enclosure that has been eliminated. When all these are taken into consideration, there are no large discrepancies in the figures presented by the different authors. Perhaps the main difficulty is that insufficient emphasis has been made relative to the basis upon which the cost comparisons have been made.

## Climatic Considerations in the Design, Operation, and Maintenance of Outdoor Steam Plants

Other than the savings in first cost, the most important factor influencing the design, operation, and maintenance of outdoor installations is climate. Sargent & Lundy, in its experience with the design and construction of some 25 units for outdoor service, believes that the outdoor plant has its place in the type of climate where it is not subjected to extremes of weather.

However, the acceptance of outdoor design is not universal. In the Southern Company system, it has been found that outdoor plants are not entirely feasible. The seasonal operational load variations are such that the minimum system demands coincide with the rainy and colder season of the year. Outages must be scheduled during this period and maintenance can be more efficiently and quickly completed where it can be performed within the protection of a building.

The question of indoor versus outdoor plants, so states M. K. Drewry, is a geographical and circumstantial one, that will never have a simple answer. For northern states, the Wisconsin Electric Power Company's experience suggests that inexpensive shelters are worth the investment. An interesting point offered by John B. Saxe is that in warm and arid areas the small saving from installing an outdoor turbine is amply warranted, particularly if the climate is being promoted and the utility is part of the act.

The effects of climatic considerations on the various phases of outdoor plants follow.

### Effect of Climate on Design

*Cold Weather.* Outdoor boiler plants have been found practical in the severe cold of Montana and the freezing weather of Utah. Operational experience gained in these plants in subzero temperatures definitely shows that particular attention must be paid to the details of protecting all piping, valves, etc., carrying liquids or gases containing moisture. Safety valves, blowdown valves, water columns, air lines, control lines, and many drain lines have frozen in these plants even though every effort has been made to have these items insulated and traced (R. A. Reid, Paul Blanchard).

It is often possible to enclose the area beneath turbine pedestals at comparatively small cost in order to provide cold-weather protection for most of the auxiliary equipment. There appears little justification for enclosing dust collectors, induced-draft fans, and tanks. The problem of cold air entering the air preheaters appears to have been satisfactorily solved by the steam air preheater (W. L. Chadwick, T. M. Morong, John B. Saxe, E. C. Duffy).

Turbine-deck snow-melting systems have been proven by experience to be of limited usefulness (E. C. Duffy).

*Temperature Extremes.* The design of the Kyrene Steam Plant in Arizona was influenced by the climatic temperature range of 20 to 120 F. Periodic rains of torrential intensity and heavy dust storms also occur. As noted previously, the major auxiliaries are enclosed below the turbine deck by a lightweight concrete-block curtain wall. This arrangement provides protection from rain and dust and better maintenance conditions for the day-to-day work on the auxiliaries. The extreme temperature ranges can affect chlorinator operation if not adequately protected (T. M. Morong).

*Mild Climates.* The over-all design of P.G.&E.'s Pittsburgh full-outdoor plant has attained a considerable degree of enclosure for operators and certain equipment by taking full advantage of numerous structural situations where low-cost enclosure could be made at desirable points (C. C. Whelchel). A porous gravel surface for the station yard is low in cost and rain water will seep into the ground without the need of a pipe drainage system (M. D. Engle).

*Warm Climates.* The boilers and heaters are the major dissipators of heat and it is practically impossible to provide satisfactory ventilation if they are enclosed (John B. Saxe, Louis Elliott). The enclosed area below turbine decks can be ventilated by hatches and/or by removable wall panels (E. C. Duffy).

*Walk-In Enclosures.* The consensus of opinion is that walk-in enclosures of some type are desirable for turbogenerators (H. G. Hiebeler, G. A. Gaffert, J. W. Keck). However, experience with an outdoor plant in Southern California has proven such enclosures are not necessary as they do not offer any more protection than can be obtained in a weatherproofed unit (W. L. Chadwick).

*Manufacturers' Design.* The major manufacturers of turbogenerators and boilers have no hesitation in building units to be reliable in operation and maintenance in the most adverse of weather conditions.

### Climatic Considerations in Construction

There are no difficulties attendant to the erection of an outdoor plant during warm and mild weather. For this reason erection costs can be held to a minimum by scheduling major construction of boilers and turbines during periods of expected nice weather (E. C. Duffy). The lack of protection afforded by an outdoor plant retards construction as the severity of climatic conditions increases. Temporary and adequate protection of

turbine unit during erection is mandatory (E. J. Garbarini). The additional cost of the temporary shelter will be apparently less if the structure can be used year after year for turbine maintenance. Shelter costs of workmen and also for other equipment increase directly with the inclemency of the weather.

*Inclement Weather.* Construction lost time, according to E. C. Duffy, will probably not exceed 5 per cent in the case of boilers and 10 to 15 per cent for turbine-generators as a result of inclement weather. Turbine-erection costs normally have been estimated $5000 to $10,000 higher because of outdoor design. Experience has shown that the installation of a full boiler roof will save erection costs if construction has to be done during periods of inclement weather.

*Winter Weather.* Experience by the Wisconsin Electric Power Company has proven the need of sheltering workmen and equipment if erection is not to be delayed during the winter. M. K. Drewry notes that 50 per cent erection-labor efficiency results from men spending half their time warming themselves.

*Rainy Weather.* In locations with considerable precipitation, John B. Saxe and E. C. Duffy confirm that it is more logical to install a permanent roof over boilers as the cost of a temporary one during construction nearly approaches that of a permanent one.

### Climatic Effects on Employee Comfort

The improvement in employee comfort and contentment in outdoor plants, while intangible, is significant. Plants in areas of limited precipitation and high average temperatures offer definite advantages in personnel comfort, particularly in the more southern states. H. G. Hiebeler claims there is practically 100 per cent preference in all ranks for the outdoor arrangement of the Houston Lighting and Power Company plants.

It is to be expected that there are annoyances to operators where extremes of temperatures are involved. Operating soot blowers and other duties while facing a hot boiler casing with winter on the back is not conducive to good health of operators (G. A. Gaffert, John B. Saxe). In the Arizona Kyrene plant the operators have experienced discomfort in going from an air-conditioned control room at 70 F into a station ambient of 100 F. According to T. M. Morong the extreme temperature variations have resulted in more colds and an increase of time off.

### Operation Under Severe Weather Conditions

*Dust Storms.* Three to five years' experience in Texas with an outdoor plant has indicated no particular troubles arising from severe dust and sand storms that would not have occurred in a totally enclosed plant. In fact the nuisance would have been worse in a conventional plant since the dust and sand would have accumulated in the enclosed areas (C. W. Geue).

*Hurricanes.* Several outdoor plants in Florida and Texas have been exposed to winds approaching 125 mph, and it has been found by experience that outdoor plants, when properly designed, are as reliable as conventional plants under hurricane conditions. No plant shutdowns have occurred that could be attributed to the plants themselves. The vulnerable equipments are the outdoor switchyards and transmission lines. Indoor plants are not always dry during hurricanes (J. W. Keck, H. G. Hiebeler).

### Climatic Effects on Maintenance

The weather has the greatest influence on the cost and duration of maintenance outages, and most, if not all, of the utilities schedule maintenance work in the milder seasons as far as system load patterns permit. G. A. Gaffert states the management of a steam plant in Louisiana consults with the weather bureau before an overhaul is planned.

*Cold Weather.* Maintenance, in general, during extremely cold weather will take longer and cost more than in a fully housed station (Louis Elliott). It has been found at Sewaren Generating Station that it takes two to three times as long to do close-tolerance work on lining-up rotary equipment (J. A. Inwright). However, even subfreezing temperatures and wet sleeting conditions are not a deterrent to any necessary maintenance. For example 18 coils were replaced in a 60,000-kw generator under these disadvantages in a Texas outdoor plant (H. G. Hiebeler). R. A. Reid doubts if cold weather is a handicap as men are more productive in cold as compared to hot conditions.

*Paint Life.* It is universally agreed that the problem of short paint life is common to all outdoor plants. At the present time, there has been no solution offered to combat the evil. It is apparent that it has to be tolerated. R. A. Reid suggests that outdoor painting costs are partially offset by not having extensive turbine and boiler structures to paint.

### Operation and Maintenance Costs

Operational costs, in general, as a result of outdoor design have decreased. This has been brought about by the compactness and optimum placement of equipment, improved instrumentation, and the very nature of the open arrangement tending toward the betterment of supervision and the observation of plant activities.

Maintenance costs are apparently increased, although diversity of opinion still exists on this score. The fact that the increased maintenance on equipment is somewhat counterbalanced by the reduction of maintenance on eliminated enclosures, plus the introduction of climatic effects, gives an explanation for this contradiction.

*Operation.* The cost of adequate centralized controls, so states T. M. Morong, has been well worth the investment in reduced personnel requirements.

No operational difficulties have appeared in the outdoor plants except that extreme temperature variations have resulted in more colds and time off for operating personnel (T. M. Morong). According to R. A. Reid, an outdoor plant subjected to the adverse weather conditions of Montana has not resulted in increased pay for the operators, and it is believed that less personnel are required.

*Maintenance.* In general, the consensus of opinion is that maintenance of outdoor equipment takes longer because it is necessary to spend additional time to protect and clean exposed parts, not normally required in a conventional plant.

It is universally accepted that cold or inclement weather has an adverse effect on outage time, particularly when close-tolerance work is attempted in extremely cold weather. J. A. Inwright notes that this latter will take two to three times as long.

The exposed breeching, ducts, and boiler casings need painting oftener than in conventional installations.

The disadvantages of outdoor maintenance are costly. However, there are a number of advantages which take away a great part of the sting. It is not unlikely that in some cases, due to climatic and other considerations, the maintenance costs will be less in an outdoor installation. Conversely, they could be appreciably greater.

The advantages of being out in the open, having natural light and sufficient space, has speeded up maintenance work. Another asset is the more pleasant working conditions. This is particularly true on outdoor boiler auxiliaries such as soot blowers, burners, fans, and so on.

Another advantage is the maintenance time saved in previous high-temperature areas. E. C. Duffy states that the saving

here outweighs lost time due to maintenance performed during low-temperature periods.

R. A. Reid doubts that cold weather is a handicap or that it increases maintenance costs.

The increased ease of routine cleaning in outdoor design by permitting the washing down of the open areas rather than sweeping or vacuum cleaning represents a saving (W. L. Chadwick).

### Maintenance of Insulation

The subject of additional maintenance cost on the outdoor pipe insulation has not been given the attention it warrants. Approximately 5 per cent of the capital investment in power plants is in pipe insulation, yet Johns-Manville Company states that the art of insulation has not progressed to the point where it is entirely acceptable to the exacting requirements of utilities. From cursory mention of the subject in the several papers on outdoor plants, the impression is given that the continual maintenance required is a necessary evil. There seems to be room for improvement. For instance, the Hunter Manufacturing Corporation states that the use of aluminum-alloy insulation in outdoor design will reduce maintenance costs and will impart sustained higher insulation efficiency.

### Construction Costs Exclusive of Climatic Considerations

There are two main reasons for adopting outdoor designs: The saving accomplished in first cost and the reduction in time and cost of the actual construction. This latter has been the subject of numerous studies and many figures have been quoted covering the estimated saving in construction costs effected by utilizing outdoor designs. The influence of the weather on construction costs is an adverse variable that, for the time being, will be left out of the picture (Louis Elliott, E. C. Gaston).

Possibly the greatest savings in construction costs are affected when a ranch-style layout can be employed. This type spreads the plant over a wider area and all major equipment, foundations, etc., are located at ground level (E. C. Gaston).

Outdoor plants tend toward simplification of design, thus automatically reducing construction costs. There remain many design features which may be changed to reduce these costs further (W. L. Chadwick, M. D. Engle).

The several basic advantages in outdoor design which contribute toward reducing the over-all construction costs are as follows:

*Reduced Construction.* Elements of construction, such as building structure, are omitted in the outdoor plant as compared to conventional plant of the same design (E. J. Garbarini).

*Increased Accessibility.* This inherent advantage in outdoor design aids the constructor in placing equipment and erecting component parts of the structure and apparatus. The improved accessibility makes it possible to use motorized moving and lifting equipment to better advantage. The elimination of structure walls extends the range of derricks and truck cranes. Trucks and truck cranes can be fully utilized to place many items of apparatus in final position. A large capacity caterpillar crane can be used during the initial plant erection, then later on in place of permanent steel structures and hoists (W. L. Chadwick, E. J. Garbarini, M. D. Engle).

*Foundations.* Since the foundation slab in outdoor design is often near ground level, the slab can be poured shortly after the construction force is organized, thus permitting the erection of boiler steel soon thereafter and the turbine-pedestal construction to follow shortly (Louis Elliott).

*Concrete Work.* The amount of reinforced-concrete floors and roof decking at considerable heights above ground level is reduced in outdoor plants (E. J. Garbarini).

*Reduced Construction Personnel.* The number of structural elements being less in outdoor design, a smaller labor crew is required. Construction supervision is noticeably more effective and there will be less interference between structural workers and equipment erectors (W. L. Chadwick, E. J. Garbarini).

*Scaffolding Costs Reduced.* The requirements for painting and electric-lighting fixtures in high places are reduced in outdoor design. This decreases scaffolding costs as well as electrical and painting costs (E. J. Garbarini).

*Lighting Costs.* The natural daylight affords better visibility and less artificial lighting is required during the construction of outdoor plants (E. J. Garbarini).

Some construction costs, will, of necessity, be more expensive in outdoor design plants than in conventional enclosed plants of the same capacity. The basic cause of this is the lack of protection resulting from eliminated enclosed structures. Some of the increased construction expenses are:

1 Providing temporary shelters for workmen, storing materials and equipment.

2 Protection of turbogenerator units during erection (E. J. Garbarini).

3 Weatherproofing of insulated steam, water, and oil lines requires additional labor and materials (Johns-Manville).

### Conflict of Opinion and Prejudice Pertaining to Outdoor Design

Outdoor design of steam plants has not found universal acceptance by the electric-power companies. There are, perhaps, many justifiable reasons to account for this. The question of indoor versus outdoor power plants, according to M. K. Drewry, is a geographical and circumstantial one that probably will never have a simple answer.

F. W. Argue believes it is unfortunate that controversy has developed regarding the feasibility of outdoor construction and that opinions have been formed without factual basis. At one extreme, there is doubt that outdoor stations are practical for other than the most favorable climate. This latter is more or less confirmed by G. A. Gaffert who notes that the outdoor plant has its place particularly in the type of climate where the plant is not subject to extremes of climate. Contrary to this, R. A. Reid has found from actual experience that outdoor plant operation is feasible for the severe climatic conditions of the Montana area. Also, E. C. Duffy intimates that outdoor plants are preferable particularly where there are long periods of hot weather as in New York.

Louis Elliott remembers in years past that in meetings of utility-industry committees, radical new ideas have more than once encountered tolerant pity from the conservatives. The installation outdoors of large boilers and turbines has run the gauntlet of ridicule, doubt, criticism, and gradual acceptance after the volume of successful installations commanded approval.

At the present there are no standards or definitions to indicate the degree of outdoorness of a steam plant. Mr. Elliott reminds us that outdoor is a convenient, and nowadays a conventional term for denoting plants in which one or more important units of equipment are installed without protection from the weather.

### Reasons Hindering Utilization of Outdoor Design

Two very different versions are offered for the delay in applying the outdoor design to power plants. J. W. Keck indicates one reason being that it was necessary to adapt much equipment for outdoor use, such as turbines, exciters, motors, instrument panels, etc. F. W. Argue believes that outdoor construction did not receive widespread acceptance until instrumentation and

automatic control had reached the stage where routine operations could be remotely controlled.

### Arguments Against Outdoor Design

E. C. Gaston explains that outdoor design has not been employed more frequently in the Southern Services, Inc. as the distribution of hydro and steam capacities and system load is such that maintenance outages on steam-electric plants have to be scheduled during the season of heavy rainfall and inclement weather. These adverse climatic conditions may so increase maintenance costs that the increase, when capitalized, would offset any saving in eliminating enclosures.

### Noise Problem

Another debatable issue is noise control. It is W. L. Chadwick's contention that this may be serious enough at some station sites practically to eliminate the possibility of outdoor design. Contrarywise, E. C. Duffy has established through the actual operation of outdoor boilers and turbines of the Long Island Lighting Company that sound emanating from such equipment is rapidly attenuated, and the noise level at various distances has created no noise problem. As a matter of fact, experiences with brick enclosures indicated that the effect was similar to a piano sounding board, resulting in amplification of the power-plant noise to surrounding areas.

### Concluding Observations

Extremely important data on the advantages and disadvantages of outdoor construction have been presented by the various authors. It is believed that many of the apparently divergent views could be reconciled in greater degree if a more careful study were made of the premises upon which each statement is based. The basic problem appears to center around the degree and type of outdoorness which will yield the minimum overall cost of production, including fixed charges, for various types of climate and system operating requirements. It would be an oversimplification of the problem to decide the case merely "for" or "against" the outdoor plant.

If a future symposium is held on this subject, it should include a very careful appraisal of the data presented by the present authors in terms of the four factors mentioned in the foregoing.

Very definite appreciation is due the many authors for their valuable contributions in this Symposium.

# Flow in Corners of Passages With Noncircular Cross Sections[1]

By E. R. G. ECKERT[2] and T. F. IRVINE, JR.,[3] MINNEAPOLIS, MINN.

**Conditions for convective heat transfer are known to be especially poor in the corner regions of noncircular passages. This situation causes the passage walls to become too hot in certain types of heat exchangers and directs attention to flow conditions in the corner regions. An experimental and theoretical investigation was conducted on the flow characteristics of triangular-shaped passages. Flow-visualization techniques revealed the remarkable fact that through a certain range of Reynolds numbers laminar and turbulent flows exist simultaneously side by side. Pressure measurements were made on two ducts to study the influence of the geometry on the hydrodynamic entrance length. The velocity field within the ducts was measured over a Reynolds number range from 500 to 43,000. An analytical study of the flow resulted in the development of a simple expression to describe the velocity field under the conditions of laminar fully developed flow in a narrow corner. This expression was confirmed experimentally using a sensitive micromanometer developed for this purpose.**

## Nomenclature

The following nomenclature is used in the paper:

$A$ = area
$d$ = diameter
$f$ = friction factor
$h$ = distance
$H$ = distance
$L$ = length of triangle height
$l$ = length of triangle base
$p$ = pressure
$r$ = radial distance
$R$ = radius of sector
$w$ = velocity in flow direction
$x$ = co-ordinate distance
$y$ = co-ordinate distance
$z$ = co-ordinate distance
$\theta$ = angle
$\mu$ = dynamic viscosity
$\nu$ = kinematic viscosity
$\rho$ = density
$\tau$ = shearing stress
$\Delta$ = finite increment

*Subscripts*

avg = average value
$d$ = duct
$h$ = hydraulic

## Introduction

Noncircular passages through which a fluid is conducted occur quite frequently in engineering applications. In heat exchangers, for instance, the ducts are very often of a noncircular shape. Correspondingly, friction and heat-transfer characteristics of such passages have been investigated for various duct cross sections in the past (1 to 4).[4] Usually in such applications, the over-all pressure drop and the average heat transfer were the only values of practical interest to the engineer.

For recent applications, however, like gas turbines or nuclear power plants, heat exchangers are needed which operate at extremely high temperature levels. As a matter of fact, the designer is in these cases interested in raising the temperature level under which the heat exchange takes place as high as possible. Usually, the limitation to this effort is set by the temperature which the material from which the heat exchanger is constructed can safely withstand. The designer is, therefore, interested in determining the location where the wall temperature within the heat exchanger will assume its highest value. In order to calculate those hot spots, the local heat-transfer coefficients have to be known.

It is to be expected that the heat transfer from a fluid flowing through a noncircular passage and cooling the duct walls will be lowest near the corner of such passages. Therefore knowledge of heat-transfer conditions in such corner regions is of special interest in the applications mentioned. Measurements on the local distribution of heat-transfer coefficients around the periphery of noncircular passages are nonexistent. For this reason, calculations (5 to 7) which had been made on the temperature distribution in the walls of polygonal passages of heat exchangers had to be based on local shearing stresses derived from measurements by Nikuradse (2 and 3). These measurements, however, have been made only at high Reynolds numbers, for which the flow is well in the turbulent range. Applications, on the other hand, have to deal frequently with flow at lower Reynolds numbers and it had to be suspected that the local cooling conditions in corners are considerably poorer for laminar flow than for turbulent ones.

For this reason, an investigation has been started with the aim to clarify flow and heat-transfer conditions in noncircular passages. Realizing that no proper understanding of convective heat transfer is possible without a good knowledge of flow conditions, this investigation was started with a study of laminar, transitional, and turbulent flow in triangular ducts. The results of this investigation are reported in the present paper. Triangular ducts with one sharp angle were chosen, since it was expected that flow conditions in a corner of small angle will differ most widely from the known conditions in a round tube.

Previous investigations on ducts with triangular cross sections were made by Schiller (1) and Nikuradse (2 and 3). Schiller measured average friction factors for a duct with an equilateral triangle as cross section having a hydraulic diameter of 0.609 in. and a side length of 1.05 in. His measurements were made

[1] This research was sponsored by the Wright Air Development Center, Air Research and Development Command.

[2] Professor of Mechanical Engineering, University of Minnesota. Mem. ASME.

[3] Instructor, Mechanical Engineering Department, University of Minnesota.

Contributed by the Heat Transfer Division of The American Society of Mechanical Engineers and presented at the Heat Transfer and Fluid Mechanics Institute, Los Angeles, Calif., June, 1955.

Note: Statements and opinions advanced in papers are to be understood as individual expressions of their authors and not those of the Society. Manuscript received at ASME Headquarters, August 22, 1955. This paper was not preprinted.

[4] Numbers in parentheses refer to the Bibliography at the end of the paper.

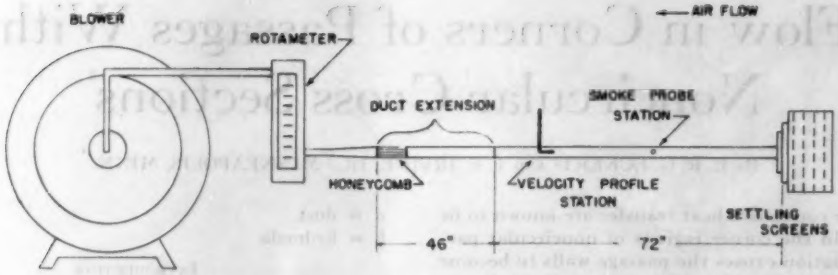


FIG. 1 SCHEMATIC OF EXPERIMENTAL APPARATUS

with water in a Reynolds number range from 4000 to 228,000. All measurements were made downstream from a position 80 hydraulic diam from the duct inlet. The Reynolds number is based on the average tube velocity and the hydraulic diameter. Nikuradse made friction measurements, also using water, on ducts with an equilateral triangle, a right isosceles triangle, and an acute triangle as a cross section. The characteristic dimensions of these duct cross sections are given in Table 1.

TABLE 1 CHARACTERISTIC DIMENSIONS OF NIKURADSE'S TRIANGLES (10)

| Type of geometry | Hydraulic diam, in. | Length of side ($l$), in. | Angle $\alpha$, deg | Length of inlet section hydraulic diam |
|---|---|---|---|---|
| | 0.615 | 1.062 | 60 | Not specified |
| | 0.344 | 0.826 | 45 | 119 |
| | 0.449 | 1.511 | 23 | 59 |

Nikuradse measured friction factors for these ducts in a Reynolds number range from 600 to 200,000. He also measured the velocity field in the exit plane of the ducts at Reynolds numbers between 20,000 and 30,000. From these measurements he obtained the local shearing stresses around the duct peripheries.

This paper discusses the experimental and theoretical studies which have been made on two ducts of triangular cross section. Both triangles were isosceles, the first having a height-to-base ratio of 5:1 and a hydraulic diameter of 0.908 in. and the second having the same hydraulic diameter with a height-to-base ratio of 2.56. The Reynolds number range extended from 500 to 43,000.

Flow-visualization techniques, pressure measurements, and probing of the velocity field were used to examine the flow of air through these ducts. Information was obtained in the laminar, transitional, and turbulent-flow range.

In order to make velocity measurements in the laminar-flow regime, it was necessary to develop a micromanometer having sufficient sensitivity to measure air velocities below 2 fps.

Concurrent with the experimental program, the velocity field in laminar flow through triangular ducts was calculated by relaxation techniques and analytical methods. The results of these calculations indicated possible generalizations of the experimental findings.

*Experimental Apparatus.* The basic flow apparatus used in these studies is shown in Fig. 1. Under the influence of a blower located downstream, air from the room was drawn through a series of seven cloth-settling screens, past a well-rounded entrance section, and into a triangular-shaped duct. After leaving the main duct in which the measurements were performed, the air traveled through a triangular extension with the same cross section and a honeycomb flow straightener. Further on in the downstream direction was a duct portion in which the cross section changed from the triangular shape to a circular one. Then the air passed through a flowmeter and returned to the room through the blower. The duct was fabricated from plexiglas and suspended rigidly by a steel frame.

As mentioned previously, two triangular ducts were used in this investigation. Both had a cross section formed of an isosceles triangle with the small angle on Duct I having a value of approximately 12 deg while the same angle on Duct II was approximately 25 deg.

Table 2 summarizes the important dimensions of both ducts. The hydraulic diameter listed in both Tables 1 and 2 is the ratio four times the cross-sectional area to circumference of the duct.

TABLE 2 INSIDE DIMENSIONS OF DUCT USED IN EXPERIMENTS

| Duct no. | Over-all length, ft | Hydraulic diam, in. | Apex angle, deg | Triangle height, in. | Triangle base, in. |
|---|---|---|---|---|---|
| I | 6.0 | 0.908 | 11.5 | 5.00 | 1.00 |
| II | 5.2 | 0.908 | 24.8 | 2.80 | 1.09 |

Holes were drilled through the walls of the duct for making static pressure measurements and for inserting probes into the main flow. Near the downstream end of the duct a slot of 0.080 in. width was cut across the top of the duct perpendicular to the flow direction. A total pressure probe was inserted through this slot into the main flow for measuring velocity profiles. While making measurements the slot was sealed with tape to avoid leakage. The probe location within the duct was determined by noting the readings on two vernier calipers which were attached to the rigid frame forming a Cartesian co-ordinate system.

*Instrumentation.* The total air flow through the duct was measured either by a rotameter, a venturi, or by determining the entrance velocity with a total pressure probe before the flow profile had developed. Comparisons between the three methods of measurements agreed to within ±2 per cent.

In order to make flow-visualization studies within the duct, cigar smoke was inserted into the stream by means of a probe. The smoke was obtained from a generator, whose general details are shown in Fig. 2. It was constructed from laboratory stands, clamps, and glassware.

Velocities within the duct were measured with a small total-head probe in conjunction with a manometer which determined the difference between the total and static pressures. It is generally desirable from the standpoint of noninterference with the flow field to make the probe diameter small with respect to the duct dimensions. On the other hand, at low velocities and small probe diameters, the effects of viscosity cause an error in the total pressure reading (9) which is troublesome to correct. As a compromise between these two restrictions, the probe dimensions were chosen as follows:

(*a*) Length of probe in the flow direction: 0.55 in.
(*b*) Outside diameter of probe: 0.049 in.
(*c*) Inside diameter of probe: 0.033 in.

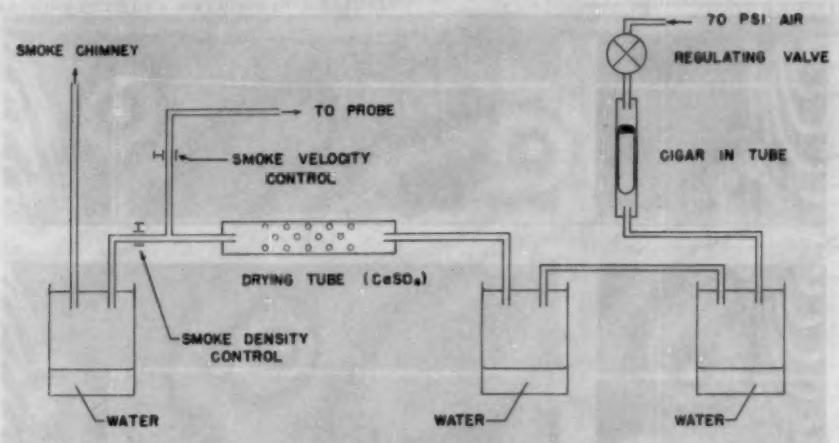


FIG. 2 SCHEMATIC OF SMOKE GENERATOR

To determine the difference between the total and static pressures, it was necessary to make measurements of very small pressure differences. A commercial micromanometer (Meriam Type A-750) was used to read pressure differences greater than 0.002 in. of water. This sensitivity was satisfactory for most of the velocity measurements in the turbulent-flow regime. In the investigation of the laminar regime, it was necessary to read pressure differences as low as 0.0002 in. of water. For this purpose a more sensitive micromanometer was developed wherein the change in liquid level rotated a floating cylinder which had a mirror attached to its top. The cylinder rotation was detected by an optical system and read by a telescope. This micromanometer, which will be described in more detail in a separate paper, can be used to measure accurately pressure differences of order $10^{-4}$ in. of water.

## RESULTS OF THE EXPERIMENTAL PROGRAM

*Flow Visualization.* The first investigations of the flow within triangular-shaped passages were made by conducting flow-visualization studies. The flow was made visible by injection of smoke through a small probe which could be moved along the height of the triangular cross section. The smoke probe was located 24 hydraulic diam from the entrance of Duct I and 35 hydraulic diam from the entrance of Duct II.

For these investigations it was essential to reduce disturbances which are carried with the air into the duct to a minimum. For this reason the settling chamber and the seven screens of very fine mesh size were arranged at the inlet to the duct. It was also found that the setup, in which the air was sucked by the blower through the duct, produced less disturbances in the air stream entering the test section than a setup in which the blower was situated upstream and pressed the air through the duct.

As the smoke probe was moved from the apex toward the base, it was first observed that over a certain distance the smoke appeared as a completely stagnant thread. As the motion toward the base continued, the smoke thread began to exhibit sinusoidal waves (similar to Tollmien-Schlichting waves) traveling downstream and fluctuating within the lengthwise plane which contains the height of the cross section. Finally, as the probe reached a position closer to the base, the amplitude of the waves increased until, at a certain point, the smoke thread diffused within a short distance downstream from the probe, indicating fully developed turbulence. Fig. 3 is a series of photographs illustrating the three types of flow described in the foregoing.

In order to determine the extent of the laminar regime near the triangle apex, a series of smoke studies was made at different Reynolds numbers. For the purpose of this study, the extent of the laminar regime was defined as the region from the apex to where the smoke thread first began to exhibit the lengthwise fluctuations. The remainder of the flow was defined as turbulent. Fig. 4 presents the curve obtained from such observations for Duct I. The amount of air flow through the duct is in this figure represented by the dimensionless parameter Re which is based on the average velocity $w_{avg}$ and on the hydraulic diameter $d_h$. The distance $x$ in which the first fluctuations of the smoke thread occurred is made dimensionless by the duct height $L$ and plotted as ordinates.

Three probes of outside diam 0.035, 0.049, and 0.065 in., respectively, were used in gathering these data. No effect of varying the probe size was noticeable. The solid lines in Fig. 5 show the curves for both ducts without the insertion of the experimental points. All measurements were made near the velocity-profile station.

It is interesting to note that the Reynolds number for which the flow is laminar in the whole cross section is quite low in comparison to values for a round tube. On the other hand, the laminar zone which decreases in size with increasing Reynolds number can still be observed for quite high Reynolds numbers.

Mention should be made at this point of the question of whether the flow was fully developed. Since in these studies it was observed that the smoke thread remained parallel to the tube axis, it was inferred that complete flow development had taken place. As will be described in a later section, further measurements were made of the longitudinal pressure gradient to investigate this consideration.

The flow visualization thus revealed the surprising and remarkable fact that in a triangular passage, laminar flow and turbulent flow exist side by side for an unlimited time (or duct length). The damping properties of the shear flow near the triangle apex are so pronounced that they do not permit even the large turbulent fluctuations which are expected in the turbulent zone to spread into the corner region. It is to be expected that such laminar regions exist generally near corners of noncircular passages. Their existence will be of considerable importance in various applications. It may, for instance, be suspected that they present a pronounced obstacle to heat transfer between duct wall and air flow near the corners.

*Velocity Profiles.* The velocity field of the flow through the

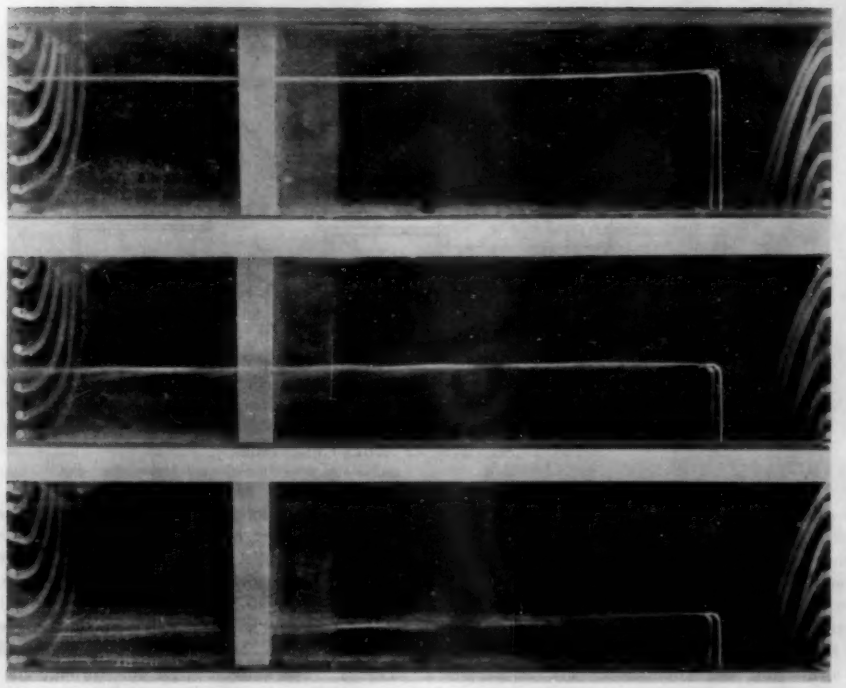

FIG. 3 PHOTOGRAPH OF THREE TYPES OF TRIANGULAR DUCT FLOW

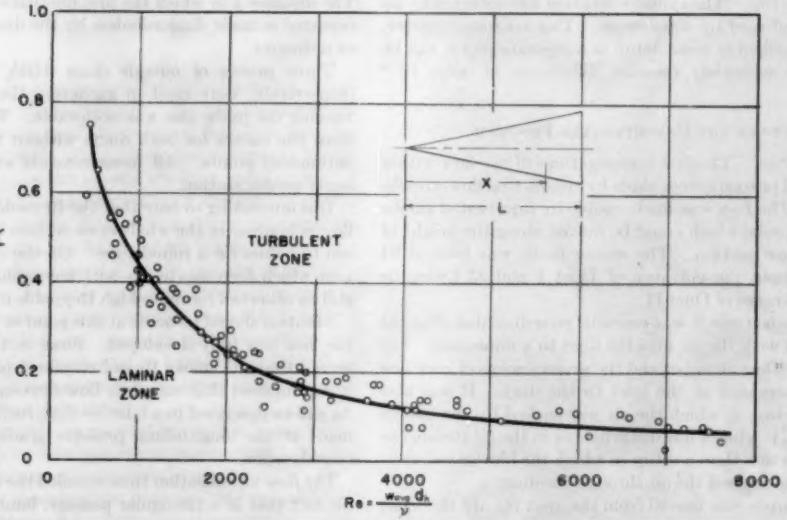


FIG. 4 DETERMINATION OF LAMINAR ZONE IN DUCT I BY FLOW VISUALIZATION

duct was measured in a plane located 71 hydraulic diam from the entrance of Duct I and 66 hydraulic diam from the entrance of Duct II. As described, provisions were made for inserting a probe into the air flow and for determining the location of the probe within the duct.

Three static pressure holes were located around the periphery of the duct in the plane containing the end of the total pressure probe. Differences between total and static pressures were read with the micromanometers previously described.

A number of velocity surveys were made at different Reynolds numbers. The Reynolds number range covered in Duct I was from 750 to 26,000 and in Duct II from 500 to 43,000. Since velocity profiles were measured in both directions perpendicular to the flow, it was possible at the end of any one survey to check the average velocity read with the rotameter or venturi against the average velocity obtained by integrating the profiles. Table 3 lists the Reynolds numbers at which the various profiles were taken and the difference in per cent between the velocities given

TABLE 3 COMPARISONS BETWEEN METHODS OF MEASURING AVERAGE FLOW VELOCITY

| Duct no. | Reynolds number | Per cent difference integration compared to rotameter or venturi |
|---|---|---|
| I | 1000 | −9.90 |
| I | 2950 | −1.44 |
| I | 4590 | −2.15 |
| I | 6600 | −7.04 |
| I | 10890 | −6.72 |
| I | 20850 | −2.82 |
| I | 26100 | −4.00 |
| II | 1000 | +0.32 |
| II | 3000 | +9.1 |
| II | 5000 | +2.1 |
| II | 10000 | +0.14 |
| II | 20580 | −0.12 |
| II | 30130 | −1.23 |
| II | 42988 | −2.46 |

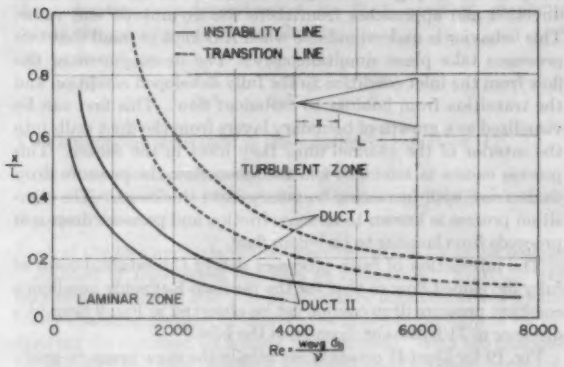


FIG. 5 DETERMINATION OF LAMINAR ZONE IN DUCTS I AND II
(Solid line—flow visualization; dotted line—velocity-profile measurements.)

by the rotameter or venturi and by integration of the profiles. With the exception of four runs in which larger deviations existed for unexplained reasons the agreement of both ways to measure the average velocity appears satisfactory.

The velocity data are presented in various ways to bring out different characteristics of the flow. Fig. 6 shows the center-line profiles from the apex to the center of the base for Duct I at various Reynolds numbers. The corresponding plot for Duct II is similar. The scale $w/w_{avg}$ applies to the profile with the lowest Reynolds number. For the other profiles the scale has to be shifted such that all profiles start with the value zero at $x/L = 0$. For the lowest Reynolds numbers (1000) in Duct I, the velocity variation starting from the apex and traveling toward the triangle base is seen to be parabolic for a considerable distance. This is in agreement with a calculation for laminar flow in a corner which will be described in the next section. As the Reynolds number increases, this parabolic variation is seen to get smaller in extent until at a Reynolds number of 26,100 no evidence of laminar flow remains which is perceptible by this method.

Short vertical lines on the profiles in Fig. 6 indicate the location at which the first fluctuations were observed by flow visualization (as indicated by Fig. 5). It will be noticed that the parabolic variation persists past the point defined as the end of the laminar regime in the smoke studies. Apparently, the flow disturbances which are perceptible by the smoke technique are not of sufficient magnitude to affect the velocity distribution seriously. This agrees with observations on the transition process from laminar to turbulent flow in other types of flow.

The dashed lines in Fig. 5 indicate the point at which the velocity profiles in both ducts begin to deviate from a parabolic variation.

Figs. 7 and 8 show velocity profiles taken along a line parallel to the triangle base for Duct I. Profiles are shown at a low and at

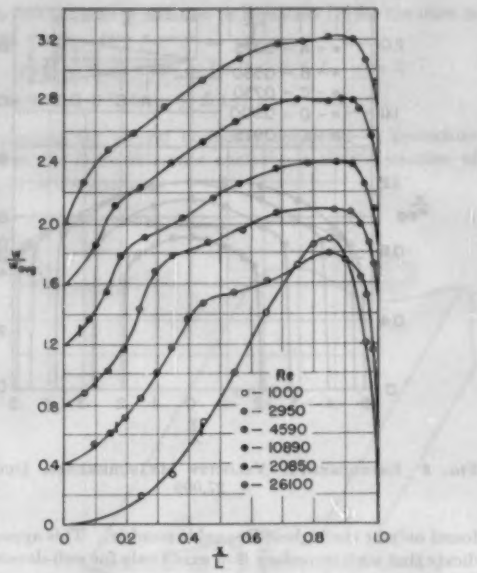


FIG. 6 EXPERIMENTAL VELOCITY MEASUREMENTS ALONG TRIANGLE HEIGHT, DUCT I

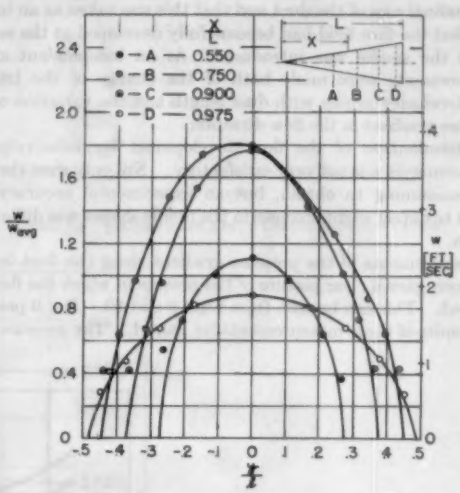


FIG. 7 EXPERIMENTAL VELOCITY MEASUREMENTS, DUCT I, RE 1000

a high Reynolds number. At the low Reynolds number the velocity profiles have a parabolic shape. An exception to this exists only for the profile at D in Fig. 7 which, under the influence of the nearby wall, assumes a fuller shape. Some of the profiles exhibit some assymmetry. No explanation for this fact is known. Fig. 8 exhibits profile shapes which are typical for turbulent flow. Interesting is the shape of the profile shown in Fig. 8 at $x/L = 0.975$. In this plane the velocities near the corner are larger than in the center. Nikuradse (2) also found from measurements at small distances from the passage wall that the velocities were larger near the corners than along the central part of the passage. He attributed this to secondary flows which move fluid particles from the core of the fluid toward the corner regions. In this investigation profiles which indicate such a secondary flow were

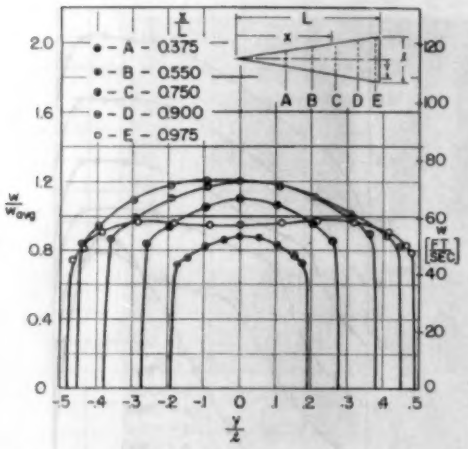


FIG. 8 EXPERIMENTAL VELOCITY MEASUREMENTS, DUCT I, RE 27,000

found only at the highest Reynolds number. This appears to indicate that such secondary flow exists only for well-developed turbulent flow.

*Pressure Drop.* It was mentioned previously that the smoke thread in the flow-visualization studies remained parallel to the longitudinal axis of the duct and that this was taken as an indication that the flow field had become fully developed at the section where the smoke was introduced. As an independent check, measurements were made both of the change of the triangle height-velocity profile with duct length and the variation of the pressure gradient in the flow direction.

Determination of the flow development by velocity-profile measurements was not very satisfactory. Not only were the data time-consuming to obtain, but an experimental accuracy sufficient to detect slight changes in the profile shapes was difficult to obtain.

Measurements of the pressure gradient along the duct length, however, gave a clear picture of the process in which the flow developed. This can be seen from Figs. 9 and 10. Fig. 9 presents the results of these measurements for Duct I. The pressure drop was determined between consecutive pressure taps along the duct. It is plotted in Fig. 9 over the location halfway between the corresponding taps. The figure indicates that for low Reynolds numbers, for which the flow is laminar in the whole duct length, the pressure drops monotonically from the duct entrance toward the exit. The asymptotic value which the pressure drop approaches for large duct lengths appears to be reached sufficiently at the exit cross section. For medium Reynolds numbers the pressure drop along the duct behaves in a peculiar way. It drops within a certain length to a minimum and then approaches the asymptotic value from below. There are indications on some curves that behind the minimum the pressure drop goes through a maximum in the downstream direction and approaches from there the asymptotic end value. This behavior is understandable when it is kept in mind that two processes take place simultaneously: The development of the flow from the inlet condition to the fully developed condition and the transition from laminar to turbulent flow. This first can be visualized as a growth of boundary layers from the duct walls into the interior of the channel until they meet in the center. This process causes in laminar as in turbulent flow the pressure drop to decrease with increasing boundary-layer thickness. The transition process is known to increase friction and pressure drop as it proceeds from laminar to turbulent flow.

The interaction of both processes delays the establishment of fully developed flow so that for the medium Reynolds numbers a constant pressure drop cannot yet be observed in Fig. 9 even at a distance of 71 hydraulic diam from the inlet.

Fig. 10 for Duct II presents essentially the same pressure-gradient condition. At the lowest Reynolds number, the flow appears to become fully developed at the duct exit. From a Reynolds number of approximately 3000 to 4300 the flow definitely is still developing at a distance of 61 hydraulic diam from the entrance and at the higher Reynolds numbers, it seems to once again be fully developed at the exit.

It has been pointed out that it was difficult to detect a change in the shape of the velocity field in the latter part of the duct within the accuracy of the measurements. Obviously pressure-drop measurements are a more sensitive indication of undeveloped or developed flow conditions.

Figs. 9 and 10 indicate that very long ducts have to be investigated if accurate knowledge on friction in the fully developed flow

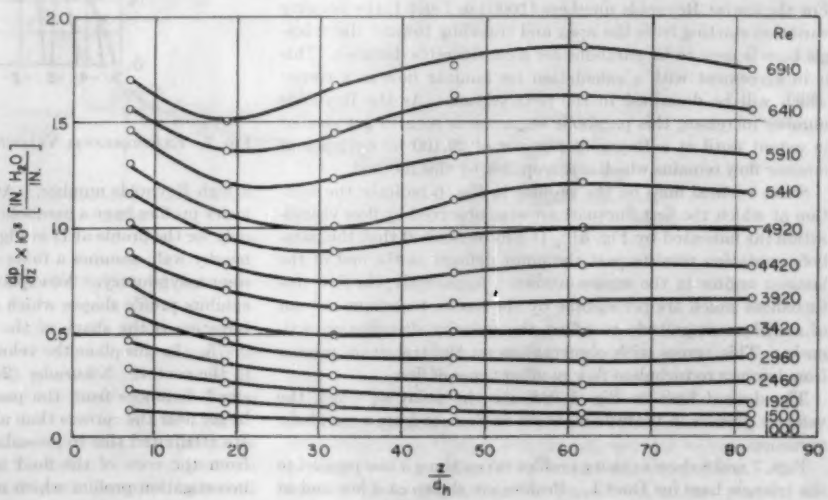


FIG. 9 LONGITUDINAL PRESSURE-DROP MEASUREMENTS, DUCT I

condition is required. The trends indicated by the figures also make it doubtful whether fully developed conditions were always obtained in the previously published measurements on friction factors in noncircular ducts.

## Theoretical Investigations

*Velocity Field.* Analytic and numerical solutions may be obtained for the triangular duct in the laminar case. Only fully developed flow will be investigated in these paragraphs. Fig. 11 shows a sketch of the triangular duct with the co-ordinate system. For the meaning of other symbols refer to the nomenclature.

For fully developed laminar flow the velocity components in the $x$ and $y$-directions are zero and the velocity component $w$ in the $z$-direction is independent of $z$. With constant property values, the velocity field is described by

$$\frac{\partial^2 w}{\partial x^2} + \frac{\partial^2 w}{\partial y^2} = \frac{1}{\mu}\frac{\partial p}{\partial z} \quad \ldots\ldots\ldots\ldots\ldots\ldots [1]$$

Two approaches were used in the solution of Equation [1]:

(*a*) Numerical solutions by relaxation.

(*b*) Solution of the differential equation with simplified boundary conditions.

Each of the two methods will be described in the following pages.

*Solution of Differential Equation by Relaxation.* Equation [1] may be transformed into a finite difference equation either by directly changing the partial derivatives into a finite form or by rederiving the equation for a finite fluid element. With the triangular shape of the duct, either a rectangular or a triangular mesh can be used to obtain the finite-difference equation. The rectangular mesh was preferred in this case for its simplicity in the numerical calculations.

Using standard relaxation techniques, the velocity distribution was calculated for Duct I. These data will be discussed in comparison with other solutions in the next sections.

*Solution of Differential Equation With Simplified Boundary Conditions.* The complete set of boundary conditions which the velocity $w$ has to fulfill in addition to Equation [1] for the duct in Fig. 11 are

1 when $y = \pm x \tan \alpha$, for $0 < x < L$; $w = 0$

2 when $x = L$, for $y \leq L \tan \alpha$; $w = 0$

By neglecting the second boundary condition—a procedure suggested in the finite-difference analysis—a simple solution of Equation [1] is obtained, i.e.

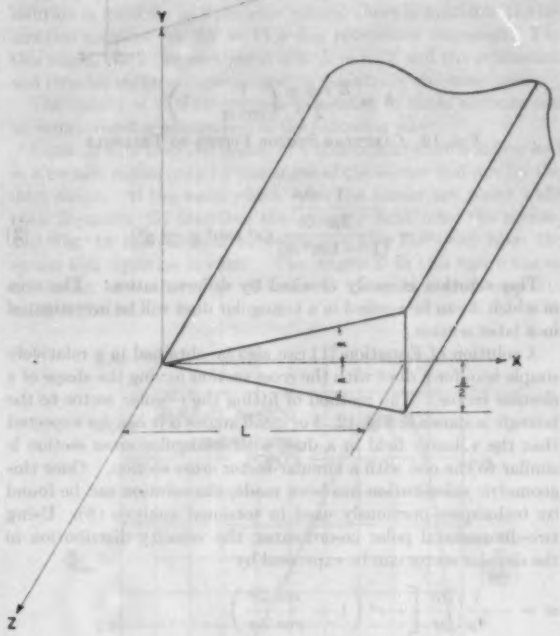


Fig. 11 Triangular Duct Co-Ordinate System

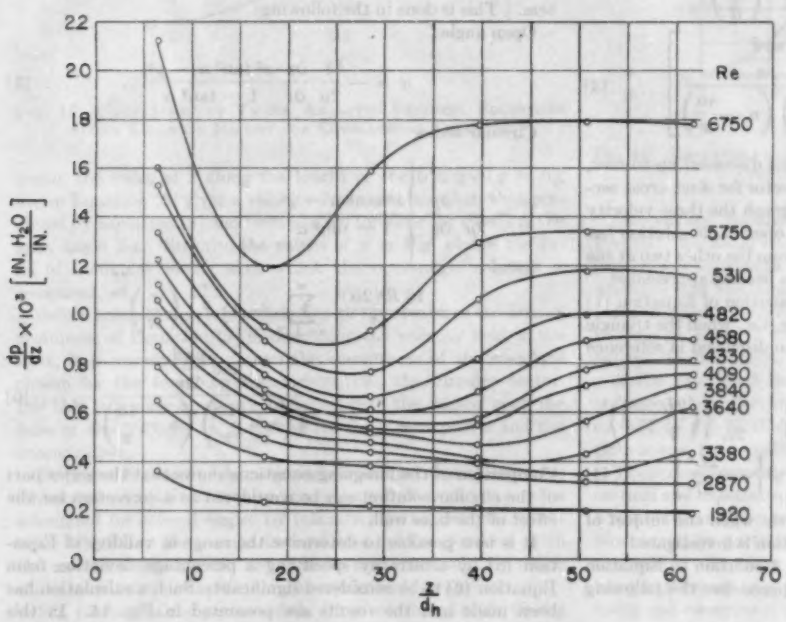


Fig. 10 Longitudinal Pressure-Drop Measurements, Duct II

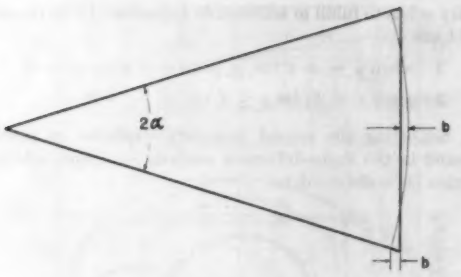


$$b = \frac{R \cos \alpha}{2}\left(\frac{1}{\cos \alpha} - 1\right)$$

FIG. 12 CIRCULAR SECTOR FITTED TO TRIANGLE

$$w = \frac{-\frac{1}{2\mu}\frac{\partial p}{\partial z}}{(1 - \tan^2 \alpha)}(x^2 \tan^2 \alpha - y^2) \quad \ldots\ldots [2]$$

This solution is easily checked by differentiation. The area in which it can be applied in a triangular duct will be investigated in a later section.

A solution of Equation [1] can also be obtained in a relatively simple way for a duct with the cross section having the shape of a circular sector. The method of fitting the circular sector to the triangle is shown in Fig. 12. For small angles $\alpha$ it can be expected that the velocity field in a duct with triangular cross section is similar to the one with a circular-sector cross section. Once this geometric substitution has been made, the solution can be found by techniques previously used in torsional analysis (8). Using two-dimensional polar co-ordinates, the velocity distribution in the circular sector can be expressed by

$$w = -\frac{1}{4\mu}\frac{\partial p}{\partial z}\left[-r^2\left(1 - \frac{\cos 2\theta}{\cos 2\alpha}\right) + \frac{16R^2(2\alpha)^2}{\pi^3}\sum_{n=1,3}^{\infty}(-1)^{\frac{n+1}{2}}\left(\frac{r}{R}\right)^{\frac{n\pi}{2\alpha}} \frac{\cos\frac{n\pi\theta}{2\alpha}}{n\left(n + \frac{4\alpha}{\pi}\right)\left(n - \frac{4\alpha}{\pi}\right)}\right] \quad \ldots\ldots [3]$$

The agreement between the three solutions discussed up to now, i.e., relaxation, open angle, and circular sector for duct cross section I can be seen from Fig. 13. In this graph the three velocity profiles for $y = 0$ are plotted. Since the open-angle solution has no cognizance of the base wall, it departs from the other two at the point where the effect of this wall begins to become appreciable.

There exists in the literature an exact solution of Equation [1] for an isosceles triangle when $\alpha = 30$ deg, i.e., when the triangle is equilateral. This solution, which is also discussed in reference (8), can be expressed by

$$w = -\frac{1}{2\mu}\frac{\partial p}{\partial z}\left[\frac{1}{2}\left\{\left(\frac{2L}{3} - x\right)^2 + y^2\right\} - \frac{1}{2L}\left\{\left(\frac{2L}{3} - x\right)^3 - 3\left(\frac{2L}{3} - x\right)^3 - 3\left(\frac{2L}{3} - x\right)y^2\right\} - \frac{2L^2}{27}\right]^3 \quad \ldots\ldots [4]$$

Equation [4] will prove to be of use shortly when the subject of the area of validity of the open-angle solution is investigated.

*Comparison of the Different Solutions.* A solution to Equation [1] is useful by the degree to which it approaches the following conditions.

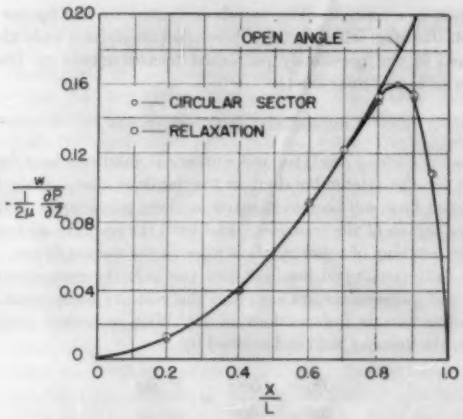


FIG. 13 COMPARISON OF THREE ANALYTIC VELOCITY SOLUTIONS ALONG TRIANGLE HEIGHT, DUCT I

1 The solution can be expressed by a simple mathematical function.

2 The solution accurately describes the velocity field within the actual duct.

Equation [2], the open-angle solution, is the most satisfactory from the standpoint of simplicity. On the other hand, Equation [3] for the circular sector would appear to be more accurate, considering as it does, the effect of the far wall. Because the simplicity of Equation [2] will be an important factor in future heat-transfer calculations, it is important to know over how large an area of the duct it accurately describes the true velocity field. To investigate this question, it will be assumed for the moment that the circular-sector solution is sufficiently accurate to serve as a standard of comparison. Later, the validity of this assumption will be discussed.

The simplest way to compare the open-angle and circular-sector solutions is to write them down in the same co-ordinate system. This is done in the following:

Open angle

$$w = -\frac{1}{2\mu}\frac{\partial p}{\partial z}\frac{x^2 \tan^2 \alpha - y^2}{1 - \tan^2 \alpha} \quad \ldots\ldots [5]$$

Circular sector

$$w = -\frac{1}{2\mu}\frac{\partial p}{\partial z}\left\{\frac{x^2 \tan^2 \alpha - y^2}{1 - \tan^2 \alpha} + \frac{16\,R^2(2\alpha)^2}{\pi^3}\sum_{n=1,3}^{\infty}(-1)^{\frac{n+1}{2}}\left(\frac{r}{R}\right)^{\frac{n\pi}{2\alpha}} \frac{\cos\frac{n\pi\theta}{2\alpha}}{n\left(n + \frac{4\alpha}{\pi}\right)\left(n - \frac{4\alpha}{\pi}\right)}\right\} \quad \ldots\ldots [6]$$

Comparison of the foregoing equations shows that the series part of the circular solution can be considered as a correction for the effect of the base wall.

It is now possible to determine the range of validity of Equation [5] by arbitrarily specifying a percentage deviation from Equation [6] to be considered significant. Such a calculation has been made and the results are presented in Fig. 14. In this

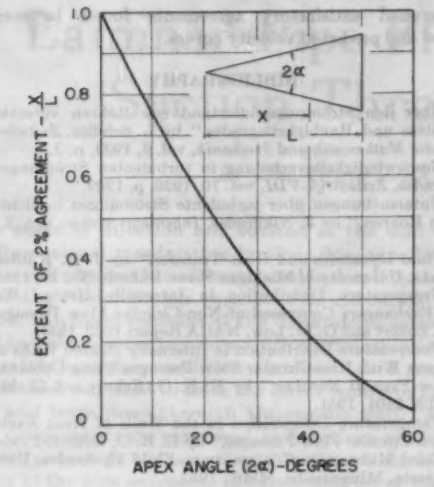


FIG. 14 AREA OF 2 PER CENT AGREEMENT BETWEEN OPEN-ANGLE AND CIRCULAR-SECTOR SOLUTIONS

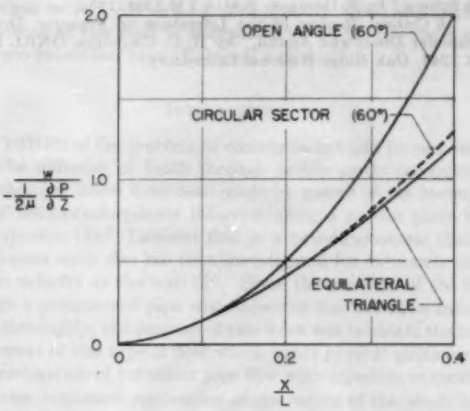


FIG. 15 COMPARISON OF THREE ANALYTIC VELOCITY SOLUTIONS ALONG TRIANGLE HEIGHT FOR EQUILATERAL TRIANGLE

graph, the value of $x$ along the height of the triangle ($y = 0$), where Equation [6] gives a velocity 2 per cent less than that predicted by Equation [5], has been plotted for different values of the apex angle $2\alpha$. Strictly, the values of $x$ in Fig. 14 are the radii of a circular sector with which the open-angle solution is compared.

Before being completely satisfied as to the results of the area of usefulness of Equation [5] in describing the velocity field in the apex, it is necessary to discuss the correctness of the standard chosen for the foregoing comparison, i.e., the circular sector. For this it is only necessary to investigate the region near the base of the triangle, i.e., between the 2 per cent points and the triangle apex.

To prove this for an arbitrary angle would involve an excessive amount of calculations, because the velocity field would have to be calculated for several angles by relaxation or by analytic methods. Therefore the comparison of the sector solution with the one for a triangle will be made for one angle only for which the exact solution is known, i.e., the equilateral triangle.

Fig. 15 shows a comparison of the three solutions for the 60-deg equilateral triangle near the apex. It is of interest to see that the circular sector and the exact solution are the same up to a value of $x/L = 0.24$, whereas the 2 per cent point at this angle is only $x/L = 0.025$ or one order of magnitude lower. The cross profiles (with $x$ = const) have also been compared for the sector and exact solution for $2\alpha = 60$ deg and $x/L = 0.24$, and they deviate from each other by no more than slide-rule accuracy or about 1 per cent.

To further substantiate the assumption that the circular-sector solution is valid up to 2 per cent points, there is available the relaxation solution for $2\alpha = 11.5$ deg previously discussed. For this angle, the 2 per cent point is $x/L = 0.72$ and the relaxation and circular-sector solutions agree to essentially the same point.

The results of the calculations presented in these sections can be summarized or generalized in the following way:

Laminar flow near the corner of a noncircular duct is influenced in a certain region only by the angle of the corner and not by the duct shape. If the walls which form the corner are plane walls then Equation [5] describes the velocity field near the corner, and Fig. 14 can be used to determine how far away from the corner this equation is valid. The length $L$ in this figure has to be chosen as the average distance of the corner from opposite walls of the duct.

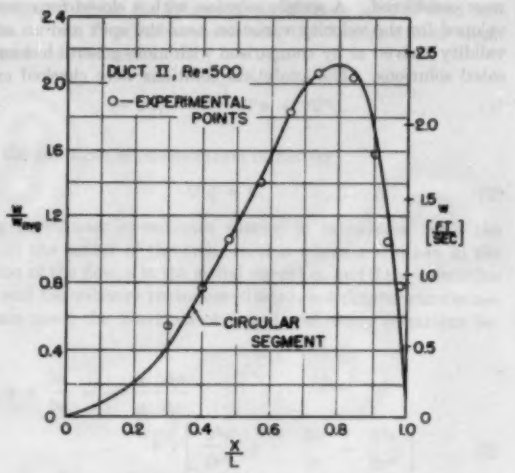


FIG. 16 EXPERIMENTAL VELOCITY MEASUREMENTS COMPARED WITH ANALYTIC SOLUTION, DUCT II

*Comparison Between Experimental and Theoretical Velocity Profiles.* By using the micromanometer developed for this purpose, it was possible to make velocity measurements in both ducts when the flow was laminar or very nearly so.

Fig. 16 shows the velocity profile taken along the height of the triangle in Duct II for the smallest Reynolds number investigated. In this figure, the experimental points are compared with a profile calculated from the appropriate circular sector. The measured velocities are corrected for probe-viscosity effects according to the method described in reference (9). The corrections lowered the smallest velocity by 16 per cent.

These measurements indicate good agreement between the theoretical and experimental points. It is interesting to refer to Fig. 5 where the smoke measurements indicate that both of these profiles should be partially turbulent. It was already discussed in connection with these measurements that turbulent fluctuations have to increase to a certain level before they influence the velocity and consequently the friction characteristics.

## Summary and Conclusions

An experimental and analytical study has been described on the internal flow characteristics of triangular ducts. Flow-visualization techniques, longitudinal pressure-drop measurements, and probing of the velocity field have all been used to investigate this flow for two ducts over a Reynolds number range from completely laminar to completely turbulent flow.

Flow-visualization measurements using smoke indicated that over a large Reynolds number range both laminar and turbulent flows exist side by side within the duct. Experimental data have been gathered for both ducts showing the extent of these flow regimes as a function of Reynolds number.

The velocity field was measured at the downstream end of the two ducts for a variety of Reynolds numbers. These measurements corroborated the existence of the two-regime flow mentioned, as well as serving as a fund of basic velocity measurements.

Pressure-gradient measurements indicated that at some Reynolds numbers the flow is not completely developed at a distance of 70 diam from the inlet.

Analytical studies were conducted on the fully developed laminar-flow problem. Relaxation procedures and solutions of the flow-differential equation with simplified boundary conditions were considered. A simple solution with a closed form was developed for the velocity variation near the apex and an area of validity arrived at by comparison with more general but complicated solutions. The analytical solutions were checked experimentally and satisfactory agreements found between the measured and predicted velocity curves.

## BIBLIOGRAPHY

1 "Über den Strömungswiderstand von Rohren verschiedenen Querschittes und Ranhigkeitsgrades," by L. Schiller, *Zeitschrift für angewandte Mathematik und Mechanik*, vol. 3, 1923, p. 2.

2 "Geschwindigkeitsverteilung in turbulenten Strömungen," by J. Nikuradse, *Zeitschrift-VDI*, vol. 70, 1926, p. 1229.

3 "Untersuchungen über turbulente Strömungen in nicht kreisförmigen Rohren," by J. Nikuradse, *Ingenieur-Archiv*, vol. 1, 1930, p. 306.

4 "Fluid Dynamics and Heat Transfer," by J. G. Knutsen and D. L. Katz, University of Michigan Press, Bulletin No. 37, 1954.

5 "Temperature Distribution in Internally Heated Walls of Heated Exchangers Composed of Non-Circular Flow Passages," by E. R. G. Eckert and G. M. Low, NACA Report 1022, 1951.

6 "Temperature Distribution in Internally Heated Walls of Heat Exchangers With Non-Circular Flow Passages Using Coolants With Very Low Prandtl Number," by E. R. G. Eckert and G. M. Low, NACA TN 2401, 1951.

7 "Temperature Distribution in the Walls of Heat Exchangers With Non-Circular Flow Passages," by E. R. G. Eckert, Proceedings of the Third Midwestern Conference on Fluid Mechanics, University of Minnesota, Minneapolis, Minn., 1951.

8 "Theory of Elasticity," by S. Timoshenko and J. N. Goodier, McGraw-Hill Book Company, Inc., New York, N. Y., second edition, 1951, p. 236.

9 "The Effect of High Viscosity on the Flow Around a Cylinder and a Sphere," by F. Homann, NACA TM 1344, 1952.

10 "A Critical Review of the Literature on Pressure Drop in Noncircular Ducts and Annuli," by H. C. Claiborne, ONRL Document 1248, Oak Ridge National Laboratory.

# Laminar Pipe Flow With Injection and Suction Through a Porous Wall[1]

By S. W. YUAN[2] and A. B. FINKELSTEIN,[3] BROOKLYN N. Y.

**The effect of injection and suction at the wall on the two-dimensional steady-state laminar flow of a fluid in a porous-wall pipe has been investigated in detail by the solution of the Navier-Stokes equations in cylindrical co-ordinates. An exact solution of the dynamic equations, reduced to a third-order nonlinear differential equation with appropriate boundary conditions, is obtained. A perturbation method was used to solve the latter equation for both small and large flows through the porous wall. The velocity components are expressed as functions of the ratio of velocity through the porous wall to the maximum axial velocity at the pipe entrance, the co-ordinates of the pipe, and the physical properties of the fluid. The results show that the effect of injection at the porous wall of the pipe is to increase the friction coefficient at the wall. For an injection ratio $Q/W = 0.01$ ($500 \leq \mathrm{Re} \leq 2500$) the friction coefficient at the wall is increased by 70–85 per cent over the zero injection case (Poiseuil e case).**

## Introduction

STUDIES of the problem of cooling rocket and jet motors by the diffusion of fluids through porous-metal combustion-chamber liners have been made by means of the investigation of the boundary-layer behavior along a porous plate with fluid injection (1).[4] Laminar flow in a two-dimensional channel with porous walls also has been investigated for extremely small suction velocity at the wall (2). Since the problem of the flow through a porous-wall pipe with injection has not been investigated thoroughly, the purpose of this work was to obtain the basic phenomena of this type of flow which would provide guidance for the investigation of turbulent pipe flow with injection or suction.

Another important application of the results of this study is to the boundary-layer control for decreasing drag and increasing lift of airplane wings. In this connection the boundary-layer flow is sucked through the surface of the wing to a duct. The ensuing flow in the duct simulates the problem of flow through a pipe with fluid injection at the walls.

In the present investigation an exact solution of the Navier-Stokes equations in cylindrical co-ordinates with injection or suction as a boundary condition at the wall was obtained. On the other hand, the problems of flow on a porous flat plate or curved wall were previously made by the approximate solution of the Prandtl boundary-layer equations.

The assumptions made in the present study were: (1) The fluid is incompressible, i.e., the mass density and the viscosity of the fluid were assumed to be constant; (2) the main flow was assumed to be laminar, and the fluid flowing in the axial direction and the fluid flowing through the porous wall were assumed homogeneous; (3) the maximum axial velocity at the entrance of the porous-wall pipe is equal to the maximum axial velocity in the Poiseuille's flow; and (4) the fluid flowing through the porous wall is uniform throughout.

## Fundamental Equations

The three-dimensional steady flow of a viscous incompressible fluid is governed by the following set of basic laws of fluid mechanics. From Newton's second law, the Navier-Stokes equations were derived as follows

$$(\vec{q}\cdot\nabla)\vec{q} = -\frac{1}{\rho}\nabla p + \nu\nabla^2\vec{q} \qquad [1]$$

From the principle of conservation of matter

$$\nabla\cdot\vec{q} = 0 \qquad [2]$$

If a curvilinear co-ordinate system is introduced with the origin at the center of the cross section where $x$ is taken in the direction of the flow, $r$ in the radial direction, and $\theta$ the azimuthal angle, and the ordinary vector curvilinear co-ordinate transformations are used, the Navier-Stokes and continuity equations become

$$u\frac{\partial u}{\partial x} + v\frac{\partial u}{\partial r} = -\frac{1}{\rho}\frac{\partial p}{\partial x} + \nu\left[\frac{\partial^2 u}{\partial r^2} + \frac{1}{r}\frac{\partial u}{\partial r} + \frac{\partial^2 u}{\partial x^2}\right] \qquad [3]$$

$$u\frac{\partial v}{\partial x} + v\frac{\partial v}{\partial r} = -\frac{1}{\rho}\frac{\partial p}{\partial r} + \nu\left[\frac{\partial^2 v}{\partial x^2} + \frac{\partial^2 v}{\partial r^2} + \frac{1}{r}\frac{\partial v}{\partial r} - \frac{v}{r^2}\right] \qquad [4]$$

and

$$\frac{\partial(ru)}{\partial x} + \frac{\partial(rv)}{\partial r} = 0 \qquad [5]$$

where $u$ and $v$ represent the $x$ and $r$-components of the velocity at any point (see Fig. 1) and $\partial/\partial\theta = 0$ because of axially symmetric flow.

The foregoing equations will be used to investigate the fluid flow in a circular pipe with a porous wall through which uniform fluid injection or suction is applied. The boundary conditions are

$$\left.\begin{aligned} &\text{At } r = 0: \quad v = \frac{\partial u}{\partial r} = 0 \\ &\text{At } r = R: \quad u = 0, \quad v = -v_0 = \text{const} \end{aligned}\right\} \qquad [6]$$

For a two-dimensional incompressible flow a stream function exists such that

---

[1] This research was conducted under the auspices of Project SQUID, jointly sponsored by the Office of Naval Research, Department of the Navy, Office of Scientific Research, Department of the Air Force, and Office of Ordnance Research, Department of the Army.

[2] Research Professor of Aeronautical Engineering, Polytechnic Institute of Brooklyn.

[3] Research Associate of Aeronautical Engineering, Polytechnic Institute of Brooklyn.

[4] Numbers in parentheses refer to the Bibliography at the end of the paper.

Contributed by the Heat Transfer Division and presented at the Heat Transfer and Fluid Mechanics Institute, Los Angeles, Calif., June, 1955, of The American Society of Mechanical Engineers.

Note: Statements and opinions advanced in papers are to be understood as individual expressions of their authors and not those of the Society. Manuscript received at ASME Headquarters, August 22, 1955. This paper was not preprinted.

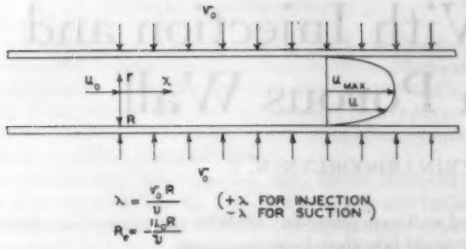


FIG. 1 FLOW ALONG A POROUS PIPE WITH INJECTION

$$ru = \frac{\partial \psi}{\partial r}, \quad -rv = \frac{\partial \psi}{\partial x} \ldots\ldots\ldots\ldots [7]$$

and the continuity Equation [5] is satisfied.

For a constant fluid injection or suction at the porous wall and the given boundary conditions, the following stream function is introduced

$$\psi = \left[A + B\frac{x}{R}\right] f(\eta) \ldots\ldots\ldots\ldots [8]$$

where $\eta = (r/R)^2$. The constant $A$ is determined from the condition at $\eta = 0$ and $x = 0$ where the maximum velocity $u_0$ for Poiseuille's flow exists. The constant $B$ is determined from the law of conservation of matter. The stream function can then be expressed as

$$\psi = \frac{R^2}{2}\left[\frac{u_0}{f'(0)} + 4v_0\frac{x}{R}\right] f(\eta) \ldots\ldots\ldots\ldots [9]$$

From Equations [7] and [9] the velocity components in the direction of flow and the radial direction are given by

$$u = u_0\left[\frac{1}{f'(0)} + 4\frac{\lambda}{\mathrm{Re}}\frac{x}{R}\right] f'(\eta) \ldots\ldots\ldots [10]$$

$$v = -2v_0\frac{f(\eta)}{\sqrt{\eta}} \ldots\ldots\ldots\ldots [11]$$

where $\lambda = v_0 R/\nu$ and $\mathrm{Re} = u_0 R/\nu$. The function $f(\eta)$ appearing in the foregoing equations is the only unknown yet to be determined in terms of the distance parameter $\eta$. Equation [11] indicates that the radial velocity becomes a function of $\eta$ only. This is because of the assumption of constant velocity $v_0$ at the wall.

By introducing the expressions of $u$ and $v$ from Equations [10] and [11] into Equations [3] and [4] there result

$$-\frac{1}{\rho}\frac{\partial p}{\partial x} = \frac{4u_0}{R^2}\left[\frac{1}{f'(0)} + 4\frac{\lambda}{\mathrm{Re}}\frac{x}{R}\right] \times [Rv_0(f'^2 - ff'') - \nu(\eta f''' + f'')] \ldots\ldots [12]$$

$$\frac{1}{\rho}\frac{\partial p}{\partial \eta} = \frac{2v_0}{R}\left[Rv_0\left(\frac{f^2}{\eta^2} - \frac{2ff'}{\eta}\right) - 2\nu f''\right] = F(\eta) \ldots [13]$$

Since the right-hand side of Equation [13] is a function of $\eta$ only, differentiation of both sides of it with respect to $x$ yields

$$\frac{\partial^2 p}{\partial x \partial \eta} = 0 \ldots\ldots\ldots\ldots [14]$$

Hence, differentiating Equation [12] with respect to $\eta$ gives

$$\frac{d}{d\eta}[Rv_0(f'^2 - ff'') - \nu(\eta f''' + f'')] = 0 \ldots\ldots [15]$$

which is to be satisfied for all $x$.

Integrating Equation [15], one obtains

$$\eta f''' + f'' - \lambda(f'^2 - ff'') = c \ldots\ldots\ldots\ldots [16]$$

for $\lambda \leq 1$, and

$$f'^2 - ff'' - \frac{1}{\lambda}(\eta f''' + f'') = k \ldots\ldots\ldots\ldots [17]$$

for $\lambda > 1$, where $c$ and $k$ are the constants of integration to be determined. The boundary conditions are obtained with the aid of Equations [6], [10], and [11]. Thus

$$\left.\begin{aligned} f(0) = f'(1) = 0; \quad \lim_{\eta \to 0} \sqrt{\eta}\, f''(\eta) = 0 \\ f(1) = \frac{1}{2} \end{aligned}\right\} \ldots\ldots [18]$$

Equation [16] is an ordinary nonlinear differential equation of the third order which resulted from the Navier-Stokes' equations and the continuity equation by the similarity transformation. With the aid of the four given boundary conditions an exact solution can be obtained and the constant of integration $c$ determined.

It can be seen that the limiting form of Equation [16], by letting $v_0$ approach to zero, is the equation describing a flow through a circular pipe with impermeable walls. The solution of this equation which satisfies all the four boundary conditions given in Equations [18] is the well-known Poiseuille's law for pipe flow. If small values of $\lambda$ are treated as a perturbation parameter a solution of Equation [16] can be obtained which will be discussed in the next section.

On the other hand, if large values of $\lambda$ are treated as a perturbation parameter the third-order differential Equation [17] is reduced to a second-order one. The solution of Equation [17] also can be obtained in the same manner since all four boundary conditions given in Equations [18] can be satisfied.

## SOLUTION FOR SMALL $\lambda$

The solution of Equation [16] can be expressed for small value of $\lambda$, by a power series developed near $\lambda = 0$ as follows

$$f = f_0 + \lambda f_1 + \lambda^2 f_2 + \ldots + \lambda^n f_n \ldots\ldots\ldots [19]$$

and

$$c = c_0 + \lambda c_1 + \lambda^2 c_2 + \ldots + \lambda^n c_n \ldots\ldots\ldots [20]$$

where the $f_n$'s and $c_n$'s are taken to be independent of $\lambda$. By substituting Equations [19] and [20] into Equation [16] and equating coefficients of like powers of $\lambda$, one obtains the following set of equations

$$\eta f_0''' + f_0'' = c_0 \ldots\ldots\ldots\ldots [21]$$

$$\eta f_1''' + f_1'' - f_0'^2 + f_0 f_0'' = c_1 \ldots\ldots\ldots\ldots [22]$$

$$\eta f_2''' + f_2'' - 2f_0' f_1' + f_0'' f_1 + f_0 f_1'' = c_2 \ldots\ldots [23]$$

The boundary conditions to be satisfied by the $f_n$'s are from Equations [18]

$$\left.\begin{aligned} f_n(0) = f_n'(1) = 0; \quad \lim_{\eta \to 0} \sqrt{\eta}\, f_n''(\eta) = 0 \\ \text{for all } n \\ f_0(1) = \frac{1}{2} \\ f_n(1) = 0, \quad n \geq 1 \end{aligned}\right\} \ldots [24]$$

The second-order perturbation solution of Equation [16] obtained by solving Equations [21] to [23] is given as follows

$$f(\eta) = \left(\eta - \frac{1}{2}\eta^3\right) + \lambda\left(-\frac{\eta}{18} + \frac{\eta^2}{8} - \frac{\eta^3}{12} + \frac{\eta^4}{72}\right) + \lambda^2\left(\frac{83}{5400}\eta - \frac{19}{540}\eta^2 + \frac{11}{432}\eta^3 - \frac{1}{144}\eta^4 + \frac{1}{720}\eta^5 - \frac{1}{10800}\eta^6\right) \quad [25]$$

$$c = -1 - \frac{3}{4}\lambda + \frac{11}{270}\lambda^2 \quad [26]$$

It is seen from the foregoing equations that the second-order perturbation solution is sufficiently accurate even for $\lambda = 1$. The velocity components in the axial and radial directions are obtained by substituting Equation [25] into Equations [10] and [11], respectively, as follows

$$\frac{u}{u_0} = \left[\frac{1}{1 - \frac{\lambda}{18} + \frac{83}{5400}\lambda^2} + 4\frac{\lambda}{\mathrm{Re}}\frac{x}{R}\right] \times \left[1 - \eta + \frac{\lambda}{36}(-2 + 9\eta - 9\eta^2 + 2\eta^3) + \frac{\lambda^2}{10{,}800}(166 - 760\eta + 825\eta^2 - 300\eta^3 + 75\eta^4 - 6\eta^5)\right] \quad [27]$$

$$\frac{v}{u_0} = -\frac{2\lambda}{\mathrm{Re}\sqrt{\eta}}\left[\eta - \frac{1}{2}\eta^2 + \frac{\lambda}{72}(-4\eta + 9\eta^2 - 6\eta^3 + \eta^4) + \frac{\lambda^2}{10{,}800}(166\eta - 380\eta^2 + 275\eta^3 - 75\eta^4 + 15\eta^5 - \eta^6)\right] \quad [28]$$

The pressure distribution in the axial and radial directions are obtained upon the substitution of Equation [25] into Equations [12] and [13], and integrating. Then one obtains

$$\frac{p(0,0) - p(x,r)}{\frac{\rho u_0^2}{2}} = \frac{8}{\mathrm{Re}}\left[1 + \frac{3}{4}\lambda - \frac{11}{270}\lambda^2\right] \times \left[\frac{1}{f'(0)} + 2\frac{\lambda}{\mathrm{Re}}\frac{x}{R}\right]\left(\frac{x}{R}\right) + 4\left(\frac{\lambda}{\mathrm{Re}}\right)^2\frac{f^2}{\eta} - \frac{8\lambda}{\mathrm{Re}^2}[f'(0) - f'(\eta)] \quad [29]$$

The pressure drop in the flow direction can be readily obtained from Equation [29], i.e.

$$\frac{p(0,r) - p(x,r)}{\frac{\rho u_0^2}{2}} = \frac{8}{\mathrm{Re}}\left[1 + \frac{3}{4}\lambda - \frac{11}{270}\lambda^2\right] \times \left[\frac{1}{f'(0)} + 2\frac{\lambda}{\mathrm{Re}}\frac{x}{R}\right]\left(\frac{x}{R}\right) \quad [30]$$

The coefficient of skin friction at the wall also can be obtained from Equation [27], and can be written

$$c_f = \frac{\tau_0}{\frac{\rho u_0^2}{2}} = \frac{4}{\mathrm{Re}}\left[\frac{1}{1 - \frac{\lambda}{18} + \frac{83\lambda^2}{5400}} + 4\frac{\lambda}{\mathrm{Re}}\frac{x}{R}\right] \times \left[1 + \frac{\lambda}{12} - \frac{13\lambda^2}{540}\right] \quad [31]$$

### Solution for Large $\lambda$

The solution of Equation [17] can be expressed for large values of $\lambda$, by a power series developed near $1/\lambda = 0$ as follows

$$f = f_0 + \frac{1}{\lambda}f_1 + \frac{1}{\lambda^2}f_2 + \ldots + \frac{1}{\lambda^n}f_n \quad [32]$$

and

$$k = k_0 + \frac{1}{\lambda}k_1 + \frac{1}{\lambda^2}k_2 + \ldots + \frac{1}{\lambda^n}k_n \quad [33]$$

where the $f_n$'s and $k_n$'s are taken to be independent of $\lambda$. By substituting Equations [32] and [33] into Equation [17] and setting all coefficients of like powers of $1/\lambda$ equal to zero, one obtains the following set of equations

$$f_0 f_0'' - f_0'^2 = k_0 \quad [34]$$

$$f_0 f_1'' - 2f_0'f_1' + f_0''f_1 + (\eta f_0''' + f_0'') = k_1 \quad [35]$$

$$f_0 f_2'' - 2f_0'f_2' + f_0''f_2 + f_1f_1'' - f_1'^2 + (\eta f_1''' + f_1'') = k_2 \quad [36]$$

The boundary conditions to be satisfied by the $f_n$'s are from Equations [18]

$$\left.\begin{aligned} &f_n(0) = f_n'(1) = 0; \quad \lim_{\eta\to 0}\sqrt{\eta}\, f_n''(\eta) = 0 \\ &\text{for all } n \\ &f_0(1) = \frac{1}{2} \\ &f_n(1) = 0, \quad n \geq 1 \end{aligned}\right\} \quad [37]$$

The first-order perturbation of Equation [17], obtained by solving the nonlinear second-order Equation [34] and the linear second-order Equation [35], is given as follows

$$f(\eta) = \frac{1}{2}\sin\frac{\pi}{2}\eta + \frac{1}{\lambda}\left\{\left[A_1 - \frac{\pi^2}{16}\int_1^\eta \frac{\xi^2 d\xi}{\sin\frac{\pi}{2}\xi}\right]\cos\frac{\pi}{2}\eta + \left[A_2 - \frac{\pi^2}{16}\int_1^\eta \frac{\xi d\xi}{\sin\frac{\pi}{2}\xi}\right]\left[\frac{2}{\pi}\sin\frac{\pi}{2}\eta - \eta\cos\frac{\pi}{2}\eta\right] - \left[\frac{3}{2} + \frac{4k_1}{\pi^2}\sin\frac{\pi}{2}\eta\right]\right\} \quad [38]$$

$$k = -0.61685 - \frac{1.3253}{\lambda} \quad [39]$$

where

$$A_1 = \frac{3}{2} - \frac{\pi^2}{16}\int_0^1 \frac{\xi^2 d\xi}{\sin\frac{\pi}{2}\xi} = 0.72708$$

$$A_2 = \frac{\pi}{4} + \frac{3}{2} - \frac{\pi^2}{16}\int_0^1 \frac{\xi^2 d\xi}{\sin\frac{\pi}{2}\xi} = 1.5125$$

and

$$k_1 = -1.3253$$

The velocity components in the axial and radial directions are obtained by substituting Equation [38] into Equations [10] and [11], respectively, as follows

$$\frac{u}{u_0} = \left[\frac{1}{0.7854 + \frac{0.8437}{\lambda}} + 4\frac{\lambda}{\mathrm{Re}}\frac{x}{R}\right]\left[\frac{\pi}{4}\cos\frac{\pi}{2}\eta + \frac{1}{\lambda}f_1' + \ldots\right] \quad [40]$$

$$\frac{v}{u_0} = -\frac{2\lambda}{\mathrm{Re}\sqrt{\eta}}\left[\frac{1}{2}\sin\frac{\pi}{2}\eta + \frac{1}{\lambda}f_1 + \ldots\right] \ldots [41]$$

The pressure distributions in the axial and radial directions are obtained upon the substitution of Equation [38] into Equations [12] and [13], and integrating

$$\frac{p(0,0) - p(x,r)}{\frac{\rho u_0^2}{2}} = \frac{8\lambda}{\mathrm{Re}}\left[0.61685 + \frac{1}{\lambda}(1.3253)\right] \times \left[\frac{1}{f'(0)} + 2\frac{\lambda}{\mathrm{Re}}\frac{x}{R}\right]\left(\frac{x}{R}\right) + 4\left(\frac{\lambda}{\mathrm{Re}}\right)^2\frac{f'}{\eta} + 8\frac{\lambda}{\mathrm{Re}^2}[f' - f'(0)] \ldots\ldots [42]$$

The pressure drop in the flow direction can be obtained readily from Equation [42], i.e.

$$\frac{p(0,r) - p(x,r)}{\frac{\rho u_0^2}{2}} = 8\frac{\lambda}{\mathrm{Re}}\left[0.61685 + \frac{1}{\lambda}(1.3253)\right] \times \left[\frac{1}{f'(0)} + 2\frac{\lambda}{\mathrm{Re}}\frac{x}{R}\right]\frac{x}{R} \ldots\ldots [43]$$

The coefficient of skin friction at the wall also can be obtained from Equation [40], which is

$$c_f = \frac{4}{\mathrm{Re}}\left[\frac{1}{0.7854 + \frac{0.8437}{\lambda}} + 4\frac{\lambda}{\mathrm{Re}}\frac{x}{R}\right] \times \left[\frac{\pi^2}{8} + \frac{1}{\lambda}(0.1854) + \ldots\right] \ldots\ldots [44]$$

## Discussion

The velocity distributions in the main flow direction at an arbitrary cross section of the pipe as calculated from Equation [27] for $\lambda = \pm 1$ and from Equation [40] for $\lambda = 10$ are shown in Fig. 2. It is noted that when $\lambda = 0$ the profile becomes Poiseuille's

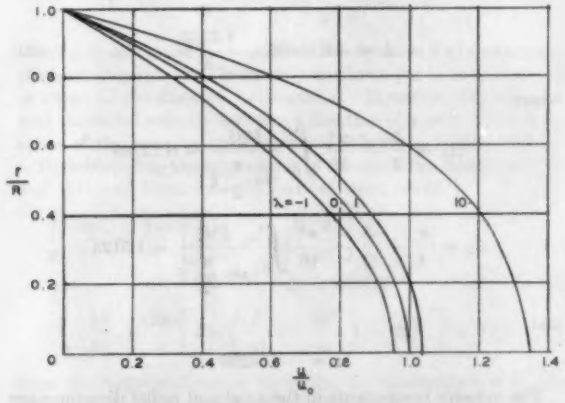


Fig. 2 Velocity Profiles Versus Length in Radial Direction for Various $\lambda$ ($\mathrm{Re} = 10^3$, $x/R = 10$)

paraboloid, and for $\lambda > 0$ (fluid being injected through the wall) the axial velocity increases and the velocity gradient at the wall increases. For $\lambda < 0$ (fluid being withdrawn through the wall) both the axial velocity and the velocity gradient at the wall decrease as compared with Poiseuille's case. This phenomenon follows the law of conservation of matter. In the present case the

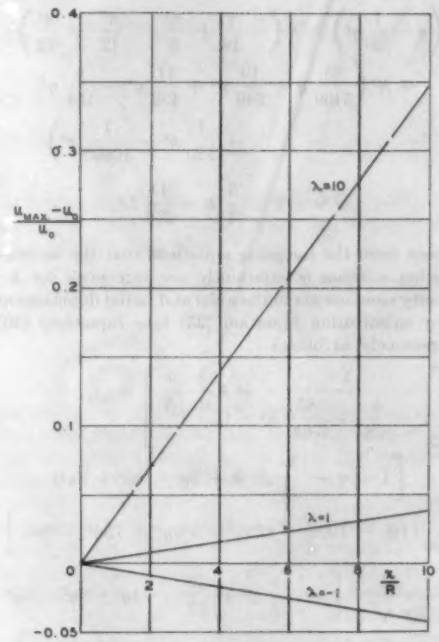


Fig. 3 Maximum Axial-Velocity Difference Versus Length in Flow Direction ($\mathrm{Re} = 10^3$)

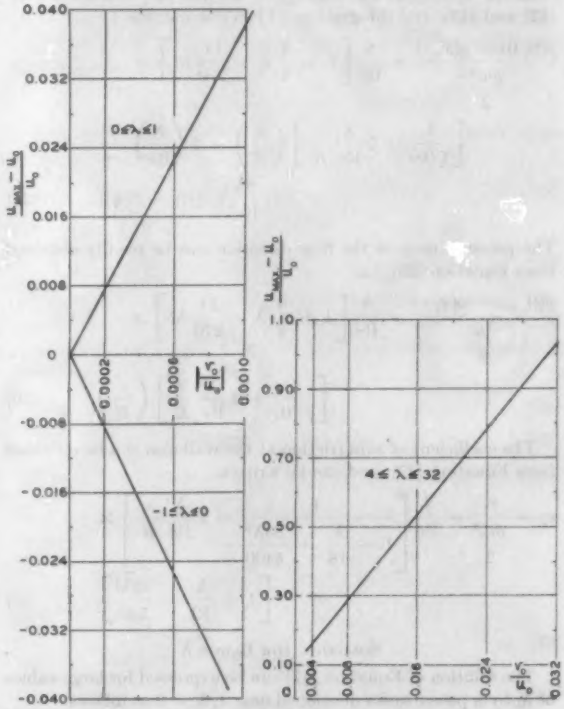


Fig. 4 Maximum Axial-Velocity Difference Versus Injection or Suction Ratio $\left|\frac{v_0}{u_0}\right|$ for Various $\lambda$ ($\mathrm{Re} = 10^3$)

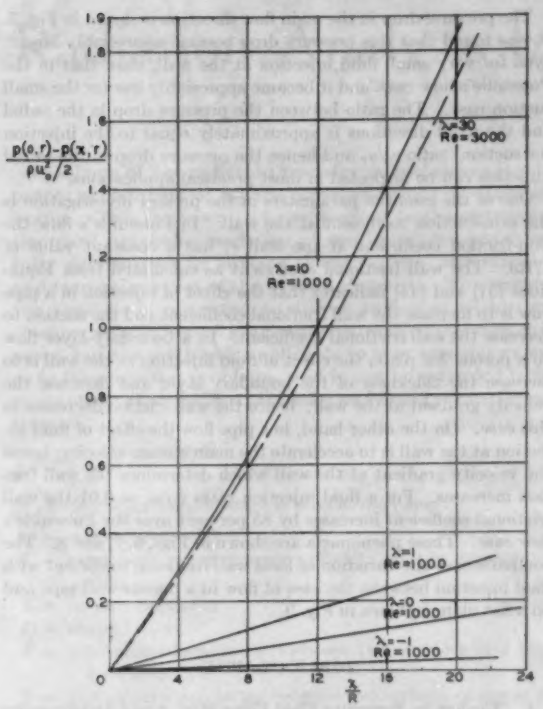


FIG. 5 AXIAL PRESSURE DROP VERSUS LENGTH IN FLOW DIRECTION FOR VARIOUS λ

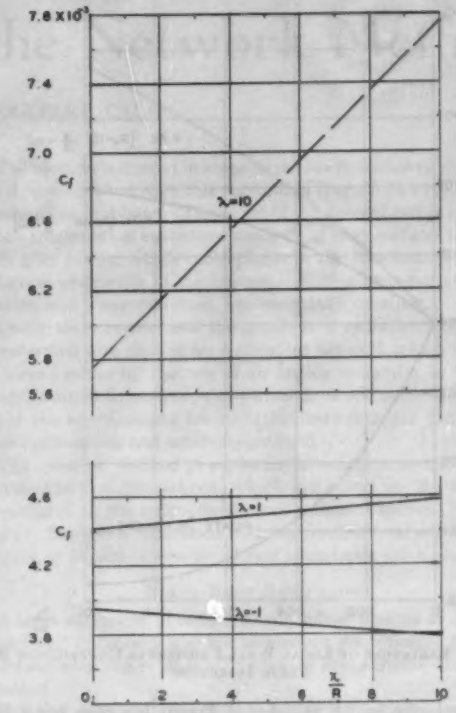


FIG. 6 VARIATION OF WALL FRICTION COEFFICIENT IN FLOW DIRECTION FOR VARIOUS λ (Re = $10^3$)

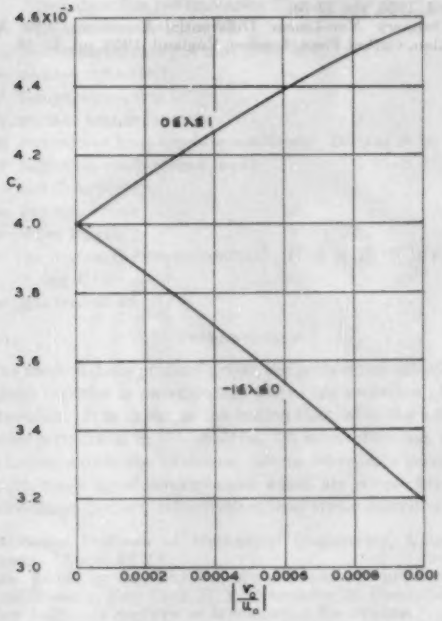


FIG. 7 VARIATION OF WALL FRICTIONAL COEFFICIENT WITH INJECTION AND SUCTION RATIO FOR $-1 \leq \lambda \leq 1$ (Re = $10^3$, $x/R = 10$)

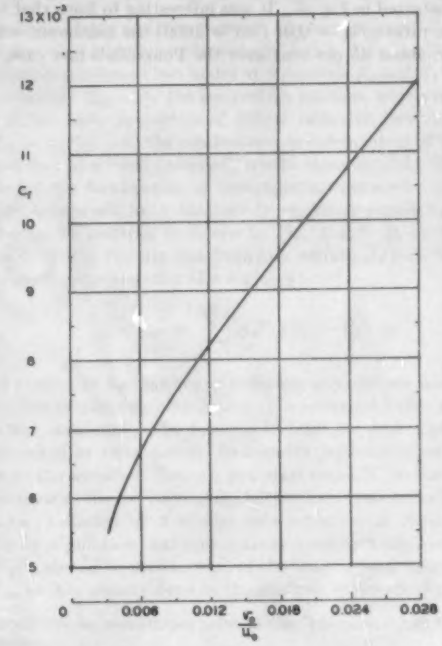


FIG. 8 VARIATION OF WALL FRICTIONAL COEFFICIENT WITH INJECTION RATIO FOR LARGE λ (Re = $10^3$, $x/R = 10$)

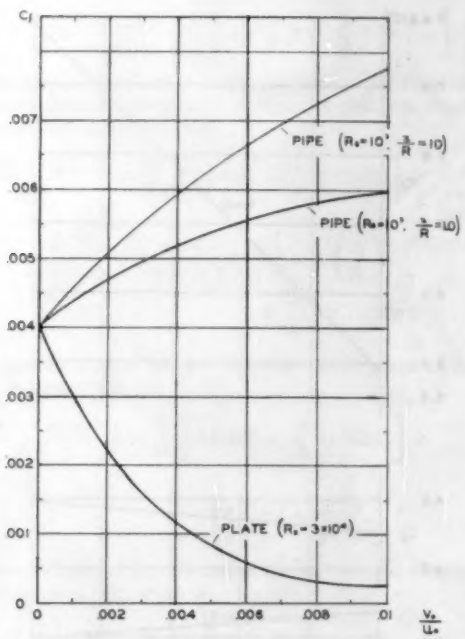


FIG. 9 VARIATION OF LOCAL WALL FRICTIONAL COEFFICIENT WITH FLUID INJECTION

radial velocity, which vanishes in Poiseuille's case, has a finite magnitude except at the center of the pipe where it vanishes.

In Fig. 3 the maximum velocity distributions along the axis of the pipe were shown. The increase of maximum velocity with the increase of fluid injection at the wall and decrease with suction were illustrated in Fig. 4. It was interesting to learn that for an injection ratio $v_0/u_0 = 0.01$ (Re = 1000) the maximum velocity increases about 35 per cent over the Poiseuille's flow case.

The pressure drop in the main flow direction is shown in Fig. 5. It was found that this pressure drop became appreciably larger, even for very small fluid injection at the wall, than that in the Poiseuille's flow case, and it became appreciably less for the small suction case. The ratio between the pressure drop in the radial and the axial directions is approximately equal to the injection (or suction) ratio $v_0/u_0$ and hence the pressure drop in the radial direction can be neglected in most practical applications.

One of the essential parameters in the present investigation is the skin-friction coefficient at the wall. In Poiseuille's flow the skin-friction coefficient at the wall $c_f$ has a constant value of 4/Re. The wall frictional coefficient as calculated from Equations [31] and [44] indicates that the effect of injection in a pipe flow is to increase the wall frictional coefficient and the suction to decrease the wall frictional coefficient. In a boundary-layer flow on a porous flat plate, the effect of fluid injection at the wall is to increase the thickness of the boundary layer and decrease the velocity gradient at the wall; hence the wall friction decreases in this case. On the other hand, in a pipe flow the effect of fluid injection at the wall is to accelerate the main stream velocity, hence the velocity gradient at the wall which determines the wall friction increases. For a fluid injection ratio $v_0/u_0 = 0.01$ the wall frictional coefficient increases by 85 per cent over the Poiseuille's flow case. These phenomena are shown in Figs. 6, 7, and 8. The comparison of the variation of local wall frictional coefficient with fluid injection between the case of flow in a porous-wall pipe and on a flat plate is shown in Fig. 9.

## BIBLIOGRAPHY

1 "Cooling by Protective Fluid Films, High Speed Aerodynamics and Jet Propulsion," by S. W. Yuan, vol. V, section F, being published by the Princeton Press, Princeton, N. J.

2 "Laminar Flow in Channels With Porous Walls," by A. Berman, *Journal of Applied Physics*, vol. 24, no. 9, September, 1953, pp. 1232–1235.

3 "Project Squid Semi-Annual Progress Report," by S. W. Yuan, October 1, 1953, pp. 52–54.

4 "Ordinary Non-Linear Differential Equations," by N. W. McLachlan, Oxford Press, London, England, 1950, pp. 43–46.

# Radiation Analysis by the Network Method

By A. K. OPPENHEIM,[1] BERKELEY, CALIF.

**Problems of net radiation transfer in enclosures involve proper accounting of all the interreflections of radiation beams. This is shown to be equivalent to the solution of electrical networks made up of conductances which are fully determined by surface-shape factors, reflectivities, and transmissivities of the system elements. The scope of the analysis is restricted to diffuse radiation within enclosures consisting of gray surfaces and containing gray gases, but the method is applicable to heat transfer as well as to illumination problems, and it can be extended to include other modes of heat transfer and energy transformation.**

## Nomenclature

The following nomenclature is used in the paper:

- $A$ = surface area, sq ft
- $E$ = black-body emissive power, $\sigma T^4$ Btu/sq ft hr, or potential, volts
- $e$ = surface emissivity
- $F$ = shape factor
- $\bar{F}$ = equivalent shape factor between two surfaces of a black enclosure
- $\bar{\bar{F}}$ = equivalent shape factor between two surfaces of a gray enclosure
- $G$ = irradiation, Btu/sq ft hr
- $H$ = enthalpy flow rate, Btu/hr
- $I$ = radiation flux, Btu/hr, or current, amp
- $J$ = radiosity, i.e., sum of emitted, reflected, and transmitted radiation flux per unit area, Btu/sq ft hr
- $Q$ = heat-transfer rate, Btu/hr
- $q$ = heat-transfer rate per unit area, Btu/sq ft hr
- $r$ = surface reflectivity
- $T$ = temperature, deg R
- $t$ = surface transmissivity
- $U$ = convective heat-transfer coefficient, Btu/sq ft hr deg F
- $Y$ = radiation conductance, sq ft
- $\alpha$ = gas absorptivity
- $\epsilon$ = gas emissivity
- $\lambda$ = wave length
- $\sigma$ = the Stefan-Boltzman constant, $1713 \times 10^{-12}$ Btu/sq ft hr deg R$^4$
- $\tau$ = gas transmissivity

## Introduction

The method deals primarily with the problem of calculating the net heat transfer in an enclosure where the radiation effects are appreciable. It is based on the notion that, with the usual idealizations introduced in the analysis, all interreflections of radiation beams within the enclosure can be taken into account by a network made up of conductances which are simple functions of surface-shape factors, reflectivities, and transmissivities.

The method is limited in scope to diffuse radiation (described in the Appendix), but with this stipulation it applies also to isotropic illumination problems. The scope of the present paper is limited to the treatment of enclosures made up of gray surfaces and filled with gray media, which corresponds to the idealization that the radiation properties of the system, i.e., the emissivities, reflectivities, and transmissivities, are essentially constant.

Under these restrictions the problem of radiation exchange is transformed into that of an equivalent network which can then be solved either by the use of an analog computer or by some computational technique of electrical network analysis. In this paper the specifications for radiation networks are derived and their applications and solutions outlined.

The network method provides an alternative to the conventional radiation calculations, which are based on the direct accounting of all the interreflections of radiation beams (1, 2, 3, 4, or 5).[2] Since it is concerned with the fundamental aspects of the subject, it is here shown developed from basic principles.

## Black-Body Enclosure

A black surface is, of course, a true diffuse emitter and, since it absorbs all the energy which it intercepts, its radiosity $J$ is equal to its emissive power $E = \sigma T^4$ where $\sigma$ is the Stefan-Boltzmann constant.

Defining a heat-transfer surface as that portion of an area which is at a constant temperature, the direct net radiant-energy exchange between any two such surfaces $A_i$ and $A_k$ of a black enclosure is

$$Q_{ik} = A_i F_{ik}(E_i - E_k) = -A_k F_{ki}(E_k - E_i) = -Q_{ki} \ldots [1]$$

The black-body emissive power $E$ can be considered then to act as a potential and the surface-shape factor $A_i F_{ik}$ as the branch conductance between two nodes at potentials $E_i$ and $E_k$ exchanging a current $Q_{ik}$. By the reciprocity relation, which represents one of the basic properties of diffuse radiation (see Appendix), $A_i F_{ik} = A_k F_{ki}$; i.e., the conductance is independent of the direction of flow as a "well-behaved" conductance should. This is the basis for the formulation of the radiation network. As an example, a network for a black-body enclosure consisting of four heat-transfer surfaces is shown in Fig. 1(*a*).[3] It becomes obvious then that the net flux from any surface $A_i$ into the black-body enclosure consisting of $n$ surfaces is

$$Q_{i-\text{net}} = \sum_{k=1}^{n} A_i F_{ik}(E_i - E_k) \ldots [2]$$

Of particular significance in radiation calculations are surfaces which act as complete reradiators. (In reference 2 they are called "no-flux surfaces.") In furnace technology such surfaces are represented by refractories. In network representation they appear as the so-called "floating potential nodes." In the presence of such nodes the net current $Q_{kl}$ between any two potential nodes can be evaluated by a similar rate equation as Equation [1], with the stipulation that the equivalent network conductance $\bar{Y}_{ik} = A_i \bar{F}_{ik}$ should be used instead of the branch conductance $Y_{ik} = A_i F_{ik}$, as it is usually done in the analysis of electrical networks.

---

[1] Associate Professor of Mechanical Engineering, University of California. Mem. ASME.

Contributed by the Heat Transfer Division and presented at the Annual Meeting, New York, N. Y., November 28–December 3, 1954, of The American Society of Mechanical Engineers.

Note: Statements and opinions advanced in papers are to be understood as individual expressions of their authors and not those of the Society. Manuscript received at ASME Headquarters, August 3, 1954. Paper No. 54—A-75.

[2] Numbers in parentheses refer to the Bibliography at the end of the paper.

[3] It should be noted that, as a matter of convenience, the values of conductances, rather than resistances, are indicated on radiation-network diagrams.

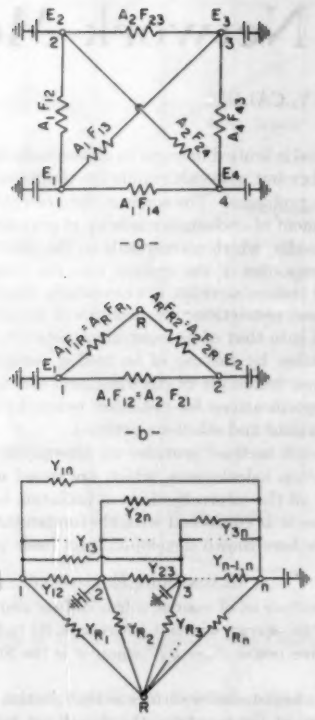


*a*—Enclosure consisting of four surfaces
*b*—Enclosure consisting of two heat-transfer surfaces and one reradiator surface
*c*—Enclosure consisting of any number of heat-transfer surfaces and only one reradiator surface

FIG. 1 NETWORKS FOR BLACK ENCLOSURES

For example, in the three-component system represented by Fig. 1(*b*) (where the equivalent conductance is equal to the total network conductance)

$$\bar{Y}_{12} = A_1\bar{F}_{12} = A_1F_{12} + \frac{1}{\dfrac{1}{A_1F_{1R}} + \dfrac{1}{A_2F_{2R}}} \quad [3]$$

while

$$E_R = \frac{F_{R1}E_1 + F_{R2}E_2}{F_{R1} + F_{R2}}$$

whence

$$T_R = \sqrt[4]{\frac{F_{R1}T_1^4 + F_{R2}T_2^4}{F_{R1} + F_{R2}}} \quad [4]$$

Equations [3] and [4] are essentially the same as Equations [12*a*], [12*b*], and [13] of reference 1. (For the latter two it has been assumed that neither $A_1$ nor $A_2$ can "see" itself, i.e., that $F_{11} = F_{22} = 0$. Consequently, $A_1F_{1R} = A_RF_{R1} = A_1 - A_1F_{12}$ and $A_2F_{2R} = A_RF_{R2} = A_2 - A_1F_{12}$, which, substituted into Equations [3] and [4], yield immediately Equations [12*b*] and [13] of reference 1.)

With these notions as a basis, the radiation exchange in an enclosure consisting of any number of black heat-transfer surfaces and reradiator surfaces can be solved by simply extending the network principle to a multicomponent system. On the basis of the reciprocal theorem (8), it follows that $\bar{Y}_{ik} = \bar{Y}_{ki}$, and consequently

$$A_i\bar{F}_{ik} = A_k\bar{F}_{ki} \quad [5]$$

A particular example of a multicomponent system for which a general solution can be easily obtained is an enclosure with a single reradiator surface. The network for such a system is shown in Fig. 1(*c*). The equivalent conductance between any two potential nodes $i$ and $k$ is here equal to the direct branch conductance $Y_{ik}$ plus the corresponding branch conductance of the generalized delta obtained from the transformation of the generalized star (8). The latter can be expressed as

$$Y_{ik}^{\Delta} = \frac{Y_{Ri}Y_{Rk}}{\sum_{k=1}^{n} Y_{Rk}}$$

Noting that $Y_{ik} = A_iF_{ik}$ and that

$$\sum_{k=1}^{n} Y_{Rk} = A_R(1 - F_{RR})$$

the equivalent conductance becomes

$$\bar{Y}_{ik} = A_i\bar{F}_{ik} = Y_{ik} + Y_{ik}^{\Delta} = A_iF_{ik} + \frac{A_RF_{Ri}F_{Rk}}{1 - F_{RR}} \quad [6]$$

which is identical with equation [12] of reference (1) or equation [4-21] of reference (2).

The case of an infinite number of refractory surfaces, i.e., when allowance is made for continuous variation of refractory surface temperature, involves the solution of nonhomogeneous integral equations (2, 9). The network principle suggests immediately a determinant solution of the problem, based on a stepwise approximation of the temperature profile. The problem is then set up in the form of a system of linear equations by applying the Kirchhoff current law to each node (representing a step in the temperature profile) which corresponds, of course, to the application of the principle of conservation of energy to each surface. Solutions of such problems given in Fig. 25 of reference (1) (Figs. 4 to 11 and equation [4–31] of reference 2) were indeed obtained by such an approximate method (9).

## GRAY-BODY ENCLOSURE

The direct radiation exchange between any two opaque and diffuse surface elements $A_i$ and $A_k$ can be expressed by a rate equation

$$dQ_{ik} = J_i d(A_iF_{ik}) - J_k d(A_kF_{ki}) = (J_1 - J_2)d(A_iF_{ik}) \quad [7]$$

which states simply that the net direct-energy exchange is due to the exchange of radiosities (see Appendix, Equation [25]). By definition the radiosity of an opaque surface is

$$J = rG + eE \quad [8]$$

where $r$ is the reflectivity, $e$ the emissivity, $G$ the irradiation, and $E$ the black-body emissive power of the surface, while the net flow of energy leaving the surface element is

$$\frac{dQ_{net}}{dA} = J - G \quad [9]$$

Care must be taken in treating Equations [8] and [9] algebraically since, in general

$$rG = \sum_{T=T_1}^{T_n} \int_0^{\infty} r(\lambda, T_s)G(\lambda, T)d\lambda$$

while

$$G = \sum_{T=T_1}^{T_n} \int_0^\infty G(\lambda, T)d\lambda$$

where $\lambda$ is the radiation wave length, $T_s$ the surface temperature, and $T$, ranging from $T_1$ to $T_n$, denotes the temperatures of radiation beams included in the total irradiation.

For a gray surface, however, $r$ = const and $r + e = 1$. The irradiation $G$, therefore, can be eliminated from Equations [8] and [9] yielding

$$\frac{dQ_{net}}{dA} = \frac{e}{r} E - \frac{1-r}{r} J = \frac{e}{r}(E - J) \ldots\ldots [10]$$

If the irradiation is uniformly distributed over the surface, i.e., $G$ = const for any point of $A$ and consequently by Equation [8] $J$ = const over $A$, Equation [10] can be integrated immediately, giving

$$Q_{net} = \frac{e}{r} A(E - J) \ldots\ldots [11]$$

Under the same circumstances Equation [7] applies in an integral form and, together with Equation [11], it provides the basis for a network representing a gray-body enclosure. This is illustrated by Fig. 2(*a*) demonstrating a network for an enclosure consisting of four gray surfaces. For this purpose, however, according to the condition preceding Equation [11], a heat-transfer surface must now be defined as that portion of an area which is not only at a constant temperature but is also uniformly irradiated. Under this restriction the effect of surface reflectivity (and emissivity) is taken into account by simply connecting the potential node $E = \sigma T^4$ to the network by means of a finite conductance $A(e/r)$, which, in the case of black enclosure, was infinite. The potential node of the corresponding black-enclosure network becomes now a floating potential node which acquires an equilibrium potential equal to surface radiosity $J$.

As a consequence of the restricted definition of the heat-transfer surface, generally the enclosure has to be defined in such a way that heat-transfer areas are small in comparison to distances between them. In principle, the accuracy of computation can be refined as much as one wishes by subdividing the heat-transfer surfaces into sufficiently small areas. This leads, after all, to a determinant solution of an integral-equation problem similar to that described at the end of the previous secton. (Incidentally, it becomes quite clear now that the reflectivity of a reradiator is completely ineffective since the addition of a conductance behind a floating potential node does not affect the network.)

For some two-component enclosures, such as two parallel, infinite planes, concentric cylinders of infinite height, or concentric spheres, the condition of uniform irradiation is satisfied for each component surface and the network is reduced to a single line of resistances in series as shown in Fig. 2(*b*). In this case the equivalent conductance is simply given by

$$\frac{1}{A_1\mathfrak{F}_{12}} = \frac{r_1}{A_1 e_1} + \frac{1}{A_1} + \frac{r_2}{A_2 e_2} \ldots\ldots [12]$$

$A_1$ representing the area of the smaller surface. The foregoing is a very well-known result. Christiansen, who published it first in 1883 (5), noted its limitation to symmetrical systems. Saunders (10) expanded the problem to nonconcentric cylinders with the restriction, however, that the reflectivity is so low that not more than one reflection need be considered. The present method permits the refinement of the analysis to any desired extent.

The network for the general case of an enclosure consisting of any number of gray heat-transfer surfaces $A_1, A_2 \ldots A_n$, and

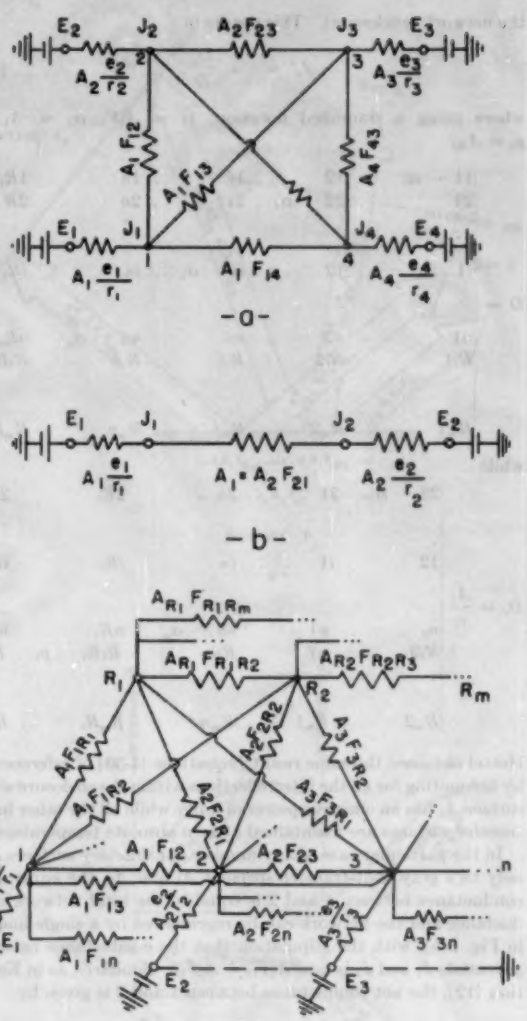


*a*—Enclosure consisting of four surfaces
*b*—Enclosure consisting of two heat-transfer surfaces
*c*—Enclosure consisting of any number of heat-transfer and reradiator surfaces

FIG. 2 NETWORKS FOR GRAY ENCLOSURES

reradiator (refractory) surfaces $A_{R1}, A_{R2}, A_{R3} \ldots A_{Rm}$, is presented in Fig. 2(*c*). The equivalent conductance $A_1\mathfrak{F}_{1i}$ between any two potential nodes 1 and $i$ can then be determined by a conventional technique of electrical network analysis (a consequence of the Thévenin theorem, reference 8) according to which the equivalent conductance $y_{1i}$ is equal to the current flowing into node $i$ when it is grounded and short-circuited with all the remaining potential nodes, as indicated by the dashed line in Fig. 2(*c*), with exception of node 1 on which a potential of unity is imposed. Thus, for any node $i \neq 1$ of the grounded short-circuited network, Fig. 2(*c*)

$$y_{1i} = A_1\mathfrak{F}_{1i} = \frac{A_i e_i}{r_i} J_i' \ldots\ldots [13]$$

while the potential $J_i'$ is obtained from the set of Kirchhoff's current law (energy-balance) equations for each node (surface) of

the network (enclosure). This results in

$$J_i' = -e_1 \frac{D_i}{D} \quad \ldots\ldots [14]$$

where using a simplified notation, $1i = A_1F_{1i}$, $\alpha_i = A_i/r_i$, $\rho_i = A_{Ri}$

$$D = \begin{vmatrix} 11-\alpha_i & 12 & \ldots 1i & \ldots 1n & 1R_1 & \ldots 1R_m \\ 21 & 22-\alpha_2 \ldots & 2i & \ldots 2n & 2R_1 & \ldots 2R_m \\ \cdot & \cdot & \cdot & \cdot & \cdot & \cdot \\ \cdot & \cdot & \cdot & \cdot & \cdot & \cdot \\ i1 & 12 & \ldots ii-\alpha_i & \ldots in & iR_1 & \ldots iR_m \\ \cdot & \cdot & \cdot & \cdot & \cdot & \cdot \\ \cdot & \cdot & \cdot & \cdot & \cdot & \cdot \\ n1 & n2 & \ldots ni & \ldots nn-\alpha_n & nR_1 & \ldots nR_m \\ R_11 & R_12 & \ldots R_1i & \ldots R_1n & R_1R_1-\rho_1 \ldots & R_1R_m \\ \cdot & \cdot & \cdot & \cdot & \cdot & \cdot \\ \cdot & \cdot & \cdot & \cdot & \cdot & \cdot \\ R_m1 & R_m2 & \ldots R_mi & \ldots R_mn & R_mR_1 & \ldots R_mR_m-\rho_m \end{vmatrix}$$

while

$$D_i = \frac{A_1}{r_1} \begin{vmatrix} 22-\alpha_2 \ldots & 21 & \ldots 2n & 2R_1 & \ldots 2R_m \\ \cdot & \cdot & \cdot & \cdot & \cdot \\ \cdot & \cdot & \cdot & \cdot & \cdot \\ 12 & \ldots i1 & \ldots in & iR_1 & \ldots iR_m \\ \cdot & \cdot & \cdot & \cdot & \cdot \\ \cdot & \cdot & \cdot & \cdot & \cdot \\ n_2 & \ldots n1 & \ldots nn-\alpha_n & nR_1 & \ldots nR_m \\ R_12 & \ldots r_11 & \ldots R_1n & R_1R_1-\rho_1 \ldots & R_1R_m \\ \cdot & \cdot & \cdot & \cdot & \cdot \\ \cdot & \cdot & \cdot & \cdot & \cdot \\ R_m2 & \ldots R_m1 & \ldots R_mn & R_mR_1 & \ldots R_mR_m-\rho_m \end{vmatrix}$$

Hottel obtained the same result (equations [4-30] of reference 2) by accounting for all the interreflections within the enclosure when surface $A_1$ has an emissive power of unity while all the other heat-transfer surfaces are maintained at zero absolute temperature.

In the particular case of any number of refractory surfaces and only two gray heat-transfer surfaces $A_1$ and $A_2$, the equivalent conductance between 1 and 2 is equal to the total network conductance and the network can be represented by a single line, as in Fig. 3(*b*), with the stipulation that the conductance between potentials $J_1$ and $J_2$ is now $A_1\bar{F}_{12} = A_2\bar{F}_{21}$. Similarly, as in Equation [12], the net conductance between 1 and 2 is given by

$$\frac{1}{A_1\mathfrak{F}_{12}} = \frac{r_1}{A_1e_1} + \frac{r_2}{A_2e_2} + \frac{1}{A_1\bar{F}_{12}} \quad \ldots\ldots [15]$$

providing thus a simple proof for equation [15] of reference (1) or equation [4-33] of reference (2).

### Gray Enclosures Filled With Gray Media

For a gray medium the emissivity $\epsilon$ is equal to absorptivity $\alpha$ and the sum of the transmissivity $\tau_{ik}$ between any two surfaces, $A_i$ and $A_k$, and the corresponding absorptivity is unity, while the radiation field is isotropic (see Appendix). Consequently, for a medium with constant absorption characteristics given by the values of $k$ and $c$ in Equation [25] (Appendix) the transmissivity and emissivity are functions of the geometry of the system, $\tau_{ik}$ being determined by Equation [24], while

$$\epsilon_{ik} = 1 - \tau_{ik} \quad \ldots\ldots [16]$$

For a gray gas the average absorption characteristics are evaluated at a given temperature level so that both $\epsilon_{ik}$ and $\tau_{ik}$ are, in general, also functions of the gas temperature.

If a gray gas at a uniform temperature is introduced into the space between two surfaces, $A_i$ and $A_k$, then only fraction $\tau_{ik}$ of the original flux from $A_i$ reaches surface $A_k$, while the rest is absorbed by the gas. In other words, if the radiosity of surface $A_i$ is $J_i$, then the portion of radiation flux transmitted to $A_k$ is $\tau_{ik}J_iA_iF_{ik}$ (Equation [33], Appendix) and the portion absorbed by gas is $\epsilon_{ik}J_iA_iF_{ik} = (1-\tau_{ik})J_iA_iF_{ik}$. In the network interpretation the conductance between any two radiosity nodes (previously $A_iF_{ik}$) becomes now $\tau_{ik}A_iF_{ik}$ while $\epsilon_{ik}A_iF_{ik}$ appears as a conductance between the radiosity node corresponding to surface $A_i$ and the node representing the gas.

Fig. 3(*a*) illustrates how each branch conductance is determined according to such a principle for the simple case of an enclosure made up of a single reradiator surface $A_R$ and a single gray heat-transfer surface $A_C$ filled with a gray gas at a temperature $T_G$. In consequence with previous arguments, rigorously such a network applies only to the case of infinite parallel walls or concentric spheres or concentric cylinder of infinite height. The next diagram, Fig. 3(*b*), is obtained simply by summing up the branch conductances, which, of course, can always be done without any loss in generality.

The more general case of an enclosure filled with a "gray gas" at a uniform temperature $T_G$, and composed of any number of gray heat-transfer surfaces $A_1$ $A_2$ . . $A_n$ and, reradiators $A_{R1}$, $A_{R2}$ . . $A_{Rm}$, can be represented by a network similar to that of Fig. 2(*c*) with, superimposed on it, a generalized star with a nodal point $G$, representing the state of the gas. For the sake of clarity the two-component networks are presented separately in Figs. 3(*c* and *d*). Each branch conductance of the "surface network" is now $A_iF_{ik}\tau_{ik}$, while each branch conductance of the "gas network" is

$$Y_{iG} = A_i\bar{\epsilon}_i = A_i\left(\sum_{k=1}^{n} F_{ik}\epsilon_{ik} + \sum_{k=1}^{m} F_{iRk}\epsilon_{iRk}\right) \quad \ldots\ldots [17]$$

For a combustion furnace, node $G$ acts as a potential node, as indicated in Fig. 3 (*d*), so the main problem is that of evaluating the equivalent conductances between this node and nodes $i, k \ldots n$, representing the heat-transfer surfaces. In the application of the conventional technique of network analysis the unit potential is imposed then on node $G$ and all the other potential nodes are

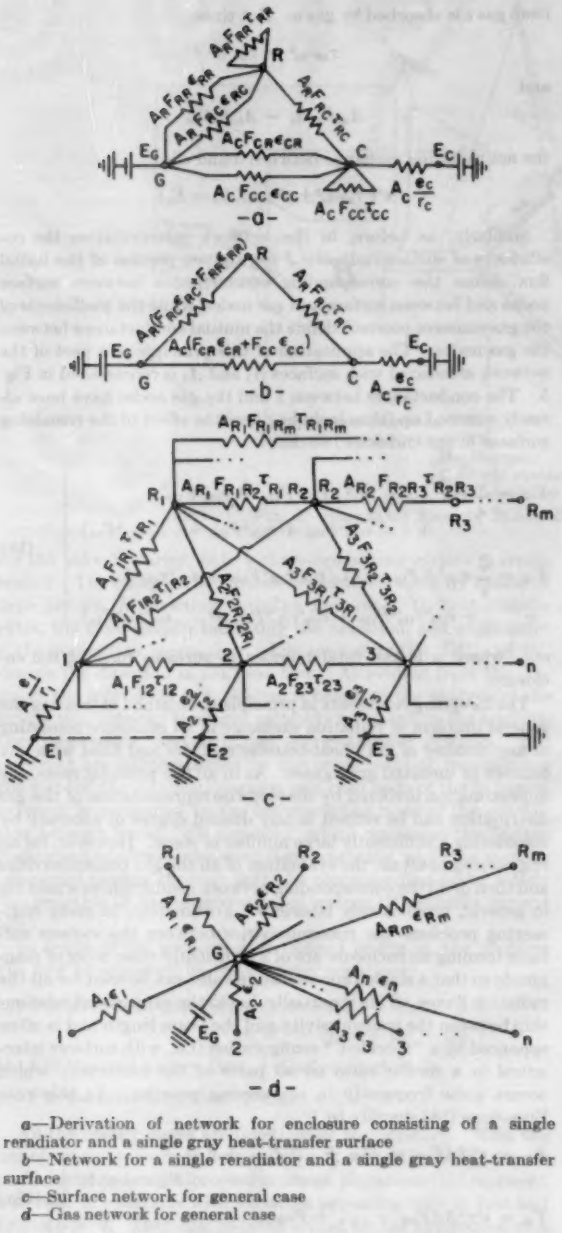


*a*—Derivation of network for enclosure consisting of a single reradiator and a single gray heat-transfer surface
*b*—Network for a single reradiator and a single gray heat-transfer surface
*c*—Surface network for general case
*d*—Gas network for general case

FIG. 3 NETWORKS FOR ENCLOSURES FILLED WITH GRAY MEDIUM AT A UNIFORM TEMPERATURE

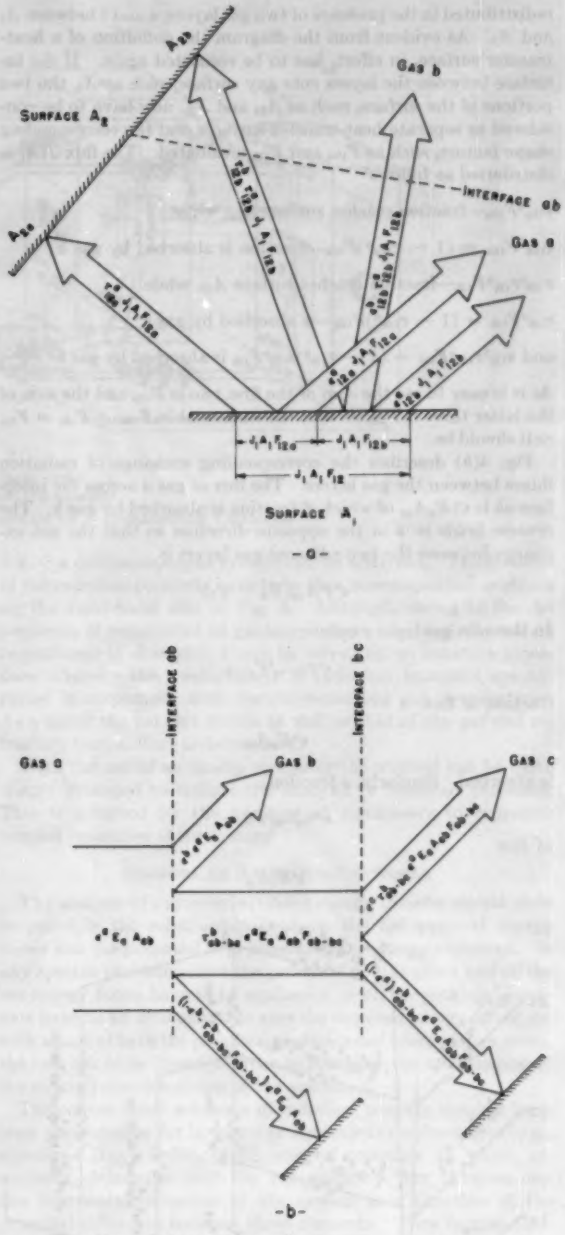


*a*—Flux from a heat-transfer surface
*b*—Flux from a constant-temperature gas layer

FIG. 4 DISTRIBUTION OF RADIATION FLUX IN AN ENCLOSURE FILLED WITH GRAY MEDIA

short-circuited as indicated by the dashed line in Fig. 3(*c*). The combined network can be solved then for any equivalent conductance in the same way as described in the preceding section. The solution agrees with that obtained by Hottel on the basis of his "determinant method."[4]

The network principle can be extended to the case of an enclosure filled with gray media having nonuniform temperature distribution. This corresponds to the stepwise approximation of an integral equation, similar in principle to the method described previously for the case of an infinite number of refractory and gray heat-transfer surfaces. The space is then considered to be filled with layers of gray media, the transmissivities (and emissivities) for a given radiation flux being constant within each layer.

Fig. 4(*a*) demonstrates how the radiation flux from surface $A_1$ is

[4] Reference (2), pp. 105–111.

redistributed in the presence of two gas layers, $a$ and $b$ between $A_1$ and $A_2$. As evident from the diagram the definition of a heat-transfer surface, in effect, has to be restricted again. If the interface between the layers cuts any surface, such as $A_2$, the two portions of the surface, such as $A_{2a}$ and $A_{2b}$, now have to be considered as separate heat-transfer surfaces and the corresponding shape factors, such as $F_{12a}$ and $F_{12b}$, evaluated. The flux $J_1A_1$ is distributed as follows[5]

$\tau_{12a}{}^a F_{12a}$—fraction reaches surface $A_{2a}$, while

$\epsilon_{12a}{}^a F_{12a} = (1 - \tau_{12a}{}^a)F_{12a}$—fraction is absorbed by gas $a$

$\tau_{12b}{}^b \tau_{12b}{}^a F_{12b}$—fraction reaches surface $A_{2b}$, while

$\epsilon_{12b}{}^a F_{12b} = (1 - \tau_{12b}{}^a)F_{12b}$—is absorbed by gas $a$

and $\epsilon_{12b}{}^b \tau_{12b}{}^a F_{12b} = (1 - \tau_{12b}{}^b)\tau_{12b}{}^a F_{12b}$ is absorbed by gas $b$

As it is easy to see the sum of the first two is $F_{12a}$ and the sum of the latter three is $F_{12b}$, so that the sum total is $F_{12a} + F_{12b} = F_{12}$, as it should be.

Fig. 4($b$) describes the corresponding exchange of radiation fluxes between the gas layers. The flux of gas $a$ across the interface $ab$ is $\epsilon^a E_a A_{ab}$ of which $\epsilon^b$ fraction is absorbed by gas $b$. The reverse holds true in the opposite direction so that the net exchange between the two adjacent gas layers is

$$\epsilon^a \epsilon^b A_{ab}(E_a - E_b)$$

In the next gas layer $c$ only

$$\epsilon^c \tau_{ab-bc}{}^b F_{ab-bc}$$

fraction of flux

$$\epsilon^a E_a A_{ab}$$

is absorbed. Similarly, a fraction

$$\epsilon^a \tau_{bc-ab}{}^b F_{bc-ab}$$

of flux

$$\epsilon^c E_c A_{cb}$$

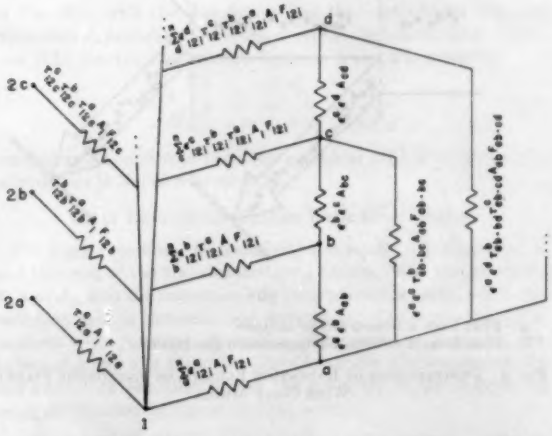


FIG. 5 NETWORK FOR ENCLOSURE FILLED WITH GRAY MEDIA
(Diagram represents only part of the network associated with one of the surfaces interchanging radiation through a number of gas layers.)

[5] The superscript denotes the portion of transmissivity or emissivity due to a given gas layer, e.g., $\tau_{12b}{}^a$ designates the fraction of the transmissivity of the flux from $A_1$ to $A_2$ let through by gas $a$, while $\epsilon_{12b}{}^a = 1 - \tau_{12b}{}^a$ is the corresponding fraction absorbed by gas $a$.

from gas $c$ is absorbed by gas $a$. But since

$$\tau_{ab-bc}{}^b = \tau_{bc-ab}{}^b$$

and

$$A_{ab}F_{ab-bc} = A_{bc}F_{bc-ab}$$

the net radiation exchange between $a$ and $c$ is

$$\epsilon^a \epsilon^c \tau_{ab-bc}{}^b A_{ab}F_{ab-bc}(E_a - E_c)$$

Similarly, as before, in the network interpretation the coefficients of surface radiosity $J$ for a given portion of the initial flux define the corresponding conductances between surface nodes and between surface and gas nodes, while the coefficients of the gas emissive power $E$ define the mutual conductances between the gas nodes. The application of this principle to a part of the network associated with surfaces $A_1$ and $A_2$ is represented in Fig. 5. The conductances between 1 and the gas nodes have been already summed up (thus including here the effect of the remaining surfaces in the enclosure) so that

$$\left.\begin{aligned} Y_{1a} &= \sum_a^n \epsilon_{12i}{}^a A_1 F_{12i} = A_1(\epsilon_{12a}{}^a F_{12a} + \epsilon_{12b}{}^a F_{12a} \\ &\quad + \ldots \epsilon_{12a}{}^a F_{12a} + \epsilon_{12b}{}^a F_{12b} + \ldots \epsilon_{1n}{}^a F_{1n}) \\ Y_{1b} &= \sum_b^n \epsilon_{12i}{}^b A_1 F_{12i} = A_1(\epsilon_{12b}{}^b \tau_{12b}{}^a F_{12b} + \epsilon_{12a}{}^b \tau_{12a}{}^a F_{12a} \\ &\quad + \ldots + \epsilon_{12b}{}^b \tau_{12b}{}^a F_{12b} + \epsilon_{12c}{}^b \tau_{12c}{}^a F_{12c} + \ldots \epsilon_{1n}{}^b \tau_{1a}{}^a F_{1n}) \end{aligned}\right\} \ldots [18]$$

etc., where $n$ is the total number of surfaces forming the enclosure.

The foregoing represents in principle the method of treating the general problem of radiation exchange in an enclosure consisting of any number of gray heat-transfer surfaces and filled with any number of unmixed gray gases. As in all the previous cases, the approximation involved by the stepwise representation of the gas distribution can be refined to any desired degree of accuracy by considering a sufficiently large number of steps. However, for an engineering analysis, the evaluation of all the gas transmissivities and then of all the corresponding network conductances would be, in general, prohibitively laborious. Fortunately, in many engineering problems the transmissivities between the various surfaces forming an enclosure are of a sufficiently close order of magnitude so that a single representative value can be used for all the radiation fluxes. This is partially due to the exponential relationship between the transmissivity and the beam length and is often enhanced by a "speckled"[6] configuration (i.e., with surfaces intermixed in a similar ratio on all parts of the enclosure), which occurs quite frequently in engineering practice. In this case Equations [18] simplify to

$$\left.\begin{aligned} Y_{1a} &= \epsilon^a A_1(F_{12a} + F_{12b} + \ldots F_{12a} + F_{12b} \\ &\quad + \ldots F_{1n}) = \epsilon^a A_1 \\ Y_{1b} &= \epsilon^b \tau^a A_1(F_{12b} + \ldots + F_{12b} \\ &\quad + \ldots F_{1n}) = \epsilon^b \tau^a A_1 F_{1-ab} \end{aligned}\right\} \ldots [18a]$$

etc., and the evaluation of all the conductances can be systematized to a fairly simple routine.

## SYSTEM WITH COMBINED ENERGY TRANSFER AND ANALOG COMPUTER

The application of the network method to a system with combined energy transfer is illustrated by a combustion chamber described schematically by the energy-block diagram, Fig. 6, where,

[6] Reference (2), p. 110.

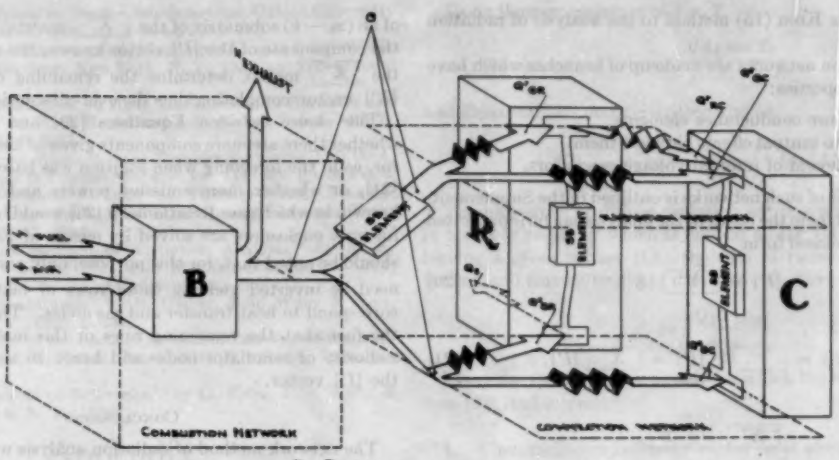


B—Burner
C—Cold surface (heat sink)
R—Refractory wall (reradiator)

FIG. 6 SCHEMATIC ENERGY BLOCK DIAGRAM OF A COMBUSTION CHAMBER

for the sake of clarity, only a three-component system is represented. The energy-flow pattern is described there by means of tape arrows, $H$ denoting enthalpy flow rates, $Q$, heat-transfer rates, the superscript $r$ indicating the radiation, and superscript $c$, the convection mechanism, while subscripts GR, GC, and RC denote the direction of net heat flow. As evident from the diagram, the solution of the problem is based on the analysis of the interaction between the three networks representing the combustion, convection, and radiation energy-transfer systems. The networks are interconnected by the triple point $G$, representing the state of the combustion gases, and each node of the radiation network is connected to the corresponding node of the convection network by an "SB element," which maintains the Stefan-Boltzmann relationship between their potentials, while the energies (currents) passing through both the corresponding nodes satisfy the principle of the conservation of energy (Kirchhoff's current law).

In terms of the nomenclature defined in Fig. 6, the problem can now be expressed by three energy equations

$$\left.\begin{aligned} &(a)\ \text{For the whole combustion system } H_{\text{fuel}} + H_{\text{air}} = H^0 = H_{\text{exh}} + Q_C + Q_S \\ &(b)\ \text{For the cold surface } Q_{RC}{}^r + Q_{GC}{}^r + Q_{GC}{}^c = Q_C \\ &(c)\ \text{For the refractory } Q_{GR}{}^r + Q_{GR}{}^c = Q_{RC}{}^r + Q_S \end{aligned}\right\} \quad \ldots [19]$$

All the energy fluxes are functions of temperature. With the use of constant, average heat capacities, convective heat-transfer coefficients, and radiation conductances, Equations [19] represent a system of equations with variables appearing only in first and fourth power. They can be often solved by the application of a semigraphical technique (11, 12) or by some iterative procedure, such as the Gauss-Seidel method (13), which may be extended to the nonlinear case represented by these equations. Thus solutions can be obtained for more general cases than those treated by conventional methods (14).

Fig. 6 can be considered as representing also the block diagram of an analog computer for the performance analysis of the combustion chamber. The SB elements represent then function-generator components satisfying the two conditions

$$E^r = \sigma(E^v)^4 \quad \text{and} \quad Q^r + Q^v = 0$$

By combining a number of such elements as those illustrated in Fig. 6 a multicomponent system can be analyzed. The $G$-nodes of the radiation networks have to be then interconnected as shown on the right-hand side of Fig. 5. Although, owing to the dependence of emissivities on gas temperature, the over-all problem is nonlinear in character, it can be solved by an iterative procedure whereby the conductances of radiation networks are adjusted in accordance with the corresponding gas temperatures. As a result the net flux profile as well as that of the gas and refractory temperature is determined.

With the use of an analog computer the method can be quite simply extended to include the analysis of transient processes. This is achieved by the addition of condensers to represent lumped capacities of the system.

## ALGEBRA OF RADIATION NETWORKS

The analysis of a system involving energy transfer should yield in principle the relationship between the net external energy fluxes and the potential field governing the energy exchange. In any specific problem either the potential field is given and all the net energy fluxes have to be evaluated, or all the potential gradients have to be determined to give the required energy fluxes, or, with a part of both the potential gradients and energy fluxes given, the rest has to be found in order to complete the specification of the over-all characteristics of the system.

The conventional solutions of radiation transfer systems have been presented so far in terms of equivalent conductances (e.g., equations [1-3], [4-78], [4-82], etc., of reference 2), which, essentially, determine only the net radiation flux between any two source-sink elements of the system as a function of the potential difference between these elements. They furnish then only a partial solution of the over-all problem which, in general, may involve a large number of elements. In order to find the net flux to any element of a multicomponent system, all the equivalent conductances with respect to this element have to be determined and the products of these conductances and the corresponding potential differences summed up. The complete over-all characteristics of the system are then obtained by repeating this procedure for each element of the system, which may involve a prohibitive amount of labor.

The concept of the radiation network permits the derivation of an over-all solution which can be applied in a systematic way to any problem pertaining to the system. This is achieved by an

application of the Kron (15) method to the analysis of radiation networks.

All the radiation networks are made up of branches which have the following properties:

1 They are pure conductance elements.
2 There are no mutual effects between them.
3 They are devoid of internal voltage generators.

Matrix analysis of such networks is outlined in the Supplement. As demonstrated there the result of the analysis can be represented in the following closed form

$$[I'] = \boxed{Y'}\,[E'] \quad \ldots\ldots\ldots\ldots\ldots\ldots [20]$$

or

$$[E'] = \boxed{Y'}^{-1}[I'] = \boxed{X'}\,[I'] \quad \ldots\ldots\ldots [21]$$

where

$$\boxed{X'} = \boxed{Y'}^{-1}$$

$$[I'] = [I'_{1n}\, I'_{2n} \ldots I_{(n-1)n}]$$

is the vector representing the external net radiation fluxes ($n$ being the total number of nodes)

$$[E'] = [E'_{1n}\, E'_{2n} \ldots E'_{(n-1)n}]$$
$$= [(E_n - E_1)(E_n - E_2) \ldots (E_n - E_{n-1})]$$

is the vector representing the differences (with respect to a single reference node $n$) between the emissive powers and/or radiosities of the system elements, and

$$\boxed{Y'} = \boxed{A}_t\,\boxed{Y}\,\boxed{A}$$

is the transformed (node-pair) admittance matrix which is obtained by an algebraic combination of the branch conductances, described in the Supplement.

Equation [20] gives at once all the solutions to the first group of problems; i.e., it determines, in effect, the net external heat flux associated with any node $j$ if all the black-body emissive powers (i.e., temperatures) and radiosities are given

$$I'_{jn} = Y'_{jn,1n}(E_n - E_1) + Y'_{jn,2n}(E_n - E_2)$$
$$+ \ldots Y'_{jn,jn}(E_n - E_j) + \ldots Y'_{jn,(n-1)n}(E_n - E_{n-1}) \ldots [20a]$$

It should be noted that in the foregoing $j$ may refer to the radiosity (where $E_j = J$) or to the reradiator node; in both these cases $I'_{jn} = 0$.

Equation [21], in turn, gives at once all the solutions to the second group of problems; i.e., it determines, in effect, any difference between emissive powers (and/or radiosities), which are required to produce a given external heat-flux distribution; e.g., for any node $j$ it yields

$$E'_{jn} = E_n - E_j = X'_{jn,1n}I'_{1n} + X'_{jn,2n}I'_{2n}$$
$$+ \ldots X'_{jn,jn}I'_{jn} + \ldots X'_{jn,(n-1)n}I'_{(n-1)n} \ldots [21a]$$

Equations like [20$a$] and [21$a$] lead also to the solution of a mixed problem wherein only some components of the $[E']$ vector, as well as of the $[I']$ vector, are given. In order that the problem be determined, the sum of such components must be equal to $m = n - 1$. If then only $k$ external fluxes are given (including zeros for all reradiator and radiosity nodes, i.e., known nonflux nodes), $k$ being an integer smaller than $m$, and therefore, if also $m - k$ differences of emissive powers are known, then Relationship [21] yields $(m - k)$ linear equations for $(m - k)$ known components of the $[E']$ vector with $(m - k)$ unknown components of the $[I']$ vector. The latter can, therefore, be determined by the inversion of an $(m - k)$ submatrix of the $\boxed{X'}$ matrix. Finally, with all the components of the $[I']$ vector known, the remaining rows of the $\boxed{X'}$ matrix determine the remaining components of the $[E']$ vector, completing thus the over-all solution.

The choice between Equations [20] and [21] depends on whether there are more components given of the external flux vector, as in the foregoing when solution was based on Relationship [21], or whether more emissive powers and/or radiosities are known, in which case Relationship [20] would be used. Networks for gray enclosures are solved by means of Equations [21]. It should be noted that, for this purpose, only part of matrix $\boxed{Y'}$ need be inverted yielding those rows of matrix $\boxed{X'}$ which correspond to heat-transfer and gas nodes. The reason for this is the fact that the remaining rows of this matrix correspond to radiosity or reradiator nodes and hence to zero components of the $[I']$ vector.

## Conclusions

The network method of radiation analysis was introduced and applied to the problem of evaluating the net heat-transfer characteristics in an enclosure consisting of any number of gray heat-transfer surfaces and filled with any number of diathermanous gray gases. A heat-transfer surface was defined for this purpose as that portion of an area which is at a constant temperature, uniformly irradiated, and in contact with a gas element at a uniform temperature. The scope of the analysis presented in the paper was limited to diffuse radiation in a system consisting of gray bodies under steady-state conditions. The conductivity for heat transfer by radiation was then shown to be a function of the system geometry and of the reflectivities and transmissivities of the elements of the system, while the potential for this transfer, a function of temperature only.

Techniques for solution of radiation networks by means of matrix algebra as well as by the use of analog computers were outlined, the latter being especially suitable for problems involving combined energy transfer.

## Acknowledgment

The author wishes to express his gratitude to his colleagues at Shell Development Company and at the University of California, especially to Dr. E. G. Chilton, Dr. D. L. Doughty, Dr. C. R. Garbett, Prof. R. V. Dunkle, and Mr. J. T. Bevans, for the many fruitful discussions which provided an invaluable source of encouragement in the progress of his work. Special thanks are also due to Dr. J. P. Roth, presently at the Institute for Advanced Study, Princeton, N. J., for his essential help and contributions in the fundamental aspects of matrix algebra.

## BIBLIOGRAPHY

1 "Radiant Heat Transmission," by H. C. Hottel; "Heat Transmission," by W. H. McAdams, chapter 3, second edition, 1942, pp. 45–86; "Chemical Engineers' Handbook," by J. H. Perry, section G, 1950, pp. 483–498; "Mechanical Engineers' Handbook," by L. S. Marks, section 4, 1951, pp. 380–392 (in the latter, the equations are numbered differently); all published by McGraw-Hill Book Company, Inc., New York, N. Y.

2 "Radiant Heat Transmission," by H. C. Hottel; "Heat Transmission," by W. H. McAdams, McGraw-Hill Book Company, Inc., New York, N. Y., chapter 4, third edition, 1953, pp. 55–125.

3 "Transfer of Heat and Mass," by E. R. G. Eckert, McGraw-Hill Book Company, Inc., New York, N. Y., first edition, 1950, pp. 193–227.

4 "Technische Strahlungsaustauschrechnungen," by E. Eckert, VDI-Verlag GMBH, Berlin, Germany, 1937.

5 "Heat Transfer and Insulation," by M. Jakob and G. A. Hawkins, John Wiley & Sons, Inc., New York, N. Y., second edition, 1950, pp. 168–189.

6 "Heat Transfer," by M. Jakob, John Wiley & Sons, Inc., New York, N. Y., vol. 1, 1949, pp. 27–29 and 52–58.

7 "Radiative Transfer," by S. Chandrasekhar, Oxford University Press, London, England, 1950, pp. 1–53 and 288–317.
8 "Principles of Electric and Magnetic Circuits," by W. B. Boast, Harper and Brothers, New York, N. Y., 1950, pp. 270–274 and 329–333.
9 "Effect of Reradiation on Heat Transmission in Furnaces and Through Openings," by H. C. Hottel and J. D. Keller, Trans. ASME, vol. 55, paper IS—55-6, 1933.
10 "Notes on Some Radiant Heat Transfer Formulae," by O. A. Saunders, Proceedings of Physical Society, vol. 41, 1929, pp. 569–573.
11 "Thermal Network Method of Furnace Heat Transfer Analysis," by A. K. Oppenheim, Shell Development Company Technical Report No. 246–52, 1952.
12 "The Network Method of Radiation Analysis," by A. K. Oppenheim, Heat Transfer and Fluid Mechanics Institute, 1954; Preprints of Papers, University of California, pp. 199–212.
13 "Linear Computations," by S. Dwyer, John Wiley & Sons, Inc., New York, N. Y., 1951, p. 252.
14 "Heat Transfer in the Radiant Section of Petroleum Heaters," by W. E. Lobo and J. E. Evans, Trans. AIChE, vol. 35, 1939, pp. 743–778.
15 "Tensor Analysis of Networks," by G. Kron, John Wiley & Sons, Inc., New York, N. Y., 1939.

# Appendix

## Definition and Properties of Diffuse Radiation

Radiation is diffuse or isotropic if the intensity of radiation at any point is independent of direction (6, 7). The intensity of

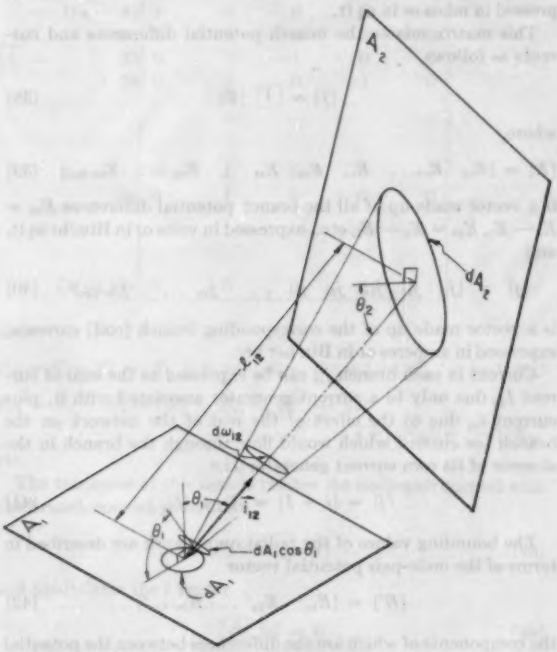


Fig. 7 Radiation Intensity Vector, $i_{12}$

radiation is a vector quantity whose position is described in Fig. 7 and magnitude $|\vec{i}_{12}|$ defined by the relationship

$$dQ_{1\to 2} = i_{12}(dA_1 \cos\theta_1)d\omega_{12} \quad [22]$$

where $dQ_{1\to 2}$ is the portion of the radiation flux from area element $dA_1$ which is intercepted by area element $dA_2$; $dA_1 \cos\theta_1$ is the projection of area element $dA_1$ as seen form $dA_2$ (i.e., into the plane perpendicular to the line $l_{12}$ joining $dA_1$ and $dA_2$), and $d\omega_{12}$ is the solid angle subtended by $dA_2$ with respect to the center point of $dA_1$.

Using the nomenclature of Fig. 7

$$d\omega_{12} = \frac{dA_2 \cos\theta_2}{l_{12}^2}$$

and Equation [22] may be written also as

$$dQ_{1\to 2} = i_{12}\frac{\cos\theta_1 \cos\theta_2}{l_{12}^2} dA_1 dA_2 \quad [23]$$

The properties of diffuse radiation are described conveniently in terms of radiosity which is defined as the total radiation flux leaving a given surface (i.e., the sum of radiation emitted, reflected, and transmitted) per unit area; that is

$$J_1 \equiv \frac{dQ_{1-\text{total}}}{dA_1} \quad [24]$$

There are two elementary cases for which the integral of Equation [23] is of interest:

1 When radiation intensity vector $\vec{i}_{12}$ is assumed constant—corresponding to radiation exchange across a nonabsorbing medium.

2 When radiation intensity vector $\vec{i}_{12}$ is assumed to be dependent only on the distance $l_{12}$, between the surface elements, Fig. 7, exchanging radiation—corresponding to diffuse radiation transfer through an absorbing medium.

These cases are then discussed in turn.

*Case 1.* If $i_{12} = i_1 = \text{const}$, then from Equation [22]

$$J_1 = i_1 \int_0^{2\pi} \cos\theta_1 d\omega_{12} = \pi i_1 \quad [25]$$

and Equation [22] becomes simply

$$dQ_{1\to 2} = J_1 d(A_1 F_{12}) \quad [26]$$

where

$$d(A_1 F_{12}) = \frac{\cos\theta_1 \cos\theta_2}{\pi l_{12}^2} dA_1 dA_2$$

or

$$A_1 F_{12} = \int_{A_1 A_2} \frac{\cos\theta_1 \cos\theta_2}{\pi l_{12}^2} dA_1 dA_2 \quad [27]$$

$F_{12}$ representing the well-known shape factor (Lambert's cosine law).

Equations [26] and [27] describe the following fundamental property of diffuse radiation through a nonabsorbing medium: The portion of radiation flux from an area element $dA_1$ which is intercepted by another area element $dA_2$ is proportional to radiosity at $dA_1$, the proportionality factor depending only on the geometry of the system.

The shape factors possess two useful properties:

(*a*) The reciprocity relationship

$$A_1 F_{12} = A_2 F_{21} \quad [28]$$

which results directly from the symmetry of Equation [27];

(*b*) The summation property

$$F_{11} + F_{12} + \ldots F_{1n} = 1 \quad [29]$$

($n$ being the number of surfaces forming an enclosure) which applies when $J_1 = \text{const}$ over surface $A_1$, since from Equations [24] and [26] it follows that

$$Q_{1-\text{total}} = J_1 A_1 = J_1 \sum_{i=1}^{n} A_1 F_{1i}$$

*Case 2.* If $i_{12}$ depends only on the distance $l_{12}$ between the surfaces exchanging radiation, i.e.

$$i_{12} = i_{10} f(l_{12}) \quad [30]$$

where, according to Equation [25]

$$i_{10} = \frac{J_1}{\pi} \quad [31]$$

is the initial intensity of radiation (at surface $A_1$), then from Equation [23]

$$dQ_{1\to 2} = \frac{i_{10} f(l_{12}) \cos\theta_1 \cos\theta_2}{l_{12}^2} dA_1 dA_2$$

or

$$Q_{1\to 2} = \int_{A_1 A_2} \frac{J_1 f(l_{12}) \cos\theta_1 \cos\theta_2}{\pi l_{12}^2} dA_1 dA_2 \quad [32]$$

Introducing the transmissivity of the medium defined by the relation

$$Q_{1\to 2} = \tau_{12} J_1 A_1 F_{12} \quad [33]$$

it follows from Equations [27] and [32] that the transmissivity in a diffuse radiation field is given by

$$\tau_{12} = \frac{\int_{A_1 A_2} \frac{f(l_{12}) \cos\theta_1 \cos\theta_2}{l_{12}^2} dA_1 dA_2}{\int_{A_1 A_2} \frac{\cos\theta_1 \cos\theta_2}{l_{12}^2} dA_1 dA_2} \quad [34]$$

The radiation-absorbing characteristics of the medium can be expressed in terms of an over-all absorption coefficient $K$ defined by the following relation

$$di = -Kidl \quad [35]$$

where $di$ denotes the decrement of radiation intensity across an increment $dl$ of radiation beam and $i$ is the intensity of radiation at a distance $l$ from the source.

The over-all absorption coefficient is expressed, in turn, as $K = kc$, where $k$ is the absorption coefficient of the absorbing molecules—in general, a function of wave length and temperature—and $c$ is the concentration of absorbing molecules. If both $k$ = const (which applies in absence of secondary processes and holds true, therefore, for monochromatic radiation) and $c$ = const (homogeneous medium) then, according to Equation [35], the field is characterized by the property that, at any point, the intensity gradient in the direction of radiation beam is proportional to local intensity. In this case Equation [35] yields

$$\frac{i_{12}}{i_{10}} = f(l_{12}) = e^{-kcl_{12}} \quad [36]$$

(Beer-Lambert law)

# Supplement

## Matrix Analysis of Radiation Networks[7]

The characteristic feature of radiation networks is the absence of mutual admittances and internal branch voltage generators. Such networks can be analyzed by an application of the Kron method (see reference 15). The purpose of this note is to describe the analytical technique involved in such an application; rigorous proofs are presented elsewhere.[8]

[7] This Supplement was prepared by the author,[1] and J. P. Roth, Institute for Advanced Study, Princeton, N. J.

[8] "An Application of Algebraic Topology to Numerical Analysis," by J. P. Roth, Proc. U. S. A. Nat. Acad. Sci., vol. 41, no. 7, July, 1955, pp. 518–521.

The branch conductances of the network define the following diagonal admittance matrix

$$\boxed{Y} =$$

| | 12 | 13 | ...1$n$ | 23 | 24 | ...2$n$ | ...$(n-1)n$ |
|---|---|---|---|---|---|---|---|
| 12 | $Y_{12}$ | 0 | 0 | 0 | 0 | 0 | 0 |
| 13 | 0 | $Y_{13}$ | 0 | 0 | 0 | 0 | 0 |
| . | | | | | | | |
| . | | | | | | | |
| . | | | | | | | |
| $1n$ | 0 | 0 | $Y_{1n}$ | 0 | 0 | 0 | 0 |
| 23 | 0 | 0 | 0 | $Y_{23}$ | 0 | 0 | 0 |
| 24 | 0 | 0 | 0 | 0 | $Y_{24}$ | 0 | 0 |
| . | | | | | | | |
| . | | | | | | | |
| . | | | | | | | |
| $2n$ | 0 | 0 | 0 | 0 | 0 | $Y_{2n}$ | 0 |
| . | | | | | | | |
| . | | | | | | | |
| . | | | | | | | |
| $(n-1)n$ | 0 | 0 | 0 | 0 | 0 | 0 | $Y_{(n-1)n}$ |

..[37]

($n$ denoting the number of nodes) the elements of which are expressed in mhos or in sq ft.

This matrix relates the branch potential differences and currents as follows

$$[j] = \boxed{Y}\,[E] \quad [38]$$

where

$$[E] = [E_{12}\ \ E_{13} \ldots\ E_{1n}\ \ E_{23}\ \ E_{24} \ldots\ E_{2n} \ldots\ E_{(n-1)n}] \ldots [39]$$

is a vector made up of all the branch potential differences $E_{12} = E_2 - E_1$, $E_{13} = E_3 - E_1$, etc., expressed in volts or in Btu/hr sq ft, and

$$[j] = [j_{12}\ \ j_{13}\ \ j_{1n}\ \ j_{23}\ \ j_{24} \ldots\ \ j_{2n} \ldots\ j_{(n-1)n}] \ldots [40]$$

is a vector made up of the corresponding branch (coil) currents, expressed in amperes or in Btu per hr.

Current in each branch $j_{ik}$ can be expressed as the sum of current $I_{ik}$ due only to a current generator associated with it, plus current $i_{ik}$ due to the effect of the rest of the network on the branch (or current which would flow through the branch in the absence of its own current generator), i.e.

$$[j] = [i + I] = [i] + [I] \quad [41]$$

The bounding values of the radiation network are described in terms of the node-pair potential vector

$$[E'] = [E_{1n}'\ \ E_{2n}' \ldots E_{(n-1)n}'] \quad [42]$$

the components of which are the differences between the potential of node $n$, taken as reference, and the potentials of all the remaining nodes, i.e., $E_{1n}' = E_n - E_1$, $E_{2n}' = E_n - E_2$, etc. and the node-pair current vector

$$[I'] = [I_{1n}'\ \ I_{2n}' \ldots I_{(n-1)n}] \quad [43]$$

the components of which are the net external currents impressed on all the nodes with exception of the reference node $n$. (Note that in both Equations [42] and [43] there is no component with a subscript $nn$.) If node $n$ represents a radiation source then for any other node $j$ representing another radiation source, $I_{jn}' < 0$ is the net external flux supplied to node $j$, while for a node $k$ representing a radiation sink $I_{kn}' > 0$ is the net flux absorbed, and for

a node $r$, representing a reradiator surface or a radiosity node $I_{rn}' = 0$.

The over-all solution of the problem is given as a relationship between the bounding values

$$[I'] = \boxed{Y'}[E'] \quad [44]$$

or its inverse

$$[E'] = \boxed{Y'}^{-1}[I'] \quad [45]$$

Matrix $\boxed{Y'}$ which appears in the foregoing as the key to the solution is obtained by the use of a transformation matrix $\boxed{A}$ relating the branch potential differences with the node-pair potentials as follows

$$[E] = \boxed{A}\,[E'] \quad [46]$$

The structure of this matrix is easy to deduce

$$\boxed{A} = \begin{array}{r|ccccc} & 1n & 2n & 3n & 4n\ldots & (n-1)n \\ \hline 12 & 1 & -1 & 0 & 0 & 0 \\ 13 & 1 & 0 & -1 & 0 & 0 \\ \vdots & & & & & \\ 1(n-1) & 1 & 0 & 0 & 0 & -1 \\ 1n & 1 & 0 & 0 & 0 & 0 \\ 23 & 0 & 1 & -1 & 0 & 0 \\ 24 & 0 & 1 & 0 & -1 & 0 \\ \vdots & & & & & \\ 2(n-1) & 0 & 1 & 0 & 0 & -1 \\ 2n & 0 & 1 & 0 & 0 & 0 \\ \vdots & & & & & \\ (n-1)n & 0 & 0 & 0 & 0 & 1 \end{array} \quad [47]$$

since

$$E_{12} = E_2 - E_1 = (E_n - E_1) - (E_n - E_2) = (+1)E_{1n}' + (-1)E_{2n}'$$

$$E_{13} = E_3 - E_1 = (E_n - E_1) - (E_n - E_3) = (+1)E_{1n}' + (-1)E_{3n}'$$

etc.

The transpose of this matrix relates the node-pair current with the branch current generators

$$[I'] = \boxed{A}_t\,[I] \quad [48]$$

and annihilates the $i$ vector

$$\boxed{A}_t\,[i] = 0 \quad [49]$$

as can be verified, say, by performing the indicated operations.

Premultiplying both sides of Equation [38] by $\boxed{A}_t$, using Equations [41] and [49]

$$\boxed{A}_t\,[I] = \boxed{A}_t\,\boxed{Y}\,[E]$$

whence with Equation [46] and [48]

$$[I'] = \boxed{A}_t\,\boxed{Y}\,\boxed{A}\,[E']$$

so that

$$\boxed{Y'} = \boxed{A}_t\,\boxed{Y}\,\boxed{A} \quad [50]$$

It should be noted that $\boxed{Y'}$ is an $(n-1)$ by $(n-1)$ matrix. It is obtained by simple multiplications shown in Equation [50] and, as demonstrated in Equation [44], it serves directly as a solution to a whole class of problems involving the determination of net fluxes induced by a given potential field.

## Discussion

VICTOR PASCHKIS.[9] The paper is very interesting because it applies a powerful technique to an important problem. It may be pointed out that this technique has been used previously for study of certain radiation problems in electric furnaces.[10,11] In this case, provision was also made in the computing network to represent conduction between different parts of the radiating body.

### AUTHOR'S CLOSURE

The author thanks Dr. Paschkis for pointing his attention to the earlier work on network analog computers for problems in radiation heat transfer. However, the technique used by Dr. Paschkis differs fundamentally from the method proposed in the present paper in that he considered node potentials as proportional to surface temperature, while, according to present method, node potentials represent radiosities and black-body emissive powers. Consequently, Dr. Paschkis had to deal with a nonlinear network which restricted considerably the scope of application, while the radiation networks described in the present paper are essentially linear and their scope is restricted only by the assumption of diffuse radiations with either gray or monochromatic system elements. In fact, his method was restricted to enclosures made up of black bodies only, and, as an example, he treated solely the simple case of such an enclosure consisting of four sources, one sink, and a single refractory surface.

Moreover, it should be noted that the present paper is by no means concerned only with analog computers—a field in which Dr. Paschkis' contributions are well known.

---

[9] Technical Director, Heat & Mass Flow Analyzer Laboratory, Columbia University, New York, N. Y. Mem. ASME.

[10] "Elektrisches Modell zur Verfolgung von Waermestrahlungsvorgaengen insbesondere in elektrischen Oefen," by Victor Paschkis, *Elektrotech. Maschinenbau*, vol. 54, 1936, pp. 617–621.

[11] "Industrial Electric Furnaces and Appliances," by Victor Paschkis, Interscience Publishers, Inc., New York, N. Y., vol. 1, 1945, p. 27; vol. 2, 1948, p. 75.

# Self-Excited Vibrations of Systems With Two Degrees of Freedom

By ERNST SALJÉ,[1] AACHEN, GERMANY

**The paper reports on an investigation of vibrations of systems with two degrees of freedom. First to be considered is the dynamic behavior of a lathe spindle. Cutting conditions are of influence, and it can be demonstrated that a lathe spindle approximates vibrations in two degrees of freedom. Thereafter, a series of tests is described that were run with turning tools of relatively great overhang and with two degrees of freedom. Finally, the mathematical concept of self-excited vibrations is given. This paper may be considered as a discussion of the particular problems investigated. It does not purport to give a general theory of self-excited vibrations of the cutting processes.**

## Introduction

RESEARCH work relating to the machinability of metals has dealt with the influence of vibrations to an increasing degree in recent years. The first comprehensive treatise about self-excited machine-tool vibrations was written by Arnold (1),[2] who gave a theoretical explanation of his test results, obtained with a turning tool having a relatively great overhang, by assuming one degree of freedom. Further papers about vibrations with one degree of freedom were published, e.g., by Chisholm (2) and Saljé (3). Self-excited vibrations of systems with two degrees of freedom were investigated by Hahn (4). While the papers (1), (2), and (4) deal with self-excited vibrations in the turning process, investigations on vibrations in the grinding process have been published by Saljé (3), (8) and Hahn (5).

Stefaniak presented a report on self-excited vibrations of systems with two degrees of freedom at a meeting on vibration engineering, held in Munich, Germany, in September, 1953. Subsequently this report has been published (6). It may be noted that previously Lysen (7) had given a report on the same subject, at the Sixth Werkzeugmaschinen-Kolloquium (Machine Tool Engineers Meeting) at Aachen.

## Self-Excited Vibrations of a Lathe Spindle

Under certain cutting conditions a lathe spindle of a given design (including the effect of the gear wheels and bearings) can vibrate with very much greater amplitudes than the amplitudes of the other machine-tool elements under the influence of the cutting forces. As an example, Fig. 1 represents the amplitudes of vertical vibrations of a lathe bed measured during the chattering of a turning tool. The measurements were taken in the $x$-$y$ plane perpendicular to the $z$-axis illustrated in Fig. 2. The points, at which the measurements are taken, are given likewise in Fig. 2

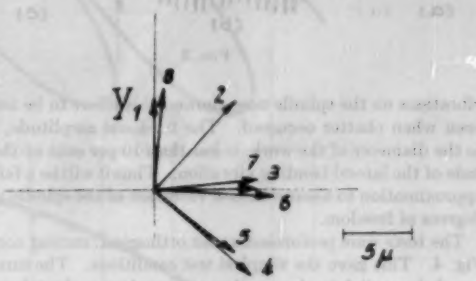


Fig. 1

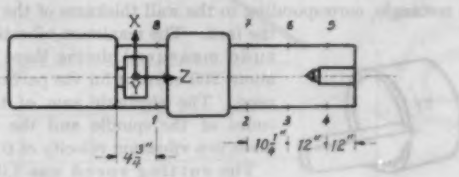


Fig. 2

and the amplitude vectors are marked with the same numbers in Fig. 1 as the points in Fig. 2. From Fig. 1 it appears that the amplitudes are 5 to 10 microns, and (200 to 400 microinches) that they are of the same magnitude in the horizontal direction. It may be noticed that a free lateral vibration of the bed, e.g., of the first order, was absent. If a free vibration or a forced vibration at the resonance point appears, the phase angle between the vectors is 0 or 180 deg; i.e., the movement of all points is given by

$$y = y_i \cos \omega t$$

According to this equation, all points must reach their maximum amplitude at the same time. Fig. 1 demonstrates the phase angle between the amplitude vectors showing that they do not follow the equation and the conditions given in the foregoing.

From this a forced vibration of the lathe bed is evident. The frequency of the self-excited periodic force differed from the natural frequency of the bed.

The lateral vibrations of the spindle nose in the $x$-$y$ plane have been measured simultaneously with the bed vibrations by capacitive electronic pickups, so that the readings are not affected by additional masses, spring constants, or damping constants, Fig. 3($a$). Oscillograms are given in Fig. 3($b$), showing amplitude values of 200 and 50 micron (0.008 to 0.002 in.) from peak to peak. According to the oscillograms, the center of the spindle was making an elliptical motion in the $x$-$y$ plane. The lengths and angular positions of the major and minor axes of this ellipse varied slightly, as illustrated in Fig. 3($c$), indicating variations of amplitude and phase angles of the vibrations measured in those two directions.

The frequency of this self-excited vibration of the spindle was in most cases slightly lower than the natural frequency. This effect will be discussed later in this paper.

Further measurements concerning the amplitudes of torsional

---

[1] Chief Research Engineer, Institute for Machine Tools and Management, Technische Hochschule.

[2] Numbers in parentheses refer to the Bibliography at the end of the paper.

Contributed by the Research Committee on Metal Processing and presented at the Annual Meeting, New York, N. Y., November 28–December 3, 1954, of The American Society of Mechanical Engineers.

Note: Statements and opinions advanced in papers are to be understood as individual expressions of their authors and not those of the Society. Manuscript received at ASME Headquarters, October 7, 1954. Paper No. 54—A-204.

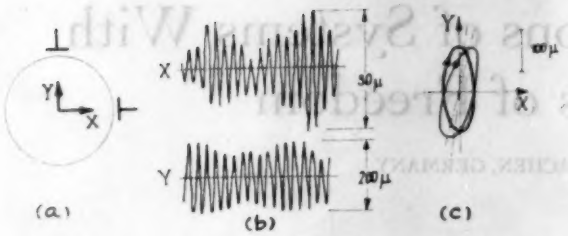


FIG. 3

vibrations on the spindle nose showed this effect to be negligible, even when chatter occurred. The torsional amplitude, reduced to the diameter of the work, is less than 10 per cent of the amplitude of the lateral bending vibration. Thus it will be a fairly good approximation to assume lateral vibration of the spindle with two degrees of freedom.

The tests were performed under orthogonal cutting conditions, Fig. 4. This gave the simplest test conditions. The turning tool was fed parallel to the turning axis against a short length of a seamless tube. Thus the cross section of the chip obtained was a rectangle, corresponding to the wall thickness of the work and the feed. The maximum vibration amplitude measured during these tests was about 260 microns for the particular lathe used. The algebraic sum of the amplitudes of the spindle and the tool post leads to a vibration velocity of 0.45 m/sec.

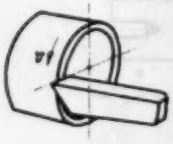

FIG. 4

The cutting speed was 1.00 to 1.15 m/sec which is much greater than the vibrational velocity. Similar results were obtained by running these tests on other lathes under the same cutting conditions. Thus a difference appears between tool vibration at high and low frequencies.

If a high-frequency vibration is present, the velocity of the vibration is limited by the cutting speed, as stated in the papers of Arnold (1) and Saljé (3). This fact may be expressed by the formula

$$v = \dot{y}_{max} = y_{max}\omega$$

For the vibrations of low frequency this criterion is invalid.

According to Arnold, the amplitudes of self-excited vibrations also can be limited by the self-excited periodic force. If the difference between the steady-state cutting force and the self-excited periodic force is less than zero, it tends to reverse the vibrational motion, and this has the same effect as a large damping constant.

Fig. 5 illustrates the amplitudes of the tool post $z$ (in the $z$-direction of Fig. 2) and of the work $y_1$ ($y$-direction of Fig. 2), which is nearly equal to the amplitude of the spindle nose, because a short length of tube was used in the tests. The plots in this diagram correspond to different cutting speeds and feeds. The slopes of $y_1$ and $z$ and their ratio of about 10:1, depend on the design of the machine. In these test series the maximum self-excited periodic force was 100 kg. The main cutting force under the same test conditions was of about the same magnitude, when chatter did not occur. The self-excited periodic forces were measured with a dynamometer having a natural frequency much higher than the frequency to be measured.

The conclusions from these and similar test series are that for lower frequencies (up to several hundred cps) and the amplitudes are limited by the self-excited periodic forces rather than by the vibrational velocity.

Further, the test series showed a nearly constant ratio between

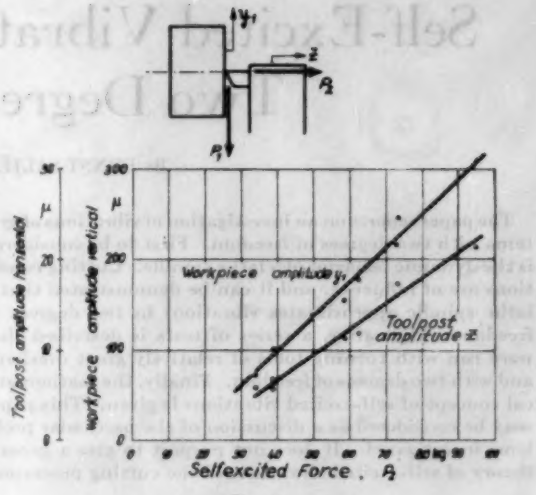


FIG. 5

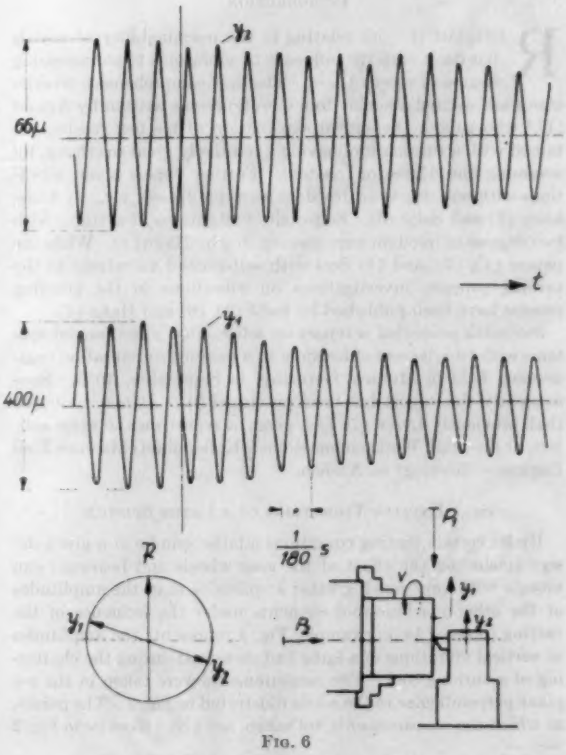


FIG. 6

the tool-post amplitudes and the spindle-nose amplitudes, measured in the same direction, so that the value of either of the amplitudes is given by measuring just one of them. As an example, Fig. 6 demonstrates a section taken from an oscillogram. Both the amplitudes are decreasing simultaneously. According to the line $A$-$A$, the phase angle between the amplitudes $y_1$ and $y_1$ is very close to 180 deg. The phase angle between the periodic force as measured and the amplitudes is approximately 90 deg as shown in the vector diagram of Fig. 6.

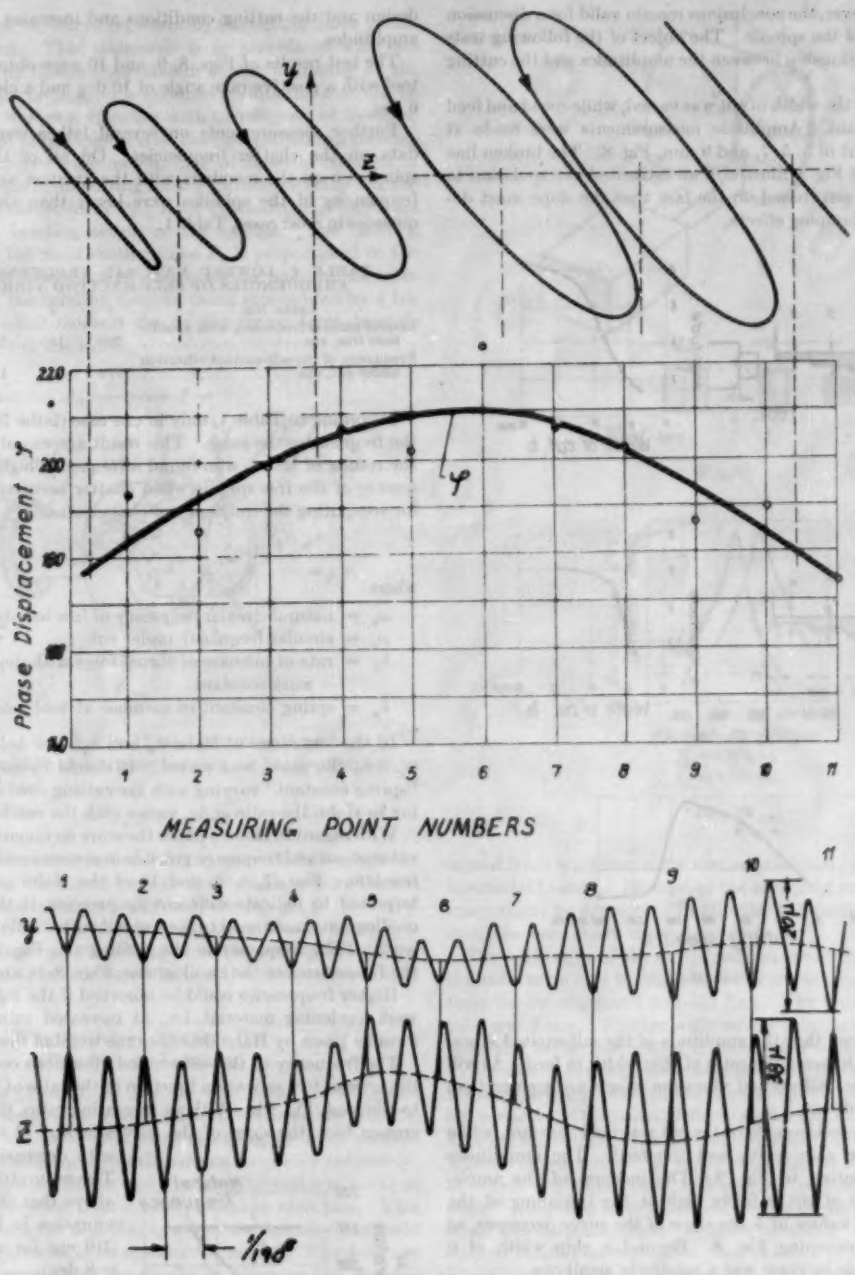


FIG. 7

As in the test results of Hahn (see his Fig. 7 in reference 4) a variation of the phase angle between the two components of the toolpost vibration, the tool vibration or the spindle vibration could be observed in the test series described later in the paper. Thus the shapes of the Lissajous figures differ from each other and the vibrating point considered may describe the pattern in any of the possible directions, Fig. 7. On the other hand, a variation of the phase-angle results from a slight variation of the frequency ratio of the two vibrations, which must remain close to one to assure low-frequency beats. If the frequency ratio exceeds 1 appreciably the ellipses are severely distorted, Fig. 15. The energy input to the self-excited vibration varies with the direction of the elliptical motion, hence altering the amplitude in most cases. The cutting conditions of these tests were the same as in the preceding test series.

As explained previously, there is a constant ratio of the amplitudes of the spindle and the tool post. Thus in the description of the following tests only the amplitude of the tool post is used in the

diagrams. However, the conclusions remain valid for a discussion of the behavior of the spindle. The object of the following tests was to find a relationship between the amplitudes and the cutting conditions.

In the first test the width of cut was varied, while speed and feed were held constant. Amplitude measurements were made at every width of cut of 3, 5, 7, and 9 mm, Fig. 8. The broken line in the diagram of Fig. 8 illustrates an estimated extrapolation to higher widths of cut, based on the fact that the slope must decrease owing to damping effects.

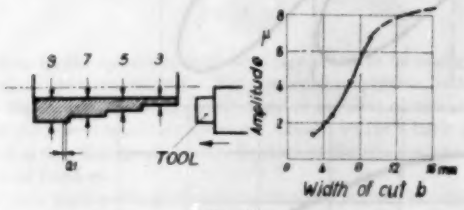


FIG. 8

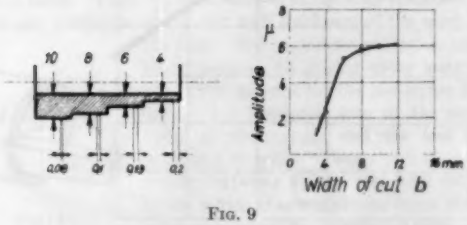


FIG. 9

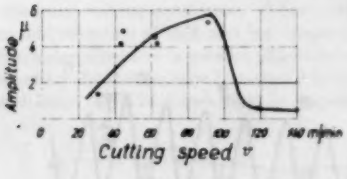


FIG. 10

It may be noticed that the amplitude of the self-excited vibration increases with increasing ratio of chip width to feed. As will be explained later, self-excited vibration effects are greater than forced-vibration effects.

Next, the cross-section area of the cut was held constant, while varying both the chip width and the feed. The amplitudes measured are plotted in Fig. 9. The increase of the amplitudes with width of cut is fairly high at the beginning of the curve; at higher values of $b$ the slope of the curve decreases, as was discussed concerning Fig. 8. Beyond a chip width of 6 mm, the amplitude increase was a relatively small one.

The effect of the cutting speed was studied in another test series. The cross section of the cut was held constant at 8 mm width and a feed of 0.1 mm per revolution. The result is illustrated in Fig. 10. The amplitude increases with the cutting speed and then decreases after reaching a maximum. This result corresponds to results obtained in previous test series, where only one degree of freedom was considered.

The amplitudes measured in the test series of Figs. 8, 9, and 10 were in proportion to the periodic forces, as shown in Fig. 5. The dynamic instability of the machine-tool members depends on their design and the cutting conditions and increases with increasing amplitudes.

The test results of Figs. 8, 9, and 10 were obtained by using a tool with a positive rake angle of 10 deg and a clearance angle of 6 deg.

Further measurements on several lathes were made to get data on the chatter frequencies. On all of these lathes the spindles were the members with the greatest amplitudes. The frequencies of the spindles were lower than their natural frequencies in most cases, Table 1.

TABLE 1 LOWEST NATURAL FREQUENCIES AND FREQUENCIES OF SELF-EXCITED VIBRATIONS

| Lathe No. | 1 | 2 | 3 | 4 | 5 |
|---|---|---|---|---|---|
| Lowest natural frequency with spindle nose free, cps | 200 | 190 | 190 | 265 | 165 |
| Frequency of the self-excited vibration under cut, cps | 174 | 170 | 190 | 256 | 132 |

According to Table 1, only in one case (lathe No. 3) were both the frequencies the same. This result agrees only partially with the results of Hahn, who found a frequency higher than the frequency of the free spindle when chatter occurred. His formula for computing the frequency of chatter was

$$\omega_c = \omega_q \sqrt{1 + k_w/k_q}$$

where

$\omega_q$ = natural circular frequency of free member
$\omega_c$ = circular frequency under cut
$k_w$ = rate of increase of thrust force with depth of cut, i.e., a work constant
$k_q$ = spring constant of member at tool point

In the test series of Hahn $k_w$ and $k_q$ were held constant and $\omega_q$, i.e., the mass, was varied. It should be noted that $k_w$ is a "spring constant" varying with the cutting conditions.[3] According to Hahn the ratio $\omega_c/\omega_q$ varies with the cutting conditions.

With regard to Hahn's paper there are no remarks on the second value of natural frequency possible in systems with two degrees of freedom. Figs. 7, 8, 9, and 10 of the Hahn paper can be interpreted to indicate different frequencies, if the width of the oscillograms is assumed to correspond with a full revolution of the work. (The frequency in the oscillogram, Fig. 7, is lower than the frequencies of the oscillograms, Figs. 8, 9, and 10.)

Higher frequencies could be observed if the cuts were made in work-hardening material, i.e., at increased values of $k_w$. The formula given by Hahn describes the trend of these relationships.

The frequency of the self-excited vibrations could be stated in the present test series as a function of the ratio of the width of cut to the feed, Fig. 11. With an increasing ratio, the frequency increases too; the slope of the curves in Fig. 11 becomes greater with decreasing rake angles. The natural frequencies were above that of the self-excited vibration in both cases (i.e., 210 cps for a rake angle of —8 deg).

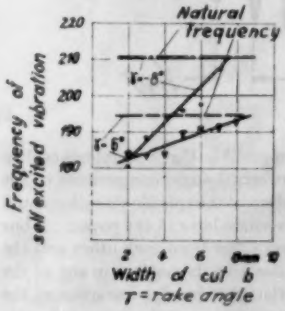


FIG. 11

The increase of the cutting forces with the feed (orthogonal cutting process) is especially high at small depths of cut (i.e., feeds). With regard to Fig. 11, we can suppose that the increase of the frequency depends

[3] Reference (8), fig. 12, p. 1077.

upon the slope of the curve representing the cutting force versus the depth of cut. This statement is in accordance with the formula given by Hahn. As stated at the beginning of the present paper, the lathe spindle executes a vibration that can be described fairly well as a vibration with two degrees of freedom.

The movement of the spindle nose can be regarded as a geometrical addition of two movements; one of them is executed in the direction of the main cutting force $P_1$ while the other has the direction of the thrust force $P_2$. Both of these components are produced by a bending action of the spindle. The bending moment due to the main cutting force $P_1$ is proportional to the length $L$ from the tool point to the supporting point of the main spindle bearing, the bending moment being represented by a triangle. The bending moment due to the thrust force depends upon the radius $r$ of the work.

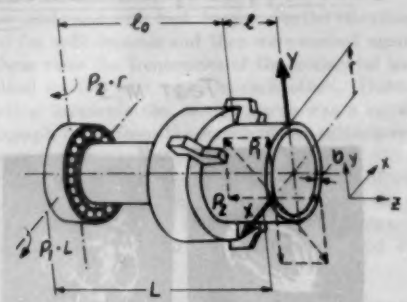


FIG. 12

According to the sketch, Fig. 12, and assuming the spindle to be clamped in the middle at the main bearing, an assumption can be made, expressed by

$$c_z > c_y$$

The spring constant and the natural frequency of the free spindle in the direction of the thrust force ($z$-direction) is greater than in the direction of the main cutting force ($y$-direction).

Even though a lathe spindle is nearly equal to a dynamic system with two degrees of freedom, when the orthogonal cutting process (see Fig. 4) is considered, it is still a relatively intricate dynamic system.

## SELF-EXCITED VIBRATIONS OF TURNING TOOLS WITH TWO DEGREES OF FREEDOM

Turning tools (Nos. 1, 2, and 3) with long overhang and different cross sections were studied in these tests, see Fig. 13. Great care had to be observed when clamping the tools because slightly altered clamping affects the natural frequency noticeably. The natural frequency of the free overhanging tool was lower in the horizontal direction than in the vertical in each case. This remained true even for tool No. 1, where the frequencies should have been equal because of its square cross section. The damping constant as computed from the amplitude diagrams (see Fig. 14)

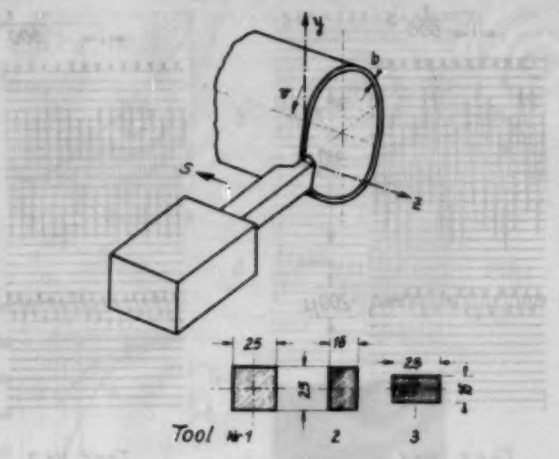


FIG. 13

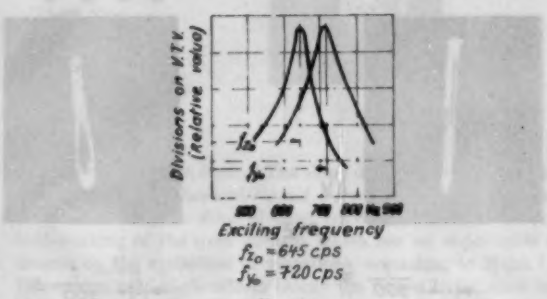


FIG. 14

of tool No. 1 is greater in the vertical direction ($y$-axis) than in the horizontal ($z$-axis). Because of the clamping conditions the contrary might be expected. In all cases the computed natural frequencies were above those measured.

The tool angles of the sharpened and honed tool were constant, the rake angle was 10 deg, and the clearance angle 6 deg. In all tests the cutting speed was 335 fpm. The wall thickness of the tube was 2 mm. Thicker walls would have caused heavy vibrations and too serious a wear of the cutting edge.

The results of one of these tests are given in Table 2. By transmitting the components of the vibration in the $y$ and $z$-direction to the vertical and horizontal deflection plates of a cathode-ray oscilloscope, respectively, the motion of the tool point in the $y$-$z$-plane appears on the screen. In many cases ellipses could be observed, of which the dimensions and angular positions remained the same. According to this the frequencies of the components were equal and the phase angles remained constant. In other cases the ellipses rotated on the screen (i.e., variable phase angles) or the Lissajous figures could not be analyzed by visual observation (i.e.,

TABLE 2 TEST RESULTS

| No. of test | No. of tool | $f_{y0}$ | $f_{z0}$ | $f_y$ under cut | $f_z$ under cut | $y_{(a)}$ (math average) | $(z_a)$ (math average) | $y/z$ | $y_{max}$ | $\frac{y}{y_{max}}$ |
|---|---|---|---|---|---|---|---|---|---|---|
| 1 | | | | 645 | 645 | 135–150 | 75–95 | 1.66 | 0.6 | 2.4 |
| 2 | 1 | 725 | 660 | 610–640 | 480–620 | 104 | 29 | 3.6 | 0.42 | 3.5 |
| 3 | | | | 530–500 | 450–500 | 160 | 105 | 1.5 | 0.59 | 2.4 |
| 4 | | | | 650 | 650 | 180 | 75 | 1.46 | 0.73 | 2.0 |
| 5 | 2 | 680–700 | 410 | 500–580 | 480–540 | 250 | 125 | 2.0 | 0.86 | 1.7 |
| 6 | | | | 410–730 | 430–470 | 165 | 115 | 1.4 | 0.76 | 1.9 |
| 7 | | | | 480–500 | 480–500 | 345 | 105 | 3.3 | 1.08 | 1.35 |
| 8 | 3 | 500 | 630 | 450 | 450 | 190 | 144 | 1.3 | 0.54 | 2.7 |
| 9 | | | | 440 | 440 | 200 | 125 | 1.56 | 0.58 | 2.4 |

$v$ = 87m/min, $b$ = 2mm, $\mu$ = micron

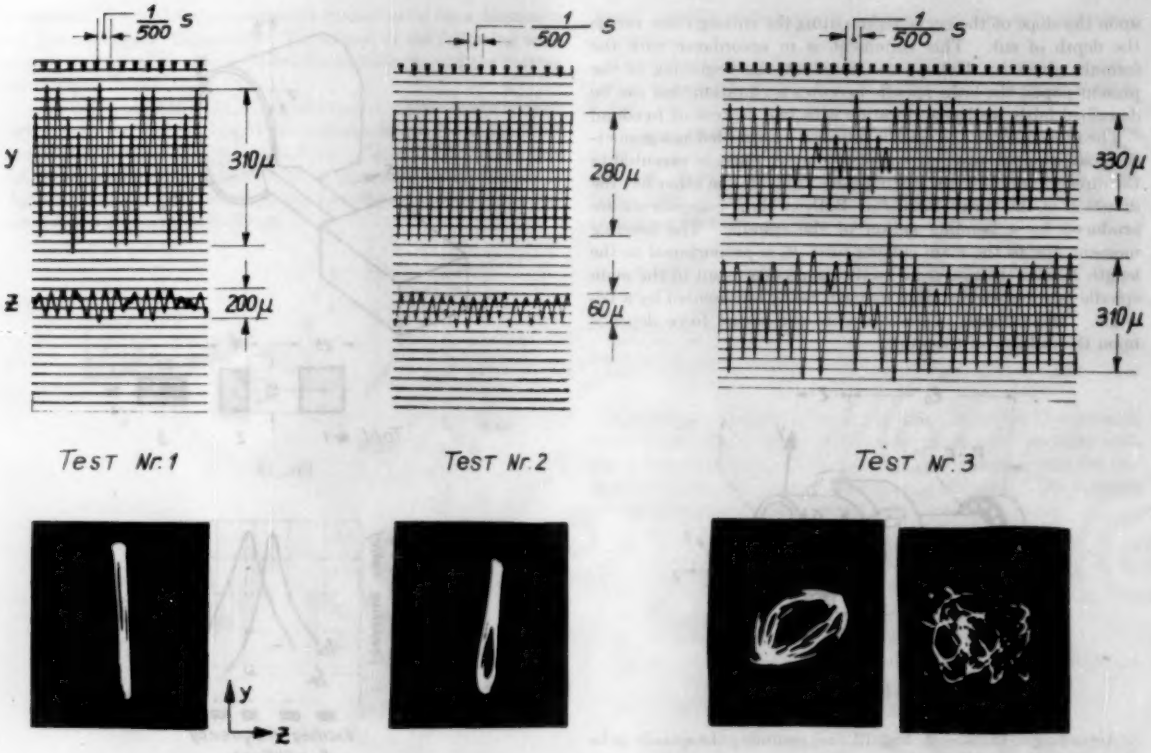


Fig. 15

speedy variations of frequencies, phase angles, and amplitudes), Fig. 15. Because of this, the behavior of the vibration is described in Table 2 by giving limiting values for the frequencies and mean values for the amplitudes. Under cut the frequencies dropped below the natural frequencies of the free tools, Table 2. The spring constant of tool No. 3 is of the same magnitude as that of the spindle and the frequency under cut was nearly equal to the natural frequency of the free tool in the $y$-direction. The frequency under cut was lower just as observed with the spindle. The frequencies of the tools Nos. 1 and 2 were also near the frequency $f_y$, but the conformity is a poorer one. Furthermore, Table 2 shows no uniform results, although the test conditions were as constant as possible. It was difficult to reproduce the experiments.

The influence of the wearland $B$ on the self-excited vibration, references (1) and (3), has been investigated in further test series, using tool No. 1. In these tests the same effects could be noted as in earlier test series made by the author (8). With a very sharply honed tool the amplitude is slightly greater than in the presence of a small wearland. With increasing wearland, the amplitude increases again, Fig. 16. In systems having two degrees of freedom the dynamic stability is affected by large wearlands. Considering only a single degree of freedom it has been stated in formerly published papers (1) and (3) that self-excited vibrations are intensified even by relatively small wearlands.

According to the tests performed so far, the frequencies and the phase angles between the $y$ and

$z$-components are not affected by the wearland. On the other hand, the ratio of the width of cut and the feed affects the frequency of the spindle vibration. The behavior of tool No. 1 was a similar one. The frequency increases with lowered feeds. Although the frequencies varied during a test they were always lower than the natural frequency. The results of a test series with variable feeds are compiled in Table 3 and Fig. 17. In spite of the relatively great scatter of the points a distinct trend appears. The frequencies of the horizontal component (i.e., in the $z$-axis) were always lower than those of the vertical. Corresponding to this, the Lissajous figures had complex shapes.

Further research work will have to be done to explain the relatively large amplitudes of the horizontal motion compared with those of the vertical motion, Table 2.

At low feeds and with high frequencies the vibrations vanished for split seconds and then were excited again. In all these cases the frequencies of the horizontal and the vertical motion were equal to each other. During the starting transients the motion curve was a spiral. A photograph taken from the screen of the cathode-ray oscilloscope is shown in Fig. 18.

These spirals indicate the number of periods of the starting transient until the maximum amplitude is reached. Furthermore, the ratio of the negative damping constant to the frequency can be estimated by means of these spirals.

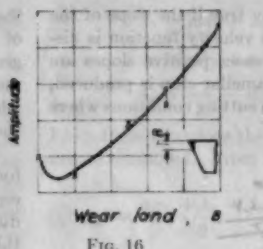


FIG. 16

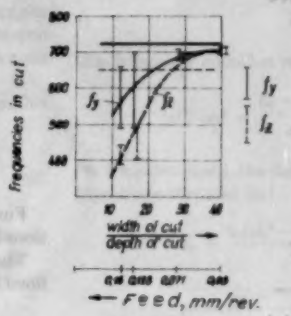


FIG. 17

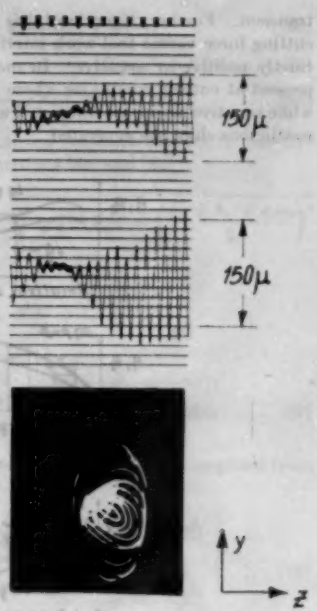


FIG. 18

## MATHEMATICAL ANALYSIS OF SELF-EXCITED VIBRATIONS OF SYSTEMS HAVING TWO DEGREES OF FREEDOM

A mathematical analysis of systems having two degrees of freedom has been made by Stefaniak (6). He considered the variation of cutting forces $P_1$ and $P_2$ due to depth of cut (i.e., the feed in the orthogonal cutting process) and velocity at the tool-work interface, and discussed the criterion of stability by means of the Hurwitz determinant.

The present paper does not follow this method. Rather, the solution of the differential equation of motion is resolved into a real and imaginary part. By so doing, it is possible to compute damping constants and frequencies.

An influence of the rake angle on self-excited vibrations is given by Fig. 11 and in the paper of Arnold (1). Therefore this influence is also considered.

Many measurements of the cutting force showed the characteristics of the curves in Fig. 19.

A widely held opinion is that the cutting forces always decrease with increasing cutting speed. But if these velocities are low an increase of the cutting forces with the velocity can be observed in many cases. The slope of the cutting force versus speed curve can vary from positive to negative and need not be the same for the forces $P_1$ and $P_2$. (For cast iron this slope is zero for all recommended cutting speeds.) Self-excited vibrations could be observed at all values of the slope.

The cutting forces always increase with depth of cut as seen in the diagram in the middle of Fig. 19. The slope of the cutting force versus depth-of-cut curve depends upon the work material and the depth of cut itself. The slope decreases with increasing depth of cut, and those of $P_1$ and $P_2$ may also differ from each other. Further, the slope of these curves includes the effect of cold-working of the work surface, which has an appreciable influence on the excitation of vibrations, according to Hahn (4). Decreasing rake angle affects chiefly the thrust force, since it is increased more than the main cutting force.

A schematic representation of the systems with two degrees of freedom considered in this paper is given in Fig. 20. One system to be considered is the tool, Fig. 20($a$), while the other is the work and the spindle, Fig. 20($b$). It should be noted that the scheme is not affected by opposite force or axis directions.

TABLE 3 TEST RESULTS WITH VARIABLE FEEDS

| No. of test | Feed $s$ | $b/s$ | $f_{y0}$ | $f_{z0}$ | $f_y$ | $f_z$ | $y(\mu)$ | $z(\mu)$ | $y/z$ | $\dot{y}_{max}$(m/s) | $v/\dot{y}_{max}$ |
|---|---|---|---|---|---|---|---|---|---|---|---|
| 1 | 0.05 | 40 | 725 | 650 | 700–708 | 700–708 | 150 | 150 | 1 | 0.68 | 2.1 |
| 2 | 0.071 | 28 | 725 | 650 | 710–690 | 710–690 | 160 | 100 | 1.66 | 0.7 | 2.05 |
| 3 | 0.125 | 16 | 725 | 650 | 490–700 | 480–400 | 160 | 145 | 1.1 | 0.7 | 2.05 |
| 4 | 0.18 | 12.5 | 725 | 650 | 480–670 | 440–490 | 170 | 130 | 1.3 | 0.72 | 2.0 |

$v$ = 87m/min, $b$ = 2mm, $\mu$ = micron

For minor changes of the cutting velocity, the depth of cut, and the rake angle, the following equations can be evaluated, if the first terms of a Taylor series are used

$$\left.\begin{aligned} P_1 &= P_{01} + \alpha_{11}\dot{y} - \beta_{11}z + \delta_{11}y \\ P_2 &= P_{02} + \alpha_{21}\dot{y} - \beta_{21}z + \delta_{21}y \end{aligned}\right\} \quad \ldots\ldots\ldots\ldots [1]$$

In the positive direction of the $y$-co-ordinate the rake angle becomes more negative and the tool-work interface velocity decreases. In the positive direction of the $x$-co-ordinate, the depth of cut decreases.

It should be noted that Equation [1] is true for small amplitudes only. In this case the curves of Fig. 19 can be replaced by their tangents. This approximation remains true only until the starting vibration transient begins its build-up, because a positive damping proportional to the amplitude is neglected. This positive damping limits the amplitude at the end of the starting

transient. Further, Equation [1] is only true if the slope of the cutting force versus tool-work interface velocity function is distinctly positive or negative. In most cases positive slopes are present at cutting conditions where a lamellar chip is produced, while negative slopes are connected with cutting conditions where continuous chips are generated.

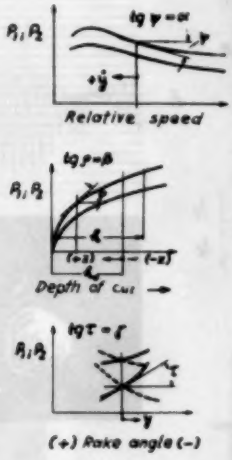


FIG. 19
(Relative speed = tool-work interface velocity.)

After the starting transient of the self-excited vibration chatter marks occur on the surface of the work, creating a forced vibration not covered by Equation [1]. However, forced vibrations cannot affect the self-excited vibration unless the work has made one revolution. In most of the tests the starting transient could be observed as completed within this period and then the starting transient was not further affected by the chatter marks.

To prove this, the following test was made: The work, shown in Fig. 4 as a short length of tube, was slotted parallel to its axis. Fig. 21 illustrates a cross section through the wall of the slotted tube. When turning this work, an alternating force is generated,

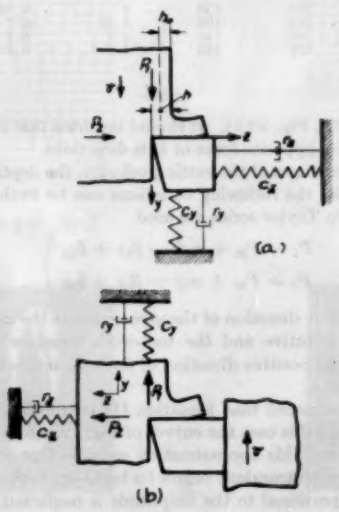


FIG. 20

the frequency given by the pitch and the revolutions per minute of the work. Beyond this, a self-excited alternating force was generated by the cutting process. The latter force was of a higher magnitude than the alternating force of the forced vibration, which vanished when its frequency differed from the frequency of the self-excited vibration.

In Equation [1] the influence of the velocity $\dot{z}$ on the cutting forces $P_1$ and $P_2$ has not been considered. Such an influence, especially that of $\dot{z}$ on $P_2$, is possible. On the other hand, many difficulties occur in trying to measure this. The analysis given in this paper does not cover this influence, because it cannot be proved by tests.

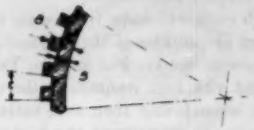

FIG. 21

Further, the influence of the tool wear on the self-excited vibrations is ignored for the time being.

The natural frequencies of the first order of a system are defined by

$$\omega_{y0} = \sqrt{\frac{c_y}{m_y}} \quad \text{and} \quad \omega_{z0} = \sqrt{\frac{c_z}{m_z}}$$

where $c_y$ and $c_z$ are spring constants and $m_y$ and $m_z$ are reduced masses.

With regard to the damping constants $r_y$ and $r_z$, the equations of motion are

$$\left.\begin{aligned} \ddot{y} + a_1\dot{y} + b_1 y + d_1 z &= 0 \\ \ddot{z} + a_2\dot{z} + b_2 z + c_2\dot{y} + d_2 y &= 0 \end{aligned}\right\} \quad \ldots\ldots\ldots\ldots [2]$$

where

$$a_1 = \frac{r_y - \alpha_1}{m_y},\ b_1 = \frac{c_y - \delta_1}{m_y},\ d_1 = \frac{\beta_1}{m_y}$$

$$a_2 = \frac{r_z}{m_z},\ b_2 = \frac{c_z + \beta_2}{m_z},\ c_2 = -\frac{\alpha_2}{m_z},\ d_2 = -\frac{\delta_2}{m_z}$$

where $\alpha_1$, $\alpha_2$, $\beta_1$, $\beta_2$, $\delta_1$, and $\delta_2$ are constants that depend on the work material and the cutting process. The constants $\alpha_1$, $\alpha_2$, $r_1$, $r_2$ can be positive or negative. The dynamic behavior of the machine tool is characterized by the constants $c_y$, $c_z$, $r_y$, $r_z$, $m_y$, and $m_z$.

With the solutions

$$z = z_0 e^{rt}$$

and

$$y = y_0 e^{rt}$$

Equation [2] becomes

$$\left.\begin{aligned} (r^2 + a_2 r + b_2)z_0 + (c_2 r + d_2)y_0 &= 0 \\ d_1 z_0 + (r^2 + a_1 r + b_1)y_0 &= 0 \end{aligned}\right\} \quad \ldots\ldots\ldots [3]$$

In order to have agreement, it is necessary that

$$r^4 + (a_1 + a_2)r^3 + (a_2 a_1 + b_2 + b_1)r^2 + (a_2 b_1 + a_1 b_2 - c_2 d_1)r + b_1 b_2 - d_1 d_2 = 0$$

This rewritten is

$$r^4 + A_3 r^3 + A_2 r^2 + A_1 r + A_0 = 0 \ldots\ldots\ldots [4]$$

According to Hurwitz, there is a stable state if the determinant is satisfied. This leads to

$$A_1A_2A_3 > A_1^2 + A_3^2A_0$$

$A_3A_2A_1$ and $A_0$ being positive. From the Hurwitz determinant one can compute the effect of varying any of the variables. Thus it is possible to determine how the stable state is affected by the variable considered. For example, if a spring constant varies, the stability may be affected in a certain range, as was demonstrated by Stefaniak (6). This is true only if in all machine-tool members transmitting the forces there exist only the same two degrees of freedom as was assumed in the analysis. If a spring constant of a member is varied too much, another member transmitting the forces, and having a different dynamic behavior, may execute self-excited vibrations and the equations of motion do not remain true as originally assumed.

Equation [4] may be solved by taking four conjugate complex roots

$$\left.\begin{aligned} r_{1,2} &= v_1 \pm i\omega_1 \\ r_{3,4} &= v_2 \pm i\omega_2 \end{aligned}\right\} \quad \ldots\ldots\ldots\ldots\ldots [5]$$

By introduction of these terms in Equation [4] and by comparing the coefficients with an equation of the fourth degree such as

$$(r - r_1)(r - r_2)(r - r_3)(r - r_4) = 0$$

one can obtain the following equations

$$\left.\begin{aligned} A_3 &= a_1 + a_2 = -2(v_1 + v_2) \\ A_2 &= a_1a_2 + b_1 + b_2 = |r_1|^2 + |r_2|^2 + 4v_1v_2 \\ A_1 &= a_1b_2 + a_2b_1 - c_2d_1 = -2(v_2|r_1|^2 + v_1|r_2|^2) \\ A_0 &= b_1b_2 - d_1d_2 = |r_1|^2|r_2|^2 \end{aligned}\right\} \quad \ldots\ldots [6]$$

FIG. 22

The real part of Equation [5] can be solved for the damping constant, while its imaginary part may be solved for the frequencies of the self-excited vibration. Fig. 22 shows the position of the vector in the complex plane at instability; i.e., $v > 0$. With regard to Fig. 18, the magnitude of the imaginary part of the vector $r$ may be estimated as much greater than its real part. This one can write

$$|r|^2 = \omega^2 \quad \ldots\ldots\ldots\ldots\ldots\ldots [7]$$

and $v_1 \ll w_1$; $v_2 \ll w_2$; $v_1 \ll w_2$; $v_2 \ll w_1$.

By doing so, the ratio $v/\omega$ of the real to the imaginary part may be estimated from the number of periods during the starting transient (3).

When substituting Equation [5] into Equation [4] we could write (see Fig. 22)

$$r_1 + r_2 = 2v_1, \quad r_3 + r_4 = 2v_2, \quad r_1r_2 = |r_1|^2, \quad r_3r_4 = |r_2|^2$$

Introduced into Equation [7], Equation [6] becomes

$$A_3 = a_1 + a_2 = -2(v_1 + v_2) \quad \ldots\ldots\ldots\ldots\ldots [8a]$$

$$A_2 = a_1a_2 + b_1 + b_2 = \omega_1^2 + \omega_2^2 \quad \ldots\ldots\ldots\ldots\ldots [8b]$$

$$A_1 = a_1b_2 + a_2b_1 - c_2d_1 = -2(v_2\omega_1^2 + v_1\omega_2^2) \quad \ldots [8c]$$

$$A_0 = b_1b_2 - d_1d_2 = \omega_1^2\omega_2^2 \quad \ldots\ldots\ldots\ldots\ldots [8d]$$

From these equations the damping constants and the frequencies can be computed. From Equations [8b] and [8d]

$$\omega_1^2, \omega_2^2 = \frac{a_1a_2 + b_1 + b_2}{2} \pm \sqrt{d_1d_2 - b_1b_2 + \left(\frac{b_2 + b_1 + a_1a_2}{2}\right)^2}$$

With the assumption

$$a_1a_2 \ll b_1 + b_2$$

this frequency equation reduces to

$$\omega_1^2, \omega_2^2 = \frac{b_1 + b_2}{2} \pm \sqrt{\left(\frac{b_2 - b_1}{2}\right)^2 + d_1d_2} \quad \ldots\ldots [9]$$

On the other hand, the damping constants may be computed from Equations [8a] and [8c]

$$\left.\begin{aligned} v_2 &= \frac{a_2(\omega_2^2 - b_1) + a_1(\omega_2^2 - v_2) + c_2d_1}{2(\omega_1^2 - \omega_2^2)} \\ v_1 &= \frac{a_2(\omega_1^2 - b_1) + a_1(\omega_1^2 - b_2) + c_2d_1}{2(\omega_2^2 - \omega_1^2)} \end{aligned}\right\} \quad \ldots\ldots [10]$$

With the coefficients of Equation [2] introduced in Equation [9] the frequency can be written in the form

$$\omega_1^2, \omega_2^2 = \frac{c_y - \delta_1}{2m_y} + \frac{c_z + \beta_2}{2m_z} \pm \sqrt{\left(\frac{c_z + \beta_2}{2m_z} - \frac{c_y - \delta_1}{2m_y}\right)^2 - \frac{\beta_1\delta_2}{m_ym_z}}$$

If the rake angle decreases with $y$ we must have

$$d_2 = -\frac{\delta_2}{m_z} < 0$$

A diagram representing Equation [9] is shown in Fig. 23. If the rake angle and $y$ are increasing, we have

$$d_1d_2 > 0$$

i.e., the circle in the diagram of Fig. 23 is replaced by a hyperbola. With

$$\delta_1 = \delta_2 = 0$$

We get

$$\omega_1^2, \omega_2^2 = b_1, b_2 = \frac{c_y}{m_y}, \frac{c_z + \beta_2}{m^3}$$

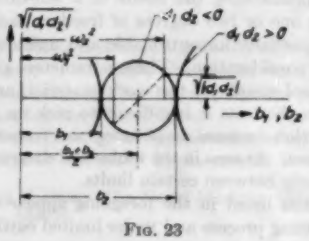


FIG. 23

The last term coincides with the frequency equation of Hahn (4). If

$$\delta_1 > 0$$
$$\delta_2 > 0$$

it can be demonstrated that the circular frequency $\omega_1$ can be lower than $\omega_{y0}$ or $\omega_{x0}$ as was found in the test series. In the case of tool No. 1 we can assume that

$$c_y = c_x$$

and

$$m_y = m_x$$

The natural frequencies under cut then become

$$\omega_1^2,\ \omega_2^2 = \omega_0^2 + \frac{\beta_2 - \delta_1}{2m} \pm \sqrt{\left(\frac{\beta_2 + \delta_1}{2m}\right)^2 - \sqrt{\left(\frac{\beta_1\delta_2}{m^2}\right)^2}}$$

Tool No. 3 is characterized by

$$c_x > c_y$$

The computed frequencies are in agreement with the other results.

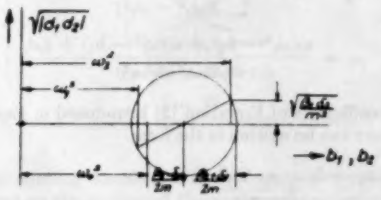


FIG. 24

At small depths of cut the values for $\beta_1$ and $\beta_2$ increase (in most cases $\beta_2$ increases more than $\beta_1$). It is demonstrated by all equations that the frequencies $\omega_1$ and $\omega_2$ increase with $\beta_1$, in other cases also with $\beta_2$. This trend is the same as in the test series.

A discussion of the damping constants can be performed in the same manner. The instability is greater for higher values of $\beta_1$ and $\beta_2$ (i.e., at lower depth and great width of cut). Even if the slope of the cutting forces versus tool-work interface velocity curve is positive, an instability may occur.

With $\beta_1$ and $\beta_2$ as variables there is a position function for the solution of Equation [4] which has the characteristics shown in Fig. 25($b$) ($v$ and $\omega$ increase with $\beta_1$ and $\beta_2$).

The position function of Equation [5] has the characteristics of Fig. 25($b$). The results of this function are illustrated in Fig. 10. For a distinct cutting speed (335 fpm at the test series) the system remains stable, the real part of $v$ being negative.

## Conclusions

Self-excited vibrations occurring in machine tools are very difficult to handle by analytical and empirical methods. When introducing simplifications, the result of a self-excited vibration system having one or two degrees of freedom can be estimated only if many partially uncontrollable and unknown parameters are taken into consideration. These parameters are functions of the machine-tool members, the work material, and the cutting conditions. In the tests it is difficult to pick up the vibrations without distortion because amplitudes and frequencies vary at appreciable rates. As seen in the tables and diagrams, the results can be given only between certain limits.

The difficulties listed in the foregoing appear even with the orthogonal cutting process and under limited cutting conditions. With tools having a nose radius, there are many more complications, because the cross section of the cut differs from a rectangle.

When using a tool with large nose radius and a long overhang, sudden vibrations of the second order appeared and disappeared after a short time interval.

However, combining tests and analytical methods, some trends could be demonstrated which may be applicable in practice. One of these results is, for example, the variation of the frequency with varying cutting conditions. Both tests and analysis indicate the variables affecting the stable state. Also, they proved the fact that self-excited vibrations may occur whether the slope of the cutting-force characteristic is positive or negative.

However, much more research work will have to be done before

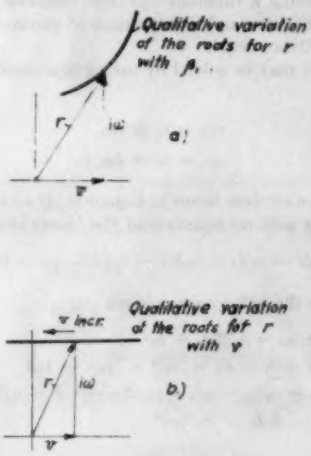


FIG. 25

the picture becomes general enough to allow the handling of all machine-tool vibration problems.

## Acknowledgment

The research underlying this paper was supported by the Deutsche Forschungsgemeinschaft and was done in part by W. Hölken, R. Piekenbrink, and U. Hölken. The mathematical formulas were revised by Dr. F. Effertz of the Mathematical Institute, Aachen Technische Hochschule. The author wishes to express his appreciation to the director of the Institute for Machine Tools, Prof. H. Opitz, for aid and encouragement. Dr. E. G. Loewen of the Machine Tool Division of the Massachusetts Institute of Technology kindly reviewed the English text of the manuscript.

## BIBLIOGRAPHY

1 "Mechanism of Tool Vibration in Cutting of Steel," by R. N. Arnold, Proceedings of The Institution of Mechanical Engineers, London, England, vol. 154, 1946, pp. 261–276.

2 "Metal Cutting and Machine Shop Productivity, the Cause of Chatter Vibrations," by A. J. Chisholm, *Machinery*, vol. 75, 1949, pp. 51–53.

3 "Ursachen und Minderung von Werkzeugschwingungen," by Ernst Saljé, Aufwand, Leistung und Wirtschaftlichkeit neuzeitlicher Werkzeugmaschinen, Verlag W. Girardet, Essen, Germany, 1953.

4 "Metal-Cutting Chatter and Its Elimination," by R. S. Hahn, Trans. ASME, vol. 75, 1953, pp. 1073–1080.

5 "On the Theory of Regenerative Chatter in Precision-Grinding Operations," by R. S. Hahn, Trans. ASME, vol. 76, 1954, pp. 593–597.

6 "Beitrag zur Theorie der selbsterregten Schwingungen," by Stefaniak, *Der Maschinenmarkt*, no. 50/51, 1954.

7 Lysen, Aufwand, Leistung und Wirtschaftlichkeit neuzeitlicher Werkzeugmaschinen, Verlag W. Girardet, Essen, Germany, 1953, pp. 186–187.

8 "Forschungsergebnisse beim Aussenrundschleifen," by Ernst Saljé, Werkstattstechnik und Maschinenbau, 43 Jg., no. 3, 1953, pp. 103–107.

## Discussion

S. Doi.[4] It appears that the author has found some experimental results which cannot be explained by Arnold's hypothesis setting forth the falling characteristic of the cutting force in its relationship with cutting speed. It seems that the author is somewhat skeptical about Arnold's hypothesis. But the author has presented little discussion on this problem. Mr. Hahn[5] and the writer[6] believe that the cause of chatter is not explained by this hypothesis. The fundamental cause of the chatter and the presence of vibrational energy are not yet widely accepted.

The author measured the horizontal and vertical vibration of workpiece simultaneously without measuring cutting force. To properly investigate the cause of chatter it is necessary to measure the cutting force and vibration simultaneously.

It is desirable that a mathematical analysis be carried out with some understanding of the fundamental cause of chatter. Evaluating $P_1 = P_{s1} + \alpha_1\dot{y} - \beta_1 z + \delta_1 y$ (Equation [1] of the paper), the author arrived at the equation of chatter (Equation [2]). Using this equation, the author has examined the stability and frequency of vibration. However, the writer is of the opinion that the values of $\alpha_1\dot{y}$, $\beta_1 z$, and $\delta_1 y$ during the chatter are of insufficient influence to develop the chatter vibration. As the author states, the amplitude of self-excited chatter is much larger than that of forced chatter.

The writer believes that the chatter vibration is a type of self-excited vibration caused by a lag in fluctuation of horizontal cutting force existing behind the horizontal vibration. Because of this lag, some amount of energy per cycle is available for maintaining or increasing the horizontal vibration of the workpiece. This delay in cutting force, the writer believes, is the peculiar phenomenon when metals are machined. If the horizontal vibration in the workpiece is initially started at its own natural frequency, the area of cut will fluctuate with that frequency, causing the vertical cutting force to do the same, resulting in the vertical vibration of the workpiece. Therefore the workpiece vibrates in the form of an ellipse (as shown in Figs. 3 and 15 of the paper) and the frequencies of components are equal.

The frequency of chatter shown in Table 1 is lower than the natural frequency of the main spindle in all cases except one case (lathe No. 3). According to the writer's experiments, the frequency of chatter is a little higher than the natural frequency and is in good agreement with Mr. Hahn's results.[5] The writer has observed that when the clearance is considerable in the main spindle bearing, or when the rigidity of the spindle in the horizontal or upward direction is much less than that in the downward direction, the frequency of chatter is lower than the natural frequency of the main spindle. The frequency of chatter depends upon the cutting condition and has no close connection with the fundamental cause of chatter.

In good agreement with the writer's experimental result are the following relations: That between the amplitude of chatter and width of cut, shown in Fig. 8; that between the amplitude of chatter and cutting speed, shown in Fig. 10, and that between the amplitude of chatter and wearland of the cutting edge shown in Fig. 16. These relations can be well explained by the writer's description.

R. S. Hahn.[7] This paper represents a considerable amount of work and the author is to be commended for the very interesting results he has presented. The general complexity of the problem of metal-cutting chatter is well illustrated by the numerous test results and graphs.

The author observes in many cases, for instance in Fig. 3, that the self-excited frequency occurring during the cutting process is less than the free "uncoupled" natural frequency, whereas he points out that Hahn (reference 4 of the paper) found the self-excited frequency to be greater than the uncoupled natural frequency. This might be explained by the fact that Hahn dealt with relatively flexible boring bars, in which case coupling with the workpiece acted as an increase in stiffness, whereas the contacting of the tool and work in the author's tests may have acted as coupling an additional mass to the system through a very stiff spring (the tool-work contact). Another feature which should be made clear regarding the various sets of tests is whether or not feedback effects from previous vibrations were possible. The writer has found that the action of chattered surfaces on the vibratory motion of the tool is very pronounced. Under feedback conditions it is possible to have self-excited vibrations at frequencies which differ somewhat from the natural frequency.

The writer agrees with the author that torsional vibrations can usually be neglected in comparison with the bending modes.

In connection with the results shown in Fig. 10, can the author connect the sudden drop in amplitude versus cutting speed with changes in the built-up edge? Or can this be explained on the basis of "destructive interference" in the feedback of energy from the vibration produced the previous revolution?

The author raises several questions about oscillograms Figs. 7, 8, 9, and 10 in Hahn's paper (4). The bars used by Hahn had essentially the same free natural frequency horizontally as they did vertically. The high-frequency pulse of "transitional" chatter in the horizontal or normal direction essentially "forced" the same frequency to appear in the vertical or tangential direction. The bar corresponding to Fig. 7 was weighted to lower its natural frequency.

The author's Equations [1] are an attempt to formulate force relations for "primary" chatter conditions; i.e., with neither "feedback" conditions nor "transitional" conditions (where a part or all of the tool is in the act of penetrating a work-hardened surface) present. In these equations the last term $\delta y$ represents the change in force due to changes in rake angle which in turn are caused by deflection of the tool. In most practical cases this effect must be extremely small. On the other hand, since the clearance angle is small to begin with and the worn flat on the clearance surface even smaller, variations in effective clearance angle due to vibration can be important. If the instantaneous clearance angle $C$ be defined as the angle between the clearance surface and the instantaneous velocity vector of the work relative to the tool it can easily be seen that

$$C = C_0 - \frac{\dot{z}}{v + \dot{y}}$$

where $C_0$ is the static clearance angle and $v$ is the work speed. For large amplitudes of vibration the second term can completely nullify the first term, i.e., as the tool vibrates into the work the effective clearance can become zero.

Instead of considering the second-order effect of variations in rake angle due to vibratory displacements it might be well to

[4] Professor of Mechanical Engineering, University of Nagoya, Chigusa-ku, Nagoya-shi, Japan.

[5] Reference (4) of the Bibliography of the paper.

[6] Memoirs of the Faculty of Engineering, University of Nagoya, Japan, vol. 5, no. 2, 1953.

[7] Consulting Engineer, The Heald Machine Company, Worcester Mass. Mem. ASME.

consider the effect of variations in depth of cut on the deflection of the tool; i.e., does an increase in depth of cut cause the tool to deflect so as to decrease or increase the depth of cut? Gooseneck tools with the "center of deflection" above the cutting edge deflect away from the work as depth of cut is increased whereas tools with the center of deflection below the cutting edge tend to deflect into the workpiece with increasing depth of cut. Such tools are said to "dig in." This condition for static stability should be insured first before considering conditions for dynamic stability.

### Author's Closure

The investigations reported and discussed in the paper were carried out two years ago. Meanwhile the field of vibrational research with reference to machine-tool development has widened considerably, increasing the complexity of the problems. Hence the results obtained at that time cannot be expected to agree completely with the relations and conclusions recently derived. It is rather evident that especially the basic relationships pertaining to machine-tool vibrations have to be sought for gradually. Therefore the author mentions in the beginning that the paper on the self-exited vibrations with two degrees of freedom should be considered as a discussion of the problems investigated.

Mr. Doi is quite right in stating that Arnold's hypothesis cannot be applied to all cases. The author is of the same opinion as Mr. Doi that the cutting force and the vibrations should be measured simultaneously. Vibrational investigations by Mr. Sokolowski (Russia) and by Mr. Doi show a lag of almost the same order of magnitude in the fluctuation between cutting force and vibrational motion. Referring to these investigations, it should be mentioned that Mr. Doi's test conditions did not meet the same requirements. The cutting speed was about 40 m/min, i.e., the range of the type 3 chip was covered, whereas cutting speeds up to 290 m/min were applied by Mr. Sokolowski, thus investigating the range most important to current practice. (Sokolowski, "Präzision in der Metallbearbeitung," Verlag Technik, Berlin—Precision in Metal Cutting.) For some materials the force-speed characteristic is a horizontal line. In these cases the coefficients $\alpha_1$ and $\alpha_2$ of Equation [1] become zero, and the expressions $\delta_1$ and $\delta_2$ can become small. However, the term $\beta$, showing how the cutting force is changed by the cutting depth, must not be neglected. The influence of the different elements may be estimated only due to the coupling of the vibratory components.

In his discussion Mr. Doi himself points out the importance of the coupling, stating that the horizontal vibration initially starts at its own natural frequency. Now the vertical cutting force is excited. There is not always an elliptical motion (see Fig. 3 of the paper) and the frequencies of the two components are different.

The frequency of chatter, Mr. Doi believes, does not depend directly on the fundamental causes of chatter, but the cutting conditions are closely related to the tendency to chatter. This fact, among others, was confirmed by Sokolowski. If, however, the tendency of the tool to chatter as well as the frequency depends on the cutting conditions, there must be a relationship between frequency and cutting conditions. In the present paper the author tried to find and illustrate these relationships.

Likewise, Mr. Hahn points out this relationship in his discussion. The solution of this problem will present considerable difficulty. As tests with boring quills of a relatively low natural frequency showed, the chatter frequencies are equal to the natural frequencies even in the case of different cutting conditions. The fact that the natural frequency in one case is smaller (according to Mr. Hahn's tests) and in another is larger than, or equal to, the chatter frequency (author's tests) leads to the assumption that not all the important components have been considered. However, the fact that the chatter frequency depends on the cutting conditions is confirmed.

In Mr. Hahn's opinion, the fact must be considered that if the vibrating uncoupled element has a small spring constant, it will acquire greater stiffness by coupling, but if the vibrating uncoupled element possesses a great spring constant, it will—after coupling—act during the cut like an element with a smaller spring constant. This explanation led to the following considerations:

Under completely equal cutting conditions the uncoupled natural frequency of the vibrating element is kept constant; however, the ratio of the spring constant to the mass is changed, thus altering the term $k_w/kg$ in Mr. Hahn's equation of frequency. In this way can be shown the cases to which Mr. Hahn's relation may be applied and how coupling and spring constant influence the frequency under the same conditions.

A feedback effect caused by chatter marks of the previous vibration will be the larger, the smaller is the ratio between the cutting depth and the depth of the chatter marks. In these cases self-excited as well as forced vibrations occur. If the forced vibration becomes larger than the self-excited vibration, the chatter frequency (in this connection no longer being a real chatter frequency in the general sense) will be determined by the frequency of the chatter marks. However, Fig. 21 of the paper shows that in spite of the periodic alternations of the chip's cross section the self-excited vibration may be of a higher magnitude. The turning tool starts to vibrate almost with its natural frequency in spite of the presence of forced vibrations.

The drop of the amplitude (Fig. 10) cannot be explained. Meanwhile, the tendency of the amplitude, plotted against the cutting speed, was proved by further investigations. Beyond this, the Russian literature also mentions these characteristics. This drop cannot be interpreted by the built-up edge, which occurs only up to a cutting speed of 50 m/min. A "destructive interference" is impossible. Each test was run for several minutes until the vibration was completely built up. The frequency of the chatter marks is equal to the chatter frequency.

The author appreciates Mr. Hahn's hint on the variation of the cutting force due to the effective clearance angle. This effect also was taken in consideration by Mr. Sokolowski. It may be assumed that the influence of the effective clearance angle is more important to chatter than that of the rake angle. Measurements of the cutting force show a sudden increase of the cutting force if the clearance angle becomes zero.

A further valuable suggestion is made by Mr. Hahn. From the investigations recently carried out, it can be seen that the magnitude and direction of the deflection of a tool with a great natural frequency, but with a relatively small static spring constant, must be considered. Some vibrational phenomena may be explained by this fact.

# A New Method of Evaluating Dynamic Response of Counterflow and Parallel-Flow Heat Exchangers

By H. M. PAYNTER[1] and YASUNDO TAKAHASHI,[2] CAMBRIDGE, MASS.

**From the exact solutions for the frequency response of counterflow and parallel-flow heat exchangers, successive parameters are calculated which give direct information for the heat exchangers regarding transient responses as well as frequency responses. The numerical evaluations of the parameters from the design data of heat exchangers are generally very simple, although the formulas themselves appear somewhat involved. Good coincidence with measured transient responses is demonstrated on an example.**

## Introduction

ONE of the authors has published[3,4] analytical solutions of heat exchangers. But numerical evaluations of these results were not simple, especially for tubular heat exchangers, Fig. 1, because they involved distributed parameter systems. A new method developed by the other author[5] can be applied to these cases to obtain a numerical basis for dynamic response calculations. Thus, for example, an estimation of the transient response, which otherwise would have required complicated calculations,[6] can be made very easily from the design parameters given in the nomenclature which follows.

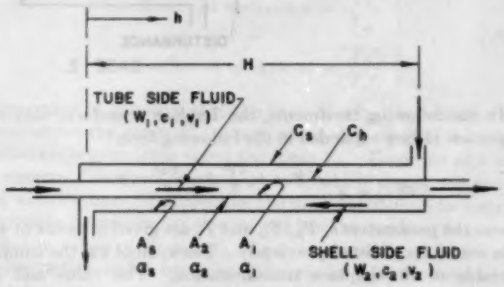


FIG. 1 COUNTERFLOW HEAT EXCHANGER SHOWING SYMBOLISM

[1] Assistant Professor of Mechanical Engineering, Massachusetts Institute of Technology. Mem. ASME.

[2] Doctor of Engineering, Professor of University of Tokyo, Japan; Fulbright Visitor, Massachusetts Institute of Technology.

[3] "Transfer Function Analysis of Heat Exchangers," by Y. Takahashi in Automatic and Manual Control, edited by A. Tustin, Butterworth Scientific Publication, 1952, p. 235.

[4] "Regeltechnische Eigenschaften der Gleich — und Gegenstromwärmeaustauschern," by Y. Takahashi, *Regelungstechnik*, heft 2, 1 Jarg., 1953, p. 32.

[5] "On an Analogy Between Stochastic Processes and Certain Dynamic Systems," by H. M. Paynter (forthcoming ASME paper).

[6] "Conduction of Heat in Solids," by H. S. Carslaw and J. C. Jaeger, Oxford, England, 1950, pp. 325–330.

Contributed by the Instruments and Regulators Division and presented at the Diamond Jubilee Semi-Annual Meeting, Boston, Mass., June 19–23, 1955, of THE AMERICAN SOCIETY OF MECHANICAL ENGINEERS.

NOTE: Statements and opinions advanced in papers are to be understood as individual expressions of their authors and not those of the Society. Manuscript received at ASME Headquarters, April 8, 1955. Paper No. 55—SA-50.

## Nomenclature

The following nomenclature is used in the paper:

$A$ = surface area of tube walls (sq ft)

$a_1 = \dfrac{kA}{W_1c_1}$; $a_2 = \dfrac{kA}{W_2c_2}$, dimensionless (dl), when both are equal, $a = a_1 = a_2$

$a_1' = \dfrac{\alpha_1 A_1}{W_1c_1}$; $a_2' = \dfrac{\alpha_2 A_2}{W_2c_2}$; $a_s = \dfrac{\alpha_s A_s}{W_2c_2}$, (dl)

$B$ = intermediate parameter (dl)

$b = b_1 + b_2$, $b_1 = \dfrac{\alpha_1 A_1}{C_h v_1}$; $b_2 = \dfrac{\alpha_2 A_2}{C_h v_1}$; $b_s = \dfrac{\alpha_s A_s}{C_s v_1}$, (dl)

$C$ = tube or shell heat capacity per unit length along the flow (Btu/ft deg F)

$c$ = specific heat of fluid (Btu/lb deg F)

$D$ = intermediate parameter (dl)

$E$ = intermediate parameter (dl)

$F$ = intermediate parameter (dl)

$f$ = intermediate parameter (dl)

$G$ = transfer functions

$g$ = intermediate parameter (dl)

$H$ = total length of flow distance in heat exchanger, ft

$h$ = running length along tube side fluid, ft

$K$ = intermediate parameter (dl)

$k$ = over-all coefficient of heat transfer (Btu/sq ft min deg F)

$L = H/v$ = distance-velocity lag of fluids, min

$M$ = intermediate parameter (dl)

$n$ = numbers of lags (dl)

$r = v_1/v_2$ (dl)

$s$ = complex variable of Laplace transformation (dl)

$T_s$ = skew time of step response relative $L_1$ (dl)

$T_d$ = dead time of lag-delay model relative to $L_1$ (dl)

$T_l$ = time constant of lag model relative to $L_1$ (dl)

$T_m$ = mean delay of step response relative to $L_1$ (dl)

$T_r$ = time constant of root-lag model relative to $L_1$ (dl)

$T_v$ = dispersion time of step response relative to $L_1$ (dl)

$t$ = running time, min

$v$ = fluid velocity, fpm

$W$ = flow rate, lb/min

$x = h/H$ (dl)

$\alpha$ = film coefficient of heat transfer (Btu/sq ft min deg F)

$\alpha$ = coefficient of skew (dl)

$\beta = (a_1 + a_2)/2$

$\delta$ = ln (steady-state change in output/steady-state change in input)

$\epsilon = (a_1 - a_2)/2$

$\theta$ = temperature of fluid (deg F)

$\mu$ = coefficient of variance (dl)

$\rho = a/(1 + a)$

$\tau = t/L_1$ (dl)

$\phi$ = pipe temperature (deg F)

$\omega$ = circular frequency

*Subscripts*

1 = tube side
2 = shell side
$h$ = tube
$s$ = shell

## Basic Assumptions

1 System parameters are uniform and constant.
2 Complete mixing in crosswise directions of each flow.
3 The heat conductivities of walls are either infinite in directions at right angles to the flow or alternatively assumed to be included in film coefficients and zero in flow directions.
4 There are no internal sources or sinks of heat.
5 Pure counter and parallel flows (Fig. 1) are considered.

## Fundamental Equations

The system parameters necessary for dynamic-response analysis under the stated assumptions are the following fifteen (see also Fig. 1).

Flow rates of fluids = $W_1$, $W_2$
Specific heats of fluids = $c_1$, $c_2$
Surface areas = $A_1$, $A_2$, $A_s$
Film coefficients = $\alpha_1$, $\alpha_2$, $\alpha_3$
Fluid velocities = $v_1$, $v_2$
Flowing distance = $H$
Solid heat capacities = $C_h$, $C_s$

These are conveniently grouped into the dimensionless forms (defined previously)

$$a_1', a_2', a_s, b_1, b_2, b_s, \tau$$

Four of them also are grouped conveniently into the following dimensionless forms[7] for d-c gain calculations and other purposes

$$\frac{a_1'b_2}{b} = a_1, \quad \frac{a_2'b_1}{b} = a_2$$

where $b = b_1 + b_2$. Almost all these parameters have been necessary for the conventional steady-state design of heat exchangers, for example, for mean temperature-difference calculations.

The running time $t$(min) and running distance along the tube-side fluid $h$(ft) also are expressed in the following dimensionless forms

$$\tau = t/L_1, \quad x = h/H$$

Now the simultaneous equations to be solved are

$$\left.\begin{aligned}
&\frac{\partial\theta_1}{\partial\tau} + \frac{\partial\theta_1}{\partial x} = a_1'(\phi_h - \theta_1)\\
&\frac{\partial\phi_h}{\partial\tau} = b_1(\theta_1 - \theta_h) + b_2(\theta_2 - \phi_h)\\
&\frac{\partial\theta_2}{\partial\tau} \pm \frac{\partial\theta_2}{\partial x} = a_2'(\phi_h - \theta_2) + a_s(\phi_s - \theta_2)\\
&\frac{\partial\phi_s}{\partial\tau} = b_s(\theta_2 - \phi_s)
\end{aligned}\right\} \quad \ldots [1]$$

[7] These are also given in the following forms

$$a_1 = \frac{kA}{W_1c_1}, \quad a_2 = \frac{kA}{W_2c_2}$$

where $k$ (Btu/min sq ft deg F) is the over-all coefficient of heat transmission of the heating surface. This form can be introduced by means of the well-known law of heat transmission, which under the assumption stated, is written as

$$1/kA = 1/\alpha_1A_1 + 1/\alpha_2A_2$$

where $1/kA$ is the equivalent resistance to heat transmission.

In these equations, $\theta_1$ and $\theta_2$ are tube-side and shell-side fluid temperatures; $\phi_h$ and $\phi_s$ are tube and shell temperatures; the double symbol $\pm$ is $-$ for counterflow (Fig. 2) and $+$ for parallel flow (Fig. 3).

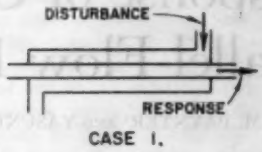


Fig. 2 Two Cases of Counterflow

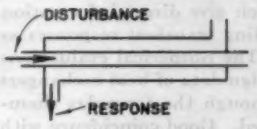


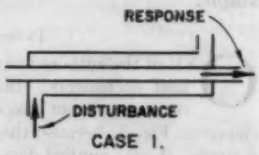


Fig. 3 Two Cases of Parallel Flow

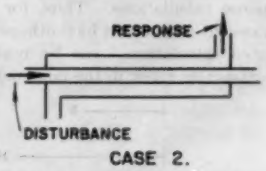


In the following treatments, the Laplace transform solutions Equation [1] are expanded in the following form

$$G(s) = e^{\delta - T_m s + \frac{T_s^2}{2}s^2 - \frac{T_a^3}{6}s^3 + \cdots} \quad \ldots [2]$$

where the parameters $\delta$, $T_m$, $T_s$, and $T_a$ are given in terms of system constants as listed previously. The symbol $s$ is the complex variable of the Laplace transformation. The value and significance of this representation has been indicated elsewhere.[8] However, one may say in summary that $\delta$ measures the steady-state amplitude ratio between response and disturbance, $T_m$ measures the mean time delay between response and disturbance, $T_s$ defines the dispersion or attenuation, and $T_a$ the assymmetry or phase nonlinearity. This characterization is very efficient for any physical process, such as those treated here, where the step response is monotonic nondecreasing in time.

## Counterflow

The Laplace transform solution (transfer function) of Equation [1] is

$$G(s) = \frac{g_{1,3}}{\frac{f_1 + f_2}{2} + \frac{\sqrt{(f_1+f_2)^2 - 4g_1g_2}}{2}\coth\frac{\sqrt{(f_1+f_2)^2 - 4g_1g_2}}{2}} \quad \ldots [3]$$

where $f_1 = \dfrac{a_1'(b_2 + s)}{b + s} + s$

$$f_2 = \frac{a_2'(b_1 + s)}{b + s} + sr + \frac{a_s}{b_s + s}$$

$$g_1 = \frac{a_1'b_2}{b + s}, \quad g_2 = \frac{a_2'b_1}{b + s}$$

and

$g_{1,2} = g_1$ when $G(s)$ is defined as

$$\begin{pmatrix}\text{Outlet temperature}\\ \text{of tube-side fluid}\end{pmatrix} \Big/ \begin{pmatrix}\text{Inlet temperature}\\ \text{of shell-side fluid}\end{pmatrix} \ldots \text{Case 1 (Fig. 2)}$$

$g_{1,2} = g_2$ for the $G(s)$ of

$$\begin{pmatrix}\text{Outlet temperature}\\ \text{of shell-side fluid}\end{pmatrix} \Big/ \begin{pmatrix}\text{Inlet temperature}\\ \text{of tube-side fluid}\end{pmatrix} \ldots \text{Case 2 (Fig. 2)}$$

Now, the parameters of Equation [2] are determined by expanding Equations [2] and [3] in series in $s$ and comparing the corresponding terms. The expansion is easier for $G^{-1}(S)$ than $G(S)$. The results yield a solution for the new parameters in the symbolic form

$$\left.\begin{aligned} \delta &= f_\delta(a_1', a_2', a_s, b_1, b_2, b_s, r)\\ T_m &= f_1(a_1', a_2', a_s, b_1, b_2, b_s, r)\\ T_s &= f_2(a_1', a_2', a_s, b_1, b_2, b_s, r)\\ T_a &= f_3(a_1', a_2', a_s, b_1, b_2, b_s, r) \end{aligned}\right\} \quad \ldots\ldots\ldots [4]$$

Details of the algebraic reduction procedure are given in Appendix 1. The simplest relation is given when solid capacities are neglected, and when the $Wc$ values and the velocities are equal for both fluids. For this case, taking $\rho = a/(1 + a)$, where $a = (kA)/(Wc)$, as abscissa, the new parameters $T_m$, $T_s$, $T_a$ are plotted in terms of conventional relative statistical measures, in Fig. 12, using coefficients of the form

$$\left.\begin{aligned} \text{Coefficient of variance } \mu &= \frac{T_s}{T_m}\\ \text{Coefficient of skew } \alpha &= \frac{T_a^3}{T_s^3} \end{aligned}\right\} \quad \ldots\ldots\ldots [5]$$

A zero value of $\mu$ means that the time distribution has no dispersion about the mean $T_m$; a zero value of $\alpha$ signifies that the distribution is symmetric about the mean $T_m$. From the plot we can observe directly that when $\rho = 0$, which occurs for small sizes, with low over-all efficiencies, the time distribution for a step disturbance is symmetric ($\alpha = 0$) and has the quickest response (minimum values of $T_m$ and $\mu$). As $\rho$ increases, $T_m$, $\mu$, and $\alpha$ all increase, with $\mu$ and $\alpha$ becoming infinitely large as the length of the exchanger becomes infinite.

## Parallel Flow

The Laplace transform solution of Equation [1] is

$$G(s) = g_{1,2}e^{-\frac{f_1 + f_2}{2}}\left[\frac{2}{\sqrt{(f_1 - f_2)^2 + 4g_1g_2}}\right] \sinh\left[\frac{\sqrt{(f_1 - f_2)^2 + 4g_1g_2}}{2}\right] \quad \ldots\ldots [6]$$

The symbols $f_1$, $f_2$, $g_1$, $g_2$, and $g_{1,2}$ are the same as defined for counterflow, see also Fig. 3.

From this equation the parameters of Equation [2] are determined in the same symbolic form as Equation [4]. Details of algebraic reduction procedure and typical special cases are given in Appendix 2.

## Numerical Example

As an example of the application of the foregoing formulas to engineering practice, one can consider the special instances of counterflow and parallel-flow exchangers with the following assumed characteristics

| | | | |
|---|---|---|---|
| $a_1 = 1.5$ | $a_1' = 6$ | $b = 27$ | $a_s = 4$ |
| $a_2 = 1.5$ | $a_2' = 2$ | $r = 3$ | $b_s = 3$ |

### Step Response in Tube-Inlet Temperature

*Counterflow Exchanger.* Applying the foregoing values to Equations [9], [12], and [13] (see Appendix 1), we obtain

$$\begin{aligned} \epsilon^\delta &= 0.61\\ T_m &= 2.28\\ T_s &= 2.16\\ T_a &= 3.08 \end{aligned}$$

The measure of spread $T_s$ and the asymmetry measure $T_a$, as before, can be expressed in terms of dimensionless coefficients, namely

$$\begin{aligned} \text{Variation } \mu &= T_s/T_m = 0.948\\ \text{Skew } \alpha &= (T_a/T_s)^3 = 2.90 \end{aligned}$$

These values can be compared, for example, to those for a unit lag, whose transform has the form

$$\text{(Lag)} \qquad G_a(s) = \frac{1}{1 + T_l s}$$

where $\mu = 1$ and $\alpha = 2$. The variation $\mu$ can be matched by adding a suitable time-delay term, since the transform for this case becomes

$$\text{(Lag + delay)} \qquad G_b(s) = \frac{e^{-T_d s}}{1 + T_l s}$$

for which

$$\begin{aligned} T_m &= T_d + T_l\\ T_s &= T_l\\ T_a &= \sqrt[3]{2}T_l \end{aligned}$$

giving

$$\begin{aligned} \mu &= T_s/T_m = T_l/(T_d + T_l)\\ \alpha &= T_a^3/T_s^3 = 2 \end{aligned}$$

Thus a lag-delay model with $\mu = 0.95$ and $\alpha = 2$ would have the form shown in Fig. 4.

However, the value of $\alpha$ for the heat exchanger indicates a curve more skewed than that expressed by a unit lag. Such a function is found in what the statisticians would call a "chi-square" distribution of one degree of freedom with the transform

$$\text{(Root lag)} \qquad G_c(s) = \frac{1}{\sqrt{1 + T_r s}}$$

having the parameters

$$\begin{aligned} T_m &= T_r/2\\ T_s &= T_r/\sqrt{2}; \qquad \mu = \sqrt{2} = 1.414\\ T_a &= T_r; \qquad \alpha = 2\sqrt{2} = 2.828 \end{aligned}$$

If this root-lag function is delayed, in addition, with the transform

$$\text{(Root-lag delay)} \quad G_d(s) = e^{-T_d s}/\sqrt{1 + T_r s}$$

the parameters become

$$\begin{aligned} T_m &= T_d + \frac{1}{2}T_r\\ T_s &= T_r/\sqrt{2}; \qquad \mu = \sqrt{2}\Big/\left(1 + 2\frac{T_d}{T_r}\right)\\ T_a &= T_r; \qquad \alpha = 2\sqrt{2} \end{aligned}$$

Thus a distribution curve of this form with $\mu = 0.95$ and $\alpha = 2.828$ is also sketched in Fig. 4.

There are many other possible distributions, all with the same values $T_m$, $T_v$, $T_a$, but differing in higher-order terms. These will all, in general, give reasonable approximations to the dynamic response of the given system, and many are susceptible to ready calculation. In the present instance, those shown in Fig. 4 come directly from functions which are readily available in tabular form and also easily realized in computing networks, etc.

*Parallel-Flow Exchanger.* The general Formulas [18] to [21] (see Appendix 2) give

$$e^{\delta} = 0.475$$
$$T_m = 2.81$$
$$T_v = 1.10$$
$$T_a = 1.02$$

with the coefficients

$$\mu = T_v/T_m = 1.10/2.81 = 0.391$$
$$\alpha = (T_v/T_a)^2 = (1.02/1.10)^2 = 0.795$$

Now, it is readily shown[5] that an $n$-lag cascade (a chi-square distribution of $2n$ degrees of freedom) has the coefficients

$$\mu = 1/\sqrt{n}, \qquad \alpha = 2/\sqrt{n}$$

In the special case of $n = 6.5$, with a transfer characteristic of the form

$$G_d(s) = \frac{1}{(1 + T_l s)^{6.5}}$$

the coefficients become

$$\mu = 0.392, \qquad \alpha = 0.784$$

and the mean time $T_m$ is given by

$$T_m = 6.5 T_l$$

Accordingly, a reasonable approximation to the parallel-flow step-response characteristic can be found in the chi-square distribution of 13 degrees of freedom with $T_l = 2.81/6.5 = 0.432$. This is indicated in Fig. 5 and compared with a lag-delay approximation with $\mu = 0.391$ and $\alpha = 2$.

### Frequency-Response Results

In terms of the same representation used for transient response, the frequency responses of heat exchangers may be found directly.

Thus, if

$$G(s) = e^{\delta - T_m s + \frac{1}{2} T_v^2 s^2 - \frac{1}{6} T_a^3 s^3 + \dots}$$
$$= e^{\underbrace{\delta + \frac{1}{2} T_v^2 s^2 + \dots}_{\text{Even}}} \; e^{\underbrace{-T_m s - \frac{1}{6} T_a^3 s^3 - \dots}_{\text{Odd}}}$$

Then, with $s = j\omega$

$$\text{Amplitude } |G(\omega)| = e^{\delta - \frac{1}{2} T_v^2 \omega^2 + \dots}$$

$$\text{Phase } \angle G(\omega) = -T_m \omega + \frac{1}{6} T_a^3 \omega^3 - \dots$$

so that the set of parameters $\delta$, $T_m$, $T_v$, $T_a$, . . . describe the frequency characteristics simply and uniquely. However, specification of only the first few parameters merely defines the low-frequency behavior, and as the frequency $\omega$ is increased, more of the time constants will be required to characterize the behavior.

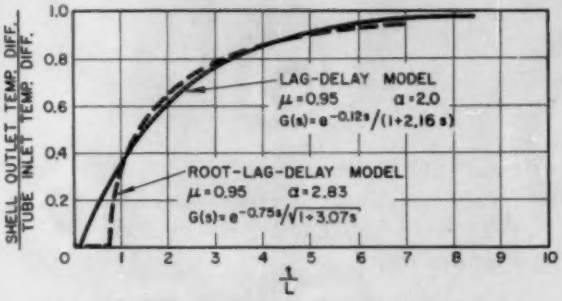


Fig. 4 Analytical Step Response for Counterflow Exchanger

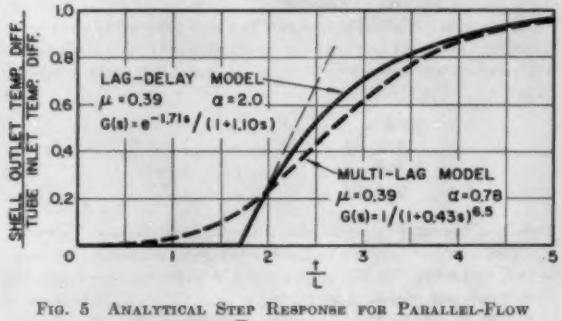


Fig. 5 Analytical Step Response for Parallel-Flow Exchanger

However, one can proceed, as was done in estimating the step response, by picking a suitable model using the low-frequency constants alone, and thus extrapolate the response to high frequencies under the tacit assumption that the model so chosen will behave at least roughly like the prototype at higher frequencies.

Then for the counterflow exchanger, there has been plotted in Fig. 6 the predicted frequency-response characteristics for the two previously determined models (Table 1).

TABLE 1 COUNTERFLOW EXCHANGER

| | Lag-delay model | Root-lag-delay model |
|---|---|---|
| Amplitude ratio | $1/\sqrt{1 + T_l^2\omega^2}$ $= 1/\sqrt{1 + 4.66\omega^2}$ | $1/\sqrt[4]{1 + T_r^2\omega^2}$ $= 1/(1 + 9.40\omega^2)^{0.25}$ |
| Phase | $T_d\omega + \tan^{-1} T_l\omega$ $= 0.12\omega + \tan^{-1} 2.16\omega$ | $T_d\omega + \frac{1}{2}\tan^{-1} T_r\omega$ $= 0.75\omega + 0.5 \tan^{-1} 3.07\omega$ |

In a directly similar fashion, the response characteristics for the parallel-flow exchanger have also been plotted in Fig. 7 from the formulas in Table 2.

TABLE 2 PARALLEL-FLOW EXCHANGER

| | Lag-delay model | Multilag model |
|---|---|---|
| Amplitude ratio | $1/\sqrt{1 + T_l^2\omega^2}$ $= 1/\sqrt{1 + 1.21\omega^2}$ | $1/(1 + T_r^2\omega^2)^{11/4}$ $= 1/(1 + 0.19\omega^2)^{2.75}$ |
| Phase | $T_d\omega + \tan^{-1} T_l\omega$ $= 1.71\omega + \tan^{-1} 1.10\omega$ | $6.5 \tan^{-1}(T_r\omega)$ $= 6.5 \tan^{-1}(0.43\omega)$ |

### Experimental Confirmation

Experiments under carefully controlled conditions have been made previously by one of the authors[3,4] upon a heat-exchanger model used both in counterflow and parallel flow. These yielded among other results the response in the shell stream outlet tem-

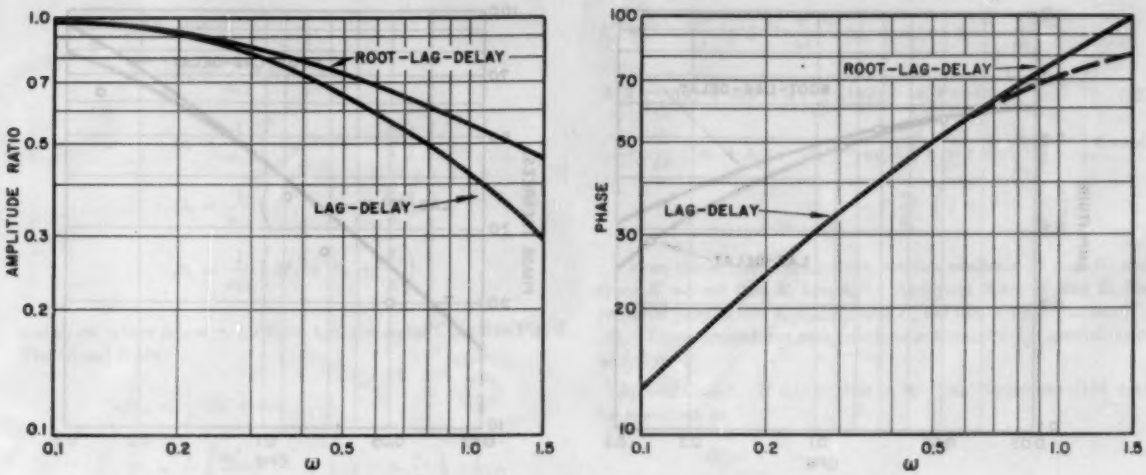


FIG. 6 ANALYTICAL FREQUENCY RESPONSE FOR COUNTERFLOW EXCHANGER

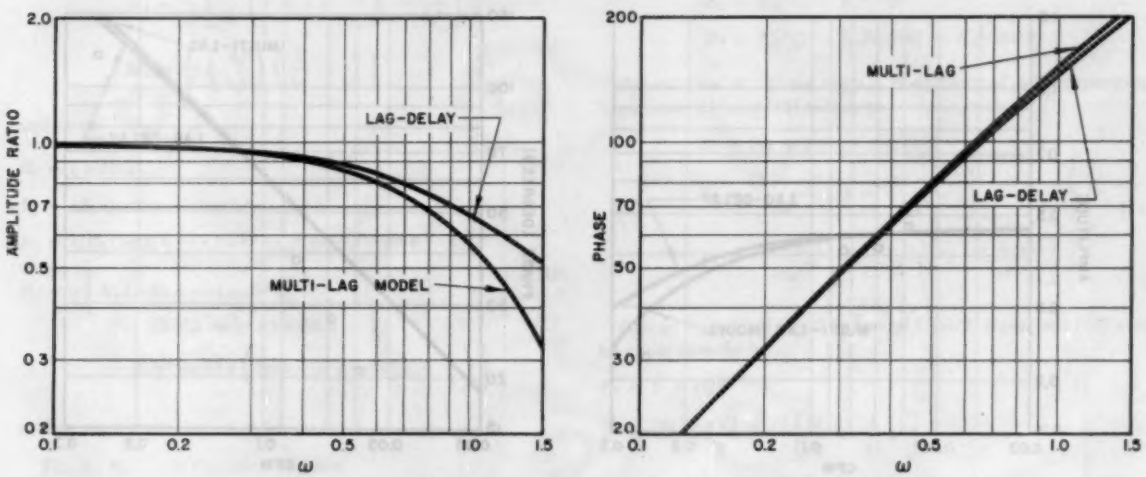


FIG. 7 ANALYTICAL FREQUENCY RESPONSE FOR PARALLEL-FLOW EXCHANGER

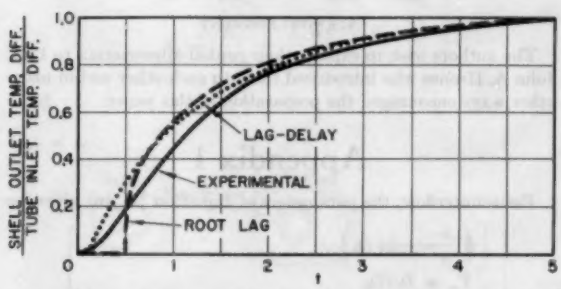


FIG. 8 COMPUTED AND EXPERIMENTAL STEP RESPONSES FOR COUNTERFLOW EXCHANGER

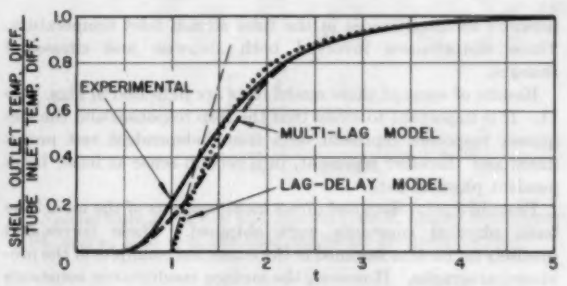


FIG. 9 COMPUTED AND EXPERIMENTAL STEP RESPONSES FOR PARALLEL-FLOW EXCHANGER

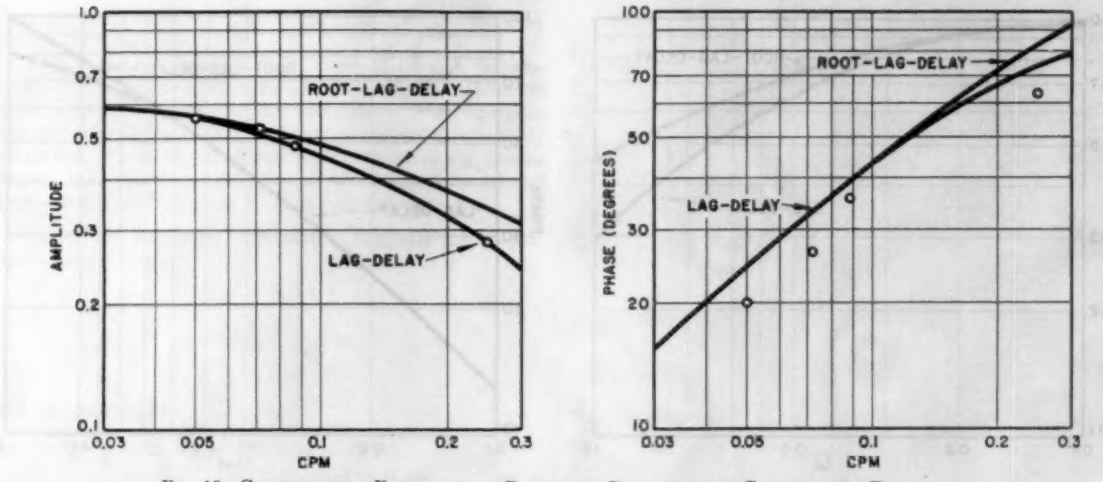


FIG. 10 COMPUTED AND EXPERIMENTAL FREQUENCY RESPONSES FOR COUNTERFLOW EXCHANGER

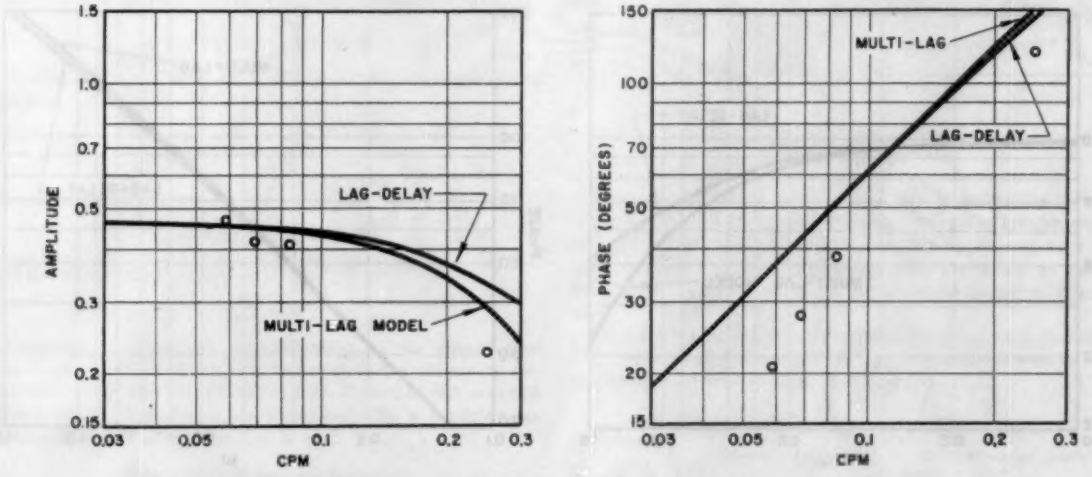


FIG. 11 COMPUTED AND EXPERIMENTAL FREQUENCY RESPONSES FOR PARALLEL-FLOW EXCHANGER

perature to disturbances in the tube stream inlet temperature. These disturbances involved both stepwise and sinusoidal changes.

Results of some of these model tests are indicated in Figs. 8 to 11. It is important to stress that the step responses and the frequency responses represent data from independent test procedures and therefore represent, in a certain sense at least, independent physical data.

From blueprint data and direct measurements of the model the basic physical constants were obtained. These correspond precisely to the data assumed in the numerical examples of the previous paragraphs. However, the surface conductance constants $\alpha_1$ and $\alpha_3$ were back-figured, at least in part, from the calculated steady-state (zero-frequency) temperature ratios. Moreover, the distance velocity lag was estimated from measurements only with tolerable accuracy at $L_1 = 0.6$ min with a probable error of at least 0.05 min.

With these restrictions understood, the predicted and measured step and frequency responses are depicted in Figs. 8 to 11.

ACKNOWLEDGMENT

The authors wish to express their cordial appreciation to Prof. John A. Hrones who introduced them to each other and in many other ways encouraged the preparation of this paper.

# Appendix 1

For counterflow, the parameters of Equation [2] are given by

$$\left.\begin{aligned} \hat{\delta} &= -\ln D_0 \\ T_m &= D_1/D_0 \\ T_e &= \sqrt{(D_1/D_0)^2 - 2D_2/D_0} \\ T_o &= \sqrt[3]{\frac{1}{3}\left(\frac{D_1}{D_0}\right)^3 - \left(\frac{D_1}{D_0}\right)\left(\frac{D_2}{D_0}\right) + \left(\frac{D_3}{D_0}\right)} \end{aligned}\right\} \quad \ldots [7]$$

and so on.

The $D_0$, $D_1$, $D_2$, $D_3$ are

$$\left.\begin{aligned} D_0 &= \frac{1}{a_{1,2}}\,(M_0 + B_0) \\ D_1 &= \frac{1}{a_{1,2}}\left(M_1 + B_1 + \frac{B_0}{b}\right) \\ D_2 &= \frac{1}{a_{1,2}}\left(M_2 + B_2 + \frac{B_1}{b}\right) \\ D_3 &= \frac{1}{a_{1,2}}\left(M_3 + B_3 + \frac{B_2}{b}\right) \end{aligned}\right\} \quad \ldots\ldots [8]$$

and so on, where $a_{1,2} = a_1$ for Case 1, $a_{1,2} = a_2$ for Case 2 in Fig. 2. The $M$ and $B$ are

$$\left.\begin{aligned} M_0 &= \frac{1}{2}\,(a_1 + a_2) \\ M_1 &= \frac{1}{2}\left(\frac{a_1' + a_2'}{b} + 1 + r + \frac{a_s}{b_s}\right) \\ M_2 &= \frac{1}{2}\left[\frac{1}{b}\left(1 + r + \frac{a_s}{b_s}\right) - \frac{a_s}{b_s^2}\right] \\ M_3 &= \frac{1}{2}\left(\frac{a_s}{b_s^2}\right)\left(\frac{1}{b_s} - \frac{1}{b}\right) \end{aligned}\right\} \quad \ldots\ldots [9]$$

and so on.

$$\left.\begin{aligned} B_0 &= \epsilon \coth \epsilon \\ B_1 &= \epsilon E_1 (\coth \epsilon - \epsilon\,\mathrm{csch}^2\,\epsilon) \\ B_2 &= \epsilon[E_2 (\coth \epsilon - \epsilon\,\mathrm{csch}^2\,\epsilon) + \epsilon E_1^2(\epsilon \coth \epsilon - 1)] \\ B_3 &= \epsilon\Big[E_3 (\coth \epsilon - \epsilon\,\mathrm{csch}^2\,\epsilon) \\ &\quad + 2E_1E_2\epsilon\,\mathrm{csch}^2\,\epsilon(\epsilon \coth \epsilon - 1) \\ &\quad + E_1^3\epsilon^2\,\mathrm{csch}^2\,\epsilon\left(\coth \epsilon - \epsilon \coth^2 \epsilon + \frac{\epsilon}{3}\right)\Big] \end{aligned}\right\} \quad \ldots [10]$$

and so on, where $\epsilon = (a_1 - a_2)/2$

The $E_1$, $E_2$, ... in Equation [10] are

$$\left.\begin{aligned} E_1 &= \frac{K_1}{2K_0}, \quad E_2 = \frac{K_2}{2K_0} - \frac{K_1^2}{8K_0^2} \\ E_3 &= \frac{K_3}{2K_0} - \frac{K_1K_2}{4K_0^2} + \frac{K_1^3}{K_0^3} \end{aligned}\right\} \quad \ldots\ldots [11]$$

and

$$\left.\begin{aligned} K_0 &= 4\epsilon^2 \\ K_1 &= -\frac{8\epsilon^2}{b} + 2(a_1 + a_2)\left[\frac{a_1' + a_2'}{b} + \left(1 + r + \frac{a_s}{b_s}\right)\right] \\ K_2 &= \frac{12\epsilon^2}{b} + \left[\left(1 + r + \frac{a_s}{b_s}\right) + \frac{2(a_1' + a_2')}{b}\right]\left[\left(1 + r + \frac{a_s}{b_s}\right) - \frac{2(a_1 + a_2)}{b}\right] \\ &\quad + \left(\frac{a_1' + a_2'}{b}\right)^2 - 2\,\frac{a_s}{b_s^2}\,(a_1 + a_2) \end{aligned}\right\} \quad \ldots [12]$$

$$\left.\begin{aligned} K_3 &= -\frac{16\epsilon^3}{b^3} + 6\,\frac{a_1' + a_2'}{b^3}\,(a_1 + a_2) - 2\,\frac{(a_1' + a_2')^2}{b^3} \\ &\quad + 2\,\frac{a_s}{b_s^3}\,(a_1 + a_2) - 2\,\frac{a_s}{b_s^2 b}\,\{(a_1' + a_2') - (a_1 + a_2)\} \\ &\quad + \frac{2}{b^2}\,\{(a_1 + a_2) - (a_1' - a_2')\}\left(1 + r + \frac{a_s}{b_s}\right) \\ &\quad - 2\,\frac{a_s}{b_s^2}\left(1 + r + \frac{a_s}{b_s}\right) \end{aligned}\right\} \quad \ldots [12] \text{ (continued)}$$

Given the system parameters, we can evaluate $M$ and $K$, and from $K$ we can find $E$, hence $B$. Applying these $M$ and $B$, the required parameters $\delta$, $T_m$, $T_s$, and $T_a$ are found by Equation [7], [8]. These procedures and relations get simpler for special cases as follows:

*Special Case 1.* If $\epsilon \doteq 0$, that is, $a_1 \doteq a_2$, Equations [10] may be rewritten as

$$\left.\begin{aligned} B_0 &= 1 \\ B_1 &= K_1/12 \\ B_2 &= K_2/12 - K_1^2/720 \\ B_3 &= K_3/12 - K_1K_2/360 + K_1^3/30240 \end{aligned}\right\} \quad \ldots\ldots [13]$$

*Special Case 2.* If we neglect the effects of solid capacities, Equations [11] and [12] reduce to

$$\left.\begin{aligned} E_1 &= (a_2 + \epsilon)(1 + r)/(2\epsilon^2) \\ E_2 &= \frac{(1 + r)^2}{8\epsilon^2}\left[1 - \frac{(a_2 + \epsilon)^2}{\epsilon^2}\right] \\ E_3 &= \frac{(1 + r)^3}{16\epsilon^4}\left[-(a_2 + \epsilon) + \frac{(a_2 + \epsilon)^3}{\epsilon^2}\right] \end{aligned}\right\} \quad \ldots [14]$$

*Special Case 3.* If $\epsilon \doteq 0$ in Special Case 2, Equations [10] may be given directly by

$$\left.\begin{aligned} B_0 &= 1 + \epsilon^2/3 \\ B_1 &= \frac{(a_2 + \epsilon)(1 + r)}{2}\left[\frac{2}{3} - \frac{4}{45}\,\epsilon^2\right] \\ B_2 &= \frac{(1 + r)^2}{4}\left[\frac{1}{3} - \frac{4}{45}\,(a_2 + \epsilon)^2 - \frac{2}{45}\,\epsilon^2 + \frac{8}{315}\,\epsilon^2\,(a_2 + \epsilon)^2\right] \\ B_3 &= \frac{(1 + r)^3}{8}\,(a_2 + \epsilon)\left[-\frac{4}{45} + \frac{16}{945}\,(a_2 + \epsilon)^2 + \frac{8}{315}\,\epsilon^2 - \frac{2078}{288225}\,(a_2 + \epsilon)^2\epsilon^2\right] \end{aligned}\right\} \quad \ldots [15]$$

*Special Case 4.* If $\epsilon = 0$ in Special Case 3, i.e., no solid capacities, and $a_1 = a_2 = a$, the final results are given directly by

$$\left.\begin{aligned} e^{-\delta} &= \frac{1 + a}{a} \\ e^{-\delta}\,T_m &= (1 + r)\left(\frac{1}{2a} + \frac{1}{3}\right) \\ e^{-\delta}\left(-\frac{T_s^2}{2} + \frac{T_m^2}{2}\right) &= (1 + r)^2\left(\frac{1}{12a} - \frac{a}{45}\right) \end{aligned}\right\} \quad \ldots [16]$$

$$e^{-\delta}\left(\frac{T_a^3}{6}-\frac{T_m T_s^2}{2}+\frac{T_m^3}{6}\right) = -(1+r)^2\left(\frac{1}{90}-\frac{2a^2}{945}\right) \quad \text{..[16] (continued)}$$

*Special Case 5.* Same as Special Case 4, and $r = 1$. Let us denote

$$e^{\delta} = \frac{a}{1+a} = \rho$$

then we have

$$\begin{aligned} T_m &= 1+\frac{1}{3}\rho \\ T_s^2 &= \frac{1}{3}+\frac{4}{3}\rho+\frac{\rho^2}{9}+\frac{8\rho^2}{45(1-\rho)} \\ T_a^2 &= \frac{32}{15}\rho+\frac{4}{3}\rho^2+\frac{2\rho^3}{27}+\frac{8\rho^2}{15(1-\rho)} \\ &\quad +\frac{8\rho^3}{45(1-\rho)}+\frac{32\rho^3}{315(1-\rho)^2} \end{aligned} \quad \text{..[17]}$$

The values of these terms are shown in Fig. 12.

# Appendix 2

For parallel flow from Equation [6] the parameters of Equation [2] are determined as follows

$$\begin{aligned} e^{\delta} &= a_{1,2}\frac{\sinh\beta}{\beta}e^{-\beta}; \qquad T_m = M_1+\frac{1}{b}-F_1 \\ \frac{T_s^2}{2} &= -M_2+F_2-\frac{1}{2}\left(F_1^2-\frac{1}{b^2}\right) \\ \frac{T_a^2}{6} &= M_3-F_3+F_1F_2+\frac{F_1}{3b^2}-\frac{2}{3b}F_1^2-\frac{1}{3b^2} \end{aligned} \quad \text{..[18]}$$

where $a_{1,2} = a_1$ for Case 1, $a_{1,2} = a_2$ for Case 2 in Fig. 3, and $\beta = (a_1+a_2)/2$.

The $M$ and $F$ in these results are

$$\begin{aligned} M_1 &= \frac{1+r}{2}+\frac{a_s}{2b_s}+\frac{a_1'+a_2'}{2b}-\frac{\beta}{b} \\ M_2 &= -\frac{a_s}{2b_s^2}-\frac{a_1'+a_2'}{2b^2}+\frac{\beta}{b^2} \\ M_3 &= \frac{a_s}{2b_s^3}+\frac{a_1'+a_2'}{2b^3}-\frac{\beta}{b^3} \end{aligned} \quad \text{.....[19]}$$

$$\begin{aligned} F_1 &= E_1(\beta\coth\beta-1) \\ F_2 &= E_2(\beta\coth\beta-1)-E_1^2\left[\beta\coth\beta-\left(1+\frac{\beta^2}{2}\right)\right] \\ F_3 &= E_3(\beta\coth\beta-1)-2E_1E_2\left[\beta\coth\beta-\left(1+\frac{\beta^2}{2}\right)\right] \\ &\quad +E_1^3\left[\left(1+\frac{\beta^2}{6}\right)\beta\coth\beta-\left(1+\frac{\beta^2}{2}\right)\right] \end{aligned} \quad \text{..[20]}$$

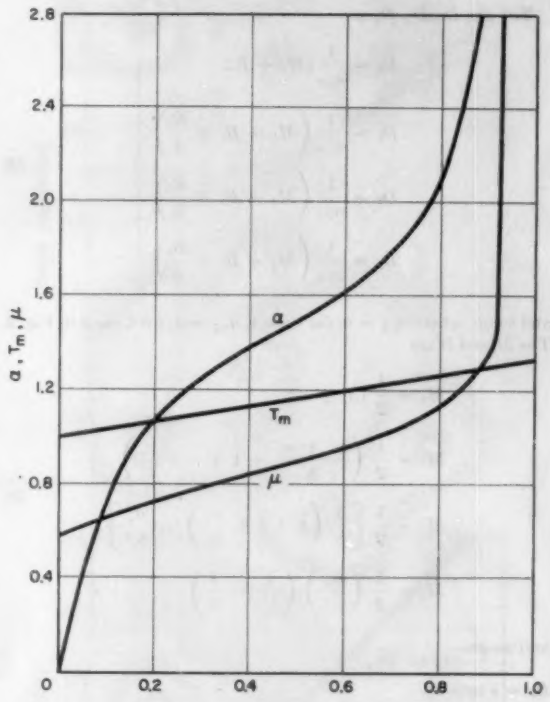


Mean delay: $T_m$
Coefficient of variance: $\mu$
Coefficient of skew: $a$

FIG. 12 DISTRIBUTION PARAMETERS FOR A SPECIAL CASE OF COUNTERFLOW

The $E_1, E_2, \ldots$ in Equation [20] are defined in the same form as Equation [11], but $K_0, K_1, \ldots$ in it are given in place of Equation [12] as follows

$$\begin{aligned} K_0 &= 4\beta^2 \\ K_1 &= 2(a_1-a_2)(1-r)-2(a_1-a_2)\frac{a_s}{b_s} \\ &\quad +\frac{2}{b}[(a_1-a_2)(a_1'-a_2')-4\beta^2] \\ K_2 &= \left[\left(1-r-\frac{a_s}{b_s}\right)+\frac{a_1'-a_2'}{b}\right]^2 \\ &\quad +(a_1-a_2)\left[2\frac{a_s}{b_s}-\frac{2}{b}\left(1-r-\frac{a_s}{b_s}\right)+\frac{4(a_1'-a_2')}{b^2}\right]+\frac{12\beta^2}{b^2} \\ K_3 &= 2\frac{a_s}{b_s^2}\left(1-r-\frac{a_s}{b_s}\right)-2(a_1-a_2)\frac{a_s}{b_s^3} \\ &\quad +\frac{2}{b}\frac{a_s}{b_s^2}\{(a_1'-a_2')-(a_1-a_2)\} \\ &\quad +\frac{2}{b^2}\left(1-r-\frac{a_s}{b_s}\right)(a_1-a_2)-\frac{16\beta^2}{b^3} \\ &\quad +\frac{6}{b^3}(a_1-a_2)(a_1'-a_2')-\frac{2}{b^3}(a_1'-a_2') \end{aligned} \quad \text{..[21]}$$

*Special Case 1.* No solid capacities

$$\left.\begin{aligned} e^{\delta} &= e^{-\beta a_{1,2}}\frac{\sinh\beta}{\beta} \\ T_m &= \frac{1+r}{2} - \frac{(a_1-a_2)(1-r)}{4\beta^2}(\beta\coth\beta-1) \\ \frac{T_s^2}{2} &= \frac{(1-r)^2}{8\beta^2}\left[1-\frac{(a_1-a_2)^2}{\beta^2}\right](\beta\coth\beta-1) \\ &\quad + \frac{(1-r)^2(a_1-a_2)^2}{32\beta^2}(1-\beta^2\operatorname{csch}^2\beta) \\ T_a^2 &= \frac{(a_1-a_2)^2(1-r)^2}{64\beta^5}\left[1+\frac{\beta^2}{3}-\beta\coth\beta\right]\times \\ &\quad \coth\beta + \frac{(a_1-a_2)(1-r)^2}{32\beta^4}\left[1-\frac{(a_1-a_2)^2}{\beta^2}\right]\times \\ &\quad [\beta^2\operatorname{csch}^2\beta-1] + \frac{(1-r)^2(a_1-a_2)}{32\beta^4}\times \\ &\quad \left[1-\frac{(a_1-a_2)^2}{4\beta^2}\right](\beta\coth\beta-1) \end{aligned}\right\} \quad \ldots [22]$$

*Special Case 2.* Same as Case 1, and $r = 1$.

$$\left.\begin{aligned} e^{\delta} &= a_{1,2}\,e^{-\beta}\frac{\sinh\beta}{\beta} \\ T_m &= 1 \\ T_s &= 0, \quad T_a = 0 \end{aligned}\right\} \quad \ldots\ldots\ldots\ldots [23]$$

# Discussion

A. R. Catheron[6] and B. D. Hainsworth.[8] This paper provides the most rigorous basis that we have yet seen for setting up working equations for the transfer functions of heat exchangers from design data. The authors should be congratulated for their step toward reducing this procedure to a practical and reliable tool.

We think that the special cases presented at the end of the paper are of perhaps greater importance than their position would indicate. We would like to ask the authors if they do not feel that the simplified equation resulting from neglecting the effects of solid capacities (Special Case 2) is justified for general use. Also, does not the use of an arbitrary mean value for the film coefficient of heat transfer introduce an error of appreciable size? The film coefficient of heat transfer for liquid flowing inside a tube varies as the inverse square root of the viscosity and as the two-thirds power of the thermal conductivity. Both properties vary with temperature, which, of course, varies along the tube.

Heat exchangers working between steam and liquid are also relatively common, but the equations presented in the paper do not apply, because the steam does not have a definite flow or temperature gradient. It would be interesting to develop this analysis for a steam-liquid heat exchanger.

## Authors' Closure

The authors are much appreciative of the discussers' comments, which raise a number of questions; in particular, (*a*) the effects of varying film coefficients, and (*b*) the effects of solid heat capacities. Regarding the first, the authors did not attempt any dynamical analysis; however, lumping or dividing the pipe length into three or more sections, using different film coefficients for each, and then calculating the performance as a whole will give one quantitative measure of the error in using mean values of the film coefficient. Both authors have performed such steady-state calculations of counter and parallel-flow heat exchangers, taking into account the nonuniform distribution of the heat-transmission coefficient, which yielded final results very close to those obtained using a mean film coefficient. Thus it is reasonable to assume not too great an error arises from this source in transient analyses.

As to the effects of solid capacities, they, of course, depend upon the ratios to other system constants. For example, if one neglects the solid capacity in an air heater, the results may suffer more serious error than in the case of liquid flow, which the discussers have selected as their example. An instance of this solid effect was demonstrated by one of the authors in Fig. 8(*d*) of his previous paper.[3]

In the case of steam-liquid heat exchangers, if the saturation steam pressure is kept fairly constant regardless of the load, the analysis may be reduced to that of simple percolation and is directly given by the present equations. On the other hand, if the steam space is approximated by an equivalent finite-heat capacitance, one of the authors' operational solutions (Case B of footnote 3) or its expanded form into the new formula (which is not included in the present paper) would give the appropriate response.

Owing to delays in the presentation of the material cited as footnote 5 in the paper, covering the underlying concepts of the operational expansion employed in Equation [2], the authors feel it would be helpful to include a summary tabulation of a number of elementary models of unit gain ($\delta = 0$) processes with step responses which are monotonic nondecreasing in time—so-called "monotone processes." This table is given as Fig. 13 of this closure.

| | NAME | STEP RESPONSE | TRANSFORM | PARAMETERS $T_m$ | $T_s^2$ | $T_a^3$ |
|---|---|---|---|---|---|---|
| 1 | Lag | 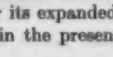 | $\frac{1}{1+T_L s}$ | $T_L$ | $T_L^2$ | $2T_L^3$ |
| 2 | Delay | 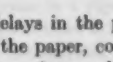 | $\epsilon^{-T_d s}$ | $T_d$ | 0 | 0 |
| 3 | Lag Delay |  | $\frac{\epsilon^{-T_d s}}{1+T_L s}$ | $T_L+T_d$ | $T_L^2$ | $2T_L^3$ |
| 4 | Two-Lag | 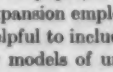 | $\frac{1}{(1+T_1 s)(1+T_2 s)}$ | $T_1+T_2$ | $T_1^2+T_2^2$ | $2(T_1^3+T_2^3)$ |
| 5 | Multi-Lag | 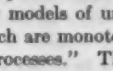 | $\left(\frac{1}{1+T_0 s}\right)^N$ | $NT$ | $NT^2$ | $2NT^3$ |
| 6 | Gaussian | 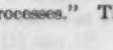 | $\epsilon^{-T_m s+\frac{1}{2}T_0^2 s^2}$ | $T_m$ | $T_0^2$ | 0 |
| 7 | Root-Lag | 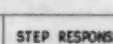 | $\sqrt{\frac{1}{1+T_r s}}$ | $\frac{1}{2}T_r$ | $\frac{1}{2}T_r^2$ | $T_r^3$ |
| 8 | Averaging | 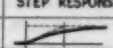 | $\frac{1}{T_f s}(1-\epsilon^{-T_f s})$ | $\frac{1}{2}T_f$ | $\frac{1}{12}T_f^2$ | 0 |

Fig. 13 Models for Monotone Processes

Some of these models, either singly or in cascade combination, have been employed in the paper. The laws of combination for the monotone parameters in such cases are most simple and direct, namely

$$c_1 \equiv T_m = T_{m1} + T_{m2} + T_{m3} + \ldots = \sum_k T_{mk}$$

$$c_2 \equiv T_s^2 = T_{s1}^2 + T_{s2}^2 + T_{s3}^2 + \ldots = \sum_k T_{sk}^2$$

$$c_3 \equiv T_a^3 = T_{a1}^3 + T_{a2}^3 + T_{a3}^3 + \ldots = \sum_k T_{ak}^3$$

$$\ldots\text{etc}\ldots$$

The coefficients $c_k$ are called the "cumulants" or "semi-invariants" of the process.

[8] The Foxboro Company, Foxboro, Mass.

It is also helpful to pass directly to the monotone parameters from any transfer characteristic of the form

$$G(s) = \frac{1}{1 + a_1 s + a_2 s^2 + a_3 s^3 + \ldots} = \frac{1}{\sum_k a_k s^k}$$

where the denominator polynomial may be either finite or infinite. For this purpose the following relationships are helpful

$$c_1 = T_m = a_1$$

$$c_2 = T_s^2 = a_1^2 - 2a_2$$

$$c_3 = T_a^3 = 2a_1^3 - 6a_1 a_2 + 6a_3$$

$$\ldots \text{etc} \ldots$$

Thus the very large number of thermal, chemical, and other industrial processes, which are characterized by monotone step responses, can be approximated very simply by a wide variety of effective models such as those of Fig. 13, all possessing the same values of $T_m$ and $T_a$, for which knowledge of merely the coefficients $a_1$ and $a_2$ suffices.

# The Dynamic Response of Industrial Thermometers in Wells

By T. C. LINAHAN,[1] PHILADELPHIA, PA.

**Previously published analyses of the dynamic response of thermometers in wells have neglected either the internal distributed well resistance or the internal bulb resistance. This paper considers an "effective" resistance and capacitance of the bulb when it is in a well. The distributed resistance and capacitance of the well are included, and an approximate second-order expression for the dynamic response is developed using a combined analytical and experimental approach. There is also a brief discussion of the film coefficient of heat transfer.**

## Introduction

THE dynamic response of a thermometer is a function of both the thermometer and the measured medium. This discussion concerns thermometers consisting of a temperature-measuring element in a protective well, where the measured medium is a fluid in forced motion. The ranges of temperatures considered are those at which the effects of radiation can be neglected. The general term, bulb, is applied to all elements whether they be bulbs of filled systems or simple butt-welded thermocouples.

Hornfeck (1),[2] Fishwick (2), Aikman (3), and others have considered bulbs-in-wells. Hornfeck and Aikman neglected the internal well resistance, while Fishwick included this resistance but only in cases where the bulb-to-well resistance could be neglected.

Aikman defines an effective capacitance of the bulb to describe its response in a well. This capacitance is determined experimentally and, in general, does not equal the value obtained by direct computation considering the heat capacities and the masses of the materials in the bulb.

This paper presents a method of treating the internal distributed resistance and capacitance of the well, and also gives a simple way of describing the bulb by an effective resistance and capacitance.

## The Film Coefficient of Heat Transfer

The film coefficient $h$ is a measure of the heat transferred from the fluid to the well. Empirical expressions for $h$ generally represent experimental data to within ±20 per cent. Of particular interest are the equations recommended by McAdams (4) which give the average film coefficient per unit area around the surface of a cylinder for Re greater than 1000 when flow is normal to the axis of the cylinder.

For liquids

$$h = \frac{0.47k}{D}\left(\frac{\rho Dv}{\mu}\right)^{0.52}\left(\frac{c\mu}{k}\right)^{0.3} \quad \ldots\ldots\ldots\ldots [1]$$

For gases

$$h = \frac{0.26k}{D}\left(\frac{\rho Dv}{\mu}\right)^{0.6}\left(\frac{c\mu}{k}\right)^{0.3} \quad \ldots\ldots\ldots\ldots [2]$$

where $v$ is the average velocity of the main body of the fluid, $\rho$ is the density, $c$ the specific heat, $\mu$ the absolute viscosity, and $k$ the thermal conductivity of the fluid. The Reynolds number, $\rho Dv/\mu$, in these equations involves $D$, the outside diameter of the cylinder.

Aikman has found that, for thermometers with their tips pointing upstream in a pipe, Equations [1] and [2] can be used to determine $h$ to within ±20 per cent if the coefficients are multiplied by 1.25, the increase being due partly to the added turbulence at the tip of the thermometer. Since $h$ depends on properties of the fluid which are functions of temperature, only a mean value can be used for a given temperature change.

Differences of opinion are expressed in texts on heat transfer concerning the values of the coefficient and the exponent of Re in Equations [1] and [2]. However, the various values do not result in greatly different film coefficients, and Equations [1] and [2] have been used successfully by several authors.

In processes where the flow pattern is random and the velocity cannot be defined in direction or magnitude, it may be possible to determine experimentally the film coefficient for a particular installation. This value then can be applied to any thermometer of the same size used in the same location in the process.

In computing response curves for this paper, experimentally determined film coefficients were used for step and frequency responses in water. They were found with the aid of specially constructed thermometers made of copper tubes with the same OD as the wells to be tested and with a $^1/_8$-in. ID. A 32-gage constantan wire soldered to the inner surface of the tube constituted a thermocouple. The response curves of this thermocouple were first-order in a well-agitated water bath and in the apparatus used for frequency-response tests (5). The first-order time constant was then divided by the heat capacity of the tube to obtain the film resistance, the reciprocal of the film coefficient.

To compute responses in air, the film coefficient was found from Equation [2] since the apparatus used for step response was designed to give crossflow. However, the film resistance in this case also was determined experimentally using the special thermocouples and was found to agree within 5 per cent of that obtained from Equation [2].

## Response of Bulbs in Wells

By assuming certain idealized conditions, the transfer of heat within a thermometer can be made analogous to the flow of current in an electrical circuit. This provides for the convenient use of the Laplace transformation and the standard solution for the equation of the circuit. Those assumptions which permit such an analogy are as follows:

---

[1] Research Engineer, Brown Instrument Division, Minneapolis-Honeywell Regulator Company; now Instructor, Villanova University, Villanova, Pa.

[2] Numbers in parentheses refer to the Bibliography at the end of the paper.

Contributed by the Instruments and Regulators Division and presented at the Diamond Jubilee Semi-Annual Meeting, Boston, Mass., June 19–23, 1955, of The American Society of Mechanical Engineers.

Note: Statements and opinions advanced in papers are to be understood as individual expressions of their authors and not those of the Society. Manuscript received at ASME Headquarters, April 12, 1955. Paper No. 55—SA-52.

1 The wells and bulbs are cylindrical.

2 Heat transfer within the thermometer is by radial conduction; axial conduction is neglected.

3 The thermal conductivity and heat capacity of the materials are considered to be linear, evenly distributed along the radius, and constant with changes in temperature.

4 The temperature of the thermometer is assumed not to affect the temperature of the main body of the fluid.

Since the only shape to be considered is a cylinder, it is convenient to define parameters on a unit-length basis, the film resistance per unit length, $R_F$, being

$$R_F = \frac{1}{\pi D_o h} \quad [3]$$

The thermal resistance of a cylindrical shell is

$$R = \frac{\ln D_o/D_i}{2\pi k} \quad [4]$$

and the capacitance per unit length is

$$C = \rho c \pi \frac{(D_o^2 - D_i^2)}{4} \quad [5]$$

where $k$, $\rho$, and $c$ are the thermal conductivity, the density, and the specific heat of the material, respectively. $D_o$ and $D_i$ are the outside and inside diameters of the shell.

In general, the bulb is thermodynamically complex. Where there is a low film resistance, for instance in well-agitated water, the response of practically all bare industrial thermometer bulbs must be described by an expression involving more than one time constant. As an example, a theory of response presented by O. Muller-Girard (6) results in a three-time constant equation for the response of certain mercury-filled thermometers. However, for the purpose of describing the response of bulbs-in-wells, the bulb can be approximated by a single time constant $T_B$ which involves only parameters of the bulb.

$$\frac{\theta_o}{\theta_i}(s) = \frac{1}{[1 + (R_F + R_S + R_2)C_1]\cosh(-\sqrt{sR_1C_1}) - \left[\frac{s(R_FC_1 + R_1C_2) + s^2R_FC_1(R_S + R_2)C_2}{\sqrt{sR_1C_1}}\right]\sinh(-\sqrt{sR_1C_1})} \quad [10]$$

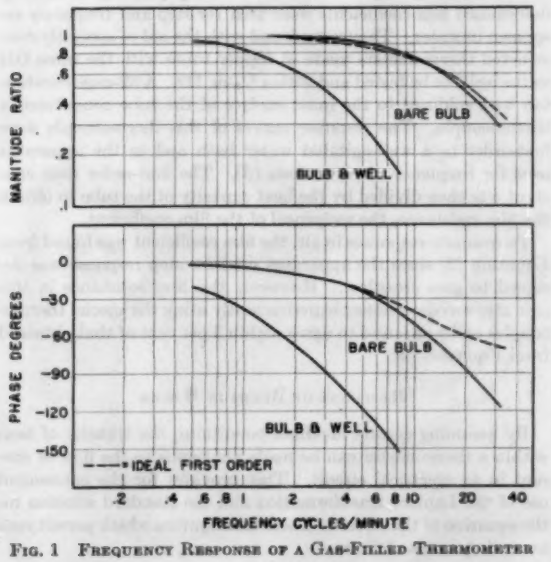


FIG. 1 FREQUENCY RESPONSE OF A GAS-FILLED THERMOMETER

Consider the experimental frequency response of a gas-filled thermometer as shown in Fig. 1. The response of the bare bulb approximates a first-order system up to frequencies at which the bulb-and-well assembly suffers much attenuation and phase lag. In this instance, a first-order approximation with time constant $T = 0.8$ sec is very good up to around 8 cycles per min (cpm). This time constant can be considered as

$$T = (R_F + R_2)C_2 \quad [6]$$

where $R_2$ and $C_2$ are the effective internal resistance and capacitance of the bulb. A further test where there is a different film resistance, $R_F'$, results in another such time constant

$$T' = (R_F' + R_2)C_2 \quad [7]$$

From Equations [6] and [7]

$$C_2 = \frac{T - T'}{R_F - R_F'} \quad [8]$$

and

$$T_B = R_2C_2 = \frac{T'R_F - TR_F'}{R_F - R_F'} \quad [9]$$

With the bulb thus defined by a single time constant, the analogous circuit is shown in Fig. 2, where $R_F$ is the film resistance, $R_1$ and $C_1$ are the internal well resistance and capacitance, $R_S$ is the bulb-to-well resistance, and $R_2$ and $C_2$ are the effective bulb resistance and capacitance, respectively. The Laplace transform solution of the circuit equations is

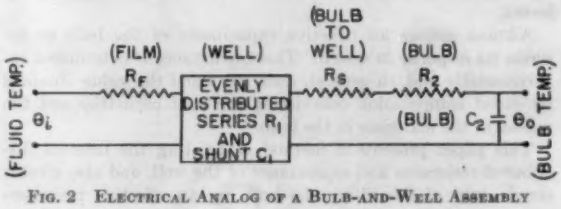


FIG. 2 ELECTRICAL ANALOG OF A BULB-AND-WELL ASSEMBLY

By expanding cosh and sinh in series and neglecting all powers of $s$ higher than 2, a second-order approximation can be made, with $T_B$ substituted for $R_2C_2$

$$\frac{\theta_o}{\theta_i}(s) \approx \frac{1}{(1 + T_1s)(1 + T_2s)} = \frac{1}{1 + (T_1 + T_2)s + T_1T_2s^2} \quad [11]$$

where

$$T_1 + T_2 = \left(R_F + \frac{R_1}{2}\right)C_1 + (R_F + R_1 + R_S)C_2 + T_B \quad [12]$$

and

$$T_1T_2 = \left[\left(\frac{R_FR_1}{2!} + R_FR_S + \frac{R_1R_S}{2!}\right)C_2 + \left(\frac{R_FC_1}{3!} + \frac{R_1C_1}{4!} + \frac{R_1C_2}{3!}\right)R_1 + \left(R_F + \frac{R_1}{2!}\right)T_B\right]C_1 \quad [13]$$

By neglecting the internal resistances of the bulb and the well, Equations [12] and [13] reduce to those used by Hornfeck, Fish-

wick, and Aikman. If all the internal resistances are zero, as is assumed in first-order approximations, $T_1T_2$ is zero and Equation [12] reduces to a single time constant

$$T = R_F(C_1 + C_2) \quad [14]$$

By neglecting $R_B$, the bulb-to-well resistance, Equations [11], [12], and [13] are useful to the manufacturer in estimating the optimum response to be expected of a particular bulb-and-well assembly when attempts are made to reduce the bulb-to-well resistance.

## Experimental and Computed Responses

All wells were 12 in. long and were immersed to a depth of 10 in. The temperature of the measured medium was determined by a bare reference thermocouple with a 63 per cent response less than 0.1 sec in water.

Fig. 3 represents a gas-filled thermometer bulb in a stainless-steel well with mercury between the bulb and the well. In Fig. 4 the same bulb is shown in another stainless-steel well with grease between the bulb and the well. The computed and experimental step responses of these assemblies in agitated water and in air, with a crossflow of 1400 fpm, are shown in Figs. 5 through 7. A few points also are plotted in Fig. 5 which were determined by computations, neglecting the internal well and bulb resistances.

Fig. 8 represents a 20-gage, butt-welded thermocouple

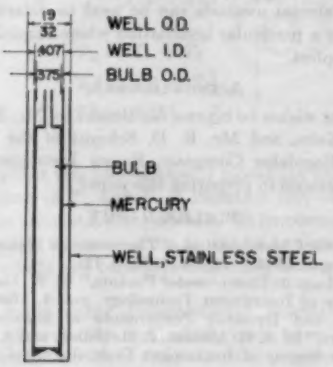


Fig. 3 Gas-Filled Thermometer in a Stainless-Steel Well With Mercury

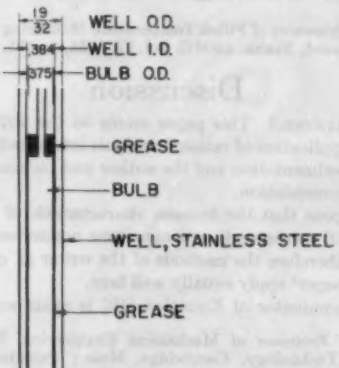


Fig. 4 Gas-Filled Thermometer in a Stainless-Steel Well With Grease

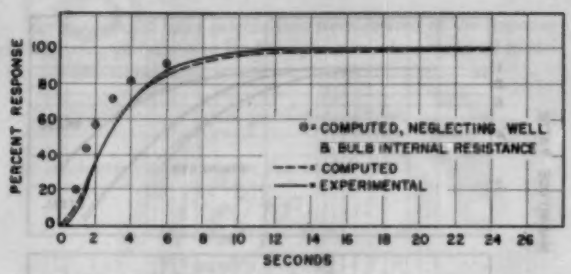


Fig. 5 Step Response in Agitated Water of the Assembly Shown in Fig. 3

(3/8-OD gas thermometer bulb in 29/32-OD × 0.407-ID stainless-steel well with mercury between bulb and well.)

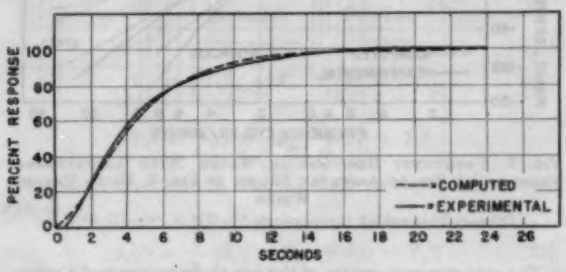


Fig. 6 Step Response in Agitated Water of the Assembly Shown in Fig. 4

(3/8-OD gas thermometer bulb in 29/32-OD × 0.384-ID stainless-steel well with grease between bulb and well.)

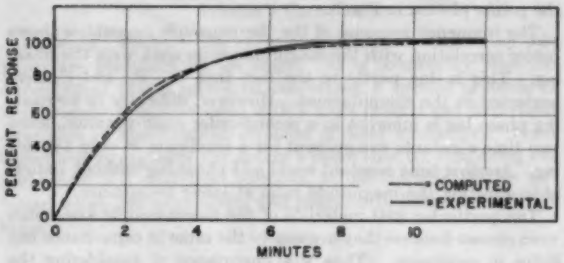


Fig. 7 Step Response in Air With Crossflow of 1400 Fpm of Assembly Shown in Fig. 4

(3/8-OD gas thermometer bulb in 29/32-OD × 0.384-ID stainless-steel well with grease between bulb and well.)

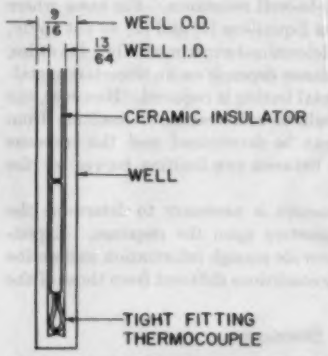


Fig. 8 Twenty-Gage Butt-Welded Thermocouple in a Well

in a well. A very tight-fitting thermocouple was made, and because of the good fit and the relatively small mass of the thermocouple, $R_B$, $R_2$, and $C_2$ were neglected in the computations. Frequency-response curves of this couple are given in Fig. 9 for three different wells with longitudinal water flow of 1.5 fps. The step response in air with the thermocouple in a stainless-steel well is shown in Fig. 10.

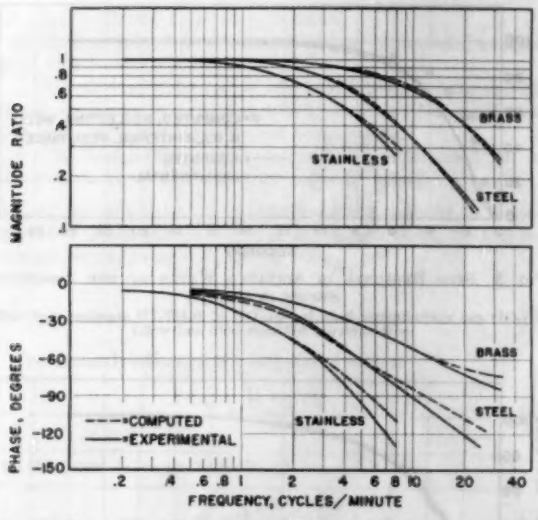


FIG. 9 FREQUENCY RESPONSE IN WATER WITH LONGITUDINAL FLOW OF 1.5 FPS OF ASSEMBLY SHOWN IN FIG. 3, USING VARIOUS WELLS

(20-gage butt-welded thermocouple 9/16-OD × 13/64-ID wells.)

The step-response curves of the gas thermometer and thermocouple assemblies show good correlation between computed and experimental results. The superior correlation obtained by including the internal well and bulb resistances instead of neglecting them is evident from comparison of the computed curve and the points plotted in Fig. 5.

The frequency response of the thermocouple assemblies shows better correlation with the magnitude ratio than with the phase lag. This is due partly to the fact that $R_B$, $R_2$, and $C_2$ were neglected in the computations. However, difficulty in correlating phase lag is inherent in a second-order approximation, since two time constants can account for a maximum of only 180 deg lag. Another time constant could add phase lag without noticeably affecting the magnitude ratio at lower frequencies.

The particular well materials of the thermocouple assemblies were chosen because they are nearly the same in capacitance but differ in resistance. Thus the importance of considering the well resistance is seen by the variation in response among the assemblies.

Two major difficulties are encountered in describing the response of bulbs-in-wells; namely, obtaining values for (*a*) the film resistance and (*b*) the bulb-to-well resistance. For cases where empirical expressions such as Equations [1] and [2] do not apply, the film resistance may be determined experimentally. Likewise, when the bulb-to-well resistance depends on an uncertain metal-to-metal contact, experimental testing is required. However, the normal variation in the bulb-to-well resistance resulting from manufacturing tolerances can be determined and the response described so that it will lie between two limiting curves for the particular assembly.

The analysis of thermometers is necessary to determine the effects of the various parameters upon the response. Experimental data alone do not provide enough information to describe the dynamic response under conditions different from those of the experiment.

## SUMMARY

The principal tenets of this paper are:

1 Although the expression for the response of a bare bulb may involve several time constants, for the purpose of describing the response in wells, the bulb can be approximated by a single time constant.

2 By considering the bulb in this manner and also by including the internal resistance of the well, better correlation between experimental and computed response is obtained than by neglecting the well and the bulb resistance.

3 The method of including the internal well resistance and capacitance was arrived at not by an arbitrary division of the well parameters but by an approximation to the complete solution of the distributed system.

4 Experimental methods can be used to determine the film resistance for a particular installation where empirical equations cannot be applied.

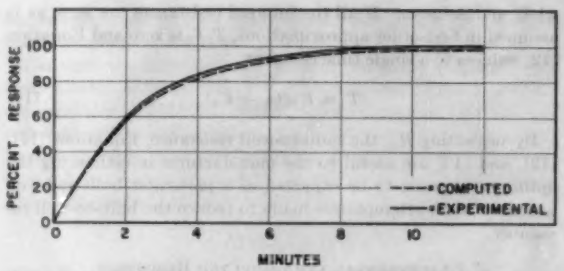


FIG. 10 STEP RESPONSE IN AIR WITH CROSSFLOW OF 1400 FPM OF ASSEMBLY SHOWN IN FIG. 3, USING A STAINLESS-STEEL WELL

(20-gage butt-welded thermocouple in 9/16-OD × 13/64-ID stainless-steel well.)

## ACKNOWLEDGMENT

The author wishes to express his thanks to Mr. S. P. Higgins, Mr. J. R. Keim, and Mr. R. D. Schmitt of the Minneapolis-Honeywell Regulator Company, Brown Instruments Division, for their assistance in preparing this paper.

## BIBLIOGRAPHY

1 "Response Characteristics of Thermometer Elements," by A. J. Hornfeck, Trans. ASME, vol. 71, 1949, p. 121.

2 "Time-Lags in Thermometer Pockets," by W. Fishwick, Trans. of the Society of Instrument Technology, vol. 4, March, 1952.

3 "Static and Dynamic Performance of Sheathed Industrial Thermometers," by A. R. Aikman, J. McMillan, and A. W. Morrison, Trans. of the Society of Instrument Technology, vol. 5, December, 1953.

4 "Heat Transmission," by W. H. McAdams, McGraw-Hill Book Company, Inc., New York, N. Y., 1942.

5 "A Thermal Sine-Wave Apparatus for Testing Industrial Thermometers," by S. P. Higgins and J. R. Keim, ASME Paper No. 54—SA-20.

6 "The Dynamics of Filled Temperature Measuring Systems," by O. Muller-Girard, Trans. ASME, vol. 77, 1955, p. 591.

# Discussion

H. M. PAYNTER.[3] This paper seems to the writer to be an exemplary application of rational analysis integrated with careful physical experimentation and the author and his associates merit deserved commendation.

It so happens that the transfer characteristic of the author's Equation [10] corresponds to a monotone nondecreasing step response and therefore the methods of the writer as outlined in a companion paper[4] apply equally well here.

If the denominator of Equation [10] is again expanded in a

[3] Assistant Professor of Mechanical Engineering, Massachusetts Institute of Technology, Cambridge, Mass.; President, Pi-Square Engineering Company, Inc. Mem. ASME.

[4] "A New Method of Evaluating Dynamic Response of Counterflow and Parallel-Flow Heat Exchangers," by H. M. Paynter and Y. Takahashi, published in this issue, pp. 749–758.

power series but where the terms are carried beyond the second degree, there results a polynomial of the form

$$\frac{\theta_o}{\theta_i}(s) = \frac{1}{1 + T_{I}s + \frac{1}{2!}T_{II}^2s^2 + \frac{1}{3!}T_{III}^3s^3 + \dots} \quad [15]$$

This may be further transformed into the monotone form

$$\frac{\theta_o}{\theta_i}(s) = e^{-T_{m}s + \frac{1}{2!}T_{s}^2s^2 - \frac{1}{3!}T_{\alpha}^3s^3 + \dots} \quad [16]$$

through the identities

$$\left.\begin{aligned} T_m &\equiv T_I \\ T_s^2 &\equiv T_I^2 - T_{II}^2 \\ T_\alpha^3 &\equiv 2T_I^3 - 3T_IT_{II}^2 + T_{III}^3 \\ &\text{etc.} \end{aligned}\right\} \quad [17]$$

As in the reference cited, $T_m$ measures the "mean delay" (i.e., the time co-ordinate of the centroid of the impulse-response curve), $\mu = (T_s/T_m)$ measures the relative "dispersion" or "spread" about the mean, and $\alpha = (T_\alpha/T_s)^3$ measures the "skew" or "asymmetry" about the mean.

The author has used what the writer would call a "two-lag" model of the process, in which

$$\frac{\theta_o}{\theta_i}(s) \approx \frac{1}{(1 + T_1s)(1 + T_2s)} \quad [18]$$

and for which

$$\left.\begin{aligned} T_m &\equiv T_1 + T_2 \\ T_s^2 &\equiv T_1^2 + T_2^2 \\ T_\alpha^3 &\equiv 2(T_1^3 + T_2^3) \\ &\text{etc.} \end{aligned}\right\} \quad [19]$$

It is obvious that this two-parameter model can be made to fit exactly the values of $T_m$ and $T_s$ of Equation [10] of the paper, but will have an erroneous value of skew. In frequency terms this means that for low frequencies the fit will be as close as possible but for intermediate and high frequencies the divergence will be measurable.

There are many other two-parameter models which are equally good theoretically but which may have special advantages for specific results or computational programs.

For example, if hand calculations were desired of the response to arbitrary variations in fluid temperature, the binominal model has obvious advantages, where

$$\frac{\theta_o}{\theta_i}(s) \approx pe^{-T_ps} + qe^{-T_qs} \quad [20]$$

The stochastic parameters for this model are

$$\left.\begin{aligned} T_m &\equiv pT_p + qT_q \\ T_s^2 &\equiv pq(T_q - T_p)^2 \\ T_\alpha^3 &\equiv pq(p - q)(T_q - T_p)^3 \\ &\text{etc.} \end{aligned}\right\} \quad [21]$$

Corresponding to the author's approximation (disregarding $\alpha$) we could take $p = q = 0.5$, for which

$$\left.\begin{aligned} T_m &= \frac{1}{2}(T_p + T_q) = T_1 + T_2 \\ T_s^2 &= \frac{1}{4}(T_q - T_p)^2 = T_1^2 + T_2^2 \end{aligned}\right\} \quad [22]$$

(Binomial) (Two-Lag)

We could then simply compute $\theta_o(t)$ corresponding to any $\theta_i(t)$ since

$$\theta_o(t) = \frac{1}{2}[\theta_i(t - T_p) + \theta_i(t - T_q)] \quad [23]$$

The foregoing remarks are all directed toward proving the soundness of the author's methods and extending the range of application of his results.

## Author's Closure

Professor Paynter's interest in and comments concerning this paper are gratefully acknowledged. It is noteworthy that the development herein presented concerning a specific problem in heat transfer is in agreement with a more general and theoretical discussion of the dynamic response of heat exchangers. Such agreement strengthens the author's belief that by combining experimental and analytical methods, sound theories can be obtained which are most useful and practical in industrial applications.

# Flow of a Compressible Fluid in a Thin Passage

By S. K. GRINNELL,[1] CAMBRIDGE, MASS.

**Pressure distribution and weight-flow rate can be predicted for laminar compressible-fluid flow in a thin passage by use of the methods presented in this paper. A simplified method can be used readily when the fluid forces due to viscous action predominate over those due to acceleration of the fluid. A more complicated trial-and-error method seems to be required for larger passages where, though the flow may be laminar, the momentum effects due to acceleration of the compressible fluid are appreciable. An experimental apparatus was used to examine the validity of the analytical work. Experimental pressure distributions agree within a maximum deviation of 10 per cent with the theoretical distributions predicted by both the comprehensive and simplified theories. Experimental weight-flow rates agree within a maximum deviation of 50 per cent with predictions of the simplified theory. Dimensionless plots of pressure distribution are presented with experimental curves of flow rate versus pressure ratio for various ratios of passage length $L$ to passage height $h$. These plots, together with simple equations, have been prepared for direct use by the designer.**

## Nomenclature

The following nomenclature is used in the paper:

$A$ = cross-sectional area of passage, sq in.
$A_\omega$ = wall area, sq in.
$b$ = width of passage transverse to flow, in.
$c$ = speed of sound, ips
$c_p$ = specific heat of gas at constant pressure, sq in/sec$^2$ deg R
$D$ = hydraulic diameter, in.
$f$ = friction factor
$g$ = acceleration due to gravity, in/sec$^2$
$h$ = height of passage, in.
$k$ = ratio of specific heats
$L$ = length of passage in direction of flow, in.
M = Mach number
$P$ = pressure, psi
$Q$ = volume rate of flow, cu in/sec
$R$ = universal gas constant, sq in/sec$^2$ deg R
Re = Reynolds number
$T$ = temperature, deg R
$u$ = fluid velocity, ips
$V$ = average fluid velocity, ips
$x$ = distance along passage in flow direction, in.
$y$ = distance from center line of passage transverse to flow, in.
$\mu$ = viscosity, lb-sec/sq in.
$\rho$ = density, lb-sec$^2$/in.$^4$
$\tau$ = fluid shear stress, psi
$\tau_\omega$ = fluid shear stress at wall, psi
$\omega$ = weight-flow rate, lb/sec

[1] Assistant Supervisor, Design Division, Dynamic Analysis and Control Laboratory, Massachusetts Institute of Technology.

Contributed by the Machine Design Division and presented at the ASME Diamond Jubilee Semi-Annual Meeting, Boston, Mass., June 19–23, 1955, of The American Society of Mechanical Engineers.

Note: Statements and opinions advanced in papers are to be understood as individual expressions of their authors and not those of the Society. Manuscript received at ASME Headquarters, March 4, 1955. Paper No. 55—SA-13.

## Introduction

With current interest and activity in the development of pneumatic components and systems, there is a need for basic information in readily usable form concerning the flow of compressible fluids in various types of flow passages. Designers of pneumatic mechanisms require information that will enable them to predict leakage flows and the distribution of pressure along leakage-flow paths. Flow past rotating and stationary shafts, flow in "hydrostatic" air bearings, leakage flow in control valves, and the flow in pneumatic resistance elements are examples of where this need has become apparent.

The general problem of gas-leakage flows in narrow channels of constant cross-sectional area was treated by A. Egli (1)[2] in 1937, with special attention to the case of leakage flows past the stems of air and steam valves. G. L. Shires (2) also has treated the flow of air in a narrow slot with particular reference to the problem of a hydrostatic compressible-fluid bearing. The work to be described in this paper is part of a thesis investigation (3) on the design of hydrostatic air bearings.

The problem treated here is that of compressible-fluid flow in a thin passage, as shown in Fig. 1. The width $b$ of the flow passage transverse to the direction of flow is of the same order of magnitude as the length of the passage in the direction of flow $L$, and the ratio of the height of the passage $h$ to the length $L$ is very small. For this range of geometric parameters, flow may be considered laminar and essentially one dimensional. As the analyses and experimental work demonstrate, the viscous-shearing forces predominate over acceleration forces when the ratio of height to length $h/L$ is very small, but the momentum forces associated with the acceleration of the fluid become more important as $h/L$ becomes larger.

## Analyses

*Adiabatic Constant-Area Flow of a Compressible Fluid With Friction.* A comprehensive analysis which has been given by A. H. Shapiro (4) for the flow of a compressible fluid in a constant-area passage includes the effects of temperature change as well as friction and momentum effects acting in the fluid. However, the solution is not in the form of explicit relationships that may be used directly for design purposes. Solutions to many problems associated with this type of flow must be found by a trial-and-error process because the stream properties and flow rate are interdependent in a nonlinear way.

The purpose of this analysis is to show how the stream properties vary along the length $L$ of a duct of constant width $b$ and constant height $h$.

The principal assumptions are as follows:

1 The flow is one dimensional and steady.
2 The working fluid is a perfect gas.

[2] Numbers in parentheses refer to the Bibliography at the end of the paper.

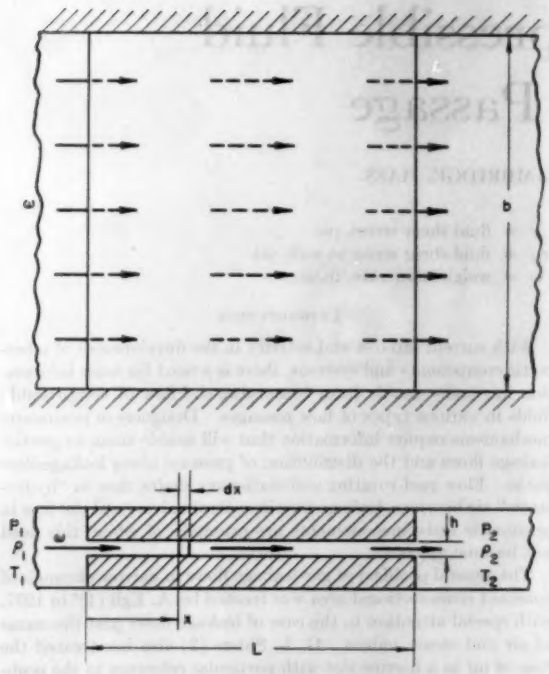


FIG. 1 FLUID FLOW IN A THIN PASSAGE

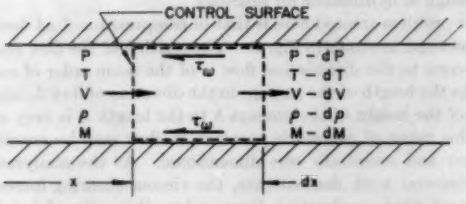


FIG. 2 ELEMENT OF FLUID

3 There are no external heat or work effects, and differences in elevation are negligible.

Two sections of the duct are considered to be an infinitesimal distance $dx$ apart, as shown in Fig. 2.

If a perfect-gas relation is assumed

$$P = \rho RT \quad [1]$$

then by logarithmic differentials

$$\frac{dP}{P} = \frac{d\rho}{\rho} + \frac{dT}{T} \quad [2]$$

From the definition of the Mach number

$$\mathbf{M} = \frac{V}{c} \text{ or } \mathbf{M}^2 = \frac{V^2}{kRT} \quad [3]$$

where

$$c = \text{sound velocity} = \sqrt{\frac{kP}{\rho}} = \sqrt{kRT} \quad [4]$$

the following equation is obtained

$$\frac{d\mathbf{M}^2}{\mathbf{M}^2} = \frac{dV^2}{V^2} - \frac{dT}{T} \quad [5]$$

The energy equation of steady adiabatic flow of a perfect gas is written

$$c_p dT + \frac{dV^2}{2} = 0 \quad [6]$$

By dividing through by $c_pT$ and by using the definition of Mach number, where $c_p = kR/(k-1)$, Equation [6] becomes

$$\frac{dT}{T} + \frac{k-1}{2}\mathbf{M}^2\frac{dV^2}{V^2} = 0 \quad [7]$$

The continuity equation is

$$\frac{\omega}{A} = \rho g V = \text{const} \quad [8]$$

Since $A$ is constant, with use of logarithmic differentials

$$\frac{d\rho}{\rho} + \frac{dV}{V} = 0 \quad [9]$$

or since

$$\frac{dV}{V} = \frac{1}{2}\left(\frac{dV^2}{V^2}\right) \quad [10]$$

$$\frac{d\rho}{\rho} + \frac{1}{2}\left(\frac{dV^2}{V^2}\right) = 0 \quad [11]$$

From Fig. 2(a), the momentum equation is written

$$-AdP - \tau_\omega dA_\omega = \frac{\omega dV}{g} \quad [12]$$

where $A$ is the cross-sectional area, $\tau_\omega$ is the shear stress exerted on the stream by the walls, and $dA_\omega$ is the wall area over which $\tau_\omega$ acts.

Now the drag coefficient, or friction factor $f$, is the ratio of the shear stress to the dynamic head of the stream and is a measure of the relative significance of viscous and momentum effects

$$f \equiv \frac{\tau_\omega}{\frac{\rho V^2}{2}} \quad [13]$$

The hydraulic diameter $D$ is defined as four times the ratio of cross-sectional area to wetted perimeter

$$D \equiv 4\frac{A}{dA_\omega}dx \text{ or } dA_\omega = \frac{4Adx}{D} \quad [14]$$

When Equations [8], [13], and [14] are introduced into Equation [12]

$$-dP - 4f\rho\frac{V^2}{2}\frac{dx}{D} = \frac{\omega}{gA}dV = \rho V^2\frac{dV}{V} \quad [15]$$

By dividing by $P$, where $V^2 = kP\mathbf{M}^2$, and by using Equation [10]

$$\frac{dP}{P} + \frac{k\mathbf{M}^2}{2}4f\frac{dx}{D} + \frac{k\mathbf{M}^2}{2}\frac{dV^2}{V^2} = 0 \quad [16]$$

The five simultaneous equations, namely, Equations [2], [5], [7], [11], and [16], may be combined to give the differential equations for $P$ and $\mathbf{M}$ as functions of $4f\,dx/D$

$$\frac{d\mathbf{M}^2}{\mathbf{M}^2} = k\mathbf{M}^2\left(\frac{1+\frac{k-1}{2}\mathbf{M}^2}{1-\mathbf{M}^2}\right)4f\frac{dx}{D} \quad [17]$$

$$\frac{dP}{P} = -k\mathbf{M}^2\left[\frac{1+(k-1)\mathbf{M}^2}{2(1-\mathbf{M}^2)}\right]4f\frac{dx}{D} \quad [18]$$

By first integrating differential Equation [17], $\mathbf{M}$ can be found as a function of $x$ if $f$ is assumed to be constant

$$\int_0^L 4f\frac{dx}{D} = \int_{\mathbf{M}_1}^{\mathbf{M}_2}\frac{1-\mathbf{M}^2}{k\mathbf{M}^2\left(1+\frac{k-1}{2}\mathbf{M}^2\right)}d\mathbf{M}^2 \quad [19]$$

The limits are as follows:

1 The entrance where Mach number is $\mathbf{M}_1$ and $x$ is zero.

2 The section a distance $L$ along the passage where Mach number is $\mathbf{M}_2$.

The integration for the special case where the final Mach number is unity gives

$$\left(\frac{4fL_{max}}{D}\right) = \frac{1-\mathbf{M}^2}{k\mathbf{M}^2} + \frac{k+1}{2k}\ln\left[\frac{(k+1)\mathbf{M}^2}{2\left(1+\frac{k-1}{2}\mathbf{M}^2\right)}\right] \quad [20]$$

where $L_{max}$ is the length required to attain a final Mach number of unity. Since $4fL/D$ is a function of Mach number only, the length of duct for a flow to pass from Mach number $\mathbf{M}_1$ to $\mathbf{M}_2$ can be found from

$$\frac{4fL}{D} = \left(\frac{4fL_{max}}{D}\right)_{\mathbf{M}_1} - \left(\frac{4fL_{max}}{D}\right)_{\mathbf{M}_2} \quad [21]$$

where $f$ is a mean friction factor.

If the passage length $L$ is greater than $L_{max}$, flow will be "choked," with the result that $\mathbf{M}_1$ and flow rate decrease as $L$ is increased. The exit Mach number $\mathbf{M}_2$ will be unity for $L$ equal to or greater than $L_{max}$.

The expression for $dP/P$ can be integrated similarly once $\mathbf{M}$ is known as a function of $x$, in order to find the pressure distribution along the passage. These expressions relating the Mach number, pressure, length of passage, and friction factor have been tabulated in Table 42 of the Gas Tables (5).

If friction factor $f$ as a function of Reynolds number Re, inlet pressure $P_1$, outlet pressure $P_2$, and the dimensions of the passage $L$, $h$, and $b$ are known, the flow rate and pressure distribution can be found by referring to Table 42 (5). An exit Mach number of unity is first assumed. The pressure ratio $P_1/P_2$ is then equal to $P/P^*$ in Table 42, where $P^*$ is the pressure when Mach number is unity, and for this value of $P_1/P_2$ there is an entering Mach number $\mathbf{M}_1$ and $(4fL_{max}/D)_{\mathbf{M}_1}$. From $\mathbf{M}_1$ and a knowledge of $T_1$, $V_1$ can be calculated from Equation [4]. For this value of $V_1$ and a corresponding Reynolds number, there is a value of friction factor $f$. With the dimensions $L$ and $h$, where $2h = D$, $4fL/D$ can be obtained. If this number is equal to $(4fL_{max}/D)_{\mathbf{M}_1}$, the exit Mach number $\mathbf{M}_2$ is unity. If $4fL/D$ is less than $(4fL_{max}/D)_{\mathbf{M}_1}$, the exit Mach number $\mathbf{M}_2$ is less than unity. If $4fL/D$ is subtracted from $(4fL_{max}/D)_{\mathbf{M}_1}$ to obtain $(4fL_{max}/D)_{\mathbf{M}_2}$, the corresponding $\mathbf{M}_2$ and $(P/P^*)_2$ can be found. If $4fL/D$ is greater than $(4fL_{max}/D)_{\mathbf{M}_1}$, the flow is choked and, by trial and error, a new $4fL/D$ must be found such that $(4fL_{max}/D)_{\mathbf{M}_1}$ and $4fL/D$ are equal for new values of $\mathbf{M}_1$ and $(P/P^*)_1$.

For any of the three cases, the flow rate is then

$$\omega = \rho_1 gbhV_1$$

and pressure distribution can be found by using intermediate values of $P/P^*$ and $4fL_{max}/D$ from Table 42.

*Simplified Analysis Neglecting Momentum Effects.* A simplified analysis that neglects momentum effects leads to explicit relationships for pressure distribution and flow rate. The Hagen-Poiseuille analysis which assumes that wall friction forces are predominant is developed for a compressible fluid in a thin passage. The assumptions are as follows:

1 Viscous-shear forces govern the flow to the extent that momentum forces can be neglected.

2 The flow is laminar and fully developed.

3 Temperature is constant throughout the flow.

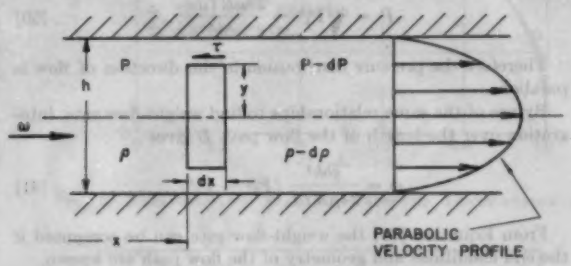


FIG. 3 ELEMENT OF FLUID

From Fig. 3, showing an element of fluid acted on by shear stress and pressure forces, the static equilibrium equation can be written as

$$2Pby - (P-dP)2by - 2\tau\, b\, dx = 0 \quad [22]$$

By Newton's (6) law of viscous flow

$$\tau = -\mu\frac{du}{dy} \quad [23]$$

where $u$ is the velocity of a particle at a distance $y$ from the center of the passage, $\mu$ is viscosity, and $\tau$ is the shear stress. When Equations [22] and [23] are combined

$$du = -\frac{y}{\mu}dy\frac{dp}{dx} \quad [24]$$

By integrating $u$ with respect to $y$ and by substituting the limits $y = h/2$, $u = 0$, the equation of the velocity distribution is

$$u = \left(\frac{h^2}{8} - \frac{y^2}{2}\right)\frac{1}{\mu}\frac{dp}{dx} \quad [25]$$

This is a parabolic distribution, as shown in Fig. 3.

The area for flow is $2by$ for an increment of flow $dQ$ so that

$$dQ = \frac{2by}{\mu}\left(\frac{h^2}{8} - \frac{y^2}{2}\right)\frac{dp}{dx} \quad [26]$$

Integrating the flow over the entire flow area, putting in limits, simplifying, and adding a minus sign because $dp/dx$ is negative in the direction of flow yield

$$Q = -\frac{bh^3}{12\mu}\frac{dp}{dx} \quad [27]$$

The equation for weight-flow rate now can be written

$$\rho_g Q = \omega = -\frac{gbh^3}{12\mu}\frac{dp}{dx} \quad [28]$$

Introduction of the perfect-gas law

$$\frac{P}{\rho} = RT \quad [1]$$

yields

$$\omega = -\frac{gbh^3P}{12\mu RT}\frac{dp}{dx} \quad [29]$$

The weight-flow rate is constant over any cross section and because of the assumption of constant temperature, the viscosity, which is principally temperature-dependent, will remain constant. Then integration to find the pressure $P$ at any point along the flow path gives

$$P = \sqrt{P_1^2 - \frac{24\mu RT\omega x}{gbh^3}} \quad [30]$$

Therefore the pressure distribution in the direction of flow is parabolic.

By use of the same relationships to find weight-flow rate, integration over the length of the flow path $L$ gives

$$\omega = \frac{gbh^3}{24\mu RTL}(P_1^2 - P_2^2) \quad [31]$$

From Equation [31] the weight-flow rate can be computed if the end conditions and geometry of the flow path are known.

## Experimental Apparatus

In order to investigate experimentally the pressure distribution and flow through a thin passage between flat plates, a simple fixture with a movable plate and a fixed plate, each $6^1/_4$ in. wide and 4 in. long, was designed, as shown in Fig. 4.

Fig. 4 Experimental Fixture

The material used in the flow-boundary surfaces was SAE 1045 hot-rolled steel stabilized by normalizing before rough and finish machining. The surfaces of the two plates were lapped together to produce very fine flat surfaces which were given a black-oxide finish to protect them from corrosion. The resulting bright black finish had a surface roughness less than 4 $\mu$ in. rms.

As shown in Fig. 4, all parts of the apparatus were made heavy enough to minimize the possibility of deflections that would invalidate the results of the experimental work.

The movable plate, which is $^3/_4$ in. thick, has an O-ring around its circumference to seal against leakage between it and the annular ring into which it fits with approximately 0.005-in. clearance all around. A second O-ring seals the space between the annular ring and the $1^1/_2$-in-thick base plate.

Three differential screws provide the adjustment for the separation between the flow plates, and three dial indicators measure the plate separation. The differential screws have a No. 6-40 thread which mates with a hole in the movable plate and a No. 8-36 thread which mates with a tapped hole in a stationary arm attached to the base plate. This arrangement, providing a motion of $^1/_{400}$ in. per revolution of the screw, allows fine adjustment of the passage height $h$.

A grid of $81^1/_{32}$-in-diam pressure-tap holes consisting of 9 rows of nine holes each on $^1/_2$-in. centers in the direction of flow and $^5/_8$-in. centers at right angles to the direction of flow covers the stationary base plate. A manifolding plate, which was lapped with the underside of the base plate after grinding to give a sealing surface, can be located by means of a rack-and-pinion arrangement to lead out pressures from 18 points, 9 from each end of the manifold plate. The apparatus schematic of Fig. 5 shows the vernier arrangement providing five positions in which two rows of holes are synchronized to feed pressures to the ends of the manifold plate. This system of pressure-tap manifolding permitted the use of 18 mercury manometers for pressure measurements instead of the 81 which would have been required without the manifold.

Two sets of three $^1/_2$-in-diam tubes lead into opposite pressure chambers through the sides of the base plate to feed air in and out of the apparatus. The pressure chambers are $^5/_{16} \times {}^1/_2 \times 6^1/_4$ in., providing large enough volume so that flow velocities before and after the flow-plate restriction are negligible.

## Instrumentation

A schematic diagram of the general instrumentation and air supply and exhaust arrangement is shown in Fig. 5.

Three dial indicators with 4-in. dials and 0.0001-in. graduations were used to measure the separation between the plates.

Eighteen vacuum-type manometers were used to measure the

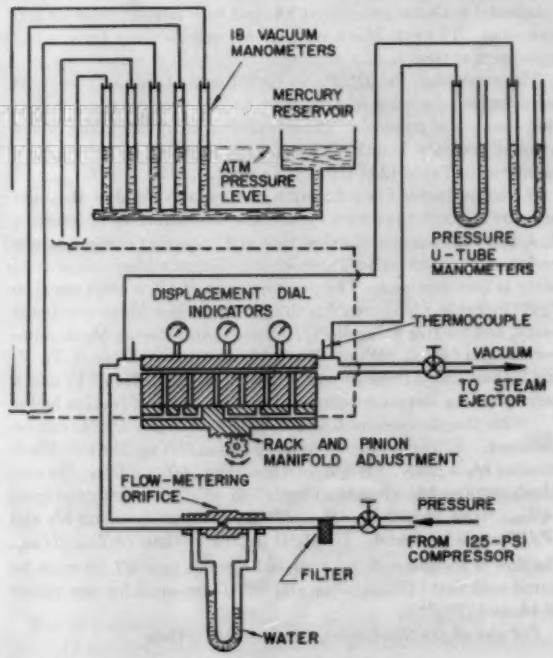


Fig. 5 Experimental Apparatus

pressure distribution. The vacuum-manometer board, shown in Fig. 4 and drawn schematically in Fig. 5, has a large reservoir of mercury maintained at atmospheric pressure. The operating supply pressures for the tests ranged from $^1/_2$ atm to 2 atm on the upstream side and from 1 atm down to $^1/_{10}$ atm on the downstream side. The mercury manometers could be read to within $^1/_{20}$ in. of mercury or approximately $^1/_{40}$ psi.

A calibrated orifice flowmeter constructed according to ASME Standards was used to measure weight-flow rate. The pressure taps before and after the orifice were connected to a differential water manometer and also to separate absolute-pressure mercury manometers.

Iron-constantan thermocouples were placed in both the upstream and downstream chambers to measure the temperature at entrance and exit of the flow passage. A Leeds & Northrup Wheatstone-bridge potentiometer circuit was used to measure the thermocouple potential within 0.1 mv.

A pressure tap was placed in both the upstream and downstream pressure chambers to determine the end pressures. These taps were connected to mercury U-tube manometers that could measure pressures as high as 2 atm or as low as perfect vacuum.

The upstream side of the apparatus was connected through orifice flowmeter, valve, and flexible hose to a 125-psi air compressor. The downstream side of the apparatus was connected through a valve to a steam ejector which is capable of handling 0.2 lb of air per sec at a pressure of 2 psia. The capacities of both compressor and ejector were more than adequate for this work because flows of less than 0.01 lb/sec were used at all times.

## Operation and Data

Pressure-distribution and weight-flow-rate data were taken with the flat-plate apparatus for operating pressure ratios $P_1/P_2$ in the range from 2 to 12. Clearance ratio $h/L$ was varied between $^1/_{4000}$ and $^1/_{667}$.

The streamlines were determined to be very nearly parallel in the major flow direction by means of very fine oil lines on the test plates made in one set of runs.

A set of runs was made with shims determining the plate separation as a check on the accuracy of the settings read from the dial indicators used for determining plate separation in the major portion of the runs.

## Results

The pressure distributions calculated from both the comprehensive and simplified analyses are compared with experimentally measured distributions in Figs. 6 and 7. The simple theory is seen to be good for very small $h/L$ ratios in the range from $^1/_{1000}$ to $^1/_{4000}$, as given in Fig. 6. For the extremely small clearances involved, the momentum effects can be neglected and the simplified theory used to predict the pressure distribution. For very small clearances, the quantity $4fL_{max}/D$ becomes very large, and errors in using Table 42 of the Gas Tables (5) are large, with the result that the comprehensive method does not give very accurate results.

However, as the clearance is increased to where $h/L$ is $^1/_{667}$, as shown in Fig. 7, the pressure distribution predicted by the simplified equation does not agree as well with the experimental pressure distribution. For these larger ratios, the complete analysis prediction of pressure distribution based on Shapiro's methods (4) agrees well with the experimental pressure distribution.

The weight-flow rate, which is predicted to be a function of the passage height cubed $h^3$ by the simplified theory, Equation [31], is found experimentally to be somewhat different, as shown in Fig. 8. It would be expected that for large $h/L$ ratios where momentum effects are important the experimental weight-flow rates would be smaller than those predicted by the simplified theory.

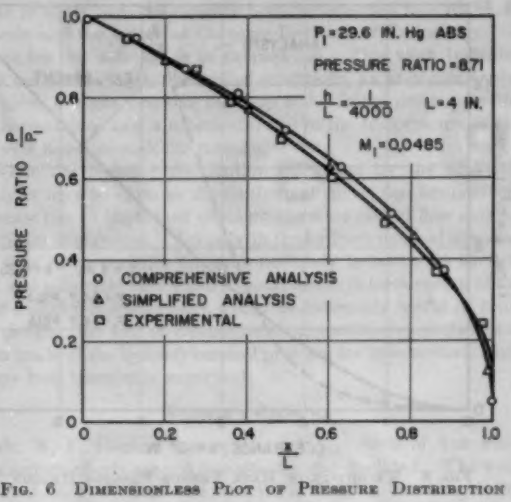


Fig. 6 Dimensionless Plot of Pressure Distribution

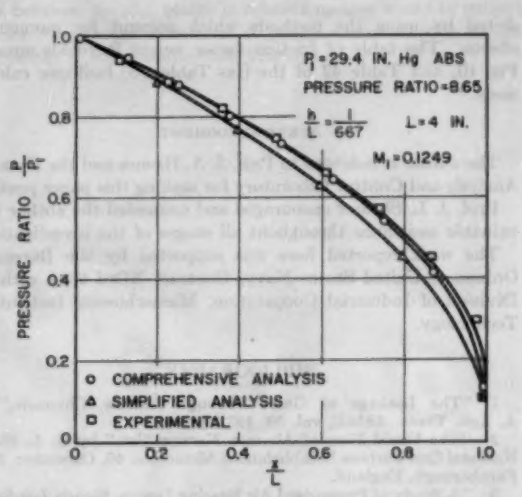


Fig. 7 Dimensionless Plot of Pressure Distribution

Experimental weight-flow rates obtained for various values of $h$ as a function of supply pressure $P_s$ are presented in Fig. 9 for a passage 4 in. long and 5 in. wide.

A plot of experimentally obtained friction factor $f$ versus Reynolds number is given in Fig. 10. The friction factors calculated from the experimental weight-flow rates agree reasonably well with the work of Egli (1), as is illustrated by a comparison of the curves of Fig. 10.

## Conclusions

A parabolic pressure distribution is accurate for passage height-to-length ratios of $^1/_{1000}$ and smaller where momentum effects can be neglected and viscous forces predominate. For this same range of passage height-to-length ratios, the simplified relationship that weight-flow rate is a function of passage height cubed proves reasonably accurate.

For larger passage height-to-length ratios where the flow is laminar, the pressure distribution and weight-flow rate can be pre-

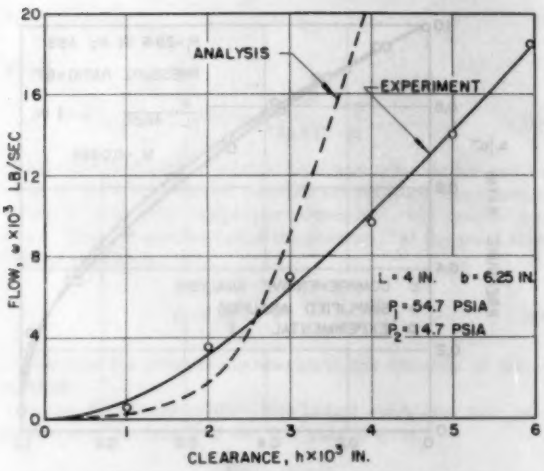


FIG. 8 WEIGHT-FLOW RATE VERSUS PASSAGE HEIGHT

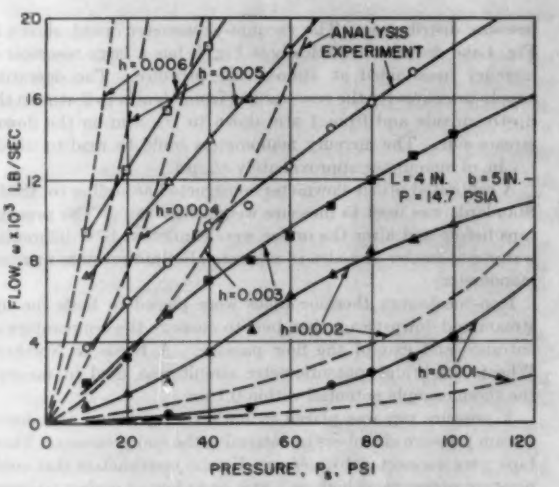


FIG. 9 WEIGHT-FLOW RATE VERSUS PRESSURE RATIO

dicted by using the methods which account for momentum effects. The table of friction factor versus Reynolds number, Fig. 10, and Table 42 of the Gas Tables (5) facilitate calculations.

### ACKNOWLEDGMENT

The author is indebted to Prof. J. A. Hrones and the Dynamic Analysis and Control Laboratory for making this paper possible.

Prof. J. L. Shearer encouraged and counseled the author with valuable assistance throughout all stages of the investigation.

The work reported here was supported by the Bureau of Ordnance, United States Navy, Contract NOrd 9661 with the Division of Industrial Cooperation, Massachusetts Institute of Technology.

### BIBLIOGRAPHY

1 "The Leakage of Gases Through Narrow Channels," by A. Egli, Trans. ASME, vol. 59, 1937, p. A-63.

2 "The Viscid Flow of Air in a Narrow Slot," by G. L. Shires, National Gas Turbine Establishment Memo No. 46, December, 1948, Farnborough, England.

3 "A Study of Pressurized Air Bearing Design, Steady Loading—No Rotation," by S. K. Grinnell, SM thesis, Department of Mechanical Engineering, Massachusetts Institute of Technology, Cambridge, Mass., January, 1954.

4 "Flow of Compressible Fluids," by A. H. Shapiro, Notes for Course 2.491, Department of Mechanical Engineering, Massachusetts Institute of Technology, Cambridge, Mass., 1952.

5 "Gas Tables," by J. H. Keenan and J. Kaye, John Wiley & Sons, Inc., New York, N. Y., 1945.

6 "The Mathematical Principles of Natural Philosophy," by I. Newton, J. Maclehose, Glasgow, Scotland, 1871.

## Discussion

W. F. HUGHES.[3] The author's simplified analysis should prove quite useful in the study of lubrication-type flows for air bearings where rather small $h/l$ values are involved, and inertial effects can be neglected. The author assumes isothermal, hence isoviscous, flow of the lubricant. For hydrostatic situations, that is, where the plates are not in relative motion, it is interesting to note that an adiabatic treatment yields results identical with the isothermal solution. In fact, the adiabatic treatment

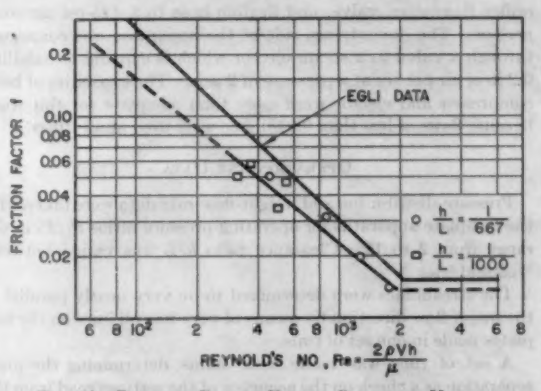


FIG. 10 FRICTION FACTOR VERSUS REYNOLDS NUMBER

shows that the isothermal solution is the only possible one compatible with energy conservation. Only in hydrodynamical situations, where the plates are in relative motion, is the adiabatic solution different from the isothermal solution. This can be shown quite readily by considering the appropriate energy equation.[4]

$$\rho c_V u \frac{dT}{dx} = -P \frac{\partial u}{\partial x} + \mu \left(\frac{\partial u}{\partial y}\right)^2$$

where the two right-hand terms represent work of expansion and shear work, respectively. This equation can be put into the form

$$\rho c_p u \frac{dT}{dx} = u \frac{dP}{dx} + \mu \left(\frac{\partial u}{\partial y}\right)^2$$

Now, if the author's expression for the velocity profile, Equation [25], is inserted into the energy equation and then integrated across the film, assuming constant specific heat and constant fluid properties across the film, the two right-hand terms cancel out leaving the temperature gradient equal to zero. (The author's expression for the velocity profile must have a negative sign inserted since the positive pressure gradient is defined in the nega-

[3] Mechanical Engineering Department, Carnegie Institute of Technology, Pittsburgh, Pa. Assoc. Mem. ASME.

[4] "Modern Developments in Fluid Dynamics," by S. Goldstein, Oxford University Press, London, England, 1938, vol. 2, p. 606.

tive $x$-direction.) Hence the flow is isothermal even if adiabatic conditions are assumed, and the results are identical with those obtained by the author.

In contrast to this behavior, the adiabatic solution is substantially different for hydrodynamical flows which give rise to increases in temperature and viscosity of the air as it flows through the passage. In actual practice, however, the flow of air under such hydrodynamical conditions will be intermediate between isothermal and adiabatic conditions since the heat generated by internal friction in the fluid will be partially stored in the fluid, increasing its internal energy, and partially conducted away through the bearing surfaces. However, the adiabatic solution considering variations in viscosity and temperature will form an upper bound to the pressure and temperature distributions and may be closer to the actual operating characteristics for certain flow conditions than the isothermal solution.

The hydrodynamical problem was first treated by Harrison in 1913[9] for the isothermal flow of air between two inclined plates in relative motion, so that the author's simplified analysis is actually a limiting case of Harrison's solution. The other extreme, that of the adiabatic flow of air between parallel plates in relative motion with a pressure differential across the moving plate or slider pad, has recently been investigated by Prof. J. F. Osterle and the writer at Carnegie Institute of Technology. A paper on this solution is in preparation. This work indicates that under these hydrodynamical conditions, an adiabatic analysis gives a slight pressure build-up which is not present for the isothermal case and a substantial rise in the temperature of the air as it flows through the passage.

While the pressure distribution calculated by the adiabatic analysis may be close to the isothermal curve, the temperature increase has an important effect on the mass rate of flow and the frictional energy loss. Actually in the hydrodynamical situation the flow characteristics fall intermediately between the isothermal and adiabatic values and a quantitative determination of the heat-transfer characteristics would be extremely useful in bearing design. As yet, no comprehensive quantitative analysis has been made of the hydrodynamical problem for intermediate cases where heat transfer is important.

[9] "The Hydrodynamical Theory of Lubrication With Special Reference to Air as a Lubricant," by M. A. Harrison, Trans. Cambridge Philosophical Society, vol. 22, 1913, p. 30.

### Author's Closure

Mr. W. F. Hughes' comments on the problem of flow when momentum effects are not important are appreciated. The work by Prof. J. F. Osterle and Mr. W. F. Hughes on compressible flow between parallel plates in relative motion would be subject matter for a paper of interest to people concerned with the development of compressible-fluid bearings.

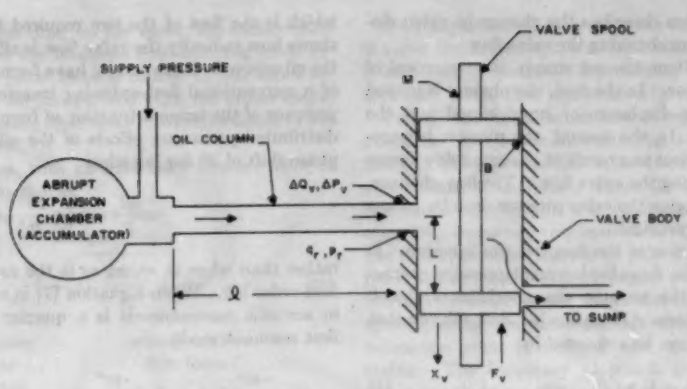


FIG. 1 SIMPLE VALVING SYSTEM

# The Effect of Oil-Column Acoustic Resonance on Hydraulic Valve "Squeal"

BY F. W. AINSWORTH,[1] MINNEAPOLIS, MINN.

**An outline is presented of a theory that oil-column resonance is one likely cause of control-valve oscillation. It is shown analytically and experimentally that acoustic resonance of the oil in the lines which are attached to the valve can cause an otherwise stable valve to squeal. Methods of eliminating the oscillation are given.**

## INTRODUCTION

ONE of the more annoying characteristics of hydraulic valves is a tendency toward violent instability. Lee and Blackburn[2] have shown that one likely cause of this oscillation hinges on the direction of spool motion relative to the direction of resulting oil flow along the spool axis. Tests by the author and others[3] have confirmed that valves are truly and extremely unstable if this direction of flow is not proper. However, the author's tests also have shown that the valves are generally unstable even when the direction of flow is proper. This condition indicates that the direction of flow does have a pronounced effect on stability; it also indicates that other very and equally important factors exist, and the search for such factors has led to the theory of oil-column resonance presented here.

## MECHANISM OF INSTABILITY

Valve instability, or squeal, occurs when a valve sustains self-excited oscillations. For example, the simple valving system shown in Fig. 1 can oscillate violently. The plunger is merely placed in the valve body, the supply pressure line energized, and the return line connected to the sump. A typical frequency of oscillation is 300 cycles per sec (cps). To the author's knowledge, no completely satisfactory explanation of the origin of this phenomenon has been given.

The results of the investigation reported here have shown that the dynamics of the oil in the lines connected to the valve, when combined with the dynamics of the plunger, can cause the system to oscillate. As a result of the inertia of the oil column, a random valve displacement causes the pressure to change at the downstream end of the column. This pressure disturbance travels upstream in the column at the speed of sound, hits the acoustic end of the column (where the oil line abruptly expands into the accumulator), and is reflected back as in an organ pipe. If the time delay of the returning pressure disturbance is such that the original valve displacement is strengthened through flow reaction forces,[2] then the resulting regeneration, by not satisfying the Nyquist stability criterion, can lead to continuous oscillation. If the natural frequency of the valve corresponds to the resonant frequency of the oil column, a highly unstable system results. The situation appears to be similar to that existing in a reed type of musical instrument, such as a clarinet, or even more to that in a tuned-reed organ pipe.

## DERIVATION OF STABILITY EQUATIONS

To solve the stability problem of Fig. 1, the Nyquist stability criterion will be applied after two transfer functions have been derived. The first transfer function describes the change in valve flow which results from changing the valve displacement.

---

[1] Research Engineer, Aeronautical Division, Minneapolis-Honeywell Regulator Company.

[2] "Transient-Flow Forces and Valve Instability," by Shih-Ying Lee and J. F. Blackburn, Trans. ASME, vol. 74, 1952, pp. 1013–1016.

Contributed by the Machine Design Division and presented at the Diamond Jubilee Semi-Annual Meeting, Boston, Mass., June 19–23, 1955, of THE AMERICAN SOCIETY OF MECHANICAL ENGINEERS.

NOTE: Statements and opinions advanced in papers are to be understood as individual expressions of their authors and not those of the Society. Manuscript received at ASME Headquarters, September 24, 1954. Paper No. 55—SA-14.

[3] "Steady-State Axial Forces on Control-Valve Pistons," by Shih-Ying Lee and J. F. Blackburn, Trans. ASME, vol. 74, 1952, pp. 1005–1011.

The second transfer function describes the change in valve displacement which results from changing the valve flow.

These two transfer functions are not simply the reciprocal of one another as it may appear. In the first, the plunger is moved by means of a brute-force-displacement input signal and the valve-flow output results. In the second, the plunger is unrestrained and free to move about as a result of changing flow forces which are caused by changing the valve flow. The flow changes, in turn, are caused by changing the valve pressure drop by means of a brute-force-pressure input signal.

The following is a derivation of the first transfer function. It involves a study both of the flow-displacement-pressure characteristics of the valve and the acoustic characteristics of the oil column. In Lee and Blackburn's[3] Equation [6], it was shown that the flow through an orifice can be expressed by

$$Q_v \propto X_v \sqrt{P_v} \quad \ldots\ldots [1]$$

where $Q_v$ is the valve flow, $X_v$ is the valve displacement, and $P_v$ is the valve pressure drop. For sinusoidal perturbations, Equation [1] can be written as

$$\Delta Q_v(j\omega) = \left.\frac{\partial Q_v}{\partial X_v}\right|_{P_v} \Delta X_v(j\omega) + \left.\frac{\partial Q_v}{\partial P_v}\right|_{X_v} \Delta P_v(j\omega) \ldots [2]$$

where $\Delta$ is the incremental notation, $j$ is the $\sqrt{-1}$, and $\omega$ is the frequency.

When dealing with the oil-column acoustic characteristics, distributed parameter effects must be considered, since the time required for a pressure wave to travel up the oil column and back is generally appreciable when compared with the time of one cycle of oscillation. Since the oil column (1) is straight-line-terminated at its upstream end by a very abrupt expansion into the accumulator, (2) is relatively long and narrow, and (3) has smooth walls, it can be treated as a simple open-ended, lossless, long transmission line or organ pipe.

For sinusoidal perturbations, the pressure and resulting flow at the receiving or downstream end of the oil column is, by the analogous electrical transmission line,[4] represented by

$$\frac{p_r(j\omega)}{q_r(j\omega)} = -jZ_0 \tan \frac{\omega l}{V} \quad \ldots\ldots [3]$$

where $p_r$ and $q_r$ are the perturbation pressure and flow at the oil-column receiving end, $l$ is the length of the oil column, $Z_0$ is the characteristic impedance of the oil column and equals $\sqrt{\rho/A^2\beta}$, $V$ is the velocity of sound through the oil and equals $1/\sqrt{\rho\beta}$, $\rho$ is the mass density of the oil, $A$ is the cross-sectional area of the oil column, and $\beta$ is the bulk modulus of the oil.

In Fig. 1 the downstream end of the oil column is connected to the valve. Thus

$$\Delta P_r(j\omega) = p_r(j\omega) \quad \ldots\ldots [4]$$

and

$$\Delta Q_r(j\omega) = q_r(j\omega) \quad \ldots\ldots [5]$$

Equations [2], [3], [4], and [5] can now be solved simultaneously to eliminate the pressure variable. This results in

$$\frac{\Delta Q_r(j\omega)}{\Delta X_r(j\omega)} = \frac{\left.\dfrac{\partial Q_v}{\partial X_v}\right|_{P_v}}{jZ_0 \left.\dfrac{\partial Q_v}{\partial P_v}\right|_{X_v} \tan \dfrac{\omega l}{V} + 1} \quad \ldots\ldots [6]$$

which is the first of the two required transfer functions, and it shows how radically the valve flow is affected by the dynamics of the oil column. Equation [6] has a form somewhat similar to that of a conventional first-order-lag transfer function except for the presence of the tangent function of frequency, which is due to the distributed parameter effects of the oil column. This causes a phase shift of 90 deg lag when

$$\frac{\omega l}{V} = \frac{\pi}{2}, \frac{3\pi}{2}, \text{ etc.} \quad \ldots\ldots [7]$$

rather than when $\omega = \infty$, as is the case with the conventional first-order lag. When Equation [7] is satisfied, the oil column is in acoustic resonance—it is a quarter wave-length line at the first resonant mode.

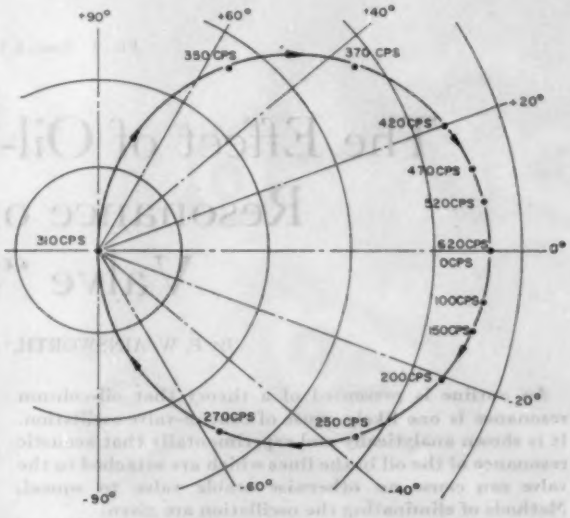


FIG. 2 FREQUENCY-RESPONSE RATIO OF VALVE FLOW TO VALVE DISPLACEMENT

A typical polar plot of Equation [6] is shown in Fig. 2 for a 45-in-long, 1/4-in-diam steel oil line, coupled to a typical 1/4-in-diam spool valve. The locus of points goes round and round and is repeated at each higher harmonic of the oil column. At low frequencies the flow is in phase with the valve displacement. At 310 cps, the quarter wave-length frequency of the 45-in. line, the flow is reduced to zero and 90 deg phase lag.

The following is a derivation of the second transfer function—the change in valve displacement which results from changing the valve flow. It involves a study of the force-flow-pressure characteristics of the valve and the mechanical force characteristics of the plunger.

In Lee and Blackburn's[3] Equation [8] it was shown that the steady-state axial force required to open a valve of the type shown in Fig. 1 is

$$F_v \propto X_v P_v \quad \ldots\ldots [8]$$

where $F_v$ is the plunger force. For sinusoidal perturbations, Equation [8] can be written as

$$\Delta F_r(j\omega) = \left.\frac{\partial F_v}{\partial X_v}\right|_{P_v} \Delta X_r(j\omega) + \left.\frac{\partial F_v}{\partial P_v}\right|_{X_v} \Delta P_r(j\omega) \ldots [9]$$

The total force acting on the valve spool in Fig. 1 is composed of an inertial force caused by the spool mass, a viscous damping

[4] "Ultra-High Frequency Radio Engineering," by W. L. Emery, The Macmillan Company, New York, N. Y., 1944, p. 140.

force caused by the viscous drag on the spool, the steady-state force of Equation [9], and the transient flow-damping force described elsewhere.[2] This latter force is caused by the rapid acceleration of the oil along the plunger axis when the orifice opens, and it is called a flow-damping force since it is proportional to the rate of change of valve flow.

The sum of these forces, with an externally applied force of zero, is zero and may be written as

$$M\frac{d^2\Delta X_v}{dt^2} + B\frac{d\Delta X_v}{dt} + \overbrace{\rho L\frac{d\Delta Q_v}{dt}}^{\text{positive flow-damping force}} + \Delta F_v = 0 \quad \ldots [10]$$

mechanical mass and viscous damping forces; steady-state flow force

where $M$ is the plunger mass, $d/dt$ is the time derivative notation, $B$ is the viscous damping coefficient, and $L$ is the flow damping length.

Equations [2], [9], and [10] can now be solved simultaneously to eliminate the force and pressure variables. This results in

$$-\frac{\Delta X_v(j\omega)}{\Delta Q_v(j\omega)} = \frac{\left.\dfrac{\partial F_v}{\partial P_v}\right|_{X_v} + j\rho L\omega}{\left.\dfrac{\partial Q_v}{\partial P_v}\right|_{X_v}} \Big/ \left[ j\omega B + \left.\frac{\partial F_v}{\partial X_v}\right|_{P_v} - M\omega^2 - \frac{\left.\dfrac{\partial F_v}{\partial P_v}\right|_{X_v}}{\left.\dfrac{\partial Q_v}{\partial P_v}\right|_{X_v}} \left.\frac{\partial Q_v}{\partial X_v}\right|_{P_v} \right] \quad \ldots [11]$$

which is the second of the two required transfer functions. It shows how the valve displacement, if not externally restrained, would react to pulsations in valve flow.

Since Equation [6] shows how the valve flow reacts to pulsations in valve displacement, it is now possible to determine if the system is stable or if the effect represented by Equation [6] can continuously excite that represented by Equation [11] or vice versa.

Perhaps the situation can best be represented by a conventional closed loop, such as is shown in Fig. 3. Here, the output of each block is the input to the other (with zero command input for convenience of analysis). From the Nyquist stability criterion, the closed-loop system will be unstable and will squeal if the open-loop frequency-response locus of Fig. 3 encloses the minus-one point (provided there is no pole of Equation [11] in the right-hand half of the complex frequency plane).

Fig. 4 shows a Nyquist diagram of the response of the open-loop system, using the same components as used for Fig. 2. The minus-one point is enclosed and, therefore, the system is unstable. The frequency at which the system will oscillate is somewhere between 270 and 310 cps, since this frequency range is closest to the minus-one point. If the locus is plotted for an oil column of zero length, the system will be found to be stable.

The two lobes on the frequency-response locus of Fig. 4 are of particular interest. These lobes are caused by the locus returning to zero at each resonant mode of the oil column. Actually, there is an infinite number of the lobes because of the infinite number of resonant modes of the oil column; however, only two are shown here for convenience.

As previously implied, Equation [11] can have a pole in the right-hand half of the complex frequency plane. This condition can be caused by the real part of the denominator of Equation [11] having a negative sign at zero frequency, and it generally occurs at large valve displacements (0.001 in. or more). The pole in the right-hand half of the plane amounts to an unstable inner loop in the open-loop system. When this occurs, the open-loop locus of the system shown in Fig. 4 should enclose the minus-one point to obtain a stable closed-loop system.

## Experimental Results

Figs. 5 and 6 show the results of the stability tests on the $^1/_4$-in. spool valve. The frequency of oscillation and the externally

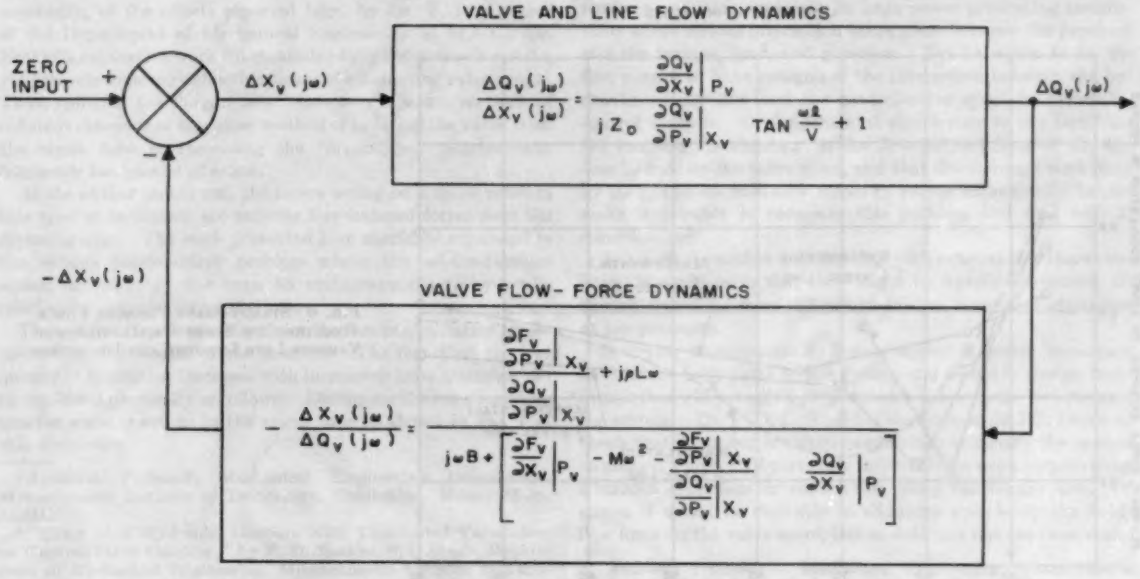
VALVE AND LINE FLOW DYNAMICS
ZERO INPUT
+
−
ΔXv(jω)
ΔQv(jω)/ΔXv(jω) = (∂Qv/∂Xv|Pv) / (jZo (∂Qv/∂Pv|Xv) TAN ωℓ/V + 1)
ΔQv(jω)
−ΔXv(jω)
VALVE FLOW- FORCE DYNAMICS
−ΔXv(jω)/ΔQv(jω) = ((∂Fv/∂Pv|Xv + jρLω) / (∂Qv/∂Pv|Xv)) / (jωB + ∂Fv/∂Xv|Pv − Mω² − (∂Fv/∂Pv|Xv)/(∂Qv/∂Pv|Xv) ∂Qv/∂Xv|Pv)

Fig. 3 Block Diagram of Closed-Loop System

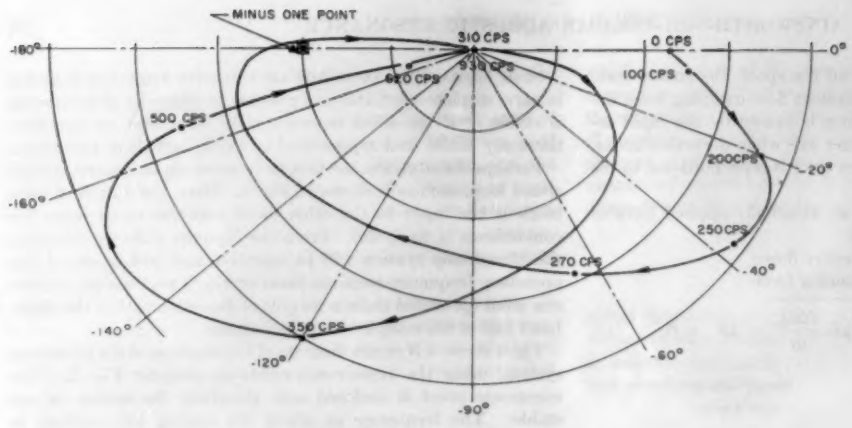


FIG. 4 FREQUENCY RESPONSE OF CLOSED-LOOP SYSTEM

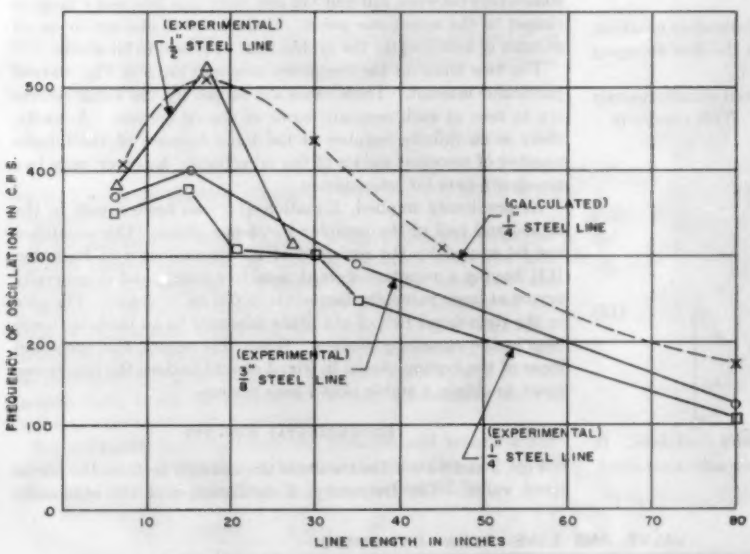


FIG. 5 SYSTEM FREQUENCY OF OSCILLATION FOR VARIOUS LINE LENGTHS AND DIAMETERS

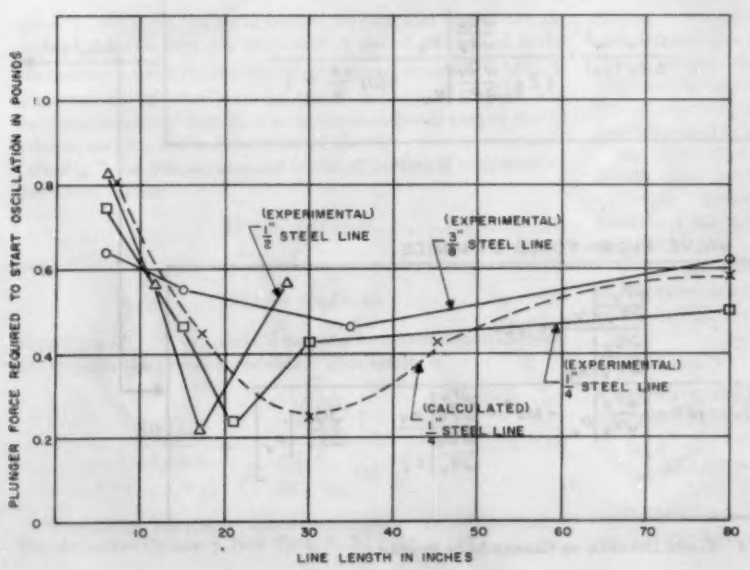


FIG. 6 STEADY-STATE PLUNGER FORCE REQUIRED TO START OSCILLATION FOR VARIOUS LINE LENGTHS AND DIAMETERS

applied, steady-state plunger force required to start the oscillation were recorded, using various line lengths and diameters. One set of calculated points also is plotted in Figs. 5 and 6 for comparison of the theoretical with the experimental results.

As can be seen, the frequency of oscillation is high, probably as a result of air entrained in the oil. Air entrained in the oil would make the oil more compressible and thus lower the velocity of sound through it. The experimental frequency of oscillation, therefore, would be lowered.

It is of particular interest to note that the frequency of oscillation generally goes down when the length of the line is increased. This is reasonable since the resonant frequency of the oil column is lowered when the length of the line is increased. Also, the force required to start the oscillation increases rapidly when the length of the line is decreased because theoretically the system must be stable when the length of the line is reduced to zero.

A steady-state plunger force is required in order to set the valve steady-state operating point, which establishes the proper and particular partial derivatives in Equations [6] and [11]. For the experiments, this force was applied through a rubber band having a very low spring rate.

### Conclusions

From the results of this study it can be concluded that the oil lines connected to the valve are a major factor in making an otherwise stable valve unstable. Therefore, to eliminate the instability, the oil lines should be (1) made as short as possible by moving the accumulator shown in Fig. 1 as close as possible to the valve, and (2) as dissipative as possible; also, adding a viscous damper to the valve plunger will help.

It is hoped that this analysis will give a basis for a better understanding of the phenomenon of valve squeal.

## Discussion

Gerhard Reethof.[5] The author has made a very definite contribution to our understanding of one further mechanism of valve instability. This paper represents a fine example of the effectiveness of "cross breeding" between the tools of the electrical engineer as applied to the mechanical-engineers' problems. Attention should be drawn to work done in parallel and independently, of the efforts reported here, by Dr. F. D. Ezekiel[6] of the Department of Mechanical Engineering at M.I.T. Dr. Ezekiel's exhaustive work substantiates fully the author's results, yet presents some very effective means of eliminating valve squeal. Thus, splitting the "organ tube" into two separate sections of different diameter or any other method of isolating the valve from the organ tube or increasing the "organ-pipe" quarter-wave frequency has proved effective.

As the author points out, the forces acting on a spool valve in this type of oscillation are entirely flow-induced forces near the metering edge. The work presented here should be expanded to the serious poppet-valve problem where the all-too-familiar squeal or "singing" has been an embarrassment to hydraulic relief-valve manufacturers and users.

The test results presented by the author are in qualitative agreement with the results of the analysis. The fact that the frequency of oscillation increases with increasing tube diameter can be explained physically as follows: During oscillation a standing quarter wave is set up in the organ tube as shown in Fig. 7 of this discussion.

[5] Assistant Professor, Mechanical Engineering Department, Massachusetts Institute of Technology, Cambridge, Mass. Mem. ASME.

[6] "Effect of a Hydraulic Conduit With Distributed Parameters on Control-Valve Stability," by F. D. Ezekiel, ScD thesis, Department of Mechanical Engineering, Massachusetts Institute of Technology, Cambridge, Mass., June, 1955.

The node is outside of the tube and moves inward with increasing tube diameter. Thus the physical length of the tube does not equal the quarter-wave length of the pressure wave causing a certain disagreement between analysis and experiment.

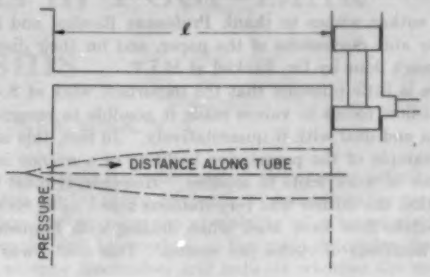


Fig. 7

The increase in frequency with increasing diameter also can be predicted from the analysis. Thus from Equation [6] and Fig. 3 of the paper the system becomes unstable when

$$Z_0 \left.\frac{\partial Q_v}{\partial P_v}\right|_{X_v} \tan \frac{\omega l}{V} = -1$$

Since

$$Z_0 = \frac{1}{A}\sqrt{\frac{\rho}{\beta}}$$

$$\frac{1}{A} \tan \frac{\omega l}{V} = \text{const}$$

Thus as $A$ increases $\tan \omega l/V$ must increase, or the frequency increases.

J. L. Shearer.[7] The fundamental concepts employed by the author in gaining a better understanding of an important hydraulic-control problem are old and well known. Liquid column dynamics have been studied thoroughly in connection with water-hammer problems, especially in large power-generating installations where serious interaction takes place between the penstock and the turbine, load, and governor. Yet he seems to be the first person to have recognized the interaction between the hydraulic supply line and the control-valve spool in hydraulic-control systems. Of fundamental significance is the fact that the coupling "mechanism" is the flow-induced force of the hydraulic fluid on the valve spool, and that the thorough work done by S.-Y. Lee on fluid-flow forces in valves undoubtedly helped make it possible to recognize this problem and deal with it quantitatively.

Although the author does not deal with exhaust-line characteristics, it would seem that they might be equally important, although somewhat more difficult to analyze because of cavitation at low pressures.

In trying to eliminate hydraulic squeal it seems important to consider both parts of the system and to apply design techniques that will provide a proper match between the two parts of the system. Dr. F. D. Ezekiel[6] has shown in an M.I.T. Doctoral thesis that a number of things can be done to modify the system to make it stable. Of particular interest is his work on providing a sudden expansion or contraction along the supply line. Of course it would be desirable to eliminate completely the fluid-flow force on the valve spool, but to date this has not been done.

[7] Assistant Professor of Mechanical Engineering, Massachusetts Institute of Technology, Cambridge, Mass. Mem. ASME.

It would seem that the results of this also could be applied to work with process-control valves, especially ones installed on long lines.

### Author's Closure

The author wishes to thank Professors Reethof and Shearer for their able discussions of the paper, and for their discussions of the work done by Dr. Ezekiel at M.I.T.

There is little question that the important work of S.-Y. Lee on fluid-flow forces in valves made it possible to recognize this problem and deal with it quantitatively. In fact, this is a very good example of the progressive build-up of a science in which one piece of work leads to another. However, it must be confessed that the author was very dubious about using S.-Y. Lee's steady-state flow force work when dealing with frequencies up in the hundreds of cycles per second. This doubt was caused by the possible large time delay required to establish the steady-state fluid flow patterns before the force can build up.

The exhaust-line characteristics would appear in the perturbation equations undistinguishable from the high-pressure line characteristics. However, in practice, the exhaust-line would cavitate and limit the amplitude of pressure oscillation to a low value which, though not as violent as squeal, could rapidly erode away the valve metering edges (which is another problem). This is in contrast to the pressure oscillation in the high-pressure line which can reach the amplitude of the supply pressure and therefore be very violent, and was the most urgent problem.

The explanation for the discrepancy between the calculated and experimental frequency of oscillation sounds very plausible. However, to be somewhat technical, all of Fig. 3, rather than just the top block, should have been used to prove the point.

# On the Maximum and Minimum Velocities and the Accelerations in Four-Link Mechanisms

By FERDINAND FREUDENSTEIN,[1] NEW YORK, N. Y.

**A method of analysis has been developed for obtaining (*a*) geometrical criteria for an extreme value of the angular velocity ratio of one link relative to another in a four-bar mechanism; (*b*) a direct method of determining the angular acceleration of the follower link of a four-bar mechanism, and maximum values of this acceleration in certain special cases. The results have been applied to a slider-crank mechanism.**

## Nomenclature

The following nomenclature is used in the paper:

Fig. 1 shows a four-bar linkage in which

$DA$ = fixed link, length equal to $d$
$AB$ = driving link, length equal to $a$
$BC$ = connecting link, length equal to $b$
$CD$ = follower link, length equal to $c$

All dimensions refer to center-line distances between pivot points.

$\phi = \angle DAB$ = displacement of driving link, radians
$\psi = \angle ADC$ = displacement of follower link, radians
$P$ = instant center or pole, located at intersection of $AB$ and $CD$
$O$ = point of intersection of $BC$ and $AD$
$OP$ = collineation axis (see reference 6)
$AA'$ = line segment parallel to $DD'$, $A'$, and $D'$ on connecting link

In the vector diagrams

$O'$ = point located at the infinitesimal distance $ds$ from $O$, both $O$ and $O'$ imagined rigidly attached to connecting link
$O''$ = point on line $OAD$, such that during infinitesimal displacement of the linkage, $O'$ moves to $O''$
$V_O$ = velocity of point $O$, on the connecting link
$V_{O1}$ = component of $V_O$, perpendicular to connecting link
$V_{O2}$ = component of $V_O$, parallel to connecting link
$v$ = angular velocity ratio, driven to driving link = $d\psi/d\phi$
$dt$ = infinitesimal interval of time
$V_{O1}dt$ = displacement of $O$, during time interval $dt$, in a direction perpendicular to connecting link
$V_{O2}dt$ = displacement of $O$, during time interval $dt$, in a direction parallel to connecting link

## Introduction

In the design of linkage mechanisms, values of the velocity and acceleration of the driven member are frequently desired. The velocity ratio (i.e., the ratio of the angular velocity of the driven link to that of the driving link) determines the mechanical advantage and thereby the operability of a given mechanism. The greatest and least values of this ratio determine the extent of the velocity fluctuation and indicate whether the motion is approximately uniform, harmonic, or irregular. The proportions of the links, on the other hand, are often determined by the magnitudes of the dynamic forces, which are functions of the accelerations in the mechanism. The methods which are presented are based on a well-known construction and concern the determination of these velocities and accelerations.

## Previous Work on Velocity Ratios

For prescribed limits of the velocity ratio in a given linkage, analytical methods for synthesizing the linkage proportions have been developed by S. Blokh (1),[2] R. Beyer (2), N. Rosenauer (3) and R. Kraus (4, 5). The latter stated (4) that at an extreme value of the velocity ratio in a drag linkage, the connecting link is perpendicular to the fixed link. This is an erroneous statement as demonstrated by N. Rosenauer (3). In so far as is known, however, the positions at which the velocity ratio become extreme have not been investigated further.

## Analysis of Extreme Values of Velocity Ratio in a Four-Bar Linkage

It is well known that in a four-bar linkage, the velocity ratio, $v$ (angular velocity of follower link divided by that of driving link) is equal to the ratio of the lengths of two parallel lines, such as $AA'/DD'$ in Fig. 1, drawn from the fixed pivots to the connecting link. Thus $v = AA'/DD'$. In the similar triangles $A'OA$, $D'OD$, $AA'/DD' = OA/OD$. Hence

$$v = \frac{OA}{OD} = \frac{OA/AD}{1 + OA/AD} \quad \ldots\ldots [1]$$

In a given linkage, $AD$ is fixed and $OA$ varies as the linkage moves. According to Equation [1], an extreme value of the velocity ratio $v$ occurs when $OA$ reaches an extreme value. The determination of the extreme-velocity position is converted, therefore, to the determination of an extreme-length position, namely, that of $OA$.

Consider point $O$ as rigidly attached to the connecting link. The velocity of $O$, $V_O$, is perpendicular to ray $OP$ and has a component $V_{O1}$ perpendicular to the connecting link and a component $V_{O2}$ parallel to the connecting link, Fig. 1. During an infinitesimal displacement of the linkage, defined by the change $d\phi$ of angle $\phi$, occurring in time interval $dt$, the motion is investigated of a point $O'$, attached to the connecting link at a distance $ds$ from $O$, such that during this displacement, $O'$ moves to $O''$ which is in line with the fixed link $AD$.

The vector $OO''$, as shown in Fig. 1, is equal to the vector sum

$$\overrightarrow{OO''} = \overrightarrow{ds} + \overrightarrow{V_{O1}dt} + \overrightarrow{V_{O2}dt} \quad \ldots\ldots [2]$$

---

[1] Assistant Professor, Department of Mechanical Engineering, Columbia University. Assoc. Mem. ASME.

Contributed by the Machine Design Division and presented at the Diamond Jubilee Semi-Annual Meeting, Boston, Mass., June 19–23, 1955, of The American Society of Mechanical Engineers.

Note: Statements and opinions advanced in papers are to be understood as individual expressions of their authors and not those of the Society. Manuscript received at ASME Headquarters, March 8, 1955. Paper No. 55—SA-20.

[2] Numbers in parentheses refer to the Bibliography at the end of the paper.

Equation [2] is based on the fact that the motion of $O'$, to a first order, is equal to the motion of $O$ and higher-order displacements are not considered. If the velocity ratio has an extreme value in Fig. 1, $OA$ is stationary relative to the first-order displacement $d\phi$ in virtue of Equation [1]. Thus $O'$ cannot be closer or further away from $A$ than $O$. Vector $V_{O2}dt$ in Equation [2] must therefore vanish (otherwise $OO'$ cannot be equal to zero). Hence $V_O$ is parallel to the connecting link $BC$, and $OP$, being perpendicular to $V_O$, is perpendicular to link $BC$. We have therefore established in a nonrigorous fashion:

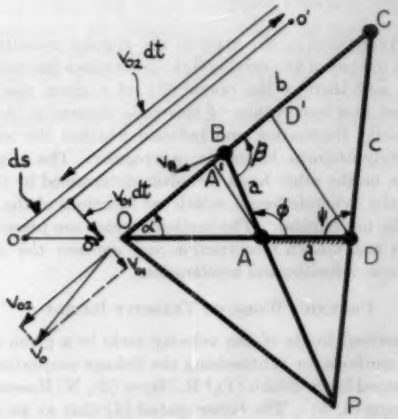


FIG. 1 FOUR-BAR LINKAGE, SHOWING CONSTRUCTION FOR VELOCITY-RATIO DERIVATIONS

*Theorem 1.* At an extreme value of the velocity ratio, $v$, in a four-bar linkage, the collineation axis ($OP$) is perpendicular to the connecting link ($BC$).

With a few additional steps we can determine a similar condition pertaining to the ratio of the angular velocity of the connecting link to that of the driving link, which is equal to $d\alpha/d\phi$ (Fig. 1).

From Fig. 1

$$\alpha = \phi + \beta - 180^\circ$$

whence

$$d\alpha/d\phi = 1 + d\beta/d\phi$$

Hence a maximum value of $d\alpha/d\phi$ occurs at an extreme value of $d\beta/d\phi$ and thus also of $d\phi/d\beta$. The extreme value of $d\phi/d\beta$ can be derived by inversion of Theorem 1, in which $AB$ is considered stationary. In this inversion, $v\,(=d\psi/d\phi) \rightarrow d\phi/d\beta$, $BC \rightarrow CD$, and $OP$ remains unchanged as it is a symmetric parameter (7). This inversion leads to the following:

*Theorem 2.* At an extreme value of the ratio of the angular velocity of the connecting link to that of the driving link in a four-bar linkage, the collineation axis ($OP$) is perpendicular to the follower link ($CD$).

$PB$ has an extreme value also. A rigorous proof of Theorem 1 is outlined in the Appendix, section 1. The truth of Theorem 2 follows by inversion. The analytical expression for the extreme value of the velocity ratio $v$ is lengthy and is derived in the Appendix, section 2.

## CONSTRUCTION OF LINKAGES WITH PRESCRIBED EXTREME VALUE OF VELOCITY RATIO, $v$

Draw the fixed link $AD$, of unit length, as shown in Fig. 2. Locate point $O$ in line with $AD$ such that $OA = v/(1-v)$, where $v$ is the extreme value of the velocity ratio. Point $O$ may be either to the left or to the right of $A$. From $O$, draw two mutually perpendicular rays, $OR_1$ and $OR_2$, at an arbitrary inclination, $\theta$, to the line of centers $AD$. Select a pole $P$ anywhere on either of the rays, say, on $OR_2$. From $P$, draw rays $PAB$, $PDC$, which intersect ray $OR_1$ at points $B$, $C$, respectively. Then $ABCD$ or $AB_1PD$ represents the desired linkage. By varying $r$ and $\theta$, the most suitable linkage proportions can be selected. Further investigation is necessary, however, to ascertain whether $v$ is a maximum, a minimum, or at a point of inflection.

Fig. 3 shows the two extreme positions of a crank-and-rocker linkage, characterized by the subscripts 1 and 2. Fig. 4 in a similar manner shows the extreme positions of a drag linkage. In a crank-and-rocker linkage, one extreme value occurs when $O$ is between $A$ and $D$. In a drag linkage, $O$ lies outside $AD$ in both

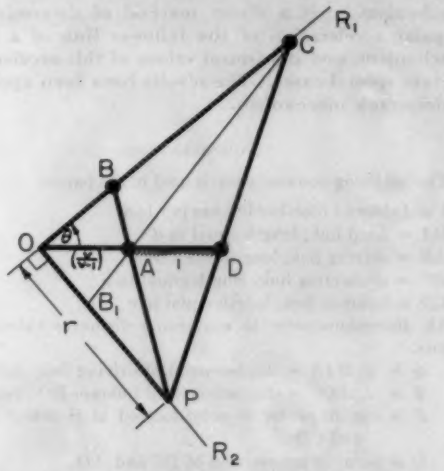


FIG. 2 CONSTRUCTION OF LINKAGE WITH PRESCRIBED EXTREME VALUE OF THE VELOCITY RATIO, $v$

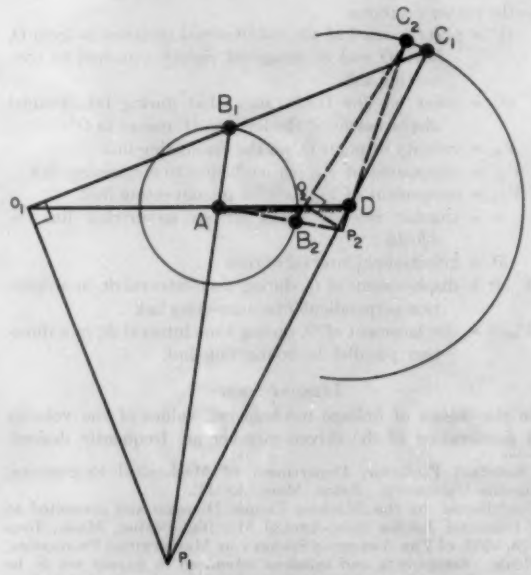


FIG. 3 EXTREME VELOCITY-RATIO POSITIONS OF A CRANK-AND-ROCKER LINKAGE

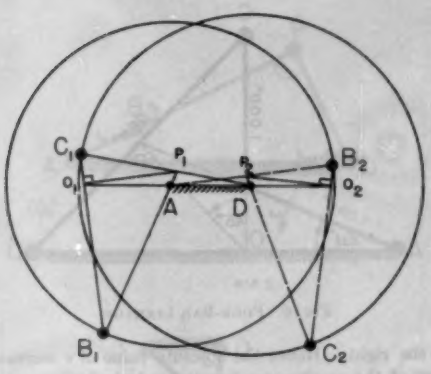


FIG. 4 EXTREME VELOCITY-RATIO POSITIONS OF A DRAG LINKAGE

positions. In both linkages, a maximum value of $v$ occurs when $O$ is to the right of $A$, assuming that $AB$ is the driving link, $AD$ horizontal, and $A$ the left pivot (the driving link of the drag linkage is assumed to be the lagging link).

## EXTENSION TO ACCELERATION ANALYSIS OF A FOUR-BAR LINKAGE

The acceleration of points on a four-bar linkage, in which the driving crank rotates at a constant angular velocity, is determined by purely geometrical considerations. A method based on these considerations can be expected to supplement the acceleration constructions using relative velocities (8, 9, 10). The method of analysis used in the previous portion of this paper, namely, the conversion of a velocity analysis to a distance analysis (i.e., to a purely geometrical analysis) will be extended in this connection. In Fig. 5, $ABCD$ is a four-bar linkage. Nomenclature is identical with that of Fig. 1. The angular velocity of the driving link, $AB$, is denoted by $\omega = d\phi/dt$ and is considered constant unless otherwise indicated. $PN$ and $MD$ are perpendicular to $BC$.

$V_B$ = linear velocity of $B$, in/sec
$V_C$ = linear velocity of $C$, in/sec
$a_{et}$ = tangential acceleration of $C$, in/sec$^2$
$\theta = \tan^{-1}(a_{en}/a_{et})$
$a_{en}$ = normal acceleration of $C$, in/sec$^2$
$\alpha_c$ = angular acceleration of follower link, rad/sec$^2$

As before, we consider the motion of a point $O'$, located infinitesimally close to point $O$ (both being attached to $BC$) such that during an infinitesimal displacement $d\phi$ of angle $\phi$, point $O'$ is displaced to $O''$, which is on the line of centers $AD$. The displacement of $O$ is shown on an enlarged vector diagram, Fig. 5. The displacement has a component $V_{O1}dt$ perpendicular to $BC$, and a component $V_{O2}dt$, parallel to $BC$, the total displacement being $V_O dt$. On the enlarged diagram, $OO''$ is shown equal to $OD$ and $O''$ is coincident with $D$.

Let the change in $OA$ during the infinitesimal displacement be equal to $dx$, where $OA = x$. Then

$$OO'' = dx \quad [3]$$

From Equation [1]

$$v = \frac{d\psi}{d\phi} = \frac{x}{x+d} = 1 - \frac{d}{x+d} \quad [4]$$

Differentiating Equation [4] with respect to $\phi$, we have

$$\frac{d^2\psi}{d\phi^2} = \frac{d}{(x+d)^2}\frac{dx}{dt}\frac{1}{\omega} \quad [5]$$

Furthermore, $V_{O1}/V_B = ON/BP$, where $V_B$ is the velocity of $B$. Therefore

$$V_{O1} = \frac{ON}{BP}a\omega \quad [6]$$

From the similar triangles $ORO''$, $OMD$, we have

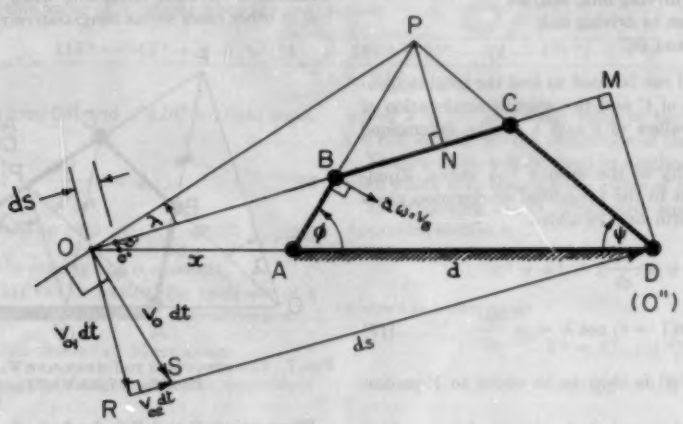


FIG. 5 FOUR-BAR LINKAGE, SHOWING CONSTRUCTIONS FOR ACCELERATION DERIVATIONS

$$MD/OD = OR/OO'' = (V_{O1}dt)/(dx) = V_{O1}/(dx/dt) \quad [7]$$

The tangential acceleration of $C$, $a_{et}$ is given by

$$a_{et} = \frac{dV_C}{dt} = \frac{d(c\omega v)}{dt} = c\omega\frac{dv}{dt} = c\omega^2\frac{d^2\psi}{dt^2} \quad [8]$$

Thus, eliminating $V_{O1}$ from Equations [6] and [7] and substituting the value of $dx/dt$ thus obtained into Equation [5], an expression for $d^2\psi/d\phi^2$ is obtained which, when substituted into Equation [8], yields

$$a_{et} = c\omega^2 ad\,\frac{ON}{PB \cdot MD \cdot OD} \quad [9]$$

Let $a_{en}$ = normal acceleration of $C = (V_C^2)/c = \omega^2 c^2$ . . . . . [10]

Since

$$v = OA/OD = (PC/c)/(PB/a) \quad [11]$$

$$v^2 = \frac{OA}{OD}\,\frac{PC}{PB}\,\frac{a}{c} \quad [12]$$

and

$$a_{cn} = \omega^2 a\,\frac{OA}{OD}\,\frac{PC}{PB} \quad [13]$$

Dividing Equation [13] by Equation [9], noting that $PN/PC = MD/c$, and simplifying, we have

$$\tan\theta = a_{cn}/a_{ct} = \frac{OA}{AD}\,\frac{PN}{ON} = \frac{v\tan\lambda}{1-v} \quad [14]$$

where $\lambda$ is the angle between the collineation axis $OP$ and link $BC$. Substituting for $a_{cn}$ and $\tan\theta$ the right-hand sides of Equations [10] and [14], the Equation $a_{ct} = a_{cn}/\tan\theta$ becomes

$$a_{ct} = c\omega^2 v(1-v)\cot\lambda \quad [15]$$

Using Equation [15] and the fact that $\alpha_c = a_{ct}/c$, we obtain the following:

*Theorem 3.* The angular acceleration of the follower link of a four-bar linkage in which the driving link rotates at constant angular velocity, is given by

$$\alpha_c = \omega^2 v(1-v)\cot\lambda \quad [16]$$

where

$\omega$ = angular velocity of driving link, rad/sec
$v$ = velocity ratio, driven to driving link
$\lambda$ = angle between $OP$ and $BC$

Equations [10, 14, 15, 16] can be used to find the total tangential or normal acceleration of $C$ and the angular acceleration of the follower link. The values of $v$ and $\lambda$ can be determined graphically.

When the angular velocity of the driving link varies, Equation [10] remains valid, but to the tangential acceleration given by Equation [15] another term must be added

$$a_{ct} = c\,\frac{d(\omega v)}{dt} = c\omega^2\,\frac{d^2\psi}{d\phi^2} + cv\,\frac{d\omega}{dt}$$

$$= c\omega^2 v(1-v)\cot\lambda + cv\,\frac{d\omega}{dt} \quad [17]$$

Similarly, the term $(v\,d\omega/dt)$ is then to be added to Equation [16].

## Example and Discussion

Let it be required to determine the angular acceleration of the follower link $CD$, Fig. 6, when the driving link is rotating at the constant rate of 10 rad/sec. This is the acceleration of interest in the stress analysis of additional rotating elements (such as gear trains, for instance) which may be actuated by the follower link.

The collineation axis $OP$ is drawn as shown. The velocity ratio, $v = OA/OD = -0.7071$, the minus sign indicating that $CD$ rotates in a direction opposite to that of $AB$. The velocity ratio is positive or negative according as $O$ lies outside or inside $AD$. $\cot\lambda = \cot\angle POC = \cot 45° = 1$. Hence, numerically

$$\alpha_c = \omega^2 v(1-v)\cot\lambda = (10^2)\,(0.7071)\,(1.707)\,(1)$$
$$= 120.7 \text{ rad/sec}^2$$

As $AB$ rotates slightly, it is clear from Fig. 6, that point $O$ moves toward the right. Hence the absolute value of $v$ increases and the sense of the acceleration is counterclockwise.

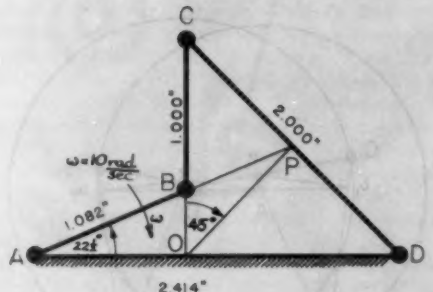


Fig. 6 Four-Bar Linkage

Conventional analyses (8) involve the following determinations:

(*a*) Component of acceleration of $B$ along $BC$.
(*b*) Angular velocity of $C$ relative to $B$.
(*c*) Acceleration of $C$ relative to $B$.
(*d*) Sum of items (*a*) and (*c*).
(*e*) Normal acceleration of $C$.
(*f*) Total acceleration of $C$, using items (*d*) and (*e*).
(*g*) Projection of this acceleration along normal to $CD$.

These proceedings involve the construction of velocities as well as intermediate calculations, but do not require the use of a formula, such as that stated in Theorem 3. The method of Theorem 3 becomes unreliable when angle $\lambda$ approaches zero, but in other cases seems comparatively rapid and simple.

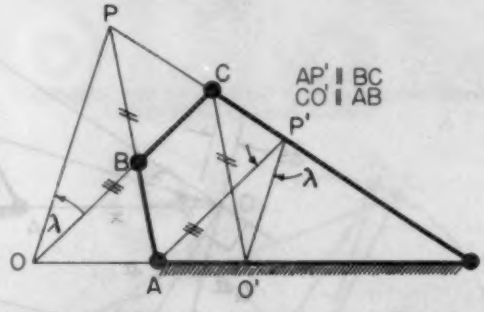


Fig. 7 Construction to Determine Value of λ When Collineation Axis Lies Far From Linkage

When points $O$ and $P$ lie far from the linkage, the construction shown in Fig. 7 can be used. In Fig. 7, $AP'$ and $BA$ are parallel to $BC$ and $CO'$, respectively. From this it follows by similar triangles that $O'P'$ is parallel to $OP$. Angle $\lambda$ can then be measured from $O'P'$ without drawing $OP$.

## Extreme Values of Angular Acceleration of Follower Link of a Four-Bar Linkage

The preceding results suggested an investigation, details of which warrant inclusion in the Appendix (section 3) only, but the results of which will be summarized briefly:

An extreme value of the angular acceleration of link $CD$ of a crank-and-rocker linkage occurs when the driving link is parallel to the connecting link and $\angle BCD$ is a right angle. For the case shown in Fig. 8(*a*)

$$\alpha_c(\max) = \frac{\omega^2 a}{bc}(a+b) \quad [18]$$

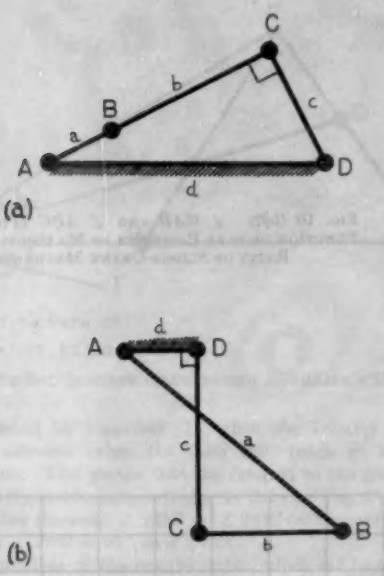


FIG. 8 LINKAGES WITH MAXIMUM VALUES OF ANGULAR ACCELERATION OF FOLLOWER LINK

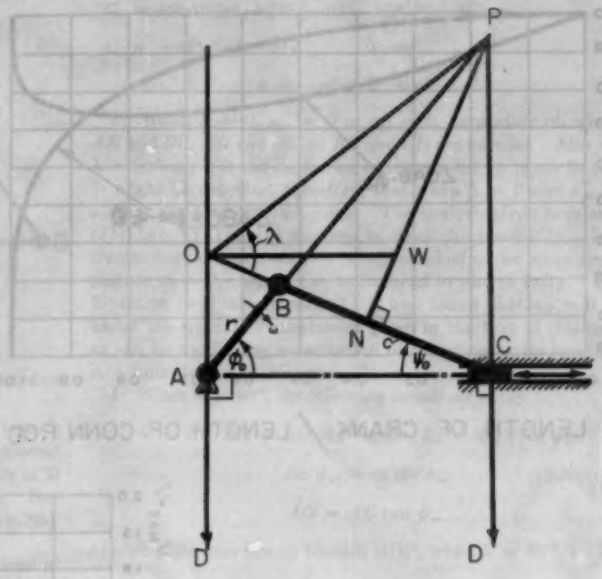


FIG. 9 SLIDER-CRANK MECHANISM

where $(a + b)^2 + c^2 = d^2$ ..... [19]

and the angular velocity of the driving link is constant.

In a drag linkage, an extreme value of $\alpha_c$ occurs when the connecting link is parallel to the fixed link and $\angle ADC$ is a right angle. For the case shown in Fig. 8 (*b*)

$$\alpha_c\,(\max) = \frac{\omega^2 d}{bc}(b + d) \quad \ldots\ldots [20]$$

where $(b + d)^2 + c^2 = a^2$ ..... [21]

and the angular velocity of the driving link is constant.

Equations [18] through [21] can be used in the synthesis of a four-bar linkage with prescribed acceleration characteristics.

### APPLICATION TO A SLIDER-CRANK MECHANISM

Fig. 9 shows a slider-crank mechanism with the equivalent four-bar linkage background.

$AB$ = driving crank, length equal to $r$
$BC$ = connecting rod, length equal to $c$
$OP$ = collineation axis of equivalent four-link mechanism
$\omega = d\phi_o/dt$ = constant angular velocity of crank $AB$, rad/sec
$v_o$ = velocity ratio (velocity of $C$ divided by that of $B$)
$V$ = maximum value of velocity ratio, $v_0$
$\lambda = \angle COP$, angle between $OP$ and $BC$
$\phi_o = \angle BAC$; when $v_o = V$, $\phi_o = \phi_m$
$\psi_o = \angle ACB$; when $v_o = V$, $\psi_o = \psi_m$
$m = r/c$
$a_b$ = acceleration of $B$, in/sec$^2$
$a_c$ = acceleration of $C$, in/sec$^2$
$v_c$ = velocity of $C$, in/sec
$OW$ = line through $O$, parallel to $AC$, $W$ being on $PN$

The maximum value of the velocity ratio, $v_o$, occurs when the collineation axis, $OP$, is perpendicular to the connecting rod $BC$, as stated in Theorem 1. The analytical formulation of this condition is derived in Appendix, section 4, and leads to the equation

$$m^2 = \frac{11V^4 - 14V^2 + 2 + \sqrt{(11V^4 - 14V^2 + 2)^2 - 4(1 - V^2)(1 + V^2)^2}}{2(1 + V^2)^2} \quad \ldots\ldots [22]$$

where $V$ is the maximum value of the velocity ratio, $v_o$, and $m$ ($= r/c$) determines the proportion of the mechanism.

This equation can be used to synthesize a slider-crank mechanism which is to have a given value of $V$.

The following set of parametric equations is derived in the Appendix, section 4

$$m^2 = t(1 + t - t^2),\ 0 \le t \le 1 \quad \ldots\ldots [23]$$

where $t$ is a parameter

$$V^2 = t(1 + t)^2/m^2 \quad \ldots\ldots [24]$$

$$\sin^2 \phi_m = t/m^2 \quad \ldots\ldots [25]$$

$$\sin(\phi_m + \psi_m) = V\sqrt{1 - t} \quad \ldots\ldots [26]$$

where $\phi_m$, $\psi_m$ are the values of $\phi_o$, $\psi_o$ when $v_o = V$.

Two graphs were constructed with the aid of these equations. Fig. 10 shows the exact values of the crank displacement ($\phi_m$) and of the angle between crank and connecting rod ($\angle ABC$ in Fig. 9) at positions of maximum velocity ratio, for different values of the mechanism proportion ratio $m$. Fig. 11 shows the maximum velocity ratio $V$ as a function of the mechanism proportion ratio $m$. In the case of harmonic motion, $m = 0$, $V = 1$, and the angles shown in Fig. 10 are right angles. The deviations from this limiting case are evident from the figures.

The acceleration of $C$, $a_c$, is equal to the acceleration $a_{cl}$ of Equation [15]

$$a_c = c\omega^2 v(1 - v)\cot\lambda \quad \ldots\ldots [27]$$

In a slider-crank mechanism, the angular velocity $v$ of the follower link is equal to zero, and the linear velocity of $C$, $v_c$ is equal

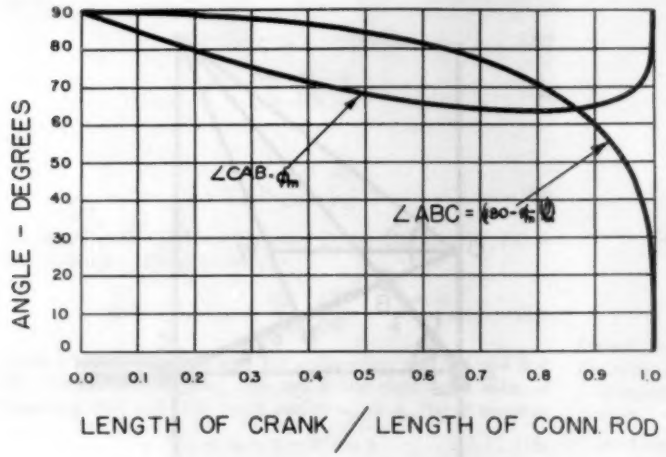


FIG. 10 (*left*) ∠ *CAB* AND ∠ *ABC* (FIG. 9) AS A FUNCTION OF *m* AT POSITIONS OF MAXIMUM VELOCITY RATIO OF SLIDER-CRANK MECHANISM

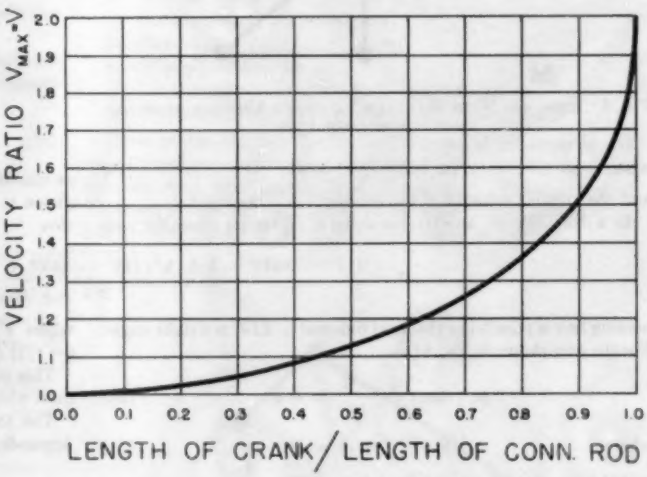


FIG. 11 (*right*) MAXIMUM VALUE, *V*, OF VELOCITY RATIO OF A SLIDER-CRANK MECHANISM AS A FUNCTION OF MECHANISM PROPORTION RATIO *m*

to ($c\omega v$). Hence Equation [27] becomes

$$a_c = v_c\,\omega \cot \lambda \left( = a_b \frac{OW}{PB} \right) \quad \ldots\ldots\ldots\ldots [28]$$

## CONCLUSION

The velocity fluctuation and the acceleration of mechanisms, the equivalent four-bar linkage background of which can be identified, can be analyzed by the methods of this paper. The investigation was suggested by a consideration of the significance of the collineation axis, *OP*, regarded as a symmetric parameter.

## BIBLIOGRAPHY

1 "On the Synthesis of Four-Bar Mechanisms" (in Russian), by S. Blokh, Bull. Academy of Science, USSR, Technical Science Division, 1940, No. 1 (listed in reference 2).

2 "Gelenkvierecke mit Vorgeschriebenen Geschwindigkeits und Beschleunigungsverhaeltnissen," by R. Beyer, *Werkstattstechnik*, vol. 37, 1943, pp. 293–295.

3 "Gelenkvierecke mit Vorgeschriebenen Groesst und Kleinstwerten der Abtriebswinkelgeschwindigkeit," by N. Rosenauer, *Werkstattstechnik*, vol. 38, 1944, pp. 25–27.

4 "Die Doppelkurbel und Ihre Geschwindigkeitsgrenzen," by R. Kraus, *Maschinenbau/Getriebetechnik*, vol. 18, 1939, pp. 37–41 (same as vol. 7 of *Reuleaux Mitteilungen*).

5 "Zur Synthese der Doppelkurbel," by R. Kraus, *Maschinenbau/Getriebetechnik*, vol. 18, 1939, pp. 93–94.

6 "Kinematics of Mechanisms," by N. Rosenauer and A. H Willis, Associated General Publications Printing, Ltd., Sydney, Australia, 1953—collineation axis on pp. 86, 191.

7 "Design of Four-Link Mechanisms," by F. Freudenstein, PhD thesis at Columbia University, publication No. 8252 of University Microfilms, Inc., Ann Arbor, Mich., 1954, p. IV–7 on "Symmetric Parameters"; p. VI–32 for Table 9.

8 "Engineering Kinematics," by A. Sloan, The Macmillan Company, New York, N. Y., 1947, pp. 280–284 on "Acceleration Analysis."

9 "Semigraphical Solution of Acceleration Problems of Plane Cam-Driven Roller Followers and Four-Bar Linkages," by Chun Hung Chiang, ASME Paper No. 54—F-15.

10 "A Uniform Method for Determining Angular Accelerations in Mechanisms," by L. R. Koenig, *Journal of Applied Mechanics*, Trans. ASME, vol. 68, 1946, pp. A-41–A-44. Discussion pp. A-309–A-313.

11 "Kinematische Getriebesynthese," by R. Beyer, Julius Springer, Berlin, Germany, 1953.

12 "On Three-Bar Motion," by A. Cayley, Proceedings of the London Mathematical Society, vol. 7, 1876, pp. 136–166.

# Appendix

1 The following concise proof of Theorem 1 is due to Prof. A. S. Hall of Purdue University and his derivation is hereby gratefully acknowledged:

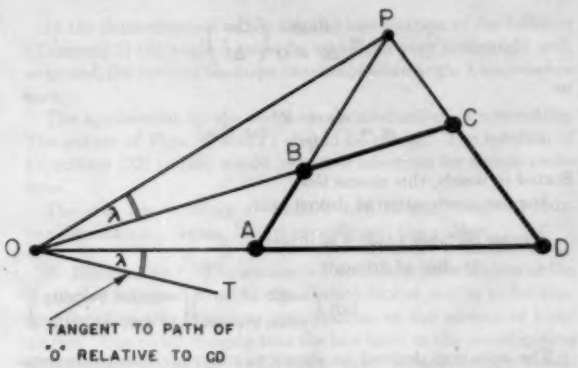


FIG. 12 FOUR-BAR LINKAGE ILLUSTRATING BOBILLIER'S THEOREM

As established by Equation [1], when the velocity ratio $v$ reaches an extreme value, $OA$ (and $OD$) reach an extreme value, likewise. This means that the tangent to the path of $O$ relative to $CD$ must be perpendicular to $OD$ (see Fig. 12). But by the Bobillier theorem, $\angle TOD = \angle POC$ (reference 6, p. 86). Hence, when $\angle TOD = 90°$, so is $\angle POC$.

2 The equations of the coupler curve, which can be found in A. Cayley (12), are given (reference 11, p. 154) in Cartesian coordinates. The $+x$-axis is in the direction $A$ to $D$, Fig. 1, the origin is at $A$, and the $+y$-axis is vertical and up. Consider point $O$ on the connecting link such that $OB = u$ and $O$ is on the $x$-axis. Writing Equation [277] (reference 11, p. 154) for $y = 0$, we obtain an equation for the abscissa $x$ of point $O$

$$u(x-d)\,[x^2+(u+b)^2-a^2] - x(u+b)\,[(x-d)^2+u^2-c^2] = 0 \quad [29]$$

According to Theorem 1, at an extreme value of the velocity ratio, $dx/du = 0$. Solving for $dx/du$ from Equation [29] and equating the numerator to zero, we have

$$(x-d)^2\,[x^2+(u+b)^2-a^2] - x[(x-d)^2+u^2-c^2] = 2ud(u+b) \quad [30]$$

Solving Equations [29] and [30] for $x$, the velocity ratio can be obtained from the equation $v = x/(x+d)$. The expression for $x$ is

$$C_1x^6 + C_2x^5 + C_3x^4 + C_4x^3 + C_5x^2 + C_6x + C_7 = 0 \quad [31]$$

where

$$C_1 = -4(d^2-b^2)^2 \quad [32]$$

$$C_2 = d[128(a^2-c^2)\,(3d^2+5b^2) - 12(d^2-b^2)n] \quad [33]$$

$$C_3 = 44b^2c^2d^2 - 12a^2d^4 + 4b^4c^2 - n^2(b^2+12d^2) - 100a^2b^2d^2 \quad [34]$$

$$C_4 = (72b^2d^2-24b^4d)\,(c^2-d^2) + 128b^4d^2 - n(a^2-b^2)\,(2b^2d+24d^3) + 4b^2dn^2 - 4dn^2 + n(18b^2c^2d - 18b^2d^3) + 80b^2d^2(a^2-b^2-n) \quad [35]$$

$$C_5 = 27b^2d^2(c^2-d^2)^2 + 48b^4d^2(c^2-d^2) - (a^2-b^2)^2(12d^4+b^2d^2) + n^2(8b^2d^2-12a^2d^2) + 36b^2d^2n(d^2-c^2) + (a^2-b^2) \times (-98b^2d^4 + 18b^2c^2d^2 + 8b^2d^2n) - 64b^4d^4 \quad [36]$$

$$C_6 = 4d^2a^2[3(a^2-b^2)\,(-n) - 8b^2(c^2-d^2)] \quad [37]$$

$$C_7 = -4d^4a^2(a^2-b^2)^2 \quad [38]$$

$$n = -a^2+b^2+c^2-d^2 \quad [39]$$

3 When $\lambda = 0$, $a_{cm} = 0$ or $a_{ci} = 0$, depending on whether $AB$ and $BC$, $AD$ and $BC$, or $BC$ and $CD$ are parallel. Also when $\lambda = 90°$, $a_{ci} = 0$ and $a_{cm}$ has an extreme value for many linkages. It might be expected, therefore, that when $\lambda = 0$ and $a_{cm} = 0$, $a_{ci}$ may reach an extreme value. The analysis given in reference (7) (chap. VI, Table 9) was used to check this possibility. In the terminology of reference (7), it was checked under what circumstances $m_3 = 0$, assuming $m_1$ to be equal to zero or unity. Using Equation [9-1] of reference (7), it was found that $a_{ci} = 0$ only under the special circumstances given in the text of this paper, as can be verified by substitution of the appropriate conditions into Equation [9-1], reference (7).

4 When $\lambda = 90°$, the following equations apply

$$V = PC/PB = AO/AB = \sin(\phi_m+\psi_m)/\cos\psi_m \quad [40]$$

$$\sin\psi_m = m\sin\phi_m \quad [41]$$

$$AO = AC\tan\psi_m \quad [42]$$

Applying the sine law to triangle $AOP$, when $\lambda = 90°$, we have

$$\frac{AO}{\sin(\phi_m+\psi_m-90°)} = \frac{AC/\cos\phi_m}{\sin\psi_m} \quad [43]$$

Combining Equations [42] and [43], we have

$$\tan\psi_m = -\frac{\cos(\phi_m+\psi_m)}{\sin\psi_m\cos\phi_m} \quad [44]$$

Eliminating $\psi_m$ from Equations [41] and [44], we obtain

$$m^4\sin^6\phi_m - m^2\sin^4\phi_m - \sin^2\phi_m + 1 = 0 \quad [45]$$

which can be written in the form

$$m^2(1-\sin^2\phi_m) = m^4\sin^4\phi_m(1-m^2\sin^2\phi_m) \quad [46]$$

Taking the square root of both sides of Equation [46], we have

$$\cos\psi_m = \cos\phi_m/(m\sin^2\phi_m) \quad [47]$$

Using Equations [47] and [41] to eliminate $\psi_m$ from Equation [40], we have

$$V = \sin\phi_m(1+m^2\sin^2\phi_m) \quad [48]$$

Squaring Equation [48] and subtracting the result from Equation [45] in order to eliminate the term in $(m^4\sin^6\phi_m)$, we obtain

$$3(m^2\sin^2\phi_m)^2 + 2(m^2\sin^2\phi_m) - m^2 - V^2m^2 = 0 \quad [49]$$

Solving for $(m^2\sin^2\phi_m)$ using Equation [49] and substituting the result into Equation [48], Equation [22] of the text is eventually obtained.

The parameter $t$, defined in Equation [25], can be defined by the equivalent equation

$$t = \sin^2\psi_m \quad [50]$$

where $0 \le t \le 1$. Equations [45, 48, 40] can be transformed into Equations [23, 24, 26] of the text. The minimum value of $\sin\phi_m$ is equal to $\sqrt{0.8}$ and occurs when $m^2 = 5/8$, as can be deduced from Equations [23] and [25].

# Discussion

ALLAN H. CANDEE.[3] The writer will discuss Theorems 1 and 3 of the paper by referring to the kinematics of toothed gearing, inasmuch as the equivalent four-bar linkage for a pair of rotating gears behaves in the same way instantaneously as other four-bar linkages. Gears may operate at a constant ratio of angular velocities in which case their pitch curves are circular, or they may have noncircular pitch curves and a varying ratio.

In noncircular gears, at a position of maximum or minimum ratio, it is obvious that the pitch curves cross the line of centers at right angles, and that they then instantaneously conform to pitch circles. With these ideas in mind we can restate Theorem 1 in the terminology of gearing as follows:

At an extreme value of the velocity ratio in a pair of noncircular gears, in the instantaneously equivalent linkage, the line connecting the pitch point $O$ to the instant center $P$ of the common normal $B$-$C$ of the tooth profiles is perpendicular to the normal itself.

This fact has long been known in the literature of kinematics and gearing. It is believed to have been discovered by Euler (1765) and it was used by Willis (1841) in a geometrical construction for locating centers of curvature in gear-tooth profiles.[4]

An easy way to arrive at the perpendicular relation described in the theorem can be shown by referring to Fig. 2 of the paper. Point $O$ is the instant center (pole) of the relative motion between links $A$-$B$ and $D$-$C$. At a maximum or minimum ratio of angular velocities point $O$ must be instantaneously at rest in the stationary line $A$-$D$, which means that the point of link $B$-$C$ at position $O$ must be instantaneously moving in the direction of $B$-$C$. Because $P$ is the instant center of $B$-$C$ relative to line $A$-$D$, line $P$-$O$ must therefore be perpendicular to $B$-$C$. The relation stated in the theorem has thus been known without benefit of mathematical analysis.

During the last Annual Meeting of the Society there was some discussion about accelerations in linkages. The writer has not had much occasion to deal with accelerations, but it occurred to him that the conditions in noncircular gearing could be used to derive an equation for the value of angular acceleration. This was done a short time later, and a brief outline of the method used may be interesting. Only a very simple diagram is needed, Fig. 13, herewith.

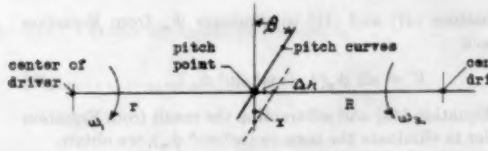


FIG. 13 DISPLACEMENTS IN NONCIRCULAR GEARS

For a small increment of time $\Delta t$, there is a displacement $\Delta x = r\omega_1\Delta t$ of the pitch curves, and a corresponding increment $\Delta r = \Delta x \tan \beta$ of the pitch radii $r$ and $R$. Originally the angular velocity of the driven gear is $\omega_2 = (r/R)\omega_1$. After the time interval

$$\omega_2 = \frac{r + r}{R - r}\,\omega_1$$

The velocity increment of the gear is $\Delta\omega = \omega_2 - \omega_2$.

Making substitutions and dividing by $\Delta t$ easily yields the angular acceleration of the gear

$$\alpha = \underset{\Delta t = 0}{\text{limit}} \left(\frac{\Delta\omega}{\Delta t}\right)$$

or

$$\alpha = \frac{r(r + R)}{R^2} \tan \beta\, \omega_1^2$$

Stated in words, this means that

Angular acceleration of driven gear

$$= \frac{(\text{center distance})(\text{radius of driver})}{(\text{radius of driven})^3} \tan\begin{pmatrix}\text{angle of}\\ \text{pitch curves}\end{pmatrix}\begin{pmatrix}\text{angular velocity}\\ \text{of driver}\end{pmatrix}^2$$

The equation derived as shown can be rewritten to conform exactly with Equation [16] of Theorem 3 of the paper. This requires recognizing ($a$) that angle $\beta$ is the complement of angle $\lambda$ of Figs. 5 and 12, ($b$) that the pitch point of the gears is located between the centers of rotation, and ($c$) that the velocity ratio $v = (r/R)$.

The writer had supposed that angular velocities in linkages were fully covered in kinematic literature, but he does not know whether the method of derivation shown in the foregoing is new or not. It seems to be shorter and simpler than the one presented in the paper.

V. L. DOUGHTIE.[5] The author is to be commended for his contribution to the study of the four-bar mechanism. He gives a simple and direct method of obtaining the angular-velocity ratios of one link relative to another and the extreme values of these ratios. The design of a linkage for prescribed extreme values of the velocity ratio is presented. He also gives a method of obtaining the angular acceleration of the follower of a four-bar mechanism in which the driving crank rotates at a constant angular velocity. This tool is also applied to the slider-crank mechanism in which the crank rotates at a constant angular velocity. For various ratios of the length of crank to connecting rod, the linear velocity ratio of the sliding member to the crankpin, the maximum value of this ratio, and the position of the crank for the maximum value of the linear velocity of the slider are obtained. The acceleration of the slider is also obtained. The comments which follow are suggestions and not criticisms of the paper.

The terms "four-link mechanisms," "four-bar mechanisms," and "four-bar linkages" have the same meaning throughout the paper. Would it be desirable to standardize some of the terms we use in "Mechanism?"

The notation could be improved. Why use $v$ for the angular velocity ratio? At one point $v$ is used as "the angular velocity of the follower," and $v_0$ is used to represent the linear-velocity ratio. Referring to Fig. 1, $O$, $O'$, $O''$ are upper case in the text but lower case in the vector diagram in Fig. 1. The letter $O$, in Fig. 5, is upper case throughout. In Fig. 5, $a$ is used for the length of the crank but in Fig. 9, $r$ is used for the length of the crank. Also, in Fig. 5, $b$ is the length of the connecting rod whereas in Fig. 9, $c$ is used. A consistent notation would cause the paper to be more easily understood.

It was hoped that the author's Theorem 1 would give a quick solution to the old problem of finding the maximum angular velocity of the follower crank of the nonparallel equal crank mechanism when the speed of the driving crank is known. Since the location of $O$ when $O$-$P$ is perpendicular to the connecting link $B$-$C$ is not definite, the method cannot be used in obtaining an accurate value.

[3] Retired, Rochester, N. Y. Fellow ASME.

[4] "A Brief Account of Modern Kinematics," by A. E. R. de Jonge, Trans. ASME, vol. 65, 1943, discussion on p. 680.

[5] Professor, Department of Mechanical Engineering, University of Texas, Austin, Texas. Fellow ASME.

In the determination of the angular acceleration of the follower (Theorem 3) the angle $\lambda$ must be measured very accurately and, as stated, the method becomes unreliable when angle $\lambda$ approaches zero.

The application to the slider-crank mechanism is interesting. The curves of Figs. 10 and 11 should be useful. The solution of Equations [22] to [26] would be rather laborious for simple problems.

Theorem 1 is certainly a valuable tool in analyzing the four-bar mechanism. Again, let me compliment the author.

N. Rosenauer.[6] The author is a notable representative of the family of kinematicians in the United States and is to be congratulated on this ingenious contribution to the science of kinematics. One could imagine that the last word in the investigation of the properties of the "collineation axis," established by Bobillier, has already been said, but the author has found an additional interesting property expressed in his Theorem I. Due tribute must also be paid to Prof. A. S. Hall for its proof given in the Appendix. All derivations in the paper are simple, straightforward and have, without any doubt, practical value since they are easily applicable.

The writer, personally, had the opportunity of checking some results of one of his latest papers No. 746 under the title "Application of Complex Variables to the Synthesis of Four-Bar Linkages With Prescribed Extreme Values of the Output Angular Velocities," which has been accepted for publication in the *Journal of Applied Mechanics*. The author's criterion (Theorem 1) works perfectly.

The derivation of the angular acceleration of the follower link as shown in Fig. 5, although not so simple, is very interesting, being connected with the direction of the collineation axis. This shows again the importance of the collineation axis and another practical application of it.

Fig. 7 shows a useful method for the determination of the direction of the collineation axis. In Fig. 5 it would be useful to repeat the notations of link $AB$:$a$ and of link $CD$:$c$ since these notations appear in the derivation of Theorem 3.

In connection with the slider-crank mechanism, the writer had again an opportunity to check some results obtained in a paper under the title "Application of Complex Variables to the Synthesis of Quick-Return Slider-Crank Mechanisms," which he is preparing for publication. Again, the author's criterion works perfectly, the only inconvenience in the case is that the collineation axis falls completely outside the drawing.

Finishing the discussion, the writer suggests the author apply his theory to the solution of the problem of designing a four-bar linkage with prescribed extreme values of the output angular velocity.

### Author's Closure

The remarks of Mr. Candee concern the well-known relations between the kinematics of linkages and those of gearing. The type of derivation suitable for inclusion in a paper depends not only upon whether it is primarily geometrical, analytical, elementary, or advanced, but is influenced also by considerations pertaining to a unified and logical development and presentation. The derivation of Theorem 1 in Mr. Candee's discussion, as well as others, both geometrical and analytical, have been intuitively clear to the author and probably also to others at the time this investigation was conducted, which time ended in the spring of 1954. The works referred to in footnote 4 in Mr. Candee's discussion deal with gearing rather than with linkages. In connection with other investigations of velocities, the author would like to refer Mr. Candee to the introduction of this paper.

The derivation of Theorem 3 given by Mr. Candee is valuable and demonstrates clearly the connection between noncircular gearing and the equivalent four-bar linkage. In this connection, the author would like to state his admiration of, and respect for, Mr. Candee's expert knowledge of the kinematics of gearing and gear generation.

The comments of Professor Doughtie (whose text on mechanisms is well known), concerning nomenclature and notation, are well taken and appreciated. The terms "four-link mechanisms," "four-bar mechanisms," and "four-bar linkages" should indeed not have been used interchangeably. These are but one instance of terms in kinematics which are not properly defined, used, and understood. This of course in no way excuses their usage in this paper.

At the 1953 Annual Meeting of the Society a suggestion was made to standardize terminology in kinematics by Mr. A. E. R. de Jonge,[7] and it is believed that such standardization would form a suitable subject matter for an ASME-sponsored project.

It is true that the symbol $v$ for angular-velocity ratio is not ideal. What other symbol would be better and would not lead to confusion with the symbol for the angular velocity of a crank? The author hopes to better his record in terminology and notation in future work, and regrets that the observations of Professor Doughtie and Dr. Rosenauer could not conveniently be incorporated into the paper at this late date.

The application of Theorem 1 to the nonparallel equal crank linkage does, it is true, lead to an indefinite position of $O$. Because of symmetry, however, it can be seen that as the links approach the in-line position, line $O$-$P$ becomes vertical and symmetrical relative to the linkage, so that in the limit point $O$ is halfway between $B$ and $D$. This leads to a maximum value of $v$ equal to $(AD + AB)/(AD - AB)$ as can be derived also from the treatment involving equivalent elliptical gearing.[8]

It was with considerable satisfaction that the author learned of the verification of some of the results by Dr. Rosenauer, one of the leading authorities in the field of kinematics. Some of Dr. Rosenauer's work in complex variables can now be studied in the English language[9] and it is to be hoped that the investigations concerning extreme values of the velocities will soon become available in the English language likewise. The author agrees with Dr. Rosenauer's comments regarding notation and intends to follow up Dr. Rosenauer's suggestion to apply the theory to the problem of designing a four-bar mechanism with prescribed extreme values of the output angular velocity.

[6] Doctor of Engineering, New South Wales University of Technology, Sydney, NSW, Australia.

[7] "An Analytical Approach to the Design of Four-Link Mechanisms," by F. Freudenstein, Trans. ASME, vol. 76, 1954, p. 492.

[8] "Elements of Mechanisms," by V. L. Doughtie and W. H. James, John Wiley & Sons, Inc., New York, N. Y., 1954, pp. 124–125.

[9] "Complex Variable Method for Synthesis of Four-Bar Linkages," by N. Rosenauer, *Australian Journal of Applied Science*, vol. 5, December, 1954, pp. 305–308.

# Long-Shoe Block Brake With Floating Anchor

By M. F. SPOTTS,[1] EVANSTON, ILL.

**It is beneficial for a brake or clutch with an internal shoe to be self-aligning and thereby affected in the least possible manner by an eccentricity of the drum or other dimensional variations in the parts of the assembly. This is achieved by connecting one end of the shoe to a floating link. In addition, the proportions should be arranged so as to cause the wear to be distributed as evenly as possible for all points of the lining. These desirable qualities can be achieved by means of the simple design equation presented here.**

## Introduction

THE theory of the long-shoe block brake must necessarily take account of the variation in pressure at different points along the shoe. Observing this requirement Huck (1)[2] was able to derive equations for the relationship between the force required to actuate the brake and the distribution of pressure along the lining. Additional theories have been presented by Waller (2), Lindemann (3), Loewenberg (4), and Acres (5). The present problem, when the shoe is supported by a floating link, was first solved by von Mehren (6) who pointed out the advantages of this type of brake. In the paper, use is made of the symmetry of the force system on the lining to effect a simplification in the design equations. A series of force polygons for a typical brake are then presented which will show how the proportions of a design should be arranged for achieving the desired operating characteristics.

## Development of Equations

Fig. 1 shows the shoe $AC$ of an internal brake of radius $r$ with end $A$ mounted in the floating link $AB$. The link is inclined at angle $\gamma$, and the pin at $B$ is rigidly attached to the foundation. The shoe encompasses an angle of 90 deg plus two angles $\alpha$ located on either side of the 90-deg angle.

In making the force analysis, it is assumed that all parts of the assembly are rigid except the lining which follows Hooke's law.

Fig. 2($a$) shows the force system for the shoe. Reaction $R$ at $A$ is inclined at angle $\gamma$. Actuating force $P$ is given the proper magnitude and direction $\beta$ to cause the normal forces on the lining to be disposed symmetrically about the center line $OD$. Such a force system causes identical elongations $\epsilon$ in the lining for points $H$ and $H_1$, say, as determined by angle $\theta$.

Wear of the lining also is disposed symmetrically about $OD$ and the greatest possible utilization of the friction material is obtained.

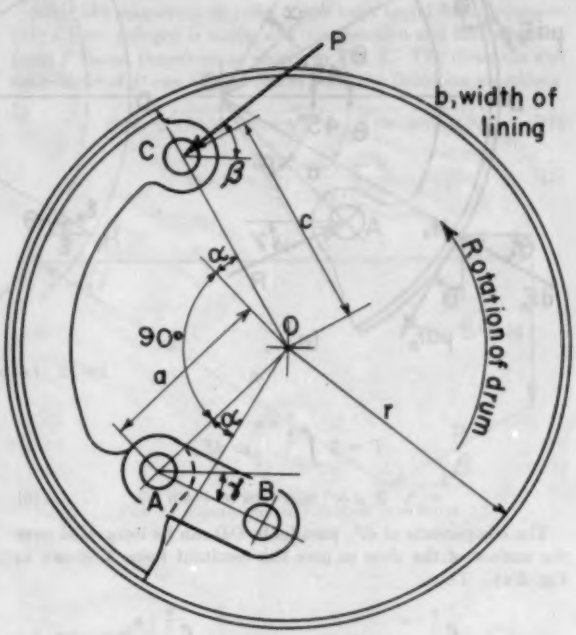


Fig. 1 Block Brake With Shoe Supported by Floating Anchor

From Fig. 2($b$), elongation $\epsilon_n$ in the radial direction, normal to the lining is equal to

$$\epsilon_n = \epsilon \cos \theta \quad [1]$$

When this equation is multiplied by the modulus of elasticity $E$, the left side $E\epsilon_n$ is equal to the normal pressure $p_n$

$$p_n = E\epsilon \cos \theta \quad [2]$$

Equation [2] is valid for point $D$ where $p_n$ becomes the maximum pressure $p_{max}$ and $\theta = 0$. Then $p_{max}$ is equal to $E\epsilon$ and when this is substituted into Equation [2], the following equation for the distribution of pressure results

$$p_n = p_{max} \cos \theta \quad [3]$$

An elemental area $dA$ of the lining is equal to $br\, d\theta$, where $b$ is the width of the lining. Let $dF_n$ represent the normal force acting on this area. Then

$$dF_n = p_n dA = br\, p_{max} \cos \theta\, d\theta \quad [4]$$

The friction force acting on the element of area is

$$\mu\, dF_n = \mu\, br\, p_{max} \cos \theta\, d\theta \quad [5]$$

where $\mu$ is the coefficient of friction.

The torque $T$ of the friction forces about the center of the drum $O$ is given by

---

[1] Professor of Mechanical Engineering, Northwestern University. Mem. ASME.

[2] Numbers in parentheses refer to the Bibliography at the end of the paper.

Contributed by the Machine Design Division, and presented at the Diamond Jubilee Semi-Annual Meeting, Boston, Mass., June 19–23, 1955, of The American Society of Mechanical Engineers.

Note: Statements and opinions advanced in papers are to be understood as individual expressions of their authors and not those of the Society. Manuscript received at ASME Headquarters, March 8, 1955. Paper No. 55—SA-21.

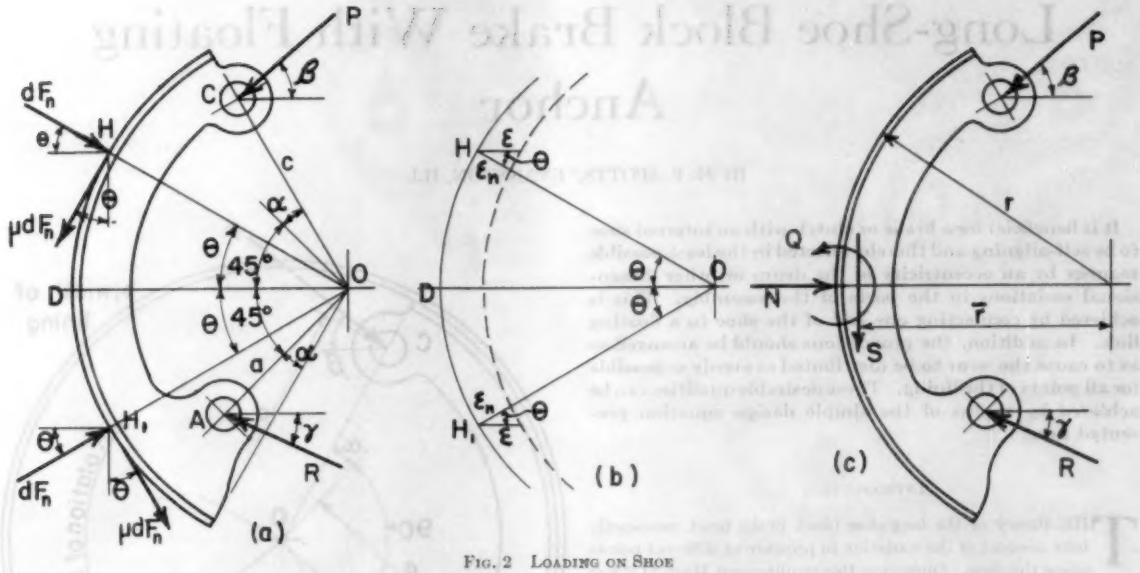


FIG. 2 LOADING ON SHOE

$$T = 2\int_0^{\frac{\pi}{4}+\alpha} \mu r\, dF_n$$

$$= \sqrt{2}\ \mu\, br^2\, p_{max}\,(\cos\alpha + \sin\alpha) \quad \ldots\ldots [6]$$

The components of $dF_n$ parallel to $OD$ can be integrated over the surface of the shoe to give the resultant force $N$ shown in Fig. 2(*c*). Thus

$$N = 2\int_0^{\frac{\pi}{4}+\alpha} \cos\theta\, dF_n = 2\, br\, p_{max}\int_0^{\frac{\pi}{4}+\alpha} \cos^2\theta\, d\theta$$

$$= \frac{1}{2}\, br\, p_{max}\left[2\left(\frac{\pi}{4}+\alpha\right) + \cos 2\alpha\right] \quad \ldots\ldots [7]$$

The components of $dF_n$ perpendicular to $OD$ add to zero. Components of $\mu\, dF_n$ parallel to $OD$ also add to zero. The components of $\mu\, dF_n$ perpendicular to $OD$ can be integrated over the surface of the shoe to give the resultant force $S$ shown in Fig. 2(*c*). Thus

$$S = 2\int_0^{\frac{\pi}{4}+\alpha} \mu\cos\theta\, dF_n = \mu N \quad \ldots\ldots [8]$$

Force $S$ acts at the center of gravity of all the components of forces $\mu\, dF_n$ perpendicular to $OD$. Let this distance be called $\bar{r}$.

Then $$\mu N\bar{r} = 2\int_0^{\frac{\pi}{4}+\alpha} \mu r\cos\theta\, dF_n \cos\theta$$

$$= 2\mu r\int_0^{\frac{\pi}{4}+\alpha} \cos^2\theta\, br\, p_{max}\cos\theta\, d\theta$$

or $$\bar{r} = \frac{2br^2 p_{max}}{N}\int_0^{\frac{\pi}{4}+\alpha} \cos^2\theta\, d\theta$$

$$= \frac{br^2 p_{max}}{3\sqrt{2}\,N}\,(\cos\alpha + \sin\alpha)(5 - \sin 2\alpha)$$

$$= \frac{T}{6S}\,(5 - \sin 2\alpha) \quad \ldots\ldots [9]$$

Attention is turned to the couples acting on the shoe. Normal forces $dF_n$ produce no couples. The components of $\mu\, dF_n$ parallel to $OD$, when integrated over the shoe, will give the moment $Q$ of Fig. 2(*c*). Thus

$$Q = 2\int_0^{\frac{\pi}{4}+\alpha} r\mu\sin^2\theta\, dF_n$$

$$= 2\mu\, r^2 b\, p_{max}\int_0^{\frac{\pi}{4}+\alpha} \sin^2\theta\cos\theta\, d\theta$$

$$= \frac{\mu\, br^2\, p_{max}}{3\sqrt{2}}\,(\cos\alpha + \sin\alpha)(1 + \sin 2\alpha)$$

$$= \frac{T}{6}\,(1 + \sin 2\alpha) \quad \ldots\ldots [10]$$

Components of $\mu\, dF_n$ perpendicular to $OD$ produce no couples.

From the foregoing equations, the following relationship can be proved

$$T = S\bar{r} + Q \quad \ldots\ldots [11]$$

The magnitude of reaction $R$ can be found by taking moments about point $C$. To do this it is necessary to know the distance $m$ in Fig. 3. Distance $e$ is first found by application of the cosine theorem

$$e = \sqrt{a^2 + c^2 + 2ac\sin\alpha} \quad \ldots\ldots [12]$$

Angle $\psi$ can be found from the following equation

$$\tan\psi = \frac{a - c(\cos\alpha - \sin\alpha)}{a + c(\cos\alpha + \sin\alpha)} \quad \ldots\ldots [13]$$

Length $m$ is then given by

$$m = e\cos(\gamma - \psi) \quad \ldots\ldots [14]$$

The moment equation about $C$ is now written and can be used for finding $R$.

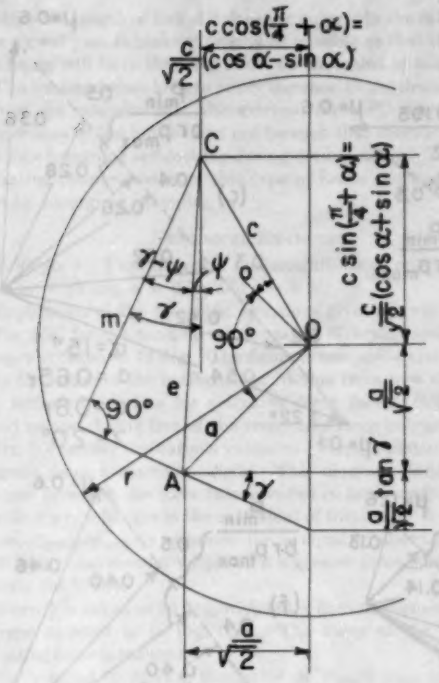


Fig. 3 Geometric Relationships

$$Rm = \frac{Nc}{\sqrt{2}}(\cos\alpha + \sin\alpha) + S\left[r - \frac{c}{\sqrt{2}}(\cos\alpha - \sin\alpha)\right] + Q$$

$$= \frac{Nc}{\sqrt{2}}[(1-\mu)\cos\alpha + (1+\mu)\sin\alpha] + T \quad \ldots\ldots [15]$$

After the magnitude of force $R$ has been found from Equation [15] a force polygon is made, and the direction and magnitude of force $P$ found therefrom as shown in Fig. 4. The direction and magnitude of $P$ can also be found from the following equations

$$P = \sqrt{(N - R\cos\gamma)^2 + (R\sin\gamma - S)^2} \quad \ldots\ldots [16]$$

$$\tan\beta = \frac{R\sin\gamma - S}{N - R\cos\gamma} \quad \ldots\ldots [17]$$

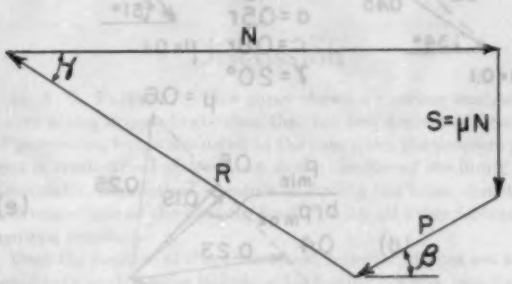


Fig. 4 Equilibrium Polygon for Shoe

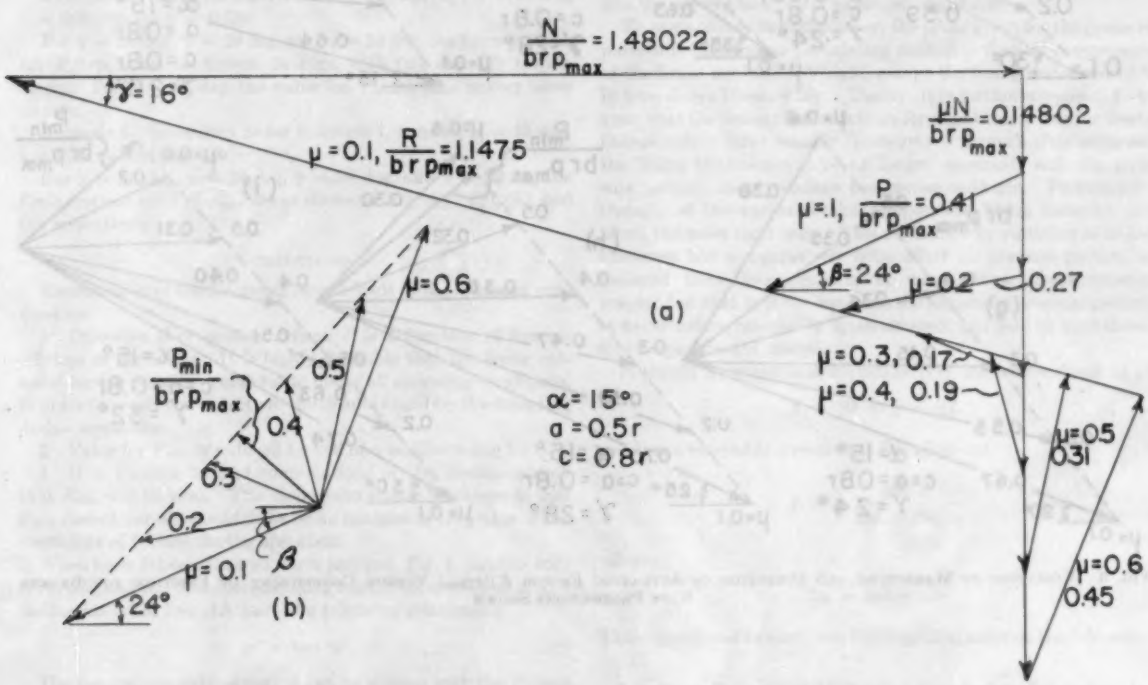


Fig. 5 Variation of Actuating Force $P$ for Brake With Data Shown

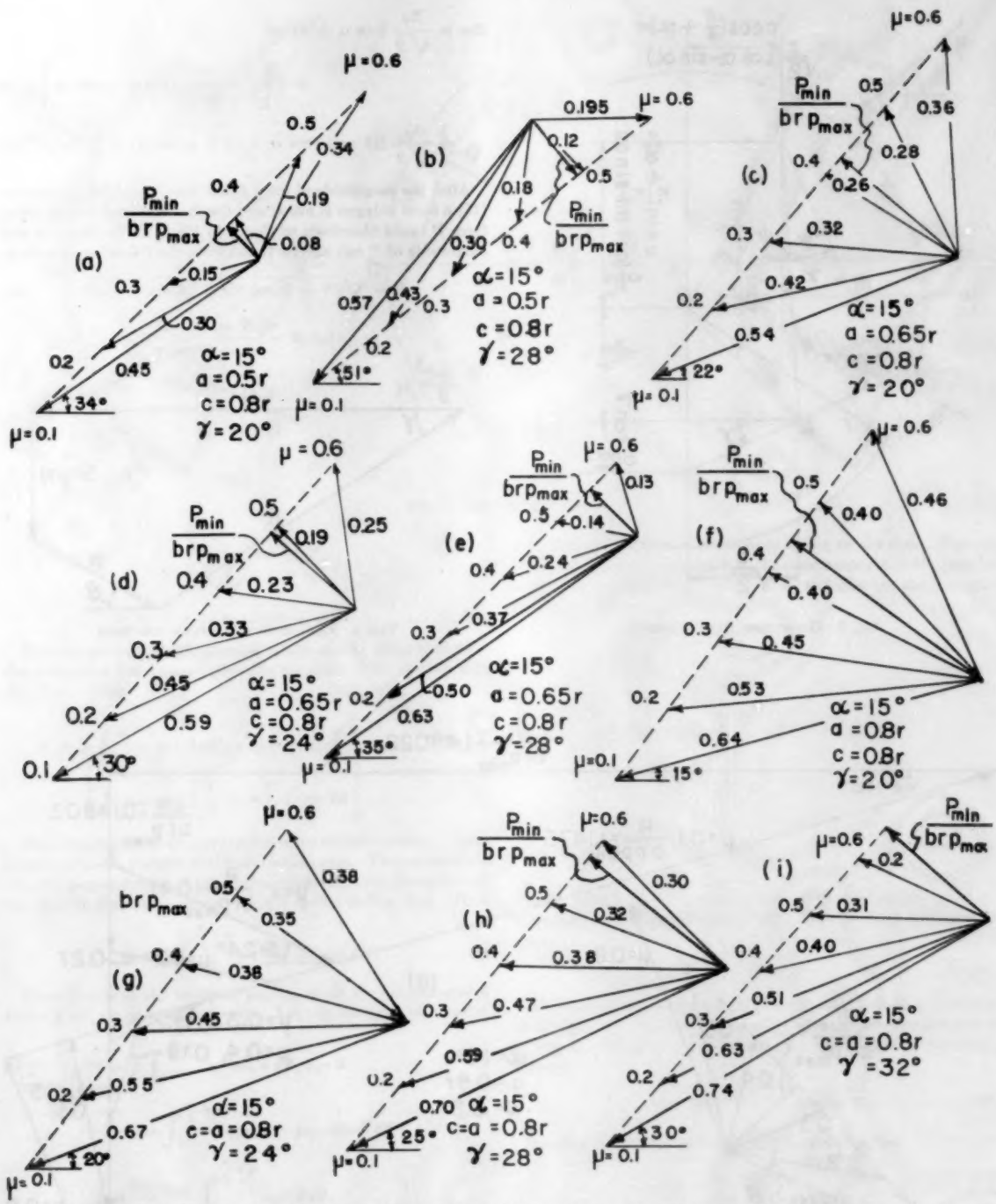


FIG. 6 [VARIATION OF MAGNITUDE AND DIRECTION OF ACTUATING FACTOR $P/br p_{max}$ VERSUS COEFFICIENT OF FRICTION FOR BRAKES WITH PROPORTIONS SHOWN

Since the length of link $AB$ does not enter into the calculations, it is a good plan to make it as long as possible so that the wear of the lining will have the least effect on the value of angle $\gamma$.

The friction forces help to apply the shoe to the drum and thus reduce the magnitude of the external force $P$. However, the proportions of the brake must not be such that there is danger of the shoe becoming self-locking during normal usage. The normal operating characteristics of this type of brake can be illustrated best by numerical examples.

### Numerical Examples

*Example 1.* Find direction and magnitude of operating force $P$ for $\alpha = 15$ deg, $a = 0.5r$, and $c = 0.8r$.

Application of the foregoing equations gives the values shown in Fig. 5($a$) for the nondimensional ratios $N/brp_{max}$ and $R/brp_{max}$ when $\gamma$ is taken as 16 deg. The figure is composite and shows results for values of the coefficient of friction from $\mu = 0.1$ to $\mu = 0.6$, inclusive. Values for actuating force factor $P/brp_{max}$ are found as the closing line of the respective force polygon.

Fig. 5($b$) shows the various values of $P/brp_{max}$ plotted as a ray diagram from a common origin. This diagram illustrates the manner in which the force factor varies in both magnitude and direction with changes in the coefficient of friction $\mu$. A minimum value, $P_{min}/brp_{max}$, is obtained for $\mu$ equal to about 0.34. For both larger and smaller values of $\mu$ a greater force is required to operate the brake.

When $\gamma$ is taken as 20 deg, with other data unchanged, the ray polygon appears as in Fig. 6($a$). The value of the minimum actuating force is reduced.

For $\gamma$ equal to 24 deg, the value of $P_{min}/brp_{max}$ is approximately zero so there would be danger of the brake locking should the coefficient of friction, for any reason, change to about 0.44.

For $\gamma = 28$ deg, the forces for various values of $\mu$ are as shown in Fig. 6($b$).

*Example 2.* Same data as for Example 1, namely, $\alpha = 15$ deg, $c = 0.8r$, except $a = 0.65r$.

For $\gamma = 20$ deg, $\gamma = 24$ deg, and $\gamma = 28$ deg, the force systems for $P/brp_{max}$ are as shown in Figs. 6($c$), ($d$), and ($e$), respectively. For $\gamma = 32$ deg the value for $P_{min}/brp_{max}$ is very close to zero.

*Example 3.* Same data as for Example 1, namely, $\alpha = 15$ deg, $c = 0.8r$, except $a = 0.8r$.

For $\gamma = 20$ deg, $\gamma = 24$ deg, $\gamma = 28$ deg, and $\gamma = 32$ deg the force systems for $P/brp_{max}$ are as shown in Fig. 6($f$), ($g$), ($h$), and ($i$), respectively.

### Conclusions

Examination of the foregoing figures leads to the following conclusions:

1 Direction $\beta$ of actuating force $P$ is a function of the coefficient of friction $\mu$. It is highly desirable that the lining material have a constant value for $\mu$, under all operating conditions, in order to retain the validity of the results found by the foregoing design equations.

2 Value for $P_{min}$ is reduced by use of a smaller value for $a$.

3 It is possible to find combinations of the constants such that $P_{min}$ will be zero. The dimensions should be chosen so that $P_{min}$ cannot vanish should there be an increase in the value of the coefficient of friction during operation.

When force $P$ becomes zero, force polygon, Fig. 4, consists only of $N$, $\mu N$, and $R$. The corresponding coefficient of friction $\mu'$ and inclination $\gamma'$ of link $AB$ have the following relationship

$$\mu' = \tan \gamma' \quad \ldots\ldots [18]$$

The moment equation about $A$ can be written with the $P$-term omitted which gives

$$a'N(1 + \mu') = \sqrt{2}\,T' \quad \ldots\ldots [19]$$

This equation applies only to a self-locking brake.

### BIBLIOGRAPHY

1 "Brakes for Heavy Vehicles," by L. C. Huck, Trans. SAE, part 1, vol. 21, 1926, p. 443.

2 "Internal Expanding Shoe Brakes for Road Vehicles," by I. M. Waller, Proceedings of The Institution of Mechanical Engineers, London, England, part 1, 1949–1950, p. 41.

3 "Internal Shoe Brakes," by H. W. Lindemann, *The Engineers' Digest*, vol. 1, 1944, p. 558.

4 "Automobile Brakes With Servo-Action," by F. Loewenberg, Trans. ASME, vol. 52, (1), 1930, APM—52-16, p. 185.

5 "Some Problems in the Design of Braking Systems," by F. A. S. Acres, *Journal Institute of Automobile Engineer*, vol. 15, 1946, p. 19.

6 "Internal-Shoe Clutches and Brakes," by O. von Mehren, Trans. ASME, vol. 69, 1947, p. 913.

## Discussion

G. A. G. Fazekas.[8] This paper shows a rigorous analysis of forces acting upon a brake shoe that has two degrees of freedom of movement, but is restricted to the case when the pressure pattern is symmetrical with respect to the bisector of the lining arc. Essentially, the method amounts to finding the locus, direction, and magnitude of the shoe-tip load $P$, with all other factors remaining constant.

Once the position of $P$ is determined, however, it does not seem possible to use the same technique for finding out how rapidly the torque or wear pattern would vary consequent upon some change in friction $\mu$. For if $\mu$ deviates from its nominal value upon which the analysis was based—as is inevitable with present friction materials—automatically, the wear pattern ceases to be symmetrical and the present analysis is no longer applicable.

To come to details of the paper, the proof given for the pressure pattern is based upon postulating explicitly that all components of the brake are infinitely rigid, except the lining material which in turn obeys Hooke's law. Tacitly, it is further supposed, however, that the lining thickness is uniform and this is true for virgin linings only. Since roughly (pressure) $\propto$ (wear), after some use the lining thickness will be no longer constant, and the pressure pattern should change too correspondingly. Fortunately, though, of the various brake components, lining materials are about the most rigid ones. This explains why variation of lining thickness has comparatively little effect on pressure pattern as deduced from measurements of wear. Wear measurements suggest too that in most instances the sinusoidal pressure pattern is, nevertheless, reasonably approximated, and may be used therefore for purposes of analysis.

It should be noted that Equation [11] can be rewritten as

$$T = Sf + Q = SL$$

and it can be readily shown that $L$ is given by

$$L = 4r \frac{\sin \alpha}{2\alpha + \sin 2\alpha}$$

where

$$2\alpha = \text{lining arc}$$

This enables one to carry out the graphical construction shown in

[8] Associate Professor of Mechanical Engineering, Polytechnic Institute of Brooklyn, Brooklyn, N. Y.

Fig. 7 from which forces on the shoe and brake torque may be obtained to any desired degree of accuracy.

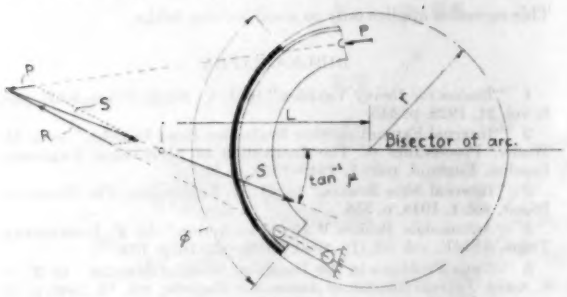


FIG. 7

It would be highly desirable indeed if $\mu$ would remain constant, as concluded by the author. Unfortunately, as yet, no such material seems to be available commercially. Even atmospheric conditions alone can induce what is referred to as the "morning sickness" of brakes. This is particularly severe with some highly self-energized brakes—having small $a$ or its equivalent. In practice, it is this very susceptibility to changes of $\mu$ that sets ndirectly a limit to $P$.

### AUTHOR'S CLOSURE

The author is grateful for the pertinent comments of Professor Fazekas.

His method of graphical analysis constitutes an alternative approach to the problem. His force designated $S$ is the resultant of the author's forces $N$ and $S$. Shifting (author's) $S$ to location $L$ has the effect of eliminating moment $Q$ from the computations. Thus

$$Q = S(L - \bar{r})$$

That this is an identity is shown by substituting $T/S$ for $L$ and the value of $\bar{r}$ from Equation [9].

# Determination of Radius of Curvature for Radial and Swinging-Follower Cam Systems

By MARTIN KLOOMOK[1] AND R. V. MUFFLEY[2]

**An exact expression is derived for the radius of curvature of disk cams with either radial or swinging followers. Several charts are included which illustrate a quick method for arriving at a solution for a particular cam contour, such as the harmonic.**

## Nomenclature

The following nomenclature is used in the paper:

- $c$ = distance from cam center to follower-arm pivot, in.
- $h$ = total output displacement, in.
- $l$ = length of follower arm, in.
- $L$ = lift (i.e., radial displacement of the follower center), in.
- $\rho$ = radius of curvature of the follower center path at any point, in.
- $\rho_{min}$ = minimum radius of curvature of follower center path over complete event, in.
- $\rho_c$ = radius of curvature of cam surface (usually the minimum value), in.
- $r_f$ = radius of cam follower roller, in.
- $R$ = radius measured from camshaft center to follower roller center, in.
- $R_0$ = radius from camshaft center to follower roller center at start of event, in.
- $y$ = displacement of output at any point, in.
- $\beta$ = total angular rotation of cam for a complete event
- $\gamma$ = angular rotation of follower arm
- $\delta$ = angle between $l$ and $c$
- $\theta$ = angular rotation of cam measured from a space fixed reference
- $\epsilon$ = angle between $l$ and $R$
- $\phi$ = angular rotation of cam measured from a line joining the follower roller and cam centers
- $\psi$ = angle between $R$ and $c$
- $\tau$ = total angular displacement of follower arm during complete event

All angles are in radians

## Introduction

The principal object of this paper is the computation of the radius of curvature of disk cams—in particular, the computation of minimum radius of curvature. This geometric property is significant for two purposes:

1 A determination of "undercut."
2 A determination of surface stress.

The meaning of undercut will be evident in the following discussion in which the geometric problem is defined.

The distance $R$ from the cam center to the follower center is the dimension commonly used in the design and manufacture of cams, rather than the distance from the cam center to the cam surface. Therefore it has been found more convenient first to trace the follower and determine the radius of curvature of the follower center path. Then for a roller follower of any diameter, the radius of curvature of the cam surface may be obtained in the following way: In Fig. 1, let $r_f$ be radius of follower, $\rho$ be radius

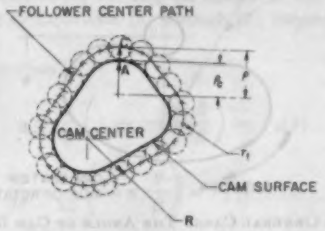


Fig. 1 General Case Showing Relation of Radius of Curvature of Cam $\rho_c$ to Radius of Curvature of Follower Center Path $\rho$ and Follower Roller Radius $r_f$

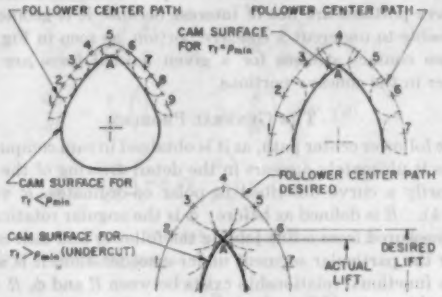


Fig. 2 Effect on Cam Profile of Increasing Follower Roller Radius While Follower Center Path Remains Constant

of curvature of follower center path at any point $C$, $\rho_c$ be radius of curvature of cam surface at $A$, point of contact of follower. Evidently both $\rho$ and $\rho_c$ have the same instant center and therefore

$$\rho_c = \rho - r_f \quad \ldots\ldots\ldots\ldots\ldots\ldots\ldots\ldots [1]$$

With $\rho$ constant, it may be seen in Fig. 2 that as the follower radius $r_f$ is increased, the radius of curvature $\rho_c$ of the cam surface becomes successively smaller. When $r_f$ is equal to $\rho$, then $\rho_c$ is equal to zero; i.e., the cam surface comes to a point. As the follower radius is increased further, the cam is undercut. That is to say, successive arcs "cut under" previously determined portions of the cam surface and reduce the lift from the value desired.

Accordingly, to prevent undercut, $r_f \leq \rho_{min}$, where $\rho_{min}$ is the minimum value of $\rho$ over the particular segment of the profile being considered. If there are a number of separate and distinct motion curves disposed around the cam, each case must be checked separately because only one segment can be represented by one continuous function.

[1] Manager, Scientific Computation Laboratory, International Business Machines Corporation, Endicott, N. Y.
[2] Staff Engineer, International Business Machines Corporation, Engineering Laboratory, San Jose, Calif. Assoc. Mem. ASME.
Contributed by the Machine Design Division and presented at the Diamond Jubilee Semi-Annual Meeting, Boston, Mass., June 19–23, 1955, of The American Society of Mechanical Engineers.
Note: Statements and opinions advanced in papers are to be understood as individual expressions of their authors and not those of the Society. Manuscript received at ASME Headquarters, March 16, 1955. Paper No. 55—SA-29.

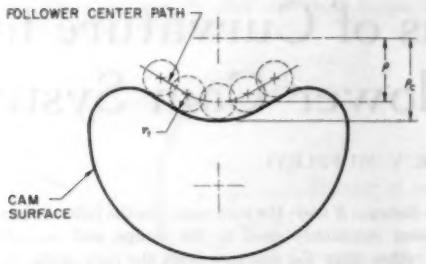


FIG. 3 IN CONCAVE PORTION OF CAM, RADIUS OF CURVATURE OF CAM IS ALWAYS GREATER THAN RADIUS OF CURVATURE OF FOLLOWER CENTER PATH

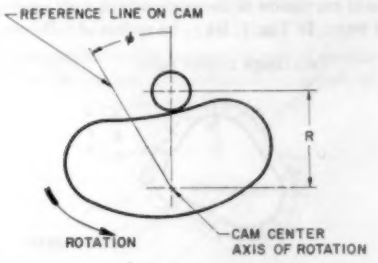


FIG. 4 THE GENERAL CASE: THE ANGLE OF CAM ROTATION $\phi$ AND THE FOLLOWER POSITION $R$

In all of the following discussion, the significant radii of curvature are those associated with convex portions of the cam surface. Concave portions are not of interest because it is geometrically impossible to undercut a concave portion, as seen in Fig. 3, and because contact stresses for a given normal force are always smaller in the concave portions.

## THE GENERAL PROBLEM

The follower center path, as it is obtained in cam computations, and as it ultimately appears in the detail drawing of the cam, is ordinarily a curve described in polar co-ordinates, $R$ versus $\phi$ (Fig. 4). $R$ is defined as before; $\phi$ is the angular rotation of the cam measured from a line joining the follower and cam centers.

For the particular segment under consideration, it is assumed that a functional relationship exists between $R$ and $\phi$, $R = G(\phi)$ and, further, that the first two derivatives are continuous

$$\frac{dR}{d\phi} = G'(\phi) \quad \text{and} \quad \frac{d^2R}{d\phi^2} = G''(\phi)$$

As shown in many calculus texts, the radius of curvature of any curve so described is given by

$$\rho = \frac{\left[R^2 + \left(\frac{dR}{d\phi}\right)^2\right]^{3/2}}{R^2 + 2\left(\frac{dR}{d\phi}\right)^2 - R\frac{d^2R}{d\phi^2}} = \frac{\{[G(\phi)]^2 + [G'(\phi)]^2\}^{3/2}}{[G(\phi)]^2 + 2[G'(\phi)]^2 - G(\phi)G''(\phi)} \quad \ldots\ldots [2]$$

Usually a cam-design problem begins with some prescribed functional relationship(s) between output displacement and time (i.e., a timing diagram). Since most cams are driven at constant angular velocity, the time function is readily converted to a relationship between output displacement and angular rotation of the cam.

Output displacement can be either rotational or translational.

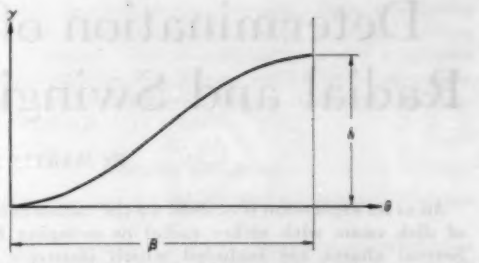


FIG. 5 THE GENERAL CASE: THE RELATIONSHIP OF $h$ TO $y$ AND $\beta$ TO $\theta$ ILLUSTRATED IN RECTANGULAR CO-ORDINATES FOR RISE PORTION OF CAM

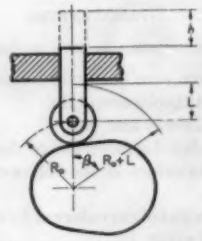


FIG. 6 RADIUS OF CURVATURE GEOMETRY FOR THE SPECIFIC CASE OF A RADIAL CAM FOLLOWER. $L$ IS SEEN EQUAL TO $h$

The particular form of the displacement-time relationship depends upon both functional requirements and inertia considerations.

One common curve is simple harmonic motion

$$y = \frac{h}{2}\left(1 - \cos \pi \frac{\theta}{\beta}\right) = F_h(\theta) \quad \ldots\ldots [3]$$

$$\frac{dy}{d\theta} = \frac{\pi h}{2\beta}\left(\sin \pi \frac{\theta}{\beta}\right) = F_h'(\theta) \quad \ldots\ldots [4]$$

$$\frac{d^2y}{d\theta^2} = \frac{\pi^2 h}{2\beta^2}\left(\cos \pi \frac{\theta}{\beta}\right) = F_h''(\theta) \quad \ldots\ldots [5]$$

where $\theta$ is the rotation of the cam from a space fixed reference, $h$ is the total displacement of the output, and $\beta$ is the total rotation of the cam corresponding to $h$. These relationships are indicated in Fig. 5.

Another frequently used motion curve is the so-called "cycloidal"

$$y = h\left(\frac{\theta}{\beta} - \frac{1}{2\pi}\sin 2\pi \frac{\theta}{\beta}\right) = F_c(\theta) \quad \ldots\ldots [6]$$

$$\frac{dy}{d\theta} = \frac{h}{\beta}\left(1 - \cos 2\pi \frac{\theta}{\beta}\right) = F_c'(\theta) \quad \ldots\ldots [7]$$

$$\frac{d^2y}{d\theta^2} = \frac{2\pi h}{\beta^2}\left(\sin 2\pi \frac{\theta}{\beta}\right) = F_c''(\theta) \quad \ldots\ldots [8]$$

Derivations follow for specific follower systems.

## RADIUS OF CURVATURE IN A RADIAL FOLLOWER SYSTEM

Consider first the simplest situation, the radial follower, in which the line of action of the follower coincides with a radial line through the cam center, Fig. 6.

Obviously, in this case, $L = h$, where $L$ is the total displacement at the cam surface, i.e., the lift or "rise." Consequently

$$R = R_0 + y = R_0 + F(\theta) = f(\theta) \quad \ldots\ldots [9]$$

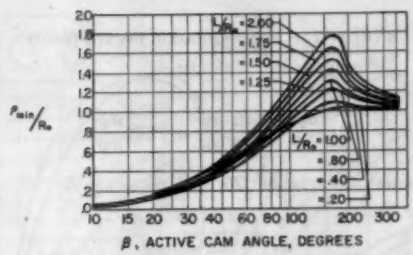


FIG. 7 MINIMUM POSITIVE RADIUS OF CURVATURE OF FOLLOWER CENTER PATH PLOTTED AGAINST ACTIVE CAM ANGLE FOR CYCLOIDAL PROFILES AND RADIAL FOLLOWER-CAM SYSTEMS

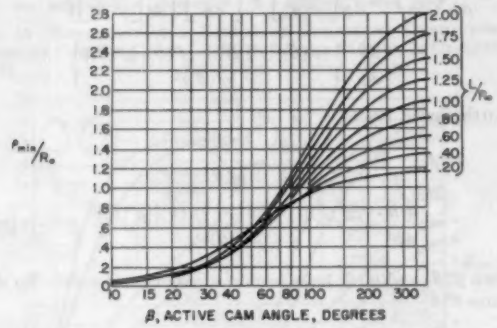


FIG. 8 MINIMUM POSITIVE RADIUS OF CURVATURE OF FOLLOWER CENTER PATH PLOTTED AGAINST ACTIVE CAM ANGLE FOR HARMONIC PROFILES AND RADIAL FOLLOWER-CAM SYSTEMS

$$\frac{dR}{d\theta} = F'(\theta) = f'(\theta) \quad [10]$$

$$\frac{d^2R}{d\theta^2} = F''(\theta) = f''(\theta) \quad [11]$$

where $R_o$ is the radius to the follower center when $\theta = 0$ (i.e., the minimum or "base" radius).

Since there is no rotation of the follower about the cam center, $\phi$ may be taken equal to $\theta$. Therefore: $G(\phi) = f(\theta)$, $G'(\phi) = f'(\theta)$, and $G''(\phi) = f''(\theta)$.

Substituting $f(\theta)$, $f'(\theta)$, and $f''(\theta)$, for the particular motion curve in the general Equation [2]

$$\rho = \frac{\{[f(\theta)]^2 + [f'(\theta)]^2\}^{3/2}}{[f(\theta)]^2 + 2[f'(\theta)]^2 - f(\theta)f''(\theta)} \quad [12]$$

Equation [12] can be evaluated for a particular motion curve by substituting the appropriate expressions for $f(\theta)$, $f'(\theta)$, and $f''(\theta)$, such as Equations [3], [4], and [5], or Equations [6], [7], and [8]. Differentiation of the resultant expressions to obtain minima yields unmanageable transcendental equations; therefore the problem was attacked with a high-speed computing machine, the IBM Model II Card-Programmed Calculator. Using a given set of parameters ($\beta$ and $L/R_o$) and a given motion curve, the value of $\rho/R_o$ was calculated corresponding to each value of $\theta$ from zero to $\beta$. This was done for an entire series of curves, and the resultant minima have been plotted as a function of $\beta$, see Figs. 7 and 8.

### RADIUS OF CURVATURE IN A SWINGING FOLLOWER SYSTEM

This system is identified with Fig. 9. The essential feature is follower rotation about some center $B$ through an angle $\gamma$, the "output displacement."

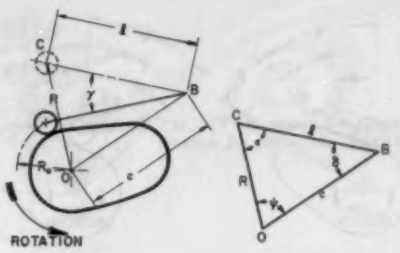


FIG. 9 RADIUS OF CURVATURE GEOMETRY FOR A SWINGING CAM FOLLOWER

In addition to the parameters ($\theta$, $\beta$, $\phi$, $R$, and $\rho$) used in a radial follower system, there are the following: $c$, $l$, $\gamma$, $\delta$, $\epsilon$, $\tau$, and $\psi$. These are defined in the Nomenclature.

Specific equations for the angular motion of the follower arm corresponding to Equations [3] through [8], respectively, are as follows:

Harmonic motion

$$\gamma = \frac{\tau}{2}\left(1 - \cos \pi \frac{\theta}{\beta}\right) = F_h(\theta) \quad [13]$$

$$\frac{d\gamma}{d\theta} = \frac{\pi\tau}{2\beta}\left(\sin \pi \frac{\theta}{\beta}\right) = F_h'(\theta) \quad [14]$$

$$\frac{d^2\gamma}{d\theta^2} = \frac{\pi^2\tau}{2\beta^2}\left(\cos \pi \frac{\theta}{\beta}\right) = F_h''(\theta) \quad [15]$$

Cycloidal motion

$$\gamma = \tau\left(\frac{\theta}{\beta} - \frac{1}{2\pi}\sin 2\pi \frac{\theta}{\beta}\right) = F_c(\theta) \quad [16]$$

$$\frac{d\gamma}{d\theta} = \frac{\tau}{\beta}\left(1 - \cos 2\pi \frac{\theta}{\beta}\right) = F_c'(\theta) \quad [17]$$

$$\frac{d^2\gamma}{d\theta^2} = \frac{2\pi\tau}{\beta^2}\left(\sin 2\pi \frac{\theta}{\beta}\right) = F_c''(\theta) \quad [18]$$

Returning to Fig. 9, the relationship between $R$ and $\gamma$ is trigonometric. From the initial data ($l$, $c$, $R_o$)

$$\delta_o = \cos^{-1}\left(\frac{l^2 + c^2 - R_o^2}{2lc}\right) \quad [19]$$

$$\delta = \delta_o + \gamma \quad [20]$$

$$R = (l^2 + c^2 - 2lc\cos\delta)^{1/2} \quad [21]$$

As the follower swings up, the ray from the cam center to the follower center must shift slightly. Hence $\phi \neq \theta$. In deriving the relationship between $\phi$ and $\theta$, reference is made to Fig. 10. In this figure the follower pivot has been shifted relative to the cam for purposes of illustration. Actually, the follower pivot is fixed. For Case 1

$$\theta + \psi_o = \phi + \psi \quad [22]$$

For Case 2

$$\theta + \psi = \phi + \psi_o \quad [23]$$

The relationship between $\phi$ and $\theta$ is seen to depend upon the relative position and rotation of the cam-and-follower system. Consequently, the case of rotation away from pivot (Case 1) must be carefully distinguished from rotation toward pivot (Case 2).

*Rotation Away From Pivot.* This is the situation in Fig. 10,

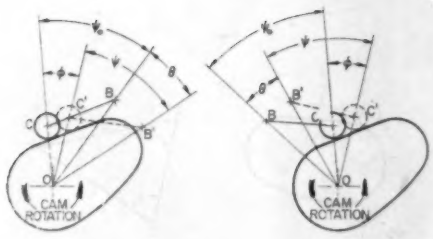


CASE 1 CASE 2

FIG. 10 SWINGING FOLLOWER SHOWN WITH ROTATION TO AND FROM THE PIVOT

Case 1, where the portion of the cam surface in contact with the roller moves "away" from the pivot $B$. The definition is not limited, of course, to the specific arrangement pictured in Case 1, but holds for any situation in which the relative motion of the cam is away from the pivot.

*Rotation Toward Pivot.* This is the situation in Fig. 10, Case 2, where the portion of the cam surface in contact with the roller moves "toward" the pivot $B$. Again, this definition includes any situation which maintains the relative position of the parts, for example, the situation which can be imagined by viewing the Case 2 sketch from the rear. Equation [23] applies to Case 2:

$\psi_0$ and $\psi$ can be computed from the $l$, $c$, $R_0$, and $l$, $c$, $R$ triangle, respectively

$$\psi_0 = \cos^{-1}\left(\frac{R_0^2 + c^2 - l^2}{2R_0c}\right) \quad [24]$$

$$\psi = \cos^{-1}\left(\frac{R^2 + c^2 - l^2}{2Rc}\right) \quad [25]$$

Therefore, since $\psi$ is a function of $R$, and $R$ is a function of $\theta$, $\phi = g(\theta)$.

Since ultimately it will be necessary to substitute $R$, $(dR)/(d\phi)$, and $(d^2R)/(d\phi^2)$ in Equation [2] for $\rho$, and since $R$ has been given by Equation [21], the next step is to determine $(dR)/(d\phi)$

$$\frac{dR}{d\phi} = \frac{\dfrac{dR}{d\theta}}{\dfrac{d\phi}{d\theta}} = \frac{f'(\theta)}{g'(\theta)} \quad [26]$$

First, for $f'(\theta)$, from Equation [21]

$$R^2 = l^2 + c^2 - 2lc\cos\delta$$

which by differentiation with respect to $\theta$ yields

$$\frac{dR}{d\theta} = \frac{lc}{R}\frac{d\delta}{d\theta}\sin\delta \quad [27]$$

Differentiating Equation [20] with respect to $\theta$

$$\frac{d\delta}{d\theta} = \frac{d\gamma}{d\theta} = F'(\theta) \quad [28]$$

Therefore

$$f'(\theta) = \frac{lc}{R}F'(\theta)\sin\delta \quad [29]$$

By differentiation of Equations [22] and [23] with respect to $\theta$

$$g'(\theta) = 1 - \frac{d\psi}{d\theta} \quad \text{(rotation away from pivot)} \quad [30]$$

$$g'(\theta) = 1 + \frac{d\psi}{d\theta} \quad \text{(rotation toward pivot)} \quad [31]$$

Also

$$\frac{d\psi}{d\theta} = \frac{dR}{d\theta}\frac{d\psi}{dR} = f'(\theta)\frac{d\psi}{dR} \quad [32]$$

Differentiating Equation [25] with respect to $R$

$$\frac{d\psi}{dR} = \frac{c^2 - R^2 - l^2}{2R^2c\sin\psi} \quad [33]$$

Finally, to determine $(d^2R)/(d\phi^2)$

$$\frac{d^2R}{d\phi^2} = \frac{d}{d\phi}\left(\frac{dR}{d\phi}\right) = \frac{d}{d\phi}\left[\frac{f'(\theta)}{g'(\theta)}\right] = \left[\frac{d\theta}{d\phi}\right]\left\{\frac{d}{d\theta}\left[\frac{f'(\theta)}{g'(\theta)}\right]\right\}$$

$$= \frac{d\theta}{d\phi}\left\{\frac{[g'(\theta)][f''(\theta)] - [f'(\theta)][g''(\theta)]}{[g'(\theta)]^2}\right\} \quad [34]$$

Furthermore, since

$$\frac{d\theta}{d\phi} = \frac{1}{g'(\theta)}$$

$$\frac{d^2R}{d\phi^2} = \frac{[g'(\theta)][f''(\theta)] - [f'(\theta)][g''(\theta)]}{[g'(\theta)]^3} \quad [35]$$

Both $f'(\theta)$ and $g'(\theta)$ have been evaluated previously. To determine $f''(\theta)$

$$f''(\theta) = \frac{d^2R}{d\theta^2} = \frac{d}{d\theta}\left[\frac{lc\sin\delta\dfrac{d\gamma}{d\theta}}{R}\right]$$

$$= \frac{Rlc\dfrac{d}{d\theta}\left(\sin\delta\dfrac{d\gamma}{d\theta}\right) - \left(lc\sin\delta\dfrac{d\gamma}{d\theta}\right)\dfrac{dR}{d\theta}}{R^2}$$

$$= \frac{Rlc\left(\sin\delta\dfrac{d^2\gamma}{d\theta^2} + \dfrac{d\gamma}{d\theta}\cos\delta\dfrac{d\delta}{d\theta}\right) - \left(lc\sin\delta\dfrac{d\gamma}{d\theta}\dfrac{dR}{d\theta}\right)}{R^2} \quad [36]$$

By substitution of Equations [28] and [29] this becomes

$$f''(\theta) = \frac{(lc\sin\delta)\left(\dfrac{d^2\gamma}{d\theta^2}\right) + (lc\cos\delta)\left(\dfrac{d\gamma}{d\theta}\right)^2 - [f'(\theta)]^2}{R} \quad [37]$$

Differentiating Equations [30] and [31] with respect to $\theta$

$$g''(\theta) = -\frac{d^2\psi}{d\theta^2} \quad \text{(rotation away from pivot)} \quad [38]$$

and

$$g''(\theta) = +\frac{d^2\psi}{d\theta^2} \quad \text{(rotation toward pivot)} \quad [39]$$

To evaluate $\dfrac{d^2\psi}{d\theta^2}$

$$\frac{d^2\psi}{d\theta^2} = \frac{d}{d\theta}\left(\frac{d\psi}{dR}\frac{dR}{d\theta}\right) = \left(\frac{d\psi}{dR}\frac{d^2R}{d\theta^2}\right) + \left(\frac{dR}{d\theta}\right)\frac{d}{d\theta}\left(\frac{d\psi}{dR}\right)$$

$$= \frac{d\psi}{dR}f''(\theta) + [f'(\theta)]\left[\frac{d}{d\theta}\left(\frac{d\psi}{dR}\right)\right] \quad [40]$$

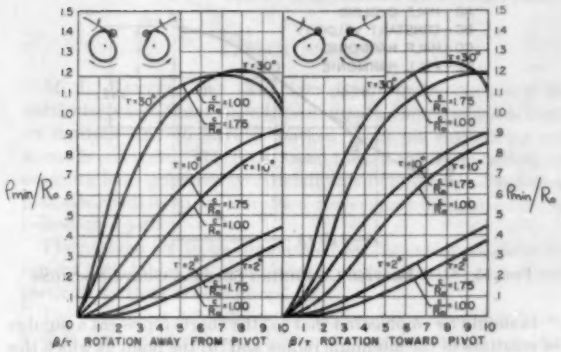


FIG. 11 REPRESENTATIVE RADIUS OF CURVATURE CHART FOR A SWINGING CAM FOLLOWER. $l/R_0 = 1.0$ AND MOTION IS CYCLOIDAL

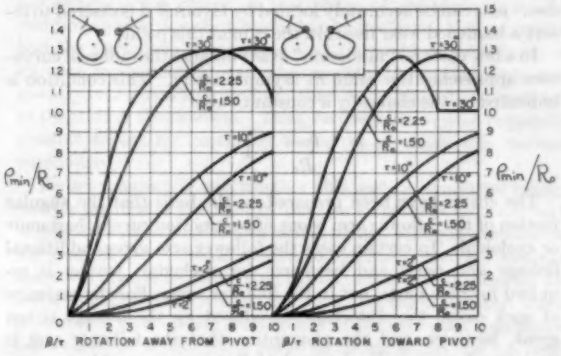


FIG. 12 REPRESENTATIVE RADIUS OF CURVATURE CHART FOR A SWINGING CAM FOLLOWER. $l/R_0 = 1.5$ AND MOTION IS CYCLOIDAL

Evaluating

$$\frac{d}{d\theta}\left(\frac{d\psi}{dR}\right)$$

$$\frac{d}{d\theta}\left(\frac{d\psi}{dR}\right) = \frac{d}{d\theta}\left(\frac{c^2 - R^2 - l^2}{2R^2 c \sin\psi}\right)$$

$$= \frac{[-4R^3c\sin\psi][f'(\theta)] - [c^2 - R^2 - l^2]\left[2R^2c\cos\psi\,\frac{d\psi}{d\theta} + 4Rc\sin\psi f'(\theta)\right]}{4R^4c^2\sin^2\psi}$$

$$= \frac{[-R^2\sin\psi][f'(\theta)] - [c^2 - R^2 - l^2]\left[\frac{R}{2}\cos\psi\,\frac{d\psi}{d\theta} + \sin\psi f'(\theta)\right]}{R^3c\sin^2\psi} \quad \ldots [41]$$

Therefore $(d^2R)/(d\phi^2)$ can now be computed and by substitution in Equation [2] the radius of curvature $\rho$ can be found (for given $l$, $R_0$, $c$, $\beta$, $\tau$, type of motion curve, direction of rotation), at any point $\theta/\beta$.

Minimum values for $\rho/R_0$ have been calculated on the IBM Model II Card-Programmed Calculator. Representative charts plotted for the cycloidal-motion curve are presented in Figs. 11 and 12. If the minimum radius of curvature obtained from the chart is greater than the base radius, the base radius is the major consideration in the design.

## NUMERICAL EXAMPLES

(*A*) *Radial Follower.* For the mechanism shown in Fig. 13, let

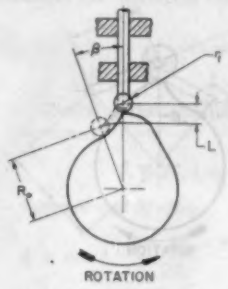


FIG. 13 RADIAL FOLLOWER CAM SYSTEM ILLUSTRATING EXAMPLE A IN TEXT

Follower radius $r_f = 0.1875$ in.
Maximum radius to follower center, $R_{max} = 1.250$ in.
Rise of cam $L = 0.200$ in.
Total cam angle $\beta = 20$ deg.
Motion curve be cycloidal.

Then $R_0 = R_{max} - L = 1.250 - 0.200 = 1.050$ in., and

$$\frac{L}{R_0} = \frac{0.200}{1.050} = 0.19$$

Find in Fig. 7, for $L/R_0 = 0.19$ and $\beta = 20$ deg

$$\frac{\rho_{min}}{R_0} = 0.16$$

Then

$$\rho_{min} = (0.16)(R_0) = (0.16)(1.050) = 0.17 \text{ in.}$$

and

$$\rho_c = \rho_{min} - r_f = 0.17 - 0.19 = (-0.02) \text{ in.}$$

This cam would be undercut because $r_f > \rho_{min}$ and $\rho_c$ is negative.

Try a larger value of maximum radius, $R_{max} = 1.500$ in.

$$R_0 = 1.500 - 0.200 = 1.300 \text{ in.}$$

and

$$\frac{L}{R_0} = \frac{0.200}{1.300} = 0.155$$

Find in Fig. 7, for $L/R_0 = 0.155$ and $\beta = 20$ deg

$$\frac{\rho_{min}}{R_0} = 0.17$$

Then

$$\rho_{min} = (0.17)(R_0) = (0.17)(1.300) = 0.22 \text{ in.}$$

and

$$\rho_c = \rho_{min} - r_f = 0.22 - 0.19 = 0.03 \text{ in.}$$

This cam would not be undercut, but, if practical, it would be desirable to reduce the follower-roller diameter from 0.375 to 0.250 in. Then $r_f = 0.125$ and $\rho_c = 0.22 - 0.12 = 0.10$ in., a better situation from the surface-stress point of view.

(*B*) *Swinging Follower.* For the mechanism shown in Fig. 14, let

Follower radius $r_f = 0.375$ in.
Total cam angle $\beta = 40$ deg
Total swing of arm $\tau = 10$ deg
Minimum radius to follower center $R_0 = 1.250$ in.
Length of follower arm $l = 1.500$ in.

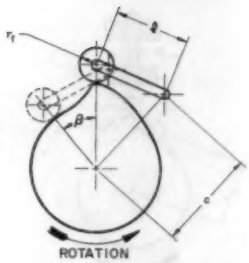


FIG. 14 SWINGING-FOLLOWER CAM SYSTEM ILLUSTRATING EXAMPLE B

Distance from cam center to arm-pivot center, $c = 2.00$ in.
The rotation be as shown in the sketch.
The motion curve be cycloidal.
Then

$$\frac{\beta}{\tau} = \frac{40 \text{ deg}}{10 \text{ deg}} = 4$$

$$\frac{l}{R_0} = \frac{1.500}{1.250} = 1.2$$

$$\frac{c}{R_0} = \frac{2.00 \text{ in.}}{1.25 \text{ in.}} = 1.6$$

TABLE 1 INTERPOLATION FOR $\rho_{min}/R_0$

| $\frac{l}{R_0}$ | $\frac{c}{R_0}$ | FROM CHART $\frac{\rho_{min}}{R_0}$ | INTERPOLATION First $\left(\frac{c}{R_0}\right)$ | INTERPOLATION Second $\left(\frac{l}{R_0}\right)$ |
|---|---|---|---|---|
| 1.0 | 1.00 | 0.35 | | |
| | 1.6 | | 0.49* | |
| 1.0 | 1.75 | 0.52 | | |
| 1.2 | | | | 0.41 |
| 1.5 | 1.5 | 0.28 | | |
| | 1.6 | | 0.30 | |
| 1.5 | 2.25 | 0.44 | | |

*Sample interpolation: $\frac{\rho_{min}}{R_0} = 0.35 + \left[\frac{1.6 - 1.00}{1.75 - 1.00}\right](0.52 - 0.35) = 0.49$

Therefore, $\rho_{min} = (0.41)(R_0) = (0.41)(1.250) = 0.51$ inches.

It will be necessary to make a double interpolation for $\rho_{min}/R_0$, as shown in Table 1. Chart values are obtained from Figs. 11 and 12.

As before

$$\rho_c = \rho_{min} - r_f = 0.51 - 0.38 = 0.13 \text{ in.}$$

In most problems a third interpolation must be used when the value of $\tau$ does not correspond to one of the three charted values, 2, 10, or 30 deg. However, the procedure is the same.

In problems where curves are matched with other curves or with straight lines, the parameters are modified before using the charts. As seen in Fig. 15, the start of the cam is re-established from point $A$ to point $E$. The location of $E$ must be computed or laid out according to the swing of the follower arm; this gives a new value of $R_0'$ to use with the new values of $\beta'$ and $\tau'$ in obtaining points from the charts.

The determination of minimum radius of curvature for the "fall" of the cam proceeds precisely as it would for the "rise" of the cam with one exception: the direction of rotation is taken opposite to that which exists in the problem under consideration.

Attention should be called to the fact that undercut can be a problem with sliding-type followers, as well as with roller followers. The analytical procedure just described for roller followers can be used for a sliding-type follower with a convex surface.

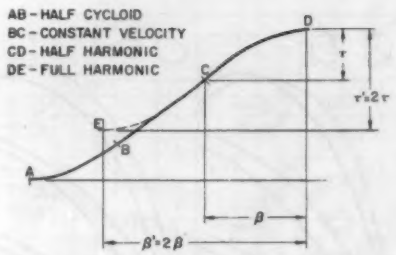


FIG. 15 CAM PROFILE COMBINING SEVERAL CURVE SECTIONS

It should be emphasized that (*a*) the charts represent a number of solutions of the minimum radius and (*b*) the point at which this minimum exists is not specified. Location of the minimum is not difficult, however. When the minimum radius of curvature $\rho_{min}$ is relatively small, it will tend to occur near the top of the cam rise. $\rho_{min}$ can be accurately located by layout if it is desired to insert a hardened wear insert in the cam at this point.

In a few cases no "minimum" exists because the radius of curvature approaches the value $R_0$ asymptotically. This condition is indicated on the charts by a constant value

$$\frac{\rho_{min}}{R_0} = 1$$

The charts have been prepared on the basis that the angular motion of the follower arm is one of two motion curves, harmonic or cycloidal. In certain cases the follower arm drives additional linkage and parts and harmonic (or cycloidal) motion is required in these parts, not in the follower arm. For the majority of such cases, the distortion introduced by the linkage is not great, however, and the assumption that the follower arm is traveling harmonically (or cycloidally) is a reasonable approximation.

The use of radius of curvature in ascertaining undercut has been shown. The radius of curvature of the cam surface is also useful for computation of contact stress by means of Hertz' equation for two cylinders in contact.

## CONCLUSIONS

An exact derivation has been given for radius of curvature of a cam-follower path. The equations are applicable to any motion curve, but the labor of computation suggests evaluation by means of a high-speed computing machine, such as the IBM Card-Programmed Calculator. The resulting data for harmonic, cycloidal, or other motion curves is then graphed to facilitate use in design, as indicated in the paper.

The graphs speed up the process of calculation to the point where it is possible to experiment with small changes in the parameters and thereby avoid serious difficulties in radius of curvature early in the design, before the cam has been detailed or calculated.

## REFERENCES

1 "An Analysis of the Dynamic Forces in a Cam-Driven System," by J. A. Hrones, ASME Paper No. 47—A-46.

2 "Curvature-Acceleration Relations for Plane Cams," by M. L. Baxter, Trans. ASME, vol. 70, 1948, pp. 483–489.

3 "Cam Curvature," by A. R. Holowenko and A. S. Hall, *Machine Design*, vol. 25, August, 1953, pp. 170–177; vol. 25, September, 1953, pp. 162–170; vol. 25, November, 1953, pp. 148–156.

4 "New Methods in Valve Design," by W. Dudley, Quarterly Trans. Society of Automotive Engineers, vol. 3, January, 1948, pp. 19–33, 51.

5 "Ein Neues Verfahren zur Aufsuchung des Krummungskreises," by W. Hartmann, *Zeitschrift-VDI*, vol. 37, 1893, pp. 95–101.

# Discussion[3]

M. L. Baxter, Jr.[4] The two papers under discussion are particularly significant since they illustrate a trend which is likely to continue and to have a marked effect on engineering and scientific advance. This is the trend toward the use of high-speed computation equipment to tabulate in advance critical and complex design data so as to reduce the engineering man-hours required on a job.

The authors are to be commended for furnishing machine designers with tables for cam pressure angles and curvatures, and particularly their maximum values.

The increasing availability of high-speed computers carries with it some implications which we as engineers should consider. In the past, an equation or formula was not of much practical use unless it could be reduced in some way to yield direct explicit results with a minimum of trial and error, and naturally considerable emphasis was placed on this phase of the derivation. In addition to reducing the labor of hand calculation, this procedure had the advantage of requiring that the problem be reduced to its real fundamentals, and the resulting equations were frequently of a much simpler form than might have been expected at the start of the problem. Then, furthermore, it was frequently possible to see by inspection the effect of changes in various parameters.

We may naturally ask whether this sort of analytical refinement is justified in the light of the new computers, or is any sort of solution satisfactory so long as it is right? Many of us would be sorry to see this attitude carried to extremes, not only because there will always be some hand calculation done, but because we feel it would represent a step backward. On the other hand, there is no doubt that certain refinements in the derivation justifiably can be omitted if the results are to be tabulated, no one will need to do it again, and there is plenty of spare computer capacity.

The formulas derived in the papers under consideration represent the modern approach. They are correct, and the results have been tabulated or graphed. The writer would like, however, to compare these formulas with those presented before this Society in 1947, and referred to by the authors as reference (2). This comparison has been difficult, not only because of the difference in symbols, but because the authors have not listed their formulas for curvature in the order of use. Nevertheless, the writer has made this comparison, using the authors' symbols throughout, and the same starting data.

The difference in length of formulas is so marked, particularly in the case of curvature, that one might suspect that both cannot be correct, or that they do a different job. Nevertheless, assurance is given that they are both correct, and that they give the same numerical answer from the same given data.

The difference can be attributed chiefly to point of view. At the time the writer's paper appeared, it was clear that hand-computation methods would have to be used, so every effort was made to reduce to a simple form. Nevertheless, by the use of appropriate kinematic and geometrical principles as well as the principles of elementary calculus, the derivations are not very long. The authors, on the other hand, knowing the power of the electronic computer, have not felt it necessary to be seriously concerned with the length of formulas so long as they are correct.

The engineer will have to decide for himself what compromise between these views to adopt on his own problems. Certainly the advent of computers promises to make many advances possible in the machine-design field which cannot be ignored.

[3] This discussion applies to ASME Papers Nos. 55—SA-29 and 55—SA-38, published in this issue, pp. 795–806.

[4] Chief Research Engineer, The Gleason Works, Rochester, N. Y. Mem. ASME.

## Comparison of Methods

### I Pressure Angle

Assuming that the following values are given or have been determined:

$$\beta,\ \tau,\ R_0,\ l,\ c,\ \delta_0,\ \delta,\ R, \text{ and } (d\delta)/(d\theta);\ \text{then}$$

*Kloomok and Muffley*

$$\psi = \cos^{-1}\frac{(c^2 + R^2 - l^2)}{2Rc}$$

$$a = \frac{\pi}{2} - \sin^{-1}\left[\frac{c}{R}\sin\delta\right] + \tan^{-1}\left[\frac{1}{\dfrac{R^2}{lc\sin\delta\dfrac{d\delta}{d\theta}} - \dfrac{c^2 - R^2 - l^2}{2Rc\sin\psi}}\right] \quad \ldots\ldots [13]$$

*Baxter*

$$\tan a = \operatorname{ctn}\delta - \frac{l\left(1 - \dfrac{d\delta}{d\theta}\right)}{c\sin\delta}$$

### II Curvature

Assuming that the following values are given or have been determined

$$\beta,\ \tau,\ R_0,\ l,\ c,\ \delta_0,\ \delta,\ R,$$

$$\frac{d\gamma}{d\theta} \text{ or } F'(\theta), \text{ and } \frac{d^2\gamma}{d\theta^2} \text{ or } F''(\theta);\ \text{then}$$

*Kloomok and Muffley*

$$\cos\psi = \frac{c^2 + R^2 - l^2}{2cR}$$

$$f'(\theta) = \frac{lc}{R}F'(\theta)\sin\delta$$

$$f''(\theta) = \frac{(lc\sin\delta)\left(\dfrac{d^2\gamma}{d\theta^2}\right) + (lc\cos\delta)\left(\dfrac{d\gamma}{d\theta}\right)^2 - [f'(\theta)]^2}{R}$$

$$\frac{d\psi}{dR} = \frac{c^2 - R^2 - l^2}{2R^2c\sin\psi} \qquad \frac{d\psi}{d\theta} = f'(\theta)\frac{d\psi}{dR}$$

$$\frac{d}{d\theta}\left(\frac{d\psi}{dR}\right) = \frac{1}{R^2c\sin^2\psi}\left\{-R^2\sin\psi\cdot f'(\theta) - [c^2 - R^2 - l^2]\left[\frac{R}{2}\cos\psi\frac{d\psi}{d\theta} + \sin\psi f'(\theta)\right]\right.$$

$$g''(\theta) = \pm\frac{d^2\psi}{d\theta^2} = \frac{d\psi}{dR}f''(\theta) + [f'(\theta)]\left[\frac{d}{d\theta}\left(\frac{d\psi}{dR}\right)\right]\begin{pmatrix}+\text{ toward pivot}\\ -\text{ away from pivot}\end{pmatrix}$$

$$g'(\theta) = 1 \pm \frac{d\psi}{d\theta}\begin{pmatrix}+\text{ toward pivot}\\ -\text{ away from pivot}\end{pmatrix}$$

$$\frac{dR}{d\phi} = \frac{f'(\theta)}{g'(\theta)}$$

$$\frac{d^2R}{d\phi^2} = \frac{g'(\theta)f''(\theta) - f'(\theta)g''(\theta)}{[g'\theta]^2}$$

$$\rho = \frac{\left[R^2 + \left(\frac{dR}{d\phi}\right)^2\right]^{3/2}}{R^2 + 2\left(\frac{dR}{d\phi}\right)^2 - R\frac{d^2R}{d\phi^2}} \quad \ldots\ldots\ldots [2]$$

*Baxter*

$$\tan a = \operatorname{ctn}\delta - \frac{l\left(1 - \frac{d\gamma}{d\theta}\right)}{c\sin\delta}$$

$$\frac{1}{\rho} = \frac{\cos a}{c\sin\delta}\left\{1 + \frac{l\cos a}{c\sin\delta}\right.$$

$$\left.\left[\frac{d\gamma}{d\theta}\left(1 - \frac{d\gamma}{d\theta}\right)\sin a - \frac{d^2\gamma}{d\theta^2}\cos a\right]\right\}$$

### Authors' Closure[5]

Our congratulations are due Mr. Baxter for his prior derivation of exactly equivalent equations for radius of curvature and pressure angle in a highly refined form.

There is no need for Mr. Baxter to become alarmed. In high-speed computers even more so than in slide-rule or desk-calculator computation, a premium is placed on efficient operation. It must be remembered that owing to the sequential character of digital computers, programming must be done in stepwise fashion, one term at a time. A reduction in the area occupied by the equations is not necessarily significant. Within this framework analytic refinement is definitely justified provided the cost of this refinement does not exceed the economy realized thereby. There are many problems presented to computers these days which, by this criterion, are borderline cases.

At any rate a highly refined analytic solution is hardly sufficient for the harried engineer. What is of much more significance to him is a method for arriving at numerical values quickly and easily. "The trend toward the use of high-speed computation equipment to tabulate in advance critical and complex design data so as to reduce engineering man-hours required on a job," which Mr. Baxter recognizes, is today indeed a reality.

[5] This closure applies to ASME Papers Nos. 55—SA-29 and 55—SA-38.

# Determination of Pressure Angles for Swinging-Follower Cam Systems

By MARTIN KLOOMOK[1] and R. V. MUFFLEY[2]

**The maximum pressure angle is required for an analysis of the forces existing in a cam system. In this paper an exact expression is derived for pressure angle in a swinging roller-follower cam system, and a chart is presented indicating a method for finding a quick numerical solution for a particular cam contour, such as the harmonic or the cycloidal.**

## Nomenclature

The following nomenclature is used in the paper:

- $A$ = point of contact of roller with cam
- $B$ = position of follower arm pivot
- $c$ = distance from cam center to follower arm pivot, in.
- $C$ = position of follower center
- $F$ = external load on radial follower stem, lb
- $l$ = length of follower arm, in.
- $N$ = normal force on roller, lb
- $O$ = cam center
- $R$ = radius measured from camshaft center to follower roller center, in.
- $R_0$ = minimum radius at start of complete event, in.
- $T$ = torque on swinging-follower arm, in-lb
- $\alpha$ = pressure angle at any point
- $\alpha_{max}$ = maximum pressure angle for event
- $\beta$ = total angular rotation of cam for a complete event
- $\delta$ = angle between $l$ and $c$
- $\epsilon$ = angle between $l$ and $R$
- $\theta$ = angular rotation of cam measured from a space fixed reference
- $\lambda$ = angle between normal to cam surface and the line $OC'$
- $\tau$ = total angular rotation of follower arm for a complete event
- $\phi$ = angular rotation of cam measured from a line joining cam and follower roller centers
- $\psi$ = angle between $c$ and $R$
- $\psi_0$ = $\psi$ when $R = R_0$

All angles are in radians

## Introduction

Of the several factors that determine the success of a cam system, one of the most important is pressure angle. Too high a pressure angle will cause high surface compressive loadings between follower and cam, and the cam shaft drive torque will be considerably increased. Accordingly, the designer should know the maximum value of pressure angle in any new cam system.

In the past, pressure angle has been determined largely by using a protractor on a layout of the cam. This practice becomes very time-consuming, however, when it is necessary to make a series of layouts to arrive at optimum proportions. Advance calculation is to be preferred if it can be kept simple.

[1] Manager, Scientific Computation Laboratory, International Business Machines Corporation, Endicott, N. Y.

[2] Staff Engineer, Engineering Laboratory, International Business Machines Corporation, San Jose, Calif. Assoc. Mem. ASME.

Contributed by the Machine Design Division and presented at the Diamond Jubilee Semi-Annual Meeting, Boston, Mass., June 19–23, 1955, of The American Society of Mechanical Engineers.

Note: Statements and opinions advanced in papers are to be understood as individual expressions of their authors and not those of the Society. Manuscript received at ASME Headquarters, March 24, 1955. Paper No. 55—SA-38.

## Radial-Follower System

Calculation of the maximum pressure angle is not difficult in the case of the roller follower traveling radially in and out from the cam center. The derivation is well known and is repeated here only as a preliminary to the derivation for the swinging follower presented later. In Fig. 1 the pressure angle is defined as the angle included between the line of action of $C$, the roller-follower center, and $CA$, the normal to the cam surface at $A$, the point of contact. In Fig. 1 the cam is actually rotating counterclockwise, but for analytical purposes the cam is considered fixed, and the follower center is considered moving around it clockwise from position $C$ to position $C'$, swinging though the small angle $d\theta$. As $d\theta$ is made smaller, $CC'$ becomes normal to $N$, and $CE$ becomes parallel to $CD$. Thus $\alpha'$ equals $\alpha$ in the limit, and

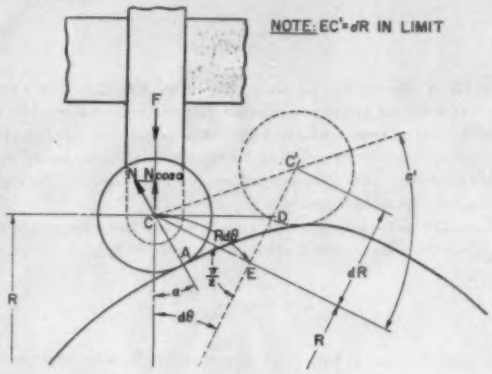


Fig. 1 Pressure-Angle Geometry for a Radial Cam Follower

$$\alpha = \tan^{-1} \frac{1}{R} \frac{dR}{d\theta} \quad \ldots\ldots [1]$$

This expression is readily evaluated for different motion curves, such as the harmonic or cycloidal, and solutions are to be found in the literature.

With the pressure angle calculated, the normal load on the roller can be determined in terms of the pressure angle and the external load on the cam-follower stem. Neglecting friction for the purposes of the present discussion

$$N = \frac{F}{\cos \alpha} \quad \ldots\ldots [2]$$

## Swinging-Follower System

The pressure angle in a swinging-follower system is completely analogous. Referring to Fig. 2, the pressure angle $\alpha$ is defined as the angle between $CA$, the normal to the curve at the

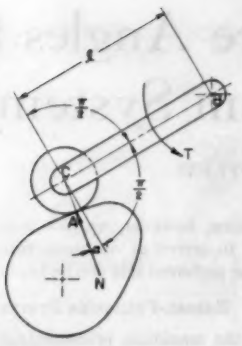


FIG. 2 TORQUE AND NORMAL LOAD FOR A SWINGING CAM FOLLOWER

point of roller contact, and the normal to $BC$, the center line of the follower arm. Taking moments about $B$, the follower arm pivot, and neglecting friction, which is usually very small

$$N = \frac{T}{l \cos \alpha} \quad [3]$$

Fig. 3 is essentially an enlargement of Fig. 2. The cam in Fig. 3 is rotating counterclockwise, but for convenience the cam is considered at rest, and the follower arm pivot is rotated clockwise a small angle $d\theta$ relative to the cam, to new position $B'$. Simultaneously, the follower roller center $C$ moves through a small angle $d\phi$ to new position $C'$.

The angle $\lambda$ in Fig. 3 is analogous to the pressure angle $\alpha$ in Fig. 1, and similarly, as $d\phi$ approaches zero, $\lambda'$ approaches $\lambda$, and

$$\lambda = \tan^{-1} \frac{1}{R} \frac{dR}{d\phi} \quad [4]$$

By examination of Fig. 3 the pressure angle may be expressed as

$$\alpha = \frac{\pi}{2} - (\epsilon - \lambda) \quad [5]$$

The follower arm is assumed to have harmonic, cycloidal, or some other prescribed angular motion with respect to the angular rotation of the cam, so that the angle $\delta$ between $l$ and $c$ can be computed as a function of $\theta$. Knowing $\delta$, the triangle $OB'C'$ in Fig. 3 may be solved for $R$, $\epsilon$, and $\psi$

$$R = \sqrt{l^2 + c^2 - 2lc \cos \delta} \quad [6]$$

$$\epsilon = \sin^{-1} \left[ \frac{c}{R} \sin \delta \right] \quad [7]$$

$$\psi = \cos^{-1} \frac{(c^2 + R^2 - l^2)}{2Rc} \quad [8]$$

Referring to Fig. 4($a$)

$$\phi = \psi_0 - (\psi - \theta) \quad [9]$$

Differentiating Equation [9] with respect to $R$

$$\frac{d\phi}{dR} = \frac{d\theta}{dR} - \frac{d\psi}{dR} \quad [10]$$

Differentiating Equation [6] with respect to $\theta$ and taking the reciprocal

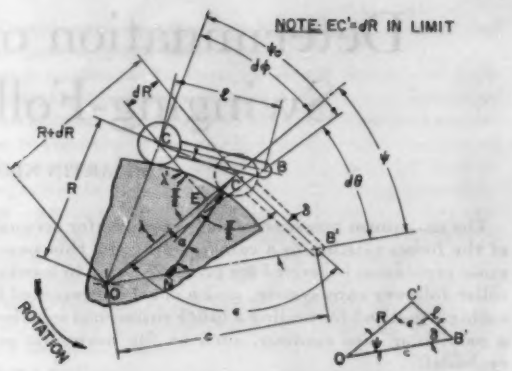


FIG. 3 PRESSURE ANGLE GEOMETRY FOR A SWINGING CAM FOLLOWER

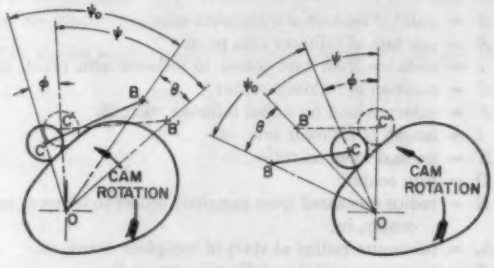


FIG. 4 SWINGING FOLLOWER SHOWN WITH ROTATION FROM AND TOWARD THE PIVOT
($a$, from pivot; $b$, toward pivot.)

$$\frac{d\theta}{dR} = \frac{R}{lc \sin \delta \dfrac{d\delta}{d\theta}} \quad [11]$$

Differentiating Equation [8] with respect to $R$

$$\frac{d\psi}{dR} = \frac{c^2 - R^2 - l^2}{2R^2 c \sin \psi} \quad [12]$$

Collecting terms from Equations [4], [7], [10], [11], and [12] and substituting in Equation [5]

$$\alpha = \frac{\pi}{2} - \sin^{-1} \left[ \frac{c}{R} \sin \delta \right] + \tan^{-1} \left[ \frac{1}{\dfrac{R^2}{lc \sin \delta \dfrac{d\delta}{d\theta}} - \dfrac{c^2 - R^2 - l^2}{2Rc \sin \psi}} \right] \quad [13]$$

Care must be taken to distinguish between rotation "away" from the follower arm pivot as in Figs. 3 and 4($a$), and rotation "toward" the pivot as in Fig. 4($b$). Considering Fig. 3 with direction of rotation reversed

$$\alpha = -\frac{\pi}{2} + \epsilon + \lambda \quad [14]$$

Referring to Fig. 4($b$)

$$\phi = \psi - (\psi_0 - \theta) \quad [15]$$

Differentiating with respect to $R$

$$\frac{d\phi}{dR} = \frac{d\theta}{dR} + \frac{d\psi}{dR} \quad \ldots\ldots [16]$$

Collecting terms from Equations [4], [7], [11], [12], and [16] and substituting in Equation [14]

$$\alpha = -\frac{\pi}{2} + \sin^{-1}\left[\frac{c}{R}\sin\delta\right] + \tan^{-1}\left[\frac{1}{\dfrac{R^2}{lc\sin\delta\,\dfrac{d\delta}{d\theta}} + \dfrac{c^2 - R^2 - l^2}{2Rc\sin\psi}}\right] \quad [17]$$

Equations [13] and [17] can be evaluated for a given motion of the follower arm by substituting the appropriate expression for $\delta$ and $d\delta/d\theta$. For example, if the motion of the follower arm is to be harmonic

$$\delta = \delta_0 + \frac{\tau}{2}\left[1 - \cos\frac{\pi\theta}{\beta}\right] \quad \ldots\ldots [18]$$

If the motion prescribed for the follower is cycloidal

$$\delta = \delta_0 + \tau\left[\frac{\theta}{\beta} - \frac{1}{2\pi}\sin\frac{2\pi\theta}{\beta}\right] \quad \ldots\ldots [19]$$

Differentiation of the resultant expression to compute a maximum yields an unwieldy transcendental equation. Rather than attempt to determine maxima in this way, a modern high-speed computer, the IBM Model II Card-Programmed Electronic Calculator, has been used to evaluate the equations for given values of the parameters $l$, $c$, $\tau$, and $\beta$ while the ratio $\theta/\beta$ is varied from 0 to 1. The individual maxima so determined have been plotted as a function of $\beta/\tau$, as seen in the representative chart, Fig. 5. In

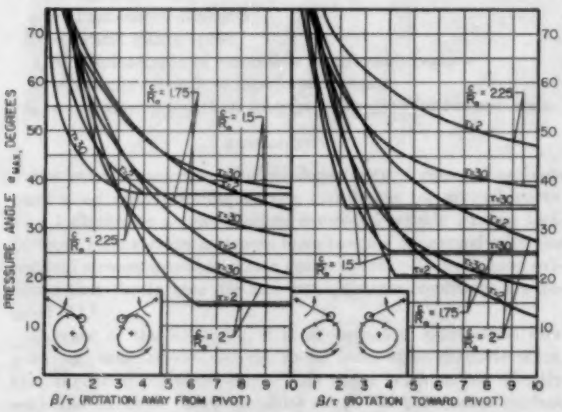


FIG. 5 REPRESENTATIVE PRESSURE ANGLE CHART FOR A SWINGING CAM FOLLOWER. $l/R_0 = 1.5$ AND MOTION IS CYCLOIDAL

these charts all linear dimensions have been converted to dimensionless form by dividing through by $R_0$. The effect of rotation toward or "from" the pivot has been accommodated by plotting two complete sets of curves on each chart.

It is emphasized that such charts can give the maximum value of pressure angle only; thus each point on each curve is the solution for a particular cam. The location of the maximum is not given, nor is it needed for most applications.

The use of the charts is indicated in the following examples:

*Example 1.* Assume a cycloidal motion is to be used for rise between two dwells. Let

$R_0 = 1.50$ in.
$l = 2.25$ in.
$c = 2.50$ in.
$\tau = 10$ deg
$\beta = 60$ deg

Rotation be away from pivot

Then $l/R_0 = 2.25/1.5 = 1.5$
$c/R_0 = 2.50/1.5 = 1.67$
$\beta/\tau = 60/10 = 6$

It is necessary to interpolate for both $c/R_0$ and $\tau$; however, this interpolation is not critical since an approximate value of the pressure angle is usually sufficient. Charted values were obtained from Fig. 5 and are given in Table 1.

TABLE 1 CHARTED VALUES FROM FIG. 5

| $c/R_0$ on chart | $\tau$ value on chart | $\alpha_{max}$ reading, deg | Interpolation: $\alpha$ for $c/R_0 = 1.67$, deg | Interpolation: $\alpha$ for $\tau = 10$, deg |
|---|---|---|---|---|
| 1.50 | 3 | 41.5 | 33.3* | 34.2 |
| 1.75 | 3 | 29.5 | | |
| 1.50 | 30 | 43.0 | 36.5 | |
| 1.75 | 30 | 33.5 | | |

* Sample interpolation:

$$\alpha = 41.5° - \left[\left(\frac{1.67 - 1.50}{1.75 - 1.50}\right)(41.5 - 29.5)\right] = 33.3°$$

*Example 2.* Half-cycloids and half-harmonics are sometimes used in conjunction with other curves. When a half-curve is to be so used, the parameters must be modified before making use of the charts.

Assume a half-harmonic is to be applied between points $C$ and $D$, Fig. 6. For computation purposes the half-curve is extended to point $E$, forming a full harmonic:

$R_0'$ is radius to follower center at point $E$

$\beta' = 2\beta$
$\tau' = 2\tau$

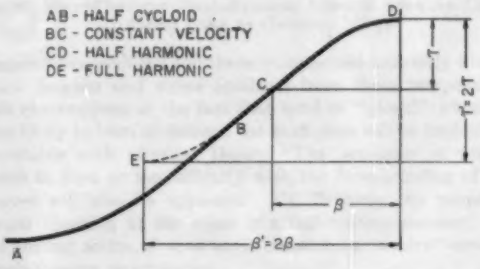


FIG. 6 GRAPHICAL ANALYSIS OF COMBINATION CAM PROFILE

Using $R_0'$, $\beta'$, and $\tau'$, the computation proceeds as in Example 1. Using the same general procedure, a check might also be made for maximum pressure angle in half-curve $AB$.

*Example 3.* Heretofore it has been tacitly assumed that the motion under consideration required a "rise" of the cam. While this is usually the more critical situation as regards forces on the

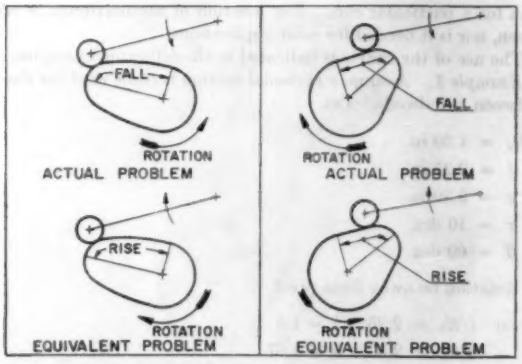


FIG. 7 CONVERSION OF FALL PORTION OF CAM TO AN EQUIVALENT RISE TO PERMIT USE OF THE CHARTS

cam and is often the only case that concerns the designer, nevertheless information is sometimes required on the "fall." The maximum pressure angle for the fall may be determined by the same method as for the rise if the direction of rotation is reversed before using the charts. Fig. 7 illustrates this point.

## CONCLUSION

An exact derivation has been given for determining pressure angle in swinging-follower cam systems. Certain of the resultant expressions have been evaluated on an IBM Model II Card-Programmed Electronic Calculator, and a typical chart is presented to illustrate the results of the computation.

## REFERENCES

1 "Pressure Angles in Cam Roller Followers," by G. V. Ono, ASME Paper No. 52—SA-33.

2 "Curvature-Acceleration Relations for Plane Cams," by M. L. Baxter, Trans. ASME, vol. 70, 1948, pp. 483–489.

# The Relation Between Grinding Conditions and Thermal Damage in the Workpiece

By R. S. HAHN,[1] WORCESTER, MASS.

**The tendency of heat checks and cracks to form in the workpiece is shown to be strongly dependent upon work speed. The durability of the cutting edges of tools is shown to be affected by the work speed during sharpening. Based on the rubbing-grain hypothesis, the "theory of heat conduction" is applied to the grinding process to show that lower surface temperatures occur when grinding is done at high work-surface speed.**

## Nomenclature

The following nomenclature is used in the paper:

$R$ = rate of metal removal
$F_n$ = normal force on wheel
$\Delta$ = dynamic curvature difference (see reference 4)
$S$ = ratio of wheel-surface speed/work-surface speed
$v_s$ = wheel-surface speed
$v$ = work-surface speed
$V = v_s + v$ = relative grit sliding speed
$l$ = half-length of heat source in direction of sliding
$\kappa$ = thermal diffusivity of work
$K$ = thermal conductivity of work
$L_g = \frac{Vl}{2\kappa}$ = dimensionless parameter for grit source
$L_w = \frac{vl}{2\kappa}$ = dimensionless parameter for wheel source
$S_s$ = shear stress between grit and work
$J$ = 778 ft-lb/Btu = Joule's constant
$\theta$ = temperature
$q$ = heat-source strength
$N$ = wheel rotary speed
$s$ = displacement of successive interference regions
$b$ = effective length of interference region
$b_0$ = maximum length of interference region for highest grain

## Introduction

For many years the grinding-department foreman has been confronted with grinding checks and burns on ground parts. Fig. 1 illustrates a heat-checked cemented-carbide cutting tool. In more recent years engineers have become concerned with the residual stresses introduced into ground parts. There is good evidence that the fatigue life and surface-stress conditions are related (1).[2]

In view of the foregoing, it is important to understand how grinding variables such as work speed, feed, wheel characteristics, etc., influence the workpiece. This paper is concerned directly with the effect of these variables on the instantaneous surface temperatures produced and thereby concerned indirectly with the actual damage and stress resulting from these temperatures. Such observations as the fact that hard or "glazed" wheels are more likely to burn or damage the workpiece will be explained in accordance with physical theory. The tendency of fine-grit wheels to burn or the difficulty with the form-grinding of deep grooves will also be apparent. Fig. 2 shows the propensity toward checking at the edges of a ball-bearing raceway. The cool cutting action of open structure such as "twelve"-structure wheels also can be explained.

Fig. 1 Heat-Checked Triple-Carbide Cutting Tool. Ground at 20 Fpm; ×20

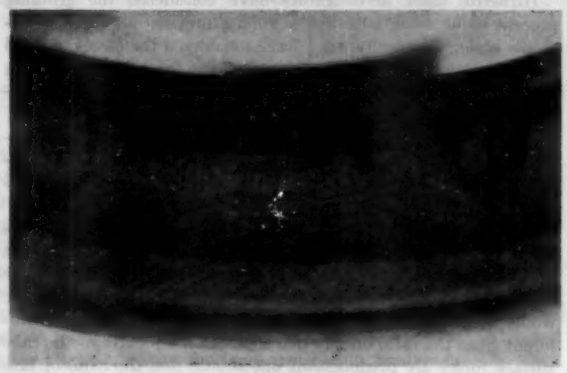

Fig. 2 Heat-Checked Ball-Bearing Groove Showing Cracks Along Edge of Groove; ×3½

## General Observations on Work Speed

The "checking" shown in Figs. 1 and 2 completely disappeared when the work speed was increased sufficiently. By work speed is meant the speed at which the workpiece is passed under the grinding wheel.

In the case of the ball-bearing groove, complete freedom from checking was obtained at a work speed of 200 fpm.

In the case of the carbide tool the work speed was in the neigh-

[1] Consulting Engineer, The Heald Machine Company. Mem. ASME.

[2] Numbers in parentheses refer to Bibliography at end of paper.

Contributed by the Metals Engineering Division and presented at a joint session of the Metals Engineering and Production Engineering Divisions and the Research Committee on Metal Processing at the Diamond Jubilee Semi-Annual Meeting, Boston, Mass., June 19–23, 1955, of The American Society of Mechanical Engineers. Note: Statements and opinions advanced in papers are to be understood as individual expressions of their authors and not those of the Society. Manuscript received at ASME Headquarters, April 27, 1955. Paper No. 55—SA-60.

borhood of 20 fpm which was nearly the maximum table speed of the reciprocating surface grinder upon which the tool was ground. This speed was not sufficient to eliminate checking.

In order to investigate further the effect of work speed, a set of 20 triple-carbide tools was ground on a rotary surface grinder at a work speed of 600 fpm. A comparison set of 27 tools was ground by conventional means at 20 fpm, the same type of diamond wheel being used for both sets. The set of 20 tools ground at high work speed yielded 20 good tools with no observable checking or cracking. The set of 27 tools ground at 20 fpm yielded 12 good tools, the rest being checked or cracked.

Next, the tools were used in a cutting test. The procedure was to observe how many parts could be bored before the tool failed. The parts were steel with a hole containing a keyway (interrupted cut). A 0.010-in. depth of cut was taken at 0.006-in. lead at 350 fpm. The tools would cut satisfactorily for a time and then would suddenly fail by chipping. The tools ground at 600 fpm produced 8.3 parts per tool. The tools ground at 20 fpm produced 3.1 parts per tool.

In view of the foregoing it can be seen that high work speeds are effective in reducing checking and cracking of heat-sensitive materials and may also influence the life of the tool or part.

## The Rubbing-Grain Hypothesis

In order to explain the pronounced effect of work speed on checking and burning, it is necessary to formulate a rational theory of grinding that fits the observations cited, as well as others.

Hitherto, most investigators have considered the grinding process to be essentially like a milling process but on a microscopic scale. Generally, they have considered the forces, normal and tangential to the wheel surface, to arise from the chips acting against the rake surface of the grit and have neglected any frictional rubbing forces on the clearance surface of the grit.

There is considerable evidence which indicates that in the grinding process it may be more realistic to consider the frictional rubbing forces on the clearance surface and neglect the cutting forces on the rake surface.

In metal cutting with single-point tools where the chip forces predominate, the tangential force is generally about twice the normal force. If such tools were simply reduced to microscopic size and the forces for a number of them added together, there would be no reason for the ratio of the total force to be any different from the ratio on any one tool. Consequently, if the rake surface forces are predominant one should find the ratio of tangential force (cutting) to normal force (thrust) to be the same as in single-point machining, namely, about two. In grinding the reverse is true—the ratio is about $^1/_2$, see Marshall and Shaw (2), and consequently, more nearly resembles the sliding-friction process where the ratio is about $^1/_4$.

Consider next the forces on a single-point tool at very small depth of cut, the tool having a very low clearance of about $^1/_2$ deg. Fig. 3 taken from Hahn (3) shows the behavior. At depths of cut less than 0.0004 in. there is no chip—metal is removed as dust in this particular case—all of the forces on the tool act on the clearance surface. Furthermore, note that the ratio of cutting force to thrust force in this region is $^1/_2$ not 2.

As a further argument in support of the rubbing-grain hypothesis, abrasive wheels are dressed by a diamond. The diamond has been observed to actually cut through the grain. It is well known that the lead of the diamond during dressing greatly influences the cutting action of a wheel. Clearly the dressing action is such as to provide zero clearance on the grain. Fig. 4, taken from Hahn (4), shows a comparison between a slowly dressed and a rapidly dressed wheel. These data were derived from tests where the wheel was pressed against the workpiece with a pre-

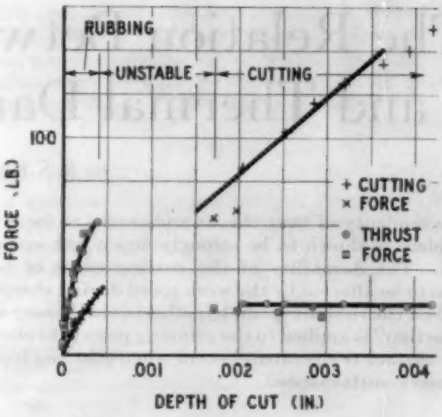


Material: Leaded bronze
Tool: Carboloy 883, 0 rake, 0.458 clearance
Speed: 20 fpm
Width of cut: $^1/_4$ in.
Highly work-hardened surface

Fig. 3 Force-Depth of Cut Relation for a Tool of Small Clearance Penetrating the Unstable "Transitional" Region

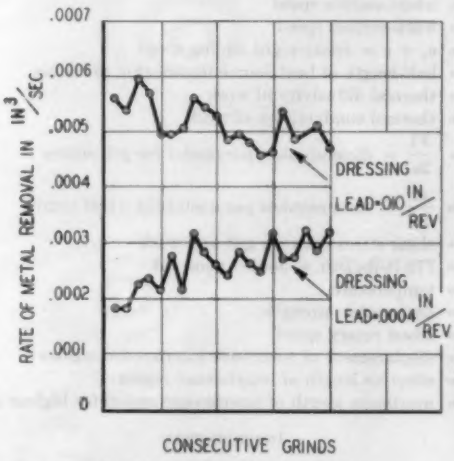


Work: SAE 4150 47-52C
Wheel: 38A60-L8VBE
Normal force: 6.16 lb

Fig. 4 Progressive Changes in Cutting Ability of Grinding Wheel Surface

scribed force and the rate of stock removal measured. For the wheel dressed at 0.0004 in/rev diamond lead, the rate of stock removal for the freshly dressed wheel is 0.00018 cu in/sec corresponding to the first point on the lower curve. Subsequent grinding actually caused the wheel to sharpen as shown. The rate of stock removal for a freshly dressed wheel with diamond lead of 0.010 in/rev is 0.00056 cu in/sec, or three times that for the slowly dressed wheel. It is clear therefore that the clearance surfaces of the grits play an important role in the grinding process.

Finally, further evidence, also in support of the rubbing-grain hypothesis, is that presented by Hahn (4) in which he experimentally found that the rate of metal removal $R$ varied with the curvature difference $\Delta$ and normal force $F_n$ according to

$$R \sim F_n \Delta^{0.13} \qquad \text{(experimental)}$$

and then proceeded to derive a theoretical formula based on the rubbing-grain hypothesis which came out to be

$$R \sim F_n^{1.4}\Delta^{0.20} \qquad \text{(theoretical)}$$

Since the agreement between the exponent of $\Delta$ is very good (although that on $F_n$ is not so good) this is taken as evidence in support of the rubbing-grain hypothesis.

### Heat Sources in Grinding

With the rubbing-grain hypothesis there are three distinct regions of interest on a grit. Fig. 5 illustrates a grit with a sizable area *OC* in rubbing contact with the workpiece. As the grit becomes dull or worn (a glazed wheel) the length *OC* probably greatly increases to *OC'*. The shear plane is illustrated at *OB* and the grit-chip interface at *OA*. These three areas *OA*, *OB*, and *OC* may be thought of as heat sources.

In contrast to the work of Outwater and Shaw (5) who considered the shear-plane source *OB*, let us consider the clearance surface source *OC*. The results of Loewen and Shaw (6), Leone (7), and Hahn (8) all agree with regard to the division of shear-plane heat at high speeds, namely, that very little shear-plane heat escapes into the workpiece. According to Loewen and Shaw (6) using their Formula [9] about 20 per cent of the shear-plane heat escapes into the work for a grain depth of cut of 0.001 in. at 5000 fpm wheel speed. Therefore most of the heat entering the workpiece must come from the source *OC* rather than the shear-plane source *OB*. The grit-chip interface source *OA* would not be expected to supply heat to the workpiece.

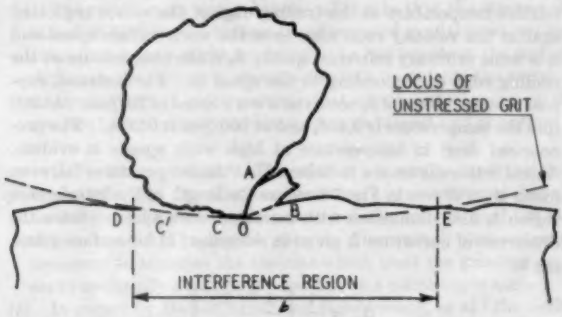


*DE* shows interference region
*OC* shows clearance heat source on grit (grit source)
*OB* shows shear-plane heat source
*OA* shows grit-chip interface heat source

Fig. 5 Illustration Showing a Grit Engaged With Workpiece

In view of the foregoing the grinding process appears, from the point of view of the workpiece, to be a tremendous barrage of small intense heat sources moving very rapidly over a short distance, the interference region *DE*, which itself is moving much more slowly along the work surface. The small intense heat sources *OC* will be referred to as grit sources in contrast to the slower moving band representing the interference region *DE* which will be termed the wheel source. The wheel source is composed of the individual grit sources. It will be seen that if the wheel turns at very high speed and is composed of fine grits closely spaced and the work speed is low, the wheel source can, to a good approximation, be represented as a continuous band source moving over the surface of the work. It will further be seen that this continuous source can be dispersed into discrete grit sources by greatly increasing the work speed.

The "theory of moving heat sources" has been worked out by Jaeger (9). Among other things Jaeger shows the temperature distribution on the surface of a semi-infinite body due to a source of heat moving along the surface. Fig. 6 illustrates the surface temperature derived from Equation [8] in reference (9) for large values of the dimensionless parameter $L_\theta$. If we assume the frictional shear stress $S_s$ between grit and work to be independent of temperature the source strength $q$ is

$$q = \frac{S_s V}{J}$$

Using this, the dimensionless temperature

$$\left[\frac{\pi K V}{2\kappa q}\,v\right]$$

in Jaeger's work becomes

$$\left[\frac{\pi k J}{2\kappa S_s}\,\theta\right]$$

and is plotted as the ordinate in Fig. 6. Since the ordinate is now free of the velocity $V$ it is clear that raising the velocity corresponds simply to larger values of $L_\theta$. In the grinding process values of $L_\theta$ for the grit sources can well be over 100 for dulled grits. Since the parameter $L_\theta$ is proportional to the product $Vl$ where $l$ is the half-length of the source in the direction of motion it is clear why dulled or glazed wheels, which have grit sources whose lengths are relatively large such as *OC'* in Fig. 5, cause more burning. Note the large increase in temperature for the larger values of $L_\theta$.

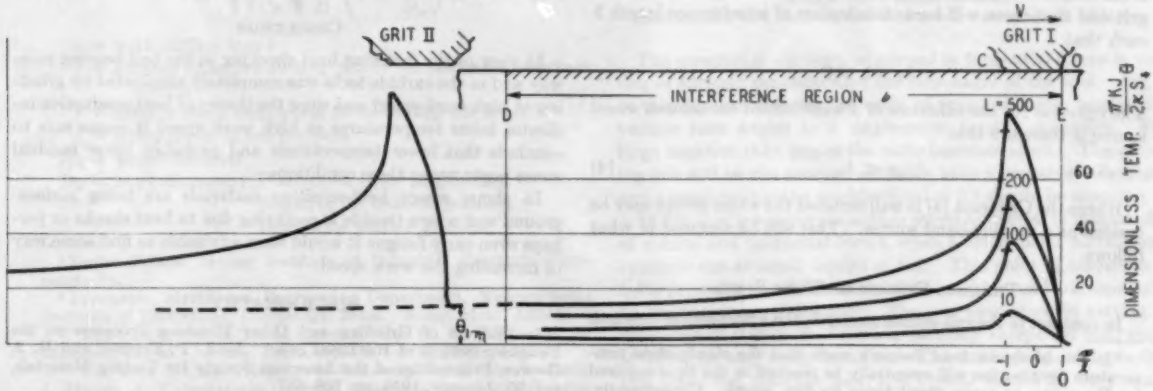


Fig. 6 Illustration Showing Surface-Temperature Distribution Due to Grit Source I. Grit II Is About Ready to Contact Work at *D*

Fig. 6 illustrates a grit source moving over an interference region ten times as long as the grit source. The Grit I is about to leave the workpiece. Grit I produces the temperature distributions shown.[3] The temperature rises very rapidly under the grit source and then falls steeply at first, as the grit passes by, and then very gradually. Following Grit I is Grit II which is about to contact the work. It will superimpose its temperature distribution upon the temperatures existing as the result of the passage of the previous grit. The minimum temperature $\theta_{1_m}$ will be seen to diminish slightly with increasing grit spacing (a shifting of Grit II to the left). After a certain time a steady-state minimum temperature $\theta_{m_s}$ will be established. The relation of $\theta_{m_s}$ to the grit spacing and other variables is obscure at present. Presumably large grit spacing, as in 12-structure wheels, would result in a lower, steady-state, minimum temperature and therefore cooler action.

The final result of many grit sources adding energy to the workpiece in discrete pulses may be treated as a uniform source of lesser intensity moving over the work, as long as the interference region for Grit II is nearly coincident with that for Grit I. The displacement of Grit II interference region relative to that of Grit I is given by

$$s = \frac{v}{\gamma N} \quad \ldots\ldots [1]$$

where $\gamma$ is the number of peripherally equispaced active grits around the circumference of the wheel, $N$ the wheel rotary speed, and $v$ the work-surface speed. If $s$ is small compared to the interference region $b$, a uniform band source of length $b$ is a good approximation. If $s$ is an appreciable fraction of $b$ or greater than $b$ the wheel source tends to disperse into a large number of independent grit sources.

The length of the interference region $b$ may be obtained by considering reference (4). In that paper the normal force on the wheel is given by Equation [13], reference (4), which is

$$F_n = \frac{\sqrt{2}}{3} \frac{k v \sigma}{h} \frac{p_0^{3/2}}{\Delta^{1/2}} \quad \ldots\ldots [2]$$

Using Equation [11], reference (4), to eliminate $p_0$ there results the expression

$$b_0 = \left[\frac{384 h}{v \sigma k}\right]^{0.2} \frac{F_n^{0.2}}{\Delta^{0.4}} \quad \ldots\ldots [3]$$

giving the length of the interference region in terms of normal force and curvature difference. It should be remembered that $b_0$ is the length of the interference region for the outermost or highest grit and that there will be a distribution of interference length $b$ such that

$$b_0 > b > 0$$

The criterion for the existence of a well-defined continuous wheel source is therefore that

$$s \ll b_0 \quad \ldots\ldots [4]$$

Where the Criterion [4] is well satisfied the wheel source may be treated as a moving-band source. This will be assumed in what follows.

## Thermal Effects of Work Speed

In contrast to the grit-source strength, the wheel-source strength is essentially independent of the velocity of the source (the work speed). In order to see directly the effect of work speed on the surface temperature due to the wheel source, Jaeger's data for a moving-band source can be made to yield Fig. 7, wherein the relative temperature at the trailing edge of the source is plotted against the velocity ratio $v/v_0$. $v$ is the work-surface speed and $v_0$ is some arbitrary reference speed; $\theta_0$ is the temperature at the trailing edge corresponding to the speed $v_0$. For instance, suppose a temperature of $\theta_0$ occurs at a work speed of 20 fpm. At 200 fpm the temperature is $0.43\theta_0$ and at 600 fpm is $0.26\theta_0$. The pronounced drop in temperature at high work speeds is evident. Actually there is reason to believe that the temperatures fall even faster than shown in Fig. 7 because the length of the interference region $b_0$ also diminishes with increased work speed. Since the difference of curvature $\Delta$ given in reference (4) for surface grinding is

$$\Delta_s = \frac{1}{a}\left[\frac{1+2S}{(1+S)^2}\right] \quad \ldots\ldots [5]$$

it can be seen that at high work speeds (smaller $S$) the curvature difference tends to increase. As a result the length of the interference region tends to decrease according to Equation [3] which produces an even faster drop in temperature as illustrated in Fig. 7 by curve $b$.

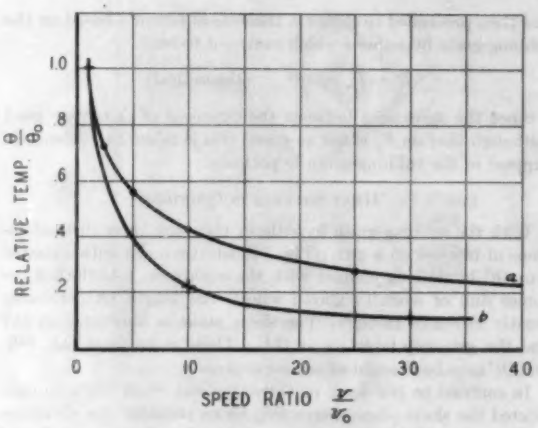


Fig. 7 Illustration Showing Rapid Fall in Surface Temperature as Work Speed Increases

(Curve $a$ is for a source whose length $l$ is constant; curve $b$ is for a source whose length $l$ diminishes with work speed.)

## Conclusion

In view of the fact that heat checking in the ball-bearing raceway and in the carbide tools was completely eliminated by grinding at high work speed and since the theory of heat conduction indicates lower temperatures at high work speed it seems safe to conclude that lower temperatures and probably lower residual stress occur under these conditions.

In shops where heat-sensitive materials are being surface-ground and where trouble is occurring due to heat checks or perhaps even early fatigue it would seem advisable to find some way of increasing the work speed.

## BIBLIOGRAPHY

1 "Effects of Grinding and Other Finishing Processes on the Fatigue Strength of Hardened Steel," by L. P. Tarasov and H. J. Grover, Proceedings of the American Society for Testing Materials, vol. 50, January, 1950, pp. 668–687.

2 "Forces in Dry Surface Grinding," by E. R. Marshall and M. C. Shaw, Trans. ASME, vol. 74, 1952, pp. 51–59

[3] It can be shown from Jaeger's work that the steady-state temperature distribution will essentially be reached in the time required for the source to move about twice its own length. Consequently, the steady-state distribution will apply except when the grit is near the initial point of engagement.

3 "Metal-Cutting Chatter and Its Elimination," by R. S. Hahn, Trans. ASME, vol. 75, 1953, pp. 1073–1080.
4 "The Effect of Wheel Work Conformity in Precision Grinding," by R. S. Hahn, Trans. ASME, vol. 77, 1955, pp. 1325–1329.
5 "Surface Temperatures in Grinding," by J. O. Outwater and M. C. Shaw, Trans. ASME, vol. 74, 1952, pp. 73–86.
6 "On the Analysis of Cutting-Tool Temperatures," by E. G. Loewen and M. C. Shaw, Trans. ASME, vol. 76, 1954, pp. 217–231.
7 "Distribution of Shear-Zone Heat in Metal Cutting," by W. C. Leone, Trans. ASME, vol. 76, 1954, pp. 121–125.
8 "On the Temperature Developed at the Shear Plane in the Metal Cutting Process," by R. S. Hahn, Proceedings of the First U. S. National Congress of Applied Mechanics, 1951, pp. 661–666.
9 "Moving Sources of Heat and the Temperature at Sliding Contacts," by J. C. Jaeger, Journal and Proceedings of the Royal Society of New South Wales, vol. 76, part 3, 1942, pp. 203–224.

## Discussion

H. R. Letner.[4] The beneficial effect of high work speed in reducing the tendency of ground surfaces to crack, pointed out by the author, emphasizes a difficulty inherent in most commercial grinding machines. We have determined the residual-stress distributions in annealed tool steel, resulting from surface grinding at work speeds from 10 to 60 fpm in 10-fpm increments, and found very little difference between them. The tests were conducted with both H and J-grade vitrified wheels, containing 46-grit aluminum-oxide abrasive. The grinding was done dry, using a wheel speed of 6000 sfpm, unit crossfeed of 0.050 in., and unit downfeed of 0.001 in.

The results were somewhat tantalizing in that the stresses obtained at 60 fpm, the highest traverse speed available on our machine, indicated a slight tendency to be less tensile at the surface. Although the reduction was too small to be outside the realm of uncertainty, it is quite possible that significant changes in the stresses take place at the high work speeds used by the author.

G. S. Reichenbach.[5] The author has emphasized the very important effect grinding conditions can have on thermal damage to the ground surface. He points out the serious need for machines capable of high work speeds. However, it does not seem necessary to abandon the theories which treat the grinding process as essentially a milling process but on a microscopic scale.

In papers by Backer, et al.[6] and Reichenbach, et al.[7] the action of a grinding wheel is shown to depend strongly on the average chip size being generated by the grinding grits. The chip thickness is taken as useful parameter to characterize chip size. For most ordinary grinding the average chip thickness is given by

$$t = \sqrt{\frac{4v}{VCr}}\sqrt{\frac{d}{D}\left(1 + \frac{D}{D_w}\right)}$$

$v$ = work surface speed
$c$ = number of active cutting points per unit area at wheel surface
$r$ = ratio of mean chip width to mean chip thickness
$d$ = wheel depth of cut per pass
$D$ = wheel diameter
$D_w$ = work diameter: Positive for external grinding
Negative for internal grinding
Infinite for surface grinding

[4] Senior Fellow, Mellon Institute of Industrial Research, Pittsburgh, Pa.
[5] Instructor, Mechanical Engineering Department, Massachusetts Institute of Technology, Cambridge, Mass. Assoc. Mem. ASME.
[6] "The Size Effect in Metal Cutting," by W. R. Backer, E. R. Marshall, and M. C. Shaw, Trans. ASME, vol. 74, 1952, p. 61.
[7] "The Role of Chip Thickness in Grinding," by G. Reichenbach, J. Mayer, S. Kalpakcioglu, and M. Shaw, published in this issue, pp. 847–859.

It is also found that the specific energy of grinding (energy per unit volume of metal removed) is high when the chip thickness is small. The reason for the high energy is not completely clear but is probably due to several causes: (*a*) There is a size effect due to the small size of chip taken, small chips having a proportionately greater shear strength than large chips. (*b*) The effect of dullness on the cutting edge of the grit becomes important when the chip thickness is reduced, so that the dullness becomes relatively larger. (*c*) Friction on the clearance face of the grit becomes a greater and greater percentage of the total work, since it will remain more or less constant while the shear work is dependent on the size of the chip.

The action of fine wheels is now easily explained. The fine-grit wheels have a larger value of $C$, and therefore produce thinner chips, which results in a high specific energy. The greater the energy input, the more the tendency for burning.

The reduction of burning with high work speeds on a surface grinder is similarly explained. Assuming that the feed $i$ is constant with time, the wheel depth of cut per pass becomes

$$d = \frac{i}{\text{rpm}} = \frac{i}{Kv}$$

where $K$ = const, depending on work diameter. Then, substituting this into the equation for $t$ and collecting all constant terms

$$t = K_1 v^{1/4}$$

Not only is the temperature under the moving wheel source reduced due to the reasons of Jaeger's moving-heat-source theory, but in addition the strength of the source is reduced.

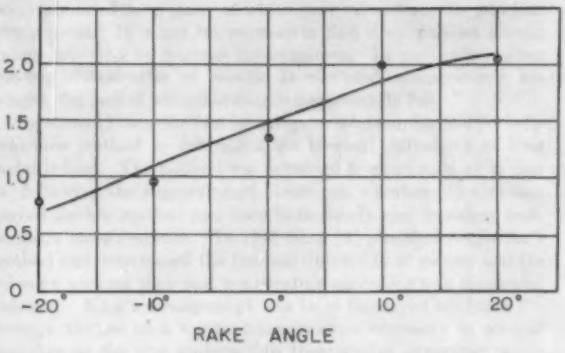


Fig. 8 Variation of Ratio of Tangential Force Over Normal Force With Rake Angle
(K2S carbide, 18-8 stainless, feed 0.0065 in.; cutting speed, 100 fpm.)

The question of the ratio of normal to tangential forces in cutting is strongly dependent on the rake angle of the tool. Fig. 8 of this discussion shows the ratio of tangential over normal for various rake angles in a single-point turning operation. For large negative rake angles the ratio becomes small. The grinding grit will on the average probably have a negative rake angle, and a small ratio in the neighborhood of 0.5 should be expected.

In Fig. 3 of the paper the author shows a reversal of magnitudes of normal and tangential forces, when a single-point cutting tool ceases to cut at small depths of cut. This point of transition is quite dependent on the stiffness of the machine used and especially on the sharpness of the tool. The tool used stopped cutting in the range of 0.0015 in. With a carefully sharpened tool, chips of 0.0001 in. may easily be taken. The cutting edge of a grinding grit being the cleavage face of a crystal should be very sharp and capable of taking very small chips. Microscopic examination

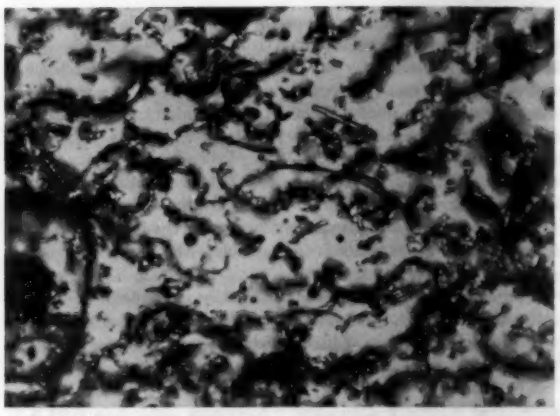

FIG. 9 GRINDING CHIPS—52100 STEEL, SPHEROIDIZED, 46-GRIT WHEEL $V$ = 6000 FPM, $v$ = 20 FPM, $d$ = 0.001 IN.; ×150

of grinding swarth (Fig. 9, herewith) indeed shows cleanly cut chips.

The method of dressing a wheel can alter over a large range the value of $C$. Rapid dressing gives $C$ a low value. This increases the chip thickness into a region of lower specific energy. Low specific energy means a high rate of metal removal in a constant-pressure grinding operation. As the wheel is used, natural wheel breakdown increases $C$ with the resultant lowering of the rate of metal removal. A very fine initial dress results in the reverse process. Both operations approach with time the same rate of metal removal as the value of $C$ becomes that produced by natural breakdown.

## AUTHOR'S CLOSURE

It is interesting to learn that Dr. Letner has found slightly lower tensile stress at the top speed of 60 fpm on his machine. The author thanks Dr. Letner for his remarks and also Professor Reichenbach, whose comments the author finds interesting.

There seem to be two viewpoints from which the grinding process can be studied. One is a kind of phenomenological viewpoint which considers the grinding energy as a starting point and does not deal with the individual forces nor their detailed origin. The other viewpoint attempts to start with the detailed workings of a representative grit and derive relations between the principal variables. These two viewpoints bear the same relation to each other as the Kinetic Theory of Gases bears to the Thermodynamics of Gases. However, any grinding theory, if it is to be realistic, whether it is based on grinding energy or otherwise, should contemplate the very real differences in behavior between sharp and dull wheels and between soft and hard wheels.

# Measuring the Thermal Diffusivity of Metals at Elevated Temperatures

By M. A. EL-HIFNI[1] and B. T. CHAO[2]

**The Angström-bar method has been modified and adapted to the measurement of thermal diffusivity of metals for temperatures ranging from 300 to 1050 F. A small, sinusoidal temperature fluctuation is superimposed on the mean temperature of a thin-wall tubular specimen by means of simultaneous heating and cooling at one end. Thermal diffusivity was calculated from the phase shift and amplitude ratio of the temperature waves determined at two measuring stations. The effect of possible surface heat loss is considered. Measurements were made on AISI 1018, 1045, 3140 steels, and 1.1 per cent carbon tool steel. Results obtained for electrolytic tough-pitch copper and 2S aluminum showed good agreement with a recent theory of Storm concerning the variation of thermal diffusivity of simple metals with temperature.**

## Nomenclature

The following nomenclature is used in the paper:

$A$ = cross-sectional area of specimen, sq ft
$A_{12}$ = amplitude ratio of temperature waves at measuring stations 1 and 2
$b$ = heat-loss factor = $\beta/\omega$
$c$ = specific heat, Btu/(lb)(deg F)
$h$ = surface coefficient of heat transfer, Btu/(hr)(sq ft)(deg F)
$K$ = thermal conductivity, Btu/(hr)(sq ft)(deg F/ft)
$l_1$ = distance between first measuring station and insulated end of specimen, ft
$l_2$ = distance between second measuring station and insulated end of specimen, ft. Hence $(l_1 - l_2)$ is distance between measuring stations
$L$ = length of tubular specimen, ft
$p$ = outside parameter of cross section of specimen, ft
$q$ = time rate of heat flow, Btu/hr
$t$ = time, hr
$T$ = temperature, deg F
$T_e$ = environment temperature, initial uniform temperature of specimen, deg F
$T_0$ = uniform temperature at heated end of specimen, measured above $T_e$
$T_1$ = amplitude of sinusoidal temperature fluctuation at heated end of specimen
$x$ = co-ordinate axis; distance measured from heated end of specimen which is taken as origin, ft
$\alpha$ = thermal diffusivity = $\frac{K}{c\rho}$, ft²/hr
$\rho$ = weight density, pcf
$\phi$ = phase angle of temperature wave, radians
$(\Delta\phi)_{12}$ = phase difference between temperature waves at stations 1 and 2
$\omega$ = $2\pi$ times frequency of temperature fluctuation, 1/hr

## Introduction

Thermal diffusivity is an important physical property in the study of transient heat flow in solids. It is the ratio of the thermal conductivity to the specific heat per unit volume of the solid; i.e., $\alpha = K/(c\rho)$. It was called by Maxwell the thermometric conductivity. The name diffusivity was first suggested by Lord Kelvin.

Data on the thermal conductivity, specific heat, and density of pure metallic elements can be found in the International Critical Tables (1).[3] Also listed are extensive references prior to 1929. The Iron and Steel Institute of Great Britain (2) reported data for a series of ferrous metals. The ASM Metals Handbook (1948 edition) tabulated data, many of which were taken from the previous two sources. It is not uncommon to find discrepancies among values reported by various investigators. In particular, when thermal diffusivities of metals at elevated temperatures are sought, the lack of adequate data is immediately felt.

Angström (3) was the first investigator who employed a periodic heat-flow method to determine the thermal diffusivity of long metallic bars. The method was extended to short rods by Weber (4) following the suggestion of Neumann. Forbes (5) also employed the bar method and used both steady and transient temperature measurements. In 1915 King (6) modified Angström's method and determined the thermal diffusivity of copper and tin wires by varying their end temperature according to a sinusoidal function. King's arrangement was later improved by Starr (7) through the use of a constant-temperature enclosure to control heat loss at the wire surface. In these earlier experiments, all measurements were made at or near room temperature.

Recently, Van Zee and Babcock (8) developed an apparatus by which the thermal diffusivity of molten glass at high temperatures could be determined. A periodic heat-flow method was reported by Sidles and Danielson (9) and measurements were performed on copper, nickel, and thorium wires for temperatures to above 1000 F. The necessary apparatus is very complex, involving elaborate and expensive instrumentation. McIntosh, Hamilton, and Sibbitt (10) also employed a periodic heat-flow method but concluded that the accuracy was inadequate to study conductivity-strain relations. The principal source of error was in the harmonic analysis of the time-temperature records. Considerable time and labor were required to analyze the data.

Use also has been made of moving heat source by Rosenthal and his collaborators (11), and satisfactory results have been claimed for metals having a diffusivity value of 0.2 sq cm/sec (0.8 sq ft/hr) or higher. The thermal diffusivity of most steels is well below this value.

[1] University of Alexandria, Alexandria, Egypt.

[2] Associate Professor of Mechanical Engineering, University of Illinois, Urbana, Ill.

Contributed by the Metals Engineering Division and presented at a joint session of the Metals Engineering and Production Engineering Divisions, and Research Committee on Metal Processing, at the Diamond Jubilee Semi-Annual Meeting, Boston, Mass., June 19–23, 1955, of The American Society of Mechanical Engineers.

Note: Statements and opinions advanced in papers are to be understood as individual expressions of their authors and not those of the Society. Manuscript received at ASME Headquarters, March 24, 1955. Paper No. 55—SA-36.

[3] Numbers in parentheses refer to the Bibliography at the end of the paper.

This paper describes an arrangement employing a "steady" sinusoidal heat flow in which due account is taken of the influence of small heat loss at the surface of a thin-walled tubular specimen. For convenience of further discussion, a short theoretical background will precede the description of the apparatus.

## Theory

The determination of thermal diffusivity by means of periodic heat-flow methods is based on the solution of the heat-conduction equations with specified boundary conditions. The latter vary with individual apparatus. When applied to wires, rods, or thin tubes whose surface is losing heat to the surrounding, the equation takes the form

$$c\rho \frac{\partial T}{\partial t} = \frac{\partial}{\partial x}\left(K \frac{\partial T}{\partial x}\right) - \frac{hp}{A}(T - T_s) \quad [1]^4$$

wherein the $x$-axis is taken along the length of the wire or tube. Since, in general, $c\rho$, $K$, and $h$ are temperature-dependent, Equation [1] is nonlinear. Analytical solution is very difficult, if not impossible, even with the simplest boundary conditions. However, if the range of temperature concerned is small, mean values of $c\rho$, $K$, and $h$ can be adopted and regarded as constants without sacrificing the desired accuracy in the final solution. In the present investigation, the specimen is first heated to a uniform temperature at which its thermal diffusivity is to be evaluated. A small, sinusoidal temperature fluctuation is then superimposed at one end of the specimen. Diffusivity calculations were based on the phase shift and the attenuation of amplitude of the temperature waves at two measuring stations obtained under the steady periodic state. Owing to the relatively small amplitudes of the superimposed temperature waves, the conditions required for the linearization of Equation [1] are satisfied. Hence, if the uniform initial temperature (which is also the environment temperature), is taken as the datum, Equation [1] becomes

$$\frac{\partial T}{\partial t} = \alpha \frac{\partial^2 T}{\partial x^2} - \beta T \quad [2]$$

with $\beta = (hp)/(Ac\rho)$. The boundary conditions are

$$\left.\begin{aligned} T(0, t) &= T_0 + T_1 \sin \omega t \\ \frac{\partial T}{\partial x}(L, t) &= 0 \\ T(x, 0) &= 0 \end{aligned}\right\} \quad [3]$$

As obtained from actual measurement under steady periodic conditions, the mean temperature varies slightly along the length of the specimen. For this reason, a constant term $T_0$ is introduced into the first boundary condition. As will be clear later, it has no effect on the calculation of diffusivity from phase shift and amplitude ratio of the temperature waves. It is included for the sake of completeness in the mathematical analysis. The second boundary condition follows from the fact that the other end of the specimen is insulated. The third equation is self-evident.

The solution of Equation [2] with Boundary Conditions [3] consists of two parts; namely, (*a*) a mean temperature distribution and (*b*) an oscillatory temperature wave, which becomes periodic when $t \to \infty$.

*Mean Temperature Distribution.* The differential equation and the boundary conditions are, respectively

$$\frac{d^2T}{dx^2} - \frac{\beta}{\alpha} T = 0 \quad [4]$$

and

$$T(0) = T_0, \quad \frac{dT}{dx}(L) = 0 \quad [5]$$

The solution is

$$\frac{T}{T_0} = \frac{\cosh (L - x)\sqrt{\frac{\beta}{\alpha}}}{\cosh L \sqrt{\frac{\beta}{\alpha}}} \quad [6]$$

*Oscillatory Temperature Wave.* The differential equation is

$$\frac{\partial T}{\partial t} = \alpha \frac{\partial^2 T}{\partial x^2} - \beta T \quad [7]$$

and the boundary conditions are

$$\left.\begin{aligned} T(0, t) &= T_1 \sin \omega t \\ \frac{\partial T}{\partial x}(L, t) &= 0 \\ T(x, 0) &= 0 \end{aligned}\right\} \quad [8]$$

Using the substitution $T = Ue^{-\beta t}$ where $U$ is a function of $x$ and $t$, Equations [7] and [8] transform into

$$\frac{\partial U}{\partial t} = \alpha \frac{\partial^2 U}{\partial x^2}$$

with

$$U(0, t) = T_1 e^{\beta t} \sin \omega t$$

$$\frac{\partial U}{\partial x}(L, t) = 0$$

$$U(x, 0) = 0$$

Applying the Laplace transformation, the subsidiary equation becomes[5]

$$\frac{d^2\bar{U}}{dx^2} - \frac{s}{\alpha} \bar{U} = 0$$

with the transformed boundary condition

$$\bar{U}(0) = T_1 \frac{\omega}{(s - \beta)^2 + \omega^2}$$

and

$$\frac{d\bar{U}}{dx}(L) = 0$$

The solution is

$$\bar{U} = T_1 \frac{\omega}{(s - \beta)^2 + \omega^2} \frac{\cosh (L - x)\sqrt{\frac{s}{\alpha}}}{\cosh L \sqrt{\frac{s}{\alpha}}} \quad [9]$$

Thence $U$ can be determined by using the inversion integral (12). Thus

$$U = \frac{T_1}{2\pi i} \int_{\gamma - i\infty}^{\gamma + i\infty} e^{\lambda t} \frac{\omega}{(\lambda - \beta)^2 + \omega^2} \frac{\cosh (L - x)\sqrt{\frac{\lambda}{\alpha}}}{\cosh L \sqrt{\frac{\lambda}{\alpha}}} d\lambda \quad [10]$$

[4] The equation can be derived easily by considering the heat balance of an element $dx$ of the wire, rod, or thin tube.

[5] $s$ being the parameter in the Laplace Transform; i.e.

$$\bar{U} = \int_0^\infty e^{-st} U(x, t) dt$$

$\lambda$ is written in place of $s$ in Equation [10] to emphasize the fact that the behavior of $\bar{U}$ is regarded as a function of a complex variable. $\gamma$ is to be so chosen that all the singularities of $\bar{U}(\lambda)$ lie to the left of the line joining $(\gamma - i\infty)$ and $(\gamma + i\infty)$.

Following the standard procedure of finding the sum of the residues at all the poles of the integrand, one finally obtains

$$\frac{T}{T_1} = A \sin(\omega t + \phi) + \frac{\pi\alpha}{L^2} e^{-\beta t} \sum_{n=1}^{\infty} e^{-\alpha\left(\frac{2n-1}{2L}\right)^2 \pi^2 t} \frac{(-1)^{n-1}(2n-1)\omega}{\omega^2 + \left[\left(\frac{2n-1}{2L}\right)^2 \pi^2\alpha + \beta\right]^2} \cos\frac{(2n-1)\pi}{2}\left(1 - \frac{x}{L}\right) \quad [11]$$

The second term on the right side of Equation [11] becomes vanishingly small when $t$ is sufficiently large. Since, in the present investigation, only the steady periodic state is of interest, the required solution is

$$\frac{T}{T_1} = A \sin(\omega t + \phi) \quad [11a]$$

where $A$ and $\phi$ are, respectively, the modulus and argument of the complex quantity

$$\frac{\cosh(L-x)\sqrt{\frac{\beta + i\omega}{\alpha}}}{\cosh L\sqrt{\frac{\beta + i\omega}{\alpha}}}$$

which can be shown to be

$$A = \left[\frac{\cosh^2(L-x)M\cos^2(L-x)M + \sinh^2(L-x)N\sin^2(L-x)N}{\cosh^2 LM\cos^2 LM + \sinh^2 LN\sin^2 LN}\right]^{1/2}$$

and

$$\phi = \arctan\left[\frac{\cosh LM\cos LM\sinh(L-x)N\sin(L-x)N - \cosh(L-x)M\cos(L-x)M\sinh LN\sin LN}{\cosh LM\cos LM\cosh(L-x)M\cos(L-x)M + \sinh(L-x)N\sin(L-x)N\sinh LN\sin LN}\right]$$

wherein

$$M = \sqrt{\frac{\omega}{2\alpha}} \frac{(1+b^2)^{1/4}}{(1 - b\sqrt{1+b^2+b^2})^{1/2}}$$

and

$$N = \sqrt{\frac{\omega}{2\alpha}} \frac{(1+b^2)^{1/4}}{(1 + b\sqrt{1+b^2+b^2})^{1/2}}$$

The amplitude ratio and phase difference of the temperature waves at two measuring stations distant $x_1$ and $x_2$ from the heated end can thus be obtained. They are

$$A_{12} = \left[\frac{\cosh^2 l_1M\cos^2 l_1M + \sinh^2 l_1N\sin^2 l_1N}{\cosh^2 l_2M\cos^2 l_2M + \sinh^2 l_2N\sin^2 l_2N}\right]^{1/2} \quad [12]$$

and

$$(\Delta\phi)_{12} = \arctan\left[\frac{\sinh l_1N\sin l_1N\cosh l_2M\cos l_2M - \cosh l_1M\cos l_1M\sinh l_2N\sin l_2N}{\cosh l_1M\cos l_1M\cosh l_2M\cos l_2M + \sinh l_1N\sin l_1N\sinh l_2N\sin l_2N}\right] \quad [13]$$

When the surface heat loss is very small, such that $b(=\beta/\omega) \ll 1$, $M$ and $N$ become identical and are both approximately equal to $\sqrt{\omega/2\alpha}$. Under such circumstances, Equations [12] and [13] become

$$A_{12} = \left[\frac{\cosh 2\delta_1 + \cos 2\delta_1}{\cosh 2\delta_2 + \cos 2\delta_2}\right]^{1/2} \quad [14]$$

and

$$(\Delta\phi)_{12} = \arctan\left[\frac{\sinh u\sin v + \sinh v\sin u}{\cosh u\cos v + \cosh v\cos u}\right] \quad [15]$$

where

$$\delta_1 = l_1\sqrt{\frac{\omega}{2\alpha}},\ \delta_2 = l_2\sqrt{\frac{\omega}{2\alpha}},\ u = \delta_1 + \delta_2, \text{ and } v = \delta_1 - \delta_2$$

It may be remarked that when $\delta_1$ and $\delta_2$ are large, say, $>5$

$$A_{12} \simeq \frac{\cosh\delta_1}{\cosh\delta_2}$$

and if, in addition, $v$ is relatively small, say, $<0.5$

$$(\Delta\phi)_{12} \simeq v = (l_1 - l_2)\sqrt{\frac{\omega}{2\alpha}}$$

While there is no theoretical difficulty in considering the effect of harmonics on both the phase shift and amplitude ratio, the procedure requires the use of a harmonic analyzer which not only entails considerable time and labor but also introduces an additional source of error. In the present work, efforts have been made to generate sinusoidal waves as accurately as possible. The recorded wave form has been carefully examined and compared with a sinusoidal curve. Distortion has been found to be so small that it can be completely ignored.

## Experimental Equipment

The experimental apparatus is designed to fulfill the various assumptions used in the theoretical analysis. A brief description is hereby given as follows:

*The Furnace.* Fig. 1 shows a vertical section through the furnace. The tubular specimen 1 was 5 in. long, $^7/_8$ in. OD, and had a relatively thin wall to insure one-dimensional heat flow. Mounted concentrically with the specimen was another tube 2 of similar material. It served to minimize the surface heat loss from the test specimen. One end of the tube-and-shield assembly was immersed in a liquid heating bath 3 to maintain a uniform temperature over the tube cross section at any given instant. It also helped to keep the temperature drop at a low value. For temperatures up to about 500 F, a low melting-point alloy containing 50 Bi, 25 Pb, 12.5 Sn, and 12.5 per cent Cd was employed. A neutral salt containing equal proportions of $NaNO_2$ and $NaNO_3$ was used for higher temperatures. The other end of the specimen was supported by a transite disk 4, which also provided for the insulation there.

Inasmuch as the entire furnace assembly was to be heated in a commercial electric furnace the temperature of which might fluctuate as much as $\pm 10$ deg F about any preset value, the outer enclosure 5 was massive for the purpose of reducing the temperature variation at its inside surface. The heating source 6 consisted of an SWG No. 18 Kanthal A wire wound around a ceramic tube. A cyclic varying current was sent through the resistance wire to generate the required temperature wave at the heating bath. Since the theory of the experiment called for a steady periodic state, the heat supplied by the electric current averaged over a complete cycle had to be removed by external means. This was accomplished by forcing cooling air through the annular space 8. Allowance for differential expansion of the various

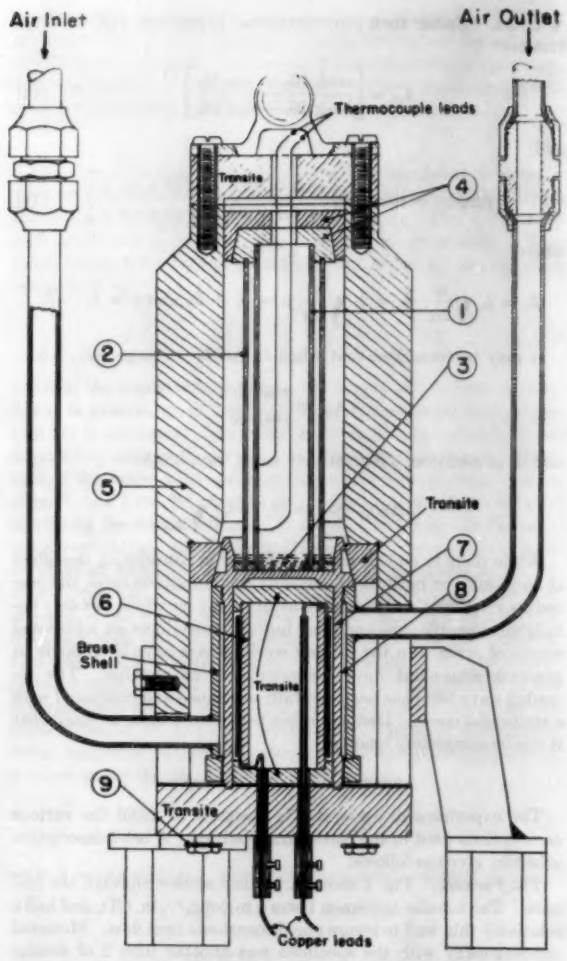


FIG. 1 VERTICAL CROSS SECTION OF FURNACE

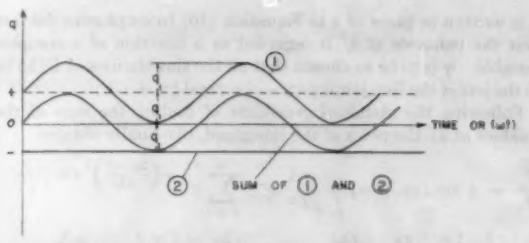


FIG. 2 SINUSOIDAL VARIATION OF HEAT SUPPLY

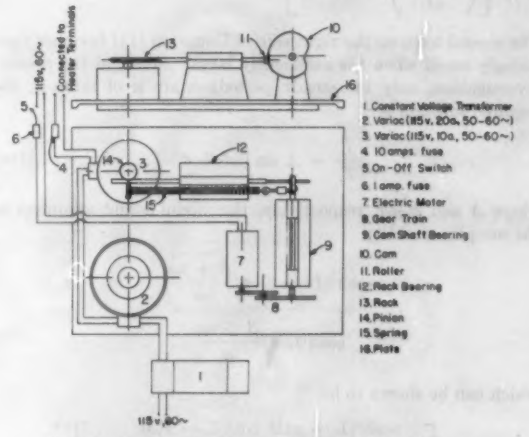


FIG. 3 ARRANGEMENT FOR VARIABLE HEAT SUPPLY

furnace components at elevated temperatures was provided for by two stainless-steel leaf springs 9.

### GENERATION OF SINUSOIDAL TEMPERATURE WAVE

Since the desired rate of heat supply was of the form $q = q_1 \sin \omega t$, the process, as such, required heating during one half cycle and refrigeration during the next half. In order to avoid the complication in mechanical construction for achieving refrigeration, the following scheme was adopted: To facilitate explanation, reference is again made to the expression $q = q_1 \sin \omega t$. By adding and subtracting a constant quantity $q_1$, one obtains

$$q = q_1(1 + \sin \omega t) - q_1 \quad \ldots\ldots\ldots\ldots\ldots\ldots [16]$$

The quantity $q_1(1 + \sin \omega t)$ varies from zero to maximum and back to zero as $\omega t$ passes through a complete cycle. This is illustrated by curve 1 in Fig. 2. Such a variation of heat supply with time can be obtained readily by altering suitably the voltage applied to the heating coil. The second term on the right side of Equation [16] is a constant and is represented by a straight line 2 in the same figure. In this apparatus it is brought into effect by forcing a constant quantity of cooling air through the annulus as described in the foregoing section. Obviously, the average heating power of the resistor is $q_1$ which is also the heat to be carried away by the cooling air in a unit time. In the present instance, $q_1$ has been found to be approximately 250 watts for a maximum temperature fluctuation of $\pm 20$ deg F at the heating bath.

It is well known that when a potential difference $V$ is impressed on a fixed resistance $R$, the rate of heat generation is $V^2/R$. Hence, for a $q$-wave as prescribed by $q_1(1 + \sin \omega t)$, the applied voltage should vary with time as according to $\sqrt{1 + \sin \omega t}$. This was achieved by the use of a cam driving an auto transformer through a rack and pinion. Fig. 3 shows diagrammatically the arrangement for the variable heat supply. This plan is similar to that used by King (6).

*Measuring and Recording Instruments.* Fig. 4 illustrates the simple measuring circuit and the instruments used. Two SWG No. 30 iron-constantan thermocouples were silver-brazed into two 0.040-in. holes accurately drilled at a distance $1 \pm 0.002$ in. apart. After brazing, the excess metal was carefully removed to insure that the original uniform cross section[6] of the tubular specimen was not disturbed. Since only the fluctuating part of the temperature was of interest, a bucking emf was introduced between the thermocouple leads and the recording instruments. This was to nullify that part of the thermoelectric effect corresponding to the mean temperature of the specimen. A bucking emf supply of the highest stability was essential. In a given test run, the actual value of the bucking emf used was measured by a separate precision potentiometer. The fluctuating part of the thermoelectric effect was recorded by two photoelectric potentiometer-type recorders.[7]

[6] All test specimens were finish-bored on a lathe followed by external grinding on a mandrel.

[7] General Electric Company, Schenectady, N. Y.

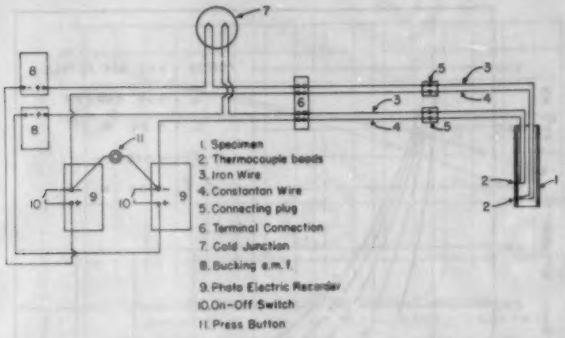


FIG. 4 MEASURING CIRCUIT

FIG. 5 COMPLETE EXPERIMENTAL ARRANGEMENT FOR DETERMINATION OF THERMAL DIFFUSIVITY OF METALS AT ELEVATED TEMPERATURES

half, the temperature of the test specimen would, for all practical purposes, settle down to a steady periodic state.

A minimum of three complete waves was recorded. Timing marks were imposed on these waves every 15 sec by momentarily short-circuiting the terminals of the photoelectric recorders. This rendered possible the accurate determination of the phase difference between the two temperature waves. Errors resulting from the nonuniformity in chart speed of the recording instruments were thus eliminated. In many cases the temperature waves had amplitudes of about 15 and 8 deg F, respectively, at the two measuring stations. The period of the sinusoidal heater varied from 540 sec for the steel specimens to 440 sec for copper. The wave form was occasionally examined and compared with a theoretical sine wave. Fig. 6 illustrates the absence of any measurable harmonics in the recorded waves.

## RESULTS AND DISCUSSION

As is evident from Equations [12] and [13], the thermal diffusivity $\alpha$ of the test specimen is not explicitly expressed in terms of the amplitude ratio or phase shift of the temperature waves; nor is the heat-loss factor $b$. Graphs have been prepared to expedite their evaluation. Figs. 7 and 8 were constructed by assigning suitable values of $\alpha$ to Equations [12] and [13] and computing the corresponding values of $A_{12}$ and $(\Delta\phi)_{12}$, $b$ being taken as a parameter. The experimental conditions are as stated. They were then used to construct a third graph (Fig. 9) in which $\alpha$ was plotted against the heat-loss factor $b$ for various values of $A_{12}$ and $(\Delta\phi)_{12}$. Hence, with the amplitude ratio and phase shift determined from the recorded waves, the evaluation of $\alpha$ became a simple matter.

It is pertinent to point out that if $\alpha$ is higher than 0.5 sq ft/hr and $b$ is less than 0.03, heat loss has relatively small effect on the phase shift under the given experimental conditions. On the other hand, when $\alpha$ is less than 0.3 sq ft/hr, the amplitude ratio is relatively insensitive to variations in heat loss and is thus more accurate for diffusivity calculation. Errors which resulted from computing diffusivity by using phase shift of temperature waves were mentioned by Starr (7) but no quantitative analysis had been given.

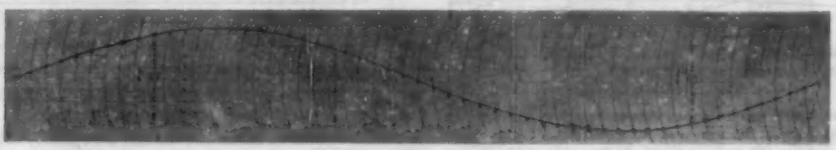

°—data plotted from actual recorded wave
~—theoretical sine wave

FIG. 6 COMPARISON BETWEEN MEASURED TEMPERATURE WAVE AND THEORETICAL SINUSOIDAL WAVE

A metering orifice of the plate type was installed in the cooling-air circuit. Its flange taps were connected to an inclined manometer. This served to indicate the air-flow rate so that operating conditions could be duplicated. Fig. 5 is a photograph of the complete experimental arrangement.

## TEST PROCEDURE

After the complete assembly was lowered carefully into the main heating furnace, connections were made to the inlet and outlet of the cooling air. The time of heating required to bring the temperature of the specimen close to that for testing varied from 1 to 2 hr, depending upon the range of temperature. The cyclic electric heater was then put into operation with the simultaneous introduction of the cooling air. After another hour and a

Fig. 9 was used in conjunction with the determination of thermal diffusivity of AISI 1018, 1045, 3140, and 1.1 per cent carbon tool steels. The results are summarized in Fig. 10. The latter steel has a reported chemical composition of 1.1 C, 0.7 Mn, 0.25 Si, and less than 0.04 P and S. The ASM Metals Handbook listed the thermal conductivity and specific heat at elevated temperatures for a similar steel containing 1.22 C, 0.35 Mn, 0.11 Cr, 0.13 Ni, 0.01 Mo, and 0.08 Cu. While the two steels are not strictly identical, it is interesting to compare the diffusivity values calculated from data on $K$, $c$, and $\rho$ with those obtained in this experiment. Fig. 11 is a comparison between the two sources.

For the electrolytic tough-pitch copper (purity 99.90 per cent) phosphorized copper tubing and 2S aluminum (purity 99.0) the heat loss had been found to be so small that it could be ignored

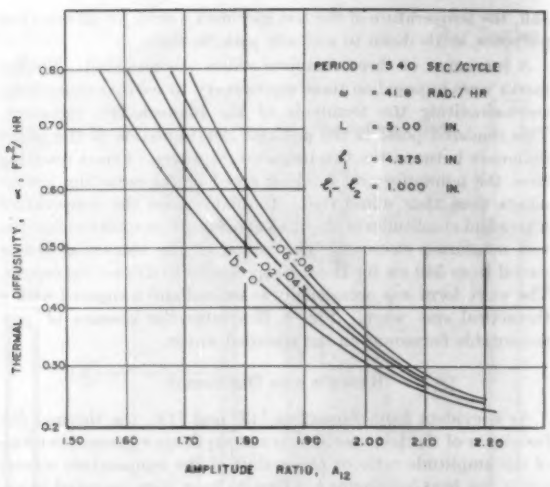


FIG. 7 INFLUENCE OF HEAT LOSS ON RELATIONSHIP BETWEEN THERMAL DIFFUSIVITY AND AMPLITUDE RATIO

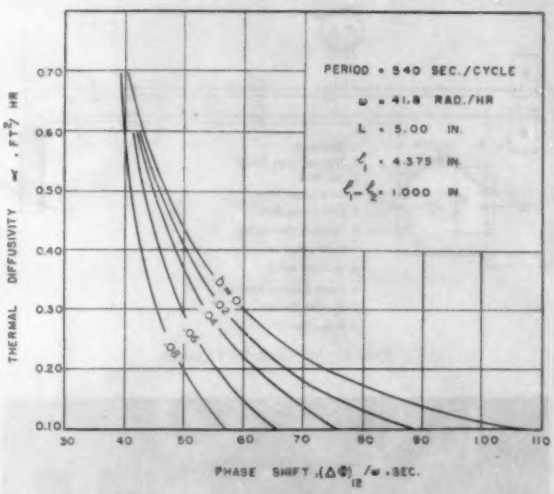


FIG. 8 INFLUENCE OF HEAT LOSS ON RELATIONSHIP BETWEEN THERMAL DIFFUSIVITY AND PHASE SHIFT

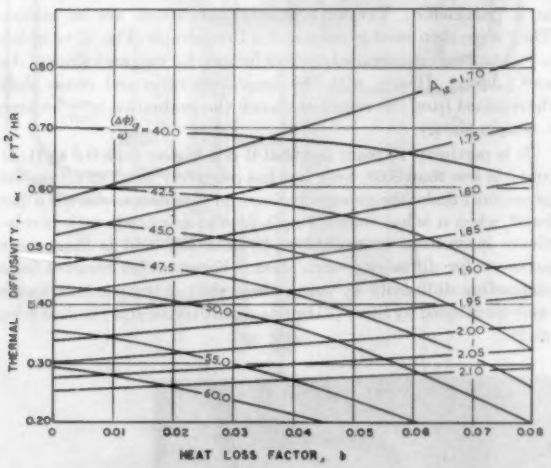


FIG. 9 SIMULTANEOUS SOLUTION OF THERMAL DIFFUSIVITY AND HEAT-LOSS FACTOR FROM AMPLITUDE RATIO AND PHASE SHIFT (Experimental conditions are same as in Figs. 7 and 8.)

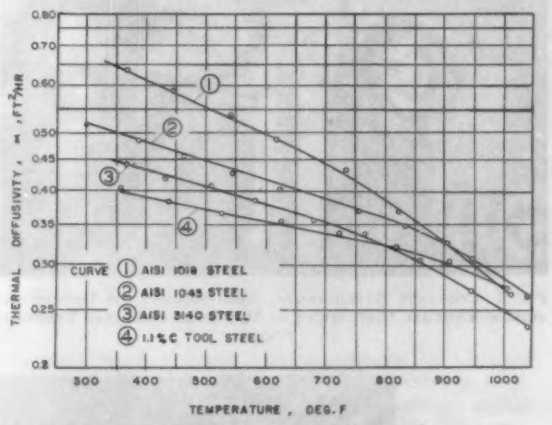


FIG. 10 EFFECT OF TEMPERATURE ON THERMAL DIFFUSIVITY OF FOUR DIFFERENT STEELS

completely in the computation. The results are shown, respectively, in Figs. 12, 13, and 14. Data on the thermal diffusivity of a high-purity copper taken from Bibliography items (9) and (13) also were plotted. The agreement is good. Bibliography (13) also listed diffusivity values for aluminum of 99.2 per cent purity. They are reproduced in Fig. 14. Some discrepancy exists in this case.

From Figs. 12 and 14 it is seen that the thermal diffusivity of electrolytic tough-pitch copper and 2S aluminum when plotted on a logarithmic scale varies linearly with temperature. This agrees with the contention of a theory expounded by Storm (13). From a theoretical consideration of the thermal conductivity of good conductors which is of the electronic origin and the specific heat at constant pressure together with the density, Storm concluded that a linear relationship between temperature and the logarithm of thermal diffusivity would exist for simple metals.

A simple metal is defined as one category of the monatomic metals whose d-shells are either completely filled or completely empty. Aluminum, copper, lead, zinc, and silver are common examples of simple metals. Otherwise, they are called transition metals. The thermal and physical properties of simple metals are, in general, less complicated than those of transition metals.

While constructional steels are essentially iron-carbon alloys with possible addition of one or more other elements, Storm has claimed that the previously described linear relation also exists for an 0.8 per cent carbon steel for temperatures ranging from 0 to about 1100 F. His calculation was based on data published by the Iron and Steel Institute of Great Britain (2). However, all the steels tested in the present investigation definitely indicate a deviation from the straight line for temperatures above 750 F.

## ACKNOWLEDGMENTS

The authors hereby express their sincere gratitude to Prof. K. J. Trigger, Department of Mechanical Engineering, University of Illinois, for his constant encouragement and for his helpful suggestions during the progress of the investigation. Acknowledgment is made to Prof. H. H. Korst, also of the Mechanical Engi-

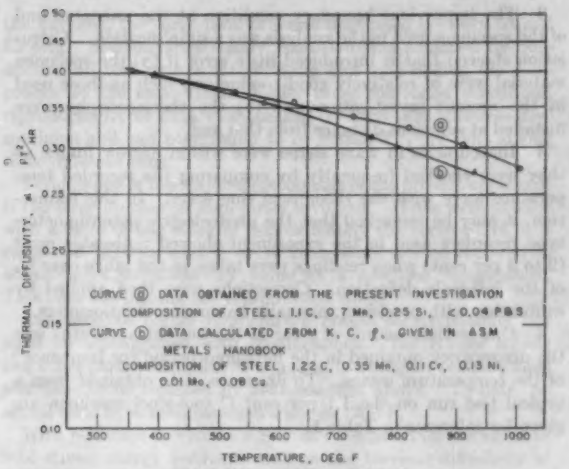
THERMAL DIFFUSIVITY, α, FT²/HR
TEMPERATURE, DEG. F
CURVE @ DATA OBTAINED FROM THE PRESENT INVESTIGATION
COMPOSITION OF STEEL: 1.1 C, 0.7 Mn, 0.25 Si, < 0.04 P & S
CURVE ⓑ DATA CALCULATED FROM K, C, ρ, GIVEN IN ASM METALS HANDBOOK
COMPOSITION OF STEEL 1.22 C, 0.35 Mn, 0.11 Cr, 0.13 Ni, 0.01 Mo, 0.08 Cu

FIG. 11 COMPARISON OF RESULTS OBTAINED FROM PRESENT INVESTIGATION WITH THOSE CALCULATED FROM $K$, $C$, AND $\rho$ GIVEN IN ASM METALS HANDBOOK

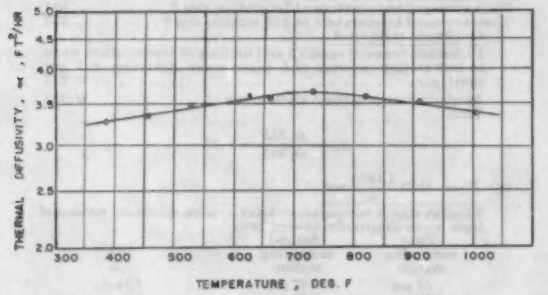


FIG. 13 EFFECT OF TEMPERATURE ON THERMAL DIFFUSIVITY OF PHOSPHORIZED COPPER

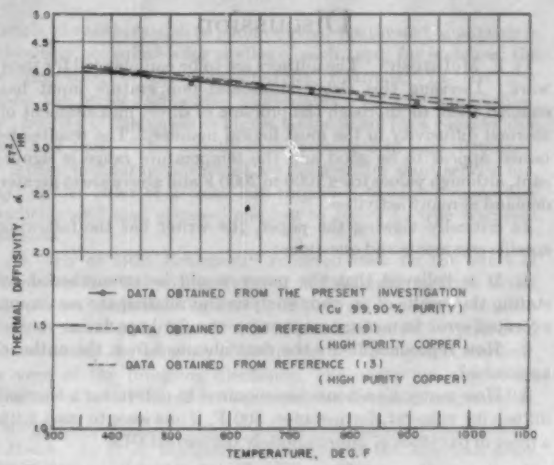
THERMAL DIFFUSIVITY, α, FT²/HR
DATA OBTAINED FROM THE PRESENT INVESTIGATION (Cu 99.90% PURITY)
DATA OBTAINED FROM REFERENCE (9) (HIGH PURITY COPPER)
DATA OBTAINED FROM REFERENCE (13) (HIGH PURITY COPPER)
TEMPERATURE, DEG. F

FIG. 12 EFFECT OF TEMPERATURE ON THERMAL DIFFUSIVITY OF HIGH-PURITY COPPER

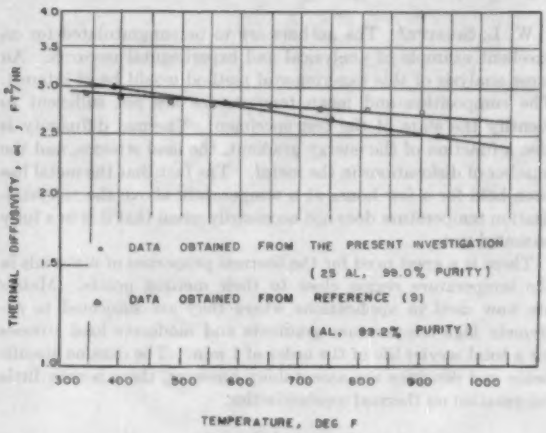
THERMAL DIFFUSIVITY, α, FT²/HR
DATA OBTAINED FROM THE PRESENT INVESTIGATION (2S AL, 99.0% PURITY)
DATA OBTAINED FROM REFERENCE (9) (AL, 99.2% PURITY)
TEMPERATURE, DEG F

FIG. 14 EFFECT OF TEMPERATURE ON THERMAL DIFFUSIVITY OF COMMERCIALLY PURE ALUMINUM

neering Department, for his helpful discussion so kindly and freely given during the preparation of the text, and to Miss Irene Cunningham for the typing of the manuscript.

This paper is based on a part of a doctoral dissertation submitted to the Graduate College of the University of Illinois in June, 1954. The work was carried out under the supervision of Prof. B. T. Chao who also formulated the mathematical phase of the investigation.

## BIBLIOGRAPHY

1 "International Critical Tables," by the National Research Council, U. S. A., McGraw-Hill Book Company, Inc., New York, N. Y., vols. 1, 2, and 5, 1929.

2 "The Physical Properties of a Series of Steels," Part II, *Journal of the Iron and Steel Institute*, vol. 154, 1946, pp. 83–121.

3 "Neue Methode, das Wärmeleitungsvermögen der Körper zu bestimmen," by A. J. Angström, *Annalen der Physik und Chemie*, vol. 114, 1861, pp. 513–530.

4 "Über das Wärmeleitungsvermögen von Eisen und Neusilber," by H. Weber, *Annalen der Physik und Chemie*, vol. 146, 1872, pp. 257–283.

5 "Experimental Inquiry Into the Laws of the Conduction of Heat in Bars, and Into the Conducting Power of Wrought Iron," by J. D. Forbes, Trans. of the Royal Society of Edinburgh, Scotland, part I, vol. 23, 1864, pp. 133–146; Trans. of the Royal Society of Edinburgh, part II, vol. 24, 1867, pp. 73–110.

6 "A Method of Measuring Heat Conductivities," by R. W. King, *Physical Review*, series 2, vol. 6, 1915, pp. 437–445.

7 "An Improved Method for the Determination of Thermal Diffusivities," by C. Starr, *Rev. Sci. Inst.*, vol. 8, 1937, pp. 61–64.

8 "A Method for the Measurement of Thermal Diffusivity of Molten Glass," by A. F. Van Zee and C. L. Babcock, *Journal of the American Ceramic Society*, vol. 34, 1951, pp. 244–250.

9 "Thermal Diffusivity of Metals at High Temperatures," by P. H. Sidles and G. C. Danielson, *Journal of Applied Physics*, vol. 25, 1954, pp. 58–66.

10 "Rapid Measurements of Thermal Diffusivity," by G. E. McIntosh, D. C. Hamilton, and W. L. Sibbitt, Trans. ASME, vol. 76, 1954, pp. 407–410.

11 "A New Method of Determining Thermal Diffusivity at Various Temperatures," by D. Rosenthal and A. Ambrosio, Trans. ASME, vol. 73, 1951, pp. 971–974.

"The Determination of Thermal Diffusivity of Aluminum Alloys at Various Temperatures by Means of a Moving Heat Source," by D. Rosenthal and N. E. Friedmann, ASME Paper No. 54—SA-56.

12 "Modern Operational Mathematics in Engineering," by R. V. Churchill, McGraw-Hill Book Company, Inc., New York, N. Y., 1944, chapter 6.

13 "Heat Conduction in Simple Metals," by M. L. Storm, *Journal of Applied Physics*, vol. 22, 1951, pp. 940–951.

# Discussion

G. E. McIntosh.[8] The authors are to be commended for their work. Devising this clever sinusoidal temperature input has enabled them to approach the problem of direct measurement of thermal diffusivity in the most logical manner. The results obtained appear to be good and the temperature range is significant, although values from 1000 to 2000 F and above are in greater demand at many activities.

In critically viewing the paper, the writer has the following specific comments and questions:

1 It is believed that the paper would be strengthened by stating the results of an error analysis and relating the maximum expected error to measurements on a standard specimen.

2 How reproducible are the data obtained from the authors' apparatus?

3 How many man-hours are required to determine a thermal diffusivity value at, for instance, 500 F, if one were to start with a piece of bar stock of approximately the correct OD?

In closing, the authors are urged to make further use of their apparatus. If at all possible, the work should be extended to higher temperature ranges.

W. L. Sibbitt.[9] The authors are to be congratulated for an excellent example of analytical and experimental research. An error analysis of this experimental method would be of interest. The composition and mean temperature are not sufficient to identify the state of the test specimen. Thermal diffusivity is also a function of the energy gradient, the load stresses, and the number of dislocations in the metal. The fact that the metal has been held for a few hours at a temperature above the recrystallization temperature does not necessarily mean that it is in a fully annealed state.

There is a great need for the thermal properties of materials in the temperature region close to their melting points. Metals are now used in applications where they are subjected to extremely high-temperature gradients and moderate load stresses for a total service life of the order of 1 min. The data on specific heats and densities are acceptable; however, there is very little information on thermal conductivities.

## Authors' Closure

The authors wish to express their appreciation to Dr. McIntosh and Professor Sibbitt for their kind remarks and pertinent comments on the paper.

Both discussers expressed the desirability of performing an error analysis which was not done owing to the complexity of the problems involved. Instead, a direct comparison with diffusivity values calculated from published data on $K$, $c$, and $\rho$ was made whenever feasible. Nevertheless, during the course of investigation, the following sources of error were noted and efforts had been made to keep them to a minimum:

1 The equations derived in the paper were based upon tubular specimens of uniform cross section. Installation of thermocouples at the temperature-measuring stations would produce some local disturbance on the supposedly linear heat flow in the specimen. Accurate analysis is difficult, but the error was presumed to be small since any excess deposit of the brazing alloy was carefully removed afterwards. Conduction error along thermocouple leads had been estimated and found to be insignificant.

2 The impervious boundary condition at the unheated end of the specimen used in the analysis was a simplification. Calculation showed that it introduced little error if (*a*) the specimen material were of relatively good conductors, such as those used in the present investigation and (*b*) the thermocouples were installed at sufficient distance from that end.

3 Inaccuracies in wave shape were within narrow limits, as they were checked frequently by comparing the recorded temperature wave with the theoretical sine wave. In this connection, it may be remarked that the photoelectric potentiometer-type recorders used in the experiment showed noticeable error (2 to 3 per cent) when readings were taken in the range over $^3/_4$ of the full-scale deflection. Corrections were then applied by calibration with precision, manually balanced potentiometers.

4 One obvious source of error in the present apparatus was the discrepancy obtained in the measured period (or frequency) of the temperature waves. To illustrate, data obtained from a typical test run on the 1.1 per cent C tool-steel specimen are given for reference in Table 1.

TABLE 1 TEST-RUN DATA

| | |
|---|---|
| Voltage of feeding variac, volts | 80.0 |
| Manometer reading, in. | 0.03 |
| Period of sinusoidal heater,[a] sec per cycle | 540 |
| Bucking emf for 1st measuring station, mv | 14.65 |
| Bucking emf for 2nd measuring station, mv | 14.60 |
| Time averaged temperature at 1st station, deg F | 534 |
| Time averaged temperature at 2nd station, deg F | 525 |
| (*i*) Amplitude ratio — $A_{12}$ | |
| Difference between maxima and minima of temperature wave at first station (average of 5 rdgs., mean deviation ± 1 per cent), mv | 0.745 |
| As above but at second station, mv | 0.382 |

Thus

$$A_{12} = \frac{0.745}{0.382} = 1.95$$

(*ii*) Phase shift $\frac{(\Delta\phi)_{12}}{\omega}$ sec

Time at which temperature wave crosses mid-axis, measured from some arbitrarily chosen zero

| First measuring station | Second measuring station | $\frac{(\Delta\phi)_{12}}{\omega}$ |
|---|---|---|
| 55 sec | 107 sec | 52 sec |
| 320 | 371 | 51 |
| 592 | 643 | 51 |
| 857 | 907 | 50 |
| 1126 | 1177 | 51 |
| | | Avg. 51.0 sec |

[a] Obtained by using stop watch and counting the number of revolutions of the driving cam (Fig. 3, item 10).

The half-periods obtained with the temperature wave at the first measuring station are, respectively, 265, 272, 265, and 269 sec. Corresponding values for the second measuring station are 264, 272, 264, and 270 sec. These values indicate a maximum deviation of +0.7 to —2.2 per cent when compared with the half-period of the sinusoidal heater, the latter being 270 sec.

While, under certain conditions as expounded in the paper, the use of amplitude ratio of the temperature waves is preferable to phase shift in diffusivity calculations, data reported herewith represent the mean value obtained by using both measurements. In general, the agreement is good. For the case of 1.1 per cent C tool steel cited in the foregoing $\alpha = 0.368$ and 0.370 sq ft per hr as computed, respectively, from the amplitude ratio and phase shift. More representative, however, is the result acquired from subsequent tests on AISI Type 430 stainless steel. At a mean temperature of 913 F, the corresponding diffusivity values are 0.242 and 0.250 sq ft per hr, indicating a mean deviation of ±1.6 per cent.

During the course of the investigation, it was immediately learned that fluctuations in air pressure had a serious effect on wave shape. The air was delivered from a compressor which was also the source of air supply to other laboratories. During

[8] Mechanical Engineer, Missile Systems Division, Lockheed Aircraft Corporation, Van Nuys, Calif. Assoc. Mem. ASME.

[9] Professor of Mechanical Engineering, Purdue University, Lafayette, Ind. Assoc. Mem. ASME.

the daytime, the surge-tank pressure fluctuated between 68 and 75 psig. Satisfactorily steady condition was achieved by conducting all test runs in late evening and by bleeding the compressor at the same time. Under these controlled conditions, reproducibility of data was checked on Type 430 stainless-steel specimen and had been found to be within $3^1/_2$ per cent among three different runs.

Perhaps one of the major shortcomings of the present apparatus is the large number of man-hours involved. If one were to start with a piece of bar stock of approximately the correct OD, it is estimated that at least 7 to 10 man-hours will be required to obtain a single diffusivity value at a specified temperature. This does not include the computation work.

Extension to higher temperature ranges seems possible but must be accompanied with modifications. The copper tubing and other parts which deteriorate rapidly at higher temperatures will have to be replaced by heat-resistant alloys. To date, no actual tests have been conducted above 1200 F.

With reference to Professor Sibbitt's comment on the effect of load stress, energy gradient, etc., on the thermal diffusivity of metals, the authors wish to point out that the present apparatus is inherently not suitable for studies of such type, for instance, the determination of stress-conductivity relations. In the first place, the present apparatus necessitates a state of equilibrium, i.e., heating of specimens at higher temperature for a considerable length of time. This usually entails changes in microstructure. It is clear that for metals which are designed for short service life, say, of the order of 1 min, but subjected to high-temperature gradients and load stresses, one has to resort to true transient methods.

As early as 1923 Bridgman[10] reported data on the effect of tension on thermal conductivity of metals, ranging from about 0.39 per cent for a 2050 kg/cm$^2$ ($\sim$29,000 psi) load in Fe to 0.015 per cent for a 770 kg/cm$^2$ ($\sim$10,900 psi) load in Pd. Evidently, for such study, an accuracy of better than $^1/_2$ per cent is required. In view of the foregoing discussion, one could not expect an accuracy of better than 2 to 3 per cent from the present apparatus.

[10] "Effect of Tension on the Thermal and Electrical Conductivity of Metals," by P. W. Bridgman, Proceedings of the American Academy of Arts and Sciences, vol. 59, 1923, p. 127.

# On the Relations Between Various Laboratory Fracture Tests

By E. M. LAPE[1] and J. D. LUBAHN[2]

**A great variety of tests were examined with the objective of finding correlations between different kinds of tests. The tests considered included notched and unnotched tensile tests, notched and unnotched bend tests, notched and unnotched disk-bursting tests, and Charpy impact tests. General correlation was obtained in only one instance, and in a few other test comparisons, correlations could be obtained only for certain metallurgical conditions. A great deal of additional work in this field is required.**

## Introduction

INABILITY to relate laboratory test results to the performance of structures in service is the most important stumbling block in developing a rational design procedure against fracturing in notch-brittle metals (1).[3] Currently we do not even understand the relationships between various simple tests commonly performed in the laboratory; certainly, until we do, there is little hope of understanding the relationship between one or more simple laboratory tests and the performance of the metal under the complex conditions that prevail in most structural parts. Obviously, the first step in developing a suitable design procedure must consist of a detailed investigation of the metal characteristics under a wide variety of laboratory test conditions. Gradually the relationships between different kinds of tests will be understood well enough to permit the prediction of one test result from the results of other kinds of tests. When this type of relationship has been established among tests that represent a sufficiently large number of factors governing fracture, it will then be possible to predict service performance, which may be viewed merely as a more complex test.

Most of the following discussion will be devoted to this subject of how to relate the results of different kinds of tests to each other. In doing so, however, one must be careful not to lose sight of the ultimate objective. It is altogether too easy to become so absorbed in discovering the relationships between two particular kinds of tests, that one disregards other factors which may be more pertinent to engineering performance, but which are not represented in the tests currently being studied. In the examples which will be given, there is a discussion of some of the factors which are currently considered to be important. Other factors, such as size or repeated loading may be just as important, if not more so.

## Degree to Which Various Tests Can Be Correlated

Let us first consider one of the very few cases where there is some evidence that the relation between two tests is understood, namely, the unnotched bend test and the unnotched tensile test. The data (2) show that the biaxiality (transverse tension over tangential tension) at mid-width of a bend specimen varies with breadth-to-depth ratio ($b/h$) from 0.5 for a very wide specimen to zero for a very narrow one. Fracture begins at the mid-width for $b/h$ ratios greater than unity, and the ductility decreases as the biaxiality increases. For $b/h$ equal to or less than unity, fracture begins at the corners, where the stress is uniaxial (transverse stresses zero) and the data indicate that the ductility for corner fracture is the same as that in a tensile test. Thus it appears that ductility is independent of stress gradient for uniaxial tension, and that narrow unnotched bend tests can be related to unnotched tensile tests.

When notches are present the situation is much more confused. There is no type of notch test whose result can be predicted consistently from the result of any other type of test, with or without a notch, although correlation does appear possible in certain cases where the ductility is exceedingly high or completely absent. In the investigations of welded ship failures, there have been numerous comparisons between such tests as the Navy tear test, the internally notched wide plate, the keyhole Charpy test, and the V-notch Charpy test. So far, these comparisons have shown that the boundary temperature between crack propagation by fibrous tearing and by sudden cleavage is approximately the same in the different tests. However, these tests give almost no information at all regarding other features of engineering performance, such as ductility and load-carrying capacity.

## Recent Notch Tests on a Special Steel

The difficulty of relating different kinds of tests, on the basis of current knowledge, can be illustrated by the following series of tests, which comprise a wide variety of tests all on the same materials. These tests were made on a special alloy steel in which a wide variety of properties (as determined by a few standard tests) could be obtained by various heat-treatments. The details of the tests are given in the Appendix, and the results are summarized in Table 1. The conditions of heat-treatment designated by A and B in Table 1 are particularly interesting, because they have the same very high value of unnotched tensile ductility, but tremendously different values of keyhole Charpy impact energy. In addition to the standard types of tests, five kinds of special tests were made for the A and B heat-treatments.

The logical first supposition as to the different impact-test results for heat-treatments A and B would be that the local strain at fracture was the same for both heat-treatments, because the tensile ductilities were equal, but that the energy to propagate the crack was very large for heat-treatment A as compared with practically none for heat-treatment B. This supposition stems from the Navy tear-test results of Kahn and Imbembo (3) on mild steel. Their tests showed that the energy to start the crack is practically independent of the test temperature. The energy to propagate the crack, however, varied from essentially zero below the transition temperature to a large value above the transition temperature. Also, one V-notch Charpy bend test on mild steel indicated that the energy to propagate the crack may be at least

[1] Thomson Laboratory, General Electric Company, Lynn, Mass.
[2] Research Associate, General Electric Company, Schenectady, N. Y. Mem. ASME.
[3] Numbers in parentheses refer to Bibliography at end of paper.
Contributed by the Metals Engineering Division and presented at a joint session of the Metals Engineering and Applied Mechanics Divisions the Diamond Jubilee Semi-Annual Meeting, Boston, Mass., June 19–23, 1955, of The American Society of Mechanical Engineers.
Note: Statements and opinions advanced in papers are to be understood as individual expressions of their authors and not those of the Society. Manuscript received at ASME Headquarters, May 17, 1955. Paper No. 55—SA-70.

TABLE 1 MATERIAL AND RESULTS

(Room-temperature tests)

Composition: 0.12% C, 0.48% Mn, 5.87% Cr, 0.95% Mo, 0.37% Ti, 0.03% B

| | A | B | C |
|---|---|---|---|
| Austenitizing temperature, deg F | 1900 | 1800 | 2[illegible] |
| Quenching medium | oil | oil | oil |
| Tempering temperature, deg F | 1300 | 1200 | 1200 |
| Tempering time, hr | 6 | 4 | 2 |
| 0.02% yield strength, 1000 psi | 43–56 | 67–78 | 93–101 |
| Tensile strength, 1000 psi | 76–83 | 90–102 | 145–149 |
| Reduction in area, per cent | 77–79 | 73–76 | 1–3[c] |
| Keyhole Charpy value, ft-lb | 36–52[a] | 2–4 | 1–2 |
| Disk-strength ratio = $\frac{\text{average tangential stress}}{\text{tensile strength}}$ | | | |
| With no stress raiser | 1.01 | 0.99 | 0.85 |
| With crack in rim | ... | 0.76 | |
| With holes and saw cut near rim | 1.00 | | |
| With saw cut in rim | 0.86 | 0.57 | |
| Notch tensile tests: 50%, 60-deg V-notches; $r/D = 0.02$ | | | |
| Notch-strength ratio = $\frac{\text{notch strength}}{\text{tensile strength}}$ | 1.55–1.69 | 1.49–1.57 | 0.84–0.90 |
| Notch ductility, per cent reduction in area | 30–53 | 0.6–1.2 | 1.0–1.3 |
| Unnotched wide-plate bending strain, per cent | >120 | >120 | |
| Notched (V-notch Charpy) slow bend ductility, per cent | 165–180 | 3–12 | |
| Maximum bending load, lb | 2220–2440 | 1740–1980 | |
| Energy absorbed in slow notch bend test, ft-lb | 38.3[b] | 1.2[b] | |

[a] One out of five tests gave only 10 ft-lb.

[b] Of the 38.3 ft-lb, 9.4 ft-lb was expended in propagating the crack, while the crack propagation was completely brittle for heat-treatment B.

[c] Two out of six tests gave 59 and 63 per cent.

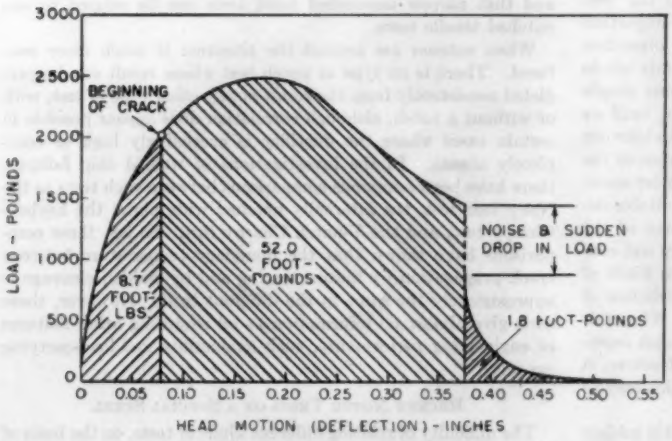


FIG. 1 ROOM-TEMPERATURE SLOW BEND TEST OF A STANDARD V-NOTCH CHARPY SPECIMEN CUT IN THE ROLLING DIRECTION FROM 4-IN. HOT-ROLLED MILD-STEEL PLATE. NOTCH IN TRANSVERSE DIRECTION OF PLATE. FROM LUBAHN (4)

five times that required to initiate fracture, even though the local strain before crack initiation was very high, 40 per cent, Fig. 1.

Thus previous tests on mild steel would indicate that the difference in impact values for conditions A and B in Table 1 would be due to differences in the mode of crack propagation. However, the results of slow notched bend tests for conditions A and B (Table 1) prove otherwise. The difference in energy absorption is due almost entirely to an enormous difference in local ductility at the root of the notch—a difference which is not indicated at all by the unnotched tensile ductility. In both specimens the crack propagated suddenly and with comparatively little energy, Fig. 2. From these data it becomes evident that impact tests are hard to interpret because impact energy is not a criterion of any single metal characteristic. For one metal the level of impact energy may measure the ductility; in another metal the impact energy may be governed almost entirely by the mode of crack propagation, while the energy to initiate the crack, even for high ductility, may have been small. The slow notched bend test provides much more information.

These same slow notched bend tests show another rather disconcerting fact. If the high strain gradient below the notch root of a rather sharply notched tensile specimen causes surface fracture, in spite of the lower ductility inside due to triaxiality, then one would certainly expect surface fracture in a notch-bend specimen, where the equally high notch-induced strain gradient is superimposed on a strain gradient due to the bending, and having the same sign. If fracture begins at the surface in notch bending, the ductility should depend only on the biaxiality in that surface. This ductility should be the same as in a very wide unnotched bend test, where the biaxiality is the same as in the notch-bend specimen (0.5).

For example, some tests on mild steel indicate that the notch bend ductility equals the unnotched bend ductility (4), provided that the specimen is not oriented in such a way that the fracture anisotropy causes an abnormal location of crack initiation (4) Fig. 3. This same equivalence may prevail for heat-treatment A, where the notch bend ductility is even greater than the strain in an unnotched specimen that has been folded flat shut (about 120 per cent). In contrast, the bend ductility values for heat-treatment B in Table 1 show that the local surface strain at fracture of the notch bend bar is many times less than the unnotched bend ductility. Thus fracture apparently did begin below the root of the notch, because of high susceptibility of the metal to triaxiality.

The ductility values in notch tensile tests also suggest that fracture begins below the surface for heat-treatment B, while surface fracture may have occurred for heat-treatment A (see Table 1). For this type of test, however, the state of affairs is not as obvious as for notch bending; there is not yet a feasible method of applying the technique of Sachs and Fried (5) to the measurement of the local surface strains in these small specimens. The reduction of area value can be related either to the local tangential strain at the notch root

$$\sqrt{1 - \frac{\%\ \text{red. of area}}{100}} = 1 + \frac{\%\ \text{tangential strain}}{100}$$

or to the average axial strain

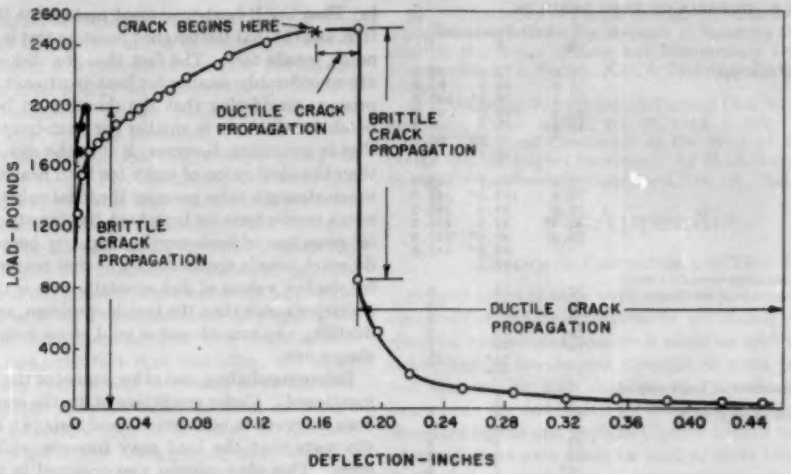


FIG. 2 SLOW BEND-TEST RESULTS FOR STANDARD V-NOTCH CHARPY SPECIMENS. EMPTY CIRCLES ARE FOR HEAT-TREATMENT A, AND FILLED CIRCLES FOR HEAT-TREATMENT B

$$1 - \frac{\%\ \text{red. of area}}{100} = \frac{1}{1 + \dfrac{\%\ \text{axial strain}}{100}}$$

but not to the local axial strain. One can easily imagine that the local axial strain was large, even for a small reduction of area, because of a high strain gradient. It is equally easy to imagine a high value of local axial strain coexisting with a small value of local tangential strain, because of a biaxiality only slightly less than 0.5. On the other hand, a large reduction-of-area value does not necessarily mean a high value of local axial strain. Because final diameter is usually measured after complete separation, the reduction-of-area value might be fictitiously high if ductile crack propagation has reduced the notch diameter while the crack is propagating, see Table 2. This phenomenon has been called the "rim effect" (6).

Regardless of the uncertainties of interpreting the reduction-of-area values in terms of local axial strain, it is still clear from the high notch-strength ratio that even for heat-treatment B the local ductility is high enough to cause a very uniform stress distribution before fracture. For very ductile metals, the stress apparently becomes quite uniformly distributed over the notch section by the time that maximum load occurs. Since maximum load occurs at about the same average strain in notched and unnotched specimens (7), the ratio of the nominal stresses at maximum load for the notched and unnotched specimens, respectively, is a rough measure of the triaxiality present (8). For very ductile metals, it has been found that this notch-strength ratio depends only on the notch depth providing the notch sharpness is less than about 6. The amount by which a notch-strength ratio value falls below this ideal value is a measure of the degree to which the stresses have failed to be uniformly redistributed before failure occurred (9). For the 50 per cent notches discussed in Table 1, the notch-strength-ratio values are at least as high as the "ideal" value of 1.5 for very notch ductile metals. Thus one must conclude either (*a*) that the low notch ductility indicated by the notch-bend tests for heat-treatment B is still enough to smooth out this initial elastic stress concentration in a notch tensile test, or (*b*) that a less severe state of stress results in a higher ductility in a notch tensile test than in a notch-bend test.

The bursting tests on unnotched disks (Table 1) show about what one would expect. For heat-treatments A and B, where the

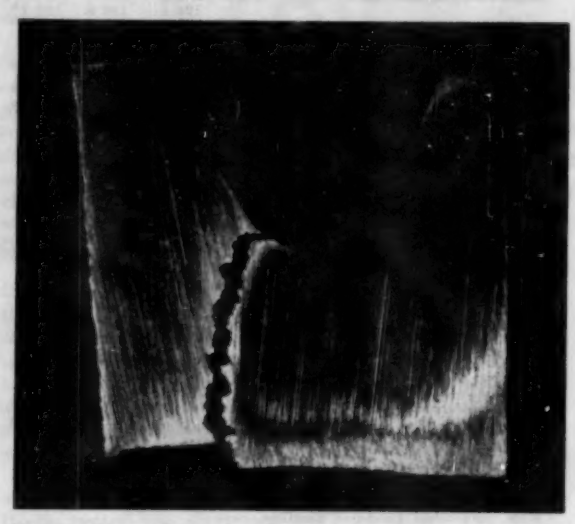

FIG. 3 SECTION THROUGH A PORTION OF A MILD-STEEL NOTCH-BEND SPECIMEN CUT FROM 4-IN. PLATE. SPECIMEN WAS GEOMETRICALLY SIMILAR TO A V-NOTCH CHARPY SPECIMEN, BEING 3.4 IN. SQUARE AND HAVING A 0.091-IN. NOTCH RADIUS. FROM LEQUEAR AND LUBAHN (4)

unnotched tensile ductility is very high, the disk-strength ratio is unity. This value means that the initially nonuniform (elastic) stresses have been sufficiently uniformly redistributed by large amounts of plastic flow that the average tangential stress at bursting of the disk equals the average stress in a tensile specimen at maximum load. This condition would be expected if the necking strain for a disk were about the same as that in a tensile specimen. Indeed this appears to be the case from measurements on both types of specimens after fracture at locations away from the necked regions (see Appendix). Thus the unnotched disk tests conform to current concepts, at least qualitatively.

For notched disks, or disks containing a stress raiser of any kind, the test results are not so easy to understand. For this type of test the criterion of the load-carrying capacity is the "disk-strength ratio." For metals with considerable ductility, the

TABLE 2 DETAILS OF TEST RESULTS

| | Heat-Treatment A | B | C |
|---|---|---|---|
| Tensile test results | | | |
| 0.02% yield strength, 1000 psi | 56.4 | 75.0 | 94.0 |
| | 53.9 | 75.0 | 95.9 |
| | 51.4 | 78.4[a] | 101.9 |
| | 53.4 | 73.0 | 98.0 |
| | 42.8[a] | 75.5 | 96.1 |
| | | 57.2[a] | 93.1 |
| | | 67.4[a] | |
| Tensile strength, 1000 psi | 77.6 | 94.7 | 148.0 |
| | 76.8 | 102.0[a] | 147.8 |
| | 76.0 | 91.8 | 145.0 |
| | 83.3[a] | 92.3 | 145.3 |
| | 79.6 | 89.6[a] | 149.4 |
| | | 92.6[a] | 147.0 |
| | | 95.1 | |
| Per cent reduction of area after complete separation | 77 | 74 | 3 |
| | 78 | 76 | 63 |
| | 79 | 73[a] | 3 |
| | 78 | 73 | 2 |
| | 78[a] | 73 | 1 |
| | | 74[a] | 59 |
| | | 76[a] | |
| Per cent reduction of diameter at beginning of necking | 4 | 3 | |
| Keyhole Charpy impact energy, ft-lb | 42 | 2 | 1 |
| | 52 | 4 | 1 |
| | 43 | 2[a] | 2 |
| | 36 | 3 | 2 |
| | 10[a] | 2 | 2 |
| | | 3[a] | |
| | | 4[a] | |
| Notch tensile test results | | | |
| Notch strength, 1000 psi | 134.0[a] | | |
| | 124.1 | 146.8 | 132.1[a] |
| | 122.5 | 139.5 | 122.8[a] |
| Per cent reduction of area at crack initiation | 19[a] | | |
| | 21[a] | | |
| Per cent reduction of area after complete separation | 38 | 1.2 | 1.3[a] |
| | 53 | 0.6 | 1.0[a] |
| | 30[a] | | |
| | 40[a] | | |
| Disk-bursting tests | | | |
| Bursting speed, 1000 rpm | | | |
| No stress raiser | 31.8 | 35.7 | 39.9 |
| 3/4-in-deep crack in rim | | 28.2 | |
| Saw cut in rim | 28.2 | 24.6 | |
| Special stress raiser (Fig. 6) | 31.2 | | |
| Average tangential stress, 1000 psi | | | |
| No stress raiser | 80.1 | 100.9 | 125.1 |
| 3/4-in-deep crack in rim | | 69.2 | |
| Saw cut in rim | 68.2 | 53.0 | |
| Special stress raiser (Fig. 6) | 83.5 | | |
| Tensile strengths of actual disks, 1000 psi | | | |
| No stress raiser | 79.0[b] | 102.0 | 147.0[b] |
| 3/4-in-deep crack in rim | | 89.6 | |
| Saw cut in rim | 79.0[b] | 92.6 | |
| Special stress raiser (Fig. 6) | 83.3 | | |
| Disk-strength ratio | | | |
| No stress raiser | 1.01 | 0.99 | 0.85 |
| 3/4-in-deep crack in rim | | 0.76 | |
| Saw cut in rim | 0.86 | 0.57 | |
| Special stress raiser (Fig. 6) | 1.00 | | |
| Per cent reduction of thickness away from local necks in unnotched disks | 8 | 6 | |
| Wide, unnotched bend-test ductility, per cent | >120[a] | >120[a] | |
| Notch-bend tests[c] | | | |
| Local strain at root of notch when crack first appears | 165 | 3 | |
| | 180 | 12 | |
| | | 4 | |
| | | 5 | |
| Energy absorbed, ft-lb | 38.3 | 1.2 | |
| Bending load, lb | 2220 | 1740 | |
| | 2440 | 1980 | |

[a] Cut from failed disks.
[b] Average of all tests (no tests from the disk in question).

disk-strength ratio is observed to be in the neighborhood of unity for the design of disks being used here. If the maximum load strain is about the same in a notched disk as in an unnotched tensile test, as is the case for notched tensile specimens, a disk-strength ratio of unity is to be expected for these thin disks, since the triaxiality, and therefore the increase in flow stress, would be expected to be small.

The disk–strength ratios for notched disks of heat-treatment A are considerably higher than those for heat-treatment B, and in some cases near unity. These data tend to indicate two things: (*a*) That the B-heat-treatment material is the more notch sensitive, and (*b*) that the notched bursting test is more severe than the notch tensile test. The fact that the disk-strength-ratio values are considerably smaller for heat-treatment B than A is not surprising, considering that the ductility in both notch-bend and notch tensile tests is smaller for heat-treatment B. The thing that is surprising, however, is that the disk-strength ratio is less than the ideal value of unity for both heat-treatments, while the notch-strength ratio assumes the ideal value of 1.5 or more in the notch tensile tests for both heat-treatments. Thus the disks suffer more loss of load-carrying capacity because of notching than do notch tensile specimens. The first reason that comes to mind for the low values of disk-strength ratio is that the disk contains a sharper notch than the tensile specimen, and that a given notch ductility can smooth out a mild stress concentration, but not a severe one.

Before concluding, one other aspect of the test results should be mentioned. Under conditions of ductile crack propagation it has been observed in both notch-bend tests (4), Fig. 1, and notch tensile tests that the load may increase while a crack is tearing open. This phenomenon also occurred in the notched-disk test with heat-treatment A. This disk was stopped and examined at 95.5 per cent of the bursting speed, and a crack was observed. Then, there was a total increase of 4.5 per cent in speed or 9 per cent in average stress before failure finally occurred. Thus the higher notched disk-strength ratio for heat-treatment A than for B apparently is partly due to the more ductile nature of the crack propagation in this material. (The slow notched bend tests, Fig. 2, also indicated that heat-treatment A was characterized by a larger fraction of ductile crack propagation than heat-treatment B.)

## Discussion and Summary

The foregoing analysis has brought to light a mass of confusing and conflicting data, only a small part of which can be rationalized satisfactorily in terms of current concepts. Out of this mass of data are emerging a few tentative generalizations, and a host of ideas as to how to pursue these concepts further, using various experimental methods to track down the factors that cause differences in the results of different types of tests.

The following tentative generalizations can be made.

1 Fracture begins at a given local strain for a given set of local conditions, irrespective of conditions in the surrounding material or the over-all size.

2 Fracture may begin either at the surface or within the volume of metal, depending upon the relative importance of two factors—strain gradient in the vicinity of the surface, and the susceptibility of the metal to triaxiality.

3 Ductility values determined from measurements of dimensions after complete separation of the specimen may be misleading if the crack propagates in a ductile manner. For example, the reduction of area measured in this way in a notch tensile specimen will be too large if the central core of metal continues to stretch while the crack is slowly progressing inward from the root of the notch (rim effect). In many cases this phenomenon will even affect the quantity which is being used to characterize the load-carrying capacity, such as the notch strength of a tensile specimen or the bursting speed in a disk test.

4 Values of energy to cause complete rupture, such as in the Charpy impact test, may be misleading; a high value of energy may be due to high ductility in one kind of metal, or to the mode of crack propagation in another metal.

Some of the experimental methods that can be used to track down further the factors that cause differences in the results of different kinds of tests are as follows:

1 In different kinds of tests, the same quantity (such as local

stress or local strain) should be measured in all cases, rather than measuring one quantity in one test and a different quantity in another test. For example, it is difficult to compare the Charpy impact test, where the total energy to rupture the specimen is measured, with the unnotched tensile test, where ultimate strength, reduction of area, etc., are measured.

2 Any suspicions as to what variable might be governing the result of a test should be checked by comparing two tests that differ only in that variable. In this way the various pertinent factors can be isolated and studied individually. For example, biaxiality is presumed to be the controlling factor in a notch tensile test when fracture begins at the surface; if the strain gradient in the normal direction is not a factor, the local strain at fracturing should be the same as in an unnotched bend test having the same biaxiality. If the comparison of these two kinds of tests proves this to be the case, the fact that biaxiality, not strain gradient, is the governing variable will be proved to be the case.

3 A valid generalization must be based on tests covering a wide variety of metal behaviors such as hardness, strain-hardening rate, tendency toward brittle crack propagation, ductility, etc.

4 The method of calculating stress and strain distributions from classical plasticity must be improved. Particularly, methods must be developed for treating situations where the elastic and plastic strains are comparable in magnitude. Some of the poorly verified assumptions used in such calculations should be checked by experiment.

5 The wider the variety of tests compared, the broader will be the engineering applicability of the generalizations derived from these tests.

6 A direct experimental method is needed for finding the location of crack initiation when the fracture begins below the surface.

### Acknowledgment

The authors acknowledge the interest and encouragement of B. M. Wundt, and also express appreciation to R. Sakamoto, W. E. Jones, and H. A. Lequear for assistance in making the tests.

### BIBLIOGRAPHY

1 "On the Applicability of Notch Tensile Test Data to Engineering Design," by J. D. Lubahn (report in preparation).

2 "An Investigation of the Stress and Strain States in Bending Rectangular Bars," by G. S. Sangdahl, E. L. Aul, and G. Sachs, Proceedings of the Society of Experimental Stress Analysis, vol. 6, no. 1, 1948, p. 1.

3 "Notch-Sensitivity of Ship Plate—Correlation of Laboratory-Scale Tests With Large-Scale Plate Tests," by N. A. Kahn and E. A. Imbembo, Symposium on "Deformation of Metals as Related to Forming and Service," held in Detroit, Mich., June, 1948, Special Technical Publication No. 87, ASTM, Philadelphia, Pa., 1949.

4 "Room-Temperature Crack Propagation and Size Effect on Mild Steel," by J. D. Lubahn, *Welding Research Supplement*, October, 1955, p. 518-s.

5 "Notch Bar Tension Tests on Annealed Carbon Steel Specimens of Various Sizes and Contours," by M. L. Fried and G. Sachs, ASTM Symposium on "Deformation of Metals as Related to Forming and Service," Special Technical Publication No. 87, ASTM, Philadelphia, Pa., 1949.

6 "An Investigation of the Technical Cohesive Strength of Metals," by D. J. McAdams and R. W. Mebs, AIME Technical Paper No. 1615, 1943.

7 "Notched Bar Tensile Properties of Various Materials and Their Relation to the Unnotch Flow Curve and Notch Sharpness," by H. Schwartzbart and W. F. Brown, ASM (to be published).

8 "The Tensile Properties of Aluminum Alloys in the Presence of Stress Raisers—Part I: The Effects of Triaxial Stress States on the Fracturing Characteristics of 24S-T," by A. E. Dana, E. L. Aul, and G. Sachs, NACA Technical Note No. 1830, March, 1949.

9 "The Effect of Notches of Varying Depth on the Strength of Heat-Treated Low Alloy Steels," by G. Sachs, J. D. Lubahn, and L. J. Ebert, Trans. ASM, vol. 34, 1945, p. 517.

10 "Correlation of Tensile Strength, Tensile Ductility, and Notch Tensile Strength With the Strength of Rotating Disks of Several Designs in the Range of Low and Intermediate Ductility," by A. G. Holms and A. J. Repko, NACA Technical Note 2791, September, 1951.

11 "Bursting Tests of Steam-Turbine Disk Wheels," by Ernest L. Robinson, Trans. ASME, vol. 66, 1944, p. 373.

12 "The Local Conditions at the Root of the Notch in a V-Notch Charpy Impact Specimen," by H. A. Lequear and J. D. Lubahn, *Welding Research Supplement*, vol. 19, 1954, p. 585.

## Appendix

### Details of Procedure and Test Results

Several types of tests were made on a special alloy steel. The composition and heat-treatments are shown in Table 1. This material was selected because it could be heat-treated to produce either high or low impact strength at room temperature, while still maintaining high ductility in a tensile test. These heat-treatments are designated by A and B, respectively, in Table 1. Standard tensile and keyhole Charpy impact tests and five types of special tests were made for each of these two heat-treatments. Some of the special types of tests were also made for a third condition of heat-treatment (C) which resulted in both low tensile ductility (except for sporadic high values) and low impact strength.

The steel was supplied in the form of 4-in-sq billets. Disk forgings were obtained by upsetting at a maximum temperature of 2100 F. The forgings were annealed at 1700 F and furnace-cooled before final heat-treatment. Some of the forgings were cut up for impact tests and notched and unnotched tensile tests, and the rest were machined to disk-bursting specimens. The smaller types of specimens were also cut out of failed disks, providing that locations away from the fractures could be found in which the tangential strain due to the bursting tests was small (less than 3 per cent).

*Standard Tests.* Unnotched tensile specimens and keyhole Charpy impact specimens were machined and tested according to the ASTM Standards. In addition to the standard measurements, the reduction in diameter away from the neck after fracture was also measured (necking strain). The tensile specimens had a 0.250-in-diam, 1-in-long smooth section. The results are shown in Table 2. Smaller specimens cut from broken disks gave results that agreed within the limit of scattering with results of tests on specimens cut from disks not tested by spinning.

*Disk-Bursting Tests.* After heat-treatment, the upset forgings were machined to disks of the following dimensions: 10 in. OD, $1^1/_2$-in. central-hole diam, and 0.375 in. thick. Two disks were severely notched by saw cutting from the outside edge with a jeweler's saw along a diameter to a depth of 0.7, the final 0.025 in. of which was 0.005 in. thick, Fig. 4. One disk had a forging crack of about $^3/_4$ in. depth in the rim, as determined by magnaflux, Fig. 5. One disk had a special stress concentration near the rim, as shown in Fig. 6. The disks with cracked or slotted rims also had two holes at the opposite edge, as shown in Fig. 5.

The disks were tested by spinning to destruction in a high-speed vacuum pit. The energy from the air-turbine drive was transmitted through a slender spindle to the disk by means of a tulip-type expansion adapter, Fig. 7. The speed of the assembly was controlled by a hand throttle on the air supply, and was measured with an electromagnetic pickup. The speed indicator could be read easily to 5 cycles per sec (cps).

The average tangential stress in the disk was calculated from the bursting speed as follows: The radial force exerted by one half of the disk upon the other is

$$\text{Force in pounds} = \frac{8\pi^2 R^2 \alpha t (b^3 - a^3)}{2g}$$

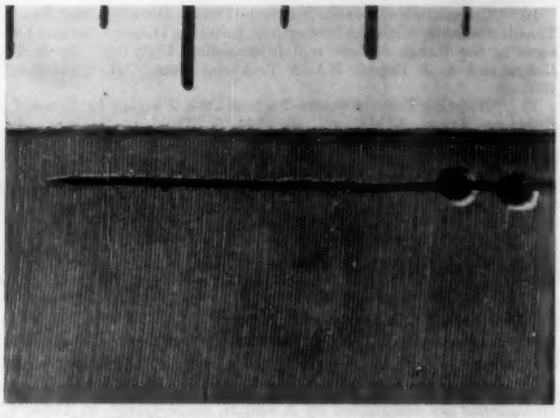

FIG. 4 SAW-CUT NOTCH IN RIM OF DISK BEFORE SPINNING (HEAT-TREATMENT A)

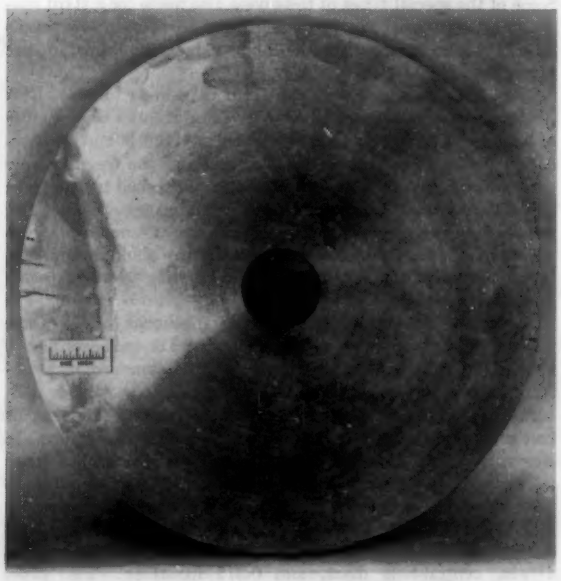

FIG. 5 RIM CRACKS OUTLINED BY MAGNAFLUX

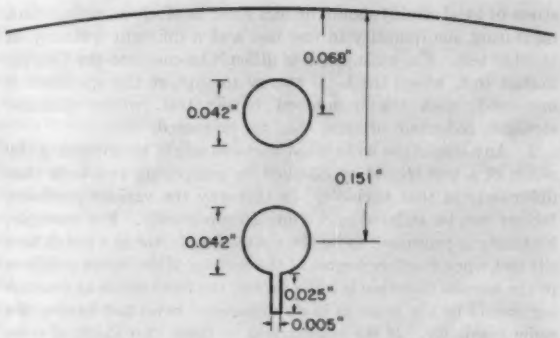


FIG. 6 SPECIAL STRESS CONCENTRATION AT RIM OF DISK. TWO IDENTICAL HOLES AT 180 DEG FROM THESE, BUT WITHOUT SAW CUT

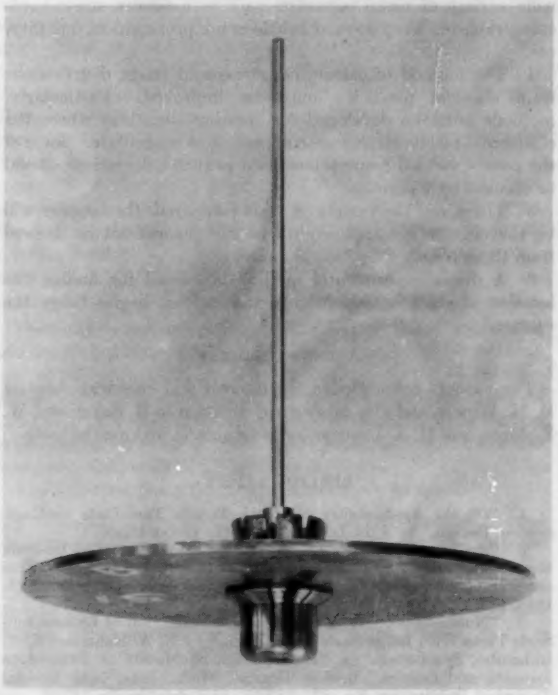

FIG. 7 TULIP-TYPE EXPANSION ADAPTER USED TO ATTACH SPINNING DISK TO ROTATING SHAFT

where $R$ = revolutions per sec; $\alpha$ = density, pci; $t$ = thickness, in.; $b$ = radius to outside, in.; $a$ = radius of hole, in; and $g$ = acceleration of gravity, ips per sec. This force acts over an area of

$$\text{Area} = t(2b - 2a)$$

in the case of the unnotched disks, and over a smaller area, that can be readily measured, in the case of the disks with various stress concentrations.

The results of the disk-bursting tests are shown in Table 2. The disk-strength ratio for unnotched disks is unity for ductile metal and less than unity for brittle material. In other words, for ductile metal the average tangential stress at bursting is as high as the tensile strength while this average stress is below the tensile strength for metal with less than a certain ductility.

These results confirm the generalization made by Holms and Repko (10) that the disk-strength ratio is unity for ductility values greater than 5 per cent On the other hand, this is not a completely valid generalization; Robinson (11) reports tests on metals with more than 15 per cent elongation in tension and disk-strength ratios as low as 0.7.

The ductile disks broke into three pieces, with 45-deg shear fractures along radial necks, Fig. 8, except for the last inch or so at the outside surface. These disks apparently suffered 6 to 8 per cent uniform reduction of thickness before local necking, according to measurements on failed disks away from the necked areas. The brittle disk broke into more than 50 pieces. The fracture surfaces were normal to the wheel surface. There was no evidence of any ductility preceding or accompanying the propagation of the cracks.

For heat-treatment A, the disk-strength ratio is as high when a hole and short saw cut are present as when they are not; only a

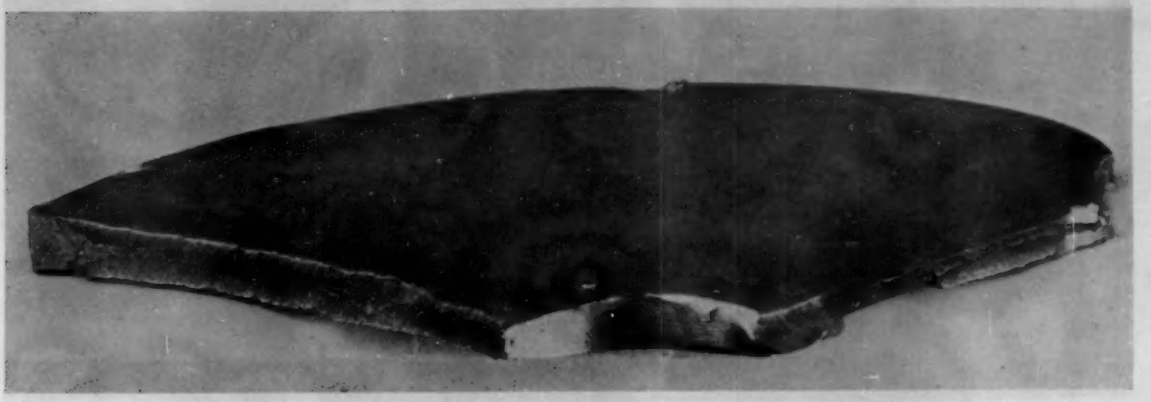

FIG. 8 DUCTILE FRACTURE IN AN UNNOTCHED DISK, SHOWING 45-DEG SHEAR FRACTURE ALONG RADIAL NECK

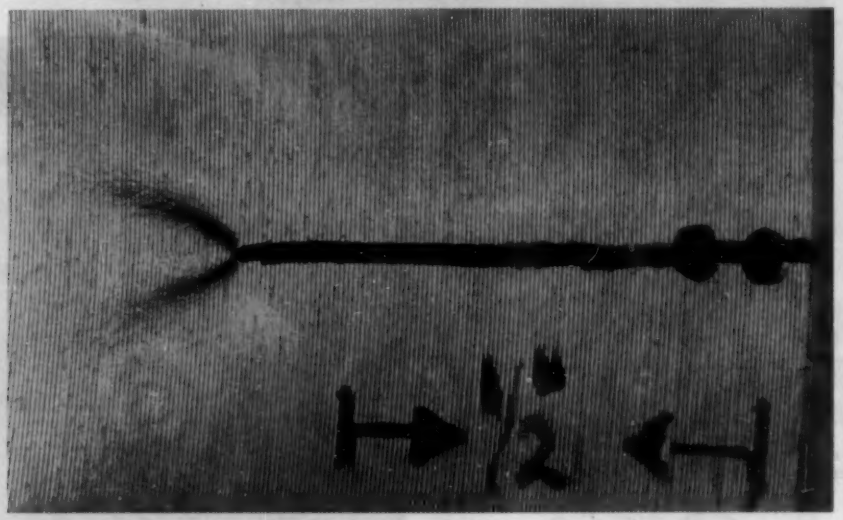


FIG. 9 SAW CUT IN RIM OF DISK (SHOWN IN FIG. 4) AFTER SPINNING AT 26,400 RPM FOR 1 MIN. SAW CUT HAS WIDENED AND CONSIDERABLE LOCAL DEFORMATION HAS OCCURRED

deep saw cut in the rim causes appreciable loss of strength. For heat-treatment B, the presence of a notch causes much more loss of bursting strength than for heat-treatment A. Sharp cracks are apparently no more severe in this respect than a saw cut, Table 2.

The slotted disk of heat-treatment A showed significant widening of the slot after spinning at 26,400 rpm (compare Figs. 4 and 9), and there was evidence of considerable deformation at the root of the slot, Fig. 9. After spinning at 27,000 rpm the disk had thinned to 0.357 at the root of the saw cut, and a crack had started. The crack was $^1/_8$ in. deep on the surfaces, and estimated to be at least $^5/_8$ in. deep at mid-thickness of the disk.

The cracked disks and slotted disks of heat-treatment B exhibited brittle primary crack propagation, starting at the base of the crack or slot, as indicated by the chevron markings, Fig. 10. The secondary cracks were ductile, as in the unnotched disks. On the other hand, the disks of heat-treatment A with stress raisers present exhibited ductile crack propagation. In the slotted disk the crack changed from normal to 45 deg shortly after leaving the notch bottom. Its propagation was accompanied by deep necking. In the disk with the special hole-and-slot stress raiser, Fig. 6, the crack did not go through one saw-cut stress raiser, Fig. 11. The slot closed up during spinning.

## UNNOTCH-BEND TESTS

The specimens were $^3/_{16} \times 2$ in. in cross section and 3 in. long. According to Sachs, et al. (2), the breadth-to-depth ratio ($b/h$) of $2/(^3/_{16})$ = approximately 11 corresponds to a biaxiality of 0.48 to 0.50, depending on the curvature. One specimen each for heat-treatments A and B was cut from a failed notched disk in such a direction that the principal bending stress was in the tangential direction of the disk, and such that the transverse direction of bending was in the radial direction of the disk.

The specimens were first bent to 120 deg in four-point loading fixtures that were especially designed for use in a furnace or liquid bath, Figs. 12 and 13. Then they were squeezed between compression heads until the machine limit of 60,000 lb was reached. No cracks were present in either specimen after the specimens had been bent flat shut, Fig. 14. This condition corresponds to about 120 per cent conventional tangential strain on the convex side.

FIG. 10 BRITTLE-CRACK PROPAGATION STARTING AT BASE OF INITIAL CRACK, AS INDICATED BY CHEVRON MARKINGS (HEAT-TREATMENT B)

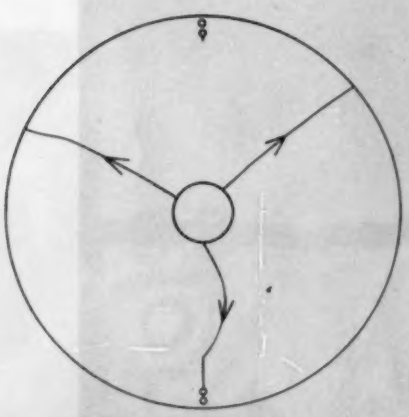

FIG. 11 FRACTURE PATTERN FOR DISK WITH SPECIAL STRESS CONCENTRATION NEAR RIM (HEAT-TREATMENT A)

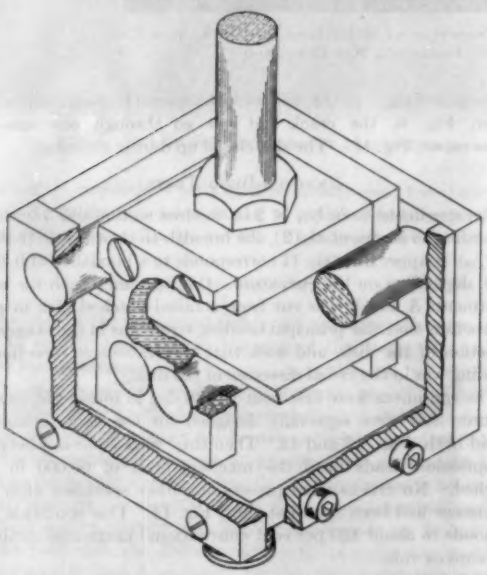

FIG. 13 UNNOTCHED BENDING FIXTURE

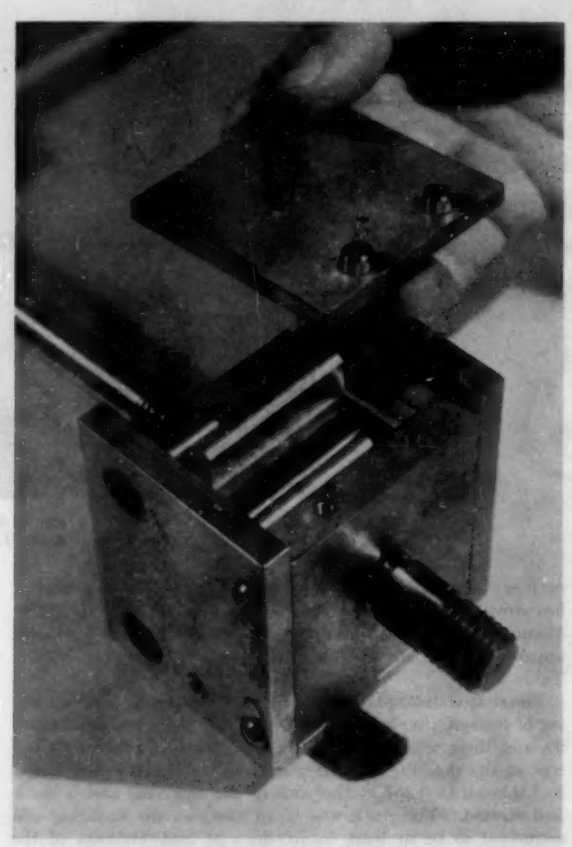

FIG. 12 UNNOTCHED BENDING FIXTURE

### NOTCH-BEND TESTS

Standard V-notch Charpy specimens were cut in the tangential direction of failed notched disks. The notch was usually cut across the specimen in the axial direction, giving orientation relationships like those in the disk tests, but a few specimens had the notch in the radial direction, giving orientation relationships like those in the unnotched bend tests. No significant behavior difference was observed for the two notch orientations.

FIG. 14 UNNOTCHED BEND SPECIMEN FOLDED FLAT SHUT

FIG. 15 NOTCHED BENDING FIXTURE

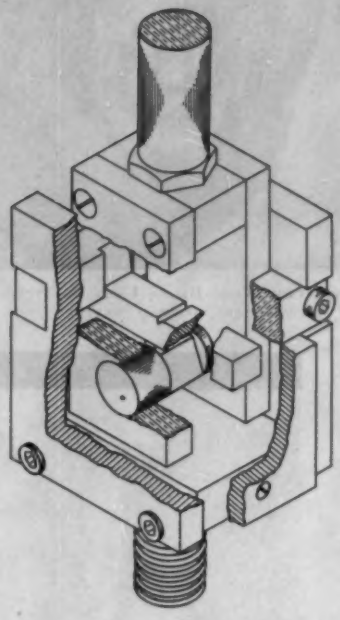

FIG. 16 NOTCHED BENDING FIXTURE

Bending was performed in special fixtures designed for use in a furnace or liquid bath, Figs. 15 and 16. The geometry of the anvils and punch was the same as in a standard Charpy impact machine.

The load was increased in small increments beginning with a load estimated to be low enough not to give any plastic strain. As plastic flow progressed, the load increments were decreased as necessary to keep the strain increments sufficiently small. After each load increment the specimen was unloaded and removed from the fixtures in order to measure bend angle and to look for cracks.

Small angles were measured with a curvature gage, Fig. 17. For this application the difference between the dial gage reading for a specimen and for a flat plate, divided by half the distance between the fixed anvils, equals the tangent of half the bend angle. The bend angle is needed to determine the local strain at the root of the notch, Fig. 18. Large bend angles were measured with a protractor which could be read to $\pm 0.2$ deg. For sudden type fractures, the load-versus-bend-angle curve could be extrapolated a short distance beyond the last point to the observed fracture load, thus giving the bend angle at fracture. In some cases, however, failure occurred suddenly at a load smaller than that reached prior to the previous unloading; and then the last measured bend angle was taken as the bend angle to fracture. For the most ductile specimens, the calibration curve did not go far enough to read off local strain for the very large bend angles observed at fracture. In these cases the approximate slope of 10 per cent local conventional strain per 1 deg of bend angle (Fig.

FIG. 17 CURVATURE GAGE BEING USED TO DETERMINE BEND ANGLE OF NOTCHED SPECIMEN

For the brittle specimens the exact moment when the crack started was very definite. There was a noise and sudden drop in load, after which a crack of considerable depth, Fig. 19, could be observed. For the ductile specimen, the final crack began to open up unobtrusively, and so the fracture bend angle was taken as the angle when a definite crack was first observed. The crack was considered to be "definite" when it was significantly deeper than the initial machining marks, which had spread open into characteristic "furrows," Fig. 20.

For heat-treatment B, the crack propagated in a brittle manner across the entire specimen, Fig. 21. For heat-treatment A, the crack propagated most of the way in a brittle manner, Fig. 21, but there was gradual tearing for a short distance at the beginning and end of the process. Also, there were shear lips on the sides, which

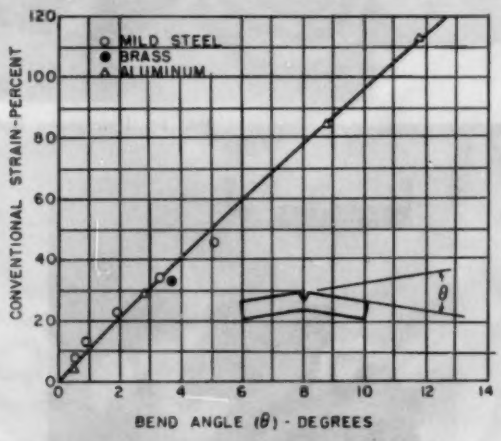


FIG. 18 CALIBRATION CURVE OF BEND ANGLE VERSUS LOCAL STRAIN AT NOTCH BOTTOM (12)

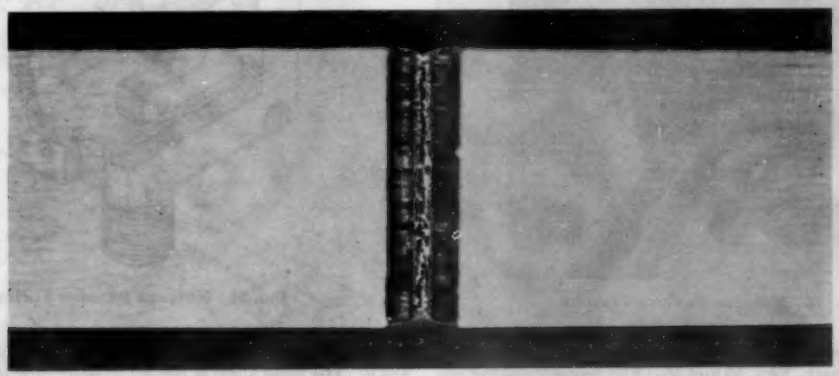

FIG. 19 BRITTLE NOTCH-BEND SPECIMEN IMMEDIATELY AFTER INITIATION OF A CRACK (HEAT-TREATMENT A)

18) was used to convert bend angle into local strain. The values of local ductility at the bottom of the notch are given in Table 2.

For the purpose of determining energy to fracture, the bend angles up to crack initiation were converted to deflections using the bending span: Deflection = (1/2) (bending span) (tan 1/2 bend angle). The additional deflection occurring during the propagation of the crack was determined from the motion of the heads of the testing machine. Fig. 2 shows load-deflection curves for heat-treatments A and B. The area under such a curve is the energy to fracture; and these energy values are given in Table 2.

were not present for heat-treatment B. Fig. 21 shows the marked distortion of the cross section resulting from the large ductility associated with heat-treatment A. The lack of such distortion for heat-treatment B is also shown by the other specimen in this figure. The difference in mode of crack propagation between specimens of heat-treatments A and B is also indicated by the load-deflection curves, Fig. 2. For heat-treatment A there were 5.4 ft-lb associated with the initial tearing and 3.2 ft-lb accompanying the final tearing. For heat-treatment B there was no indication of any slow tearing prior to complete sudden ruptur-

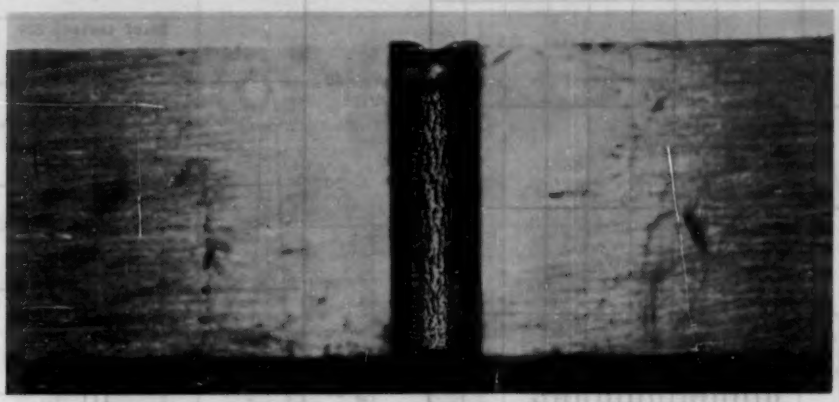

FIG. 20 DUCTILE NOTCH-BEND SPECIMEN AFTER CONSIDERABLE STRAIN BUT BEFORE INITIATION OF A CRACK. "FURROWS" IN NOTCH BOTTOM ARE MACHINING MARKS WHICH HAVE OPENED UP INTO BLUNT GROOVES

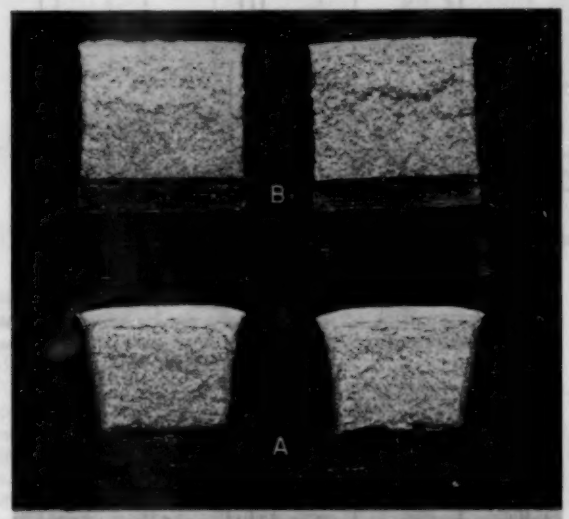


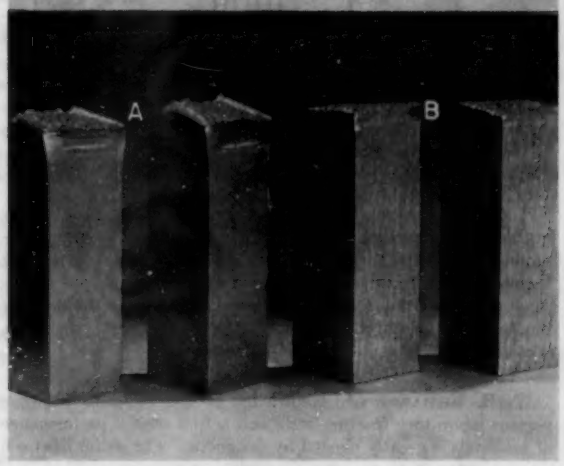


FIG. 21 COMPARISON OF FRACTURE SURFACES OF NOTCHED BEND SPECIMENS FOR HEAT-TREATMENTS A AND B

ing. Thus the energy of crack propagation was less than that stored elastically in the system.

### NOTCH TENSILE TESTS

The notch was a 60-deg annular V-groove cut in a 0.250-in-diam, 1-in-long cylindrical section. The notch had a 0.005-in. root radius. The specimen diameter at the root of the notch was 0.175 in., thus giving a notch depth of 51 per cent.

In most of the tests, only the maximum load and reduction of area after separation were measured. In a few tests on ductile specimens, however, the load-diameter curves were determined, and the point of crack initiation was observed. These latter tests (Table 2) showed that part of the "ductility," measured after separation, is fictitious. It is due to the rim effect (6).

The results of all the tests are given in Table 2. They show that the ductility under notch conditions is much lower for heat-treatment B than for heat-treatment A. However, the ductility in either case apparently is high enough to smooth out the initial stress concentration, because the notch-strength ratio is very high for both A and B heat-treatments. This is not so for heat-treatment C. In this case the notch-strength ratio is far below the ideal value of 1.5. This must be due to a still lower notch ductility for heat-treatment C than for B, although the measured values do not show it. (However, they are too small to be very reliable.)

## Discussion

E. P. KLIER,[4] V. WEISS,[4] and G. SACHS.[5] This paper is a very interesting and stimulating contribution to the evaluation of the old standard and of recently developed laboratory tests. It is evident from the paper that a large number of factors is responsible for any failure and, therefore, that the selection of a single test method is not sufficient to establish the fracture characteristics of a material.

The writers would like to present a contribution concerning the accuracy and reproducibility of notch-tension and Charpy impact tests. A great number of tests of these types have been performed on 4340 steel at Syracuse University.[6]

An evaluation of these tests revealed that considerable scatter

[4] Syracuse University, Syracuse, N. Y.

[5] Director of Metallurgical Research, Syracuse University, Syracuse, N. Y. Mem. ASME.

[6] The work was supported by the Bureau of Aeronautics, U. S. Navy, under Contract No. NOas 54-424-c. The steel was hardened to strength levels between approximately 200,000 and 300,000 psi.

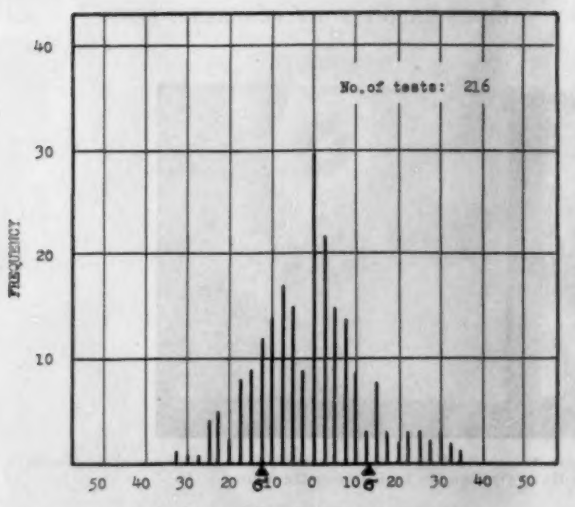


FIG. 22 DISTRIBUTION OF V-NOTCH CHARPY IMPACT TEST VALUES OF 4340 STEEL, TESTED AT ROOM TEMPERATURE

was encountered for impact tests, even at room temperature, while the consistency of the results of notch-tensile tests was very much better.

For a given heat-treatment the maximum number of parallel impact tests in this study was 10 and that of notch-tensile tests was 5. Frequency plots of such a small number of test values, of course, were irregular. Therefore, to achieve the desired statistical comparison, a large number of values was needed. To obtain such an expanded set of test values the following procedure was used:

1 Each set of test data was averaged and the average value was assigned "zero" deviation.

2 The percentage deviation from this value was determined for each test of the set.

3 Such results of a number of sets, differing in heat-treatment, were plotted in the same co-ordinate system.

Frequency plots, such as presented in Figs. 22, 23, and 24, herewith, were thus obtained for the impact test at room temperature, the notch-tension test at room temperature and —100 F and at —320 F. The frequency plots of the data are compared in Fig. 25. In addition, Table 3 of this discussion lists the percentage of test values, as derived from Fig. 25, which lie within the indicated deviations.

TABLE 3 PER CENT OF INDICATED TEST DATA WHICH LIE WITHIN SPECIFIED DEVIATION FROM MEAN VALUE

| Deviation, per cent | ±2.5 | ±5 | ±10 |
|---|---|---|---|
| Impact test (RT) | 20 | 39 | 65 |
| Notch-tensile test (—320 F) | 45 | 64 | 85 |
| Notch-tensile test (RT, —100 F) | 73 | 93 | 100 |

From this evaluation of the test results it is evident that the reproducibility of a notch-tensile test performed at room temperature and at —100 F is considerably superior to the repoducibility of the V-notch Charpy test. The consistency of the notch-tensile test performed at —320 F is intermediate.

J. M. LESSELLS.[7] This paper is of engineering interest since it gives a summary of the various tests which may be used in determining the suitability of a particular steel.

[7] President, Lessells and Associates, Inc., Boston, Mass.; Associate Professor of Mechanical Engineering, Emeritus, Massachusetts Institute of Technology, Cambridge, Mass. Fellow ASME.

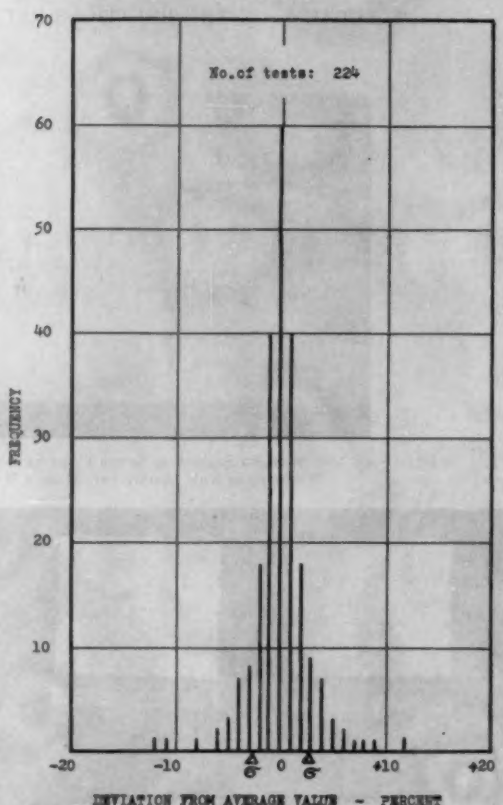


FIG. 23 DISTRIBUTION OF NOTCH-TENSILE-TEST RESULTS OF 4340 STEEL, TESTED AT ROOM TEMPERATURE AND —100 F

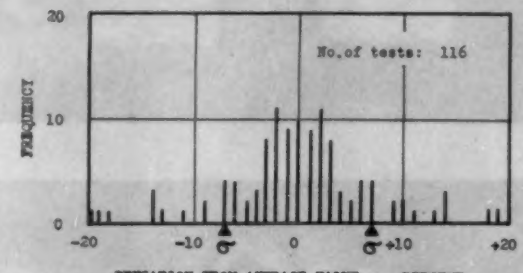


FIG. 24 DISTRIBUTION OF NOTCH-TENSILE-TEST RESULTS OF 4340 STEEL, TESTED AT —320 F

The authors seem to be a little severe regarding the utility of the notched bar-impact test. While the values of energy cannot be applied directly to design, the test was capable of detecting the notch brittle conditions associated with certain nickel-chrome steels and more recently has been used a great deal in the study of the brittle fracture of ship plate steels. The test, therefore, is of considerable engineering importance.

W. B. RICHARDSON.[8] Knowledge of the relations between various laboratory fracture tests and actual service performance of materials is greatly needed by designers. The writer has been

[8] Mechanical Engineer, U. S. Naval Ordnance Laboratory, White Oak, Silver Spring, Md. Assoc. Mem. ASME.

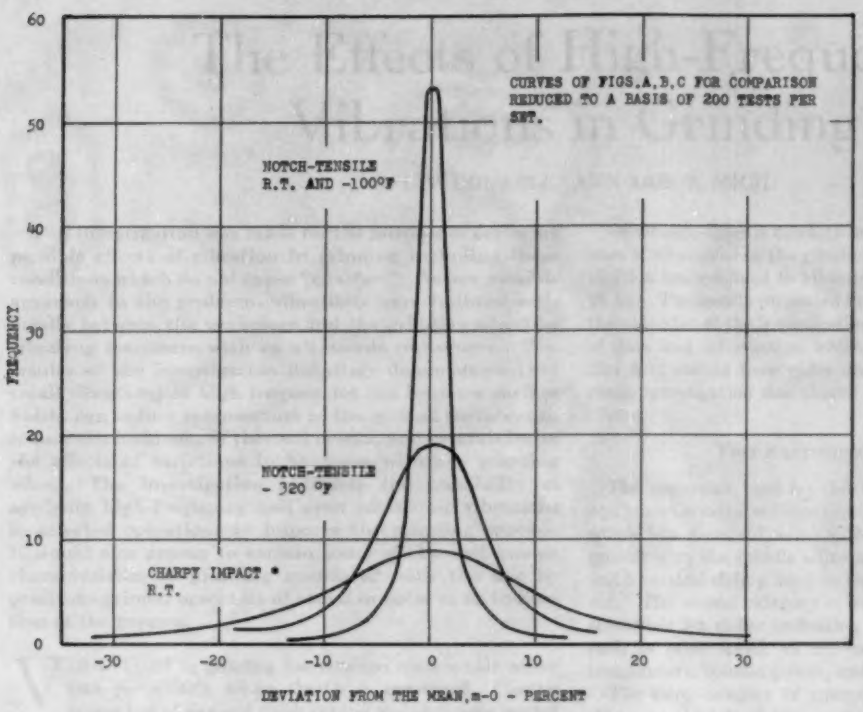


FIG. 25 COMPARISON OF DISTRIBUTION CURVES FOR RESPECTIVE SETS OF DATA

trying to collect data in this field for use in design of missiles and projectiles. Lack of correlation between various tests, as discussed by the authors, makes development of rational design procedures difficult.

One of the factors governing failure of materials used in projectiles is the rapid rate and short duration of loading It is not true shock, since the loading pulse may last about 15 millisec in a medium-caliber gun. In most cases the actual design is based on the static strength of the material, using impact and ductility values to check for unusual brittleness. In some experimental designs, however, the calculated stresses have exceeded the static strength of the heat-treated alloy steel in the shell wall by as much as 15 per cent with no evidence of failure. For instance, one specimen of Aircraft Quality AISI 4340 quenched and tempered to a hardness of $R_c$ 42-44 was fired from a gun. The compressive stress in the aft portion of the hollow cylinder reached a maximum of at least 225,000 psi. The specimen was recovered and showed a slight plastic deformation of a form discussed by Timoshenko.[9] A tensile specimen of the same material had a yield point of 175,000 psi and tensile strength of 187,000 psi.

As usual with simulated service tests, the foregoing test had several features which make complete analysis difficult, such as the fact that the load was compressive and also varied from a maximum at the base to a minimum in the nose. Our experience with various types of loading leads us to the belief that the short duration of the load is probably the most important single factor causing the increases in strength which we commonly find.

There has been a considerable amount of research on the effects of dynamic loads on the mechanical properties of materials.[10,11,12,13] Most of the results show somewhat less increase in the strength of the heat-treated medium carbon-alloy steels than our results seem to show. Freudenthal[14] has a good general discussion of the problems involved, stressing the fundamental requirement for more detailed knowledge of the complete equations of state relating stress and strain with time and temperature.

The writer would like to see the authors continue their efforts to correlate results of the various laboratory fracture tests. It also might help if they could include a more explicit study of the time and temperature variables.

### AUTHORS' CLOSURE

Professor Lessells' point, that impact tests are useful for comparing materials, is well taken. In general, a steel which has a higher impact strength will also exhibit better performance in service.

The authors did not intend to criticize the impact test from the viewpoint of material selection, but rather from the viewpoint of its usefulness for design purposes. The designing engineer is usually concerned with such quantities as load or deflection at fracture. In only a few cases does energy to fracture enter into design calculations.

[9] "Theory of Elastic Stability," by S. Timoshenko, Article 81, p. 439, "Symmetrical Buckling of Cylindrical Shell Under Uniform Axial Compression," McGraw-Hill Book Company, Inc., New York, N. Y., 1936.

[10] "The Effect of Axial Dynamic Loads on the Mechanical Properties of Certain Steels," by R. C. Smith, T. E. Pardue, and I. Vigness, Naval Research Laboratory Report 4468 (unclassified), Washington, D. C., 1954.

[11] "Analysis of Plastic Deformation in a Steel Cylinder Striking a Rigid Target," by E. H. Lee and S. J. Tupper, *Journal of Applied Mechanics*, Trans. ASME, vol. 76, 1954, p. 63.

[12] "The Tensile Impact Properties of Some Metals and Alloys," by D. S. Clark and D. S. Wood, Trans. ASME, vol. 42, 1950, pp. 45–74.

[13] "Explosive Impact Tests," by P. R. Shepler, Proceedings of The Society for Experimental Stress Analysis, vol. 5, no. 1, 1947, pp. 1–25.

[14] "The Inelastic Behavior of Engineering Materials and Structures," by A. M. Freudenthal, John Wiley & Sons, Inc., New York, N. Y., 1950, pp. 167–170.

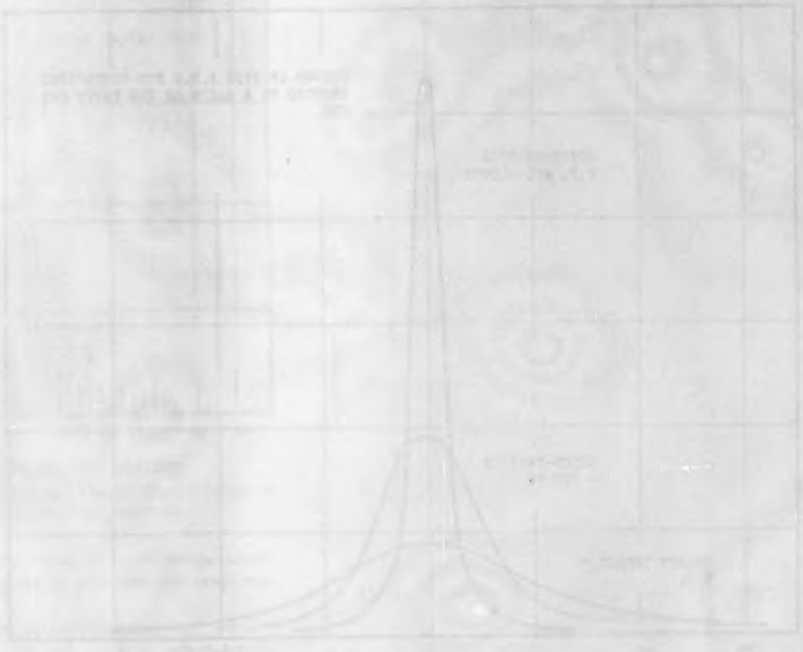

# The Effects of High-Frequency Vibrations in Grinding

By L. V. COLWELL,[1] ANN ARBOR, MICH.

**This investigation was made for the purpose of exploring possible effects of vibration in grinding including those conditions which do not cause "chatter." As one possible approach to the problem, vibrations were induced artificially between the workpiece and the grinding wheel by vibrating specimens with an ultrasonic transducer. The results of the investigation definitely demonstrate that small vibrations at high frequencies can improve surface finish, can reduce temperature in the ground surface, can reduce the incidence of thermal cracks, and can minimize the effects of variations in hardness within a grinding wheel. The investigation indicates the possibility of applying high-frequency and even ultrasonic vibrations to selected operations to improve the grinding process. It would also appear to explain some of the well-known characteristics of grinding associated with the use by precision-grinder operators of sound or noise as an indication of the process.**

VIBRATION in grinding has received considerable attention particularly where chatter is concerned. Chatter causes loss of size and finish control and obviously cannot be tolerated. Little difficulty is experienced with this type of vibration today.

There have been several types of evidence which seem to indicate that vibration problems still exist in grinding even in the absence of the strong resonant vibrations which cause chatter. One type of evidence concerns the proper grinding wheel for a specific production-grinding job. For example, a group of centerless grinders may be finishing automotive wrist pins. Experience indicates that a particular wheel is best for this job; however, if one of these grinders is replaced by a new grinder of identically the same model and manufacture, the grinding wheel that has become standard for the job does not work as well on the new grinder as it did on the machine it replaced. After the new grinder has been in operation for a period of time, then the standard wheel does perform well. Presumably, the change in the machine during the so-called run-in period is associated with the bearings and could be a vibration problem.

Another type of evidence that vibrations may still be effective in the absence of sustained chatter is the common fact that a skilled grinder operator literally "grinds by ear." In other words, the operator relies on the sounds to guide him. These sounds are, of course, created by vibrations in the grinding zone. They may be wheel vibration, or some combination of wheel, spindle, and work vibrations. A simple survey of the intensity of sound at different frequencies in a grinding operation has shown substantial intensity at frequencies even up to 20 kilocycles (kc) which is beyond the threshold of human hearing.

[1] Professor, Department of Production Engineering, College of Engineering, University of Michigan. Mem. ASME.

Contributed by the Research Committee on Metal Processing and presented at the Diamond Jubilee Semi-Annual Meeting, Boston, Mass., June 19–23, 1955, of THE AMERICAN SOCIETY OF MECHANICAL ENGINEERS.

NOTE: Statements and opinions advanced in papers are to be understood as individual expressions of their authors and not those of the Society. Manuscript received at ASME Headquarters, March 1, 1955. Paper No. 55—SA-12.

Obviously, there is much to be learned further about the influence of vibrations on the grinding operation. The present investigation was confined to vibrations in the range between 10 and 18 kc. The results presented in this paper are preliminary since the objective of the investigation was first to determine the type of data and information which could be related to vibration. The first results were quite unexpected in nature so that the entire investigation was altered to determine the scope of these effects.

## Test Equipment and Procedure

The apparatus used for this study is shown in Fig. 1. The equipment consists of three types. First is the grinding machine which is a standard 8-in. × 24-in. reciprocating-table surface grinder with the spindle adjustable longitudinally for cross-feed and a vertical sliding head on the column for control of depth of cut. The second category of equipment includes numerous instruments for either indicating or recording of pertinent data such as table speed, vibrations of various machine elements, temperature, spindle power, and so on.

The third category of equipment is the electrical apparatus shown at the left of the grinder for inducing vibrations in the machine. It was established in preliminary study that the amplitude of vibrations occurring naturally in the grinder at no time exceeded 2 to 3/10,000 in. so that the grinder itself could be considered to be substantially rigid and to such an extent that the vibratory motions between the work and wheel could be induced without undue effects from the natural machine vibrations. The electrical equipment shown at the left in Fig. 1 was used to drive a so-called transducer shown in the close-up of Fig. 2.

The transducer consists of laminations of 0.005-in-thick sheets of pure nickel. These laminations or the stack, as it is sometimes called, are wound with copper wire to form a coil. Alternating current applied to the coil causes the nickel laminations alternately to contract and expand, giving rise to vibratory motion of the two ends of the stack in the direction of the axis of the coil. Devices of this type are in general use and the method has been known for a number of years.

Work specimens were mounted on top of the stack as shown in Fig. 2. In this particular setup, a relatively thin steel specimen rests on a laminated bakelite base which in turn is held to the top of the stack by means of screws and Cycleweld. The Cycleweld was used in all junctions with the transducer. By this means, it was possible to vibrate work specimens at amplitudes up to approximately 0.001 in. at frequencies in the range from 10 to 18 kc per sec (kcs).

In general, the test procedure involved mounting the work specimen on the transducer and proceeding to grind as in any ordinary surface grinding. All so-called conventional grinding, that is without induced vibration, was accomplished in the same manner except that the transducer was not vibrated. This was done so that the only significant difference between the two grinding conditions would be that of induced vibration.

## Preliminary Tests

Initial observations were confined to surface-roughness measurements and microscopic examination of the grinding swarf or

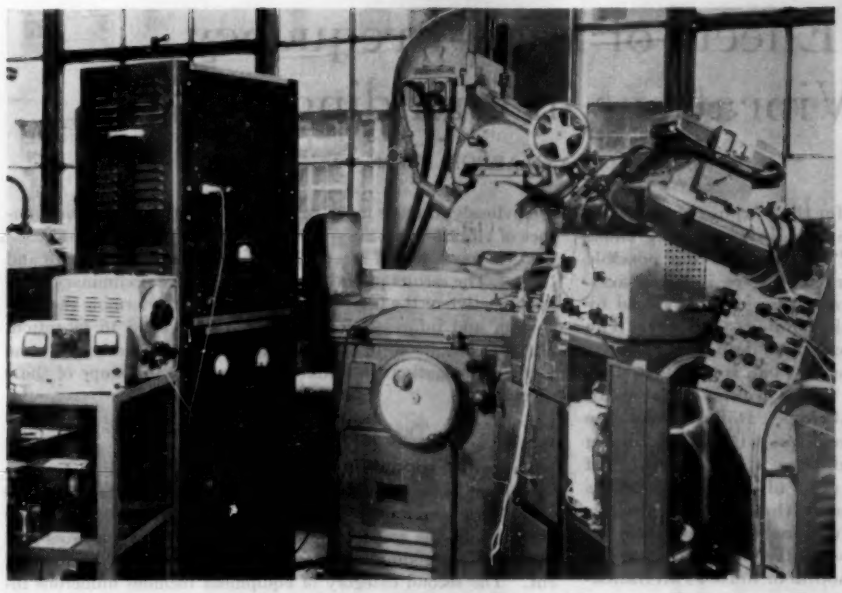

FIG. 1 LABORATORY EQUIPMENT FOR STUDYING EFFECT OF INDUCED ULTRASONIC VIBRATIONS IN SURFACE GRINDING

(Electrical apparatus at left of grinder provides high-frequency power to transducer which vibrates work specimen radial to grinding wheel. Instruments to right of grinder record input power to spindle and work temperature.)

TABLE 1 SURFACE-FINISH SUMMARY—TEST SERIES 1

| Material | Wheel grade | Vibrated, V conventional, C | Roughness, $d = 0.0002$ | Microin., $d = 0.0005$ | RMS, $d = 0.002$ |
|---|---|---|---|---|---|
| 1020..... | F | C | 26 | 26 | 23 |
| 1020..... | F | V | 20 | 24 | 22 |
| 1020..... | J | C | 18 | 36 | 40 |
| 1020..... | J | V | 18 | 19 | 30 |
| 52100..... | F | C | 21 | 63 | 40 |
| 52100..... | F | V | 16 | 38 | 16 |
| 52100..... | J | C | 18 | 21 | 23 |
| 52100..... | J | V | 14 | 25 | 13 |

dust obtained during dry grinding. The preliminary tests made with a vibration range of approximately 0.001 in. at a frequency of between 10 to 11 kc gave some unexpected results both as to surface finish and apparent temperature. Table 1 is a summary of the surface-roughness measurements made on surfaces ground in the first series. It will be noted that the roughness was reduced from 40 to 16 microinches, a reduction of 60 per cent, when grinding hardened 52100 steel with an F-grade aluminum-oxide wheel with the specification DA60-F9-V20. The depth of cut was 0.002 in. and the cross-feed was 0.050 in. A similar effect persisted at two shallower cuts of 0.0005 in. and 0.0002 in., shown respectively in columns 5 and 4 of Table 1. The figures just quoted represent the greatest improvement in surface finish observed in this series.

In addition to the surface-finish improvements, microscopic examination of the grinding swarf and visual observation of the spark stream indicated lower temperatures as a result of induced vibration. This is supported by Figs. 3 and 4, although the pictures do not confirm this as clearly as visual examination in a microscope. Fig. 3 shows a sample of swarf from hardened 52100 steel ground without vibration at 0.002 in. depth of cut. It should be noted that there is a substantial number of spheroids, many of which are quite large. Their shape indicates that the material was molten. A larger percentage of

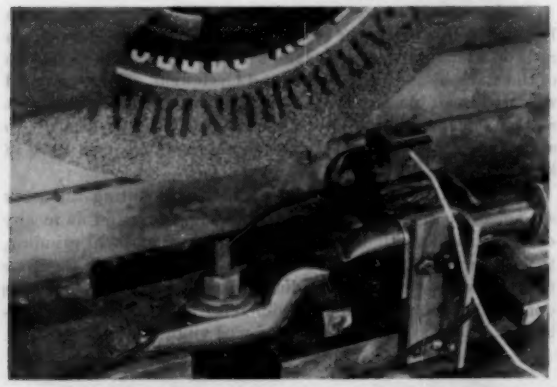

FIG. 2 MAGNETOSTRICTIVE TRANSDUCER WITH "TEMPERATURE" SPECIMEN CYCLEWELDED TO LAMINATED PLASTIC SUPPORT

(A thermocouple is imbedded in center of underside of test specimen.)

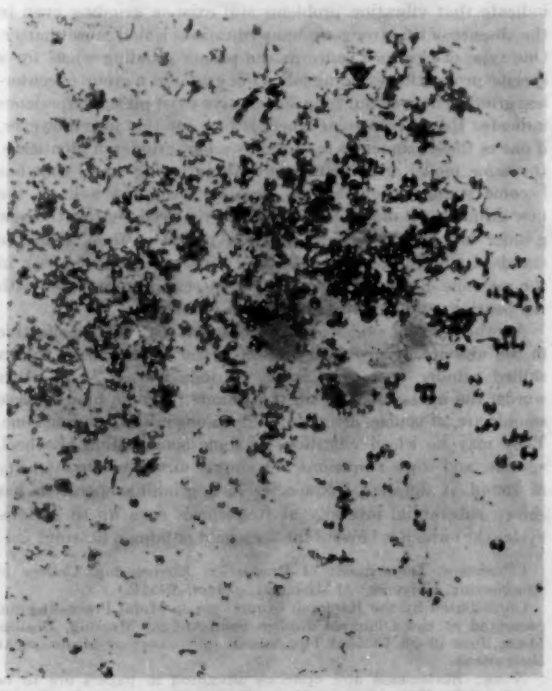

FIG. 3 SAMPLE OF SWARF FROM HARDENED AISI 52100 STEEL GROUND WITHOUT VIBRATION AT 0.002 IN. DEPTH OF CUT

(Note numerous large spheroids ×10.)

FIG. 4 SAMPLE OF SWARF FROM HARDENED AISI 52100 STEEL GROUND WITH INDUCED VIBRATION AT 0.002 IN. DEPTH OF CUT ×10

spheroids indicates a generally hotter condition, or perhaps more appropriately, a greater quantity of heat.

Fig. 4 shows the results of grinding at the same conditions except with induced vibration. Note a much smaller percentage of spheroids and generally smaller chips. In both figures, the somewhat blurred white blotches are particles either of abrasive or bond.

There was some doubt as to the significance of the improved surface finish and apparently lower temperature since only a very narrow range of grinding conditions was represented in this first series of tests. Consequently, numerous additional tests were made over a broad range of conditions including depth of cut, cross-feed, table speed, work material, and so on. The initial results as to improved surface finish and apparent lower temperature persisted in varying degrees throughout the broader range of conditions. This result stimulated interest in confirming the apparent temperature reduction not only as a temperature manifestation, but also in terms of residual stress. By this time grinding ratio also became of interest owing to the persistence of the effect of vibration and indications that vibration caused the wheel to break down more rapidly. Superimposed on all these questions was the question as to why induced vibration created these effects. Subsequent tests were designed to confirm the apparent reduction in temperature, to determine the effect on grinding ratio, and to gain further evidence as to how they came about.

### THE EFFECT OF VIBRATION ON GRINDING TEMPERATURE

Fig. 5 shows the surface of two specimens of hardened AISI 52100 steel. The upper specimen was ground conventionally while the lower one was vibrated. They were ground dry at a depth of 0.002 in. It will be noted that patches of oxides are visible only on the conventionally ground specimen. These are typical of the consistent pattern seen on ground surfaces when conditions produce temperatures on the verge of being too severe. The pitch of the dark patches is the distance traveled by the work during one revolution of the grinding wheel. The work was traversed in a direction across the picture from left to right. This phenomenon was studied at depths of cut ranging from 0.0002 in. up to and including 0.008 in. The extent of the oxide patches increased with the depth of cut during conventional grinding. They never appeared when vibration was imposed.

Another type of evidence supported observations that temperatures with the vibrated specimens were lower; this information came directly as a result of collecting the grinding swarf. It was collected in small beakers placed at a constant distance from the grinding specimen and intercepting the spark stream. It was noted that particles of steel were fused to the wall and to the bottom of the beaker. It was further noted that the amount of material fused to the beaker was substantially greater when grinding Ti 150A titanium. Fig. 6 is a picture looking at the bottom of two beakers used to collect the swarf from the vibrated and conventially ground specimens. The beaker at the left was used for a vibrated specimen and the one at the right is from a conventionally ground specimen. It will be noted that the bottom of the right-hand beaker shows many black specks. These were spheroids of molten titanium which fused with the glass and were flattened out upon impact. Only three such fusions were found in the beaker for the vibrated specimen.

Two groups of tests were conducted with thermocouples imbedded in the test specimens as shown in the close-up of Fig. 2. Plunge-grinding tests were made in steps of 0.002 in. at a work speed of 22 fpm. The test specimens were $^1/_4$ in. square by 0.125 in. thick, with a thermocouple hole $^1/_{16}$ in. diam. drilled into the middle of the underside. The end of the thermocouple was

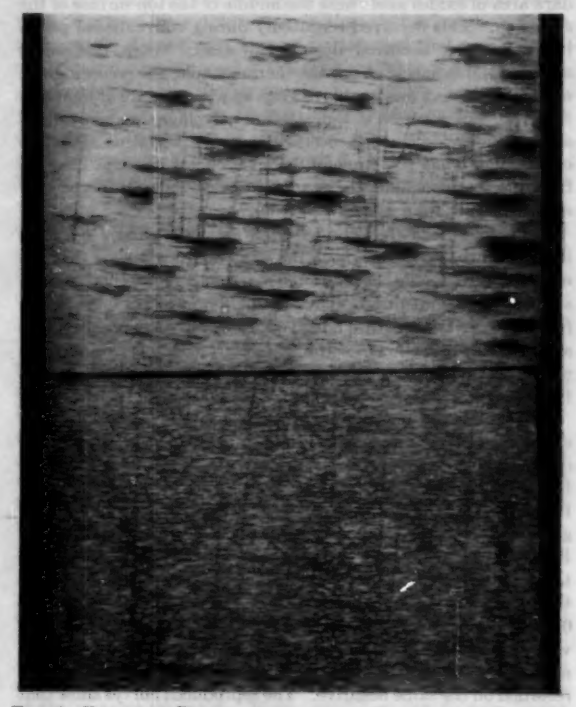

FIG. 5 VIEWS OF GROUND SURFACES OF HARDENED AISI 52100 STEEL

(Upper surface was ground conventionally and shows oxides from overheating due to loaded region of wheel. Lower surface ground with same wheel and induced vibration is free from burned areas. Wheel used for this test was deliberately chosen on hard side.)

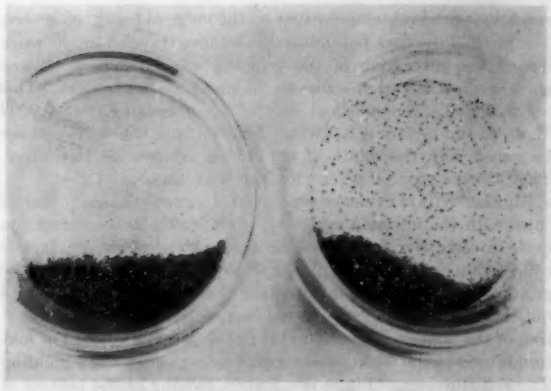

FIG. 6 SWARF SAMPLES COLLECTED DURING GRINDING OF TI 150A TITANIUM

(Sample for conventional grinding is shown in beaker at right; molten spheres fused to bottom of beaker. Cooler swarf obtained during vibration did not fuse to bottom of beaker at the left.)

resistance-welded to the bottom of the thermocouple hole. Initially, there was 0.030 in. of metal between the end of the thermocouple and the ground surface.

The first tests were preliminary in nature and were made while using a Speedomax recorder. Observations were made also of input power. All tests made during vibration of the work specimen gave definite repeatable temperature indications. On the other hand, the same tests without vibration resulted in varying peak temperatures. For example, it will be noted in Fig. 2 that a dark area of oxides exists near the middle of the top surface of the specimen. This occurred repeatedly during conventional grinding, but never occurred during vibration. When the oxides occurred immediately above the thermocouple, the recording pen of the Speedomax was unable to keep up with the rate of temperature rise, but even so it indicated a very high temperature of approximately twice that occurring during vibration. On the other hand, when the circle of oxides occurred at some distance from the thermocouple, the resulting peak temperature was only slightly higher than during vibration.

If it is assumed that the oxidized area was caused by local loading on the grinding wheel, the work speed was such that the oxidized area would be expected to occur repeatedly at substantially constant pitch. Thus it would appear that one reason for the lower temperature observed with vibration is continuous and uniform breakdown of the wheel surface, thus avoiding abnormal wear and resulting higher temperatures from those portions of a grinding wheel which may be duller than the average.

A second series of temperature tests using imbedded thermocouples was made with an oscilloscope to indicate the temperature change. The temperature curves were recorded with a Polaroid-Land camera with the setup pictured in Fig. 1. The results of these tests followed closely the experience in the preliminary group. A typical temperature versus time record is given in Fig. 7. The two curves shown were obtained from consecutive tests, the first by conventional grinding and the second by vibration. During the conventional grinding the thermocouple was 0.014 in. from the ground surface, while during the next pass with vibration it was only 0.011 in. from the surface and 50 per cent more metal was removed. The two temperature curves were recorded on the same negative. The reproduced curves show that the peak temperature for conventional grinding was approximately 475 F. It was evident that a loaded zone, if this was the cause, did contact the workpiece above the thermocouple during the conventional grinding test.

### EFFECTS OF VIBRATION ON RESIDUAL STRESSES

It was decided to conduct one series of tests for the purpose of determining the difference in residual stress between a conventionally ground specimen and one ground with vibration. Not only are residual stresses of interest, per se, but also, it is known that the magnitude of residual tensile stress is determined by the amount of overheating or temperature level. Consequently, the earliest indications of temperature difference pointed toward a significant difference in residual stress as between conventional and vibrated grinding.

Two specimens were prepared for this study. They were $^7/_8$ in. square by 0.060 in. thick, made from fully hardened SAE X 4340 steel, and were approximately 55 $R_c$. The specimens were Cyclewelded to bakelite supports, which, in turn, were mounted on the transducer for grinding. One specimen was ground conventionally and the other with vibration. Both specimens were ground at the following conditions:

| | |
|---|---|
| Grinding wheel | Carborundum DA60-J9-V20 |
| Wheel speed | 6000 fpm |
| Table speed | 20 fpm |
| Depth of cut | 0.002 inch per pass (5 test passes) |
| Cross-feed | 0.050 inch per stroke |
| Fluid | Dry grinding |

Observations were made of input power, and watch glasses were

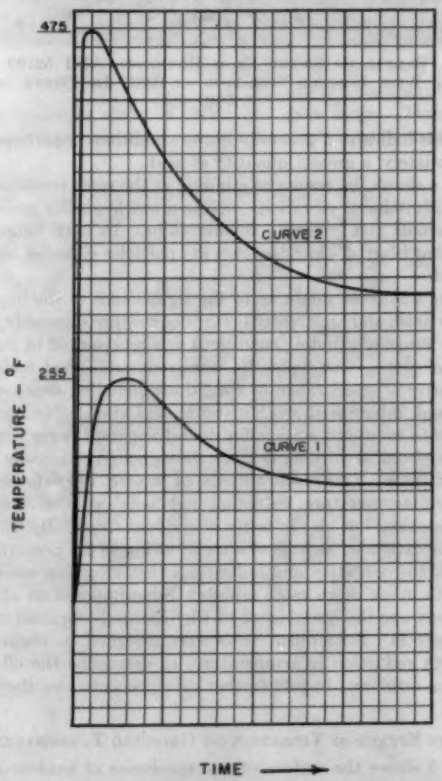


FIG. 7 OSCILLOSCOPE TRACES OF TEMPERATURE RISE IN GROUND SPECIMEN OF AISI 4340 STEEL HARDENED TO 55 $R_c$

(Curve 2 is for conventional grinding with end of thermocouple being 0.014 in. from surface after a 0.002-in-deep cut. Curve 1 was obtained on subsequent pass with work vibrated while removing 0.003 in. depth of material. Both tests were made at a table speed of 22 fpm.)

used to intercept the stream of grinding swarf. The curvature of the underside of the test specimens was determined before and after grinding, so that the change in curvature could be used as a measure of the residual stress.

It was noted that the input power was appreciably less when vibration was used. Similarly the watch-glass test indicated lower temperatures during vibration. Analysis of the curvature change gave the following results for curvature in the direction of wheel velocity:

$$\text{Conventional} = 38 \times 10^{-4}$$
$$\text{Vibrated} = 26 \times 10^{-4}$$

Another group of tests also gave good indications of difference in residual stress. This group was run for the purpose of comparing the effect of vibration on a resinoid wheel with that obtained for a vitreous-bonded wheel. For this purpose two 52100 full-hard specimens were ground at a work speed of 20 fpm, cross-feed of 0.050 in., depth of cut of 0.002 in., since these same conditions had been used previously with the J-grade vitrified wheel. A Carborundum A60-T3-BT wheel was used. It was intended to

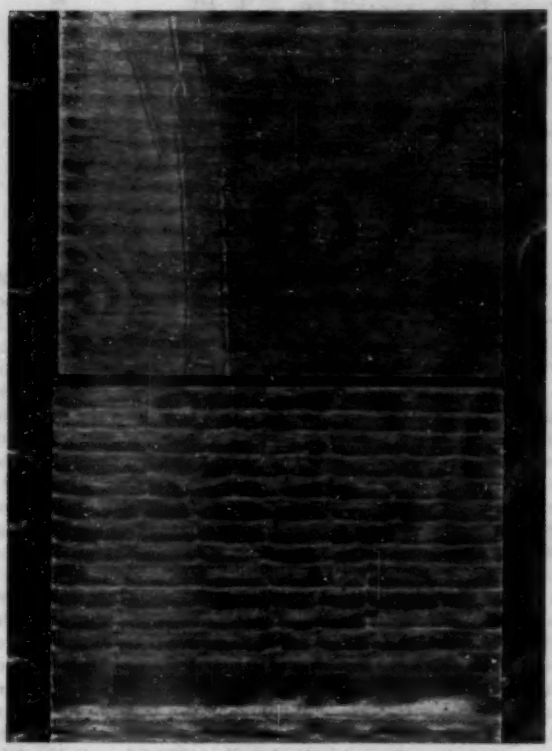

FIG. 8 BOTH SPECIMENS GROUND WITH RESIN-BONDED WHEEL

(Badly cracked specimen at bottom was ground without vibration. Specimen at top ground with induced vibration produced residual stresses low enough to permit necking in full-hard AISI 52100 steel. Both specimens ground with a hard-grade resinoid-bonded wheel to accentuate "burning" conditions.)

precut five passes, followed by five test passes, as was done with the vitreous wheel. However, the test specimen was so badly cracked and overheated after just two passes by conventional grinding that the test was stopped. For this reason the subsequent vibration test also was limited to two passes. The resulting specimens are shown in Fig. 8. The specimen at the bottom was ground conventionally while the one at the top was ground with vibration. It will be observed that the conventionally ground specimen was so severely stressed that cracks occurred in all directions. Some of these cracks penetrate more than $^1/_{16}$ in. below the surface.

The specimen ground with vibration shows three cracks completely across the surface and a fourth one approximately one-half way across. Only two of these cracks were evident immediately after grinding and, at that time, they had extended from one edge about a third of the way across the surface. Within 12 hr the rest of the cracks developed. These surfaces were studied under the microscope and it was noted that there was considerable localized "necking" in the vicinity of the cracks on the vibrated specimen. This is a rare occurrence since it is generally believed that fully hard steel will not undergo any elongation or reduction of area prior to fracture. It is a coincidence that the level of residual stress was such that some creeping and relaxation could take place. It is obvious that the level of stress in the vibrated specimen was considerably less than in the one ground conventionally. Further, it is obvious that vibration is effective with resin-bonded wheels as well as with vitrified wheels.

In all previous tests in evaluating the effects of vibration, the workpiece was mounted on top of the transducer and vibrated radially to the grinding wheel. The question arose as to whether the vibration would be similarly effective if the workpiece were vibrated across the face of the wheel. Consequently, the transducer was mounted on an angle plate so that grinding could be performed on what would otherwise be the side of the specimen. Vibration did improve the surface finish as in previous tests. However, it was demonstrated that the workpiece literally vibrates in all directions and further that the vibration energy is reflected from the various surfaces of the test specimen. In other words the "side" of the workpiece showed the same manifestations of vibration as did the top in the other orientation of the transducer. Tentatively, it may be assumed that a similar attempt to vibrate the work specimen parallel to the direction of grinding would yield similar results.

Two $^1/_8 \times {}^1/_8 \times {}^5/_8$-in. tips of Carboloy 78B tungsten carbide were brazed to the top of cold-rolled steel supports. The two carbide specimens were ground with a Carborundum DA60-J9-V20 wheel at a depth of 0.002 in. The one specimen ground conventionally developed many hairline cracks across the grinding direction. The specimen ground with vibration developed no cracks. This result raised the question as to whether the cracks in the one specimen might not have been caused by brazing; consequently, the two specimens were ground a second time using vibration on the specimen that had been cracked with the result that the cracks were removed by grinding. The use of conventional grinding on the other specimen that did not show any cracks in the first grind once more produced many cracks. It is well known that thermal cracks constitute a widespread problem in the sharpening of carbide tools in industry even where silicon-carbide and diamond wheels are used. Aluminum-oxide wheels are never recommended for this purpose; yet the use of vibration permitted the use of aluminum oxide for grinding the tungsten-carbide tips without producing thermal cracks.

### EFFECT OF VIBRATION ON GRINDING RATIO

Most of the test results reported up to this time involve relatively little metal removal and the grinding wheels were dressed with a diamond prior to each test so that the wheels did not reach equilibrium during these tests. In any event, the grinding ratio was determined for a number of them by chemical analysis of the samples of swarf. These results varied from a higher grinding ratio for vibration compared to conventional grinding to substantially less than that obtained for conventional grinding. However, it appeared generally true that vibration caused more wheel breakdown than conventional grinding.

One series of tests was devoted entirely to a study of the effects of vibration on grinding ratio. The results of this series are recorded in Table 2. Two specimens of hardened 52100 steel were ground, one conventionally and one vibrated. Fifty-eight test passes were made on each specimen. Four samples of swarf were collected in each case. The first sample involved only one pass across the work. The second sample consisted of the next two passes, the third sample included the next five passes, and the fourth sample included the next 50 passes. All eight samples were analyzed by chemical tests after reducing the oxides in a hydrogen atmosphere. It will be noted that the grinding ratio as shown in the third column of Table 2 increased from 5.8 to 39.8 in the successive samples obtained for conventional grinding. Similarly, the ratio varied from 2.18 to 24.35 for the vibrated specimen. It is probable that the two higher figures in each series are the most representative; that is, the grinding ratio for conventional grinding was approximately 40 as compared to approximately 25 for the vibrated specimen.

TABLE 2 GRINDING-RATIO STUDY

| Test code | No. of passes in sample | Grinding ratio = volume of metal / volume of abrasive |
|---|---|---|
| JAk1C | 1 | 5.80 |
| JAk2C | 2 | 10.51 |
| JAk3C | 5 | 13.63 |
| JAk4C | 50 | 39.80 |
| JAk1V | 1 | 2.18 |
| JAk2V | 2 | 3.24 |
| JAk3V | 5 | 10.68 |
| JAk4V | 50 | 24.35 |

## Theoretical Aspects

Laboratory tests demonstrate without question that vibrations at ultrasonic frequencies during grinding affect the temperatures, the residual stress, the roughness of the ground surface, and the effective condition of the grinding wheel. These things having been observed, it appears there should be some theoretical basis for predicting such results.

*Geometry of Grinding.* First, let us consider the geometry of a grinding cut. C. T. Yang and M. C. Shaw[2] have reported the following equations expressing the theoretical length and thickness, respectively, of the chip taken by an abrasive grain during grinding

$$l = \sqrt{D\,d}\ \text{in} \quad [1]$$

where $D$ = wheel diameter, in. and $d$ = depth of cut, in.

$$t = \sqrt{\frac{4v}{VCr}}\sqrt{\frac{d}{D}}\ \text{in} \quad [2]$$

where

$D$ = wheel diameter, in.
$d$ = depth of cut, in.
$v$ = work speed, fpm
$V$ = wheel speed, fpm
$C$ = number of abrasive grains per sq in. of wheel surface
$r$ = ratio of width to depth of grinding scratch

The significance of these quantities is given in Fig. 9(*a*) showing the theoretical proportions of a grinding cut without vibration. Calculations using these equations are given in Tables 3 and 4.

Table 3 contains values of the theoretical length of arc of contact for depths of cut ranging from 0.0002 to 0.008 in. For example, the length of contact is 0.049 in. for the 0.0002-in. depth of cut and 0.310 in. for the 0.008-in. depth of cut at the other extreme. The third column of Table 3 gives the time of contact of the abrasive grain during its traverse of the contact surface based on a wheel speed of 6000 fpm. The times are given in microseconds or 0.000001 sec. It will be noted that the times vary from 41 up to 258 microsec for the range of depth of cut given in Table 3.

TABLE 3 THEORETICAL LENGTH OF CONTACT, $l$

(Between abrasive wheel and work)

| Depth of cut, $d$, in. | Length of contact, $l$, in. | Time of contact, microseconds |
|---|---|---|
| 0.0002 | 0.049 | 41 |
| 0.0005 | 0.077 | 64 |
| 0.0010 | 0.109 | 91 |
| 0.0020 | 0.154 | 128 |
| 0.0040 | 0.219 | 182 |
| 0.0080 | 0.310 | 258 |

Length of contact $l = \sqrt{D\,d}$
Wheel diameter $D$ = 12 in.

TABLE 4 THEORETICAL THICKNESS OF CHIP, $t$

(Depth of cut = 0.0005 in.)

| Work speed, fpm | Chip thickness, microinches: Parallel to work speed[a] | Minimum[b] | Probable[c] |
|---|---|---|---|
| 20 | 62 | 0.9 | 55 |
| 40 | 124 | 1.7 | 82 |
| 60 | 186 | 2.5 | 96 |
| 80 | 248 | 3.4 | 110 |

[a] $t = v/V\sqrt{C}$

[b] $t = 2v\sqrt{d}/V\sqrt{DC}$

[c] $t = 2\sqrt{v\sqrt{d}/\sqrt{VCr}\sqrt{D}}$

where

$V$ = wheel speed, ips = 1200
$v$ = work speed, ips
$d$ = depth of cut, in. = 0.0005
$D$ = wheel diameter, in. = 12
$C$ = grain/sq in. = 3000
$r$ = ratio of mean width to depth of scratch = 10

The values in Table 4 are theoretical chip thicknesses which occur at table speeds from 20 to 80 fpm, a typical range for surface grinding. The figures in the second column are values of $X$ as shown in Fig. 9(*a*). These are given in microinches and might be considered to represent an approximate upper limit for the thickness of chip. The third column contains a set of numbers designated as the minimum thickness of chip based on the improbable situation wherein all of the abrasive grains are lined up one behind the other in the direction of cutting velocity. The last column designates a probable thickness based on Equation [2]. It shows a range from 55 to 110 microinches for the work-speed range of 20 to 80 fpm. The two facts that appear to be most significant in Tables 3 and 4 are the very short time of contact and the unusually small thickness of chip.

Initially it was believed that change in direction of an abrasive grain relative to its unvibrated path might be responsible for the effectiveness of vibration since it was theorized that a change of direction could either prevent the formation of built-up edge or more readily remove it. This appears unlikely when one analyzes a vibration with a range of 0.001 in. at a frequency of 10 kc. Fig. 9(*b*) is a velocity diagram drawn to scale relative to the theoretical, unvibrated path. It indicates that the velocity of the lateral or vibratory motion does not exceed $^1/_{40}$ that of the wheel speed. A similar diagram could be drawn to scale for the displacement; however, this would show even less deviation than the velocity diagram of Fig. 9(*b*), when it is recalled that the displacement is multiplied by the angular frequency to obtain the velocity.

An exaggerated path diagram is plotted in Fig. 9(*c*), where the lateral motion due to vibration is greatly expanded in relation to the movement along the path of contact. It will be recalled from Table 4 that the maximum chip thickness at a depth of cut of 0.008 in. would be only 110 microinches or approximately 0.0001 in. Consequently, if the work being ground is actually vibrated over

[2] "The Grinding of Titanium Alloys," by C. T. Yang and M. C. Shaw, Trans. ASME, vol. 77, 1955, pp. 645–660.

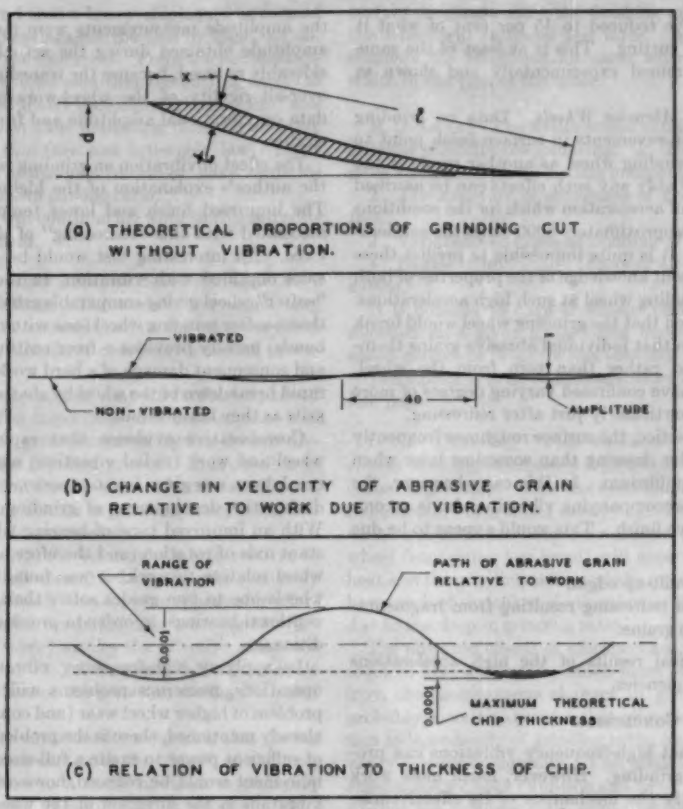


FIG. 9 GEOMETRICAL RELATIONSHIPS IN GRINDING
(Vibrations assumed to be 10 kc with a range of 0.001 in.)

a range of 0.001 in. relative to the grinding wheel, then it simulates a condition wherein the abrasive grain dips down toward the work, cuts for a short distance, and then leaves the workpiece entirely.

Consider what this behavior would mean with a depth of cut of 0.008 in. at the grinding conditions represented in Table 4. It will be recalled from Table 3 that this depth of cut would cause an abrasive grain to be in contact with the workpiece 258 microsec during steady-state or nonvibrated grinding. The period of a half-cycle at a frequency of 10 kc is 50 microsec. Thus, at the conditions represented in Fig. 9(*c*), a single "dip" would involve appreciably less than 50 microsec. Assuming that an abrasive grain had made one such dip it would then start another just 100 microsec after beginning the first one, and so on, so that as many as three such dips could be made in a single traverse at a depth of cut of 0.008 in.

Two other characteristics of the conditions just described serve to explain the observed reductions of temperature. First, it will be noted that the abrasive grain cuts for approximately 20 microsec at the 0.008 in. depth, during a single dip, then leaves the work for the remaining 80 microsec of a given cycle before beginning the next dip. Thus, even at this extreme depth of cut, the workpiece has a period of time to cool off. This period is four times as long as the interval during which heating took place. With conventional grinding the work would be exposed to the high temperature continually during the traverse of an abrasive grain.

The other significant characteristic is the fact that an abrasive grain in making successive passes across the contact surface would achieve randomness in the thickness of chip it would remove. This thickness would vary from zero to at least twice that indicated in Fig. 9(*c*). Consequently, the amount of energy required to cut a given volume of metal would be reduced. The temperature level would drop as a result of the reduction in the total amount of heat released. Wattmeter records appear to confirm this conclusion although part of the observed reduction in power requirements could have been brought about by increased average sharpness of the abrasive grains.

Professor Shaw[3] also reports Equation [3] as representing the peak temperature in grinding. This is presumed to apply for steady-state conditions within a moving heat source. Consequently, it makes no specific provisions for time-dependent variations within

$$\theta_m = \sqrt{\frac{\pi}{4}} \sqrt{\frac{Vl}{k_3 P_3 c_3}} \left(\frac{u_f}{J}\right) \left(\frac{rl^2}{A}\right) + \theta_0 \quad \ldots\ldots [3]$$

where

$k_3$ = thermal conductivity of abrasive
$p_3c_3$ = volume specific heat of abrasive
$u_f$ = friction energy unit volume of metal cut, pci
$A$ = area of contact between chip and abrasive grain, sq in.
$\theta_0$ = ambient temperature of abrasive

the source itself. However, it is to be noted that the peak temperature increases as the square root of the length of contact. Thus, if the time value of the dip, shown in Fig. 9(*c*), is compared as a length of contact with that of a complete cycle, then

peak temperature would be reduced to 45 per cent of what it would be for steady-state cutting. This is at least of the same magnitude as that determined experimentally and shown in Fig. 7.

*Effect of Vibrations on Abrasive Wheels.* Data on grinding ratio plus the observed improvements in surface finish point to altered condition of the grinding wheel as another result of the ultrasonic vibration. Probably any such effects can be ascribed directly to the magnitude of acceleration which for the conditions of most of these tests was approximately 5000 times the acceleration of gravity or 5000 $g$. It is quite impossible to predict these results quantitatively without knowledge of the properties of both the work material and grinding wheel at such high accelerations. It is not entirely unexpected that the grinding wheel would break down more rapidly or even that individual abrasive grains themselves might be fractured rather than torn from the wheel. Studies of grinding ratio have confirmed varying degrees of more rapid wheel breakdown, particularly just after redressing.

In ordinary grinding practice, the surface roughness frequently is greater immediately after dressing than sometime later when the wheel has reached equilibrium. In this case, however, the greater wheel breakdown accompanying vibration also is accompanied by improved surface finish. This would appear to be due to two things:

1 Fewer and smaller built-up edges.

2 Continuous, uniform redressing resulting from fragmentation of individual abrasive grains.

Both of these are logical results of the high accelerations achieved at ultrasonic frequencies.

## Conclusion

There is little doubt that high-frequency vibrations can produce desirable results in grinding. However, much more work needs to be done to clarify the mechanism of its effectiveness. Considerably more than that needs to be done to learn how to apply it to industrial grinding. It is fascinating to consider that, even now, we may be deriving the benefits of ultrasonic vibrations in industrial grinding without knowing it.

## Acknowledgment

The author gratefully acknowledges the financial support, cooperation, and encouragement given this investigation by The Carborundum Company, Niagara Falls, N. Y.

# Discussion

W. R. Backer[3] and Hans Ernst.[4] This paper presents some interesting data on the utility of controlled vibration in the metal-cutting process. Several of the reported effects of vibration on the grinding operation, such as the improved finish and reduced workpiece damage due to heating, lend positive support to commercial application of this principle. Others, including more rapid wheel wear and the technical difficulties of inducing the vibrations, in controlled direction and at useful energy levels, may detract from the value of its commercial use.

The test results presented are of a survey nature, and it is hoped that further work is in progress. The tests on surface finish show little advantage on 1020 steel compared to the harder materials. The question arises as to whether the process is significantly advantageous on softer workpieces. There is also a question on the vibrational amplitude obtained in the tests. If the amplitude measurements were made prior to grinding, the amplitude obtained during the actual cut may have been considerably reduced, because the transducer then had to oppose the over-all rigidity of the wheel-work-machine system. Further data on vibrational amplitude and frequency effects are also desirable.

The effect of vibration on grinding ratio is very interesting, and the author's explanation of the higher wheel wear is plausible. The improved finish and lower temperatures may likewise be associated with this "redressing" of the wheel by the vibratory force. An interesting test would be the comparison of the results obtained with vibration, to those when grinding with a "softer" wheel giving comparable grinding ratio. It is well known that a softer grinding wheel (one with more friable grits or weaker bonds) usually provides a freer cutting action, with less heating and consequent damage of a hard workpiece, because of the more rapid breakdown of the wheel by shattering or breaking out of the grits as they become dull.

Corroborative evidence that rapid radial motion between wheel and work (radial vibration) may cause more rapid wheel breakdown was given by an experience in the writer's laboratories during the development of grinding-machine spindle bearings. With an improved type of bearing which provided a more constant axis of rotation (and therefore a more constant position of wheel relative to work) it was found necessary to use grinding wheels one to two grades softer than previously used with conventional bearings, in order to provide comparable grinding conditions.

In applying high-frequency vibration to practical grinding operations, numerous problems will arise. In addition to the problem of higher wheel wear (and consequent higher wheel costs) already mentioned, there is the problem of providing a transducer of sufficient power to excite a full-sized workpiece; the power requirement would be reduced, however, if further tests show that vibration in the direction of the wheel axis is equally effective. The vibration frequency must be considerably higher than the resonant frequency of any significant elastic system in the machine, to prevent marring the workpiece. Preferably, it should be above the sonic range (say, about 20,000 cycles per sec) in order to avoid objectionable noise.

On the positive side, corroborative evidence that high-frequency vibration may advantageously affect a metal-cutting process is given by our experience some years ago with vibration applied to other forms of metal-cutting tools. In a series of experiments in 1934, in which a longitudinal vibration with a frequency of 1500 cps and amplitude of about 0.005 in. was applied to a

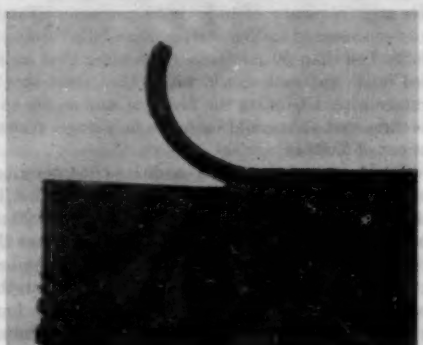

Fig. 10 Chip Formed by Manual Pressure of Workpiece Against Vibrating Cutting Tool

(Material: Hard bronze; width of cut, 1/2 in.; depth of cut, 0.040 in.; cutting ratio, 1.0.)

[3] Senior Research Engineer, The Cincinnati Milling Machine Company, Cincinnati, Ohio. Assoc. Mem. ASME.

[4] Director of Research, The Cincinnati Milling Machine Company, Cincinnati, Ohio. Fellow ASME.

planer-type tool, it was found that a heavy chip could be formed by merely pressing a workpiece against the tool by hand, an obvious impossibility without the vibration. From the accompanying illustration, Fig. 10, it will be seen that the cutting ratio (as shown by the chip-length ratio and the chip-thickness ratio) was approximately equal to unity, thus indicating that the effective friction between chip and tool face was extremely low. Later studies with vibrations at ultrasonic frequency have similarly shown an appreciable increase in cutting ratio.

We hope that the author will continue his work in this interesting and potentially useful field.

R. S. Hahn.[8] The author has certainly discovered some very interesting and important effects. The work of the author may have industrial application on one hand, and on the other may help in understanding the basic details of every-day grinding operations.

The results obtained by the author may be further explained by focusing attention on the important part the clearance surface (i.e., the surface on the grits generated by the dresser diamond) of the grit plays in the grinding process. It is possible to explain the soft or hard action for the vibrated and nonvibrated conditions, and the attendant change in grinding ratio, burn, and finish on happenings at the clearance surface.

The author shows in Fig. 9(*b*) the velocity of a grit relative to the work. Although the actual normal velocity may be relatively small, on the "going into the work" stroke very appreciable effective negative clearance angles occur (in this case $\tan^{-1} 1/_{20}$). On the "going out of the work" stroke the effective clearance angles are naturally positive; i.e., during one half of the cycle there is interference on the heel of the grits and during the other half there is clearance.

The action observed can be explained by supposing that during the in-stroke when interference occurs on the "heel" of the grit, the heel spalls or flakes off either as a result of stress or of highly localized temperature, or both. It is known that wheel wear during certain precision-grinding operations often amounts to something around 0.001 in. Thus whole grits cannot be tearing loose. The writer has also observed[6] that wheels dressed at a small diamond lead actually become "sharper" as they are used after dressing. This again suggests a breaking down of the heel of the grits, thus relieving the interference.

As a result of the foregoing it is natural to expect the grinding ratio to be lower (i.e., more wheel wear and a softer action). Furthermore, since the dimension of the rubbing area of the grit in the direction of motion will be reduced by spalling off of the heel, the temperature developed will be less according to the moving source theory.[7]

The tests described by the author were performed on a surface grinder where it is conventional to prescribe a certain down feed (wheel depth of cut) and then to take passes of the table simultaneously with increments of cross-feed. Under these conditions heavy forces are induced near the leading edge of the wheel with lesser ones near the trailing edge. If the wheel is free-cutting by virtue of a comparatively small amount of interference on the heel of the grits, the nonlinear distribution of induced force across the wheel width will differ from the distribution for a hard acting wheel or under nonvibrating conditions. The surface roughness is likely to depend on these force distributions. In the case of a free cutting action (soft) it seems reasonable to expect a lower surface roughness since the finishing grits at the trailing side of the wheel will be under less force. It would be interesting to compare the roughness for cases where the wheel cuts its full width in one pass of the table.

R. O. Lane.[8] The writer would caution future investigators to consider carefully the following: 1 The different types of abrasives available from all leading companies.

2 The structure or structures of grinding wheels used in the test.

3 Variations in types of bonding of the abrasive particles.

4 Degree of uniformity of any or all wheels used in all investigation.

It is possible to have erroneous results from improper wheel selection on a given metal being investigated in lieu of the so-called correct or proper wheel selected.

The author is to be complimented on the presentation of a very fine paper.

L. P. Tarasov.[9] This excellent pioneering study shows clearly that high-frequency vibrations can reduce the heat generated in grinding. This has been found to be accompanied by a reduction in the grinding ratio, which is the same as an increase in wheel wear. It has long been known that a change to a softer wheel (containing less bond) will generally also reduce both the heat and the grinding ratio, and the question naturally arises as to how much of the effect of vibration on the generation of heat was due to the drop in grinding ratio.

The observed effects of vibration are very pronounced with respect to heat generation, much more so than might be expected from the simultaneous changes in grinding ratio. Hence it is probably correct to assume that vibration can affect heat generation independently of grinding ratio, but it would be desirable to verify this experimentally. This could be done by repeating the experiment without vibration and using a sufficiently softer wheel so that the grinding ratio would be the same as for the harder wheel used with vibration. A comparison of heat effects would then show the direct effect of vibration.

The entirely different appearance of the cracks in the two specimens in Fig. 8 of the paper shows that there was some difference in the effect of grinding, with and without vibration, but it is doubtful that this can be ascribed to vibration on the basis of the evidence presented. Practically nothing is known about the detailed mechanism of formation of such cracks, but both crack patterns shown are typical of those often seen in nonvibrated badly cracked specimens. Only a few cracks are present in the upper or vibrated specimen but they are much wider than those in the other one. The crack width is some measure of the stress that was relieved elsewhere in the surface when the crack was formed. Just as much stress may have been relieved by the formation of the very few wide cracks in the upper piece as by the numerous narrow cracks in the lower one, and no light is thrown on the relative magnitude of the stresses prior to cracking. Hence no conclusions can rightfully be drawn from a comparison of these two crack patterns other than that the stresses were in some way different. The crack width, for example, might be determined by the nature of the stress gradient perpendicular to the surface, but this is only a speculation. A far more detailed understanding of the relationships between surface cracks and stresses will be necessary before the former can be used even as rough measuring sticks for the latter.

It might also be mentioned that the observed necking or plastic flow is not surprising in view of the marked softening of the steel

[8] Research Engineer, Heald Machine Company, Worcester, Mass. Mem. ASME.

[6] "The Effect of Wheel-Work Conformity in Precision Grinding," by R. S. Hahn, Trans. ASME, vol. 77, 1955, pp. 1325–1329, Fig. 5.

[7] "The Relation Between Grinding Conditions and Thermal Damage in the Workpiece," by R. S. Hahn, published in this issue, pp. 807–812.

[8] Vice-President, Macklin Company, Jackson, Mich.

[9] Metallurgical Engineer, Research and Development Department, Norton Company, Worcester, Mass. Mem. ASME.

to a depth of several thousandths of an inch, as judged from the severity of the burn pattern. The deformation occurred in steel that may easily have been softened to Rockwell C50.

The writer would like to suggest that a simple way of determining relative heat effects such as are of interest here is to measure the depth of grinding burn; i.e., the depth to which overtempering caused by grinding heat can be detected in hardened steel after suitable sectioning and etching. It is just as quantitative as the thermocouple method, which measures the average temperature in a layer located a considerable distance below the ground surface.

### Author's Closure

Thanks are due to all those who have contributed discussions of this paper. Their contributions represent serious thought, and the many suggestions are definitely useful in interpreting observations whose causes are not yet clearly defined. The closure will take up the several questions in the order that they were raised by the discussers.

First the comments by Mr. Backer and Mr. Ernst. It should be emphasized that this paper was not in any sense intended to promote commercial application of high-frequency vibrations in industrial grinding, although some applications would seem to be feasible. Instead, it was believed that the observations made in this study help to explain many of the phenomena well known to precision-grinder operators under the general heading of "grinding by ear." The author agrees with the discussers that attempts at commercial application where such vibrations do not occur naturally to significant extent will be met with complex problems of both a technical and economic nature. Such problems might very well prevent practical use in some areas.

It was pointed out by Mr. Backer that there might have been a substantial attenuation of amplitude of vibration during actual cutting. The amplitude of the work was not monitored during these tests, but it is doubtful that there was any significant attenuation since it will be recalled that the accelerations were of the magnitude of 5000 "g's," or in other words, 5000 times the acceleration of gravity. Consequently, the forces developed by the transducer are also very large, about 500 lb in this case, so it would not be expected that grinding forces, which are also relatively low, would have any appreciable effect. Rather, it is to be expected that power limitations would assert themselves before any difficulties from limited force capacity would arise. Even so, there could be rather little power demand from the transducer in the grinding area except where there was a large coefficient of friction to convert this energy into heat. The earlier investigation reported by the discussers as illustrated in Fig. 10 would appear to confirm the assumption that the amplitude would not be attenuated appreciably by the act of grinding.

Attention also was called to the fact that softer wheels break down more rapidly, resulting in a sharper average condition for the abrasive, and that this can be expected to reduce cutting temperatures. That observation is also most certainly true and it is difficult to say as to how much the temperature reduction observed in this test was due to sharper abrasive and how much was due to shorter exposure to the peak temperature created where vibration was superimposed.

Mr. Backer referred to the difficulties that may be encountered in attempted commercial application of high-frequency vibrations to grinding. Certainly the number and complexity of problems will increase with the complexity of the grinding operation. It can be expected that considerable development effort will be required before extensive use can be made, if at all. Despite the magnitude of the development problems, it is believed that commercial application to such operations as the grinding of carbide tools can be made almost immediately with little development effort. Other and more complex operations may come in due time.

Dr. Hahn has called attention to what might prove to be a very important aspect of this problem. He points out that the relative motion between the work and the wheel caused by the vibration creates interference on the approach between the work and the heel or flank of the abrasive grain since diamond dressing is known to produce substantial areas of zero relief. It is quite possible that this interference, coupled with the high accelerations, does remove such interfering material, thus accomplishing two desirable effects; one, a resharpening of the abrasive grain, and the other, a reduction in the amount of rubbing and associated heating.

Mr. Lane reminds us that this investigation covered a very limited range of bonded abrasive properties and grinding conditions. This fact leaves doubt as to the extent to which high-frequency vibrations would bring about desirable results over the broad ranges of these variables. It can be expected that such investigations as are desired for commercial purposes will eventually be made, and one would expect further clarification of the mechanism from tests conducted at substantially different conditions.

The author was pleased to learn that Dr. Tarasov has arrived at substantially the same conclusion—that vibration does have an independent effect in reducing the temperature, but, as he pointed out, this conclusion can be further confirmed by tests with softer wheels which will give about the same grinding ratio as a harder wheel with superimposed vibration.

It is regrettable that the photographs of the cracked specimens as shown in Fig. 8 are poor. Dr. Tarasov got the impression that the cracks in the vibrated specimen were much wider than in the nonvibrated specimen. As a matter of fact, the exact opposite is true, and what appears to be a wide crack in the upper half of Fig. 8 is in reality a shadow created by angular lighting and noticeable localized necking or plastic flow in the vicinity of the crack. It is the belief of the author that it was a coincidence that the residual stress level in the vibrated specimen was almost identically that of the yield or fracture stress of this material. A somewhat higher stress level presumably would not have resulted in sufficient time for a substantial amount of plastic yielding to take place. The author believes that this interpretation is confirmed by the fact that the cracks in the nonvibrated specimen occurred almost instantly during grinding, whereas none of the cracks in the vibrated specimen showed up until quite some time later; there was one small short crack within an hour and the rest of the cracks developed within the next 24 hours. The author wishes to thank Dr. Tarasov for his helpful suggestions as to additional techniques which can be used to refine the information that can be obtained from an investigation of this type.

# The Role of Chip Thickness in Grinding

By G. S. REICHENBACH,[1] J. E. MAYER,[2] S. KALPAKCIOGLU,[3] AND M. C. SHAW[4]

**Grinding chips are classified into five types depending upon their relative thickness-to-length ratio and equations are derived for computing the length or thickness of chips of all types for external, surface, internal, and plunge-grinding operations. Representative experimental grinding data are presented and discussed to illustrate the use of the equations and to emphasize the importance of chip thickness as a grinding parameter. The force on a single grain is derived and the result applied to explain relative wheel hardness.**

## Nomenclature

The following nomenclature is used in the paper:

$v$ = work speed, fpm { + if opposite direction to $V$ ; − if same direction as $V$ }

$V$ = wheel speed, fpm

$l$ = undeformed chip length, in.

$D$ = wheel diameter, in.

$D_w$ = work diameter, in. { + for external grinding ; ∞ for surface grinding ; − for internal grinding }

$D_t$ = diameter of trochoidal path cut by abrasive grain

$t$ = undeformed chip thickness, in.

$d$ = wheel depth of cut, in.

$i$ = infeed per pass or revolution, ipr

$C$ = mean number of cutting points per sq in.

$r$ = ratio of mean chip width to chip thickness

$m$ = distance between successive grains on wheel surface, in.

$p$ = pitch on workpiece = $\frac{2v}{VCrt}$ for all cases

$f$ = infeed rate in plunge grinding

$B$ = nondimensional group = $\frac{2v}{VCrd\sqrt{Dd}}$

$K$ = quantity that varies between 1 and 2, depending on value of $v/V$

$K_0, K_1, K_2, K_3, \ldots$ = constants

$n$ = exponential coefficient

$b$ = work width, in.

$b'$ = mean width of groove cut by single grit, in.

$F_p$ = tangential force on wheel, lb

$F_Q$ = radial force on wheel, lb

$F_g$ = tangential force on individual grain, lb

$F_r$ = relative grain force, sq in.

$\Delta$ = curvature difference = $\frac{2}{D} - \frac{2}{D_t}$, $(\text{in.})^{-1}$

$\theta_1, \theta_2$ = small angles subtended at center of wheel and work, respectively, by undeformed chip length ($l$)

$R$ = rate of metal removal, $\text{in.}^3$ per min

$h$ = mean height of imperfection left behind upon ground surface, in.

*Additional Equations*

Value of $B$ for case I: $B_I = \frac{0.018}{\sqrt{1 + D/D_w}}$ (5% discrepancy)

Value of $B$ for $t/d = 1$: $B_{III} = \frac{1}{\sqrt{1 + D/D_w}}$

Value of $B$ for $p = l$ (case IV): $B_{IV} = \frac{2\left(1 + \frac{v}{V}\right)}{\sqrt{1 + D/D_w}} = 2\left(1 + \frac{v}{V}\right) B_{III}$

Per cent difference between $D_t$ and $D = \frac{2v}{V}(1 + D/D_w) \times 100$

Force per grain = $F_g = 2ul^2r$

Relative grain force = $F_r = \frac{v}{VC}\sqrt{\frac{d}{D}(1 + D/D_w)}$

## Introduction

While it has long been known that the thickness of the individual chips that are produced in a grinding operation is an important variable (see later section for historical survey) it was not until relatively recently (1, 2, 3)[5] that the significance of this variable with regard to grinding energy and surface temperatures was demonstrated.

In reference (1) a dynamometer for measuring separately the radial and tangential grinding-force components was described and representative results for surface grinding presented. Simpler, more sensitive, and more rugged instrumentation for measuring grinding forces subsequently have been built for reciprocating and rotary surface grinding as well as for internal grinding and plunge grinding with abrasive belts. A representative surface-grinding dynamometer of recent design has been described (4).

In the second paper (2) the specific energy or energy consumed per unit volume of metal removed in grinding ($u$) was found to be an important quantity which is defined as follows

$$u = \frac{VF_p}{vbd} \quad [1]$$

where

$V$ = wheel speed

$v$ = work speed

[1] Instructor in Mechanical Engineering, Massachusetts Institute of Technology, Cambridge, Mass. Assoc. Mem. ASME.

[2] Private, U. S. Army, 9111 TU-QMC Headquarters Res. and Dev. Command, Natick, Mass.

[3] Mechanical Engineer, Galata, Persembe Pazar, Zencefil Sokak 6, Istanbul, Turkey. Assoc. Mem. ASME.

[4] Professor of Mechanical Engineering, Massachusetts Institute of Technology, Cambridge, Mass. Mem. ASME.

Contributed by the Research Committee on Metal Processing and presented at the Diamond Jubilee Semi-Annual Meeting, Boston, Mass., June 19–23, 1955, of THE AMERICAN SOCIETY OF MECHANICAL ENGINEERS.

NOTE: Statements and opinions advanced in papers are to be understood as individual expressions of their authors and not those of the Society. Manuscript received at ASME Headquarters, March 24, 1955. Paper No. 55—SA-37.

[5] Numbers in parentheses refer to the Bibliography at the end of the paper.

$F_p$ = tangential component of force on grinding wheel
$b$ = width of cut
$d$ = wheel depth of cut

This quantity was found to be a strong function of the maximum undeformed chip thickness $t$, which for the surface-grinding experiments considered in reference (1 and 2) was found to be

$$t = \sqrt{\frac{4v}{VCr}}\sqrt{\frac{d}{D}} \quad \ldots\ldots [2]$$

where

$D$ = wheel diameter
$C$ = number of cutting points per square inch on face of wheel as determined from a soot track
$r$ = ratio of mean width of cut to depth of cut produced by an individual abrasive grain as determined from a taper section of a ground specimen

The relation between $u$ and $t$ for a reciprocating surface grinding operation is shown in Fig. 1. Here the specific energy is seen to rise rapidly with decrease in $t$ and then to remain constant with further decrease in $t$.

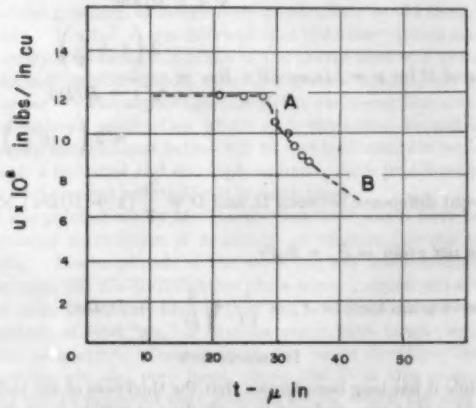


FIG. 1 VARIATION OF SPECIFIC GRINDING ENERGY ($u$) WITH MAXIMUM CHIP THICKNESS ($t$)—FROM REFERENCE (2)

In this paper the equations for chip length and chip thickness for internal and external grinding operations will be derived, and changes in the previous analysis that are necessary when $v/V$ becomes large or $d$ very small will be considered. These results will then be used to explain certain experimental grinding data.

## UNDEFORMED CHIP LENGTH

In Fig. 2($a$) is shown the surface-grinding case previously considered (2). In this instance the undeformed chip length $l_s$ was found to be

$$l_s = \sqrt{Dd} \quad \ldots\ldots [3]$$

Fig. 2($b$) is for external grinding (where $v \ll V$). If the work were stationary the arc of contact $l_s$ would be $OA$, but since the work also moves it will extend the additional distance $AB$. Hence

$$l_s = OA + AB \quad \ldots\ldots [4]$$

If $T$ is the time it takes the wheel to travel distance $OA$, then

$$OA = VT \quad \ldots\ldots [5]$$

and

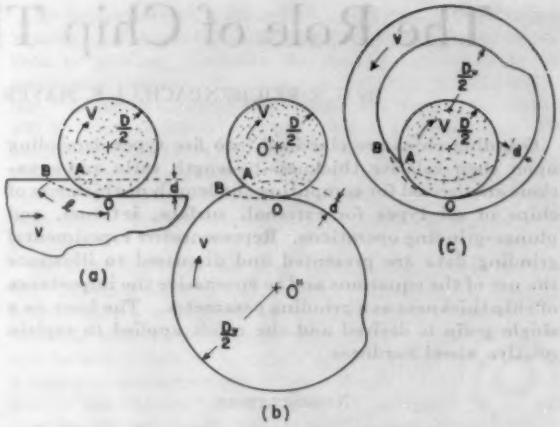


FIG. 2 CHIPS PRODUCED DURING ($a$) SURFACE GRINDING, ($b$) EXTERNAL GRINDING, AND ($c$) INTERNAL GRINDING OPERATIONS, WHEN $v \ll V$

$$AB = vT \quad \ldots\ldots [6]$$

thus eliminating $T$

$$AB = \frac{v}{V}(OA) \quad \ldots\ldots [7]$$

or, from Equations [4] and [7]

$$l_s = \left(1 + \frac{v}{V}\right) OA \quad \ldots\ldots [8]$$

Arc $OA$ is very nearly equal to the chordal distance $OA$ corresponding to a penetration of the two circles by an amount $d$. Neglecting second-order terms

$$OA = \sqrt{\frac{Dd}{1 + \frac{D}{Dw}}} \quad \ldots\ldots [9]$$

and hence for external grinding

$$l_e = \sqrt{\frac{Dd}{1 + \frac{D}{Dw}}}\left(1 + \frac{v}{V}\right) \quad \ldots\ldots [10]$$

Similarly, for internal grinding, Fig. 2($c$)

$$l_i = \sqrt{\frac{Dd}{1 - \frac{D}{Dw}}}\left(1 + \frac{v}{V}\right) \quad \ldots\ldots [11]$$

It is worth noting that a general expression can be written that holds for all types of peripheral grinding if certain conventions are adopted. This equation is

$$l = \sqrt{\frac{Dd}{1 + \frac{D}{Dw}}}\left(1 + \frac{v}{V}\right) \quad \ldots\ldots [12]$$

where

1 $Dw$ is negative for internal grinding
2 $Dw$ is infinite for surface grinding
3 $Dw$ is positive for external grinding
4 $v$ is positive for up grinding ($v$ and $V$ in opposite directions)
5 $v$ is negative for down grinding ($v$ and $V$ in same direction)

Of course $(v/V)$ may be neglected since in deriving this equation it was assumed $v << V$.

Equation [12] is for case (I) of Fig. 3 were distance $AB << OA$. In this instance chord $OA$ is given by Equation [9], and the value of $l$ by Equation [12]. The other cases of Fig. 3 are for progressing greater values of $v$ relative to $V$. If we consider the last case V where $AB > OA$ it is evident that chord $OA$ is twice as great as that for case I and hence for case V

$$l = OA + AB = 2\sqrt{\frac{Dd}{1 + D/Dw}}\left(1 + \frac{v}{V}\right) \quad [13]$$

This equation also holds for case IV, but for other intermediate cases the coefficient on the right side of the equation will be less than 2. In the general case which covers all conditions of Fig. 3

$$l = K\sqrt{\frac{Dd}{1 + D/Dw}}\left(1 + \frac{v}{V}\right) \quad [14]$$

where $K$ is a constant that varies from 1 (for case I where $AB << OA$) to 2 (for cases IV or V where $AB > OA$).

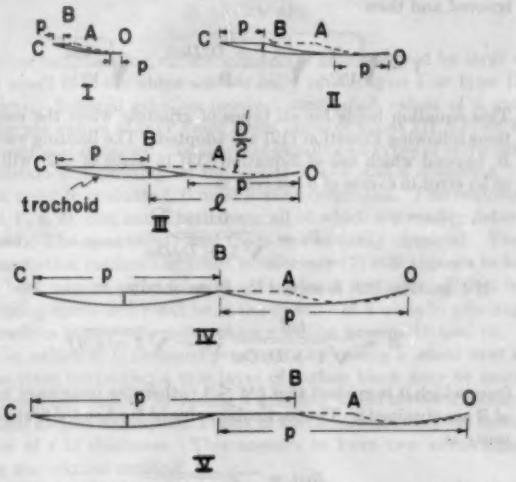


Fig. 3 Types of Chips Produced When Work Speed ($v$) Is Increased Progressively Relative to Wheel Speed ($v$)
(Quantity $p$ is distance work moves between passage of successive grains.)

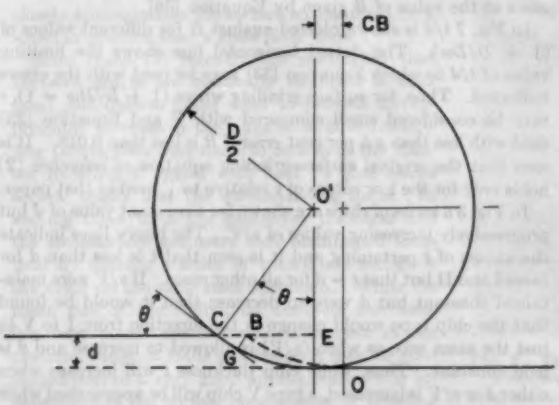


Fig. 4 Chip Thickness in Surface Grinding When $v \ll V$

Equation [14] is the most general expression for chip length $l$, and holds for chips of all size and for internal, external, or surface grinding if the conventions listed under Equation [12] are followed.

### Undeformed Chip Thickness

In deriving Equation [2] it was assumed that distance $CB$ was very small compared with distance $OB$ (i.e., $v \ll V$). For such a case, Fig. 4, the maximum chip thickness $t$ is

$$t = BG = CB \sin\theta \quad [15]$$

but

$$\sin\theta = \frac{CE}{\frac{D}{2}} \quad [16]$$

and

$$BE = (l - AB) \cong l \quad [17]$$

since $AB << l$.

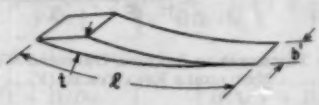


Fig. 5 Mean Shape of Chip Corresponding to Fig. 4

If there are $C$ cutting points per square inch on the wheel face and the average chip is as shown in Fig. 5, having a width $(b')$,[6] then the distance between successive cutting points on the wheel face is $1/(b'C)$. The corresponding distance on the work surface will be $v/V$ times this value and hence

$$p = CB = \frac{v}{Vb'C} \quad [18]$$

However, we may write

$$b' = r\frac{t}{2} \quad [19]$$

where, as previously mentioned, $r$ is the mean ratio of width to depth of cut, and $t$ is the maximum chip thickness.

Combining Equations [15] to [19], inclusive, we have

$$t^2 = \frac{4vl}{VCrD} \quad [20]$$

and substituting for $l$ (surface grinding) from Equation [12], noting that here $v << V$

$$t = \sqrt{\frac{4v}{VCr}}\sqrt{\frac{d}{D}} \quad [21]$$

If Equation [21] is applied to a case where $v$ is relatively large compared with $V$, it sometimes happens that the predicted value of $t$ exceeds $d$, which is unreasonable. The difficulty lies in the

[6] While actual chips will vary in width along their length rather than being of constant width $b'$, it is convenient that we choose for our model statistical chip one of constant width. This picture simplifies the calculations since triangular regions of metal are then not left behind on the surface to be removed by later grains. A treatment such as that presented here assumes that all chips are the same and the fact that there is really some variation from chip to chip is assumed to alter the results very little on a relative basis. The assumption that the mean chip is of constant width would appear to be consistent with adoption of a mean chip in the first place.

fact that in deriving Equation [21] certain assumptions were made which are not justified unless $v << V$. Fig. 6 shows a case for surface grinding where $CB$ is large as a result of $v$ being relatively large. The former method takes distance $BG$ as equal to $t$ which in this case is a poor approximation, being too large by the

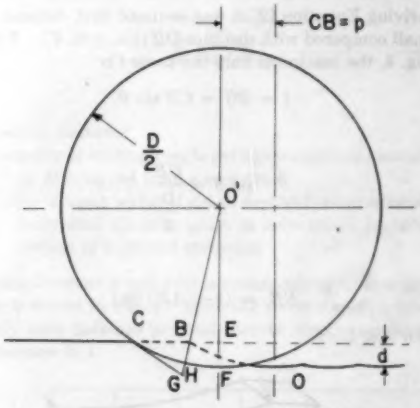


FIG. 6 CHIP THICKNESS IN SURFACE GRINDING WHEN (v) IS NOT NEGLIGIBLE RELATIVE TO (V)

amount $GH$. Even though the expression for $BH$ is more complex than that for $BG$, it must be used in finding $t$ in this case, and

$$t = BH = \frac{D}{2} - O'B \quad \ldots\ldots [22]$$

If distance $CB$ is represented by $p$ (for pitch) then

$$t = \frac{D}{2} - \sqrt{\overline{BE}^2 + \overline{E'O}^2} = \frac{D}{2} - \sqrt{(CE - p)^2 + \left(\frac{D}{2} - d\right)^2} \quad \ldots\ldots [23]$$

or, expanding the quantity under the radical

$$t = \frac{D}{2} - \frac{D}{2}\sqrt{1 + \frac{d^2 + (CE)^2 + p^2 - Dd - Z(CE)p}{\left(\frac{D}{2}\right)^2}} \quad \ldots [24]$$

$$= \frac{D}{2} - \frac{D}{2}\sqrt{1 + x} \quad \ldots\ldots [25]$$

Since $x$ is always small compared with unity we may expand the radical into a series ignoring higher-order terms

$$t = \frac{D}{2} - \frac{D}{2}\left(1 + \frac{x}{2} - \ldots\right) \quad \ldots\ldots [26]$$

or

$$t = \frac{Dd - (CE)^2 - d^2 + 2(CE)p - p^2}{D} \quad \ldots\ldots [27]$$

The quantity $d^2$ will be much smaller than the other terms in the numerator and since $(CE)^2$ is equal to $Dd$

$$t = \frac{2\sqrt{Dd}\,p - p^2}{D} \quad \ldots\ldots [28]$$

From Equations [18] and [19]

$$p = \frac{2v}{VCrt} \quad \ldots\ldots [29]$$

and therefore

$$\frac{t}{d} = \frac{2B}{t/d} - \frac{B^2}{(t/d)^2} \quad \ldots\ldots [30]$$

where

$$B = \frac{2v}{VCrd\sqrt{Dd}} \quad \ldots\ldots [31]$$

If $B << t/d$ (i.e., if $v << V$) the second term on the right side Equation [30] may be ignored and then Equation [30] reduces to Equation [21] for surface grinding.

The foregoing derivation may be extended to external and internal grinding by a similar although more tedious analysis. When this is done we obtain

$$\frac{t}{d} = \frac{2B}{\frac{t}{d}}\left(1 + \frac{D}{Dw}\right)^{1/2} - \frac{B^2}{(t/d)^2}\left(1 + \frac{D}{Dw}\right) \quad \ldots [32]$$

where $Dw$ has a positive sign for external grinding, a negative sign for internal grinding, and is infinite for surface grinding.

If $B << t/d$ or $v << V$ the last term of this equation may be ignored and then

$$t = \sqrt{\frac{4v}{VCr}}\sqrt{\frac{d(1 + D/Dw)}{D}} = \sqrt{\frac{4vd}{VCrl}} \quad \ldots\ldots [33]$$

This equation holds for all types of grinding when the conventions following Equation [12] are adopted. The limiting value of $B$, beyond which use of Equation [33] in place of [32] will lead to an error in excess of 5 per cent is

$$B_{\mathrm{I}} = \frac{0.019}{\sqrt{1 + D/Dw}} \quad \ldots\ldots [34]$$

If Equation [32] is solved for $B$ we obtain

$$B = \frac{t/d}{\sqrt{1 + D/Dw}}\left(1 - \sqrt{1 - t/d}\right) \quad \ldots\ldots [35]$$

from which it is evident that $t/d \leq 1$ (otherwise imaginary values of $B$ are obtained). The particular value of $B$ when $t/d$ first equals unity is

$$B_{\mathrm{III}} = \frac{1}{\sqrt{1 + D/Dw}} \quad \ldots\ldots [36]$$

It can be shown that when $t/d$ is plotted against $B$ for different values of $(1 + D/Dw)$, $t/d$ reaches the limit with zero slope in all cases at the value of $B$ given by Equation [36].

In Fig. 7 $t/d$ is shown plotted against $B$ for different values of $(1 + D/Dw)$. The dotted horizontal line shows the limiting value of $t/d$ to which Equation [33] may be used with the errors indicated. Thus, for surface grinding where $(1 + D/Dw = 1)$, $v$ may be considered small compared with $V$ and Equation [33] used with less than a 5 per cent error if $B$ is less than 0.018. It is seen that the original surface-grinding equation of reference (2) holds only for the low values of $v$ relative to $V$ used in that paper.

In Fig. 3 a series of chips are shown for a constant value of $d$ but progressively increasing values of $v/V$. The heavy lines indicate the values of $t$ pertaining and it is seen that $t$ is less than $d$ for cases I and II but that $t = d$ for all other cases. If $v/V$ were maintained constant but $d$ were to decrease then it would be found that the chip type would change in the direction from I to V in just the same way as when $(v/V)$ is allowed to increase and $d$ is held constant. Thus, while chip thickness $t$ will increase when either $d$ or $v/V$ is increased, a type V chip will be approached when $(v/V)$ increases or $d$ decreases.

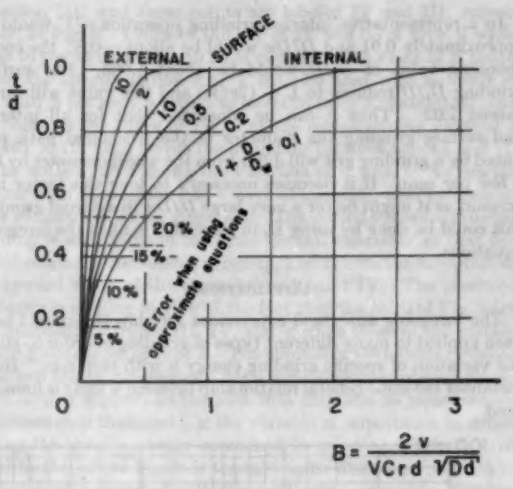


FIG. 7 VARIATION OF $t/d$ WITH NONDIMENSIONAL QUALITY $B = 2v/(VCd\sqrt{dD})$

Since reciprocating surface grinding is characterized by large $d$ and small $v/V$ the chips are normally of the type I or type II variety. Internal grinding involves very small values of $d$ and moderate values of $(v/V)$ and hence chips of types III, IV, or V are normally obtained. In external grinding all types of chips can be obtained depending on the values of $v/V$ and $d$ obtaining.

In order to evaluate $t$, $B$ must first be computed. This requires that $V$, $v$, $D$, $Dw$, and $d$ be known, all of which are readily determined. The quantities $r$ and $C$ are not so easily obtained. The taper-section method described in reference (2) still appears to be the best way of estimating $r$. Many such tests reveal that in snagging operations $r$ will be in the vicinity of 8 while in grinding operations involving smaller chips $r$ will be beween 10 and 15.

The values of $C$ obtained previously by rolling a wheel over a glass plate containing a thin layer of carbon black may be more precisely determined by rolling a grinding wheel across a freshly ground surface coated with a layer of soot approximating the mean value of $t$ in thickness. This appears to have two advantages over the original method.

1 Unusually high points on the wheel can penetrate the steel surface in a more characteristic manner than when hard glass is used.

2 The geometry of a ground surface more closely approximates the surface encountered by a wheel in practice than a glass plate does.

Since Hahn (5) recently has postulated that abrasive grains are elastically mounted in their bond, and deform under load to provide an appreciable increase in the number of effective cutting points, tests were made to determine the manner in which $C$ varied with load. Fig. 8 shows several tracks and the corresponding loads. In making these tests the soot-layer thickness and the steel-surface geometry were maintained identical by making a series of tracks one alongside the other on the same steel specimen. While the mean size of the individual contacts increases, few new points are observed to appear in the practical range of loads and hence it may be concluded that to a very good approximation $C$ is independent of the normal components of grinding force.

For a type V chip, Fig. 3, the area of the metal removed will be $(2/3dl)$ to a very good approximation, and from continuity considerations this area must be related to the infeed $i$, as follows

$$^1/_4dl = {}^1/_4il + (p - l) \quad [37]$$

When the value of $p$ is substituted from Equations [18] and [19] and the value of $l$ from Equation [13] we obtain

$$d = \left(\frac{3}{4}\frac{B\sqrt{1 + D/Dw}}{1 + \frac{v}{V}} - \frac{1}{2}\right)i \quad [38]$$

This equation reduces to $d = i$ for cases IV or below, for case V $d$ will always be found to be greater than $i$ since there are gaps between successive chips.

For cases I to IV of Fig. 3, the value of mean wheel depth of cut $d$, will be equal to the infeed per revolution of the work $i$. For case V $d > i$ since the entire surface is not cut.

The limiting case for which $p = l$ is case IV and it is of value to know the magnitude of $t$ or $B$ in this instance

$$p = \frac{2v}{VCrt} = 2\sqrt{\frac{Dd}{1 + D/Dw}}\left(1 + \frac{v}{V}\right) \quad [39]$$

or since $d = t$ for this case

$$t = \left[\frac{v\sqrt{1 + D/Dw}}{VCr\sqrt{D}\left(1 + \frac{v}{V}\right)}\right]^{2/3} = \left[\frac{B\sqrt{1 + D/Dw}}{2\left(1 + \frac{v}{V}\right)}\right]^{2/3}d \quad [40]$$

from which it follows that

$$B_{1V} = \frac{2\left(1 + \frac{v}{V}\right)}{\sqrt{1 + D/Dw}} \cong \frac{2}{\sqrt{1 + D/Dw}} \quad [41]$$

Plunge grinding is a type sometimes used in tool grinding and snagging operations involving an abrasive belt. This type of grinding is characterized by

1 A workpiece fed directly into the abrasive surface at a rate $(f)$ without lateral feed.

2 Chips of constant thickness throughout their length.

3 Chips of length equal to the mean length of the workpiece in the direction of grinding.

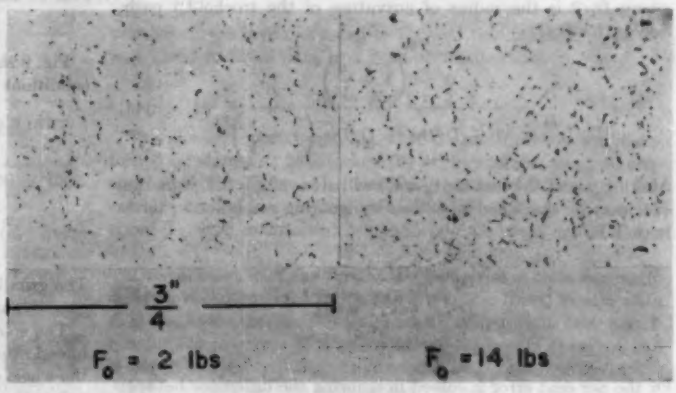


FIG. 8 TRACKS MADE BY A FRESHLY DRESSED GRINDING WHEEL ROLLED ACROSS A SOOT-COVERED STEEL SURFACE PREVIOUSLY GROUND BY THE SAME WHEEL

(The different tracks correspond to different normal loads between wheel and work. Work material, 1020 SAE steel; abrasive, aluminum oxide; grain size, 46; wheel hardness, I; wheel width, 3/4 in.)

If the maximum chip thickness is $t$, then it may be shown readily that for plunge grinding

$$t = \sqrt{\frac{2f}{VCr}} \quad [42]$$

where $f$ is the infeed in inches per minute.

### Significance of Trochoidal Path

All of the foregoing equations are summarized for convenience in the Appendix.

In the derivations two assumptions were made:

1 That in all grinding operations chips are so small compared with wheel and work diameters that chordal distances may be substituted for arc lengths, except in plunge grinding.

2 That the distance the work moves while a chip is actually being produced is small; or, stated another way, that the actual trochoidal path that a grit takes is closely approximated by a circular arc the radius of which is equal to that of the wheel.

One need only compare values of $l$ with values of $D$ or $Dw$ to be satisfied that in all cases the angle the wheel or work turns through in producing a chip is very small. The significance of assumption 2 is not so evident and hence this will be discussed further. The paths shown in Fig. 3 would be circular arcs were it not for the fact that the work moves horizontally while the chip is being generated. The resulting path is that of a trochoid, and difference between circular arcs $OA$ and trochoids $OB$ is shown greatly exaggerated in Fig. 3. Since the angle subtended by $OB$ is in reality very small (see item 1) the trochoid may be clearly approximated by a circular arc, but the diameter of the equivalent circle $D_e$ would be greater than that corresponding to the wheel diameter (i.e., diameter of circle $OB$ > diameter of circle $OA$ in Fig. 3). In all of the foregoing derivations this difference between the radius of curvature of the trochoid and the wheel was ignored. In order to determine the nature of this approximation we may make use of equations derived by Hahn (5) for the curvature difference $\Delta$, between the wheel surface and the trochoid generated by an abrasive particle. When these equations for external surface and internal grinding are rewritten in terms of the symbols and sign conventions adopted here it is found that

$$\Delta = \frac{2}{D} - \frac{2}{D_t} = \frac{2}{D}\left[1 - \frac{1}{\left(1 + \frac{v}{V}\right)^2}\right]\left(1 + \frac{D}{DW}\right) \quad [43]$$

where $D_t/2$ is the radius of curvature of the trochoidal path. Solving for $D_t/D$

$$\frac{D_t}{D} = \frac{\left(1 + \frac{v}{V}\right)^2}{1 + D/Dw - D/Dw\left(1 + \frac{v}{V}\right)^2} \quad [44]$$

Making use of the fact that $(v/V)$ will always be <0.1, Equation [44] may be simplified as follows by ignoring second-order terms in $(v/V)$

$$\frac{D_t}{D} = \frac{1 + \frac{2v}{V}}{1 - 2\frac{v}{V}\frac{D}{Dw}} \quad [45]$$

Or the per cent error involved in ignoring the difference between $D_t$ and $D$ is

$$\frac{D_t - D}{D_t} \times 100 = \frac{2v}{V}\left(1 + \frac{D}{Dw}\right) \times 100 \quad [46]$$

In a representative internal-grinding operation $v/V$ would be approximately 0.01 and $D/Dw$ would be about —0.8; the corresponding value of $D_t/D$ would be about 1.005. For surface grinding $D_t/D$ reduces to $1 + (2v/V)$ and this value will rarely exceed 1.02. Thus it can be concluded that for all internal and surface grinding the diameter of the trochoidal path produced by a grinding grit will differ from the wheel diameter by but a few per cent. If it becomes necessary to take this factor into account as it might be for a very large $D/Dw$ in external grinding this could be done by using $D_t$ in place of $D$ in all of the foregoing equations.

### Applications

The foregoing analytical expressions for chip thickness $t$ have been applied to many different types of grinding in order to study the variation of specific grinding energy $u$ with chip size. In all instances the same general relationship between $u$ and $t$ is found to hold.

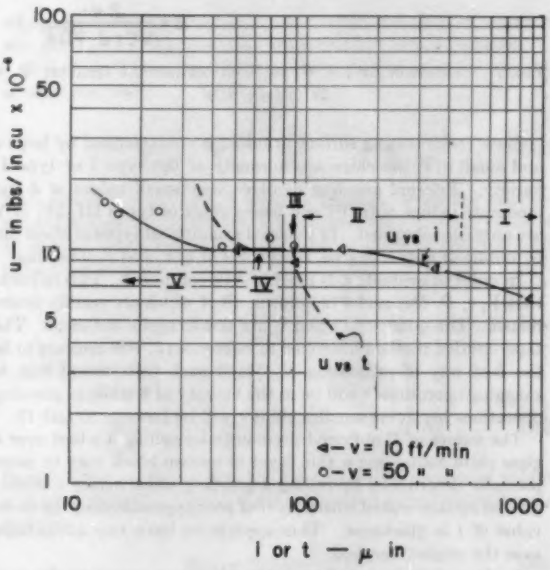


Fig. 9 Internal-Grinding Data Obtained Under the Conditions of Table 1

Fig. 9 shows some internal-grinding results obtained under the conditions of Table 1.

TABLE 1 INTERNAL-GRINDING CONDITIONS FOR FIG. 9

Wheel diameter ($D$), 0.72 in.
Work diameter ($Dw$), 1.20 in.
Wheel speed ($V$), 5500 fpm (30,000 rpm)
Work speed ($v$), 50 fpm and 10 fpm
Abrasive, white $Al_2O_3$
Grain size, 30
$C$, 1000 grains per sq in.
$r$, 15

The grinding forces were measured by means of a special strain-gage dynamometer fitted to a Bryant internal-grinding machine.

The solid curve and data points show the variation of $u$ with infeed rate ($i$, ipr). For all grinding cases from I to IV of Fig. 3, the wheel depth of cut $d$ is equal to the infeed rate $i$, and for such points the value of $B$ may be found readily. The critical value of $B$ corresponding to case IV is found to be 3.18 from Equation [41], while the value of $B$ for which $t = d$ is 1.58 from Equation [36]. The corresponding values of $d$ may be computed from

Equation [31] and these points are labeled IV and III, respectively, in Fig. 9. Chips to the left of IV will be of type V while those to the right of III will be of type II. The value of $B$ below which the approximation $v \ll V$ may be used with an error of less than 5 per cent is found to be 0.028 from Equation [34], and the point on the curve of Fig. 9 at the corresponding value of $d$ ($= 465 \times 10^{-6}$ in.) marks the boundary between types I and II.

The dotted curve shows the variation of $u$ with $t$. Values for this curve in the regions I to V were obtained by use of the equations summarized in the Appendix. The dotted curve for internal grinding is seen to have the same general character as that obtained originally for surface grinding, Fig. 1, with the exception of the upward trend of the curve beyond point IV. The observed similarity is striking in view of the fact that the chips of Fig. 9 are predominantly of types III, IV, and V while those in the surface grinding tests were of type I. The similarity that exists between these two sets of curves despite the wide difference of chip shape, lends further support to the idea that chip size as measured by maximum chip thickness $t$, is the variable of importance in determining the specific energy consumed in grinding. The upward trend to the left of Fig. 9 is thought to be due to an increase in friction work associated with the relatively longer type V chips.

The per cent difference in the trochoid $D_t$ and wheel $D$ diameters may be found from Equation [46] for the tests of Fig. 9. When this is done for the larger speed case ($v/V = 0.0001$), the per cent difference is found to be $0.73D/2$, which is certainly negligible.

Representative data obtained by internal, surface, and belt grinding are given in Fig. 10 for the grinding conditions of Table 2. The values of $t$ were computed using the equations of the Appendix.

TABLE 2 GRINDING CONDITIONS FOR FIG. 10

| | Internal | Surface | Belt |
|---|---|---|---|
| $Dw$, in. | 1 | ∞ | ∞ |
| $D$, in. | 0.75 | 8 | 8 (backing wheel) |
| $v$, fpm | 79 | 4 | 0 (plunge) |
| $V$, fpm | 5500 | 6300 | 11000 |
| $d$, $10^{-6}$ in. | 5 to 33 | 250 to 2000 | 1 to 15 ipm (infeed) |
| $C$, per in.$^2$ | 1500 | 2000 | 120 |
| $r$ | 15 | 15 | 6 |
| $b$, in. | 0.475 | 0.5 | 3/8-in. rod |
| Wheel or belt specification | 38A46-I12VBEP | 32A46-H8VBE | 3M-36 |

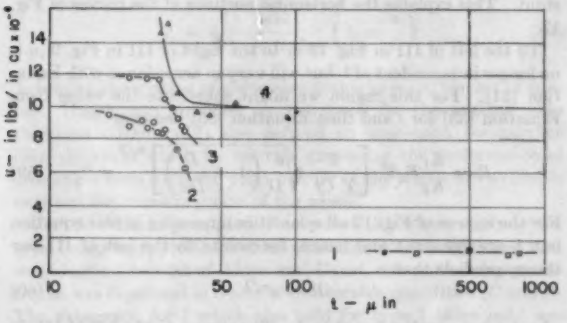


FIG. 10 VARIATION OF SPECIFIC GRINDING ENERGY ($u$) WITH MAXIMUM CHIP SIZE $t$ FOR BELT (1), SURFACE (2, 3), AND INTERNAL (4) GRINDING OPERATIONS

For belt grinding (curve 1) the values of $t$ are so large that $u$ is essentially independent of $t$. The two surface-grinding curves were obtained under conditions that were believed to be the same. However, different operators obtained all the data at widely different times. The curves are seen to be quite similar with the exception of the constant value of $u$ approached to the left. This value is sensitive to the exact method of dressing and this alone could account for the difference in the energy values shown. Slight variations in the relative humidity also have been found to give different energy curves when grinding in air, the specific energy being higher on days of high relative humidity.

The internal grinding data of Fig. 10 are representative of industrial practice and correspond to type V chips over the entire range of grinding. These results are seen to be similar to those of Fig. 9 despite the considerable difference in grinding conditions. The upward trend of the internal-grinding curve is thought to be characteristic of this type of grinding and the type V chip. Below a particular value of $t$, grains began to plow and rub rather than to produce true chips. The value of $t$ at which this occurs, and at which the energy per unit volume rises steeply, is apparently greater for type V chips than for type I or type II chips.

Certain experiments of Hahn (5) which already have been referred to will now be considered in light of the foregoing theory. In one set of experiments Hahn used wheels of constant size (1.5-in. diam) and varied the work diameter $Dw$, through a wide range of values for both internal and external cases. In these tests both $v$ and $V$ were maintained constant, as was the normal force between wheel and work, $F_n$. When the rate of metal removed $R$, was plotted against curvature difference $\Delta$, curves such as those shown in Fig. 11 were obtained. The vertical displacement of the

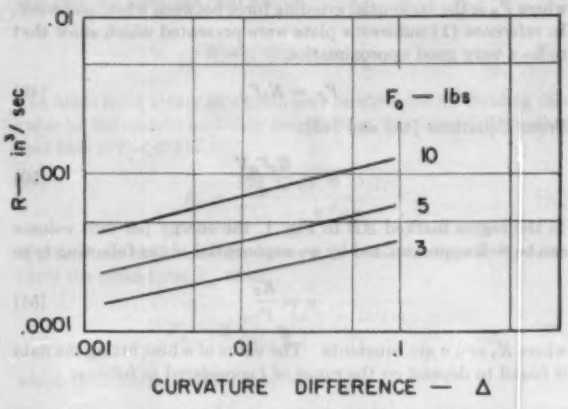


FIG. 11 VARIATION OF RATE OF METAL REMOVED ($R$) WITH CURVATURE DIFFERENCE ($\Delta$) FOR INTERNAL AND EXTERNAL-GRINDING EXPERIMENTS IN WHICH NORMAL FORCE BETWEEN WHEEL AND WORK WAS MAINTAINED CONSTANT—FROM REFERENCE (5)

parallel curves is proportional to $F_Q$, and the following equation was found to fit all data to a good approximation

$$R = K_s F_Q \Delta^{0.18} \quad [47]$$

In a second series of tests, Fig. 12, the wheel diameter was maintained constant at 1.25 in. while the work diameter was held constant at minus 3.5 in. in an internal-grinding operation. In this case the normal force between wheel and work $F_Q$, and the wheel speed $V$, were maintained constant but the work speed $v$ was varied.

The variation in $R$ observed in the first series of tests was really due to a variation in $t$. The reason $R$ was also found to vary with $\Delta$ is due to the fact that $t$ as well as $\Delta$ changes when $D/Dw$ is altered. The influence of $\Delta$ in Equation [47] is only apparent and is due to the fact that $\Delta$ and $t$ vary with $D/D_w$ in a similar way.

From Equation [1] it follows that

$$u = \frac{F_p V}{R} \quad [48]$$

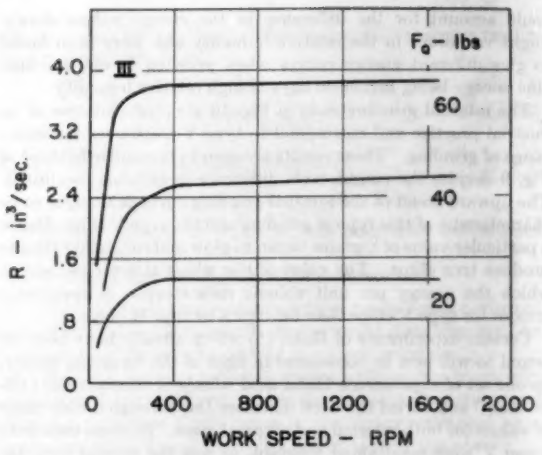


FIG. 12 VARIATION OF RATE OF METAL REMOVED ($R$) WITH WORK SPEED WHEN INTERNAL GRINDING SAE 4140 STEEL OF RC47-52 FROM REFERENCE (5)

where $F_P$ is the tangential grinding force between wheel and work. In reference (1) numerous plots were presented which show that to be a very good approximation

$$F_P = K_1 F_Q \quad [49]$$

From Equations [48] and [49]

$$R = \frac{K_1 F_Q V}{u} \quad [50]$$

In the region marked $AB$ in Fig. 1, the energy per unit volume can be well approximated by an exponential of the following type

$$u = \frac{K_2}{t^n} \quad [51]$$

where $K_2$ and $n$ are constants. The value of $n$ best fitting the data is found to depend on the range of $t$ considered as follows:

| $t \times 10^6$, in. | $n$ |
|---|---|
| 20 to 40 | 0.9 |
| 40 to 70 | 0.7 |
| 70 to 100 | 0.6 |

From Equations [33], [48], [49], and [51] it can be shown that when all quantities except $F_Q$ and $D/Dw$ are held constant

$$t = F_Q^{\frac{1}{4-n}} \left(1 + \frac{D}{Dw}\right)^{1/4} \quad [52]$$

Similarly, from Equation [43] it follows that when all quantities except $F_Q$ and $D/Dw$ are constant

$$\Delta \sim 1 + D/Dw \quad [53]$$

and hence

$$t \sim F_Q^{\frac{1}{4-n}} \Delta^{1/4} \quad [54]$$

Combining Equations [50] and [51]

$$R = \frac{K_1}{K_2} F_Q V t^n \quad [55]$$

or from Equation [54]

$$R = (K_2 V) F_Q^{\frac{4}{4-n}} \Delta^{n/4} \quad [56]$$

For very fine grinding ($t$ = 20 to 40$\mu$ in.)

$$R = K_3 V F_Q^{1.33} \Delta^{0.33} \quad [57]$$

while for coarser grinding ($t$ = 70 to 100$\mu$ in.)

$$R = (K_3 V) F_Q^{1.18} \Delta^{0.18} \quad [58]$$

In comparing this equation with Hahn's empirical Equation [47] it should be noted that in these tests $V$ was held constant. Both the derived exponents of $F_n$ and $\Delta$ are seen to be in good agreement with the experimental values.

The fact that the analytical exponents in Equations [57] and [58] are slightly greater than the experimental estimate of 1.0 may be accounted for in two ways:

1 In arriving at Equation [56] it was assumed that the number of cutting points per square inch $C$ would be independent of the normal force $F_Q$. While this is a good first approximation, we know that if $C$ does vary slightly with increase in $F_Q$ it will be to increase, and an increase in $C$ with $F_Q$ will lower the exponent of $F_Q$ in the direction of 1.

2 The experimental scatter of Dr. Hahn's data leading to Equation [47] is such that we cannot clearly distinguish between an exponent of 1.0 and a slightly higher value.

While Equation [47] is quite correct, it is misleading to express this relation in terms of curvature difference $\Delta$ since this quantity is physically insignificant. Although an appreciable difference in $\Delta$ is evident in Equation [43] for external surface and internal grinding on a relative basis, when the absolute values are considered, Equation [46], the differences are found to be insignificant. A preferable expression to Equation [47] is that of Equation [55] which features the real variable of importance, $t$.

The second set of data presented by Dr. Hahn, Fig. 12, also can be explained in terms of the $u$ versus $t$ relationship for internal grinding. The break in the curves of Fig. 12 marked III correspond to point III in Fig. 9. Values to the right of III in Fig. 12 correspond to values to the left of III in Fig. 9, and in this region $u$ will be essentially constant. From Equation [53] it is evident that $R$ will remain constant as long as $F_Q$, $V$, and $u$ remain constant. This explains the horizontal portions of the curves of Fig. 12.

To the left of III in Fig. 12 or to the right of III in Fig. 9 ,$u$ is no longer independent of $t$, but will vary in accordance with Equation [51]. For this region we might substitute the value from Equation [33] for $t$ and then Equation [55] becomes

$$R = \frac{K_1}{K_2} F_Q V \left[\frac{4}{V C r} \sqrt{\frac{d}{D}\left(1 + \frac{D}{Dw}\right)}\right]^{n/2} v^{n/2} \quad [59]$$

For the curves of Fig. 12 all quantities appearing in this equation but $b$ are constant and hence, for points to the left of III our theory predicts that

$$R \sim v^{n/2} \quad [60]$$

where $n$ is a number less than 1. The curves to the left of III in Fig. 12 are seen to correspond in shape to Equation [60] when $n$ is less than 1. Thus the $u$ versus $t$ relationship for internal grinding is seen to explain in all details the experimental data of Hahn shown in Fig. 12.

## HISTORICAL BACKGROUND

The first paper published concerning the size of grinding chips appears to have been written by Alden (6) in 1914. From the geometry of two intersecting circles the following equation for maximum chip thickness $t$ was derived for external grinding

$$t = \frac{v}{V} m \sin(\theta_1 + \theta_2) \quad [61]$$

where

$m$ = spacing of successive grits on wheel circumference
$\theta_1$ = angle $00' B$ in Fig. 2 (*b*)
$\theta_2$ = angle $00'' B$ in Fig. 2 (*b*)

While this equation is difficult to use, since a convenient method of finding $m$ is not given and the small angles $\theta_1$ and $\theta_2$ are difficult to measure, Alden did direct attention to the importance of chip thickness in grinding. Alden assumed that the maximum force per grain would vary directly as $t$.

In 1915 Guest (7) independently discussed the importance of maximum chip thickness in England and presented the following equation for external grinding

$$t = 2m \frac{v}{V} \sqrt{\frac{d}{D}(1 + D/Dw)} \quad [62]$$

While this equation reduces to that of Alden it is preferable in that it replaces $\theta_1$ and $\theta_2$ by quantities that are more easily determined. However, this expression like Alden's involves the ill-defined quantity $m$. Guest assumed that the maximum force per grain would vary as $t^2$.

In 1920 Chapman (8) published an expression for $t$, which also contained an $m$. Krug (9) of Germany apparently presented the first expression for $t$ in which an $m$ did not appear, but this was done by assuming arbitrarily that the mean grain spacing is always on half the arc of contact, and that grains are spherical in shape. Krug's equation is not reproduced here since certain errors in the derivation were subsequently found (10).

In 1938 Hutchinson (11) presented the following expression for chip length in surface grinding

$$l_c = \sqrt{dD}\left(1 \pm \frac{v}{V}\right) \quad [63]$$

the plus sign pertaining to the case where the work moves in a direction opposite to the wheel and vice versa. For external grinding Hutchinson found

$$l_c = \sqrt{\frac{dD}{1 + D/Dw}}\left(1 \pm \frac{v}{V}\right) \quad [64]$$

Assuming the spacing of successive grains to equal the arc of contact, Hutchinson obtained an expression for the average chip thickness. Heinz (12) also derived an expression for average chip thickness which he used in discussing the performance of grinding wheels from the point of view of the chip space available between the abrasive grains of the wheel.

The derivations presented in reference (2), which apply to the type I chip only, yielded a value of maximum chip thickness that was identical to that of Alden and Guest, except that the quantity $m$ was expressed in terms of measurable quantities ($C$ and $r$). The expression for $l$ which also held for type I chips only was identical to that presented by Hutchinson. Hutchinson's Equation [64] for external grinding is seen to be included as a special case in Equation [12] of this paper.

In reference (5) Hahn suggested that type V chips were obtained under certain conditions in internal grinding. In the present paper chips are classified into five types and expressions for maximum chip thickness $t$, and undeformed chip length $l$, are derived for all types of chips as well as for all types of grinding. These results are summarized in the Appendix.

All workers up to Hahn (5) not only approximated the trochoidal path of the individual grain by a circular arc but assumed that this arc had the radius of curvature of the wheel. In the present paper this question is discussed and it is concluded that except in extreme cases of external grinding these approximations are justified. For the few cases where the trochoidal path must be considered we can still use a circular arc but the wheel radius should then be replaced by the trochoidal radius of curvature. The method of doing this is considered in this paper.

## Force on a Single Grain

While experimental grinding-force data were not available until reference (1), early workers speculated on how the maximum force per grain varied with maximum chip thickness for the case of type I chips. For example:

1 Alden assumed that the maximum force on a single grain $F_g$ varied directly as $t$.

2 Guest assumed that $F_g$ varied as $t^2$.

The work done per unit time in a grinding operation (type I chips) is

$$\text{Work/time} = uvbd \text{ (12), in-lb/min} \quad [65]$$

The number of chips produced per minute will be

$$\text{No. chips/min} = 12\, VbC \quad [66]$$

and thus the work per chip will be

$$\text{Work/chip} = u \frac{vd}{VC} \quad [67]$$

The mean force acting on a grain may be obtained by dividing this value by the undeformed chip length from Equation [12] (noting that here $v/V << 1$)

$$\bar{F}_g = \frac{urd}{VC} \frac{\sqrt{(1 + D/Dw}}{\sqrt{dD}} \quad [68]$$

If we assume the maximum force on an individual grain $F_g$, to be twice the mean force $\bar{F}_g$, then

$$F_g = 2 \frac{ur}{CV} \sqrt{\frac{d(1 + D/Dw)}{D}} \quad [69]$$

which from Equation [33] may be written

$$F_g = 2ut^2r \quad [70]$$

Whether Alden or Guest is correct in his assumption depends upon the region in which grinding is taking place. For very fine grinding $u$ is independent of $t$ so that Equation [70] reduces to

$$F_g = Kt^2 \quad [71]$$

which is in agreement with Guest's assumption. For somewhat coarser grinding $u = K_2/n$ (Equation [51]), $n$ being between 0.6 and 0.9. If $n$ is taken equal to 0.9, Equation [70] reduces to

$$F_g = Kt^{1.1} \quad [72]$$

which is very close to Alden's assumption. It should be expected that in the early days limitations of machines and wheels put most grinding operations in the fine regions, corresponding to Equation [71] or [72].

If we assume that $r$ (the ratio of mean scratch width to depth) is a constant for a given grinding wheel, then from Equations [51] and [70] we may write

$$F_g = K_3 \left[\frac{v}{VC} \sqrt{\frac{d}{D}(1 + D/Dw)}\right]^{1-\frac{n}{2}} \quad [73]$$

where $K_3$ is a constant and will have different values depending on the relative size of the chip as shown in Fig. 13. For any given

type of grinding, however, $n$ will be constant and the relative magnitude of $F_s$ will depend only on the quantity within brackets which we may call the "relative grain force" $F_r$

$$\text{Relative grain force} = F_r = \frac{v}{VC}\sqrt{\frac{d}{D}(1 + D/Dw)} = \frac{vd}{VCl} \quad \ldots [74]$$

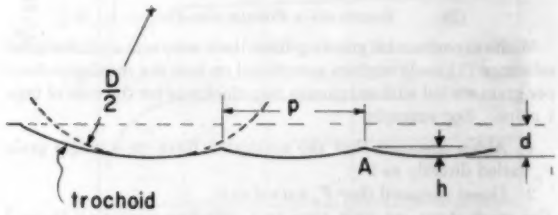


FIG. 13 SURFACE IMPERFECTIONS OF HEIGHT (h) LEFT BEHIND UPON GROUND SURFACE

By increasing $F_r$ a given wheel will behave softer. It is thus seen that the principal ways of decreasing the effective hardness of a grinding wheel are

1 To increase the work speed ($v$).
2 To decrease the wheel speed ($V$).
3 To decrease the number of cutting points per square inch of wheel surface by dressing, change of grain size, or change of grain spacing (wheel structure).
4 To increase the wheel depth of cut ($d$).
5 By increasing the curvature of the wheel or work surface (i.e., by decreasing $D$ or decreasing $Dw$). In this connection it should be recalled that in internal grinding $Dw$ is negative and hence relative wheel hardness will decrease when $Dw$ is increased in internal grinding.

Equation [74] explains and correlates many well-known grinding rules of the workshop such as the few examples mentioned in the following:

1 Why internal-grinding wheels are normally harder in action than surface-grinding wheels (if all quantities other than $Dw$ are the same).
2 Why a wheel dressed with a coarse feed appears softer than the same wheel dressed with fine feed.
3 Why finishing operations call for wheels that are either softer than those used in roughing operations when the grain size is kept the same, or can have the same hardness if the grain size is reduced in proportion to the volume of metal removed. In this connection it might be noted that there is an increasing trend to use softer wheels of larger grain size in finishing operations rather than the other possibility.
4 Hardened steels are commonly ground with softer wheels than unhardened steel in fine grinding operations. Reference (1) reports that for fine grinding the forces, and hence specific energy, are independent of work hardness. Therefore, since in grinding hardened steels it is extremely important to avoid burning or overtempering the surface, it is more important that grains break loose as soon as they become slightly dull in the case of hardened steels than when grinding softer steels whose heat-treatment need not be preserved.

## SURFACE ROUGHNESS

In any grinding operation high points as shown at $A$ in Fig. 13 will be left upon the finished surface. The mean height of such points $h$, is related to the surface finish produced and hence expressions for $h$ will be considered here. We already have obtained an expression for the pitch $p$, for any characteristic points on the ground surface (Equations [18] and [19]) and hence by reference to Equation [12] we have for any type of grinding

$$p = \frac{2v}{VCrt} = 2\sqrt{\frac{Dh}{1 + D/Dw}}\left(1 + \frac{v}{V}\right) \quad \ldots [75]$$

or

$$\sqrt{h}t = \frac{v\sqrt{1 + D/Dw}}{V_{cr}\sqrt{D}\left(1 + \frac{v}{V}\right)} \quad \ldots [76]$$

For type I chips ($v$ — $V$) we can substitute for $t$ from Equation [33] and then[7]

$$\frac{h}{d} = \frac{(t/d)^2}{16} \quad \ldots [77]$$

For chips of type II it follows from Equation [31] which define $B$ that

$$\frac{h}{d} = \frac{B^2(1 + D/Dw)}{4\left(\frac{t}{d}\right)^2\left(1 + \frac{v}{V}\right)^2} \quad \ldots [78]$$

while for the special type III chip

$$t/d = 1 \text{ and } B^2 = \frac{1}{1 + D/DW}$$

and thus

$$\frac{h}{d} = \frac{1}{4(1 + v/V)^2} \quad \ldots [79]$$

Finally, for type IV and V chips it is evident that

$$\frac{h}{d} = 1 \quad \ldots [80]$$

The quantity $h$ given in Equations [77 to 80] represents the mean peak-to-valley distance of the material left behind on the finished surface based upon purely geometrical considerations. The actual maximum peak-to-valley roughness will differ from the computed values for the following reasons:

1 Due to vibration of the wheel relative to the work.
2 Due to built-up edge on certain abrasive grains.
3 Due to deviations of the actual grinding wheel from the simplified average model assumed here. Occasional grains of unusual setting in depth and of unusual spacing will cause the maximum observed $h$ to deviate from that computed.

However, despite these effects it is felt that Equations [77 to 80] are useful in comparing the relative changes in surface roughness to be expected by changes in grinding conditions under ideal conditions.

## ACKNOWLEDGMENT

The authors wish to acknowledge generous support in portions of the work reported here by The Bryant Chucking Grinder Company, Springfield, Vt., in other portions by The Carborundum Company, Niagara Falls, N. Y., and The Timken Roller Bearing Company, Canton, Ohio.

[7] This equation is somewhat different from that given in reference (13). The differences arise from a change in the assumed chip shape. Throughout this paper a rectangular chip section has been assumed for the average chip considered for reasons given in footnote[6] while in reference (13) a triangular chip section was used.

# Appendix

SUMMARY OF EQUATIONS AND NOMENCLATURE FOR EXTERNAL SURFACE AND INTERNAL GRINDING

| Chip type | Condition | Chip length | Wheel depth of cut | Max chip thickness | $h/d$ |
|---|---|---|---|---|---|
| I | $t \ll d$, $p \ll l$ | $l = \sqrt{\frac{Dd}{1 + D/Dw}}$ | $d = i$ | $t = \left[\frac{4v}{V\,Cr}\sqrt{\frac{d(1 + D/Dw)}{D}}\right]^{1/2}$ | $h/d = \frac{(t/d)^2}{16}$ |
| II | $t < d$, $p < l$ | $l = K\sqrt{\frac{Dd}{1 + D/Dw}}\left(1 + \frac{v}{V}\right)$ | $d = i$ | $\frac{t}{d} = \frac{2B\sqrt{1 + D/Dw}}{t/d} - \frac{B^2(1 + D/Dw)}{(t/d)^2}$ (See Fig. 7) | $h/d = \frac{B^2(1 + D/Dw)}{4\left(\frac{t}{d}\right)^2\left(1 + \frac{v}{V}\right)^2}$ |
| III | $t = d$, $p < l$ | $l = K\sqrt{\frac{Dd}{1 + D/Dw}}\left(1 + \frac{v}{V}\right)$ | $d = i$ | $t = d$ | $h/d = \frac{1}{4\left(1 + \frac{v}{V}\right)^2}$ |
| IV | $t = d$, $p = l$ | $l = 2\sqrt{\frac{Dd}{1 + D/Dw}}\left(1 + \frac{v}{V}\right)$ | $d = i$ | $t = d$ | $h/d = 1$ |
| V | $t = d$, $p > l$ | $l = 2\sqrt{\frac{Dd}{1 + D/Dw}}\left(1 + \frac{v}{V}\right)$ | $d = i\left[\frac{3B\sqrt{1 + D/Dw}}{4\left(1 + \frac{v}{V}\right)} - \frac{1}{2}\right]$ | $t = d$ | $h/d = 1$ |

For plunge grinding: $t = \sqrt{\frac{2i}{V\,Cr}}$

## BIBLIOGRAPHY


1 "Forces in Dry Surface Grinding," by E. R. Marshall and M. C. Shaw, Trans. ASME, vol. 74, 1952, p. 51.

2 "The Size Effect in Metal Cutting," by W. R. Backer, E. R. Marshall, and M. C. Shaw, Trans. ASME, vol. 74, 1952, p. 61.

3 "Surface Temperatures in Grinding," by J. O. Outwater and M. C. Shaw, Trans. ASME, vol. 74, 1952, p. 73.

4 "Machine Tool Dynamometers," by N. H. Cook, E. G. Loewen, and M. C. Shaw, *American Machinist*, May 10, 1954.

5 "The Effect of Wheel-Work Conformity in Precision Grinding," by R. S. Hahn, Trans. ASME, vol. 77, 1955, pp. 1325–1329.

6 "Operation of Grinding Wheels in Machine Grinding," by G. I. Alden, Trans. ASME, vol. 36, 1914, p. 451.

7 "The Theory of Grinding With Reference to the Selection of Speeds in Plain and Internal Work," by J. J. Guest, Proceeding of The Institution of Mechanical Engineers, London, England, 1915, p. 543.

8 "Cylindrical Grinding in 1920," by W. H. Chapman, Trans. ASME, vol. 42, 1920, p. 595.

9 "Beitrage zur Kenntnis des Schlerfens," by C. Krug, *Maschinenbau*, September, 1925, p. 875.

10 Communication by A. Hoffman, *Maschinenbau*, January, 1933.

11 "Do We Understand the Grinding Process?" by R. V. Hutchinson, *SAE Journal*, vol. 42, 1938, p. 89.

12 "Metal Cutting With Abrasive Wheels," by W. B. Heinz, Trans. ASME, vol. 65, 1943, p. 21.

13 "The Grinding of Titanium Alloys," by C. T. Yang and M. C. Shaw, Trans. ASME, vol. 77, 1955, pp. 645–660.


# Discussion

W. R. BACKER.[8] The authors have presented an analysis of grinding geometry based on a single average grit removing an average chip. This type of analysis is very useful to those working in grinding mechanics, because many different setups can be compared in terms of the fundamental quantities of actual chip dimensions. While chip geometry is only one phase of the study of the grinding process, it is an important one and is worthy of the attention it has received in this and other recent publications.

The authors assumed average-chip form, Fig. 5, shows a constant-width chip in which the width increases with maximum chip thickness per Equation [19]. Considering, as an example, a finish surface-grinding operation, an increase in the downfeed per pass could increase $t$ and require a larger $b'$ without changing the initial grit-work contact geometry. This means the grit must anticipate the maximum chip thickness or that Equation [19] of the paper really means an increasing chip width with chip thickness. As an alternative derivation of the chip geometry for this case, consider the metal-removal rate in grinding

$$\text{Metal-removal rate} = vbd \quad \ldots\ldots [81]$$

The number of chips produced per unit time is $bVC$, so the volume of the average chip is as follows

$$\text{Volume of chip} = \frac{vbd}{bVC} = \frac{vd}{VC} \quad \ldots\ldots [82]$$

The average cross-sectional area of the undeformed chip is the following

$$\text{Average-chip area} = \frac{vd}{VCl} \quad \ldots\ldots [83]$$

For the surface-grinding example, considering the average area,

[8] Senior Research Engineer, The Cincinnati Milling Machine Company, Cincinnati, Ohio. Assoc. Mem. ASME.

the product of average thickness $t_a$, and average width $b_a'$

$$t_a b_a' = \frac{vd}{VC\sqrt{Dd}} = \frac{v}{VC}\sqrt{\frac{d}{D}} \quad [84]$$

Assume that the instantaneous chip width $b_i'$ is a linear function of instantaneous chip thickness $t_i$

$$b_i = \frac{r}{2} t_i \quad [85]$$

This gives a chip of increasing cross section with distance along the contact path for "up" grinding. Cross section varies linearly along this path, so

$$b_a' t_a = {}^1/_2 t b' = {}^1/_2 t \frac{r}{2} t \quad [86]$$

Thus, Equation [84] of this discussion becomes

$${}^1/_4 r t^2 = \frac{v}{VC}\sqrt{\frac{d}{D}}$$

or

$$t = \sqrt{\frac{4v}{VCr}}\sqrt{\frac{d}{D}} \quad [87]$$

This is identical with the authors' Equation [21]. The cross-sectional area must thus have increased with the square of the instantaneous chip thickness and not linearly with it as proposed in Fig. 5.

The authors' derivation of the relative-grain-force index, Equation [74], is of interest in connection with Equation [83] of this discussion. The relative grain force is, of course, the average chip cross-sectional area. A better relative-grain-force index might have been the following

$$F_r = \frac{uvd}{VCl} \quad [88]$$

The reintroduction of the specific energy $u$ makes this term the actual force on the average grit, allowing for workpiece variables and other parameters affecting grain force.

It is believed that the value of the authors' analysis would have been enhanced, especially for research workers, if the instantaneous chip thickness had been considered as the fundamental geometrical quantity in grinding rather than the maximum chip thickness. If grinding properties are known as a function of instantaneous chip thickness, a solution for any particular setup can be determined easily.

O. W. Boston.[9] The authors of the paper conclude that the average thickness of chip is a criterion for evaluating the power required to remove metal in grinding. The writer wishes to point out a paper covering a similar subject related to milling by Mr. F. A. Parsons.[10] Mr. Parsons computes the average thickness of chip (ATC) as a function of the feed and depth of cut and then plot the net energy required at the tool point to remove various metals, such as free-cutting brass, cold-rolled steel (low-carbon), SAE 1020 steel, and cast iron, for various values of ATC but for three different depths of cut, namely, 0.010, 0.100, 1.000 in., respectively.

For example, the curve of cubic inches of metal removed per horsepower-minute for milling free-cutting brass takes the form of one straight line when plotted over ATC on log-log paper for a depth of cut of 0.010 in. A second straight line somewhat below the first is obtained for a depth of cut of 0.100 in. and a third straight line still lower is obtained when the depth of cut is 1.000 in. This indicates that, for a given depth of cut, a straight line is obtained when the feed is varied to get different values of ATC. For a constant value ATC, such as 0.0006, the cubic inches per horsepower-minute for cutting brass are 2.5 for a depth of 0.010 but only 2.0 when the depth is 0.100 in. Again, 2.5 cu. in. of brass are removed per unit horsepower when the ATC is 0.0006, 0.0013, and 0.0023 in., respectively, for the three depths of cut. This indicates that the ATC is not a safe method for computing the power for metal removal. The results for the other metals show also that ATC is not a safe basis for computing energy values. The cold-rolled steel being milled with lard oil is one exception to this rule, as the variation of depth does not destroy the continuity of the three curves. (This discussion was given in a paper by the writer and C. E. Kraus.[11])

The discussion given by Dr. Hahn, showing that friction between the work and the flank of the abrasive grain is an important factor when grinding, may indicate that the problem of chip removal by negative-rake abrasive particles involving end friction may follow one law while chip removal with the sharp cutting edges, such as those of a milling cutter, may follow another.

R. S. Hahn.[12] The authors have presented an excellent paper, giving for the first time formulas for the length and thickness of the various types of chips. In most cases these formulas are based upon circular arcs and chords which replace the grain loci. It may be interesting to compare Equations [10], [11], [12], or [14] of the paper with the more-exact equations derived from the trochoidal expressions for the locus of a point on the wheel relative to the workpiece which have been given (authors' reference 5). For internal grinding the path is

$$y = \frac{(1+\eta)^2 - (1-\rho)}{2a(\rho+\eta)^2} x^2 = I_i x^2 \quad [89]$$

where

$$\eta = \frac{\text{wheel rotary speed}}{\text{work rotary speed}}$$

$$\rho = \frac{R}{a} = \frac{\text{work radius}}{\text{wheel radius}}$$

and where the origin of co-ordinates is taken at 0, Fig. 2(*c*). By finding the $x$ co-ordinate of the point of intersection of this curve, Equation [89] of this discussion, with the circular bore of the hole the length of arc $OB$ or chip length may be approximated by

$$l_i = \sqrt{\frac{d}{I_i - \frac{1}{D_w}}} \quad [90]$$

Similar equations may be derived for external and surface grinding, thus

External

$$l_e = \sqrt{\frac{d}{I_e + \frac{1}{D_w}}}$$

[9] Professor and Chairman, Department of Mechanical and Production Engineering, University of Michigan, Ann Arbor, Mich. Fellow ASME.

[10] "Power Consumed in Milling," by F. A. Parsons, *American Machinist*, vol. 53, 1920, p. 315.

[11] "The Elements of Milling," by O. W. Boston and C. E. Kraus, ASME Paper RP-54-4, Trans. ASME, vol. 54, 1932.

[12] Research Engineer, The Heald Machine Company, Worcester, Mass. Mem. ASME.

Surface

$$l_e = \sqrt{\frac{d}{I_e}}$$

where

$$I_e = \frac{(1-\eta)^2 - (1+\rho)}{2a(\rho+\eta)^2}$$

$$I_e = \frac{\left(\frac{V}{v}\right)^2}{2a\left(1+\frac{V}{v}\right)^2}$$

These equations are based not on the true trochoidal equations but actually on parabolic approximations to the true trochoid as evidenced by Equation [89]. In so far as chip length is concerned either circular or parabolic loci give adequate accuracy. In dealing with the difference between adjacent loci in order to get the running chip thickness along the chip there may be some discrepancies between the circular-arc locus and the more accurate parabolic locus. Since neither expression is particularly cumbersome it would seem preferable to use the more accurate parabolic formulas, which are valid for a wide range of conditions. The expression for the running chip thickness as a function of the distance $x$ along the length of the chip is, for internal grinding

$$t(x) = m\frac{v}{V}\left(2I_i - \frac{1}{R}\right)x - I_i\left(\frac{mv}{V}\right)^2$$

The derivation of Equation [18] seems obscure. The chips apparently have a width $b'$ which is distinctly different from the transverse grain spacing. It would seem natural to obtain the longitudinal grit spacing as

$$\frac{1}{\text{transverse spacing} \times \text{grit surface density } (c)}$$

According to the authors' Equations [18] and [19], when $b'$ is eliminated, the pitch $p$ or spacing of marks produced on the work by peripherally adjacent grits is a function of the chip thickness $t$. It does not seem that this can be true since the pitch is entirely unrelated to chip thickness.

Concerning Equations [57] and [58] it should be pointed out that these are not purely theoretical equations showing agreement with the observed experimental fact that $R \sim \Delta^{0.2}$ since $\eta$ has been found by experiment. These equations actually show that the author' experimental data, which yielded the values of $\eta$, are in accord with the curvature effects as reported by the writer (authors' reference 5).

## Authors' Closure

The shape for the average chip proposed by Mr. Backer is as shown in Fig. 14($a$) while that used by the authors is shown in Fig. 14($b$). Each of the two proposed mean chip geometries leads to the same volume per chip and hence the difference is one of shape rather than volumetric content. A basic property that the average chip must satisfy is the possibility of a number of identical average chips being fitted together on the ground surface to yield the unground surface without voids. Fig. 14($b$) satisfies this requirement while Fig. 14($a$) does not.

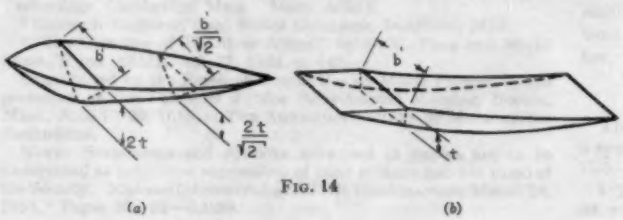


Fig. 14

($a$) ($b$)

At first one may be troubled by the fact that whereas many (although not all) actual chips may have the appearance of Fig. 14($a$) none will have the appearance of Fig. 14($b$). However, it is not necessary that the average chip look like any real chip any more than it is necessary that the average man look like any particular man.

The authors agree with Professor Boston that the average chip thickness is not alone a reliable method for predicting power requirements in grinding. In fact, Fig. 10 shows that for a given chip thickness the specific energy may have several values depending upon conditions such as wheel sharpness, grinding fluid, or type of grinding. The real value of the equations is to show the direction in which grinding energy will change when a variable such as work speed or wheel depth of cut is changed. If the chip thickness decreases as a result of such a change, then the specific energy will increase or remain the same depending on the magnitude of chip thickness obtaining. Thus the equations show the relative importance of several operating variables.

Reasons for the shape of the specific energy-chip thickness curve was not discussed in the paper, but rather the data were presented as experimental fact. Several possible reasons suggest themselves. First, a size effect as suggested in reference (2) probably operates, particularly in the flat region of the curve and in region I of Fig. 9. Secondly, the cutting edge of a grain may not be perfectly sharp, and dullness present would become relatively important as the chip thickness decreased. Thirdly, there is undoubtedly some rubbing on the clearance faces of the grains as Dr. Hahn suggests, and this would be expected to represent a larger fraction of the total-energy input as the size of chip decreases. The rising region of the energy curve closest to the origin, region V of Fig. 9, is thought to be predominantly due to this sort of rubbing action. As a wheel sparks out energy continues to be consumed with practically no metal removal. In the limit this would lead to an infinite value of specific energy.

Equation [88] suggested by Mr. Backer as a measure of the relative force on a single grain is the same as the authors' Equation [68] when the expression for chip length Equation [12] is substituted. As stated in the text, Equation [74] is meant to be used only for a given type of grinding (such as fine surface grinding). In such instances the range of $t$ involved will not be great, $u$ may be considered constant, and Equation [74] employed. If grain-force values covering a wide range of $t$ are of interest then Mr. Backer's Equation [88], or the authors' Equation [68], is to be preferred. As Mr. Backer indicates, values of energy could be related to instantaneous values of $t$ rather than to maximum values of $t$. While such a picture would be of theoretical interest the end results would not be as convenient to apply to grinding problems.

As Dr. Hahn points out, the equations presented could be modified to involve the parabolic approximation to the trochoid but it is questionable whether the results obtained would differ significantly from those presented, particularly in view of the qualitative way in which the results are intended to be used.

In the derivation of Equation [18] the mean pitch per grain is obtained by considering a peripheral path on the wheel of width $b'$ and finding the average number of grains which lie within this path. It appears physically reasonable that the width of path ($b'$) be proportional to chip thickness, for if a scratch is made on the surface and the wheel rotated until a second grain passes through the same scratch, the wider the scratch the sooner a second grain will pass within the boundaries of the first scratch.

# Inorganic Grinding Fluids for Titanium Alloys

By M. C. SHAW[1] and C. T. YANG[2]

**Dilute aqueous solutions of certain inorganic salts are very effective in decreasing the rate of grinding-wheel wear and providing decreased surface roughness in the finishing of titanium-alloy surfaces. A systematic study of a large number of salt solutions has revealed that such solutions act by the formation of adsorbed cationic and anionic layers on the aluminum-oxide and titanium surfaces, respectively. These layers prevent the abrasive and chip surfaces from coming close enough together to form strong bonds, which when broken, remove pieces of abrasive from the system. In the choice of a suitable material, ion size and effective charge are found to be two items of major importance. Barium was found to be the most effective element in the periodic table for adsorption on aluminum oxide, while the phosphate radical was the most effective anion investigated for adsorption on a titanium-alloy surface. Long chains attached to each of these ions should increase the effectiveness of the simpler ions considered here. The relation between corrosion inhibition and the screening of titanium surfaces in grinding is discussed.**

## Introduction

In a previous paper[3] the grinding of titanium alloys was discussed with particular reference to grinding-wheel wear. It was found that good finish always accompanied a low rate of wheel wear and vice versa. Low wheel speeds (2000 fpm), the proper type of aluminum-oxide abrasive (white), and a good cutting fluid were found to be the most important ways of decreasing wheel wear when grinding titanium. The improved results were in all cases explainable in terms of a decrease in the tendency for bonding between the abrasive and the metal ground. In this paper the action of dilute water solutions in decreasing grinding-wheel wear will be discussed in greater detail.

The tendency for a grinding wheel to wear is conveniently expressed in terms of a grinding factor ($G$)

$$G = \frac{\text{volume of metal removed}}{\text{volume of grinding wheel consumed}} \quad \ldots\ldots [1]$$

This nondimensional ratio can be determined under a standard set of conditions and the resulting values used to compare the effectiveness of a series of fluids or other grinding variables.

For some time it has been known that materials commonly used to inhibit rusting of steel surfaces by water solutions such as sodium nitrite and organic nitrite amines are effective as grinding fluids for titanium alloys. Tarasov[4] was the first to use such solutions in titanium grinding. When sodium nitrite is used in this manner it is customary to employ about 5 per cent of the active ingredient. Most of the tests[3] were therefore made using a 5 per cent sodium-nitrite solution.

## Preliminary Tests

At the beginning of the present investigation tests were made upon a number of materials in order to determine the range of effectiveness of grinding fluids. These tests were performed under the conditions of Table 1 and the results obtained are also given in this table. The principal conclusions to be drawn from these preliminary tests are as follows:

1 Ordinary soluble oils are poor fluids for grinding titanium alloys.

2 Distilled water is inferior to air.

3 Certain inorganic salts, principally those of the heavy alkali metals such as sodium and potassium are most interesting.

4 Both the anion (negatively charged particle) as well as the cation (positively charged ion) appear to be important in determining the effectiveness of a given salt.

TABLE 1 PRELIMINARY TESTS

Type of grinding: Cylindrical grinding, 2-in-diam wheel
Type of wheel: White aluminum oxide, 46 grit, K hardness, 5 structure, vitreous bond
Work material: Ti 150A
Wheel depth of cut (d): 0.0005 in.
Axial feed ($d_a$): 0.050 ipr
Wheel speed (V): 2200 fpm
Work speed (v): 30 fpm

| Fluid | $G$ |
|---|---|
| Water | 0.5 |
| Air | 0.9 |
| Soluble oil | 1.1 |
| 5% aluminum chloride | 1.4 |
| 5% ammonium chloride | 1.5 |
| 5% sodium nitrite | 1.7 |
| 10% sodium nitrite | 2.0 |
| 10% sodium nitrate | 2.5 |
| 10% potassium nitrite | 3.3 |

Even though highly chlorinated and sulphonated oils give results almost as good as the sodium and potassium-nitrite solutions it was decided not to study these materials further inasmuch as they represent a fire hazard in conjunction with titanium. If titanium is ground at normal speeds (6000 fpm) the sparks are brilliant and there is real danger of the grinding swarf becoming ignited if a combustible lubricant such as oil is used. At the speeds recommended for titanium grinding (2000 fpm) the chips do not glow at all and there is no danger from fire even when a combustible fluid such as oil is used. However, it is thought best to use only non-combustible fluids in grinding titanium since it is so easy for a workman inadvertently to use too high a speed and thus set a fire.

## Systematic Study of Inorganic Salts

The encouraging results of the preliminary tests indicated that a systematic study of inorganic salts should be made. The salts

---

[1] Professor of Mechanical Engineering, Massachusetts Institute of Technology, Cambridge, Mass. Mem. ASME.

[2] Research Engineer, Ford Motor Company, Dearborn, Mich.

[3] "The Grinding of Titanium Alloys," by C. T. Yang and M. C. Shaw, Trans. ASME, vol. 77, 1955, p. 645.

Contributed by the Research Committee on Metal Processing and presented at the Diamond Jubilee Semi-Annual Meeting, Boston, Mass., June 19–23, 1955, of The American Society of Mechanical Engineers.

Note: Statements and opinions advanced in papers are to be understood as individual expressions of their authors and not those of the Society. Manuscript received at ASME Headquarters, March 24, 1955. Paper No. 55—SA-39.

[4] "How to Grind Titanium," by L. P. Tarasov, *American Machinist*, vol. 96, 1952, p. 135.

that were effective ionize readily in water to produce positively and negatively charged particles as follows

$$CA \xrightarrow[\text{water}]{} [C^+] + [A^-] \quad [2]$$

where CA represents a salt, C represents the portion that ionizes to form a positively charged particle (cation), and A represents the portion that becomes negatively charged (anion). For example, sodium nitrite which has been previously mentioned would ionize as follows

$$NaNO_2 \xrightarrow[H_2O]{} [Na^+] + [NO_2^-] \quad [3]$$

It was decided that the cation should be varied first over a wide range of elements holding the anion fixed and then the reverse procedure should be followed. Inasmuch as a wide range of nitrates is readily available it was decided to use the nitrate radical for the constant anion in the first series of tests and likewise, inasmuch as sodium salts are most common, it was decided to use sodium for the constant cation in the second series of tests.

In order that the concentration of the active ingredient be the same in all tests it was decided to use solutions of equal molarity. (A 1-molar solution contains a number of pounds of salt equal to its molecular weight in 1000 lb of solution) one-tenth molar solutions were used in all cases. Thus the sodium nitrite (MW = 69.01) solution investigated here contained 0.69 per cent by weight of the salt.

Surface grinding was chosen for these tests since the $G$-values could be more reproducibly determined under such conditions. The standard conditions under which all tests were performed are as follows:

Wheel: 7 in. diam. 3¹/₄ in. wide, white aluminum oxide, 60 grit, L hardness, 5 structure number, vitreous bond
Work material: 2 in. × 2 in. × 4 in., Ti RC 130B
Wheel speed: 2000 fpm
Work speed: 400 ipm
Cross-feed: 0.05 in/pass
Downfeed: 0.001 in.
Dressing: 4 cuts of 0.001 in. each using face of pyramidal diamond
Fluid required: 2 gal

After dressing the wheel under carefully controlled conditions it was used to remove 0.002 in. from the work surface in two steps in order to bring its surface to a constant condition. Then, after measuring the diameter of the wheel with a micrometer, the test was started. Twenty layers each of 0.001 in. depth were removed, after which the wheel was again measured. If the wheel wear was not sufficient a second series of twenty layers was removed. The amount of material removed from the work was determined by direct measurement rather than from the downfeed read from the machine. From these data it was possible to compute the values of $G$. Between fluids the wheel and all apparatus were carefully cleaned with water.

The results of the first and second series of tests are summarized in Table 2 together with some miscellaneous results (series 3). In all cases $G$ is expressed relative to the value obtained with distilled water.

The manner in which $G$ varies with concentration is illustrated in Fig. 1 for two different solutions. In the case of $NaNO_2$, there is little influence of material added in excess of 0.5 M (4 per cent by weight). The curve for barium hydroxide is similar to that for sodium nitrate and it is expected that in this case too, $G$ will continue to rise with concentration well beyond the maximum concentration of solution tested (0.1M). From Fig. 1(*a*) the value of $G$ at the optimum concentration of 0.5 is seen to be about 2.5 times that for a 0.1M solution. Thus we might expect the value of Table 2 to be greater by a factor of about 2.5 if the concentration is increased to 0.5M. The solutions of Table 2 are all more dilute than would be used in practice since dilute solutions are easier to work with.

TABLE 2 GRINDING RESULTS WITH 0.1M SOLUTIONS OF INORGANIC SALTS

| Series 1: Cation Varied | | Series 2: Anion Varied | |
|---|---|---|---|
| Salt | $G$ | Salt | $G$ |
| $LiNO_3$ | 1.58 | $Na_3PO_4$ | 3.20 |
| $NaNO_3$ | 2.14 | $Na_2S$ | 3.00 |
| $KNO_3$ | 3.06 | $Na_2SO_4$ | 2.95 |
| $CaNO_3$ | 2.78 | $Na_2B_4O_7$ | 2.69 |
| $AgNO_3$ | 0.99 | $Na_2CrO_4$ | 2.68 |
| $NH_4NO_3$ | 1.05 | NaOH | 2.65 |
| $Mg(NO_3)_2$ | 1.31 | $NaCO_3$ | 2.56 |
| $Ca(NO_3)_2$ | 2.08 | $NaNO_2$ | 2.44 |
| $Sr(NO_3)_2$ | 2.83 | NaCl | 2.22 |
| $Ba(NO_3)_2$ | 3.55 | $NaNO_3$ | 2.14 |
| $Co(NO_3)_2$ | 0.96 | **Series 3: Miscellaneous** | |
| $Cu(NO_3)_2$ | 0.98 | Air | 1.33 |
| $Cd(NO_3)_2$ | 1.04 | Distilled water | 1.00 |
| $La(NO_3)_2$ | 2.24 | $K_3(PO_4)$ | 3.60 |
| $Ce(NO_3)_3$ | 2.14 | $Ba(OH)_2$ | 3.15 |
| $Al(NO_3)_3$ | 1.12 | BaS | 2.86 |
| $Fe(NO_3)_3$ | 0.93 | $BaH\,PO_4$ | 1.11 |
| $Th(NO_3)_4$ | 1.36 | 10% water-base fluid | 1.27 |
| $Pb(NO_3)_4$ | 1.17 | 100% grinding oil | 1.97 |

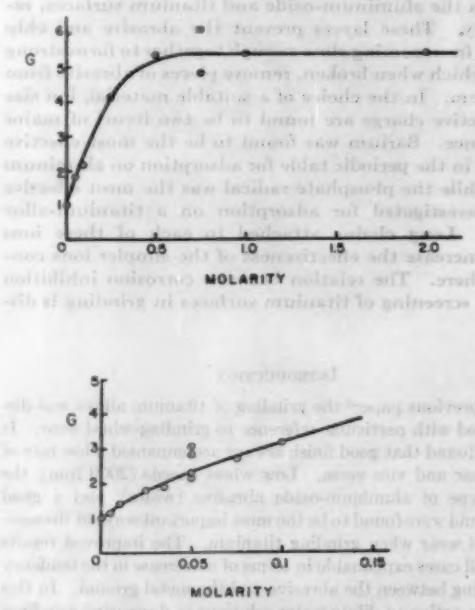


FIG. 1 VARIATION OF GRINDING FACTOR ($G$) WITH CONCENTRATION OF AQUEOUS SOLUTIONS. ALL VALUES ARE GIVEN RELATIVE TO $G$ FOR DISTILLED WATER
[(*a*) Sodium nitrate solutions; (*b*) barium hydroxide solutions.]

## CATIONIC ADSORPTION

First, let us observe the correlation that exists between the results of Table 2 (series 1) and the position of the metal in the periodic table, Fig. 2. The vertical bars shown are proportional in height to the $G$-values of Table 2 (series 1). The most effective elements are seen to be those to the left and toward the bottom of the table. After examining the variation of many properties with position in the periodic table it was found that the most closely parallel variation was found to exist between ion size and $G$-value. The variation of ion size with position in the periodic table is shown in Fig. 3 which is based on values reported by Pauling.[5] Here it is seen that, in general, the larger metal ions are found in the lower left portion of the periodic table, in the very region where the larger values of $G$ are found.

[5] "Nature of the Chemical Bond," by L. Pauling, Cornell University Press, Ithaca, N. Y., second edition, 1948.

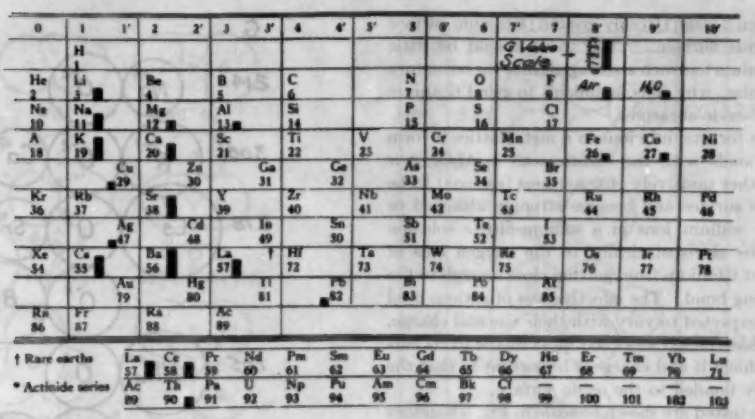


FIG. 2 VARIATION OF GRINDING FACTOR (*G*) WITH POSITION OF CATION IN THE PERIODIC TABLE

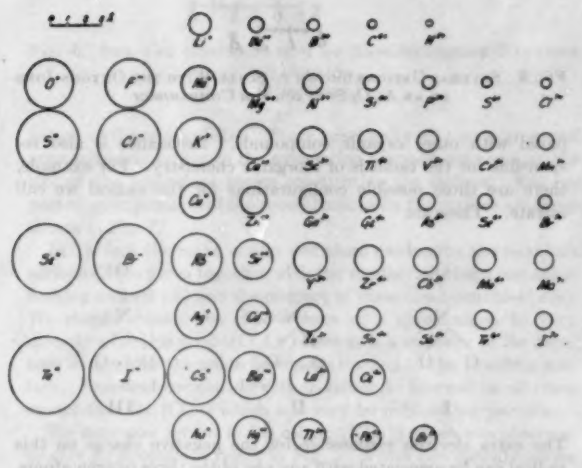

FIG. 3 VARIATION OF ION SIZE WITH POSITION IN THE PERIODIC TABLE
(After Pauling, footnote 5.)

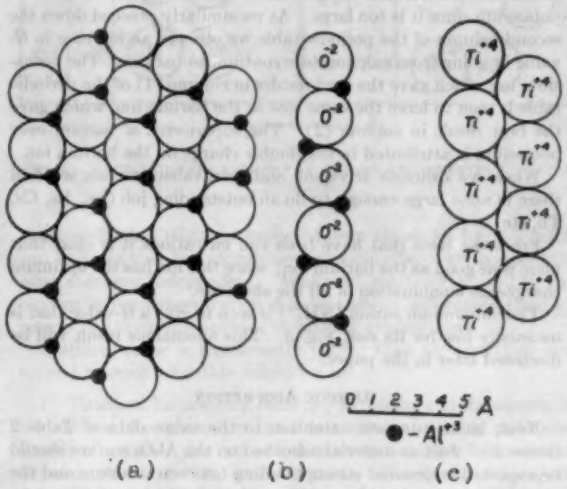


FIG. 4 ALUMINUM OXIDE AND TITANIUM SURFACES SHOWN TO SCALE
[(a) Plan view of $Al_2O_3$ surface; (b) side view of $Al_2O_3$ surface; (c) side view of titanium-metal surface (free electron cloud not shown).]

Next, let us consider why there is such good correlation between ion size and *G*-value. It is well known that aluminum oxide used in grinding wheels is $\alpha$ corundum ($Al_2O_3$) which consists of a hexagonal close-packed array of oxygen ions with aluminum ions interspersed in $^2/_3$ of the cusps between oxygen ions. The oxygen ions [$O^{=}$] are very large compared to the aluminum ions [$Al^{3+}$] as may be seen by reference to Fig. 3. Two views of an aluminum-oxide surface are shown to scale in Fig. 4. Since the components of aluminum oxide are true ions having been formed by the transfer of electrons from oxygen to aluminum atoms, the bonding responsible for the strength of this material is purely electrostatic. This type of bond is frequently referred to as an ionic bond. What we encounter in coming close to an aluminum-oxide surface is a close-packed array of oxygen ions. The aluminum ions may be ignored since they are very small and buried between oxygen ions.

Also shown to scale in Fig. 4 is a titanium surface. Titanium, being a metal, is held together by a different type of bonding force known as the metallic bond. The building blocks in a metal are positive ions produced from the neutral metal elements by removal of the valence electrons. Titanium having four valence electrons gives rise to positive ions having a quadruple charge when the valence electrons are removed. In the case of a metal, valence electrons do not transfer to other elements as in the case of an ionic crystal, but distribute themselves throughout the metal much as the molecules are distributed in a gas. The metallic bonding force arises from the interaction of the free cloud of valence electrons and the positively charged ions. The result is a structure that is close-packed and strong. The size of the ions in a metal lattice differ considerably from those in an ionic crystal since each is subject to entirely different forces. The titanium surface shown in Fig. 4 corresponds to the size of the titanium ion in a metal lattice as determined by x-ray diffraction studies.[6]

Comparison of the titanium-ion size with that of the oxygen ion in $Al_2O_3$ shows that the two are about the same. This provides the good fit essential for the formation of strong electrostatic bonding forces. The large charge difference between titanium (plus 4) and oxygen (minus 2) ions adds to the tendency for

[6] "Structural Inorganic Chemistry," by A. F. Wells, Oxford University Press, London, England, second edition, 1950.

strong bonding between a clean (freshly ground) titanium surface and an aluminum-oxide surface. Thus there should be little wonder as to why titanium has such a strong affinity for refractory oxides and, in particular, why it is so difficult to grind titanium alloys with refractory-oxide abrasives.

Just as it is possible for titanium ions in a metal lattice to form strong electrostatic bonds with the surface ions in $Al_2O_3$, it is equally possible for other positively charged ions (cations) to be attached to the oxide surface and become strongly attached or adsorbed. Thus the sodium ions in a sodium-nitrite solution can attach themselves electrostatically to the oxygen ions of $Al_2O_3$ and thus prevent titanium from getting close enough to the surface to form a strong bond. The effectiveness of cations used in this way might be expected to vary with their size and charge. Size is important in that the ion adsorbed must fit the oxide surface and completely shield it and charge is important in that the layer must be strongly bonded to the oxide surface.

A few of the cations tested are shown to scale in Fig. 5 together with the *G*-values observed. The improvement observed as we proceed from sodium to potassium is due to a better match between the sodium and oxygen ions. Cesium is not as good as potassium since it is too large. As we similarly proceed down the second column of the periodic table we observe an increase in *G*-value in going from calcium to strontium to barium. The potassium ion which gave the best results in column (1) of the periodic table is seen to have the same size as the barium ion, which gave the best result in column (2). The superiority of barium over potassium is attributed to the double charge on the barium ion.

When we examine trivalent and tetravalent metals we find there is none large enough to do an outstanding job (i.e., La, Ce, Th, etc).

From the tests that have been run on cations it is clear that none is as good as the barium ion; since this ion has the optimum charge-size combination of all the elements.

The ammonium cation $[NH_4^+]$ is seen to give a *G*-value that is unusually low for its size, Fig. 5. This anomalous result will be discussed later in the paper.

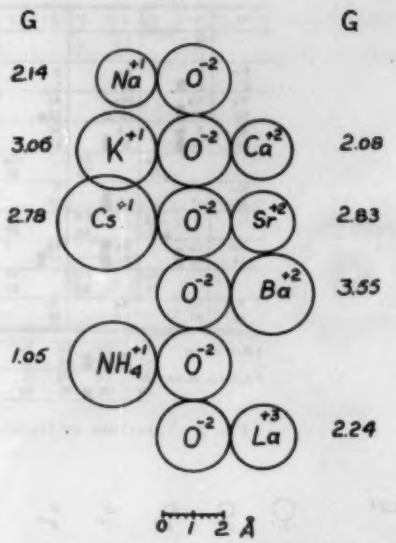


FIG. 5 SEVERAL CATIONS SHOWN TO SCALE WITH THE OXYGEN IONS OF AN $Al_2O_3$ SURFACE FOR COMPARISON

## ANIONIC ADSORPTION

Next, let us turn our attention to the anion data of Table 2 (series 2). Just as material adsorbed on the $Al_2O_3$ surface should be expected to prevent strong bonding between titanium and the abrasive, we also should expect material adsorbed on the titanium metal surface to be effective. We should further expect those anions most closely matching titanium in size and having the greatest charge to be the most effective. The comparison of results with regard to ion size is quite simple as before, but the matter of effective ion charge requires further discussion.

When we examine the anionic parts of the salts of Table 2 (series 2), we find that unlike the cations most of them consist of groups of elements called radicals rather than being simple elements themselves. A typical radical is $[NO_3^{-1}]$. This group of elements is held together by still another type of force known as a covalent bond. This is the type of bond found in practically all organic compounds. Ordinarily it is a relatively weak type of bonding force and accounts for the low strengths and decomposition temperatures of organic materials such as lubricating oils and waxes. The ordinary covalent bond arises from a sharing of electrons between two elements such as carbon and hydrogen in an organic compound.

In certain instances a valence electron responsible for bonding is shared between more than one pair of elements and when this happens it is said that the electron resonates between two or more positions. When resonance exists the binding forces are greatly enhanced and a much more stable structure exists. Resonance is responsible for the relatively great stability of benzene compared with other organic compounds. Resonance is also responsible for the radicals of inorganic chemistry. For example, there are three possible configurations for the radical we call nitrate. These are

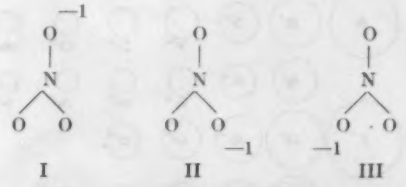


The extra electron responsible for the negative charge on this radical can be associated with any one of the three oxygen atoms. Thus any particular oxygen atom has a negative charge associated with it only $^1/_3$ of the time and hence the effective negative charge on a single oxygen atom is $-^1/_3$. The resonance between structures I, II, and III is responsible for the chemical stability of the nitrate ion and for the fact that it takes part in many chemical reactions as a unit and without decomposition.

The effective charges on any of the oxygen atoms of the negative radicals of Table 2 (series 2) can be similarly computed. As a further example we might consider the phosphate radical $[PO_4^{=}]$. In this case we have four oxygen atoms on which three charges are distributed equally in time, and hence the effective charge on a single oxygen atom is $(-^3/_4)$.

A further consideration that concerns us is the size of the elements constituting the principal inorganic radicals. The size and configuration of a number of negative radicals is shown in Fig. 6 which is from the work of Bragg. In those radicals involving oxygen (i.e., the angular $[NO_2^-]$, the planar $[NO_3^-]$, or tetragonal $[SO_4^=]$ radicals, etc.) and another element, the oxygen is large while the other element (metal) is relatively small. Thus, with regard to size, we are essentially dealing with oxygen ions of equal size arranged into different configurations in the case of all of the negative radicals of Table 2.

In Fig. 7 the anions tested are shown to scale in conjunction with the ions in a metallic titanium surface. The corresponding

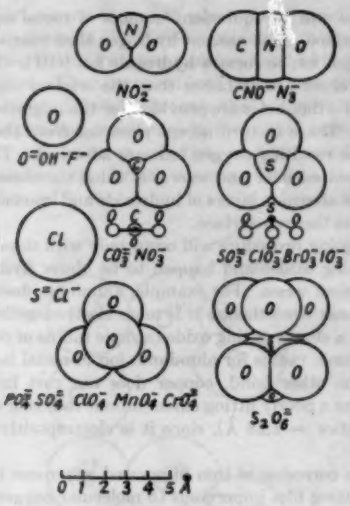


FIG. 6 SIZE AND CONFIGURATION OF REPRESENTATIVE NEGATIVE RADICALS
(After Bragg.)

values of $G$ are also listed. Since practically all ions correspond approximately in size to the oxygen ion we need not consider the size of the individual atoms constituting the cations. The expected arrangements of the several anions on the surface are those shown in Fig. 7.

In Table 3 the mean charge per atom contacting the titanium surface ($A$) is given together with the number of atoms per anion making contact ($B$) and the product of these two quantities ($AB$). We should expect the effectiveness of a given anion to vary directly with this product ($AB$) since it is a measure of the firmness with which the anion becomes attached to the titanium surface. Excellent correlation with $G$-values is observed for all cases except that for $[Cl^{-1}]$ which is a very large ill-fitting particle.

We may now return to the cation $[NH_4^+]$ which was observed to give an anomalous result in Fig. 5. From size considerations alone we should expect the ammonium radical to give a $G$-value between that for potassium and cesium, see Fig. 5, or to yield a $G$-value of about 3. However, the observed value was closer to 1. The reason for this lies in the resonating structure of this radical.

TABLE 3 REACTION BETWEEN EFFECTIVE BONDING CHARGE PER ANION AND GRINDING FACTOR

| Anion | A Mean charge per atom | B Number of bonding atoms per anion | Product $AB$ = effective bonding charge | $G$ |
|---|---|---|---|---|
| $PO_4^{\equiv}$ | $-3/4$ | 3 | 2.25 | 3.20 |
| $S^=$ | $-2$ | 1 | 2.00 | 3.00 |
| $SO_4^=$ | $-1/2$ | 3 | 1.50 | 2.95 |
| $CrO_4^=$ | $-1/2$ | 3 | 1.50 | 2.68 |
| $OH^-$ | $-1$ | 1 | 1.00 | 2.68 |
| $CO_3^=$ | $-1/2$ | 2 | 0.67 | 2.56 |
| $NO_2^-$ | $-1/2$ | 1 | 0.50 | 2.44 |
| $Cl^-$ | $-1$ | 1 | 1.00 | 2.22 |
| $NO_3^-$ | $-1/3$ | 1 | 0.33 | 2.14 |

The $[NH_4^+]$ group consists of a large nitrogen atom surrounded by four small hydrogen atoms in the form of a tetrahydron. A single positive charge resonates between the four hydrogen atoms, and thus the effective charge on a single hydrogen atom is only $(+1/4)$. Hence the $[NH_4^+]$ group behaves as though it were a potassium ion with a positive charge of $1/4$ instead of 1.

## GENERAL DISCUSSION

The values of $G$ given in Table 2 (series 3) are in general agreement with what might be expected from the series 1 and 2 tests, but indicate that the anionic and cationic effects are not strictly separable and independent. While all solutions are 0.1M the change in ion concentration due to valence differences must of course be taken into account in making comparisons.

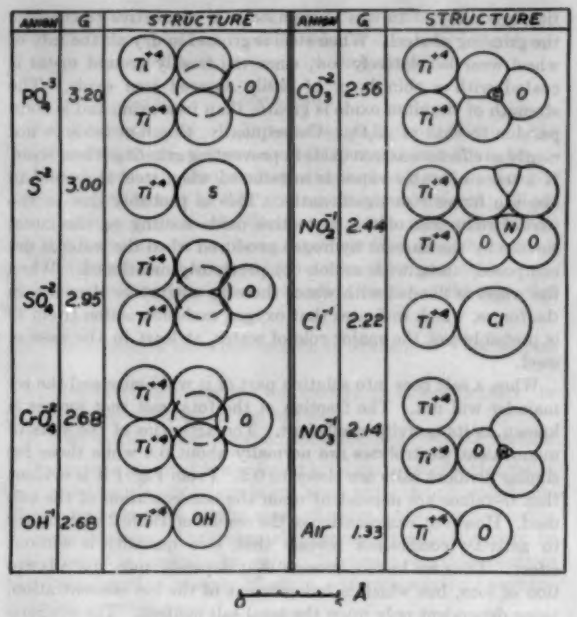


FIG. 7 EXPECTED ARRANGEMENT OF ANIONS ADSORBED ON TITANIUM SURFACE

Distilled water is significantly poorer than air and there are several reasons why this might be so:

1 Titanium has a strong tendency to oxidize and the oxygen in the air would produce a thin oxide coating on freshly produced titanium surfaces, thus providing a screening layer between the titanium and aluminum-oxide surfaces. We should not expect this action to be too effective, however, since in most instances the nascent titanium surfaces will be in contact with aluminum oxide immediately upon being formed and hence will form a strong bond with the oxygen surface of the $Al_2O_3$ rather than with the oxygen in the air. The presence of water would exclude atmospheric oxygen and thus prevent the limited beneficial effect of its presence in dry grinding.

2 Water vapor is known to decompose into its elements at elevated temperatures in the presence of titanium. The nascent hydrogen atoms that would thus be formed are known to be very small and would rapidly diffuse interstitially between titanium ions to form a titanium hydride. The presence of the hydrogen atoms in the titanium surface would enhance the positive charge associated with this surface and tend to cause even stronger bonds with the negative oxygen ions of the $Al_2O_3$ surface. Nascent hydrogen is also a positive fluxing agent.

3 Water at high temperatures will react with aluminum oxide to form the hydroxide. This material is very weak and such a reaction should increase the frequency with which particles of $Al_2O_3$ would be plucked from the surface following the formation of welds between the titanium and the abrasive.

While it is not possible to say which of the foregoing actions is most likely, it is expected that they may all contribute more or less to the poor performance of pure water as a grinding fluid for

titanium alloys. In this connection it is instructive to consider the grinding of steel. When steel is ground in dry air the rate of wheel wear is relatively low, since the freshly ground metal is coated with a thin layer of easily sheared iron oxide. The strength of titanium oxide is greater than iron oxide and is comparable to that of $Al_2O_3$. Consequently, titanium oxide is not nearly as effective as iron oxide in preventing grinding-wheel wear. If a trace of water vapor is introduced when steel is ground in air, the forces rise significantly. This is probably due to the partial reduction of the protective oxide coating on the metal surface by the nascent hydrogen produced when the water is decomposed, along with action (3) previously mentioned. When the wheel is flooded with water there is no further decrease in the forces, which indicates that oxygen exclusion action (item 1) is probably not the major role of water, at least in the case of steel.

When a salt goes into solution part of it will ionize and the remainder will not. The fraction of the total salt that ionizes is known as its activity coefficient. The activities of the salts of monovalent electrolytes are normally about 0.8 while those for similar divalent salts are closer to 0.5. From Fig. 1 it is evident that $G$-values are dependent upon the concentration of the salt used. However, examination of the results of Table 2 with regard to activity coefficients reveals that this quantity is without effect. Thus we have a process that depends upon the adsorption of ions, but which is independent of the ion concentration, being dependent only upon the total salt content. The explanation of this paradox would seem to lie in the fact that the relaxation time required for ionization is small compared with the time a particle is in close contact with the surface. Thus, while the total salt concentration would be important in influencing the probability of a particle contacting the surface at a point where needed, the question as to whether the contacting particle was ionized or undissociated upon striking the surface would be unimportant.

### Relation With Corrosion Inhibition

While there is considerable similarity between the action of corrosion inhibitors and the action of the inorganic salts of this investigation there are also important differences. For example, it is well known that whereas a very small concentration (0.1 per cent or less) of sodium nitrite ($NaNO_2$) will inhibit the corrosion of iron or steel immersed in aerated water, sodium nitrate ($NaNO_3$) is not effective in this regard. Yet, it will be observed in Table 2 (series 2) that sodium nitrate and sodium nitrite are almost equally effective in grinding. To understand the reason for this we should consider briefly the nature of the sort of corrosion considered here and the action of a corrosion inhibitor such as sodium nitrite.

When an iron specimen is exposed to dry air the rate of oxidation of its surface is very low. This rate is almost equally low in deaerated water, but is greatly accelerated when oxygen or air is entrained in the water. Corrosion is particularly rapid at the point where the specimen protrudes through a fluctuating surface since the degree of aeration is then high. If the iron surface was generated in air or exposed to air before being immersed it will be covered by a layer of adsorbed oxygen ions. However, these oxygen ions are a poor fit on the iron ions of the surface (atomic radius of oxygen ion = 1.40 Å,[7] atomic radius for iron ion in metal lattice = 1.26 Å) and hence holes will exist through which small particles can migrate.

The small particles that migrate to the surface in this case are oxygen molecules and hydrogen ions. Upon reaching the surface each hydrogen ion takes up an electron from the free electron gas of the metal and an equivalent number of metal ions are freed from the surface. The nascent hydrogen then reacts with an adjacent oxygen ion to form a hydroxide ion [$\overline{OH}$]. This particle fits the metal surface no better than the original oxygen ion, see Fig. 6, and further holes are provided for the migration of oxygen molecules. These in turn accept electrons from the metal surface and the resulting oxygen ions are adsorbed. The foregoing cycle is repeated over and over. A thick membrane of "rust" consisting of alternate layers of hydroxide and iron ions eventually developed on the iron surface.

The foregoing procedure will occur only with those metals that have ill-fitting oxides and happen to be above hydrogen in the electrochemical series. For example, aluminum does not behave in this manner even though it is more electronegative than iron, since it has a closely fitting oxide (atomic radius of oxygen ion = 1.40 Å; atomic radius for aluminum ion in metal lattice = 1.43 Å). On the other hand, copper does not rust in water even though it has a poorly fitting oxide (atomic radius of copper ion in metallic lattice = 1.28 Å), since it is electropositive relative to hydrogen.

Now, the corrosion of iron in aerated water can be prevented if a close-fitting film impervious to molecular oxygen and hydrogen ions is laid down on the surface. Sodium nitrite provides such a coating, Fig. 8. Such a layer can be adsorbed from a

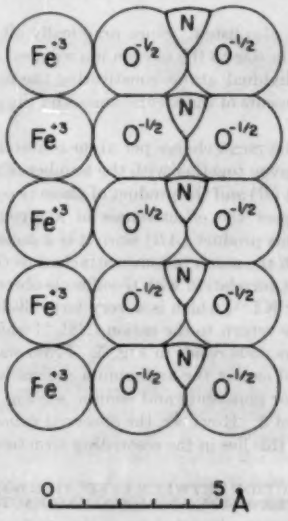


Fig. 8 Adsorbed Layer of Nitrite Ions on Iron Surface

dilute aqueous solution of a nitrite (such as sodium nitrite) or by pretreating the iron with concentrated nitric acid. In the latter case the iron is said to be rendered passive. Since concentrated nitric acid is known to be reduced by iron to form nitrite ions it would seem that iron is rendered passive in the same way when either treated by concentrated nitric acid or a dilute solution of an ionizable nitrite.

The mutual repulsive forces of oxygen atoms in the [$NO_2^-$] ions, each of which has an effective resonant charge of $-1/2$, cause an extremely close-packed arrangement and close-knit protective layer. The size of the oxygen atoms will be less in this close-packed array than in the free state, i.e., as in Fig. 6, and hence a good fit will occur on the metal surface. The close packing will not only insure a completely filled layer, but will augment the attractive electrostatic force between the inner oxygen atom and the metal surface in anchoring the coating in place.

[7] Å the Angstrom unit = $10^{-8}$ cm or 0.004 microinch.

When sodium nitrate is used in place of sodium nitrite an ill-fitting array, as shown in Fig. 9, results which is not capable of preventing the migration of oxygen molecules and hydrogen ions to the metal surface. The nitrate ion is effective, however, in raising the $G$-value since diffusion through the adsorbed film is not present in the grinding problem as in the case of corrosion. The nitrate ion is not quite as effective in titanium grinding as the nitrite ion since the former is not as firmly attached to the titanium surface.

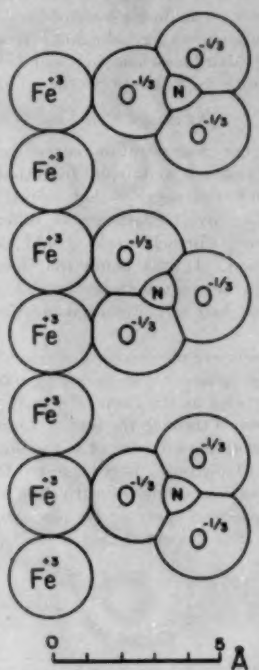


FIG. 9 ADSORBED LAYER OF NITRATE IONS ON IRON SURFACE

The effectiveness of the nitrite ion in inhibiting iron against corrosion is enhanced when an organic chain is attached to one end of the nitrite ion. This can be accomplished by reacting sodium nitrite with an organic amine to form a compound sometimes called a nitrite amine or sometimes called an ammonium nitrate

$$R-NH_2 + NaNO_2 \rightarrow R-NH_2-NO_2-Na \quad [4]$$

alkyl amine + sodium nitrite → sodium alkyl ammonium nitrite

where $R$ represents an organic chain. Sometimes all three positions on the amino nitrogen are substituted by organic groups as in the well-known vapor phase inhibitor tricyciohexylammonium-nitrite. The ammonium nitrite ionizes in water to give an ammonium-nitrite anion $[R-NH_2-NO_2^-]$ that adsorbs on an iron surface as in Fig. 8, except that $R$-chains extend outward from the outer oxygen atoms. These chains offer a further barrier to the passage of oxygen molecules or hydrogen ions to the metal surface and help hold the protective layer on the surface. Actually, the nitrite group is soluble in water and if fresh water should be substituted for the inhibited nitrite solution, rusting could occur. The organic chain attached to the nitrite group renders the ammonium-nitrite complex hydrophobic or water-repellent which in turn keeps the protective layer in place on the surface even in the presence of uninhibited water.

This development in the field of corrosion inhibition suggested that cations for grinding titanium should also have long chains attached, and work is under way with such materials.

## CONCLUSION

The systematic study of dilute inorganic aqueous solutions has revealed that these solutions are effective grinding fluids for titanium alloys due to the formation of adsorbed layers on both the aluminum oxide and freshly ground titanium surfaces. These adsorbed layers screen the titanium and abrasive surfaces and prevent strong bonds from being established between them which when ruptured result in rapid loss of abrasive material.

Three considerations govern the effectiveness of the adsorbed layer:

1 The ability of the adsorbing ion to fit the ions of the surface closely.

2 The effective charge per ion tending to anchor in place the screening ions adsorbed on the surface.

3 The length of the adsorbed ion extending from the surface.

The barium ion $[Ba^{++}]$ was found to be the most effective cation for protecting aluminum-oxide surfaces, while the phosphate ion $[PO_4^{\equiv}]$ was found to be the most effective anion for protecting titanium surfaces. Unfortunately, barium phosphate cannot be used since it is insoluble in water. Barium-hydroxide solutions have been found to be quite effective, and such solutions are noncorrosive on steel parts.

The concentration of the active ingredient was found to be important, best results being obtained with about $^1/_2$ molar concentrations.

Item 3 has not as yet been completely investigated, but initial tests reveal that even better results than those reported here are obtained by using a positive ion consisting of a long chain with a barium atom at the end or a negative ion consisting of a long-chain water-soluble organic phosphate or diphosphate.

## ACKNOWLEDGMENT

The authors wish to express their sincere gratitude to the Shell Oil Company for the grant that made this research possible.

# Discussion

L. P. TARASOV.[8] The authors have presented an entirely new picture of the functioning of the best type of water-base grinding fluid that has been found for grinding titanium. Their systematic investigation of a wide variety of inorganic compounds has led them to propose a theory based on the matching of ionic sizes, supplemented by the effect of the magnitude of ionic charge. These two factors are certainly important, but it would seem that other factors like polarizability and work function could also modify the effectiveness of the various ions in adhering to the surface.

Although the best results were obtained with solutions of barium salts, it must be remembered that these are extremely toxic and therefore they should not be used in production grinding until they have been approved by the industrial health authorities for use under whatever safeguards may be deemed necessary.

It should be pointed out that the results given in Table 2 for the 10 per cent water-base fluid (presumably a soluble oil) and for a straight grinding oil are representative of the many products in these two categories that are totally unsuitable for titanium grinding even though they are perfectly satisfactory with

[8] Metallurgical Engineer, Research and Development Department, Norton Company, Worcester, Mass. Mem. ASME.

steel. We have found, as a result of extensive laboratory testing, that only certain soluble and grinding oils are really suitable for titanium, and with these it is possible to attain far higher grinding ratios. For grinding conditions that were quite similar to those used by the authors, we have been able to obtain the following grinding ratios:

| | |
|---|---|
| Soluble oil (10 per cent concentration) | 4–5 |
| Sulfochlorinated grinding oil | 15–20 |
| Very highly chlorinated grinding oil | 25–35 |

Presumably the authors' poor results in this respect can be attributed to a deficiency of suitable surface-chemical activity in the products used.

The authors have found that increasing the concentration of sodium nitrate beyond 0.5 $M$ did not lead to any further increase in the grinding ratio. We have investigated the effect of concentration only for sodium nitrite and have not found any evidence of such a saturation value. Surface-grinding tests made in 1952 on Ti-150A with a 32A60-K8VBE wheel running at 2500 sfpm gave us the following values of $G$ for several molar concentrations, the highest corresponding to 40 per cent by weight of the salt:

| Molar concentration | $G$ |
|---|---|
| 0.00 | 1.4 |
| 0.29 | 4.9 |
| 0.58 | 5.7 |
| 2.32 | 7.6 |
| 5.80 | 9.3 |

The relationship between log $G$ and log concentration was linear from the highest concentration tried down to 0.3 $M$. This linearity may have been fortuitous but there was certainly no evidence that $G$ had leveled off beyond a certain concentration.

Since it is difficult to see why sodium-nitrite and nitrate solutions should differ so markedly with respect to the effect of concentration, it would be desirable to extend the sodium-nitrate results to higher concentrations. If the leveling-off effect is verified, it would mean that the inorganic salts found by the authors to be most effective at a concentration of 0.1 $M$ would not necessarily maintain their ranking at the much higher concentrations of commercial interest.

It is pointed out by the authors that sodium nitrite is improved as a rust inhibitor for iron by the addition of an amine. In titanium grinding, we have found that the grinding ratio is not affected in the least by adding a suitable amine, whether to a sodium-nitrite solution or to a grinding oil. It will be interesting to see if attaching other long-chain compounds to the cations, as suggested by the authors, will improve the grinding action.

### Authors' Closure

The fact that the concentration curve for sodium nitrite obtained by Dr. Tarasov is so different from that obtained by the authors for sodium nitrate suggests that the order of effectiveness of the different salts investigated may be different at high and low concentrations. Further work should be performed to answer this question. It was found that long ethylene-oxide chains attached to the phosphate group did provide a water-soluble barium phosphate salt of unusual effectiveness in titanium grinding.

With regard to adverse physiological effects of aqueous barium solutions, the only danger lies in breathing air containing very finely divided particles in the form of a mist. Such materials should not be absorbed through the skin. A mist will be dangerous if particles of solution are present in the air in the size range from about $^1/_2$ to 10 microns. It is suggested that a determination of the fluid particle size entrained in the air in the vicinity of the grinding-machine operator be made by an industrial-hygiene expert if it is suspected that a health hazard exists in any particular case.

# Selective Silica Carry-Over in Steam

By E. E. COULTER,[1] E. A. PIRSH,[2] and E. J. WAGNER, JR.[3]

**The distribution ratios of the concentrations of silica in steam to those in boiler water were determined over a range of pressures from 300 to 3140 psi, of silica concentrations in the water from 12 to 1000 ppm, and of pH values of the water from 7.8 to 12.1. Mechanical carry-over, determined by using a radioactive tracer, was insufficient to necessitate corrections to the vaporous silica carry-over data at pressures above 500 psi.**

## Introduction

STUDIES of power-station operating problems have shown that troublesome turbine-blade deposits, composed principally of silica, are formed under certain conditions of boiler operation. The severity of the silica-deposit problem has been observed to increase with increasing silica concentration of the boiler water and increasing operating pressure. The work of a number of investigators has shown that silica carry-over under such conditions is selective, the ratio of the amount of silica in the steam to that in the boiler water being greater than the corresponding ratios for other boiler-water constituents (1, 2, 3).[4] Such selective carry-over is generally believed to be due to vaporization of silica from the boiler water into the steam.

Although the problem has been investigated widely, the previous data are not complete over the range of modern boiler operation, and often the data of several investigators fail to agree. Therefore, as the first logical step in searching for a solution of the selective silica carry-over problem, a test program to determine the distribution ratios of silica concentrations in steam to those in boiler water over a wide range of conditions was undertaken and completed.

## Apparatus

The principal components of the test apparatus were a small electrically heated, natural-separation boiler, an air-cooled condenser, and sampling systems for boiler water and steam, as shown in Fig. 1. The equipment was designed for a maximum pressure of 3200 psi and a maximum steaming capacity of 100 lb/hr at 2500 psi.

Operating pressure was regulated automatically by varying the speed of the blower which supplied cooling air to the condenser, thereby controlling condensing rate. The electronic blower-speed control received its signal from a pressure recorder. The condenser was installed at a higher elevation than the boiler, so the condensate returned by gravity to the boiler.

Provision was made for continuous, simultaneous sampling of boiler water and steam. Each sampling system contained a condensing or cooling coil, flow-control valve, thermometer well,

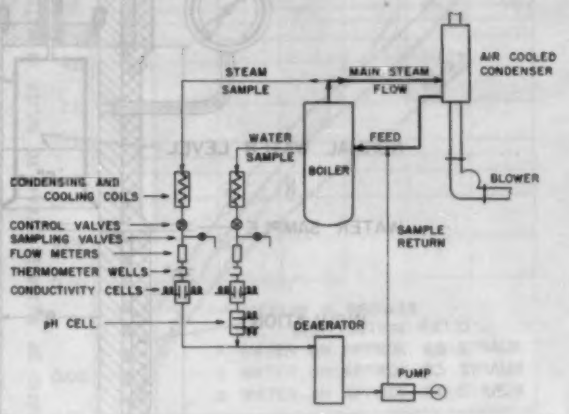


Fig. 1 Flow Diagram of Silica Carry-Over Test Apparatus

conductivity cell, flowmeter, and sample valve used to remove samples of steam condensate or boiler water from the system for silica analysis. To minimize contamination of the sample all parts upstream of the sample valves were stainless-steel or plastic tubing. In addition, a flow cell for obtaining pH of the boiler water was installed. After passing through the sampling system the samples were combined and admitted to a deaerator from which the discarded samples were returned to the boiler by a pump.

Steam was generated in the small test boiler shown in Fig. 2. Previous investigators (1, 2, 3) had experienced difficulty in obtaining accurate data because condensate, which formed on the walls of the upper unheated portions of their boilers due to heat loss, tended to absorb appreciable amounts of silica from the steam. Therefore a concentric stainless-steel liner was installed in the boiler and extended from below the water level to the steam-sampling point at the top. All steam generated was collected inside the liner and flowed upward to the steam-sampling point. The loosely fitting downward-turned elbow on the end of the steam-sampling line prevented condensate from dripping into the steam space and allowed amounts of steam in excess of the steam sample to flow to the main steam line supplying the condenser and to surround and eliminate heat loss from the liner.

Electric resistance heaters were evenly spaced on the outside boiler surface below the water level and provided a maximum heat flux of 20,000 Btu per hr per sq ft. Power to the heaters was controlled manually.

All samples were analyzed for soluble or reactive silica by the reduced silico-molybdate colorimetric method using a Beckman Model DU spectrophotometer and 100-mm cells (4). This method has sufficient sensitivity to enable measurement of silica concentrations to ± 0.002 ppm.

## Procedure

The test work consisted of two phases; the determination of the amount of silica carried over in steam at various boiler-water conditions, and the utilization of a radioactive tracer to determine the extent of mechanical, or dropwise, carry-over of boiler water.

*Silica Carry-Over Phase.* In all of the silica carry-over tests

[1] Mechanical Engineer, The Babcock & Wilcox Company, Alliance, Ohio. Assoc. Mem. ASME.

[2] The Babcock & Wilcox Company, New York, N. Y.

[3] Test Engineer, The Babcock & Wilcox Company, Alliance, Ohio. Now at U. S. Naval Station, Newport, R. I. Assoc. Mem. ASME.

[4] Numbers in parentheses refer to the Bibliography at the end of the paper.

Contributed by the Power Division and presented at the Diamond Jubilee Semi-Annual Meeting, Boston, Mass., June 19–23, 1955, of The American Society of Mechanical Engineers.

Note: Statements and opinions advanced in papers are to be understood as individual expressions of their authors and not those of the Society. Manuscript received at ASME Headquarters, March 8, 1955. Paper No. 55—SA-19.

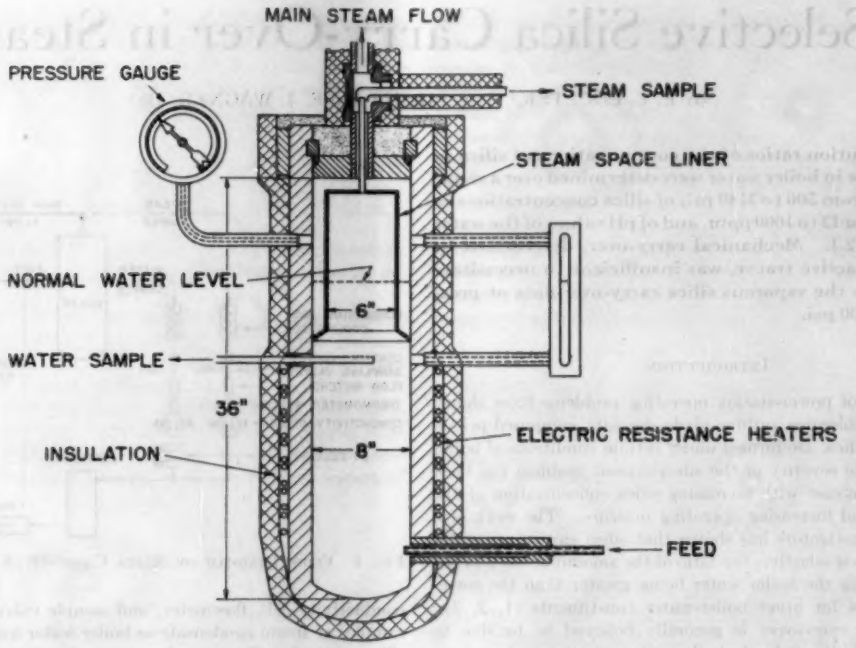


FIG. 2 TEST BOILER FOR SILICA CARRY-OVER

the boiler water was made up of distilled water that was passed through a mixed-bed ion-exchange column to reduce the conductivity to less than 0.1 micromho per cm. Only silica in the form of reagent-grade silicic acid or sodium silicate ($Na_2SiO_3 \cdot 9H_2O$) and sodium hydroxide were added to the water to produce the desired silica concentration and pH.

With seven different water solutions the boiler was operated at a constant steaming rate of 5 lb per hr and the total steam flow was sampled. One test was made with a variable steaming rate of 40 to 85 lb per hr during which the steam-sample rate was held at 5 lb per hr. The boiler-water characteristics and test conditions are summarized in Table 1.

The boiler was filled to the operating level with a water solution of one half the silica concentration desired for that test and then vented of gases by opening the steam-sample line or the condenser vent to the atmosphere while heat was applied to the boiler. Simultaneously, the one-half concentration water was pumped into the boiler to replace the vented steam until the boiler water reached the desired silica concentration. The boiler was brought up to the lowest test pressure by increasing the heat input, while maintaining the level by controlling the continuous sample flows.

To maintain a constant silica concentration in the boiler the deaerator reservoir was filled with the one-half concentration water and the steam and water were sampled at equal rates. The average concentration of the total sample leaving the boiler was approximately the same concentration as the water pumped in from the deaerator.

After reaching the desired test pressure and steaming rate the boiler conditions were held constant for at least 1 hr or until the conductivity of the steam and water samples became constant. Samples of steam condensate and boiler water were then withdrawn into 8-oz polyethylene bottles for silica analysis. During the first run at least two sets of samples were analyzed at each test point, but this was later reduced to one set after it was established that the two sets of samples consistently checked. After samples were withdrawn the boiler operating conditions were changed and the sampling process was repeated until the desired range of pressure or steaming rates was covered.

*Radioactive Tracer Phase.* Operation of the apparatus with a radioactive tracer was similar to that previously described for silica carry-over. The boiler water was a solution of radioactive phosphorus ($P^{32}$) in the form of a phosphate with sodium hydroxide added to adjust the pH to 11.0. Fifty millicuries of activity were used which produced a total boiler-water phosphate concentration of about 0.05 ppm.

The boiler was operated at the same steaming rates and pressures as for the silica carry-over tests. The conductivity and pH cells were removed from the sample lines, and samples of only 1/3 oz were withdrawn into glass bottles. Boiler conditions were held

TABLE 1 SILICA CARRY-OVER TEST CONDITIONS

| $SiO_2$ conc. in boiler water, ppm | Form of $SiO_2$ added to boiler water | Avg pH of boiler water | Test press, psig | Avg steaming rate, pph |
|---|---|---|---|---|
| 114–151 | Silicic acid | 7.8 | 500 to 2500 | 5 |
| 12–24 | Sodium silicate | 9.0 | 1500 to 3140 | 5 |
| 50–76 | Sodium silicate | 10.2 | 300 to 3000 | 5 |
| 109–194 | Sodium silicate | 11.2 | 300 to 3000 | 5 |
| 135–172 | Sodium silicate | 12.1 | 500 to 2500 | 5 |
| 622–996 | Sodium silicate | 12.1 | 2000 to 3000 | 5 |
| 119–154 | Silicic acid | 12.1 | 500 to 3000 | 5 |
| 131–160 | Sodium silicate | 11.1 | 500 to 2500 | 40–85 |

constant for at least 1½ hr at each test point before withdrawing samples.

The samples were analyzed only for total radiation by evaporating 1 ml of the sample or of a diluted sample in a planchet and assaying the residue with a Geiger-Müller type scaler. By using identical planchets for each sample and a holder that established a fixed geometrical relationship between the planchet and the Geiger-Müller tube, relative values were obtained for the steam condensate and boiler-water sample activity.

## Discussion of Results

The phenomenon of silica vaporization in a steam atmosphere has been a much investigated subject, but data have often disagreed and did not cover the full range of pressure and water conditions at which modern high-pressure boilers are operated. Straub and Grabowski's work (1, 2) was the most comprehensive with respect to boiler operation although most of their data were obtained at one pressure of 1540 psi. Jacklin and Browar (3) and Splittgerber (5) present results which vary widely from Straub's, but several factors have been recognized that could cause the variance. Brady (6) points out the necessity of controlling, or at least of measuring, the water pH, and Straub has shown the misleading effect of condensation in the steam space of the test vessel. Besides these, the question could be raised about the existence of mechanical carry-over in each test vessel. In the present investigation an attempt has been made to profit from the past work by eliminating each of the suggested sources of disagreement.

A summary of all the test points taken at a constant boiler steaming rate of 5 lb per hr is shown in Fig. 3. The ratio of silica

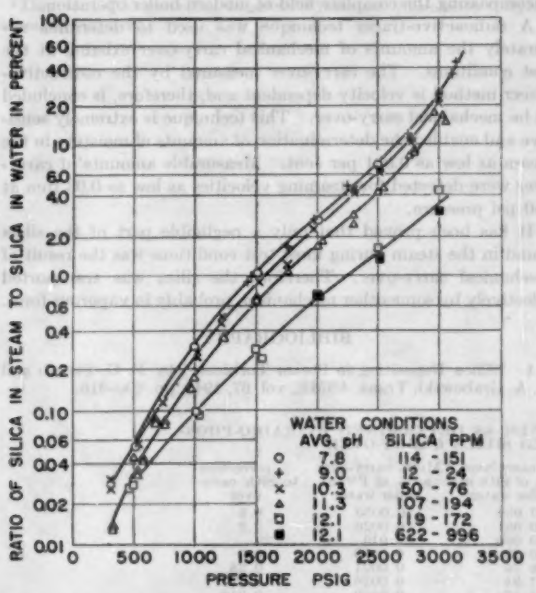


Fig. 3 Effect of Pressure, Water pH, and Silica Concentration in Water on Silica Ratio Determined at a Constant Steaming Rate of 5 Lb/Hr

concentration in steam to that in the boiler water is plotted versus pressure with four curves, each representing a different boiler-water pH. The data show an almost logarithmic increase of the silica-distribution ratio with pressure and an increase in this ratio as the water pH decreases. The effect of water pH on the silica ratio becomes greater at the higher pH values where an

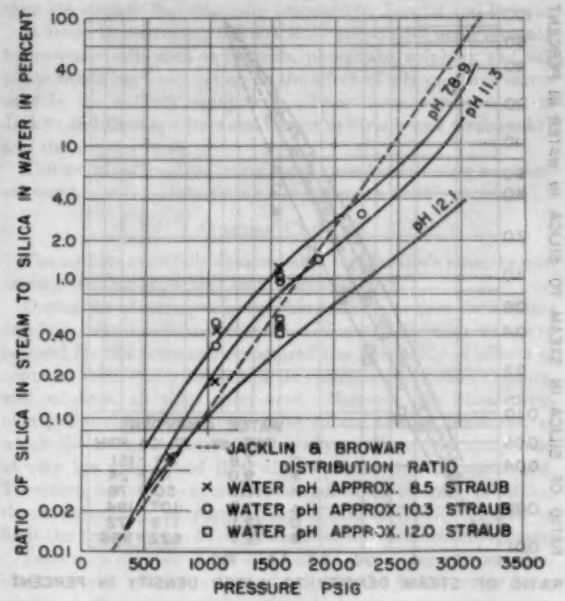


Fig. 4 Comparison of Silica Carry-Over Results With the Results of Previous Investigators

increase of pH from 11.3 to 12.1 reduces the silica ratio by 50 per cent, while an increase of pH from 7.8 to 9 shows no measurable effect. Between the limits of 10 to 1000 ppm silica in the water the silica concentration itself does not affect the distribution ratio, nor does the form in which the silica is added (silicic acid or sodium silicate) affect the distribution ratio.

The data of Straub and Grabowski (1) which were obtained by using only sodium silicate and sodium hydroxide in the boiler water are shown in Fig. 4 with several curves reproduced from Fig. 3 for comparison. The present data are in general agreement with Straub's even with respect to the effect of pH. The straight-line distribution ratio proposed by Jacklin (3) is also shown to indicate the amount the present data deviate from this straight line and also to show the magnitude of the pH effect which was not considered by Jacklin.

Several investigators (7, 8) have found that the equilibrium amount of silica in steam is a function of the steam density. It also might be expected that the silica-distribution ratio would be a function of the ratio of the density of water to that of steam, and this relationship is shown by a log-log plot in Fig. 5. When plotted in this manner the characteristic S-shape of the curves in Fig. 3 is eliminated.

One of the principal reasons for questioning the accuracy of previous selective silica carry-over data was the inability of the investigators to prove definitely the presence or absence of mechanical carry-over during their tests. Instead of assuming that mechanical carry-over is made negligible by operating at low steaming velocities as was done previously, a method was sought to determine its extent in the test boiler. Since the sensitivity of the electrical conductivity method for determining mechanical carry-over is much less than the sensitivity of the silica-measuring method, it is not applicable to this problem. Therefore mechanical carry-over was measured by a new technique, in which radioactive phosphorus ($P^{32}$) was added to the boiler water in the form of phosphate, and the amount of tracer material in condensed steam samples was measured. The sensitivity of this method surpasses by far that of any method used previously, and

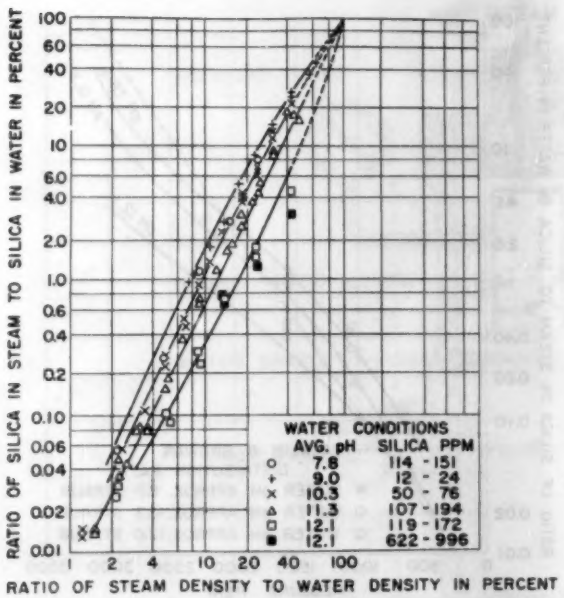


FIG. 5 SILICA RATIO VERSUS DENSITY RATIO

phosphate concentrations in the steam samples could be determined to the nearest one part in ten trillion ($10^{-7}$ ppm). Although the activity of radioactive phosphate decreases rapidly (14.3-day half-life), it was possible to measure to 0.001 per cent moisture in the steam throughout the duration of the test. Per cent moisture is determined directly by the ratio of the activity of the condensed steam samples to that of boiler-water samples, obtained simultaneously.

The supposition that the radioactive phosphate tracer is a reliable measure of mechanical carry-over is substantiated by the velocity dependence of phosphate carry-over as shown in Fig. 6. The amount of carry-over at a constant pressure of 750 psi is shown in terms of per cent moisture in the steam plotted against the average steam velocity through the 6-in-diam steam space of the boiler. The presence of mechanical carry-over at steam velocities below 1 fpm indicates that low steaming rates will not eliminate mechanical carry-over completely.

Because the amount of silica vaporized into the steam increases logarithmically with pressure, the per cent error in silica carry-over measurements caused by mechanical carry-over decreases at the higher pressures. A comparison of the per cent error in silica carry-over measured at various steaming rates is shown in Table 2. All data shown in Figs. 3, 4, and 5 were taken with a steaming rate of 5 lb per hr. At this rate mechanical carry-over was sufficient to cause an 8.6 per cent error in measured silica carry-over at 500 psi and 3.2 per cent error at 750 psi. At increased steaming rates a 29 per cent error occurs at 500 psi, but

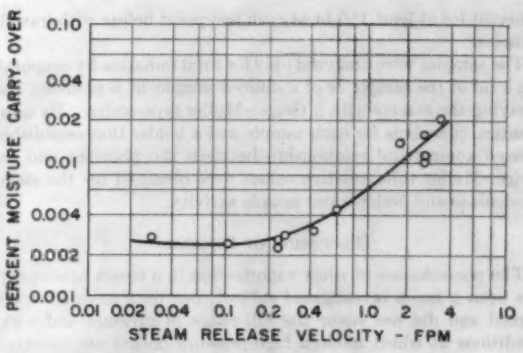


FIG. 6 EFFECT OF STEAM-RELEASE VELOCITY ON MECHANICAL CARRY-OVER, EXPRESSED AS MOISTURE CARRY-OVER, AT A CONSTANT PRESSURE OF 750 PSIG AS DETERMINED BY RADIOACTIVE-TRACER METHOD

the error decreases rapidly to 0.012 per cent at 2500 psi. Although some mechanical carry-over was found at all test conditions, the effect on silica carry-over measurements was negligible for pressures above 500 psi. Therefore only the silica carry-over data for pressures of 500 psi and below were corrected for mechanical carry-over.

## SUMMARY AND CONCLUSIONS

The distribution ratios of the concentrations of silica in steam to those in boiler water were determined over a range of variables encompassing the complete field of modern boiler operation.

A radioactive-tracer technique was used to determine accurately the amounts of mechanical carry-over existing at the test conditions. The carry-over measured by the radioactive-tracer method is velocity dependent and, therefore, is concluded to be mechanical carry-over. This technique is extremely sensitive and enabled the determination of amounts of moisture in the steam as low as 0.001 per cent. Measurable amounts of carry-over were detected for steaming velocities as low as 0.03 fpm at 750 psi pressure.

It has been proved that only a negligible part of the silica found in the steam during most test conditions was the result of mechanical carry-over. Therefore the silica was transported selectively by some other mechanism, probably in vaporous form.

TABLE 2 EFFECT OF MECHANICAL CARRY-OVER AS DETERMINED BY RADIO-PHOSPHATE TRACER ON MEASURED SILICA CARRY-OVER

| Press, psig | Steaming rate, pph | Avg steam velocity, fpm | $SiO_2$ carry-over as % of $SiO_2$ in boiler water | Mech. carry-over as % of $P^{32}$ in boiler water | % correction to $SiO_2$ carry-over |
|---|---|---|---|---|---|
| 500 | 5.5 | 0.41 | 0.058 | 0.0050 | 8.6 |
| 750 | 5.0 | 0.25 | 0.081 | 0.0026 | 3.2 |
| 500 | 49 | 3.7 | 0.066 | 0.019 | 29 |
| 1000 | 67 | 2.5 | 0.23 | 0.0070 | 3.0 |
| 1500 | 50 | 1.1 | 0.74 | 0.0021 | 0.28 |
| 2000 | 82 | 1.3 | 1.94 | 0.0026 | 0.13 |
| 2500 | 85 | 0.95 | 4.25 | 0.0050 | 0.012 |

## BIBLIOGRAPHY

1 "Silica Deposition in Steam Turbines," by F. G. Straub and H. A. Grabowski, Trans. ASME, vol. 67, 1945, pp. 309–316.

2 "Steam Turbine Blade Deposits," by F. G. Straub, University of Illinois Bulletin No. 364, June, 1946.

3 "Correlation of Silica Carry-Over and Solubility Studies," by C. Jacklin and S. R. Browar, ASME Paper No. 51—A-91, unpublished.

4 "A Spectrophotometric Determination of Small Amounts of Soluble Silica in Water," by H. E. Robison, E. A. Pirsh, and E. J. Grimm, ASME Paper No. 51—A-92, unpublished.

5 "The Volatility of Silicic Acid (Die Flüchtigkeit der Kiesel-

saüre)," by A. Splittgerber, *Archiv für Warmewirtschaft und Dampfkesselwesen*, vol. 22, 1941, p. 66.

6 "Chemical Nature of Silica Carried by Steam," by E. L. Brady, *Journal of Physical Chemistry*, vol. 57, 1953, pp. 706–710.

7 "A Portion of the System Silica-Water," by G. C. Kennedy, *Economic Geology*, vol. 45, 1950, pp. 629–653.

8 "The Solubility of Quartz and Some Other Substances in Superheated Steam at High Pressures," by G. W. Morey and J. M. Hesselgesser, Trans. ASME, vol. 73, 1951, pp. 865–875.

## Discussion

CLARENCE JACKLIN.[9] The authors are to be congratulated on the excellent design of their test apparatus for determining silica carry-over and their careful and precise test procedure. The relatively precise results indicate all the factors which influence silica carry-over were well controlled in this test work. The data also covers the full range of pressure, pH, and silica concentrations likely to be encountered in boilers where silica carry-over is a problem. These results are an important addition to the fundamental knowledge on this subject.

In Fig. 4 of the paper the authors show the straight-line distribution ratio proposed by Jacklin and Browar along with curves from their own results and points from Straub and Grabowski's work. The writer would like to offer a word of explanation about the straight-line distribution ratio. It was originally based on the assumption that values of silica in the steam from our experimental boiler were low because of steam washing. Later calculations and the authors' data show the error of this assumption. The writer considers the authors' curves to be a much more accurate representation of the distribution ratio than the straight line originally proposed by Jacklin and Browar.

It would be interesting to know if the presence of other common boiler-water salts such as chloride, phosphate, sulphite, and sulphate would have any action on the effect of pH on silica carry-over in the authors' equipment. These salts were present in Jacklin and Browar's tests and absent in Straub and Grabowski's and the authors' tests.

The use of radioactive-tracer techniques for detecting mechanical carry-over is an interesting new approach to this problem.

[9] Director of Engineering Research, National Aluminate Corporation, Chicago, Ill.

### AUTHORS' CLOSURE

The authors gratefully acknowledge Mr. Jacklin's remarks concerning the test apparatus and procedure.

During the planning stages of this research project the authors carefully considered the composition of synthetic boiler waters to be used for the tests and recognized the possibility of effects of common boiler-water salts, such as chloride, phosphate, sulphite, and sulphate, on silica carry-over. However, the silica carry-over problem is known to be most severe at high pressures, at which the concentrations of boiler-water salts are normally held at very low values, and their effects should thus be minimized. Therefore, in order to avoid a time-consuming program of testing the large number of possible combinations, it was decided to limit the test program to solutions of caustic and sodium silicate.

Tests on a number of full-size boilers containing various combinations and concentrations of salts in the boiler water have produced silica carry-over results which are in excellent agreement with the laboratory results. Consequently, the authors have concluded that, if silica carry-over is affected by boiler-water salts other than those used in the laboratory tests, the effects are minor and do not significantly alter the values reported.

# Demineralized Make-Up for 1250-PSI Installation at East Millinocket Mill of Great Northern Paper Company

By E. F. DAVIDSON,[1] BOSTON, MASS.

**In 1952 the Great Northern Paper Company planned an increase in manufacturing capacity at its East Millinocket mill from 325 to 900 tons per day of newsprint, necessitating an enlargement of its steam-generating plant. Results of studies showed that new boilers should supply 1250 psi, 850 F steam to noncondensing extraction turbine-generators, and that the maximum amount of by-product power should be generated up to the limitation imposed by steam flow through the turbines as required for process. The problem of supplying relatively large quantities of feedwater make-up of suitable quality was a major consideration. Shortly before 1952, a number of high-capacity water-treatment installations of the demineralizing type had been installed, which provided operational background for justifying the 1250-psi steam plant from this standpoint.**

## Introduction

GREAT Northern Paper Company's manufacturing plants are located at Millinocket and East Millinocket, Maine, on the West Branch Penobscot River and at Madison, Maine, on the Kennebec River. The power requirements for the two Penobscot River mills have been supplied principally in the past by a series of hydroelectric generating stations using the West Branch flow supplemented by some steam and diesel generation. The power supply for the Madison mill is not connected with the other two plants.

The boilers at both Millinocket and East Millinocket generated at low pressure (200 psi) to supply process steam to digesters, paper machines, and winter-heating loads. Small condensing turbine-generators and back-pressure units also were supplied, when needed, by the 200-psi-pressure steam. These sources of electric power were expensive to operate and were regarded only as emergency stand-by.

When Great Northern Paper Company planned, in 1952, to increase its manufacturing capacity at the East Millinocket mill from about 325 tons to 900 tons per day of newsprint, studies were made to determine the most suitable method of meeting increased process-steam and power requirements. Since the increase in paper-producing facilities necessitated an enlargement of the steam-generating plant, consideration was given to the use of high-pressure boilers with steam-turbine generators supplying extraction and exhaust steam for process while generating by-product electric power. Process steam was required at 200 psig to supply digesters and individual paper-machine mechanical-drive turbines, and at 40 psi for driers and heating, to be obtained in part from the mechanical-drive turbine exhaust, with the balance supplied from the main turbine exhaust.

The pressures investigated were 600, 850, and 1250 psi, on the basis of turbine-industry standard ratings.

Results of investigation showed that the new boilers at East Millinocket should be designed to supply 1250 psi, 850 F steam to noncondensing extraction turbine-generators, and that the maximum amount of by-product power should be generated up to the limitation imposed by steam flow through the turbines, as required for process.

It was decided in December, 1952, to proceed with the installation of two 300,000-lb-per-hr boilers and two 12,500-kw turbines, each arranged for automatic 200-psi extraction and 40-psi exhaust, both being variable within limits. Equipment was to be installed in two steps; one boiler and one turbine for the first step of the expansion to be completed in the middle of 1954, and the second boiler approximately one year later for the second step, with the second turbine to be installed at some future date if or when needed.

Because of the limited time available for completion of construction and also because of lower cost of fuel oil relative to coal, at the time, it was concluded that the boilers should be designed on the basis of fuel-oil firing only, initially, but with provision made for later addition of coal-handling equipment, coal bunkers, pulverizers, and associated apparatus. This decision resulted in substantial economies in the initial plant cost. Even though the coal facilities were not provided, future price developments may make the use of coal attractive and the door has been left open for its employment.

The problem of supplying relatively large quantities of feedwater make-up of suitable quality was a major consideration. Shortly before 1952 a number of high-capacity water-treatment installations of the demineralizing type had been installed, which provided operational background for justifying the 1250-psi steam plant from this standpoint.

## River-Water Supply

The source of raw water available for the preparation of approximately 20 per cent demineralized make-up required is the Penobscot River, which is impounded by a dam at the mill. As shown by typical water analysis in Table 1, concentrations of total dissolved mineral constituents are relatively low, thus favoring the utilization of the ion-exchange process for the economical production of condensate quality make-up. Suspended solids and other foreign matter consist of small amounts of silt and fibrous fragments from bark and leaves, and organic materials from decaying vegetable matter, respectively.

---

[1] Engineer, Mechanical Division, Stone & Webster Engineering Corporation.

Contributed by the Power Division and presented at the Diamond Jubilee Semi-Annual Meeting, Boston, Mass., June 19–23, 1955, of The American Society of Mechanical Engineers.

Note: Statements and opinions advanced in papers are to be understood as individual expressions of their authors and not those of the Society. Manuscript received at ASME Headquarters, May 20, 1955. Paper No. 55—SA-75.

TABLE 1 TYPICAL WATER ANALYSES

| Constituent | Penobscot River water | Treated and filtered water | Demineralized water |
|---|---|---|---|
| | Ppm as $CaCO_3$ | | |
| Calcium, Ca | 12 | 12 | Trace |
| Magnesium, Mg | 6.5 | 6.5 | Trace |
| Sodium, Na | 9.5 | 36.5 | Trace to 2.0 |
| Total cations | 28.0 | 55.0 | 2.0 |
| Bicarbonate, $HCO_3$ | 10.0 | 10.0 | 0 to 2.0 |
| Sulphate, $SO_4$ | 15.0 | 42.0 | Trace |
| Chloride, Cl | 3.0 | 3.0 | Trace |
| Total anions | 28.0 | 55.0 | 0 to 2.0 |
| | Parts per million | | |
| Dissolved solids | 50 | 85 | 0 to 2 |
| Suspended solids | 2 to 20 | 1 | 0 |
| Color | 35 to 50 | 3 to 5 | 2 to 4 |
| Oxygen consumed from permanganate | 18 | 3.5 to 6.5 | 2.8 to 4.0 |
| Free Carbon Dioxide, $CO_2$ | 3.0 | 12.5 | 0 |
| Silica, $SiO_2$ | 3 to 6 | 5.0 | 0.02 to 0.1 |
| Iron, Fe | 0.3 | 0.1 | Trace |
| Total hardness, as $CaCO_3$ | 18.5 | 18.5 | Trace |
| Conductivity, micromhos/-CM | ... | ... | 2 to 10 |
| pH | 5.7 to 6.7 | 6.2 | 5.5 to 9.0 |

The organic materials, indicated generally by color bodies and chemical-oxygen demand of the water, are undesirable in boiler water at pressures above 400 psi and are recognized factors that may reduce the capacities and expected life of strong base anion resins utilized in demineralizers and affect appreciably demineralizer-effluent quality. It is imperative, therefore, that suitable chemical pretreatment be employed to reduce or remove completely the objectionable constituents from surface waters which will be demineralized.

### Preliminary Investigations

A laboratory-scale test program was initiated to determine suitable treatment methods and optimum dosages of chemicals required.

Coagulation of water-color bodies, which are negatively charged colloids, was accomplished by the application of acidic coagulants such as aluminum or ferric sulphate at relatively low pH with the required dosage usually proportional to water color. Sufficient alkali was added to react with the coagulant and adjust pH. Because of the difficulty in densifying bulky color flocs, particularly in water near the freezing temperature, a coagulant aid was found necessary to produce a tough, dense, readily settleable floc. Activated silica prepared by total reaction of the sodium-oxide content of sodium silicate with sodium bicarbonate was found satisfactory for treating the colored river water.

Laboratory coagulation tests with the various treating chemicals showed that 60 ppm of aluminum sulphate, 10 to 16 ppm of alkali as sodium hydroxide, and 10 ppm to 12 ppm of activated silica utilized at pH of 6.2 resulted in good coagulation of the suspended solids and reduced chemical-oxygen demand and color to less than 5 ppm. Further reduction in chemical-oxygen demand and color in applying chlorine in quantities up to and including breakpoint and superchlorination followed by activated carbon feed was negligible. Partial chlorination of river water was considered essential, however, to prevent fouling of full-scale treating equipment and pressure-type filters.

### Pretreatment and Demineralizing Plant

The plan, arrangement, and simplified flow diagram of the pretreatment and demineralizing plant designed and installed at East Millinocket to produce boiler feedwater make-up from Penobscot River water are shown in Figs. 1 and 2, respectively. All equipment is installed indoors for convenience of operation and protection against freezing.

The pretreatment equipment designed for continuous net-output capacity of 280 gpm consists of one 4-ft-diam × 18-ft-deep steel flash mixing tank equipped with motor-driven agitator, two 13-ft-6-in-diam × 16-ft-deep "Accelator"-type clarifiers of steel construction designed for operation either singly or in parallel, three 8-ft-diam × 4-ft straight-side pressure-type filters, two wet-type feeds for alum coagulant, one wet-type feed for sodium hydroxide, equipment for preparing and feeding activated silica, level controls, and raw-water, indicating and recording flowmeter with automatic controls for proportioning chemicals to the river water delivered to the flash mix tank.

A clear well is provided below floor grade adjacent to the filters for storing 30,000 gal. Demineralizer supply and filter backwash pumps are located above the clear well.

The demineralizing equipment includes duplicate two-bed demineralizers, each consisting of 6-ft-diam cation and anion exchange units containing 70 cu ft of Nalco HCR high-capacity polystyrene resin and 85 cu ft of Nalco SBR Type I highly basic resin, respectively. Manifolds are equipped with Conoflow air-operated Saunders valve nests. Other equipment includes cycle timers for automatic control during regeneration, strong acid and caustic controlled volume pumps, regenerant mixing chambers, controls, and instruments. Semiautomatic operation is provided with push-button initiation of regeneration cycles and return to service. Maximum flow rate of 200 gpm is obtained through one pair of exchangers during regeneration of the second pair.

Horizontal steel tanks are installed for storage of 10,000 gal each of 66 deg Bé sulphuric acid and 50 per cent caustic.

A 10,000-gal acidproof tile-lined concrete tank is provided below ground grade for retention of the strong acid and caustic waste regenerants where excess acid is completely neutralized with hydrated lime prior to discharge to the mill-sewer system.

During the pretreatment process, river water is delivered to the bottom inlet of the flash mix tank located ahead of the clarifiers where alkali, alum, and chlorine solutions are introduced in proportion to water flow to develop pin-point floc during a 5-min detention time. Addition of activated silica is made to the mix-tank effluent discharging to the Accelators designed for detention of 2 hr to coagulate and settle the color bodies and suspended material. Clarified effluent from the Accelator flows by gravity through pressure-type sand filters to the clear well. Filtered water is pumped from storage through the two-bed demineralizers and delivered for boiler water to a 30,000-gal condensate return tank.

With continuous operation, complete control of the treatment process is maintained with one full-time day-shift water-plant operator and intermittent checking by a boilerhouse operator during night shifts.

A typical analysis of river, treated and filtered water, is given in Table 1.

### Performance

Performance of the Accelator clarifying units operating at design capacity with river-water temperatures ranging from near freezing to 75 F has shown that the equipment is capable of delivering effluent with less than 5-ppm turbidity as guaranteed. The conservative upflow rate of about 1 gal per sq ft per min, together with 2-hr detention, has proved of distinct advantage in handling the lightweight floc resulting from precipitation of organic material in the river water.

Operating experience has shown, however, the necessity for maintaining uninterrupted feed of chemicals and correct dosages, suitable slurry concentrations in the Accelator and control of automatic proportional blowdown of excess precipitates to obtain acceptable water from the pretreatment process.

During initial operation of the demineralizing equipment in

August, 1954, performance-test runs showed that the equipment failed to fulfill two requirements specified for the plant and guaranteed by the manufacturers, namely, that total dissolved impurities in the demineralized water would average 1 ppm and not exceed 2 ppm (as $CaCO_3$), and net exchange capacity of each anion unit would be 902 kg (as $CaCO_3$).

Initially dissolved solids content of demineralized water averaged 3 ppm because of high sodium leakage from the cation unit, a common occurrence when cations, particularly sodium in the resin bed, are not thoroughly eliminated during regeneration by the normal dosages of acid used. Since sodium in the water being demineralized constituted about 65 per cent of the total cations, it was assumed that a greater proportion of residual sodium remained in the lower layers of the resin bed following regeneration. Hydrogen ions produced in the upper part of the bed during the normal-run exchange with the sodium ions left in the lower part of the bed and result in high "leakage." Performance was considerably improved by remixing the resins with a short backwash following the cation regeneration and fast rinse.

The degree of leakage during the operating cycle which followed was reduced approximately 50 per cent and demineralized water quality improved as shown by a reduction in conductivity from average of 15 to 6 micromhos per cm.

Performance runs showed also that net exchange capacities of the anion units were about 10 per cent below specification guarantees covering the Type I highly basic resin. Although design ratings were 11 kg per cu ft, actual test runs produced slightly less than 10 kg per cu ft based on a normal silica end point of 0.1 ppm.

Several capacity runs conducted under careful supervision in November, 1954, checked results obtained during initial operation. At this time the anion-resin beds were sampled and determinations made in the laboratory to evaluate for basicity and total exchange capacity for comparison with the original resin sampled when the plant was first placed in operation. These tests showed a loss in basicity and total exchange capacity of 22 and 12.5 per cent, respectively.

Subsequent treatment of the resin samples in laboratory columns with warm 10 per cent salt solution followed by 5 per cent acid solution removed appreciable amounts of color bodies which apparently had accumulated during preliminary operation and fouled the resins. Several cycles of the salt-acid treatment followed by caustic regeneration restored the total exchange capacity to 11 kg per cu ft as shown by laboratory column tests using a "test" water for exhausting the resin bed.

A total of about 25 lb of sodium chloride, 35 lb of sulphuric acid, and 13 lb of caustic soda per cu ft of resin was found necessary during treatment to remove substantially all of the organic color from the resin.

Test runs made on the plant demineralizer units in February, 1955, after 6 months of operation showed total exchange capacities were still dropping and were 17 per cent below guarantees. It was decided therefore to treat the resin in No. 1 anion unit with the salt and acid solutions in accordance with a method worked out by Cochrane Corporation, the equipment suppliers. About a month was required to obtain a shipment of high-purity salt required for the treatment so that actual clean-up work was not started until April, 1955. At that time resin capacities were found to have further decreased to 27 per cent below guarantee.

In brief the method used for treatment consisted of dumping 800 lb of No. 1 grade rock salt on top of the anion bed, introducing hot (160 F) demineralized water to dissolve the salt to produce a 10 per cent solution and percolating the salt solution slowly down through the resin to waste. Color determinations made on the waste solutions showed from 2000 to 50,000 ppm of color extracted during this treatment.

A 5 per cent sulphuric-acid solution was next introduced to remain in contact with the resin bed for 2 hr followed by a thorough rinse and a double regeneration using a total of 10 lb of caustic soda per cu ft of resin.

Three complete treatment cycles were required to bring about substantial reduction in the amounts of color removed and improvement in total exchange capacity of the anion resin. Following the third treatment the total exchange capacity obtained during a test run was 5 per cent below guarantee. Since tests showed that color had not been completely removed from the anion resin, the unit was given a fourth treatment, but no improvement in length of run was noted.

Waste effluent color in ppm, flow rates, and concentrations of salt and acid cleaning solution used for each of the four treatments are shown in Table 2. Currently chemical-oxygen-demand tests are being conducted on some of the highly colored samples to determine whether results can be related to color index.

Table 3 gives a record of the test runs following each of the four treatment cycles.

The loss in net-output capacity due to organic fouling of the anion resin has not caused serious curtailment in production of sufficient make-up for the present boiler load. However, with two boilers and increased demand for make-up in the near future, the loss has become a matter of some concern. Present plans are to treat the anion-resin beds periodically with the salt and acid solutions and equipment is being installed to facilitate the treatment process.

Characteristic of results obtained with the use of the highly

TABLE 2 TREATMENT DATA

| Time | Per cent NaCl | Effluent color, ppm | Per cent $H_2SO_4$ | Flow, gpm |
|---|---|---|---|---|
| **Treatment No. 1—Prior to Run 80** | | | | |
| 9:30 | 1.1 | 2,000 | | 14.0 |
| 10:00 | 10.4 | 23,000 | | 14.0 |
| 10:30 | 14.4 | 15,000 | | 14.0 |
| 11:00 | 0.4 | 240 | | 14.0 |
| 11:30 | 0.0 | 15 | | 14.0 |
| Acid for 2 hr | | | 5.3 | 14.0 |
| 1:30 rinse | | | | 14.0 |
| 1:50 rinse | | | | 60.0 |
| 2:00 rinse | | | 0.0 | 170.0 |
| 3:00 unit regenerated (usual procedure) | | | | |
| **Treatment No. 2—Prior to Run 81** | | | | |
| 11:10 | 0.0 | 2 | | 14.0 |
| 11:35 | 2.9 | 2,500 | | 14.0 |
| 12:00 | 15.6 | 50,000 | | 14.0 |
| 12:30 | 16.5 | 50,000 | | 14.0 |
| 1:10 | 0.0 | 35 | | 14.0 |
| Acid for 1 hr | | | 5.0 | 14.0 |
| 2:10 rinse | | | 5.0 | 14.0 |
| 2:40 rinse | | | 5.9 | 14.0 |
| 3:10 rinse | 1.2 | | 2.0 | 28.0 |
| 3:40 rinse | 0.0 | | 0.7 | 28.0 |
| 3:50 rinse | 0.0 | | 0.2 | 170.0 |
| 4:00 unit regenerated (usual procedure) | | | | |
| **Treatment No. 3—Prior to Run 82** | | | | |
| 10:45 | 0.0 | 100 | | 14.0 |
| 11:15 | 10.5 | 11,000 | | 14.0 |
| 11:45 | 17.4 | 30,000 | | 14.0 |
| 12:00 | 12.5 | 20,000 | | 14.0 |
| 12:25 | 0.58 | 60 | | 14.0 |
| Acid for 1 hr | | | 5.1 | 14.0 |
| 1:45 rinse | | 8.0 | 5.1 | 14.0 |
| 2:15 rinse | Trace | 5.0 | 5.9 | 28.0 |
| 2:45 rinse | 0.0 | 3.0 | 1.2 | 28.0 |
| 3:45 rinse | 0.0 | | 0.2 | 170.0 |
| 3:55 unit regenerated (usual procedure) | | | | |
| **Treatment No. 4—Prior to Run 89** | | | | |
| 10:15 | 0.23 | 1,000 | | 10 |
| 10:30 | 1.1 | 6,000 | | 10 |
| 10:45 | 10.0 | 15,000 | | 10 |
| 11:00 | 20.0 | 22,000 | | 10 |
| 11:15 | 12.0 | 21,000 | | 10 |
| 11:40 | 11.0 | 21,000 | | 10 |
| 11:50 | 9.6 | 20,000 | | 10 |
| 12:00 | 7.3 | 10,000 | | 10 |
| 12:15 | .30 | 75 | | 10 |
| Acid for 1 hr and rinsed | | | | |
| 2:30 unit regenerated (cation single) (anion double) | | | | |

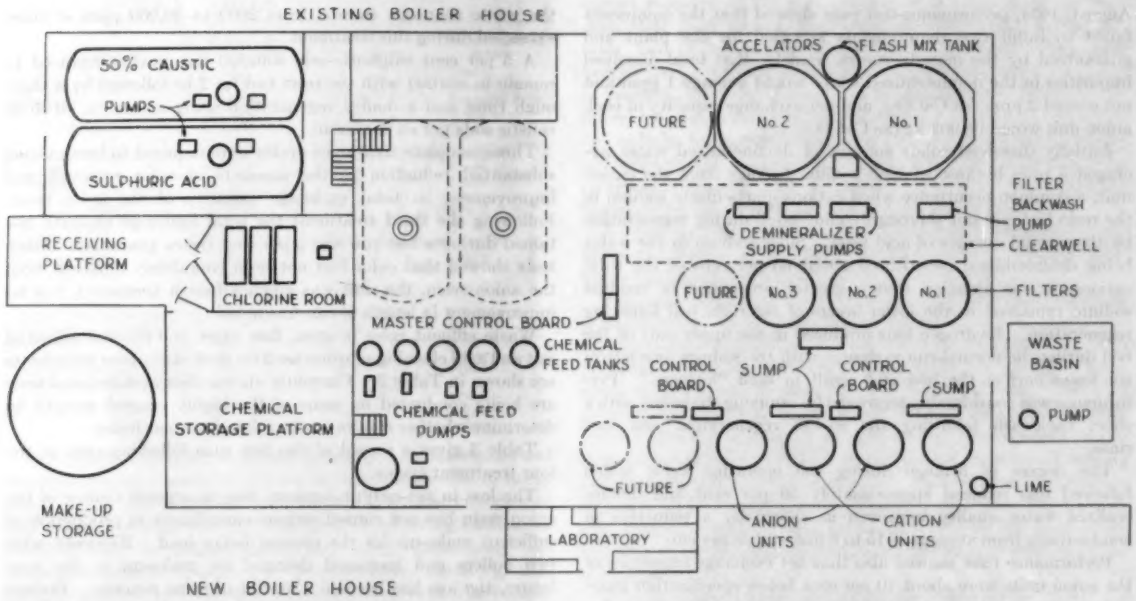


FIG. 1 PLAN ARRANGEMENT—RIVER-WATER TREATMENT AND DEMINERALIZING PLANT

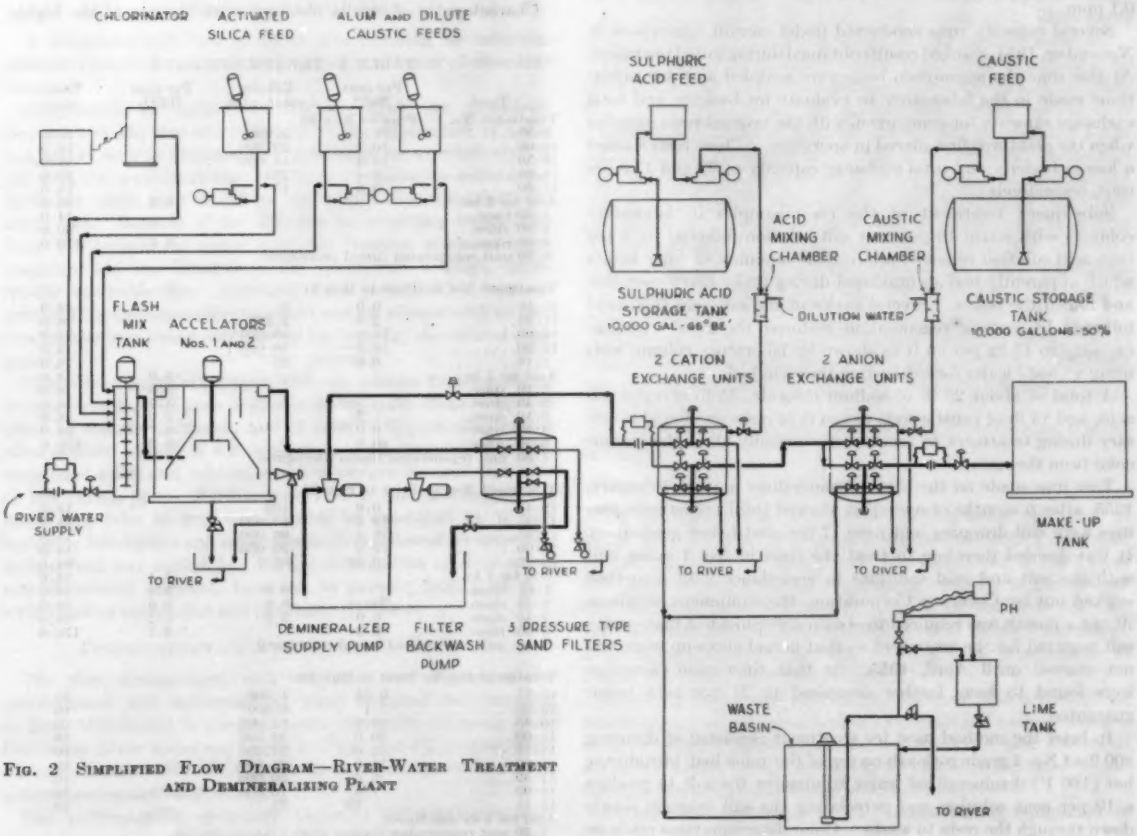


FIG. 2 SIMPLIFIED FLOW DIAGRAM—RIVER-WATER TREATMENT AND DEMINERALIZING PLANT

TABLE 3 RECORD OF TEST RUNS—DEMINERALIZING UNIT NO. 1 GREAT NORTHERN PAPER COMPANY

| Run no. | Date | Anions, gr/gal | Net output between regeneration, M gal: Guarantee—Unit No. 1 | Net output between regeneration, M gal: Actual—Unit No. 1 | Per cent under guarantee—Unit No. 1 |
|---|---|---|---|---|---|
| 80..... | 3/31/55 | 3.56 | 253 | 184 | 27.3 |
| 81..... | 4/1/55 | 3.18 | 283 | 205 | 27.5 |
| 82..... | 4/4/55 | 3.72 | 242 | 231 | 4.5 |
| 83 to 88, inc. | | | Not included as test runs | | |
| 89..... | 4/27/55 | 3.65 | 247 | 235 | 4.9 |
| 90..... | 4/30/55 | 3.90 | 231 | 214 | 7.4 |

basic anion resins, silica residuals in the demineralized water average about 0.05 ppm with maximum concentration of 0.1 ppm; thus, with 20 to 30 per cent demineralized make-up boiler water, silica concentrations have been consistently maintained within the control limits of 3 ppm without excessive blowdown.

About 2 to 4 ppm color and 5 ppm chemical-oxygen demand persist with demineralized water as shown by the analysis in Table 1, although no adverse effect on boiler operation has been noted in the 6 months of high-pressure operation. Traces of organic acids, which are not completely removed by anion exchange, resulted in lowering pH of finished water to 5.5 during a normal run. This was particularly noticeable with reduction of sodium leakage from the cation unit.

### Steam and Condensate System Clean-Up

Years of mill operation with Corliss reciprocating-engine drives for the paper machines utilizing 10 to 12-psi exhaust steam for heating paper-machine drier cylinders had resulted in fouling the steam and condensate systems as well as the driers, with oil and oily sludges.

During the mill-expansion program, existing paper-machine drives were replaced with modern steam-turbine drives, thus removing the source of oil contamination of condensate returns to be used in the high-pressure boilers. A problem of some magnitude concerned clean-up of the steam and condensate systems, and the drier cylinders of the four existing paper machines to remove accumulations of oil, sludges, scale, iron oxide, and dirt.

In April, 1954, before replacement of the Corliss engines, a cleaning program was initiated to test the effectiveness of cleaning chemicals. Solutions of Oakite No. 19, alkaline phosphate, and Oakite No. 8, a detergent, in concentrations of 1 lb and 0.25 lb per gal, respectively, were injected at rates of 18 gal per hr into the 10-psi exhaust header delivering steam to the paper machines. Two periods of application, one of 72 hr and one of 56 hr, were used initially during which condensate was discharged to waste.

Sampling points in the system were selected at the steam-header oil trap, paper-machine drier rolls, sectional condensate headers under the paper machines, and the main condensate header. Oil determinations were made on 800-cc samples of condensate using an extraction method with purified ether to remove oil.

The results of tests showed average oil concentration of samples taken at the various points before chemical addition was 9.2 ppm. The daily average for one week after termination of chemical addition was 3.3 ppm and later increased to about 5 ppm. A sample taken from the oil trap at the end of the exhaust-steam header prior to introduction of cleaning solution contained 488 ppm of oil; after treatment average oil concentrations were about 15 ppm. All sampling points showed large increases of oil concentration during chemical addition with a general increase for about five days.

As the Corliss engines for each of the four paper machines were replaced with steam turbines the cleaning program was continued, reducing concentrations of oil in the condensate to approximately 2 to 3 ppm. To clean the systems more efficiently, it was necessary to mix several hundred gallons of hot cleaning solution and circulate it through the drier cylinders of each paper machine and the condensate system during week-end shutdowns of the machine. Also, where convenient, condensate lines and traps were dismantled and cleaned mechanically to remove oily sludges. Cleaning was continued until late October, 1954, when analyses of condensate samples showed less than 1 ppm of oil. Except for short periods after week-end shutdown, condensate returns remained clear and free from oil contamination and were accepted for use in the high-pressure boiler.

With the elimination of oily exhaust steam and the removal of oily deposits from the piping and equipment, it became necessary to provide other protection against corrosion and iron pickup. In accordance with current practice a neutralizing amine is introduced to the high-pressure boiler drum to raise pH of condensed steam to 8.5.

Recent analysis of condensate samples shows average iron content is 0.26 ppm.

### Conclusion

From discussion of the water-plant design, operation, and performance covered in this paper, it is apparent that there are challenging problems to be met and solved by both the plant designer and operator in treating successfully certain classes of natural surface-water supplies prior to demineralization.

Preliminary investigations at East Millinocket as well as eight months of plant-scale operation during which approximately 35,000,000 gal of Penobscot River water have been processed satisfactorily by demineralization for high-pressure boiler operation have demonstrated the nature of these problems and revealed some of the answers.

The exacting specifications required for waters applied to the highly basic anion resins used in demineralizers have made the problem of chemical pretreatment particularly critical and one demanding extreme vigilance on the operator's part to assure success of plant operation.

### Acknowledgment

The author wishes to express appreciation to Mr. Roy V. Weldon, Executive Vice-President, Great Northern Paper Company, for his advice in preparing this paper and thank his associates in the Engineering Department and the Research and Control Department, Messrs. W. F. Daniell, Manager of Engineering, J. H. Heuer, Manager of Research and Control, D. F. Pollard, Technical Director, Roy Illingworth, Chief Chemist, and Carl Reed, Chemist, for their co-operation in conducting laboratory and field investigations and supplying data and material used.

## Discussion

S. B. Applebaum.[3] We are indebted to Mr. Davidson of Stone and Webster and his associates at the Great Northern Paper Company for this interesting preliminary account of their experiences with the Cochrane demineralizer.

When it was reported that the capacity was below normal it was at first felt that addition of more anion resin would be a solution of the problem. However, when Mr. Crits, of Cochrane's Research Department, visited the plant and returned with representative core samples of the resin for work in the laboratory, the real cause of the shortage of capacity was determined. It was

[3] Director, Water Treatment Division, Cochrane Corporation, Philadelphia, Pa. Mem. ASME.

apparent that the difficulty was due to fouling of the anion resin by color and organic matter. The problem was how best to remove this fouling impurity from the resin. Painstaking tests with various cleaning reagents in varying strengths and amounts and for varying contact periods were made until the successful method described by Mr. Davidson was determined in the Cochrane laboratory. The use of salt first followed by acid and then by caustic succeeded in dislodging the organic matter from the pores of the anion resin. Salt causes the resin particles to contract and caustic causes them to swell. This alternate contraction and swelling of the resin was successful. Capacity tests in column resin tubes were made to prove that the cleansing method finally developed would restore the capacity. We are glad that it was equally successful on a large scale with the actual plant.

The next question is what can be done to reduce this organic fouling in the future. Even though the pretreatment plant is reducing the color and organic matter to a substantial degree it is apparent that the anion resin is still continuing to absorb some of the residual color and organic matter even if only by 2 or 3 ppm. When this is multiplied by millions of gallons passing through the resin beds an accumulation of color takes place which blocks the active reacting sites in the resin particles, reducing their capacity for acid and silica adsorption.

Mr. Davidson states that the preliminary laboratory study of the necessary pretreatment before designing the plant showed that alum coagulation was sufficient and that superchlorination followed by activated carbon accomplished negligible additional reduction of color and organic matter. However, in the writer's opinion, it is precisely this small additional improvement in the pretreatment that is now necessary.

Additional tests are now being made in that direction and it is hoped the final report on this interesting installation at some future technical meeting will round out this initial progress report by Mr. Davidson by revealing a successful solution of the pretreatment problem so that the frequency of cleansing of the anion resin will be reduced to a minimum.

### Author's Closure

The comments and suggestions made by Mr. Applebaum are greatly appreciated. We wish also to express appreciation for the co-operation and interest shown by the Cochrane Corporation in making Mr. G. Crits, research engineer, available to take an active part in connection with the resin-fouling problem which occurred following preliminary operation of the demineralizing-plant equipment. The salt and acid treatment for cleaning the fouled resin developed by Mr. Crits proved to be a satisfactory method for restoring the exchange capacity of the anion units. In consideration of Mr. Applebaum's faith in the value of activated carbon for removing the final traces of organic contaminants in the clarified and filtered river water, this medium will be evaluated on small-scale laboratory-column tests.

# Power Removal From Boiling Nuclear Reactors

By P. C. ZMOLA[1] and R. V. BAILEY[2]

**The principal features of a nuclear reactor from which power is removed by boiling of the coolant within the active core are discussed. For most applications, the coolant is also the moderator and possibly the fuel carrier, and the objective is to devise a core arrangement which will permit operation at the highest power density for a given average fluid density. Calculations based on simple theoretical models are presented in performance-chart form to display the relation of influencing variables. Experimental results obtained from systems in which boiling was produced by electrical resistance heating of the liquid or simulated by bubbling air through the apparatus are summarized. A method for calculating the density distribution in a boiling system which takes into consideration explicitly the relative velocity of the vapor and liquid is presented.**

## Nomenclature

The following nomenclature is used in the paper:

$A$ = cross-sectional area of reactor core, sq ft
$A_1$ = cross-sectional area of downcomer at its top, sq ft
$A_2$ = cross-sectional area of riser at its top, sq ft
$f$ = vapor fraction, dimensionless
$g$ = gravitational force per unit mass, 32.2 ft sec$^{-2}$
$h_{fg}$ = latent heat of vaporization, Btu lb$^{-1}$
$J_0$ = Bessel function of first kind, order zero
$K_f$ = flow-loss coefficient based on circulation of liquid only, dimensionless
$K_h$ = flow-loss coefficient based on homogeneous flow, dimensionless
$K_s$ = flow-loss coefficient based on slip flow, dimensionless
$m$ = ratio of circulation flow rate to net steam flow rate, dimensionless
$P$ = average power density, Btu sec$^{-1}$ ft$^{-3}$ = 0.0373 $Kwl^{-1}$
$P_t$ = total power input which results in boiling, Btu sec$^{-1}$
$p$ = pressure
$R$ = core radius, ft
$r$ = radius, ft
$r'$ = fractional core radius, dimensionless
$u_g$ = $U_g/f$ = actual average velocity of vapor, ft sec$^{-1}$
$u_f$ = $U_f/(1-f)$ = actual average velocity of liquid, ft sec$^{-1}$
$u_r$ = actual average relative velocity of vapor to liquid, ft sec$^{-1}$
$U_f$ = velocity of liquid based on entire flow cross section, ft sec$^{-1}$
$U_g$ = velocity of vapor based on entire flow cross section, ft sec$^{-1}$
$U_0$ = reference circulating liquid velocity, ft sec$^{-1}$
$U_s$ = slip factor, ft sec$^{-1}$
$U_1$ = velocity at $A_1$, ft sec$^{-1}$
$U_2$ = velocity at $A_2$, ft sec$^{-1}$
$v_f$ = specific volume of liquid, ft$^3$ lb$^{-1}$
$v_g$ = specific volume of vapor, ft$^3$ lb$^{-1}$
$v_{fg}$ = specific-volume change in evaporation, ft$^3$ lb$^{-1}$
$w$ = mass rate of vapor generation per unit volume, lbs sec$^{-1}$, ft$^{-3}$
$Z$ = height of reactor core or active boiling height, ft
$Z_0$ = total test-section height, ft
$z$ = height, ft
$z_b$ = height above test-section inlet at which boiling is initiated, ft
$\beta$ = $A_1/A_2$
$\eta$ = fraction of vapor entrained in liquid and recirculated, dimensionless
$\rho$ = fluid density, pcf
$\rho_f$ = density of liquid, pcf
$\rho_g$ = density of vapor, pcf
$\rho_i$ = average density of riser, pcf
$\rho_0$ = average density of downcomer, pcf
$\bar{\rho}$ = average density of reactor-core fluid, pcf

*Subscripts*

$f$ = liquid
$g$ = vapor
1 = entrance to downcomer
2 = exit of riser

## Introduction

The incentive in employing boiling as a method of heat removal from the core of a water-cooled nuclear reactor arises from the effort to reduce the fixed cost of the reactor plant without a sacrifice in operating cost or dependability. In comparison with nonboiling water-cooled reactors the savings in initial investment arises from two sources: (1) For a given maximum temperature restriction the thermal efficiency of the boiling plant is higher, thus requiring a smaller plant for a given net output while the system operating pressure is lower. (2) One or more costly components such as circulating pumps and heat exchangers can be eliminated.

However, the basic simplicity of the boiling system is purchased at the expense of some design latitude in the direction of system stability and neutron economy. Stability and time-dependent operating conditions will not be considered here except to mention that several reactors have operated satisfactorily under boiling conditions. For a system in which the coolant is also the moderator the neutron economy is strongly dependent upon the density of the boiling mixture and hence upon the rate of heat removal. In a reactor in which the coolant does not function as the principal moderator it is possible to design the system such that the neutron economy is independent of the coolant density. Our attention here, however, is directed toward coolant-moderated boiling reactors.

The design objective is to devise a core arrangement from which the maximum power can be extracted for a given mean density of the boiling mixture. The fissionable material or "fuel" in the

[1] Sr. Development Engineer, Oak Ridge National Laboratory, Oak Ridge, Tenn. (operated by Carbide and Carbon Chemicals Company, for the U. S. Atomic Energy Commission). Assoc. Mem. ASME.

[2] Professor of Chemical Engineering, Tulane University, New Orleans, La.

Contributed by the Power Division and presented at a joint session of the Power and Nuclear Engineering Divisions at the Diamond Jubilee Semi-Annual Meeting, Boston, Mass., June 19–23, 1955, of The American Society of Mechanical Engineers.

Note: Statements and opinions advanced in papers are to be understood as individual expressions of their authors and not those of the Society. Manuscript received at ASME Headquarters, June 16, 1955. Paper No. 55—SA–80.

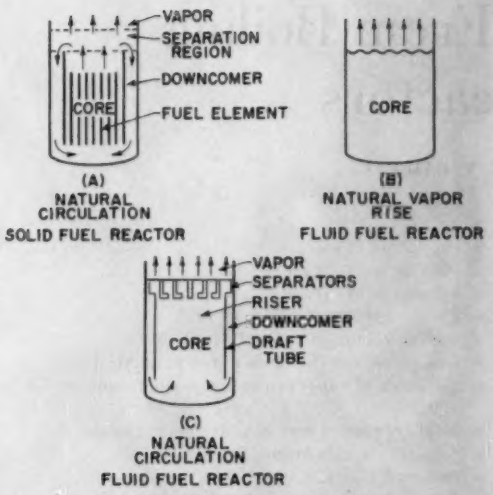


FIG. 1 SCHEMATIC DIAGRAM OF CORE ARRANGEMENTS FOR BOILING REACTORS

core can be disposed as a solid in the form of plates or rods or as a fluid in the form of solution or slurry. A schematic diagram of the core arrangement of a solid-fuel reactor is shown in Fig. 1(A). The fuel elements are disposed in the core vessel so that as boiling takes place from the surfaces of the fuel elements a circulation is established. Vapor separated from the boiling mixture in the region above the core passes into the steam dome and the remaining liquid enters the downcomer to be recirculated through the core. Clearly, a pump can be employed to augment the natural circulation.

For fluid-fuel or homogeneous reactors in which the fuel is uniformly dispersed in the moderator-coolant, two core arrangements appear feasible. In the core arrangement shown in Fig. 1(B) the natural vapor rise is depended upon to remove the steam, there being no ordered motion of the fuel mixture. If a concentric baffle or draft tube is employed to separate the core into a riser and downcomer region, as in Fig. 1(C), a gross circulation of the boiling-fuel solution can be established as in the core of the solid-fuel reactor. However, in this case, there is fuel in the downcomer as well as in the riser.

While the choice of the core arrangement for a particular application depends upon a rather large number of factors, most of which are not of direct concern in this study, it is possible to make some generalizations which indicate the constraints on the power-removal system of a boiling reactor. For large reactors, such as those that would be used in a central-power station, the long-term economy indicates a low-fuel enrichment with a conversion ratio (fissionable atoms produced from neutron capture in fertile material to fissionable atoms burned) close to 1. In such reactors heavy water would ordinarily be the moderator. This means that to reduce costs, the total inventory of fuel and heavy water as well as fuel enrichment should be held to a minimum consistent with good neutron economy. All of these factors are improved by a high moderator density. For small reactors using fuel substantially enriched in the fissionable isotope, a high moderator density is required to minimize the fuel inventory. Consequently, it is necessary to maintain a high boiling-mixture density and high utilization of fuel and special materials.

For purposes of convenience, the removal of vapor from the core can be considered as consisting of two steps: (1) The vapor generated in the interior of the reactor must be moved to the surface of the core, and (2) after having reached a surface, the vapor must be removed from the entraining liquid. The relative importance of these two problems depends upon the design of the particular reactor under consideration. Since the vapor generation is proportional to the volume of the core and the vapor separation is proportional to the surface area, the separation problem becomes more severe in comparison with vapor transport as larger reactor sizes are considered. This matter of physical size and configuration permeates most considerations both with regard to the necessity of including some devices for vapor separation and the extent to which circulation can be employed as a means of vapor transport. Accordingly, the mechanisms of vapor transport and method of vapor separation have been considered separately. The emphasis has been placed on the vapor-transport problem.

## VAPOR TRANSPORT IN THE CORE

Vapor generated in the interior of the reactor will rise as a result of its buoyancy. In addition to this natural vapor rise, the gross motion or circulation of the liquid can contribute to the vapor transport. A natural circulation can be achieved if the flow can be directed to take advantage of the variation of fluid density within the core. If necessary, circulation can be forced by means of a pump.

*Preliminary Calculations.* A simple analytical model can be used to determine in a preliminary manner the influence of pertinent variables such as core size, operating pressure, and physical properties of the coolant. It is postulated that vapor transport takes place by natural circulation only and that the boiling mixture flows as a homogeneous fluid, i.e., that adjacent liquid and vapor move at the same velocity. The calculation is based on a cylindrical reactor which is partitioned by a draft tube as in Fig. 1(C). The boiling liquid flows upward in the center, liberates a substantial part of the vapor at the top surface, and flows downward in the annular region between the draft tube and the wall of the core vessel. The details of the calculation are shown in Appendix A. The results can be displayed in the form of performance charts. Such a performance chart is shown in Fig. 2 for the case of a uniform vapor generation throughout the core (including the downcomer). Fig. 3 displays a similar chart for the core in which the vapor formation at any point is proportional to $J_0(2.405r')\sin(\pi z')$ where $r'$ is the fractional core radius and $z'$ is the fractional height. This is the power distribution one expects from an unreflected cylindrical reactor in which the moderator and fuel density are uniform. Of course, in a boiling reactor neither the power distribution nor density distribution is uniform. The actual power distribution depends upon a rather complicated function of the fluid density but these two postulates represent limits of the actual power distribution. Riser and downcomer areas were arbitrarily taken equal.

For both power distributions the expressions relating the average power density $P$ to the average fluid density decrease $(1 - \bar{\rho}/\rho_f)$ have the form

$$\frac{Pv_{fg}}{h_{fg}}\left[\frac{K_h Z}{2g}\right]^{1/3} = \Phi\left(1 - \frac{\bar{\rho}}{\rho_f}, \eta\right) \quad [1]$$

$K_h$ is a flow-loss coefficient and is equal to the number of velocity heads lost in one circulation pass. It is based on the mixture velocity at the top of the riser. $\eta$ is the fraction of the vapor entrained in the liquid and recirculated. The dependent parameter $m\ v_f/v_{fg}$ shown on the performance charts is a generalized recirculation ratio.

The rather gross assumptions that were made to permit reasonably simple calculation preclude accurate estimates of absolute values for attainable power densities in particular systems. How-

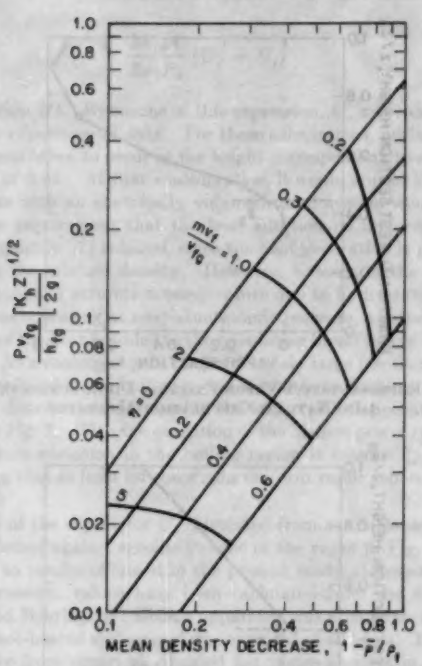


FIG. 2 PERFORMANCE CHART FOR NATURAL-CIRCULATION BOILING REACTOR BASED ON HOMOGENEOUS FLOW. POWER GENERATION UNIFORM, $\beta = 1$

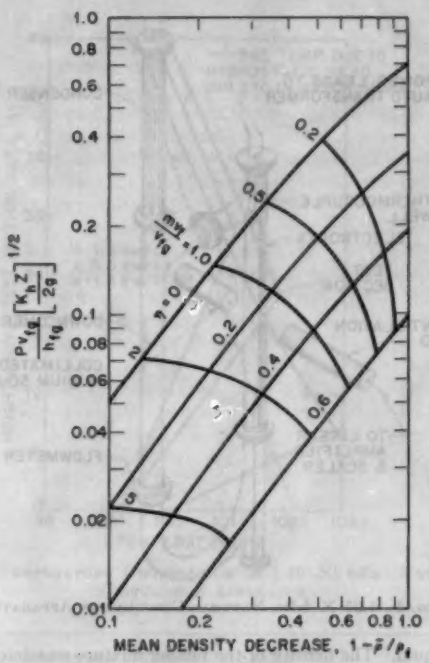


FIG. 3 PERFORMANCE CHART FOR NATURAL-CIRCULATION BOILING REACTOR BASED ON HOMOGENEOUS FLOW. POWER GENERATION PROPORTIONAL TO $J_0(2.405r')$ SIN $(\pi z')$, $\beta = 1$

ever, the objective of the calculation was to determine the pertinent variables entering the power-removal picture.

The pressure influence enters through the ratio $h_{fg}/v_{fg}$. The reality of this pressure effect depends strenuously upon the postulation that the relative velocity between the vapor and liquid is small in comparison with the circulation velocity.

The influence of hydrodynamic losses is reflected in the loss coefficient $K_h$. Its value is dependent upon the geometry of the specific system and whether additional resistances such as vapor separators are required in the circulation circuit.

The power-removal capability of a unit falls off rather rapidly with increasing vapor entrainment in the downcomer. Following current steam-generator practice, $\eta$ should have a value close to zero; in any event, it is likely that $\eta > 0.2$ will be excessive. Vapor separators can be employed to reduce vapor recirculation. However, they must be capable of operating under conditions of low total-pressure drop or the value of the loss coefficient $K_h$ will become too large for effective operation. Referring to the performance charts, it can be seen that for a given-average density decrease, a vapor entrainment of $\eta = 0.2$ reduces the power-density equivalent to about a fourfold increase in the loss coefficient $K_h$.

The operating mean-density decrease for a specific reactor is set by nuclear requirements. The range of interest is $0.15 < (1 - \bar{\rho}/\rho_f) < 0.40$. From the performance charts the corresponding values of the recirculation ratio $m$ fall between 10 and 100 over a range of pressures. This indicates the premium that exists to employ natural convection since a circulating pump must handle large flow rates of essentially saturated water, and if coolant holdup is important, in a radiation field.

The power density varies inversely with the square root of the height and is independent of the diameter. For homogeneous flow when heat is generated in the downcomer a subsidiary calculation indicated that the optimum ratio of riser to downcomer areas was approximately 3 instead of 1 as assumed for the calculations presented. However, the relationship of the various variables was not influenced sufficiently to warrant either a recalculation or inclusion of the ratio as a parameter.

*Experimental Work.* In order to check the realism of the analytical considerations and to obtain further information on the dependence of power-removal capability upon average fluid density, several experimental systems were studied. Results presented here were obtained from two systems in which volume boiling was produced by electrical resistance heating of dilute acid and salt solutions. Both were natural-circulation systems and were generally similar in design. The test section of one was $1.25 \times 4$ in. in cross section while that of the other was $6 \times 6$ in. The test sections in both were 4 ft high.

A schematic drawing of the $1.25 \times 4$-in. system is shown in Fig. 4. The circulation loop consisted of two vertical legs of 4-in. glass pipe 6 ft high with connecting sections at the top and bottom. Stainless-steel electrodes were mounted in one leg. Each of the two electrodes was made by welding a flat strip of steel across the chord of a longitudinal strip cut from a length of pipe. The curved portion of the electrodes roughly conformed to the inside diameter of the glass pipe and the flat section formed the test region. A flowmeter was installed in the downcomer leg. The flowmeter used was either an orifice or a cooling coil with thermocouples mounted upstream and downstream. A reflux condenser was mounted above the downcomer leg.

Vertical density distributions through the test section were obtained by measuring the attenuation of a collimated gamma-ray beam by the boiling fluid. The gamma source was iridium 192. The detector was a scintillation counter employing a thalium-activated sodium-iodide crystal. The output from the photomultiplier tube was fed to a linear amplifier and then to a scaler with an internal timing circuit. At each station a count rate was obtained with the test section empty and also completely filled

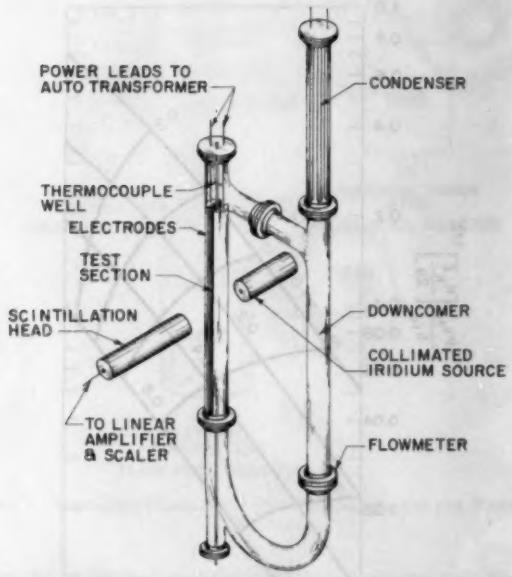


FIG. 4 1.25 × 4-IN. NATURAL-CIRCULATION APPARATUS

with liquid. The density of the boiling mixture was determined from the count rate obtained under operating conditions by assuming the count-rate increases as a simple exponential with increasing fraction vapor. The assumption of a simple exponential was shown to be valid in subsidiary experiments. The fraction vapor could be measured with a precision of 3 per cent without difficulty.

Temperature traverses of the test section were made in a few runs with a movable thermocouple within a 4-mm-OD glass tube which passed vertically through the center of the test section.

Experiments were also performed with four static systems in which air was supplied at the bottom of the test vessel and bubbled through the liquid. System diameters were 4, 6, 24, and 69 in. The 6-in. system was square in cross section; 6 in. was the hydraulic diameter. Active heights investigated ranged from 0.5 to 8.7 ft. The density of the liquid-gas mixture was determined by measuring the liquid level before and during the passage of air through the system.

*Summary and Analysis of Available Experimental Information.* It was observed that for static systems the vapor velocity $U_g$ based on the entire cross-sectional area of the test region could be represented by

$$U_g = U_s \frac{f}{1-f} \quad [2]$$

where $f$ is the fraction vapor and $U_s$ is only a slowly varying function of the geometry and fluid properties. The true average vapor velocity $u_g$ is

$$u_g = \frac{U_g}{f} = \frac{U_s}{1-f} \quad [3]$$

On the premise that the velocity of the vapor relative to the liquid $u_r$ ($u_r = u_g$ in static systems) should be the same in dynamic as in static systems, the expression for this slip velocity in a dynamic system is

$$u_r = \frac{U}{f} - \frac{U_f}{1-f} = \frac{U_s}{1-f} \quad [1]$$

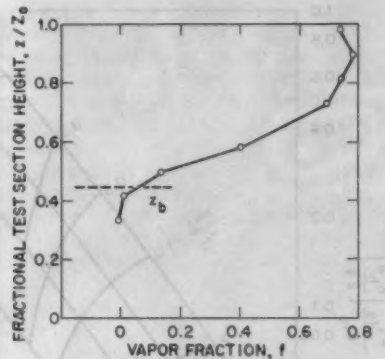


FIG. 5 REPRESENTATIVE VAPOR-FRACTION DISTRIBUTION IN 1.25 × 4-IN. NATURAL-CIRCULATION APPARATUS

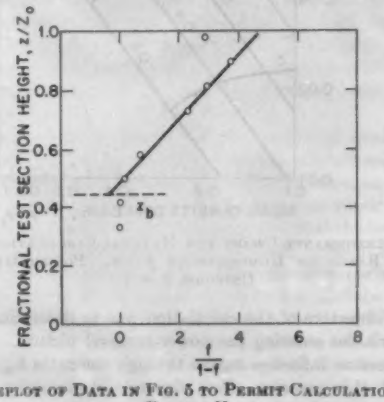


FIG. 6 REPLOT OF DATA IN FIG. 5 TO PERMIT CALCULATION OF SLIP FACTOR $U_s$

where $U_f$ is the liquid velocity based on the total cross-sectional area of the test section. Accordingly, the vapor velocity for a dynamic system is given by

$$U_g = (U_f + U_s) \frac{f}{1-f} \quad [5]$$

For the particular case in which the power input to the system is uniform, the vapor velocity, as a function of the height from the inlet of the test section $z$ is given by

$$U_g = \frac{P_g \rho_f (z - z_b)}{A h_{fg} \rho_g Z} \quad [6]$$

where $P_g$ is the total power from which vaporization results, $A$ is the cross-sectional area of the flow channel, $z_b$ is the point of initiation of boiling, and $Z$ is the total boiling height. Equations [5] and [6] can be combined to give

$$\frac{(z - z_b)}{Z_0} = \frac{Z h_{fg} A}{Z_0 \rho_g P_t} (U_f + U_s) \frac{f}{1-f} \quad [7]$$

which defines the vertical vapor-fraction distribution and hence the density distribution. $Z_0$ is the total test-section height.

A representative density distribution obtained from the 1.25 × 4-in. circulating system is shown in Fig. 5. Each point represents the average of four values obtained from four traverses made during the run. The data have been replotted in Fig. 6 to correspond in form to Equation [7]. The slope of the line representing the data corresponds to the factor

$$\frac{Zh_{fg}A}{Z\omega_g P_t}(U_f + U_s)$$

in Equation [7]. By means of this expression, $U_s$ was calculated from the experimental data. For these calculations, initiation of boiling was taken to occur at the height corresponding to a vapor fraction of 0.05. At first consideration, it would appear that experiments with an electrically volume-heated system would not meet the requirement that the heat addition be uniform upon which Equation [7] is based, since the heat generation is proportional to the mixture density. However, because of the appreciable change in saturation temperature due to hydrostatic head in systems operating at near-atmospheric pressure, a rather large fraction of the heat is added to the circulating liquid before boiling begins. As a consequence, a proportionately large fraction of the vapor produced in the boiling region results from flashing. Temperature distributions obtained in the 1.25 × 4-in. apparatus are shown in Fig. 7. With the exception of the highest power run, the temperature variation in the boiling region is reasonably linear indicating that at least for some runs uniform vapor generation is achieved.

Values of the slip factor $U_s$ calculated from available data are shown plotted against specific volume of the vapor in Fig. 8. In addition to results obtained in the present study at near-atmospheric pressure, values have been calculated from the data of Cook[3] and Behringer.[4] Cook's apparatus was a natural-circulation surface-heated system and was operated at 600 psia. Boiling took place from electrically heated flat plates about 4 in. wide. Two combinations of plate-spacing and height were employed, namely, $^1/_8$-in. channel, 5 ft high, and $^7/_{16}$-in. channel, 4 ft high. Water entering the test section was slightly subcooled in all of the runs. The Behringer apparatus was a natural-vapor-rise system in which vapor was generated at the bottom and bubbled through a tube initially filled with water to a height of 8.2 ft. Tube diameters of 2.25, 2.72, and 3.25 in. were used and the pressure range from atmospheric to 600 psia was covered. For this system values of $U_s$ could be calculated by means of Equation [2] since the vapor fraction did not change with height.

Since the slip velocity must go to zero at the critical pressure, the line representing the data has been extrapolated to pass through this point. Data for pressure above 600 psia are not available. Slip factors above this pressure should be considered plausible values. Greater weight was given to slip factors calculated from the Behringer data since they were subject to fewer assumptions regarding the operating conditions of the system. The range within which half the slip-factor values calculated from circulating-system data fell is indicated by brackets. All values were used in calculating the average at a given pressure since it was difficult to establish to what degree the actual operating condition corresponded to the assumptions upon which Equation [7] is based. In natural-vapor-rise systems all data fell within 20 per cent of the average value.

The influence of geometry and fluid physical properties other than vapor specific volume on the slip factor appear small. Subsidiary tests with a static system in which air was bubbled through glycerin and methanol as well as water gave similar values of the slip factor. In these tests the surface tension varied by a factor of 2.5 and the dynamic viscosity by a factor of 500. Results of experiments with the air-water apparatus indicate that

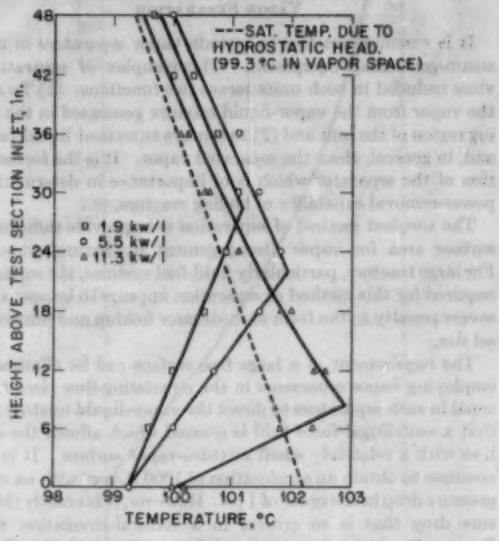
---SAT. TEMP. DUE TO HYDROSTATIC HEAD. (99.3 °C IN VAPOR SPACE)
□ 1.9 kw/l
○ 5.5 kw/l
△ 11.3 kw/l
HEIGHT ABOVE TEST SECTION INLET, in.
TEMPERATURE, °C

FIG. 7 TEMPERATURE DISTRIBUTION IN 1.25 × 4-IN. NATURAL-CIRCULATION APPARATUS

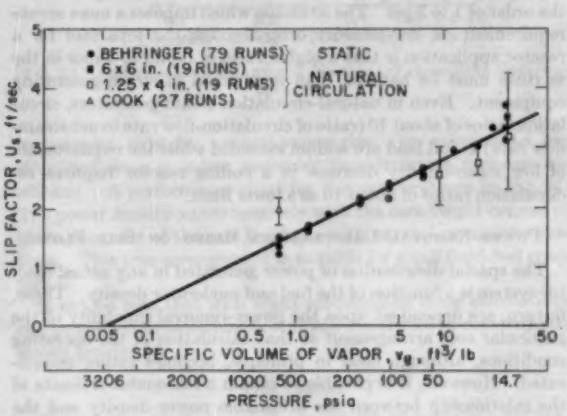
• BEHRINGER (79 RUNS)
■ 6 x 6 in. (19 RUNS)
□ 1.25 x 4 in. (19 RUNS)
△ COOK (27 RUNS)
STATIC
NATURAL CIRCULATION
SLIP FACTOR, $U_s$, ft/sec
SPECIFIC VOLUME OF VAPOR, $v_g$, ft³/lb
PRESSURE, psia

FIG. 8 SLIP FACTOR $U_s$ FOR STEAM-WATER MIXTURES AS A FUNCTION OF PRESSURE

the slip factor is independent of height and decreases slightly with increasing diameter.

It is interesting to notice that implicit in the vapor-transport picture represented by Equation [5] is that the ratio of vapor velocity to liquid velocity is constant.[5]

The method of calculating the vapor transport as a function of the boiling-mixture density outlined here should be considered tentative; the work is clearly preliminary. However, the method does appear to preserve the features of boiling-liquid flow essential to calculating the mixture density in the range of interest in boiling-reactor calculations. It has the advantage of separating the calculation of the density distributions from that of pressure drop in circulating systems; the coupling between the two is a reference circulating liquid velocity $U_s$. In the case of natural-vapor-rise systems, no pressure-drop calculation is necessary.

[3] W. H. Cook, Argonne National Laboratory, personal communication.

[4] "Wasserumlauf in Dampfkesseln," by E. Schmidt, P. Behringer, and W. Schurig, *VDI Forschungsheft 365*, 1934. A translation of this paper is on file at the Technical Library, Y-12 Plant, Carbide and Carbon Chemicals Company, Oak Ridge, Tenn.

[5] At a cross section where the vapor fraction is $f$, the actual average vapor velocity is $u_g = U_s/f$; the actual liquid velocity is $u_f = U_f/1 - f$. Accordingly, the ratio of vapor velocity to liquid velocity is $(U_f + U_s)/U_f$.

### Vapor Separation

It is common practice to include vapor separators in modern steam-generating equipment. The complex of separation devices included in such units serves two functions: (1) To remove the vapor from the vapor-liquid mixture generated in the steaming region of the unit and (2) to remove entrained liquid particles and, in general, clean the separated vapor. It is the former function of the separator which is of importance in determining the power-removal capability of boiling reactors.

The simplest method of separation is to provide sufficient free-surface area for vapor disengagement by natural vapor rise. For large reactors, particularly fluid-fuel systems, the surface area required for this method of separation appears to impose a rather severe penalty in the form of moderator holdup and pressure-vessel size.

The requirement of a large free surface can be eliminated by employing vapor separators in the circulating-flow circuit. It is usual in such separators to direct the vapor-liquid mixture flow so that a centrifugal-force field is created which affords the separation with a relatively small mixture-vapor surface. It is rather common to obtain an acceleration of 1000 ft/sec$^2$ with an over-all pressure drop in the order of 1 psi. However, it is exactly this pressure drop that is so critical in a natural-circulation system. For most systems the pressure difference available for operating the separator plus-flow losses in the remainder of the system is in the order of 1 to 3 psi. The situation which imposes a more severe requirement on low-pressure drop through the separator for a reactor application is that a higher ratio of liquid to vapor in the mixture must be handled than is common in steam-generating equipment. Even in natural-circulation steam generators, circulation ratios of about 10 (ratio of circulation-flow rate to net steam-flow rate) at full load are seldom exceeded while the requirements of low mean-density decrease in a boiling reactor requires recirculation ratios of about 10 as a lower limit.

### Power-Removal Calculations Based on Slip Flow

The spacial distribution of power generated in any actual reactor system is a function of the fuel and moderator density. These, in turn, are dependent upon the power-removal capability of the particular core arrangement so that calculation of the operating conditions, although clear in principle, becomes rather complicated. However, it is possible to obtain a reasonable estimate of the relationship between the attainable power density and the average boiling-mixture density for a number of core arrangements by postulating that the energy is added in some simple manner.

The power-removal capability of the three core arrangements discussed in the introduction have been calculated employing the two-phase flow model given by Equation [5] under the postulation that the power generation is uniform. The calculations are outlined in Appendix B. For both the solid and fluid-fuel natural-circulation systems it was postulated that no vapor was entrained at the top of the downcomer ($\eta = 0$). In the fluid-fuel system, for which a performance chart is shown in Fig. 9, the ratio of riser to downcomer area was arbitrarily taken as three ($\beta = 1/3$). The region of uniform heat generation extended over the downcomer. The power density is based on the entire core volume. A performance chart for the solid-fuel system is shown in Fig. 10. The power density is based on the riser (fuel-region) volume only; no heat is generated in the downcomer.

These performance charts are similar in form to those prepared on the basis of homogeneous flow with the exception of an additional parameter $K_s U_s^2/2gZ$ by which the influence of the slip factor is taken into consideration.

The power density for a given-average fluid-density decrease

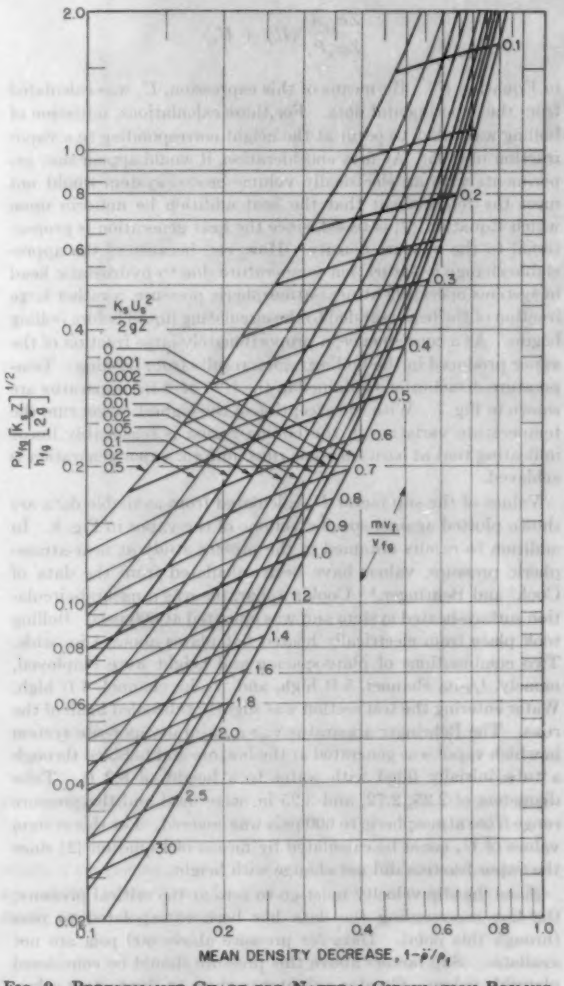


Fig. 9 Performance Chart for Natural-Circulation Boiling Reactor Based on Slip Flow. Power Generation Uniform in Riser and Downcomer, $\beta = 1/3$

and operating pressure can be calculated by means of the performance charts in the following manner.[6]

1 For a given-average density decrease an approximate value of $m$ can be found from the circulation-rate parameter $mv_f/v_{fg}$ corresponding to a value of $K_s U_s^2/2gZ = 0$.

2 For a given operating pressure and a specified distribution of vapor generation, the pressure loss in one circulation pass is a unique function of the weight-flow quality at the top of the riser. The weight-flow quality is equal to $1/m$. Charts of multipliers that can be applied to a calculated single-phase pressure drop to obtain the two-phase pressure drop have been prepared by Martinelli and Nelson.[7] Employing these charts or an equivalent method of calculation, the flow-loss coefficient $K_s$ can be obtained.

[6] An example is worked in Appendix C.

[7] "Prediction of Pressure Drop During Forced-Circulation Boiling of Water," by R. C. Martinelli and D. B. Nelson, Trans. ASME, vol. 70, 1948, p. 695. The details in the calculation of the loss coefficient $K_s$ from the multipliers given in the above paper are shown in Appendix C.

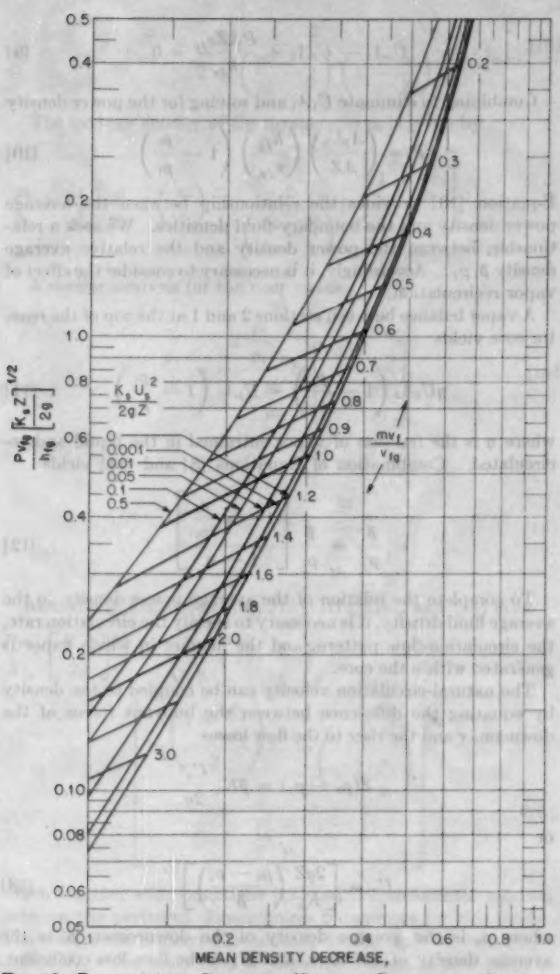


FIG. 10 PERFORMANCE CHART FOR NATURAL-CIRCULATION BOILING REACTOR BASED ON SLIP FLOW. POWER GENERATION UNIFORM IN RISER. NO POWER GENERATED IN DOWNCOMER

3 $U_s$ is a function of operating pressure only and can be obtained from Fig. 8. The parameter $K_s U_s^2/2gZ$ can then be calculated and an improved value of $m$ can be obtained from the performance chart.

4 An improved value of $K_s$ is then calculated. This process is rapidly convergent and two iterations are usually sufficient.

5 The power density can now be calculated from the value of the ordinate

$$\frac{Pv_{fg}}{h_{fg}}\left[\frac{K_s Z}{2g}\right]^{1/2}$$

corresponding to the mean density decrease $(1 - \bar{\rho}/\rho_f)$ and the parameter $K_s U_s^2/2gZ$.

Fig. 10, the performance chart for the solid-fuel reactor, can be used to calculate the power density attainable in a single channel as a function of the average density in that channel. Such a relationship can be used to take into consideration the radial power distribution in a reactor core. To account for a nonuniform vertical power distribution a new chart must be prepared.

For the reactor-core arrangement in which the generated vapor is removed only by natural-vapor rise, the calculations are simplified since it is not necessary to calculate a flow-loss coefficient. A performance chart for this case is shown in Fig. 11. The power density varies inversely with the core height instead of the square root of the core height as with natural-circulation systems. This core arrangement is suitable for small fluid-fuel reactors.

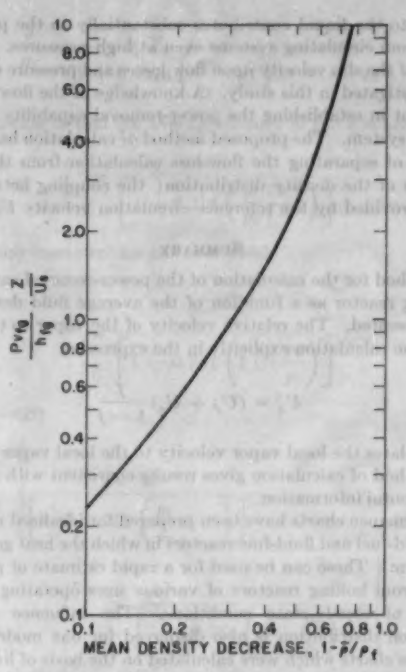


[FIG. 11 PERFORMANCE CHART FOR NATURAL-VAPOR-RISE BOILING REACTOR

It can be seen that with slight modification these calculations can be applied to determination of flow conditions in conventional steam generators.

## DISCUSSION

The relationship between the transport of vapor in a boiling-liquid mixture and the mixture density as given by Equation [5] is supported by existing experimental information. The relationship must be considered tentative in the sense that a prudent designer would like the range and limits of applicability more completely defined and the experimental information upon which it is based more firmly established. Briefly, the principal features of the proposed flow model are:

1 The relative velocity of the vapor to the liquid depends primarily upon the local vapor fraction and not upon the circulating flow rate.

2 The value of the slip factor $U_s$ depends primarily upon the specific volume of the vapor and only weakly upon geometry and other physical properties.

3 A corollary of (2) is that the ratio of the local vapor velocity to the local liquid velocity is essentially constant with distance along the channel.

Further experiments with circulating systems are needed over a range of pressures. In particular, no complete data exist for pressures over 600 psia.

As applied to reactors, it appears that the velocity of the vapor

relative to the liquid contributes substantially to the power removal from circulating systems even at high pressures. The influence of the slip velocity upon flow losses and pressure drop was not investigated in this study. A knowledge of the flow losses is important in establishing the power-removal capability of a circulating system. The proposed method of calculation has the advantage of separating the flow-loss calculation from the determination of the density distribution; the coupling between the two is provided by the reference circulation velocity $U_0$.


### Summary

A method for the calculation of the power-removal capacity of a boiling reactor as a function of the average fluid density has been presented. The relative velocity of the vapor to the liquid enters the calculation explicitly in the expression

$$U_g = (U_f + U_0)\frac{f}{1-f}$$

which relates the local vapor velocity to the local vapor fraction. The method of calculation gives results consistent with available experimental information.

Performance charts have been prepared for idealized models of both solid-fuel and fluid-fuel reactors in which the heat generation is uniform. These can be used for a rapid estimate of power removal from boiling reactors of various sizes operating under a variety of steady-state conditions. The influence of heat-generation distribution is also displayed for one model in performance charts which were calculated on the basis of homogeneous flow.



### Acknowledgments

The authors wish to acknowledge the work of M. Richardson and H. A. MacColl, who helped assemble and run most of the experimental apparatus, and of W. S. Brown, who helped in some of the early studies.


# Appendix A

### Homogeneous Flow-Reactor Models

To analyze the case in which all of the vapor transport is provided by natural circulation of the core fluid, the following postulations were made:

1 The reactor core is cylindrical. The core fluid flows in an annular downcomer region to the bottom of the reactor core, reverses, and flows through the riser region in the center to the top of the reactor core.

2 At the top of the downcomer, the average fluid velocity normal to the annular cross-sectional area $A_1$ is $U_1$. At the top of the riser, the average fluid velocity normal to the central cross-sectional area $A_2$ is $U_2$. All of the circulating fluid passes through $A_1$ and $A_2$, respectively.

3 As the fluid flows from area $A_2$ to $A_1$, a vapor separation is affected and an equal mass rate of saturated liquid is added so that the average density of the fluid increases from $\rho_2$ to $\rho_1$.

4 The circulation velocities are sufficiently greater than the vapor velocities relative to the liquid that the fluid may be considered homogeneous.

5 The reactor core has a uniform cross-sectional area $A = A_1 + A_2$.

Conservation of mass requires that

$$U_1A_1\rho_1 = U_2A_2\rho_2 \quad [8]$$

A volumetric balance requires that

$$U_1A_1 - U_2A_2 + \frac{PAZv_{fg}}{h_{fg}} = 0 \quad [9]$$

Combining to eliminate $U_1A_1$ and solving for the power density

$$P = \left(\frac{A_2U_2}{AZ}\right)\left(\frac{h_{fg}}{v_{fg}}\right)\left(1 - \frac{\rho_2}{\rho_1}\right) \quad [10]$$

Equation [10] provides the relationship between the average power density and the boundary-fluid densities. We seek a relationship between the power density and the relative average density $\bar{\rho}/\rho_f$. Accordingly, it is necessary to consider the effect of vapor recirculation.

A vapor balance between sections 2 and 1 at the top of the reactor core yields

$$\eta U_2A_2\left(1 - \frac{\rho_2}{\rho_f}\right) = U_1A_1\left(1 - \frac{\rho_1}{\rho_f}\right) \quad [11]$$

where $\eta$ is the fraction of vapor entrained in the liquid and recirculated. Combination of Equations [8] and [11] yields

$$\frac{\bar{\rho}}{\rho_f} = \frac{\bar{\rho}}{\rho_1}\left[\frac{1 - \eta\dfrac{\rho_1}{\rho_2}}{1-\eta}\right] \quad [12]$$

To complete the relation of the average power density to the average fluid density, it is necessary to specify the circulation rate, the circulation-flow pattern, and the manner in which vapor is generated within the core.

The natural-circulation velocity can be coupled to the density by equating the difference between the buoyant forces of the downcomer and the riser to the flow losses

$$Z(\rho_0 - \rho_i) = \bar{\rho}K_h\frac{U_2^2}{2g}$$

or

$$U_2 = \left[\frac{2gZ}{K_h}\left(\frac{\rho_0 - \rho_i}{\bar{\rho}}\right)\right]^{1/2} \quad [13]$$

where $\rho_0$ is the average density of the downcomer, $\rho_i$ is the average density of the riser, and $K_h$ is the flow-loss coefficient. Although the flow losses enter Equation [13] in a rather rudimentary fashion, the essential influence of the variables is preserved. For a given system, the turning, friction, and acceleration losses all depend in first approximation on the product of the density and the square of the velocity.

For the specification of the circulation-flow pattern and the manner in which vapor is generated within the reactor core, two models are considered.

*Case I.* The rate of vapor formation occurs uniformly throughout the reactor core and the cross-sectional area of the riser $A_2$ is equal to that of the downcomer $A_1$.

Considering a differential height of the annular downcomer and writing a volumetric balance for this element gives

$$\frac{d}{dz}(A_1U) - \frac{PA_1v_{fg}}{h_{fg}} = 0 \quad [14]$$

where $U$ is the velocity in the upward direction.

Conservation of mass for the downcomer requires

$$UA_1\rho + U_1A_1\rho_1 = 0 \quad [15]$$

Noting that $A/A_1 = 2$, a combination of Equations [10], [14], and [15] and a subsequent integration with respect to the height $z$ yields

$$\frac{\rho}{\rho_1} = \frac{2}{2 + \left(\frac{\rho_1}{\rho_2} - 1\right)\left(1 - \frac{z}{Z}\right)} \quad \ldots\ldots [16]$$

The average density of the downcomer $\rho_0$ is given by

$$\frac{\rho_0}{\rho_1} = \int_0^1 \frac{\rho}{\rho_1}\, d\left(\frac{z}{Z}\right) = \frac{2}{\left(\frac{\rho_1}{\rho_2} - 1\right)} \ln\left[\frac{1 + \frac{\rho_1}{\rho_2}}{2}\right] \quad \ldots\ldots [17]$$

A similar analysis for the riser yields

$$\frac{\rho_i}{\rho_1} = \frac{2\,\frac{\rho_2}{\rho_1}}{1 - \frac{\rho_2}{\rho_1}} \ln\left[\frac{2}{1 + \frac{\rho_2}{\rho_1}}\right] \quad \ldots\ldots [18]$$

Also

$$\frac{\bar{\rho}}{\rho_1} = \frac{\rho_0 + \rho_i}{2\rho_1} = \frac{\ln \frac{\rho_1}{\rho_2}}{\frac{\rho_1}{\rho_2} - 1} \quad \ldots\ldots [19]$$

Assembling Equations [10], [13], [17], [18], and [19] gives

$$\frac{Pv_{fg}}{h_{fg}}\left[\frac{K_h Z}{2g}\right]^{1/2} = \frac{1}{\sqrt{2}}\left(1 - \frac{\rho_2}{\rho_1}\right) \left[\frac{\ln\left(\frac{1 + \frac{\rho_1}{\rho_2}}{2}\right) - \ln\left(\frac{2}{1 + \frac{\rho_2}{\rho_1}}\right)}{\ln \frac{\rho_1}{\rho_2}}\right]^{1/2} \quad \ldots\ldots [20]$$

which together with Equations [12] and [19] defines the relation between the pertinent dimensionless parameters for this model. The results are displayed graphically in Fig. 2.

*Case II.* The mass rate of vapor formation at any point is directly proportional to $J_0(2.405r')$ sin $(\pi z')$, where $r'$ is the fractional core radius $r/R$, and $z'$ is the fractional core height $z/Z$. The cross-sectional area of the riser $A_2$ is equal to that of the downcomer.

In a manner similar to that of Case I, conservation of mass for the downcomer demands

$$U_1 A_1 \rho_1 \int_{\rho_1}^{\rho} \frac{d\rho}{\rho^2} = Cv_{fg} R^2 Z \int_1^{z'} \left[\int_{r'=0.707}^{1} 2\pi r' J_0(2.405r')\, dr'\right] \sin \pi z' dz' \quad \ldots\ldots [21]$$

where $C$ is a constant. Performing the indicated integration

$$U_1 A_1 \rho_1 \left(\frac{1}{\rho_1} - \frac{1}{\rho}\right) = -0.0928 C v_{fg} R^2 Z(1 + \cos \pi z') \quad \ldots\ldots [22]$$

The average power density is

$$P = Ch_{fg} \int_0^1 \int_0^1 2r' J_0(2.405r') \sin \pi z' dr' dz' = \frac{Ch_{fg}}{3.63} \quad \ldots\ldots [23]$$

Combination of Equations [8], [11], [22], and [23] gives

$$\frac{\rho}{\rho_1} = \frac{1}{1 + 0.1073\left(\frac{\rho_1}{\rho_2} - 1\right)(1 + \cos \pi z')} \quad \ldots\ldots [24]$$

Integrating to find the average density of the downcomer

$$\frac{\rho_0}{\rho_1} = \frac{1}{\left[1 + 0.214\left(\frac{\rho_1}{\rho_2} - 1\right)\right]^{1/2}} \quad \ldots\ldots [25]$$

A similar treatment for the riser yields

$$\frac{\rho_i}{\rho_1} = \frac{\frac{\rho_2}{\rho_1}}{\left[1 - 0.784\left(1 - \frac{\rho_2}{\rho_1}\right)\right]^{1/2}} \quad \ldots\ldots [26]$$

Accordingly

$$\frac{\bar{\rho}}{\rho_1} = \frac{1}{2}\left\{\frac{1}{\left[1 + 0.214\left(\frac{\rho_1}{\rho_2} - 1\right)\right]^{1/2}} + \frac{\frac{\rho_2}{\rho_1}}{\left[1 - 0.784\left(1 - \frac{\rho_2}{\rho_1}\right)\right]^{1/2}}\right\} \quad \ldots\ldots [27]$$

Equations [10], [13], [25], and [26] give

$$\frac{Pv_{fg}}{h_{fg}}\left[\frac{K_h Z}{2g}\right]^{1/2} = \left(1 - \frac{\rho_2}{\rho_1}\right)\left(\frac{\rho_1}{\bar{\rho}}\right)^{1/2} \left\{\frac{1}{\left[1 + 0.214\left(\frac{\rho_1}{\rho_2} - 1\right)\right]^{1/2}} - \frac{\frac{\rho_2}{\rho_1}}{\left[1 - 0.784\left(1 - \frac{\rho_2}{\rho_1}\right)\right]^{1/2}}\right\}^{1/2} \quad \ldots\ldots [28]$$

Equations [12], [27], and [28] define the relation between the dimensionless parameters for this model. The results are displayed graphically in Fig. 3.

The circulation ratio $m$ is defined by

$$m = \frac{\text{circulating flow rate}}{\text{steam rate}} = \frac{U_2 A_2 \rho_2}{\frac{PAZ}{h_{fg}}} \quad \ldots\ldots [29]$$

Substituting for $U_2$ from Equation [13] and rearranging

$$\frac{Pv_{fg}}{h_{fg}}\left[\frac{K_h Z}{2g}\right]^{1/2}\left[\frac{mv_f}{v_{fg}}\right] = \frac{1}{2}\left[\frac{\rho_0 - \rho_i}{\bar{\rho}}\right]^{1/2}\left(\frac{\rho_2}{\rho_f}\right) \quad \ldots [30]$$

Substitution of Equation [13] into Equation [10] gives

$$\frac{Pv_{fg}}{h_{fg}}\left[\frac{K_h Z}{2g}\right]^{1/2} = \frac{1}{2}\left[\frac{\rho_0 - \rho_i}{\bar{\rho}}\right]^{1/2}\left(1 - \frac{\rho_2}{\rho_1}\right) \quad \ldots [31]$$

Combining Equations [30] and [31] gives

$$\frac{mv_f}{v_{fg}} = \frac{\frac{\rho_2}{\rho_1}\left(\frac{\rho_1}{\rho_f}\right)}{\left(\frac{\rho_1}{\rho_2} - 1\right)} \quad \ldots\ldots [32]$$

which is plotted as a dependent parameter in Figs. 2 and 3.

# Appendix B

## Slip-Flow-Reactor Models

Calculation of the relationship between the power density and the mean fluid density for the case in which the relative velocity of the vapor is taken into consideration is similar to that for homogeneous flow. Referring to Appendix A, only postulation 4 is replaced by considering the vapor velocity at any cross section of the flow path is given by Equation [5]. For simplicity, calculations are based on $\eta = 0$, and uniform vapor generation ($w$ = const).

Conservation of mass requires

$$\frac{d}{dz}\left[\frac{U_f}{v_f} + \frac{U_g}{v_g}\right] = 0 \quad [33]$$

In the downcomer the velocity will be considered positive downward so that Equation [5] becomes

$$U_g = (U_f - U_s)\frac{f}{1-f} \quad [34]$$

A volumetric balance of vapor generated in the downcomer yields

$$\frac{dU_g}{dz} = -wv_g \quad [35]$$

Eliminating $U_f$ in Equation [33] by substitution from Equation [34], performing the indicated differentiation, and combining with Equation [35] gives

$$\frac{U_g}{v_g}\frac{d}{dz}\left(\frac{1-f}{f}\right) - \left[\frac{v_f}{v_g} + \left(\frac{1-f}{f}\right)\right]w = 0 \quad [36]$$

Relating the circulation-flow rate to the liquid velocity at the entrance to the downcomer, $U_0$, the conservation-of-mass expression becomes

$$\frac{U_0}{v_f} = \frac{U_g}{v_g} + \frac{U_f}{v_f} \quad [37]$$

Elimination of $U_f$ between Equations [34] and [37] gives

$$U_g = \frac{U_0 - U_s}{\left[\frac{v_f}{v_g} + \left(\frac{1-f}{f}\right)\right]} \quad [38]$$

which can be substituted into Equation [36] to obtain the expression

$$\int_{\infty}^{\frac{1-f}{f}} \frac{d\left(\frac{1-f}{f}\right)}{\left[\frac{v_f}{v_g} + \left(\frac{1-f}{f}\right)\right]^2} = \int_Z^z \frac{wv_g}{U_0 - U_s}\,dz$$

Performing the indicated integration and eliminating the vapor fraction $f$ by means of the relation $\rho = \rho_f(1-f) + \rho_g f$ results in an expression for the density distribution in the downcomer

$$\frac{\rho}{\rho_f} = \left[1 + \frac{wZv_{fg}}{U_0 - U_s}\left(1 - \frac{z}{Z}\right)\right]^{-1} \quad [39]$$

The average downcomer density is given by

$$\frac{\rho_0}{\rho_f} = \int_0^1 \frac{\rho}{\rho_f}\,d\left(\frac{z}{Z}\right) = \frac{U_0 - U_s}{wZv_{fg}}\ln\left[1 + \frac{wZv_{fg}}{U_0 - U_s}\right] \quad [40]$$

In the riser, the density distribution and average density can be obtained in a manner similar to that for the downcomer with the exception that the circulation velocities of the vapor and liquid are considered positive upward. This results in the slip factor $U_s$ preserving the positive sign in Equation [5] and the vapor-balance expression becoming

$$\frac{dU_g}{dz} = wv_g \quad [41]$$

The conservation-of-mass expression related to the liquid-flow rate at the entrance to the downcomer becomes

$$\frac{U_0\beta}{v_f} = \frac{U_g}{v_g} + \frac{U_f}{v_f} \quad [42]$$

where $\beta$ is the area ratio $A_1/A_2$. The corresponding expression for the vapor velocity is

$$U_g = \frac{U_0\beta + U_s}{\left[\frac{v_f}{v_g} + \left(\frac{1-f}{f}\right)\right]} \quad [43]$$

Performing the analogous operations yields the density distribution

$$\frac{\rho}{\rho_f} = \left[\frac{\rho_f}{\rho_2} - \frac{wZv_{fg}}{U_0\beta + U_s}\left(1 - \frac{z}{Z}\right)\right]^{-1} \quad [44]$$

and the average density

$$\frac{\rho_i}{\rho_f} = -\frac{U_0\beta + U_s}{wZv_{fg}}\ln\left[1 - \frac{wZv_{fg}}{U_0\beta + U_s}\left(\frac{\rho_2}{\rho_f}\right)\right] \quad [45]$$

for the riser.

The vapor liberated from the core at the top of the riser must be equal to that generated in the core

$$wZ(\beta + 1) = \frac{U_{g2}}{v_g} \quad [46]$$

substituting for $U_{g2}$ from Equation [43] and expressing $f_2$ in terms of density at the top of the riser, $\rho_2$, the expression becomes

$$\frac{wZv_{fg}}{U_0\beta + U_s} = \left(\frac{\rho_f}{\rho_2} - 1\right)\left(\frac{1}{\beta + 1}\right) \quad [47]$$

At the bottom of the core the density in the riser and downcomer must be equal; accordingly, by Equations [39] and [44]

$$\left(\frac{\rho_f}{\rho_2} - 1\right) = \frac{wZv_{fg}}{U_0 - U_s} + \frac{wZv_{fg}}{U_0\beta + U_s} \quad [48]$$

Substitution of Equation [47] into Equation [48] gives

$$\frac{wZv_{fg}}{U_0 - U_s} = \left(\frac{\rho_f}{\rho_2} - 1\right)\left(\frac{\beta}{\beta + 1}\right) \quad [49]$$

Notice that Equation [47] can be substituted into Equations [44] and [45], and Equation [49] can be substituted into Equations [39] and [40] to give density distributions and average densities as a function of the riser outlet-density ratio $\rho_2/\rho_f$. Specifically

$$\frac{\rho_0}{\rho_f} = \frac{1}{\left(\frac{\rho_f}{\rho_2} - 1\right)\left(\frac{\beta}{\beta + 1}\right)}\ln\left[1 + \left(\frac{\rho_f}{\rho_2} - 1\right)\left(\frac{\beta}{\beta + 1}\right)\right] \quad [50]$$

and

$$\frac{\rho_i}{\rho_f} = -\frac{1}{\left(\frac{\rho_f}{\rho_2}-1\right)\left(\frac{1}{\beta+1}\right)} \ln\left[1-\left(1-\frac{\rho_2}{\rho_f}\right)\left(\frac{1}{\beta+1}\right)\right] \quad \ldots\ldots [51]$$

The average density in the reactor is

$$\frac{\bar{\rho}}{\rho_f} = \left(\frac{\beta}{\beta+1}\right)\frac{\rho_0}{\rho_f} + \left(\frac{1}{\beta+1}\right)\frac{\rho_i}{\rho_f} = \frac{-1}{\left(\frac{\rho_f}{\rho_2}-1\right)} \ln\frac{\rho_2}{\rho_f} \quad \ldots\ldots [52]$$

Finally, the natural-circulation velocity can be coupled to the density by equating the difference between buoyant forces in the downcomer and riser to the circulating-flow losses[8]

$$Z(\rho_0 - \rho_i) = K_s \rho_f \frac{U_0^2}{2g}$$

or

$$U_0 = \left[\frac{2gZ}{K_s}\left(\frac{\rho_0}{\rho_f} - \frac{\rho_i}{\rho_f}\right)\right]^{1/2} \quad \ldots\ldots [53]$$

Substituting this expression into Equation [47] and recalling that $w = P/h_{fg}$, there results

$$P\frac{v_{fg}}{h_{fg}}\left[\frac{K_s Z}{2g}\right]^{1/2} = \left(\frac{1}{\beta+1}\right)\left[\beta\left(\frac{\rho_0}{\rho_f} - \frac{\rho_i}{\rho_f}\right)^{1/2} + \left(\frac{K_s U_s^2}{2gZ}\right)^{1/2}\right]\left(\frac{\rho_f}{\rho_2}-1\right) \quad \ldots\ldots [54]$$

Equations [50], [51], [52], and [54] provide the relationship between power density and average fluid density for this model in which vapor is uniformly generated throughout the reactor core. Results of a calculation for which $\beta = 1/3$ are displayed graphically in Fig. 9. This model is appropriate for a fluid-fuel reactor of the type illustrated schematically in Fig. 1(*c*).

The circulation ratio $m$ is defined by

$$m = \frac{\text{circulating flow rate}}{\text{steam rate}} = \frac{\rho_f U_0 h_{fg}}{PZ}\left(\frac{\beta}{\beta+1}\right) \quad \ldots\ldots [55]$$

Substitution for $U_0$ from Equation [53] gives

$$\frac{Pv_{fg}}{h_{fg}}\left[\frac{K_s Z}{2g}\right]^{1/2}\left[\frac{mv_f}{v_{fg}}\right] = \left(\frac{\beta}{\beta+1}\right)\left(\frac{\rho_0}{\rho_f} - \frac{\rho_i}{\rho_f}\right)^{1/2} \quad \ldots\ldots [56]$$

This expression can be combined with Equation [54] to give

$$\frac{mv_f}{v_{fg}} = \frac{1}{\frac{\rho_f}{\rho_2}-1} - \left(\frac{1}{\beta+1}\right)\frac{\left[\frac{K_s U_s^2}{2gZ}\right]^{1/2}}{\frac{Pv_{fg}}{h_{fg}}\left[\frac{K_s Z}{2g}\right]^{1/2}} \quad \ldots\ldots [57]$$

which is in a form convenient for plotting as a dependent parameter. This has been done in Fig. 9.

Only slight modification need be made in the relations presented in the foregoing to be applicable to a solid-fuel reactor of the type illustrated schematically in Fig. 1(*a*). Again, vapor generation is postulated uniform, but only in the riser. No vapor is generated in the downcomer. $U_0$ is based on the inlet area of the fuel region at the bottom of the core. Since only liquid enters at the bottom of the riser, from Equation [44] there results

$$\frac{\rho_f}{\rho_2} - 1 = \frac{wZv_{fg}}{U_0 + U_s} \quad \ldots\ldots [58]$$

The average density in the riser is also the average density in the core; from Equations [45] and [58]

$$\frac{\bar{\rho}}{\rho_f} = \frac{\rho_i}{\rho_f} = -\frac{U_0 + U_s}{wZv_{fg}} \ln\left[1 - \frac{wZv_{fg}}{U_0 + U_s}\left(\frac{\rho_2}{\rho_f}\right)\right] = -\frac{1}{\left(\frac{\rho_f}{\rho_2}-1\right)} \ln\frac{\rho_2}{\rho_f} \quad \ldots\ldots [59]$$

Substituting Equation [53] for $U_0$ into Equation [58] and employing $w = P/h_{fg}$ gives

$$\frac{Pv_{fg}}{h_{fg}}\left[\frac{K_s Z}{2g}\right]^{1/2} = \left[\left(1-\frac{\rho_i}{\rho_f}\right)^{1/2} + \left(\frac{K_s U_s^2}{2gZ}\right)^{1/2}\right]\left(\frac{\rho_f}{\rho_2}-1\right) \quad \ldots\ldots [60]$$

which along with Equation [59] provides the relationship between power density and average fluid density for this model. It will be noticed that with the exception of a new definition of $U_0$, the relations for this model follow from the previous one by letting $\beta = 0$. These relationships are displayed graphically in Fig. 10 in the form of a performance chart.

The dependent parameter involving the circulation ratio becomes

$$\frac{mv_f}{v_{fg}} = \frac{1}{\frac{\rho_f}{\rho_2}-1} - \frac{\left[\frac{K_s U_s^2}{2gZ}\right]^{1/2}}{\frac{Pv_{fg}}{h_{fg}}\left[\frac{K_s Z}{2g}\right]^{1/2}} \quad \ldots\ldots [61]$$

Another core arrangement, one employing natural-vapor rise, can be examined for power-removal capability by further modification of the foregoing expressions. The natural-vapor-rise system is shown schematically in Fig. 1(*b*). In this case $U_0 = 0$ and Equation [58] becomes

$$\frac{\rho_f}{\rho_2} - 1 = \frac{wZv_{fg}}{U_s}$$

which upon rearrangement and substitution of $w = P/h_{fg}$ is

$$\frac{Pv_{fg}}{h_{fg}}\frac{Z}{U_s} = \left(\frac{\rho_f}{\rho_2}-1\right) \quad \ldots\ldots [62]$$

The mean density is given by Equation [59]. The results for this model are displayed graphically in Fig. 11.

# Appendix C

## Sample Calculation

To calculate the power-removal capability of a boiling reactor it is necessary to evaluate the pressure drop in one circulation pass of the boiling mixture. This pressure drop enters the performance calculation through the flow-loss coefficient $K_s$ which is defined by

$$\Delta p_{\text{loss}} = K_s \rho_f \frac{U_0^2}{2g} \quad \ldots\ldots [63]$$

It is convenient to employ the method of Martinelli and Nelson.[7] Expressed in their symbols, the pressure drop during flow of a boiling mixture $\Delta P_{TP}$ is given as

[8] $K_s$ and $K_h$ have not been defined in a completely equivalent manner. For the case $\eta = 0$, it can be shown that

$$K_h/K_s = (\bar{\rho}/\rho_2)(\rho_f/\rho_2)\beta^3$$

TABLE 1 VALUES OF $\Delta P_{TPF}/\Delta P_0$ AS A FUNCTION OF $1/m$ AND $p$

| Steam quality, per cent by weight flow | Pressure, psia | | | | | | | |
|---|---|---|---|---|---|---|---|---|
| | 14.7 | 100 | 500 | 1000 | 1500 | 2000 | 2500 | 3206 |
| 1 | 4.7 | 2.8 | 1.79 | 1.45 | 1.28 | 1.17 | 1.08 | 1.00 |
| 5 | 16.5 | 7.4 | 3.42 | 2.30 | 1.77 | 1.43 | 1.21 | 1.00 |
| 10 | 33.0 | 13.8 | 5.13 | 3.10 | 2.23 | 1.72 | 1.39 | 1.00 |
| 20 | 68.5 | 25.9 | 8.90 | 4.92 | 3.18 | 2.27 | 1.70 | 1.00 |
| 30 | 108 | 39.5 | 12.1 | 6.40 | 4.00 | 2.68 | 1.90 | 1.00 |
| 40 | 152 | 52.5 | 15.1 | 7.70 | 4.74 | 3.15 | 2.20 | 1.00 |
| 50 | 198 | 65.0 | 18.0 | 8.96 | 5.40 | 3.55 | 2.48 | 1.00 |
| 60 | 246 | 76.0 | 21.2 | 10.3 | 6.10 | 3.92 | 2.62 | 1.00 |
| 70 | 293 | 87.2 | 24.2 | 11.9 | 6.93 | 4.36 | 2.82 | 1.00 |
| 80 | 337 | 97 | 27.3 | 13.2 | 7.62 | 4.70 | 2.95 | 1.00 |
| 90 | 377 | 108 | 29.2 | 14.0 | 8.00 | 4.98 | 3.10 | 1.00 |
| 100 | 408 | 118 | 31.0 | 14.9 | 8.50 | 5.26 | 3.22 | 1.00 |

TABLE 2 VALUES OF MULTIPLIER $r$ AS A FUNCTION OF $1/m$ AND $p$

| Steam quality, per cent by weight flow | Pressure, psi | | | | | | | |
|---|---|---|---|---|---|---|---|---|
| | 14.7 | 100 | 500 | 1000 | 1500 | 2000 | 2500 | 3206 |
| 1 | 0.04 | 0.023 | 0.0130 | 0.0093 | 0.0067 | 0.0041 | 0.0021 | 0 |
| 5 | 0.16 | 0.068 | 0.0316 | 0.0211 | 0.0153 | 0.0100 | 0.0064 | 0 |
| 10 | 0.41 | 0.118 | 0.0498 | 0.0313 | 0.0227 | 0.0163 | 0.0100 | 0 |
| 20 | 1.30 | 0.280 | 0.093 | 0.054 | 0.037 | 0.026 | 0.017 | 0 |
| 30 | 2.70 | 0.522 | 0.146 | 0.084 | 0.054 | 0.037 | 0.025 | 0 |
| 40 | 4.60 | 0.850 | 0.209 | 0.112 | 0.074 | 0.049 | 0.033 | 0 |
| 50 | 7.03 | 1.250 | 0.291 | 0.150 | 0.096 | 0.064 | 0.043 | 0 |
| 60 | 9.95 | 1.730 | 0.384 | 0.193 | 0.121 | 0.080 | 0.053 | 0 |
| 70 | 13.40 | 2.27 | 0.494 | 0.241 | 0.149 | 0.098 | 0.064 | 0 |
| 80 | 17.20 | 2.90 | 0.618 | 0.296 | 0.180 | 0.117 | 0.076 | 0 |
| 90 | 21.80 | 3.63 | 0.762 | 0.360 | 0.215 | 0.139 | 0.088 | 0 |
| 100 | 26.7 | 4.40 | 0.903 | 0.420 | 0.253 | 0.162 | 0.102 | 0 |

$$\Delta P_{TP} = \Delta P_0 \left(\frac{\Delta P_{TPF}}{\Delta P_0}\right) + r\frac{G^2}{g} \quad [64]$$

where

$\Delta P_0$ = pressure drop in the flow circuit for flow of saturated water at total flow rate

$\left(\frac{\Delta P_{TPF}}{\Delta P_0}\right)$ = multiplier for single-phase pressure drop to yield two-phase frictional pressure drop; plotted as a function of system pressure and exit weight-flow quality in Fig. 4 of Martinelli and Nelson[9]

$r$ = multiplier to account for loss due to acceleration of the fluid during evaporation; plotted as a function of system pressure and exit weight-flow quality in Fig. 6 of the previous paper[9]

$G$ = total weight rate of flow per unit area

As applied to the present calculation the following equivalence exists

$$G = \rho_f U_0 \quad [65]$$

$$\Delta P_0 = K_f \rho_f \frac{U_0^2}{2g} \quad [66]$$

where $K_f$ is the flow-loss coefficient for the flow circuit based on liquid flow only. Substituting Equations [65] and [66] into Equation [64], rearranging, and equating the result to Equation [63] yields

$$K_s = \left[K_f \left(\frac{\Delta P_{TPF}}{\Delta P_0}\right) + 2r\rho_f\right] \quad [67]$$

which is a function of system pressure and $1/m$ for a given reactor.

As a sample calculation, the power density in a fluid-fuel-reactor core, 10 ft high and 10 ft diam, will be obtained for operation at an average density decrease of 0.30 and 1000 psia; $\beta = 1/3$ and vapor generation uniform.

1 For $(1 - \bar{\rho}/\rho_f) = 0.30$ and $K_s U_s^2/2gZ = 0$, $mv_f/v_{fg} = 1.0$ from Fig. 9. At 1000 psia, $m = 1.0\, v_{fg}/v_f = 0.424/0.0216 = 19.6$; $1/m = 0.051$.

2 From Martinelli and Nelson,[7] Figs. 4 and 6, $\Delta P_{TPF}/\Delta P_0 = 2.3$ and $r = 0.021$, respectively, for exit quality 0.051 and pressure 1000 psia. Evaluating the loss coefficient based on flow of the liquid:

| | |
|---|---|
| Downcomer friction | 0.3 |
| Turn at bottom | 1.0 |
| Riser friction | <0.1 |
| Separators | 3.0 |
| Total | $K_f \approx 4.5$ |

From Equation [67]

$$K_s = [4.5(2.3) + (2)0.021/0.0216] \approx 12$$

3 From Fig. 8, $U_s = 1.0$ at 1000 psia, accordingly

$$\frac{K_s U_s^2}{2gZ} = \frac{12(1)}{64.4(10)} = 0.019$$

From Fig. 9 the improved value of $mv_f/v_{fg} = 0.52$. Repeating steps 2 and 3 for $m = 10$ gives $K_s = 17$ and $K_s U_s^2/2gZ = 0.026$.

4 From Fig. 9 the ordinate has the value 0.24 from which

$$P = \frac{(0.24)(0.0373)(650)}{0.424}\left[\frac{64.4}{17(10)}\right]^{1/3} = 8.5\ Kw/l$$

[9] Numerical values of the multipliers calculated by Martinelli and Nelson[7] on which their Figs. 4 and 6 are based are reproduced here in Tables 1 and 2, respectively.

# BOOKS Engineers need today. Are YOU availing yourself of them?

For the knowledge and experience of over 400 experts with major problems of the mechanical engineering field, look to...

## TRANSACTIONS OF THE ASME FOR 1955

The 224 papers in this volume put you on the advances and trends throughout the field, supply information that will help you develop a broad background, give you the benefit of original viewpoints, and provide a unique collection of procedures and solutions for attacking your own problems. Investigations reported and problems dealt with in its 2100 pages are those concerned with airplane-engine structures, nuclear and steam power plants, piping, turbines, turbomachinery, automatic control, heat transfer, mechanics, lubrication, mechanisms, metal cutting, fuels, feedwater treatment, corrosion, cavitation, metal testing and fatigue, rubber and plastics.

$15.00—$7.50 to ASME members

The findings of original researches and the current approach to problems by the use of new analytical tools and procedures are accessible to you in the

## PROCEEDINGS OF THE SECOND U. S. NATIONAL CONGRESS OF APPLIED MECHANICS

Each of the 99 papers in this 825-page book is an individual treatise which can be studied independently. Collectively they form an invaluable record of recent advances made in connection with significant problems encountered throughout modern applied mechanics including kinematics, dynamics, vibration, wave motion; mechanical properties of material and failures; stress analysis, elasticity, plates and shells; plasticity, fluid flow, aerodynamics, and heat transfer.

$9.00 to members and nonmembers

Specific information about properties of metals, tables on design standards, and help to make your product design more efficient will be found in these three volumes of the ASME Handbook

## METALS ENGINEERING-DESIGN

Topics covered are high-temperature considerations, elasticity, residual stresses, vibration, fatigue, shot peening, cold working, nitriding, flame strengthening, impact, corrosion, nondestructive testing, surface finish and mass production, and design procedures.

1953 $10.00

## METALS PROPERTIES

Supplies data on more than 500 metals, including the chemical composition of each metal; its brittleness; heat-treatment and other characteristics; industrial uses; and treatment temperatures for forging, annealing, quenching; and other pertinent information. Additionally, there is material on end-quench hardenability which shows the relative depths to which various carbon and alloy steels harden; and information on notch toughness, corrosion fatigue, low and high-temperature properties, and damping, where it is applicable to the metal under consideration.

1954 $11.00

## ENGINEERING TABLES

Includes many of the tables of recognized design standards of the type not commonly found in handbooks. They are arranged conveniently in the following fifteen sections, with tables which apply to the design of specific parts grouped together: Bar stock and shafting; bearings; spur, helical, and herringbone, bevel and worm gears; cylindrical fits; key and keyseating; belts; springs; aircraft and mechanical tubing; electrical motors; and gaskets.

1956 $12.00

A picture of what frequency response is and how it can be used is offered in...

## FREQUENCY RESPONSE

In 372 pages, this book deals with problems of calculating transient response from frequency response, choosing optimum controls for given physical systems, calculating nonlinear phenomena, limited motion movements in a nonlinear control system, and using the frequency method to analyze intermittent regulating systems. It discusses the application of experimental methods; includes a survey of sine-wave generators; covers frequency response design criteria and standards for presentation of data.

1956 $7.50

A complete and lucid treatment of the problems of stability, accuracy, and speed control, and the influence of sources of error is presented in...

## DYNAMICS OF AUTOMATIC CONTROLS

Beginning with the discussion of the functional elements of a control, the book then surveys and describes the mathematical methods for handling control problems; considers the important components of the control loop and special control problems; examines causes of nonlinearities in the control loop; treats on-off regulator and its field of application; deals with the theory of excursion-dependent periodic controller; covers applications of various types of control; and includes formulas for the Laplace transformation, concepts concerning difference equations, and a table of the principle transfer systems.

1948 $6.00

For information on the developments in heat transfer and in the design of apparatus relating thereto, your source is...

## GENERAL DISCUSSION ON HEAT TRANSFER

Here, in 500 pages, eminent engineers of twelve countries review the progress made during the period 1940–1950, discuss methods of utilizing the knowledge gained, survey the numerous engineering applications of heat transfer, appraise new fundamental discoveries in the field, and consider modern methods of approach to heat transfer problems. In addition to 93 contributions, the volume includes all of the discussions and the authors' replies.

1951 $10.00

For expert information on reducing or eliminating air contamination read...

## PROBLEMS AND CONTROL OF AIR POLLUTION

Here will be found a discussion of the present gaps in our knowledge of air pollution and the need for further research in many directions ...new and authoritative material on the treatment and recovery of sulphur dioxide—widely recognized as one of the most formidable challenges to effective air-pollution control, many helpful ideas on new developments in control and the experiences in air-pollution abroad, a summary of the British smog problem and the remedies proposed, and suggestions for avoiding pitfalls in community relations over air-pollution problems.

1955 $7.50

For help that cuts cost, steps up production, and standardizes practice consult the

## MANUAL ON THE CUTTING OF METALS

Consideration is given to the mechanical characteristics and structures of the metals to be cut—irons and steels, high-nickel alloys, copper and its alloys, magnesium, and plastics. The influence of the composition and microstructure of each metal on the wear of the cutting tool, chip formation and control, and surface finish is explained. Cutting fluids, and the cutting speed tool life for various cutting fluids are thoroughly discussed. Speeds and feeds for machining a variety of metals are recommended. Three hundred and thirty tables give data on feeds, speeds, and depths of cut to be used when turning steels and cast irons in general use.

1952 $10.00

20% discount allowed to members

**THE AMERICAN SOCIETY OF MECHANICAL ENGINEERS 29 WEST 39TH STREET NEW YORK 18, NEW YORK**